# Geomechanics to solve geological structure issues: forward, inverse and restoration modeling

Frantz Maerten

**UNIVERSITE MONTPELLIER II**
**SCIENCES ET TECHNIQUES DU LANGUEDOC**

**THESE**

**pour obtenir le grade de**

**DOCTEUR DE L'UNIVERSITE MONTPELLIER II**

**Discipline : Structure et évolution de la lithosphère**
**Ecole doctorale : SIBAGHE**

présentée et soutenue publiquement

par

**Frantz MAERTEN**

Le 17 juin 2010

**Titre :**

# Geomechanics to solve geological structure issues: forward, inverse and restoration modeling

## JURY:

| | | |
|---|---|---|
| **M. Jean Chéry** | U. Montpellier, France | Directeur de thèse |
| **M. David D. Pollard** | U. Stanford, USA | Codirecteur de thèse |
| **M. Bruno Lévy** | INRIA, France | Rapporteur |
| **M. Yves Leroy** | ENS Paris, France | Rapporteur |
| **M. Xavier Legrand** | Repsol, Madrid | Examinateur |
| **M. Marc Daignières** | U. Montpellier, France | Examinateur |

## RÉSUMÉ

### Utilisation de la géomécanique pour résoudre des problèmes liés aux structures géologiques: modélisation directe, inversion et restauration

Différentes applications de l'élasticité linéaire en géologie structurale sont présentées dans cette thèse à travers le développement de trois types de codes numériques. Le premier utilise la modélisation directe pour étudier les déplacements et champs de contraintes autour de zones faillées complexes. On montre que l'ajout de contraintes inégalitaires, telles que la friction de Coulomb, permet d'expliquer l'angle d'initiation des dominos dans les relais extensifs. L'ajout de matériaux hétérogènes et d'optimisations, telles la parallélisation sur processeurs multi-cœurs ainsi que la réduction de complexité des modèles, permettent l'étude de modèles beaucoup plus complexes. Le second type de code numérique utilise la modélisation inverse, aussi appelée estimation de paramètres. L'inversion linéaire de déplacements sur les failles ainsi que la détermination de paléo-contraintes utilisant une approche géomécanique sont développées. Le dernier type de code numérique concerne la restauration de structures complexes plissés et faillées. Il est notamment montré qu'une telle méthode permet de vérifier l'équilibre de coupes géologiques, ainsi que de retrouver la chronologie des failles. Finalement, nous montrons que ce même code permet de lisser des horizons 3D faillés, plissés et bruités en utilisant la géomécanique.



**MOTS-CLÉS:** Géologie structurale, élasticité linéaire, modélisation directe, inversion, restauration

## ABSTRACT

### Geomechanics to solve geological structure issues: forward, inverse and restoration modeling

Different applications of linear elasticity in structural geology are presented in this thesis through the development of three types of numerical computer codes. The first one uses forward modeling to study displacement and perturbed stress fields around complexly faulted regions. We show that incorporating inequality constraints, such as static Coulomb friction, enables one to explain the angle of initiation of jogs in extensional relays. Adding heterogeneous material properties and optimizations, such as parallelization on multicore architectures and complexity reduction, admits more complex models. The second type deals with inverse modeling, also called parameter estimation. Linear slip inversion on faults with complex geometry, as well as paleo-stress inversion using a geomechanical approach, are developed. The last type of numerical computer code is dedicated to restoration of complexly folded and faulted structures. It is shown that this technique enables one to check balanced cross-sections, and also to retrieve fault chronology. Finally, we show that this code allows one to smooth noisy 3D interpreted faulted and folded horizons using geomechanics.



**KEYWORDS:** Structural geology, linear elasticity, forward modeling, inverse modeling, restoration modeling

*"Imagination is more important than knowledge"*

Albert Einstein

# Preface

This thesis is comprised of work that started a while ago, when I was unemployed after a bachelor degree in geophysics and geology at the University of Montpellier II. It has been continued at Stanford University within the research group of Pr David D. Pollard for four years, mainly on correcting, rewriting, enhancing and optimizing an existing 3D boundary element code. Then, several publications have emerged while at Igeoss, a start-up that we created in 2004 in Montpellier with my brother Laurent (who did his PhD with Pr David Pollard), and David Pollard himself.

After my return to France from Stanford to start Igeoss, the idea of doing a PhD came to my mind when I realized that a *VAE* ("valorisation des acquis et de l'experience" which can be translated to "appreciation of achievements and experiences") was now possible in France to obtain the equivalent of a master degree in order to start a PhD. Marc Daignières, a professor at the University of Montpellier II, successfully supported my request against a faculty commitee and I was able to start in November 2006, under the direction of Jean Chery (France) and Dave Pollard (USA).

Walking in the world of geomechanics, numerical methods, optimizations and programming without any knowledge and background is not so simple, but can lead to new insights with the help of the imagination (hence the quote of this thesis). Eleven papers are presented and one is in the appendix, which show the usefulness of linear elasticity. Although during this period three other papers were published (see appendix C), I do not include them within this thesis as I was only a little bit involved.

I particularly show in this thesis that using the simple conceptual model of linear elasticity can lead to many application codes which are used to better understand geological structures using either forward, inverse or restoration modeling. The large number of publications using such codes by researchers around the world (more than one hundred twenty), demonstrates their importance. A complete list of publications in different geological domains can be obtained on the Igeoss support website at https://support.igeoss.com.

Doing this thesis was the opportunity to start the company **Igeoss** in 2004 in Montpellier, and to continue the **research** on iBem3D, Dynel2D and Dynel3D while giving **13** international conferences and writing **11** papers as well as a **patent** for the estimation of the state of stress in complex reservoirs using measures from well bores and faults geometry.

Finally, Igeoss integrated **Schlumberger**, the world's leading supplier of technology in the oil and gas industry worldwide, after the acquisition in April 2010.

# Acknowledgments

I wish to thanks, first, Dave Pollard who gently guided me in the comprehension of structural geology and geomechanics while at Stanford University. He accepted to take me in his Rock Fracture Project (RFP) group while I was programming graphical interfaces in a small company in Montpellier, and without any knowledge in numerical codes and geomechanics. I think that his choice was mainly motivated by the fact that (1) Laurent, my brother, was already working with him as a '*very good*' PhD student, and that (2) during my free time in France, I was coding a new numerical code in 2D and 3D, namely Dynel. My brother Laurent is also greatly acknowledged, and it is still a pleasure to work together: him, the *structural geologist*, and me the *analytical geologist*.

While at Stanford University (USA) and in Montpellier (FRANCE), I met many students, researchers and people from the industry who provided me a diversity of viewpoints in the domains of structural geology, geophysics and computer sciences. They include (alphabetical ordered): Fabrizio Agosta, Marco Antonellini, Atilla Aydin, Taixu Bai, Loic Bazalgette, Nicolas Bellahsen, Stephan Bergbauer, Stephan Bourne, Jean Chéry, Michele Cooke, Juliet Crider, Marc Daignières, Nick Davatzes, Russell Davies, Guillaume Deconchy, Guilhen De Joussineau, Xavier Du-Bernard, Peter Eichhubl, Patricia Fiore, Eric Flodin, Juan Mauricio Florez, Paul Gillespie, Radu Girbacea, Brita Graham, Paul Griffiths, Joel Ita, Hervé Jourde, Simon Kattenhorn, Ole Kaven, Sotiris Kokkalas, Sébatien Lacase Serge Lallemand, Xavier Legrand, Bruno Levy, Lidia Lonergan, Michel Lopez, Peter Lovely, Stephen Martel, Maurice Mattauer, Matteo Molinaro, Jordan Muller, Ovunc Multu, Rodrick Myers, Ian Mynatt, Fabien Pauget, Jean-Pierre Petit, Jean-Christophe Perez, Phil Resor, Paul Segall, Michel Seranne, Roger Soliva, Kurt

Sternlof, Lans Taylor, Haiquing Wu, Scott Young, Amgad Younes, Wenbing Zhang, Marc Zoback, and certainly many other people...

I thanks people who accepted to review this work in a short time: Bruno Levy and Yves Leroy, as well as the "examinateurs": Xavier Legrand, Loic Bazalgette (Shell) and Marc Daignières. And, of course, my principal advisor, Jean Chery, from the University of Montpellier II.

Many thanks to Roger Soliva from the University of Montpellier who helped me to understand some geological features in the field, and who provided helpful feedback before the PhD defense. It is always a great pleasure to discuss "structural geology" with him.

I also thanks the *Igeoss* team for the hard work they provided: Alexandre Baranov, Jean-Pierre Joonnekindt, Dieter Knoll, Thomas Laverne, François Lepage, Frederic Marmond, Michael Palomas, Emanuel Quetelard, and especially David Desmarest who teach me the object oriented languages while at "After Development" in Montpellier. He was my mentor and is now a precious element at Igeoss.

Igeoss consortium members are acknowledged for their support in the development of iBem3D, Dynel2D and Dynel3D: BG-Group, BhpBilliton, Chevron, ConocoPhillips, Eni, ExxonMobile, Repsol, Shell and Total.

People from the *CEEI*, *LRI* and the "Region Languedoc Roussillon" are also acknowledged: Josick Paoli (Région Languedoc Roussillon) who trusted and helped us to start Igeoss, the team of Cap Alpha and Cap Omega, the team of LRI and especially Géraldine Karbouch, Jean-Paul Mikallef from Transfert LR.

Noel Lichau is also acknowledged. He helped me to discover the structural geology while doing *speleology*.

Many thanks to my father and mother in law, Freddy and Eliane Genieys, who helped me to find an equilibrium during these hard years, and with whom I use to rock climb.

Finally, I thanks my wife and my children for their patience and comprehension during these hard years of continuous work: Claire, Lila and Tristan. Claire is a **very precious help**.

By the way, I do not recommend to start a company and to do a PhD thesis while working for that company, remodeling an old house, having 2 babies during that time, taking care of 150 olive trees, giving free math courses for families with no resources and being in charge of starting a Geosciences *cluster* in the *Région Languedoc Roussillon*. Good luck Sébastien...

This thesis is dedicated to my parents...

# CONTENTS

# Introduction

Physical theories always deal with simplifications of nature, simply because modeling a complicated structure such as the earth at a large scale using a microscopic atomistic molecular model is unrealistic. Therefore, researchers tend to capture the most important properties of real objects, and use them in a conceptual theoretical, then analytical and numerical model, the goals being to **explain** and **predict** physical phenomena.

We can distinguish two types of physical models that provide foundations for all physical theories for modeling the material behavior: (1) microscopic discrete models, and (2) macroscopic continuum models. At the microscopic scale, the particles are moving according the influence of their mutual interaction forces given by the quantum mechanics. At a much larger scale, objects are governed by continuum theories (solid mechanics, fluid mechanics, elasticity, thermodynamics, electromagnetism, acoustic, and so forth). These theories tend to describe the behavior of objects in our perception of four dimensional space-time. Matter and energy are considered as a continuum in this framework, and therefore mathematical representation of physical quantities is by means of continuous (or piecewise continuous) functions of space and time.

These kind of problems can be solved exactly by mathematical manipulations (**analytical models**), but the mathematical tools usually limit the possibilities to oversimplified models. Therefore, various techniques of **discretization** have been proposed and developed, leading to **numerical models** involving approximation that approach the true analytical solution as the number of discrete variables increases. The goal of these methods is to numerically solve the partial differential equations (PDE). Well known methods are the Finite Difference Method (FDM), the Finite Element Method (FEM) and the Boundary Element Method (BEM).

The FDM is the earliest classical numerical treatment for solving PDE, and it replaces the continuum solution by a set of lattice points. At each point, any differential operators are replaced by finite difference operators, leading to a set of difference equations which can be easily solved.

In FEM, the solution domain is discretized into a number of uniform or nonuniform finite elements that are connected by mean of nodes, and the change in the dependent variable with regard to location is approximated within each elements using a shape function.

The BEM uses the fact that equations in differential forms can often be transformed into integral forms. It transforms the differential operator defined in the domain into an integral operator defined on the boundary. Hence, in BEM, only the boundary of domains of interest need to be discretized.

Both FEM and FDM are similar in a sense that the entire solution domain has to be

discretized, and a mesh is needed. In BEM, only the bounding surfaces (in 3D) are used.

The focus of this thesis is the **continuum mechanics** applied to the comprehension of **geological phenomena**, using partial differential equation-based (PDE) modeling with boundary conditions. More precisely, we are interested in **quasi-static** phenomena (e.g. co-seismic events) in the **sub-surface** using **linear elasticity**, which proves to be a good approximation and can provide new insights for the comprehension of earthquakes and volcanoes or to study the state of perturbed stress field around a complexly faulted area.

Three kind of numerical codes are developed: (1) forward modeling, (2) inverse modeling and (3) restoration modeling.

1. **Forward** modeling studies the fault response to an imposed far field stress or strain given the fault geometry and the boundary conditions. Result of such simulations can be used, for example, to predict fractures due to faulting, or to study fault triggering in an earthquake process.

2. **Inverse** modeling is a form of *parameters estimation* of what is usually imposed or computed on faults in the forward sense (i.e. far field stress, fault slip distribution). Given some observed deformation at Earth's surface due to faulting at depth, the aim is to invert for the slip distribution onto the faults that induced such observed displacements, or to invert for a tectonic loading (also called paleostress in the literature) which activated the faults which, in turn, generated the deformations at the ground surface.

3. **Restoration** modeling is the study of the geological structures (geometry) back in time using special boundary conditions onto a model which are related to geological phenomena (e.g. sedimentation, erosion). This type of modeling allows one, for example, to validate the structural interpretation of geological structures, to predict fractures due to folding, or to determine the faults chronology as we go back in time. It is also used to localize and correct anomalous zones of high stress/strain concentration on 3D faulted and folded horizons, and therefore, operates has a geomechanically-based smoothing filter.

# Contents of the thesis

This thesis is divided into three main parts containing a total of eleven papers that are either published, submitted or in preparation. Another paper in preparation is presented in appendix, which complete the work done during this thesis.

**Part I** is devoted to forward modeling using an elastostatic Boundary Element Method (BEM) called iBem3D (the successor of Poly3D originally developed at Stanford University), and is composed of five chapters. We show, in this first part of the thesis, that the conceptual model using the boundary element method can be extended to incorporate (i) preventing of element interpenetration while allowing opening mode (ii) the static friction with varying friction coefficient and cohesion, and (iii) the material heterogeneity using complex shaped interfaces between regions of different material properties. A special chapter is devoted to the optimization and parallelization of such a code, which is useful for modeling material heterogeneity. Finally, a chapter applies the static friction to the study of fracture orientation in extensional relays.

**Part II** of this thesis studies the inverse modeling using the same boundary element code, and is subdivided in three chapters related to (i) slip inversion, (ii) paleostress estimation and (iii) slip recovery. A chapter is devoted to the application of the slip inversion applied to the Nias earthquake (Indonesia). Appendix A presents an optimization technique of the slip inversion using the procedures described in part I.

**Part III** uses another numerical method, namely the Finite Element Method (FEM), to restore structural interpretations for validation or prediction of fractures related to folding (chapter 10). Chapter 11 also presents another application to restore 3D surfaces (unfaulting and unfolding simultaneously) in order to localize anomalous geometries. It proposes an algorithm to correct for the initial geometry by minimizing a user selected criteria (e.g. stress, strain, area change, ...). These two tools are very useful for the correction of faults geometry before doing any forward or inverse modeling using the boundary element codes presented in part I and II.

## Part I: **forward modeling** using linear elasticity with a boundary element code.

### Chapter 1 presents the foundation of this thesis. We show that using the analytical formulation of the displacement field induced by an angular dislocation in a homogeneous elastic whole- or half-space, it is possible to construct 3D complex surfaces of displacement discontinuity made of triangular elements. This formulation allows surfaces of discontinuity to have complex shapes and tip-lines, as opposed to Okada's formulation, currently the standard method in

geophysics, where rectangular elements are used inducing inevitably overlaps and gap between the elements. Application of such a code is wide in the domains of structural geology and geomechanics. We present some of the major applications that have already been published by a large community around the world.

Chapter 2 proposes an iterative method to solve the system of linear equations. This technique allows one to reduce the model complexity from $O(n^3)$, while using the Gauss elimination or LU decomposition, to $O(kn^2)$, where $k$ is the number of iterations required for the iterative solver. Moreover, this solver allows the incorporation of inequality constraints on traction (e.g. static Coulomb friction) and displacement (e.g. non-interpenetration of the elements). As we will see, it also facilitates the parallelization on multi-core architectures.

Chapter 3 presents an application of the inequality constraints from chapter 2 to the orientations of branching fractures at strike slip relay zones between reactivated en echelon stylolites and joints. The chosen area is "Les Matelles" located near Montpellier, France. Specifically, it is shown that the orientation of the domino within the relay zone is function of the friction.

Chapter 4 shows that the initial implementation of the boundary element code, which was done for an homogeneous isotropic material, can be extend to heterogeneous isotropic materials using special boundary conditions at interfaces separating regions of different material properties. These interfaces are discretized as 3D triangulated surfaces that can have any shape.

Chapter 5 is devoted to the optimization of forward modeling. Even if using an iterative approach (chapter 2) decreases the model complexity, it remains a major drawback for computing large models made of hundreds of thousands triangular elements, the memory needed being the same as when using direct matrix inversion. Furthermore, the post-processing at observation grids can be a penalization for the user, especially if the number of observation points is large. This chapter presents the optimization of the computation by using approximations and parallelization on multi-core processors, for both the system resolution and post-processing. It is shown that the model complexity is reduced from $O(kn^2)$, for an iterative solver, to $\sim O(kn)$, and that

the post-processing at observation points (field points) is drastically reduced and is a function of the position of the grids relative to the sources (surface discontinuities).

Part II: **Inverse modeling** using linear elasticity with a boundary element code.

Chapter 6 presents the advantages of doing linear slip inversion on complex fault geometries. Given some observations of deformations at the ground surface (e.g. GPS, tiltmeters, satellite images, ...) as well as the fault geometries, we invert for slip distributions onto the faults that generated such measured deformations. Specifically, it is shown that such an approach using triangular elements is more precise than traditional methods using rectangular-planar elements. The code is applied to the Hector Mine earthquake, CA, and performs better than when using rectangular elements.

Chapter 7 presents an application of the slip inversion for the Nias earthquake which occurred in 2005 in Indonesia. This study adds evidence that the earthquake probably did not break the surface, and this has implications for tsunami generation.

Chapter 8 presents a geomechanically-based technique to recover for the paleostress that induced observed displacements onto the faults from seismic interpretation. This technique is limited to one tectonic event, but can give a good estimate of what could have been the orientation and magnitude of the tectonic loading using mechanical interactions. While doing the stress inversion, we invert at the same time for the unknown displacement discontinuities onto the faults (e.g. strike-slip).

Chapter 9 presents another way of doing paleo-stress estimation using the principle of superposition that applies in linear elasticity. This new method can take into account various data sets such as fracture and secondary fault plane orientation that formed in the vicinity of active faults, GPS, InSAR, fault throw and slickenlines. It is shown that multiple tectonic events can be recovered and the data may be segregated into their respective events. Furthermore, such a method allows one to do real-time computation of the faults slip and perturbed stress field while the user changes the imposed far field stress.

Part III: **Restoration modeling** using linear elasticity with a finite element code.

Chapter 10 is devoted to the validation of interpretations using a restoration technique. Doing forward modeling, as describe in chapter 1, shows the importance of the fault and fracture geometry to the resulting computed displacement discontinuity onto them, and consequently to the associated perturbed stress field. For the majority of the numerical simulations, it is mandatory to validate such interpretations before analyzing the result of a forward numerical simulation.

Chapter 11 presents a geomechanically-based smoothing filter for noisy 3D surfaces. It is shown that the filter removes geometrical artifacts where, for example, high stress concentration occurs after unfolding and unfaulting, while smoothing fault cut-offs and transforming high displacement gradients at crack-tips into a more realistic geometry.

Additionally, we present in appendix A, an on-going project related to part II (Inverse modeling using Boundary Element Method) for doing fast slip inversion using an iterative solver. In appendix B, we present a sensitivity analysis for fault sealing and leakage for both nuclear waste disposal and exploitation of natural resources.

The conclusions and perspectives are developed in part IV.

# Part I

## Forward modeling using Boundary Element Method

# Aperçu

La première partie de cette thèse est consacrée à la modélisation directe en développant et utilisant iBem3D (ex-Poly3D), une méthode d'éléments frontières (BEM). Etant donné la géométrie 3D des failles ainsi que le champ de contraintes à l'infini, il est possible de déterminer les champs de déplacement et de contraintes perturbés autour de zones complexes faillées (chapitre 1). Des améliorations de ce code sont proposées dans le chapitre 2, où les contraintes inégalitaires sont ajoutées dans la formulation, ce qui permet de simuler la friction Coulombienne et la non-interpénétration des plans de failles lors d'un régime compressif. Dans le chapitre 3, nous donnons une application directe du frottement pour étudier les angles de branchement des dominos dans un relais extensif. Les améliorations comprennent aussi l'ajout de matériaux hétérogènes à l'aide d'interfaces 3D triangulées séparant deux régions ayant des propriétés mécaniques différentes (chapitre 4). Du fait qu'une telle amélioration induit un accroissement non négligeable dans le nombre d'inconnues, des optimisations sont nécessaires (réduction de la complexité ainsi que parallélisation sur des architectures multi-cœurs). Ces optimisations sont présentées dans le chapitre 5.

L'annexe B présente une utilisation élégante des contraintes inégalitaires pour l'analyse de sensibilité de differents paramètres. On utilise *Scribble*, un langage en Javascript pour iBem3D, permettant d'exécuter rapidement des milliers de modèles. Dans cette modélisation, trois paramètres interdépendants sont analysés pour étudier à la fois les risques sismiques liés au stockage de déchets nucléaires et l'exploitation des ressources naturelles: (1) l'épaisseur de la glace au-dessus des failles, (2) la friction sur les failles et (3) la cohésion.

# Overview

The first part of this thesis is dedicated to forward modeling using iBem3D (former Poly3D), a Boudnary Element Method (BEM). Having the faults geometry as well as the far field stress, it is possible to determine the displacement and perturbed stress field around complex faulted areas (chapter 1). Enhancements of iBem3D are proposed in chapter 2, where inequality constraints are added in the formulation, allowing Coulomb frictional behavior and non-interpenetration of elements making a fault in a compressional regime. In chapter 3 we give a direct application of the friction to study the different branching angles for the initiation of the jogs in extensional relays. Enhancements also include heterogeneous materials by using complexly-shaped 3D interfaces separating two regions with different materials properties (chapter 4). Since such an extension induces a non-negligible jump in the number of unknowns, optimizations are necessary (complexity reduction as well as parallelization on multicore architectures). This is done in the chapter 5.

Appendix B presents an elegant application of the inequality constraints for sensitivity analysis. It uses *Scribble*, the Java-script language for iBem3D, to quickly run thousands of models. In this particular modeling, three inter-dependent parameters are analyzed for both nuclear waste disposal and exploitation of natural resources: (1) ice thickness above the faults, (2) fault friction and (3) fault cohesion.

# Chapters

# CHAPTER 1

# IBem3D, a three-dimentional iterative boundary element method using angular dislocations for sub-surface structures modeling

F. Maerten[1,2], L. Maerten[1], D. D. Pollard[3], Y. Lagalay[4]

(1) Igeoss, Montpellier, FRANCE
(2) University of Montpellier II, Geosciences, FRANCE
(3) Stanford University, CA, USA
(4) EMEA Oil & Gas Group, Paris, FRANCE

To be submitted to Journal of Structural Geology

Figure 1.7 and 1.8 with permission of Journal of Structural Geology.
Figure 1.9 and 1.11 with permission of Journal of Geophysical Research.
Figure 1.10 with permission of Earth and Planetary Science Letters.
Figure 1.12 with permission of AAPG Bulletin.

**Preamble**

The following chapter presents the foundation of this thesis. We show that using the analytical formulation of the displacement field induced by an angular dislocation in a homogeneous elastic whole- or half-space, it is possible to construct 3D complex surfaces of displacement discontinuity made of triangular elements. This formulation allows surfaces of discontinuity to have complex shapes and tip-lines, as opposed to the Okada's formulation, where rectangular elements are used inducing inevitably overlaps and gaps between the elements. Application of such a code is wide in the domains of structural geology and geomechanics. We review some of the major applications that have already been published by a large community around the world.

## About...

**Poly3D** versus **iBem3D**

Historically, the development of **Poly3D** started in 1993, and was written at Stanford University by Andrew Lyle Thomas (Thomas, 1993) using the C language and based on the work of Jeyakumaran (Jeyakumaran et al., 1992). In 1998, Yann Lagalay came at Stanford for one year to work on the "Shadow's effect" problem (see section 1.9). A year after, I came in the group of Dave Pollard, and started to correct some bugs, optimize the fundamental equations and rewrite the core code in pseudo C++ (C++ wrapper around the C language).

Since then, the code was entirely rewritten in C++ while at Igeoss, adopting the triangular elements instead of the more general polygonal formulation, for speed and design considerations. Several enhancements are now part of the new code, such as a fast iterative solver, parallelization on multicore architectures, $\mathcal{H}$-Matrix optimization, heterogeneity of materials, inequality constraints (static friction) and paleo-stress evaluation. The new code is now named **Ibem3D**...

For this paper, Laurent Maerten wrote the "Applications" part while Dave Pollard enhanced the manuscript and wrote the introduction, the verification part as well as the conclusions.

# Article Outline

## 1.1 Résumé

Le but de cet article est de décrire iBem3D, un code C++ modulaire basé sur la théorie des dislocations angulaires pour la modélisation en trois dimensions des fractures et failles dans un milieu infini ou semi-infini, élastique, hétérogène et isotrope. Nous présentons aussi les améliorations apportées à ce code ainsi que le grand nombre d'applications dans le domaine de la géologie structurale depuis la première implémentation en 1993 sous le nom de Poly3D. Le principal avantage d'utiliser une telle formulation pour décrire les failles et fractures, réside dans la possibilité de modéliser des géométries complexes sans trou ni recouvrement entre les éléments adjacents discontinus, ce qui est très problématique pour les modèles utilisant des dislocations rectangulaires. Fiabilité, vitesse de calcul, simplicité et exactitude des résultats sont améliorés dans la dernière version de ce code.

Les applications industrielles comprennent la modélisation des failles sous-sismiques, la modélisation des réservoirs fracturés, l'interprétation et la validation de la connectivité des failles et de la compartimentation des réservoirs, l'étude des zones déplétées, la réactivation des failles et la stabilité des puits de forage sous pression. Les applications académiques comprennent l'étude des tremblements de terre et la surveillance des volcans, l'atténuation des risques sismiques ainsi que la modélisation de stabilité des glissements de terrain.

## 1.2 Abstract

The purpose of this paper is to describe iBem3D, a C++ and modular computer program based on the theory of angular dislocations for three-dimensional fracture and fault modeling in an elastic, heterogeneous, isotropic whole- or half-space, and to present the extensions as well as the wide range of applications in structural geology since its first implementation in 1993 under the name Poly3D. The main advantage of using this formulation for describing faults and fractures resides in the possibility of modeling complex geometries without gaps and overlaps between adjacent triangular dislocation elements, which is a significant shortcoming for models using rectangular dislocation elements. Reliability, speed, simplicity and accuracy are enhanced in the latest version of the computer code. Industrial applications include subseismic fault modeling, fractured reservoir modeling, interpretation/validation of fault connectivity and reservoir compartmentalization, depleted area and fault reactivation, and pressurized well bore stability. Academic applications include earthquake and volcanoe monitoring, hazard mitigation and slope stability modeling.
**Keywords**: 3D-BEM, Geomechanics, Faults interaction, Sub-surface modeling

## 1.3 Introduction

The rapidly increasing number of geologic, seismologic and geodetic data sets with abundant and very precise spatial information on fault geometry and slip distributions promote the development of more complex geometric and kinematic models of modern earthquake ruptures and paleoseismic events. These data sets indicate that faults commonly are composed of multiple discrete segments, each with a curved surface and curved tipline. Construction of model fault segments using multiple rectangular dislocations (Okada, 1985) introduces non-physical gaps and overlaps with associated stress concentrations and irregularities in slip distributions that may differ significantly from those in nature (Maerten et al., 2005). Discretization of fault segments into a set of triangular dislocations enables one to approximate the curviplanar surfaces and curved tiplines to a precision that is consistent with the data (Jeyakumaran et al., 1992; Thomas, 1993; Maerten et al., 2005, 2009; Maerten, 2010).

The C computer code that was originally developed at Stanford University by Andrew Thomas (Thomas, 1993) in 1993 was called Poly3D. The idea of using the angular dislocation formalism to construct complex planar dislocations with constant displacement discontinuity was first used by Jeyakumaran et al. (Jeyakumaran et al., 1992) in 1992.

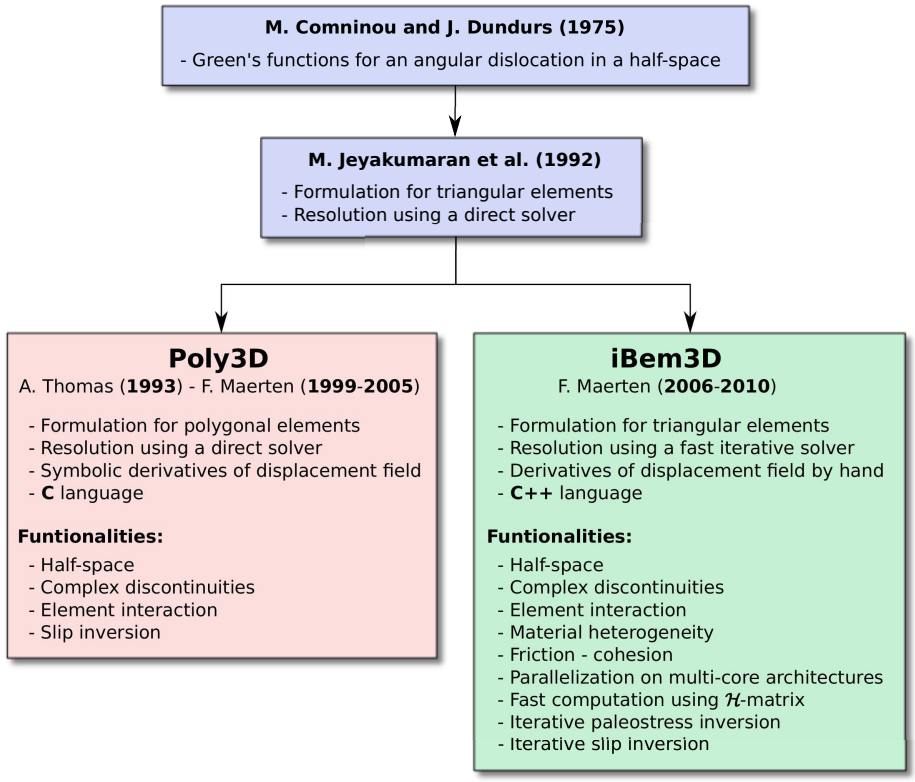


FIGURE 1.1: Poly3D versus iBem3D. Both of them are based on Comninou and Dundurs work (Comninou and Dundurs, 1975) and Jeyakumaran (Jeyakumaran et al., 1992). While Poly3D employs polygonal elements, iBem3D uses triangular elements and relies exclusively on an iterative solver. Compared to Poly3D, where the equations for the displacement field were symbolically derived using a computer program, iBem3D uses hand made derivatives (now running 4 times faster) and incorporates many enhancements.

Since then, due to the rapid evolution of computer power and the constant demand for doing more complex and larger models, a new code has emerged, following the work of Jeyakumaran (Jeyakumaran et al., 1992) for triangular elements. To develop the new code, iBem3D, the C++ object oriented language was chosen and an iterative solver now replaces the older direct solver (Gauss elimination). C++ allows modularity of the code (Maerten and Maerten, 2008a; Maerten et al., 2009; Maerten, 2010) while the iterative solver permits running larger models in a shorter time (Maerten et al., 2009). The equations for the displacement field provided by Comninou and Dundurs (Comninou and Dundurs, 1975) were entirely derived by hand for optimization considerations, whereas Poly3D equations were symbolically derived using a dedicated software. The call to the core equations now runs four times faster. Comparisons of Poly3D and iBem3D are summarized in Figure 1.1 where the technological differences are highlighted.

In this paper, we summarize the theory behind iBem3D along with verifications (section 1.4), and present the latest improvements such as the implementation of material heterogeneity, static friction, optimizations and parallelization, linear-slip inversion and paleostress recovery (section 1.5). Finally, the wide range of academic, research and industrial applications are discussed in section 1.6.

## 1.4 Theory behind iBem3D

The theory of dislocations in elastic materials has been used widely over the past half century to evaluate the displacement, strain and stress fields around faults in Earth's lithosphere. Steketee discussed this theory and potential applications to geophysical problems in two papers (Steketee, 1958b,a). He reviewed Volterra's formulation for the dislocation problem and presented a method for the construction of Green's functions for the semi-infinite space containing a surface of displacement discontinuity (the dislocation). The Green's functions can be integrated to calculate the displacement field around the planar surface of discontinuity. These displacement fields satisfy the Navier equations which are the governing equations for linear elastic theory. Spatial derivatives of the displacement components provide the strain components, and incorporation of Hooke's law for a homogeneous and isotropic elastic material gives the stress components. Thus, Steketee's work illustrates how the mathematical tools of dislocation theory enables one to compute the displacement, strain and stress fields around idealized faults in an elastic half-space, but it does not make explicit comparisons to geophysical data.

Chinnery used some results of Steketee to derive the particular solution for a vertical rectangular strike-slip fault of arbitrary dimensions and depth (Chinnery, 1963). He computed and illustrated the displacement and stress fields, and compared the surface displacements fields to those measured geodetically near active faults (Chinnery, 1961, 1963). The theoretical exposition of Steketee and the correlations to observations made by Chinnery had profound effects on the geophysical research community as they set the stage for the use of dislocation theory as one of the principal tools for the mechanical analysis of faulting. This usage has continued from the early nineteen sixties to the present day with many notable successes. Integration of Volterra's dislocation over rectangular surfaces in the half-space has been used in these studies (Maruyama, 1964; Press, 1965; Savage and Hastie, 1966, 1969; Mansinha and Smylie, 1971; Davis, 1983; Ma and Kusznir, 1993). Okada has reviewed this literature and perfected the analytical expressions for deformation at the surface of the half-space due to inclined shearing and opening rectangular dislocation surfaces (Okada, 1992).

For 2D solutions, a widely used numerical technique is the boundary element method (BEM) (Crouch and Starfield, 1983), which has been used to model fault behavior (Mavko, 1982; Bilham and King, 1989), overlapping spreading centers (Sempere and Mac Donald, 1986), the emplacement of igneous dikes (Delaney and Pollard, 1981) and the growth of joint sets (Olson and Pollard, 1989; Wu and Pollard, 1995) and veins (Olson and Pollard, 1991). One form of BEM is based on the dislocation and is called the displacement discontinuity method (DDM).

The method pioneered by Steketee and Chinnery involves complicated and lengthy integrations even for simple geometrical figures such as rectangles. A different approach, originally presented by Burgers (Burgers, 1939), was adopted by Yoffe (Yoffe, 1960) for the problem of an angular dislocation in the infinite elastic medium. This solution was then used to construct, in principle, the solution for dislocation polygons and polyhedra in the infinite medium. More recent contributions to the material science literature consider triangular loops of dislocation directly (Wong and Barnett, 1984; Barnett, 1985) instead of superposition of angular dislocations, but do not offer a general solution for the half-space problem. Comnimou and Dundurs extended the use of angular dislocation to the half-space problem (Comninou and Dundurs, 1975) and thereby paved the way for applications of this approach to geophysical problems in general and faulting in particular.

iBem3D is a computer program that calculates the displacements, strains and stresses induced in an elastic whole- or half-space by planar triangular-shaped elements of displacement discontinuity. Those elements are constructed by superposition of angular dislocations following the method described by Jeyakamuran, Rudnicki, and Keer (Jeyakumaran et al., 1992), and later by Thomas (Thomas, 1993). The elastic fields around the elements are derived from the solution for a single angular dislocation in an elastic half-space or whole-space (Yoffe, 1960; Comninou and Dundurs, 1975). Geologically, a triangular element may represent some portion of a fracture or fault surface across which the discontinuity in displacement is approximately constant.

Several triangular dislocation elements may be used to model faults or fractures, or even may be joined to form a closed surface that may represent either a finite elastic body or a void in an otherwise infinite or semi-infinite elastic body. This superposition provides the means to model geological structures with complex, three dimensional boundaries and shapes that are not possible to model effectively with the rectangular surface that has been extensively used in dislocation modeling of faults and fractures in the earth (Okada, 1985, 1992). Attempts to model curved surfaces with rectangular elements, except in the simplest cases, result in gaps and overlaps. In contrast, Fig. 1.2 shows how a complex 3D fault surface may be approximated with triangular elements with no gaps or overlaps. The

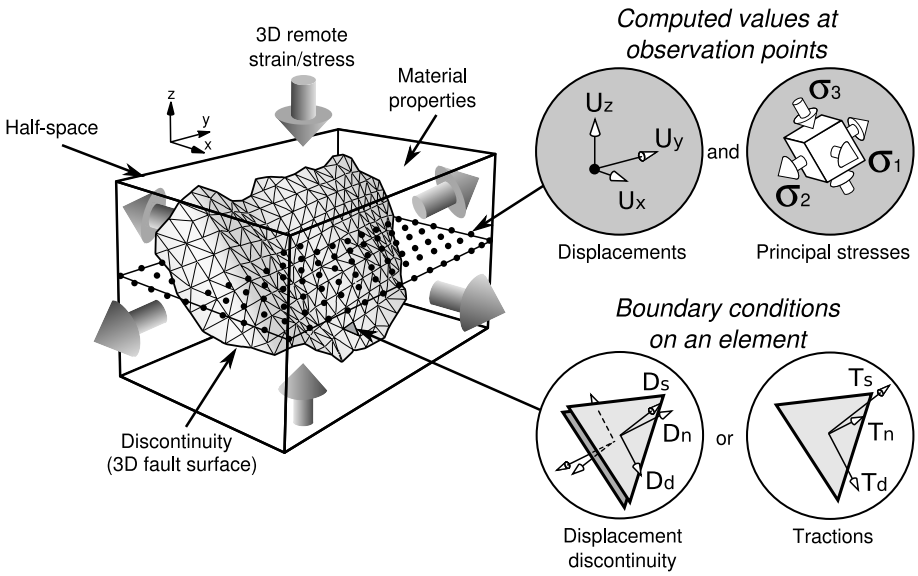


FIGURE 1.2: Construction of a complex fault geometry using triangular elements and schematic representation of a surrounding observation grid. Boundary conditions on triangular elements are a combination of displacement and traction. At each observation point, displacement, strain and stress can be computed as a post-process. Also shown is the 3D remote strain/stress

discretization of a three-dimensional fault surface into triangular boundary elements allows the construction of a surface with any desired tipline and shape. Boundary conditions, i.e., displacement discontinuities that are constant over an entire element or tractions at the center of each element, are prescribed according to the local coordinate system attached to the element (Fig. 1.4d). Additionally, remote stresses and/or strains can be prescribed. Output at observation points (black dots in Figure 1.2) can be displacement, strain, stress, principal strain and principal stress (Fig 1.2).

### 1.4.1 Angular, biangular and triangular dislocations

Among the different ways to build a triangular element with angular dislocations, the simplest (Fig. 1.3) is created by superposition of three angular dislocations as described by Yoffe (Yoffe, 1960). All three angular dislocations lie in the same plane, here the $(x, y) - plane$, and the dislocation surfaces (lightly shaded areas) extend to infinity. This construction does not enable a solution for the half-space problem as the lines of some dislocations would cross the traction-free surface when the element is inclined. Consequently, Comninou (Comninou and Dundurs, 1975) did not adopt this simple representation in their solution for the angular dislocation in the half-space. Instead, they used an angular dislocation with one vertical leg perpendicular to the surface of the half-space. An angular dislocation $(A, \alpha, \beta)$ (Fig. 1.4a) lies in a vertical plane that makes an angle

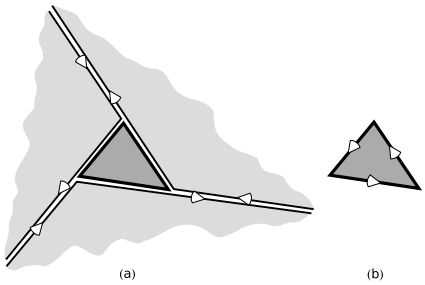


FIGURE 1.3: Triangular element construction according to Yoffe (Yoffe, 1960). All three angular dislocations lie in the same plane. This construction does not enable a solution for the half-space problem as the lines of some dislocations may cross the traction-free surface when the element is inclined

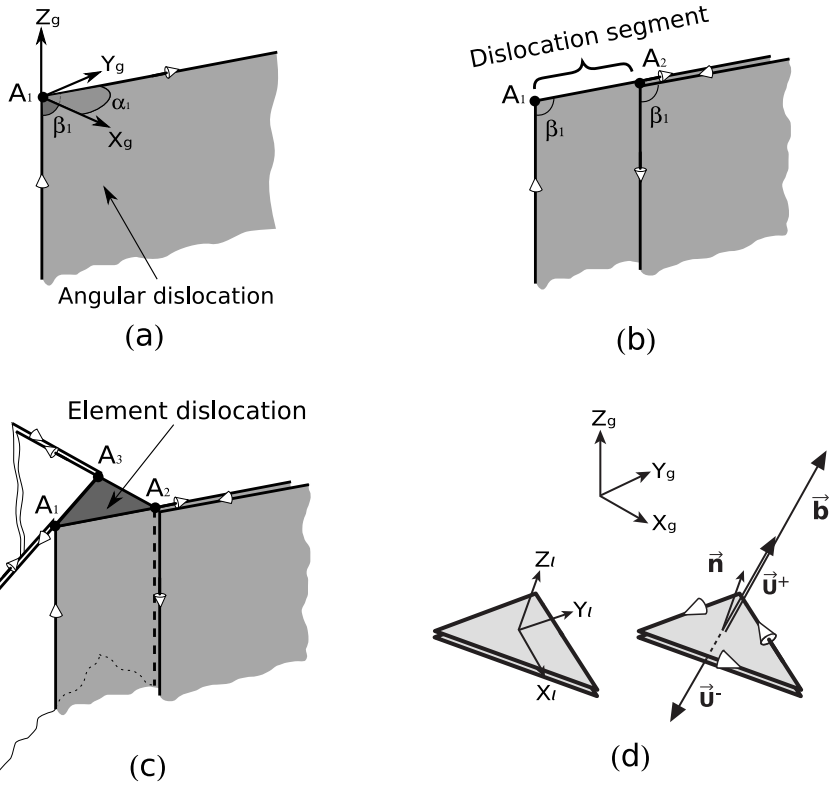


FIGURE 1.4: Angular, biangular, triangular dislocations and local coordinate system used in iBem3D. (a) Angular dislocation representation, with its semi-infinite vertical and inclined legs initiating at point A. (b) Biangular dislocation construction from two angular dislocations. The inclined leg cancels at point B. (c) Triangular dislocation construction from three biangular or six angular dislocations. All inclined and vertical legs cancel, leaving a triangular loop represented by the element, where a constant Burgers's vector is applied. (d) Representation of the element local coordinate system and the Burgers vector

$\beta$ in the horizontal plane to the global $y - axis$, with one leg perpendicular to the free surface. The two legs of the angular dislocation subtend an angle $\alpha$, and extend to infinity from a common vertex $A$. The uniform displacement discontinuity across the dislocation is given by its Burgers vector. Given a point $M$ in the elastic body, the displacement

component $\mathring{\mathbf{u}}_\mathbf{i}$ due to an angular dislocation $(A, \alpha, \beta)$ (Fig. 1.4a), is given by:

$$\mathring{\mathbf{u}}_\mathbf{i}(\mathbf{M}) = \sum_{j=1}^{3} \mathring{\mathbf{U}}_\mathbf{ij}(\mathbf{M}, \mathbf{A}, \alpha, \beta)\mathbf{b}_\mathbf{j} = \mathring{\mathbf{U}}_\mathbf{ij}\mathbf{b}_\mathbf{j} \text{ (Einstein notation)} \tag{1.1}$$

and is a linear function of the Burgers vector $\mathbf{b}$. Coefficients of the matrix $\mathring{\mathbf{U}}_\mathbf{ij}$, called the *displacement influence matrix*, are given by Comninou & Dundurs (Comninou and Dundurs, 1975). Note that the half-space problem is solved using image dislocations and a solution to the Boussinesq problem to remove tractions from the free surface (Comninou and Dundurs, 1975). The Boussinesq solution provides corrective terms for the free surface so that no shear stresses appear on it, and the image dislocations remove the normal tractions.

The strain field at point M can be computed by partial derivation of (1.1) by using the linearized *Green-St Venant* strain tensor:

$$\mathring{\epsilon}_\mathbf{ij} = \frac{1}{2}(\nabla\mathring{\mathbf{u}} + \nabla\mathring{\mathbf{u}}^\mathbf{t}) = \sum_{\mathbf{k=1}}^{\mathbf{3}} \mathring{\mathbf{E}}_\mathbf{ijk}(\mathbf{M}, \mathbf{A}, \alpha, \beta)\mathbf{b}_\mathbf{k} = \mathring{\mathbf{E}}_\mathbf{ijk}\mathbf{b}_\mathbf{k} \tag{1.2}$$

where $\nabla\mathring{\mathbf{u}}$ is the deformation gradient tensor. $\mathring{\mathbf{E}}_\mathbf{ijk}$ represents the *strain influence matrix* due to an angular dislocation and is derived from:

$$\mathring{\mathbf{E}}_\mathbf{ijk} = \frac{\mathbf{1}}{\mathbf{2}}\left(\frac{\partial\mathring{\mathbf{U}}_\mathbf{ik}}{\partial\mathbf{x}_\mathbf{j}} + \frac{\partial\mathring{\mathbf{U}}_\mathbf{jk}}{\partial\mathbf{x}_\mathbf{i}}\right) \tag{1.3}$$

For linear elastic materials, the stress components are related to the infinitesimal strain components using constitutive equations called Hooke's Law. The general form of Hooke's Law is simplified for an isotropic material, so there are only two material constants. The isotropic elastic material is one in which the elastic constants are the same regardless of direction. Given the Hooke's law

$$\sigma_{ij} = 2G\epsilon_{ij} + \lambda\epsilon_{kk}\delta_{ij} \tag{1.4}$$

the stress tensor is given for infinitesimal deformation as

$$\begin{aligned}\mathring{\sigma}_\mathbf{ij} &= 2G\mathring{\epsilon}_\mathbf{ij} + \lambda\mathring{\epsilon}_\mathbf{kk}\delta_\mathbf{ij} = \sum_{\mathbf{k=1}}^{\mathbf{3}} \mathring{\mathbf{S}}_\mathbf{ijk}(\mathbf{M}, \mathbf{A}, \alpha, \beta)\mathbf{b}_\mathbf{k} \\ &= \mathring{\mathbf{S}}_\mathbf{ijk}\mathbf{b}_\mathbf{k}\end{aligned} \tag{1.5}$$

where $G$ is the shear modulus, $\lambda$ the Lamé's constant, $\delta_{ij}$ the Kronecker delta, and $\mathring{\epsilon}_{\mathbf{ij}}$ is given by (1.2). $\mathring{\mathbf{S}}_{\mathbf{ijk}}$ represents the *stress influence matrix* due to an angular dislocation.

A biangular dislocation, having two vertical legs, perpendicular to the free surface, constructed from two angular dislocations $(A_0, \alpha, \beta)$ and $(A_1, \alpha, \beta)$ (Fig. 1.4b). The resulting displacement at point M is simply the superposition of contributions from the two angular dislocations:

$$\begin{aligned}\bar{\mathbf{u}}_{\mathbf{i}}(\mathbf{M}) &= \sum_{j=1}^{3}[\mathring{\mathbf{U}}_{\mathbf{ij}}(\mathbf{M}, \mathbf{A_0}, \alpha, \beta) - \mathring{\mathbf{U}}_{\mathbf{ij}}(\mathbf{M}, \mathbf{A_1}, \alpha, \beta)]\mathbf{b_j} \\ &= \sum_{j=1}^{3} \bar{\mathbf{U}}_{\mathbf{ij}}(\mathbf{M}, \mathbf{A_0}, \mathbf{A_1}, \alpha, \beta)\mathbf{b_j} = \bar{\mathbf{U}}_{\mathbf{ij}}\mathbf{b_j}\end{aligned} \tag{1.6}$$

Using the same process of superposition, a triangular element $\{A_0, A_1, A_2\}$ in the whole- or half-space is build with three biangular dislocations (Fig. 1.4c). The superposition of these dislocations are vertical surfaces defining a volume. This volume is semi-infinite and vertically trending compared to the global coordinate system. The coincident legs under each vertex cancel leaving a displacement discontinuity only in the triangle. The Burgers vector $\mathbf{b}$ is constant over the triangular dislocation. The superposition of these dislocations are vertical surfaces defining a volume. This volume is semi-infinite and vertically trending compared to the global coordinate system.

The total displacement at point M resulting from a triangular dislocation made of three dislocation segments, is therefore given by

$$\mathbf{u}_{\mathbf{i}}(\mathbf{M}) = \sum_{j=1}^{3}\sum_{k=1}^{3} \bar{\mathbf{U}}_{\mathbf{ij}}(\mathbf{M}, \mathbf{A_k}, \mathbf{A_{k+1}}, \alpha_{\mathbf{k}}, \beta_{\mathbf{k}})\mathbf{b_j} = \mathbf{U_{ij}}\mathbf{b_j} \tag{1.7}$$

the strain by

$$\epsilon_{\mathbf{ij}}(\mathbf{M}) = \sum_{k=1}^{3}\sum_{l=1}^{3} \bar{\mathbf{E}}_{\mathbf{ijk}}(\mathbf{M}, \mathbf{A_l}, \mathbf{A_{l+1}}, \alpha_{\mathbf{l}}, \beta_{\mathbf{l}})\mathbf{b_k} = \mathbf{E_{ijk}}\mathbf{b_k} \tag{1.8}$$

and the stress by

$$\sigma_{\mathbf{ij}}(\mathbf{M}) = \sum_{k=1}^{3}\sum_{l=1}^{3} \bar{\mathbf{S}}_{\mathbf{ijk}}(\mathbf{M}, \mathbf{A_l}, \mathbf{A_{l+1}}, \alpha_{\mathbf{l}}, \beta_{\mathbf{l}})\mathbf{b_k} = \mathbf{S_{ijk}}\mathbf{b_k} \tag{1.9}$$

For a model made of $n$ triangular dislocation elements, the displacement at any point $M$ is determined by superposition, i.e. by contribution of all the elements within the elastic body:

$$\mathbf{u_i(M)} = \sum_{m=1}^{n} \mathbf{U_{ij}^m b_j^m} = \mathbf{U_{ij}^m b_j^m} \tag{1.10}$$

where $\mathbf{U_{ij}^m}$ are the displacement influence coefficients due to the $m^{th}$ element, and $\mathbf{b_j^m}$ is the $j^{th}$ Burgers vector component. The strain and stress also are given by the contribution of all elements.

The Burgers vector $\mathbf{b}$, for a given element $e$, can be divided into two displacement vectors, $\mathbf{u}^+$ on the positive side of the element and $\mathbf{u}^-$ on the negative side, and these are related by:

$$\mathbf{b} = \mathbf{u}^+ - \mathbf{u}^- \tag{1.11}$$

In order to retrieve these vectors, one first calculates the displacement $\mathbf{u}^+$ at the element's centroid using equation (1.10) with an infinitesimal positive shift along the element's normal as described in section 1.9.2.2 of the appendix. The displacement on the negative side, $\mathbf{u}^-$, is then calculated using the prescribed boundary value and (1.11).

Note that one must use the corrective displacement presented in appendix if the observation point $M$ is under the triangulated surfaces of discontinuity in the elastic half-space, since the displacement field is not correctly calculated. This problem is directly linked to the construction of the triangular element and the interpretation of the solid angle used to define Burgers'function (see appendix).

### 1.4.2 Element boundary conditions

Each triangular dislocation is defined with three boundary conditions using the element local coordinate system. This is constructed with $x$ along the dip (direction of greatest inclination in the element plane), $z$ along the element's normal, and $y$ is the cross-product of $z$ and $x$. The $y$-axis is oriented toward north if the element is horizontal with respect to the global coordinate system (Fig. 1.4d). Boundary conditions consist of the displacement discontinuity component or traction component in each coordinate direction. When all triangular dislocations within the model are prescribed with displacement discontinuities, the displacement at any point within the elastic field is entirely defined by equation (1.10). However, when triangular elements have prescribed traction boundary condition,

one must first determine the corresponding Burgers components that produce these tractions, and then proceed with (1.10).

Using Cauchy's formula by resolving the stress tensor $\sigma_{ij}$ (Eq. 1.9) on the triangular element's plane using its centroid as the collocation point, the element's traction can now be defined by:

$$\mathbf{t_i} = \sigma_{ij}\mathbf{n_j} = (\mathbf{S_{ijk}b_k})\,\mathbf{n_j} = (\mathbf{S_{ijk}n_j})\,\mathbf{b_k} = \mathbf{T_{ij}b_k} \tag{1.12}$$

where $\mathbf{n_j}$ represents the element's normal components and $\mathbf{T_{ij}} = \mathbf{S_{ijk}n_j}$ is the *traction influence matrix*.

Using the traction formulation for a triangular dislocation, the total traction at the center of a triangular element is simply the total traction exclusive of that imposed by the remote loading at the center:

$$\mathbf{t_i} = \mathbf{T_{ij}^m b_j^m} \tag{1.13}$$

A system of linear equations is then constructed using (1.13), and solved for the unknowns Burgers vector components

$$\{\mathbf{t}\} = [\mathbf{T}]\{\mathbf{b}\} \tag{1.14}$$

In equation (1.14), $\{\mathbf{t}\}$ represents the column of the initially prescribed traction vectors (see next section 1.4.3), $[\mathbf{T}]$ is a *dense matrix* of traction influence coefficients, and $\{\mathbf{b}\}$ the column of the unknowns Burgers vectors.

### 1.4.3 Remote loading

Initial boundary conditions are prescribed for each triangular element of the model based upon the stress field $\sigma^{\mathbf{R}}$ that exists throughout the body before any slip or opening of the elements. This remote stress is applied to the model by prescribing boundary conditions that are the tractions resolved from this remote stress on the elements using Cauchy's formula (1.12). Then, one uses equation (1.14) to solve the system. Given the far field remote stress $\sigma^{\mathbf{R}}$ and the normal $\mathbf{n}$ of an element $e$, the initial traction for this element is given by $\mathbf{t} = -\sigma^{\mathbf{R}}\mathbf{n}$. Therefore, the initial traction boundary vector for a given element opposes the prescribed resolved far field stress onto this element, leading to equilibrium. If a remote strain $\epsilon^{\mathbf{R}}$ is prescribed, one first calculates the corresponding remote stress $\sigma^{\mathbf{R}}$ using Hooke's Law (1.4) and then proceeds as above.

### 1.4.4 Post-processing at observation points

After the system (1.14) is solved, displacement, strain and stress components can be computed anywhere within the elastic solid, by using the principle of superposition. For a given observation point (field point), the resulting component is the sum of contributions from all influencing elements (sources). For the displacement, equation (1.10) is used directly. For strain and stress, equation (1.15) and (1.16) are used respectively:

$$\epsilon_{\mathbf{ij}}(\mathbf{M}) = \sum_{m=1}^{n} \mathbf{E}^{\mathbf{m}}_{\mathbf{ijk}} \mathbf{b}^{\mathbf{m}}_{\mathbf{k}} + \epsilon^{\mathbf{R}}_{\mathbf{ij}} = \mathbf{E}^{\mathbf{m}}_{\mathbf{ijk}} \mathbf{b}^{\mathbf{m}}_{\mathbf{k}} + \epsilon^{\mathbf{R}}_{\mathbf{ij}} \tag{1.15}$$

$$\sigma_{\mathbf{ij}}(\mathbf{M}) = \sum_{m=1}^{n} \mathbf{S}^{\mathbf{m}}_{\mathbf{ijk}} \mathbf{b}^{\mathbf{m}}_{\mathbf{k}} + \sigma^{\mathbf{R}}_{\mathbf{ij}} = \mathbf{S}^{\mathbf{m}}_{\mathbf{ijk}} \mathbf{b}^{\mathbf{m}}_{\mathbf{k}} + \sigma^{\mathbf{R}}_{\mathbf{ij}} \tag{1.16}$$

where $\mathbf{E}^{\mathbf{m}}_{\mathbf{ijk}}$ and $\mathbf{S}^{\mathbf{m}}_{\mathbf{ijk}}$ represent the strain and stress influence matrices at field point $M$ due to a source element $m$, respectively, and $\epsilon^{\mathbf{R}}$ and $\sigma^{\mathbf{R}}$ the remote field strain and stress, respectively. In equation (1.15) and (1.16), the perturbed strain/stress field due to slipping triangular elements is simply superimposed on the remote stress/strain field.

### 1.4.5 Benchmarking the code

The basic element used by iBem3D is a planar dislocation loop with a triangular tipline. The analytical equations for the displacement, strain, or stress fields around such an element are not written down because the element is actually made up of a set of angular dislocations and the effect of these are numerically summed within the code. Therefore we must use a simpler dislocation solution for the purpose of benchmarking the code and find a way to compare that to the output of iBem3D. Figure 1.5 shows a single dislocation line extending along the $z$ coordinate axis with a tangent vector in the positive coordinate direction. The edge dislocation is positive with a Burgers vector directed along the $x$ coordinate axis. For comparison to this dislocation line we choose the simplest iBem3D element, an equilateral triangular element with unit side length, $a = 1$. This element lies in the ($x$, $z$)-plane with one side parallel to the $z$ coordinate axis. The tangent vector along that side points in the positive coordinate direction and the dislocation there is a pure edge dislocation with Burgers vector directed along the $x$ coordinate axis. The origin of coordinates is placed at the midpoint of that side. Because the dislocation line is infinite in length and the side of the triangular element is finite, we must restrict our range to the region immediately surrounding the side of the element at the midpoint.

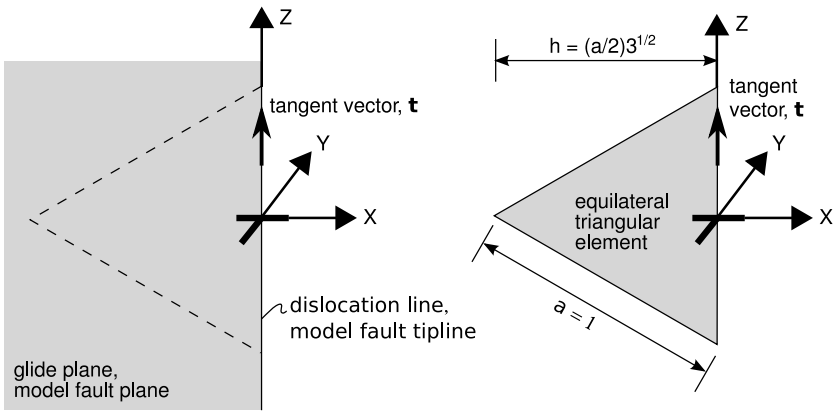


FIGURE 1.5: Single edge dislocation e and iBem3D triangular element

For the purposes of bench marking, we choose the displacement field and the strain field associated with the straight edge dislocation line (Weertman & Weertman (Weertman and Weertman, 1964), p. 35-37). The stress components are proportional to the strain components through Hooke's Law (eq. 1.4), so using one or the other is sufficient. The displacement components are:

$$\begin{cases} u_x = -\frac{b}{2\pi}\left[\tan^{-1}\left(\frac{y}{x}\right) + \frac{\lambda+\mu}{\lambda+2\mu}\left(\frac{xy}{x^2+y^2}\right)\right] \\ u_y = -\frac{b}{2\pi}\left[\frac{\mu}{2(\lambda+2\mu)}\ln\left(\frac{x^2+y^2}{C}\right) + \frac{\lambda+\mu}{\lambda+2\mu}\left(\frac{y^2}{x^2+y^2}\right)\right] \\ u_z = 0 \end{cases} \tag{1.17}$$

Here $\lambda$ and $\mu$ are Lamés elastic constants ($\mu$ also is referred to as the shear modulus) and $b$ is the magnitude of the Burgers vector for the edge dislocation. The constant $C$ is an arbitrary (rigid) translation that does not appear in the strain equations because they are derivatives of the displacements. Because the dislocation line is infinite in extent the displacement parallel to this line is zero. The strain components are:

$$\begin{cases} \epsilon_{xx} = +\frac{by}{2\pi}\left[\frac{(3\mu+2\lambda)x^2+\mu y^2}{(2\mu+\lambda)(x^2+y^2)^2}\right] \\ \epsilon_{yy} = -\frac{by}{2\pi}\left[\frac{(\mu+2\lambda)x^2-\mu y^2}{(2\mu+\lambda)(x^2+y^2)^2}\right] \\ \epsilon_{xy} = -\frac{bx}{2\pi}\left[\frac{2(\mu+\lambda)(x^2+y^2)}{(2\mu+\lambda)(x^2+y^2)^2}\right] \\ \epsilon_{xz} = \epsilon_{yz} = \epsilon_{zz} = 0 \end{cases} \tag{1.18}$$

Note that the shear strain component along the line $y = 0$ is proportional to $b/x$, so as the distance to the dislocation line becomes very small the strain becomes very large. In fact there is a singularity in all the strain components at the dislocation line. While this is mathematically correct it is non-physical, so we must restrict attention to the region at some distance from the dislocation line where the strain (and stress) components are of reasonable magnitude for the assumptions of linear elastic deformation to be meaningful.

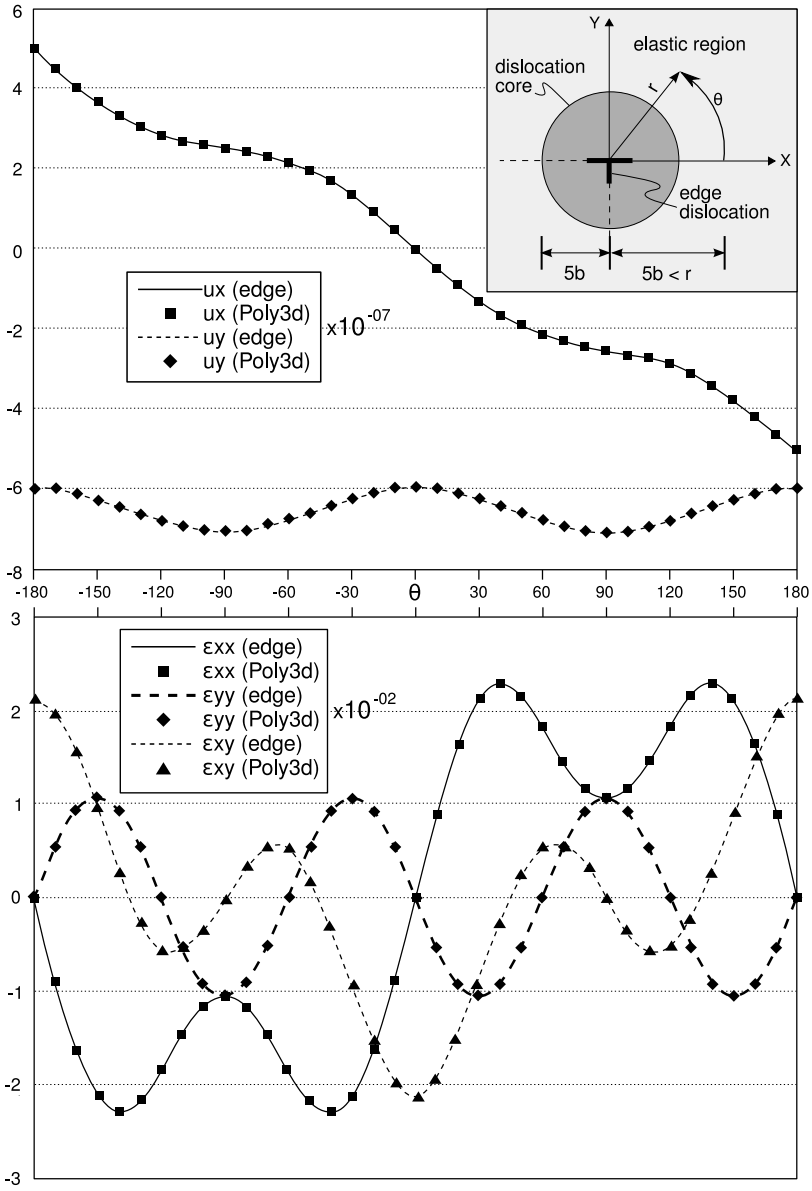


FIGURE 1.6: Verification of displacement (top) and strain (bottom) field equations for an edge dislocation with $r = 5b$

It is generally agreed (Weertman and Weertman, 1964) that this distance is some multiple of the Burgers vector, say about $r > 5b$, and the region inside this radius is called the dislocation core. Furthermore, the elastic fields are based upon the concept of a continuum, which breaks down for still smaller volumes where inhomogeneity of the crystalline lattice becomes relevant. Therefore, to avoid the dislocation core, but remain close to the dislocation line relative to the length scale of the triangular element we specify a range $r \geq 5b$ (inset of Fig. 1.6).

For the iBem3D parameters, the elastic moduli $\lambda$ and $\mu$ are chosen to be 20,000 MPa. The dislocation has prescribed displacement boundary conditions with Burger's vector equals

to $b = (10^{-6}, 0, 0)$. The observation points are located on a circle in the $(x, y)$-plane such that $r = 5.10^{-6}$ and $-180 < \theta < 180$, with a point every $10^o$ (inset of Fig. 1.6).

The displacement distributions for the two non-zero components are shown in Figure 1.6, top. These components are referred to the global coordinate system. The analytical solution results are shown as continuous smoothed line and the iBem3D results are superimposed as symbols. Note that the component $u_x$ varies from $+b/2$ at $\theta = -180^o$ to $-b/2$ at $\theta = +180^o$, thus accounting for the displacement discontinuity. The component $u_y$ is continuous across the glide plane. The graphical comparison indicates that iBem3D reproduces the analytical results quite well, and inspection of the numerical computations demonstrate that the two solutions are identical to four significant figures. The distributions of the strain components just outside the dislocation core are shown in Figure 1.6, bottom. Again the analytical results are plotted as smooth curves and the iBem3D results are superimposed as symbols. The graphical comparison indicates that iBem3D reproduces the analytical results quite well, and inspection of the numerical computations demonstrates that the two solutions are identical to four significant figures.

A similar bench marking procedure was carried out using the analytical solution for the single screw dislocation (Weertman & Weertman (Weertman and Weertman, 1964), p. 32-35). Once again iBem3D reproduced the displacement and strain fields everywhere just outside the dislocation core to four significant figures or better. These two tests demonstrate that the physical fields of displacement and strain (and by implication stress) in the region very near the edge of a triangular element are calculated by iBem3D with results that are consistent with the fields for pure edge and screw dislocation lines. By implication, we expect the physical fields near an edge of an element with an oblique Burgers vector will be consistent with the fields for the mixed dislocation.

In a similar way the displacement and stress components from iBem3D were compared to those components from the analytical solution for a two-dimensional strip of displacement discontinuity (Crouch & Starfield (Crouch and Starfield, 1983), p. 79-83). The comparison was made at a radial distance $r = 2a$ from the middle of the strip. Again the match is identical to four significant figures. We suggest that these comparisons provide a robust bench marking of the mathematical equations and coding in iBem3D for the near field of the element tipline and the intermediate field of the discontinuity.

## 1.5 Enhancements to iBem3D

As mention in previously, iBem3D incorporates several new enhancements compare to Poly3D, thanks to the C++ object oriented design. Those are summarized below.

### 1.5.1 Heterogeneous material

Solutions for heterogeneous materials can be formulated using triangulated interfaces between regions (Maerten and Maerten, 2008b). An interface is defined as a doubly triangulated surface (one for each region), perfectly coincident, but with opposite normals. Each region is characterized by a homogeneous and isotropic material but the elastic moduli may be different in each. The interface between two different regions transmits the mechanical influence of one region on the other by computing the corresponding Burgers's vectors for two adjacent elements on the interface using continuity and equilibrium conditions prescribed in the global coordinate system:

$$\begin{cases} \mathbf{u_1^-} = \mathbf{u_2^-} & \text{(continuity conditions)} \\ \mathbf{t_1} + \mathbf{t_2} = \mathbf{0} & \text{(equilibrium conditions)} \end{cases} \tag{1.19}$$

In equation (1.19), $\mathbf{u_1^-}$ and $\mathbf{t_1}$, part of region 1, represent the displacement computed on the negative side of each element and the traction, respectively. This formulation leads to separate models for each region that are linked through the continuity and equilibrium conditions at the interface (Maerten and Maerten, 2008b).

### 1.5.2 Friction and non-interpenetration

Friction and non-interpenetration present a subset of inequality constraints on traction and displacement, respectively, for the general contract problem in mechanics. While solving such problems, different algorithms can be used to incorporate these constraints. The most popular ones are the Lagrange Multipliers, the Penalty Method and the Complementarity Problem (Wriggers, 2002). However, these methods incorporates either new equations into the system, artificial parameters, or the necessity to explicitly construct the system matrix. In (Maerten et al., 2009), we use another technique based on successive corrections of the solution. Compared to other techniques of contact management, this new simple methodology, which does not use any incremental trial and error procedures, brings more flexibility, while making the system more stable and less subject to round-off errors, without significant computational overhead.

The incorporation of inequality constraints on traction and displacement now extends the existing wide range of applications of iBem3D. For example, static friction can be used to model the cohesive end zone (CEZ) of a fault (Martel, 1997; Davatzes and Aydin, 2003; Cooke, 1997), where the greater friction reduces slip such that a (non-physical) infinite stress state is avoided. This enhancement also can be used to study frictional behaviors when faults or opening fractures approach interfaces separating regions of different material properties (Maerten and Maerten, 2008b), or to understand the role of static friction on fracture orientation in extensional relays along strike-slip faults (Soliva et al., 2010). This tool will enable investigations leading to more accurate estimation of seismic hazard in regions of active faults, better recovery of petroleum reserves from fractured reservoirs, improved access to geothermal energy and reduced costs for remediation of contaminants on fractured aquifers.

### 1.5.3 Linear slip inversion

Retrieving the slip distribution onto three-dimensional faults, given measurements of ground displacements (e.g., from Global Positioning System (GPS) or synthetic aperture radar interferometry (InSAR)) associated with tectonic events such as earthquakes is of great interest. Three dimensional indirect boundary element methods are a good candidate for the inversion. Usually, a weighted least squares approach combined with a Tikhonov regularization is used (Johnson et al., 2001; Maerten et al., 2005). Then, the system has to be solved with a constrained solver in order to reach a realistic convergence. In (Maerten et al., 2005), we extend the forward formulation to linear slip inversion, and show that using such a formulation is more precise than using rectangular elements (Okada, 1985). For instance, gaps and overlaps between adjacent elements, which lead to to numerical artifacts, do not exist on triangulated discontinuities. Consequently, this technique more precisely captures information close to the fault elements.

### 1.5.4 Paleostress

Given data that constrains the faults geometry, as well as the boundary conditions on the elements making up the fault, the choice of what remote stress or strain to apply to the model may be problematic. In (Kaven, 2009), we show that using an iteratively coupled double systems, it is possible to estimate the paleostress given measures of the displacement discontinuity on some parts of faults. For example, throw or dip-slip measurements may be available from reflection seismic interpretation. While inverting for the

paleostress, we simultaneously recover for the unknown displacement discontinuities onto the faults. This technique allows one to extend the faults geometry, if necessary, and to compute the unknown dip- and strike-slip.

### 1.5.5 Optimization

Working with heterogeneous materials (section 1.5.1) requires triangulated interfaces with traction boundary conditions for all three axes for all the elements. Because the interface is decomposed into pairs of perfectly coincident discontinuities with opposite normals, the number of unknowns grows rapidly. As a result, the system of equations to solve requires a huge memory to store the dense system matrix and a long time to compute the solution. Furthermore, post-processing at observation points can require lengthy computational time. We described in (Maerten, 2010) the $\mathcal{H}$-Matrix (Hackbusch, 1999) combined with the Adaptive Cross Approximation (Bebendorf, 2000, 2008; Bebendorf and Rjasanow, 2003) to significantly reduced the memory needed to store the dense matrix and the time needed to solve the system of equations. This technique also is applied to the post-processing at observation points, decreasing drastically the computational time. Furthermore, in (Maerten, 2010), it is shown that this optimization can easily be parallelized on multi-core architectures.

## 1.6 Applications

Numerical models of rock deformation based on continuum mechanics can provide significant means for the understanding of geologic structures and phenomena in the context of theoretical research, teaching, hydrocarbon exploration and production as well as civil engineering. Since 1993, scientists and engineers using Poly3D/iBem3D have been intensively active, publishing more than 250 scientific papers, theses and abstracts related to fracture mechanics and numerical modeling of tectonic processes. In this section, we summarize both the research and the industry main applications illustrated by selected figures. For an exhaustive list of Poly3D/iBem3D related publications, please visit the following Internet link: http://www.igeoss.com/igeoss/research/publications.html

### 1.6.1 Research and Academic applications

#### 1.6.1.1 Teaching

Computational science methods are often used to investigate and illustrate complex geological phenomena. To provide geology students with opportunities to both visualize and explore such phenomena, several teachers among them Dr. Linda Reinen from Pomona College, USA (Reinen, 2008) and Dr. Michele Cooke from University of Massachusetts, USA, have incorporated the program Poly3D/iBem3D into their undergraduate Structural Geology course.

#### 1.6.1.2 Fracture mechanics

A major and straightforward use of elastic dislocation is to study fracture mechanics. Since its first version, Poly3D/iBem3D has been thoughtfully used to understand the mechanics of (i) natural fault propagation (Willemse and Pollard, 2000), (ii) echelon normal fault arrays (Willemse et al., 1996; Willemse, 1997; Crider, 2001), (iii) intersecting faults (Maerten et al., 1999; Maerten, 2000), (iv) secondary fracture development (Martel and Boger, 1998; Kattenhorn et al., 2000; Bourne and Willemse, 2001; Soliva et al., 2010), (v) orthogonal cross joints (Bai et al., 2002) and (vi) normal fault linkage (Crider and Pollard, 1998) and spacing (Soliva et al., 2006).

As a representative example, Bai et al. (Bai et al., 2002) demonstrate that orthogonal cross joints do not necessarily require a systematic rotation of the regional stress field by 90°. They show that for vertical systematic joints developing in horizontal strata under triaxial remote stress, where the least compressive stress is perpendicular to the fracture planes, there is a local stress change for a critical ratio of fracture spacing to height preventing the development of new parallel joints and promoting the development orthogonal cross joints (Figure 1.7).

#### 1.6.1.3 Structural geology

Understanding geological structures and processes normally requires the combination of geological observations from outcrop, core, air photo or industry data such as seismic reflection data, with idealized numerical models of rock deformation based on continuum mechanics. Elastic models are often used because they are computationally simple and adequately explain most of deformation observed in nature. For instance, faults are

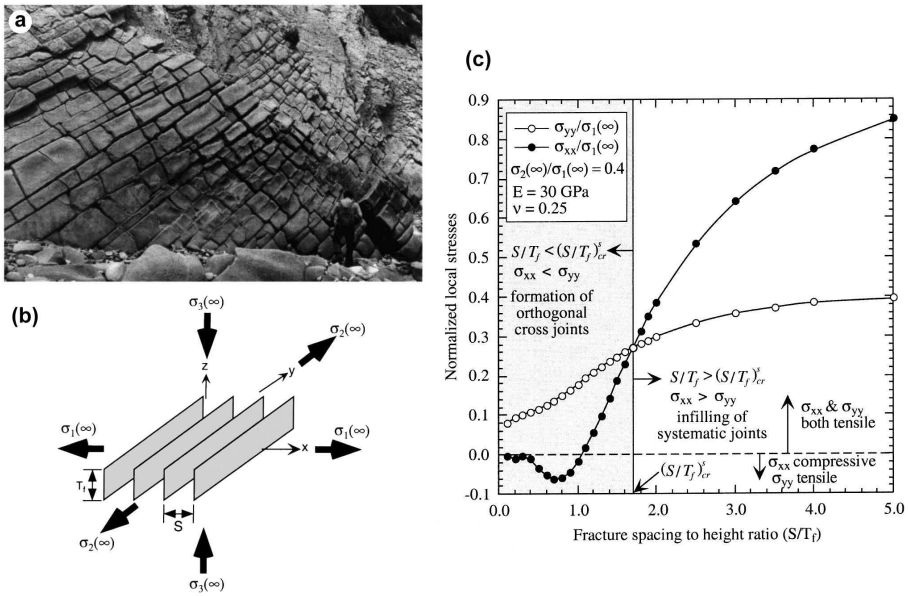


FIGURE 1.7: (a) Orthogonal cross joints in a steeply inclined carbonate bed from the Monterey Formation, California. (b) Model configuration with four fractures of the same dimension placed in the whole space of homogeneous, isotropic and elastic medium. (c) Results of local stress switch between adjacent equally-spaced fractures. The sign convention used here is that tensile stresses are positive and compressive stresses are negative. Figure modified from Bai et al., 2002 (Bai et al., 2002).

modeled as three-dimensional surfaces of displacement discontinuity in a homogeneous, isotropic, linear elastic material. This provides a first-order understanding of how fault accommodate slip, interact, concentrate stress and deform the surrounding rock mass. Perhaps of greatest importance is the fact that the solutions to the elastic boundary value problem comply with Newtons laws of motion and they have an explicitly defined constitutive law relating stress and strain in three dimensions.

Therefore, geologists have been using Poly3D/iBem3D to understand observed geological structures such as fault-related folding and associated secondary fractures (Savage and Cooke, 2003; Bellahsen et al., 2006; White and Crider, 2006; Allward-Fiore, 2006; Mynatt et al., 2007; Shackleton and Cooke, 2007), deformation associated with thrust faults (Griffith and Cooke, 2004; Olson and Cooke, 2005), strike slip faults (Brankman and Aydin, 2004) and normal faults (Resor, 2003; Grant and Kattenhorn, 2004; Soliva et al., 2008; Marshall and Cooke, 2008; Meigs et al., 2008). Figure 1.8 illustrates how mapped displacement profiles along overlapping faults in Vallo di Diano, Italy, have been geomechanically reproduced using linear elasticity (Soliva et al., 2008).

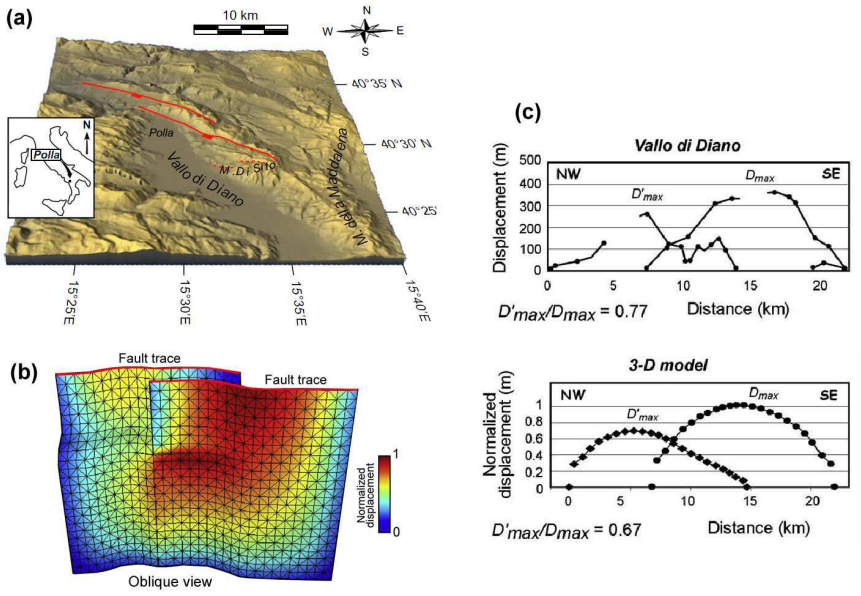


FIGURE 1.8: (a) Location and overview of the Vallo di Diano segmented normal fault zone on a digital elevation model. The overlapping normal fault segments are mapped with red lines at the base of the fault scarps. (b) Three-dimensional view of the fault surface, the mesh used in the model and computed displacement distribution. (c) Comparison between Earth's surface scarp topography profiles and displacement computed at the surface in the model. Figure modified from Soliva et al., 2008 (Soliva et al., 2008).

#### 1.6.1.4 Active tectonics and earthquakes

The increasing availability of spatially rich geodetic data, specifically dense Global Positioning System (GPS) networks and synthetic aperture radar interferometry (InSAR), offers researchers opportunities to construct increasingly complex geometric and kinematic models of earthquake ruptures. Unfortunately, these high quality data now available to geophysicists and geologists are not fully exploited in forward and inversion procedures when using geomechanical methods based on rectangular dislocation segments (Okada, 1985; Johnson et al., 2001; Jónsson et al., 2002). Indeed, these methods, which tend to oversimplify fault geometries, can lead to inconsistencies when inverting for slip on earthquake faults, and they preclude a more complete understanding of the role of fault geometry in the earthquake process.

With the use of angular dislocations (Comninou and Dundurs, 1975; Thomas, 1993; Maerten et al., 2005), discontinuities can be discretized into triangular elements allowing for the construction of three-dimensional fault surfaces that more closely approximate curviplanar surfaces and curved tiplines without introducing overlaps or gaps, consistent with the full extent of available data. The strengths of this method has been successfully demonstrated for more than 10 years for (i) simulating stress transfer from one rupture

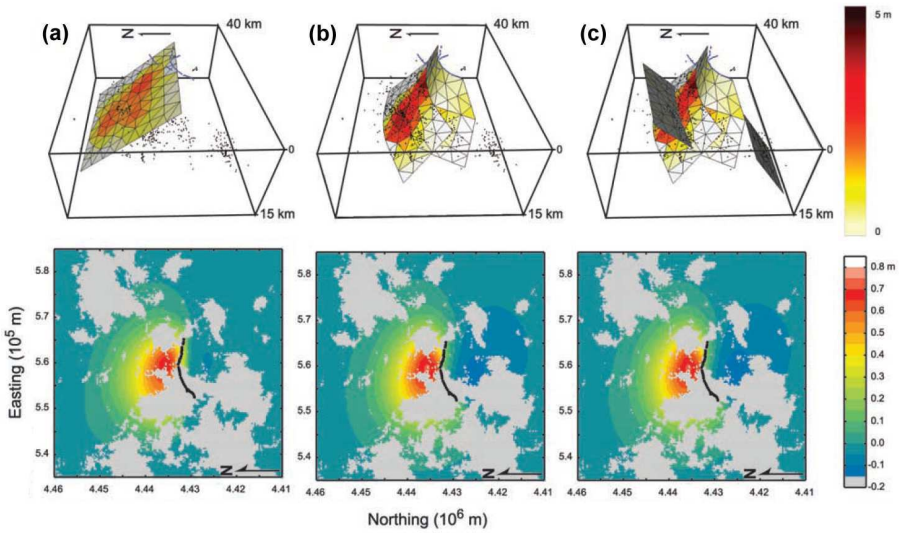


FIGURE 1.9: Inversion results of the 1995 Kozani-Grevena earthquake, Greece for three models: (a) the best fit planar model from nonlinear inversion, (b) a three-fault model including major fault segments interpreted from aftershock hypocenters and surface ruptures, and (c) a five-fault model including two antithetic faults also interpreted from aftershock distributions. For each model, two images are presented: (top) an oblique view of the model looking toward the east with the slip distribution calculated from linear inversion of InSAR data, aftershock hypocenters, and surface rupture traces; (bottom) the results of the forward model illustrating predicted surface deformation (range change) with areas of no InSAR data in gray. Figure modified from Resor et al., 2005 (Resor et al., 2005).

to nearby fault (Price and Bürgmann, 2002; Muller et al., 2003; Muller and Aydin, 2004; Muller et al., 2006), (ii) modeling stress distribution around active faults (Fielding et al., 2004; Lovely et al., 2009; Fielding et al., 2009), (iii) appraising different rupture geometry (Rigo et al., 2004; Muller and Aydin, 2005; Akoglu et al., 2006; Marshall and Cooke, 2008; Dair and Cooke, 2009), (iv) modeling rupture slip distribution (Burgmann et al., 2000; Schmidt et al., 2005; Kreemer et al., 2006; Zhang et al., 2008; Cheng et al., 2009), and (v) using slip inversion to model coseismic deformation associated with recent earthquake as illustrated in Figure 1.9 (Maerten et al., 2005; Resor et al., 2005; Cakir et al., 2006).

#### 1.6.1.5 Volcanoes

Swelling or collapse of volcanoes is often related to magma migration within and outside the magma chamber. Therefore, analyzing the ground surface deformation along the flanks of volcanoes over time can provide very good insight on the potential eruptions. As for earthquake studies, GPS networks, InSAR data and microseismicity are commonly used to study the volcanoes activity. Similarly, the same geomechanical tools based on elastic dislocation can be used to model magma activities and potential interaction with

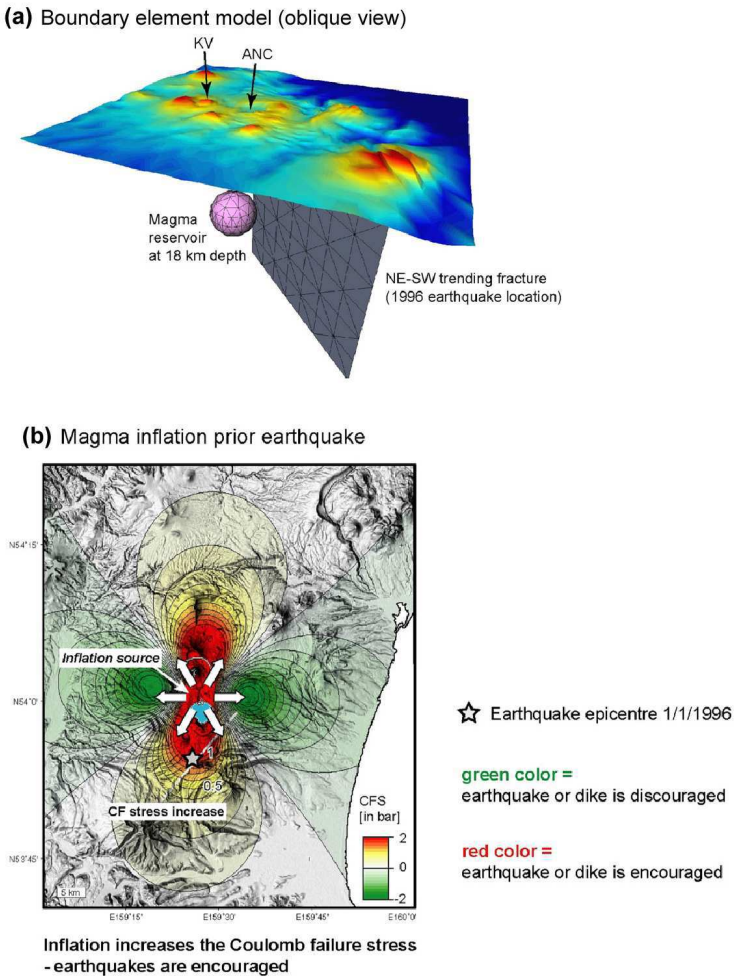


FIGURE 1.10: 1996 earthquake-eruption sequence at the Karymsky Volcanic Group, Kamchatka. (a) Numerical model construction. Perspective view of the boundary element model setup. (b) Modeling results. Model simulation of inflation of a deep magma reservoir. Coulomb failure stress change (CFS) calculated at faults parallel to the NESW (N040) fracture system (red = faults are brought closer to failure, indicating CFS increases; green = CFS decreases). Faulting is encouraged in exactly the area of the 1996 earthquake main shock. Inflation therefore encouraged this earthquake. Figure modified from Walter et al., 2007 (Walter, 2007).

nearby faults or dikes as illustrated in Figure 1.10 (Cailleau et al., 2007; Diez et al., 2005; Klügel et al., 2005; Lundgren and Lu, 2006; Walter and Amelung, 2006, 2007; Walter, 2007; Yun et al., 2006).

### 1.6.2 Industry and engineering applications

#### 1.6.2.1 Subsurface fault interpretation

Complex geological structures, where faults are known to be challenging as they often are poorly imaged, are known to be potentially good hydrocarbon reserves. As an example, spatial continuity and linkage of faults may substantially affect fluid flow either by compartmentalizing the reservoir, or by increasing the tortuosity of flow pathways, whether the faults act as seals or conduits. In such context, it is essential to check the consistency of the subsurface structural interpretations as it will improve reservoir flow simulation models and, in turn, significantly reduce the number of wells required to drain reserves.

Maerten et al. (Maerten, 2000) demonstrate how geomechanical models based on elastic dislocation can be applied to improve the subsurface interpretation understanding and obtain more realistic reservoir models. They have developed a method to infer, in three dimensions, the fault tip-line geometry below the seismic resolution as well as potential fault linkage. A 3D numerical model of the faulted reservoir and its surroundings is constructed using seismic interpretation. Such a model, combined with an appropriate set of boundary conditions is used to compute the fault slip distribution as well as vertical displacement field. By comparing the interpreted fault slip distribution to the computed slip distribution adjacent to potential intersection lines, the geomechanical models can constrain the geometry of the faults as well as the location of the intersection line between faults (Figure 1.11). The interpreted structure contour map and theoretical displacement field also are compared to constrain the fault geometry.

#### 1.6.2.2 Subsurface small-scale fracture modeling

Natural fractures such as small-scale faults and joints are known to be capable of significantly altering the flow of hydrocarbons, either during the migration from the source to the reservoir rock or during production of the reservoir. Therefore, understanding and quantifying the spatial and temporal development of these features as well as their properties (e.g. geometry, throw, aperture, permeability, etc.) can have great economic impact on the recovery of natural reserves. During the past ten years, methodologies based on elastic dislocation have been developed, taking into account mechanical concepts and the fundamental physical laws that govern fracture development to more realistically model the spatial and temporal development of structural heterogeneities and to address these economic issues.

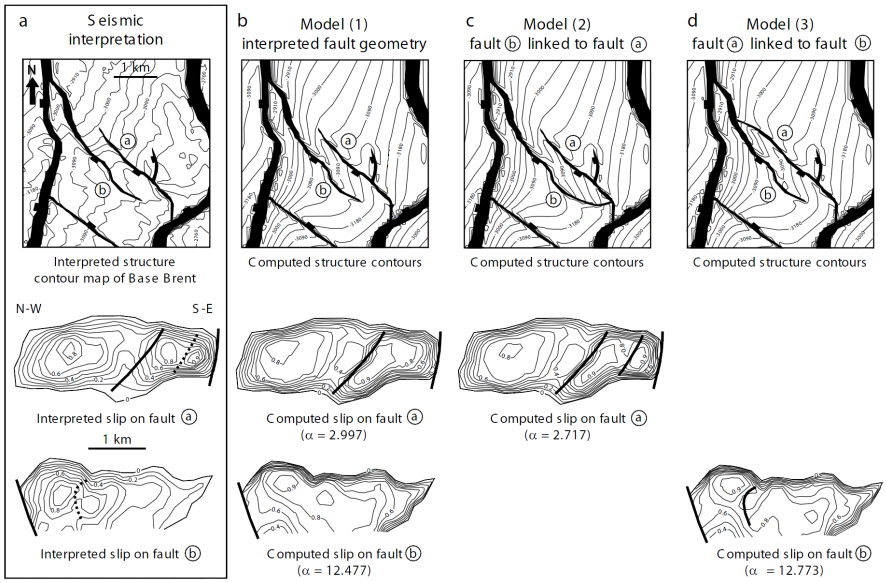


FIGURE 1.11: Analysis of the Oseberg reservoir compartmentalization, Northern North Sea. (a) Interpreted structure contour map and normalized contoured slip distribution on faults a and b. (b) Computed vertical displacement field and normalized slip distribution on faults a and b from a first model using the interpreted fault geometries. (c) Computed values from a second model using fault b linked to fault a. (d) Computed values from a third model with fault a linked to fault b. Qualitative and quantitative comparisons suggest that fault b is likely to be linked to fault a. Figure modified from Maerten et al., 2000 (Maerten, 2000).

The basic methodology consists of calculating the stress distribution at the time of fracturing using the available reservoir structure data such as faults, fractures and folds, and rock properties and the tectonic setting that can be characterized by stress or strain magnitude and orientation. Then, the calculated stress fields, perturbed by the main structures, combined with rock failure criteria are used to model natural fracture networks (i.e. type, orientation, location, and spatial density). Applications to both outcrops (Kattenhorn et al., 2000; Bourne and Willemse, 2001; Davatzes et al., 2005) and reservoirs (Maerten et al., 1999; Bourne et al., 2000; Maerten et al., 2002, 2006) demonstrate how geomechanics can provide a high degree of predictability of natural fracture networks. Poly3D/iBem3D has been successfully applied to model subseismic faults (Maerten et al., 1999, 2006) in Northern North Sea highly faulted reservoirs (Figure 1.12) as well as undetected joints in naturally fractured carbonate reservoirs (Bourne and Willemse, 2001).

#### 1.6.2.3 Perturbed stress field and fracture reactivation

In hydrocarbon reservoirs, fracture reactivation can have a significant effect on the flow properties. The two main factors that allow quantitative modeling of fracture reactivation are the geometry of preexisting natural fractures and the present day perturbed stress

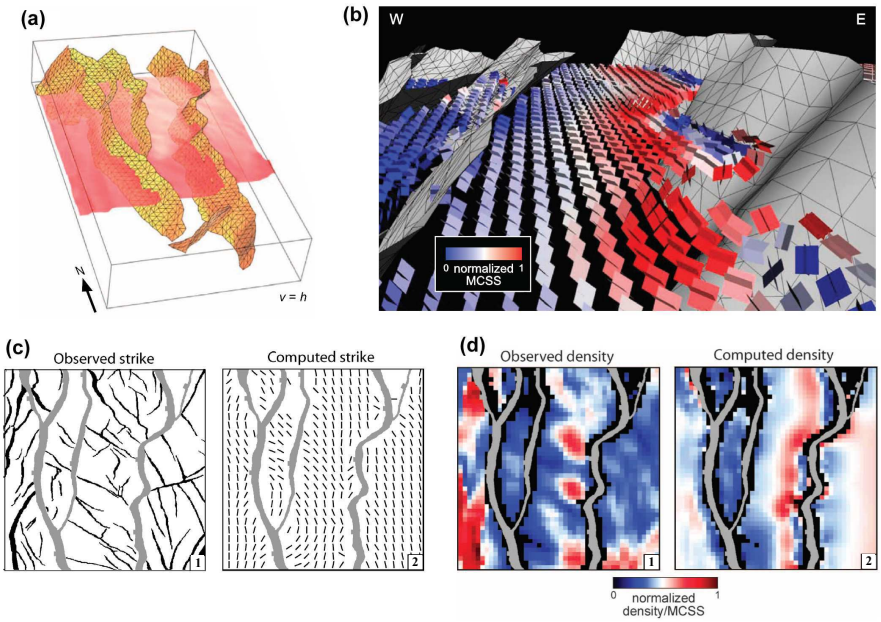


FIGURE 1.12: Subseismic fault modeling of the Oseberg reservoir, Northern North Sea. (a) Three-dimensional view of the model mesh made of triangular elements. Base Brent horizon (red) used as observation surface. (b) Three-dimensional visualization of the predicted failure planes at observation points. Conjugate planes represent the two Coulomb failure planes color coded by the magnitude of the normalized MCSS. (c) Comparison between observed and computed fault strike. (1) Fault map. (2) Computed fault strike using the major approximately north-south (gray) faults and a remote loading with a N80E direction of extension. (d) Comparison between observed and computed fault density. (1) Density of the observed Upper Jurassic (black) faults. (2) Computed fault density. All densities are normalized. Figure modified from Maerten et al., 2006 (Maerten et al., 2006). AAPG@2006, reprinted by permission of the AAPG whose permission is required for further use.

fields. The later can have different origins but it is always caused by local deformation such as the one observed around active faults, cavities, wellbore and salt formations for instance. As a direct application of elastic dislocation, Tamagawa and Pollard (2008) (Tamagawa and Pollard, 2008) show that in the Yufutsu field, Japan, nonproductive wells were drilled in the area where the regional stress state prevails, and the most productive well penetrates the area near the tips of active faults, where the stress concentrations lead to enhancements in fracture permeability by opening or shearing.

#### 1.6.2.4 Risk assessment

The design of roads, dams, tunnels and underground repositories to safely store waste requires the conservative assessment of the risks that landslides, natural fracture reactivation and earthquakes might pose. With that respect, researchers and engineers

have efficiently used geomechanics and elastic dislocation to study landslide from a theoretical aspect (Martel, 2004) and to evaluate slope instability of the Corinth Canal, Greece, due to nearby fault activation (Tselentis and Gkika, 2005). Over the past decade, Poly3D/iBem3D has been used to carefully evaluate the potential risk of fracture reactivation over time, during glacial loading and unloading cycles, at the Olkiluoto high-level nuclear waste repository site, Finland (La Pointe et al., 2002; Soliva et al., 2010).

## 1.7 Conclusions

The C computer code Poly3D has been applied to a wide variety of problems in academic and industrial structural geology since 1993, with over 120 published papers that acknowledge use of the code. Now iBem3D, a C++ computer code, provides a new formulation of the three dimensional problem of multiple triangular dislocations arranged to model faults and fractures in an elastic whole- or half-space using the boundary element method. It offers significant enhancements over Poly3D including modularity, an iterative solver, greater model size and complexity, reliability, speed, simplicity, and accuracy. We anticipate that iBem3D will provide structural geologists with an even more versatile tool for solving problems of faulting and fracturing in Earth's brittle crust.

The problem in the calculation of the displacement field under triangular dislocation surfaces in an elastic half space made of superposed angular dislocations has been identified and solved. It was directly linked to the construction of the triangular surface and interpretation of the solid angle used to define the Burgers's function $\phi$.

## 1.8 Acknowledgments

The authors would like to thank M. David Barnett and Huajian Gao of Stanford University, Department of Material Sciences for their help in understanding the dislocation theory. We would also like to thanks all the iBem3D and Poly3D users who contributed over a decade to make this code even more stable by reporting problems.

# References


Akoglu, A. M., Cakir, Z., Meghraoui, M., Belabbes, S., El Alami, S. O., Ergintav, S., and Akyuz, H. S. (2006). The 1994-2004 al hoceima (morocco) earthquake sequence: Conjugate fault ruptures deduced from insar. *Earth and Planetary Science Letters*, 252:467–480.

Allward-Fiore, P. (2006). *3D characterization and mechanics of brittle deformation in thrust fault related folds*. PhD thesis, Stanford University, CA, USA.

Bai, T., Maerten, L., Gross, M. R., and Aydin, A. (2002). Orthogonal cross joints: Do they imply a regional stress rotation? *Journal of Structural Geology*, 24:77–88.

Barnett, D. (1985). The displacement of a triangular dislocation loop. *Phil. Mag. A*, 51:383–387.

Bebendorf, M. (2000). Approximation of boundary element matrices. *Numeri Math*, 86(4):565–589.

Bebendorf, M., editor (2008). *Hierarchical Matrices, a means to efficiently solve elliptic boundary value problems*. Springer, Berlin Heidelberg.

Bebendorf, M. and Rjasanow, S. (2003). Adaptive low-rank approximation of collocation matrices. *Computing*, 86(4):1–24.

Bellahsen, N., Allward-Fiore, P., and Pollard, D. D. (2006). From spatial variation of fracture patterns to fold kinematics: A geomechanical approach. *Geophysical Research Letters*, 33:L02301.

Bilham, R. and King, G. (1989). The morphology of strike slip faults: examples from the san andreas fault, california. *J. Geophys. Res.*, 94:10204–10226.

Bourne, S. J., , Rijkels, A., Stephenson, B. J., and Willemse, E. J. M. (2000). Predictive modeling of naturally fractured reservoirs using geomechanics and flow simulation. *GeoArabia*, 6(1):87–102.

Bourne, S. J. and Willemse, E. J. M. (2001). Elastic stress control on the pattern of tensile fracturing around a small fault network at nash point, uk. *Journal of Structural Geology*, 23:1753–1770.

Brankman, C. M. and Aydin, A. (2004). Uplift and contractional deformation along a segmented strike-slip fault system: the gargano promontory, southern italy. *Journal of Structural Geology*, 26:807–824.

Burgers, J. (1939). Internal strains in solids. *Proc. Acad. Science*, 42:293.

Burgmann, R., Schmidt, D. A., Nadeau, R. M., D'Alessio, M., Fielding, E. J., Lawrence, S., Manaker, D., McEvilly, T., and Murray, M. H. (2000). Earthquake potential along the northern hayward fault. *Science*, 289:1178–1182.

Cailleau, B., La Femina, P. C., and Dixon, T. H. (2007). Stress accumulation between volcanoes: an explanation for intra-arc earthquakes in nicaragua? *Geophysical Journal International*, 169:1132–1138.

Cakir, Z., Meghraoui, M., Akoglu, A. M., Jabour, N., Belabbes, S., and Ait-Brahim, L. (2006). Surface deformation associated with the mw 6.4, february 24, 2004 al hoceima (morocco) earthquake deduced from insar: Implication for the active tectonics along north africa. *Bulletin of Seismological Society of American*, 96:59–68.

Cheng, L.-W., Lee, J.-C., Hu, J. C., and Chen, H.-Y. (2009). Coseismic and postseismic slip distribution of the 2003 mw = 6.5 chengkung earthquake in eastern taiwan: Elastic modeling from inversion of gps data. *Tectonophysics*, 466:335–343.

Chinnery, M. (1961). The deformation of the ground around surface faults. *Bull. of Seism. Soc. of America*, 51:355–372.

Chinnery, M. (1963). The stress changes that accompany strike-slip faulting. *Bull. of Seism. Soc. of America*, 53:921–932.

Comninou, M. and Dundurs, J. (1975). The angular dislocation in a half space. *Journal of Elasticity*, 5(3):203–216.

Cooke, M. (1997). Fracture localization along faults with spatially varying friction. *J. Geophys. Res.*, 22:425–434.

Crider, J. G. (2001). Oblique slip and the geometry of normal fault linkage: mechanics and a case study from the basin and range in oregon. *Journal of Structural Geology*, 23:1997–2009.

Crider, J. G. and Pollard, D. D. (1998). Fault linkage: Three-dimensional mechanical interaction between echelon normal faults. *Journal of Geophysical Research*, 103:24,373–24,391.

Crouch, S. L. and Starfield, A. M., editors (1983). *Boundary element methods in solid mechanics*. George Allen and Unwin, London.

Dair, L. and Cooke, M. L. (2009). San andreas fault topology through the san gorgonio pass, california. *Geology*, 37:119–122.

Davatzes, N. C. and Aydin, A. (2003). The formation of conjugate normal fault systems in folded sandstone by sequential jointing and shearing. *J. of Geophysical Research*, 108.

Davatzes, N. C., Eichhubl, P., and Aydin, A. (2005). Structural evolution of fault zones in sandstone by multiple deformation mechanisms: Moab fault, southeast utah. *Geological Society of America Bulletin*, 117:135–148.

Davis, P. (1983). Surface deformation associated with a dipping hydrofracture. *J. Geoph. Res.*, 88:5826–5834.

Delaney, P. and Pollard, D. (1981). Deformation of host rocks and flow of magma during growth of minette dikes and breccia-bearing intrusions near ship rock, new mexico. *U.S. Geological Survey Professional Paper*, 1202:61p.

Diez, M., La Femina, P. C., Connor, C. B., Strauch, W., and Tenorio, V. (2005). Evidence for static stress changes triggering the 1999 eruption of cerro negro volcano, nicaragua and regional aftershock sequences. *Geophysical Research Letters*, 32:L04309.

Fielding, E. J., Lundgren, P., Burgmann, R., and Funning, G. J. (2009). Shallow fault-zone dilatancy recovery after the 2003 bam earthquake in iran. *Nature*, 458:64–68.

Fielding, E. J., Wright, T. J., Muller, J. R., Parsons, B. E., and Walker, R. (2004). Aseismic deformation of a fold-and-thrust belt imaged by synthetic aperture radar interferometry near shahdad, southeast iran. *Geology*, 32:577–580.

Grant, J. V. and Kattenhorn, S. A. (2004). Evolution of vertical faults at an extensional plate boundary, southwest iceland. *Journal of Structural Geology*, 26:537–557.

Griffith, W. A. and Cooke, M. L. (2004). Mechanical validation of the three-dimensional intersection geometry between the puente hills blind-thrust system and the whittier fault, los angeles, california. *Bulletin of the Seismological Society of America*, 94:493–505.

Hackbusch, W. (1999). A sparse matrix arithmetic based on h-matrices: Part 1: Introduction to h-matrices. *Computing*, 62:89–108.

Jeyakumaran, M., Rudnicki, J. W., and Keer, L. M. (1992). Modeling slip zones with triangular dislocation elements. *Bulletin of the Seismological Society of America*, 82:2153–2169.

Johnson, K., Hsu, Y., Segall, P., , and Yu, S. (2001). Fault geometry and slip distribution of the 1999 chi-chi, taiwan, earthquake imaged from inversion of gps data. *Geophys. Res. Lett.*, 28:2285–2288.

Jónsson, S., Zebker, H., Segall, P., and Amelung, F. (2002). Fault slip distribution of the 1999 mw 7.1 hector mine, california, earthquake, estimated from satellite radar and gps measurements. *Bull. Seism. Soc. Am.*, 92:1377–1389.

Kattenhorn, S., Aydin, A., and Pollard, D. (2000). Joints at high angles to normal fault strike: an explanation using 3d numerical model of fault perturbated stress field. *Journal of Structural Geology*, 22:1–23.

Kaven, O. (2009). *Geometry and mechanics of three-dimensional faults: implications for slip, aftershocks, and paleostress*. PhD thesis, Stanford University, CA, USA.

Klügel, A., Walter, T. R., Schwarz, S., and Geldmacher, J. (2005). Gravitational spreading causes en-echelon diking along a rift zone of madeira archipelago: an experimental approach and implications for magma transport. *Bulletin of Volcanology*, 68:37–46.

Kreemer, C., Blewitt, G., and Maerten, F. (2006). Co- and postseismic deformation of the 28 march 2005 nias mw 8.7 earthquake from continuous gps data. *Geophysical Research Letters*, 33:L07307.

La Pointe, P., Cladouhos, T., and Follin, S. (2002). Development, application, and evaluation of a methodology to estimate distributed slip on fractures due to future earthquakes for nuclear waste repository performance assessment. *Bulletin of the Seismological Society of America*, 92:923–944.

Lovely, P. J., Pollard, D. D., and Mutlu, O. (2009). Regions of reduced static stress drop near fault tips for large strike-slip earthquakes. *Bulletin of the Seismological Society of America*, 99:1691–1704.

Lundgren, P. and Lu, Z. (2006). Inflation model of uzon caldera, kamchatka, constrained by satellite radar interferometry observations. *Geophysical Research Letters*, 33:L06301.

Ma, X. and Kusznir, N. (1993). Modeling of near-field subsurface displacements for generalized faults and fault arrays. *Journal of structural geology*, 15:1471–1484.

Maerten, F. (2010). Adaptive cross approximation applied to the solution of system of equations and post-processing for 3d elastostatic problems using the boundary element method. *Engineering Analysis with Boundary Elements*, 34:483–491.

Maerten, F. and Maerten, L. (2008a). Iterative 3d bem solver on complex faults geometry using angular dislocation approach in heterogeneous, isotropic elastic whole or half-space. In Brebbia, editor, *Boundary Elements and other Mesh Reduction Methods XXX*, pages 201–208, Southampton. BEM 30, WITpress.

Maerten, F. and Maerten, L. (2008b). Iterative 3d bem solver on complex faults geometry using angular dislocation approach in heterogeneous, isotropic elastic whole or half-space. In Brebbia, editor, *Boundary Elements and other Mesh Reduction Methods XXX*, pages 201–208, Southampton. BEM 30, WITpress.

Maerten, F., Maerten, L., and Cooke, M. (2009). Solving 3d boundary element problems using constrained iterative approach. *Computational Geosciences*.

Maerten, F., Resor, P. G., Pollard, D. D., and Maerten, L. (2005). Inverting for slip on three-dimensional fault surfaces using angular dislocations. *Bulletin of the Seismological Society of America*, 95:1654–1665.

Maerten, L. (2000). Variation in slip on intersectiong normal faults: Implications for paleostress inversion. *Journal of Geophysical Research*, 105(25):553–565.

Maerten, L., Gillepsie, P., and Pollard, D. (2002). Effect of local stress perturbation on secondary fault development. *Journal of Structural Geology*, 24:145153.

Maerten, L., Gillespie, P., and Daniel, J.-M. (2006). 3-d geomechanical modeling for constraint of subseismic fault simulation. *AAPG Bulletin*, 90:1337–1358.

Maerten, L., Willemse, E. J. M., Pollard, D. D., and Rawnsley, K. (1999). Slip distributions on intersecting normal faults. *Journal of Structural Geology*, 21:259–271.

Mansinha, L. and Smylie, D. (1971). The displacement fields of inclined faults. *Bull. Seism. Soc. of America*, 61:4731–4743.

Marshall, S. T. and Cooke, M. L. (2008). Effects of nonplanar fault topology and mechanical interaction on fault-slip distributions in the ventura basin, california. *Bulletin of the Seismological Society of America*, 98:1113–1127.

Martel, S. (1997). Effects of cohesive zones on small faults and implications for secondary fracturing and fault trace geometry. *Journal of Structural Geology*, 19:835–847.

Martel, S. J. (2004). Mechanics of landslide initiation as a shear fracture phenomenon. *Marine Geology*, 203:319–339.

Martel, S. J. and Boger, W. A. (1998). Geometry and mechanics of secondary fracturing around small three-dimensional faults in granitic rock. *Journal of Geophysical Research*, 103:21,299–21,314.

Maruyama, T. (1964). Statical elastic dislocations in an infinite and semi-infinite medium. *Tokyo Daigaku Jishin Kankyoso Iho*, 42:289–368.

Mavko, G. (1982). Fault interaction near hoolister, california. *J. Geoph. Res.*, 87:7807–7816.

Meigs, A. J., Cooke, M. L., and Marshall, S. T. (2008). Using vertical rock uplift patterns to constrain the three-dimensional fault configuration in the los angeles basin. *Bulletin of the Seismological Society of America*, 98:106–123.

Muller, J. R. and Aydin, A. (2004). Rupture progression along discontinuous oblique fault sets: implications for the karadere rupture segment of the 1999 izmit earthquake, and future rupture in the sea of marmara. *Tectonophysics*, 391:283–302.

Muller, J. R. and Aydin, A. (2005). Using geomechanical modeling to constrain the fault geometry within the marmara sea, turkey. *Journal of Geophysical Research*, 110:B03407.

Muller, J. R., Aydin, A., and Maerten, F. (2003). Investigating the transition between the 1967 mudurnu valley and 1999 izmit earthquakes along the north anatolian fault with static stress changes. *Geophysics Journal International*, 154:471–482.

Muller, J. R., Aydin, A., and Wright, T. J. (2006). Using an elastic dislocation model to investigate static coulomb stress change scenarios for earthquake ruptures in the eastern marmara sea region, turkey, buiter, s. j. h. & schreurs, g. (eds). *Geological Society of London Special Publication - Analogue and Numerical Modelling of Crustal-Scale Processes*, 253:397–414.

Mynatt, I., Hilley, G., and Pollard, D. D. (2007). Inferring fault characteristics using fold geometry constrained by airborne laser swath mapping at raplee ridge, utah. *Geophysical Research Letters*, 34:L16315.

Okada, Y. (1985). Surface deformation due to shear and tensile faults in a half-space. *Bulletin of the Seismological Society of America*, 75:1135–1154.

Okada, Y. (1992). Internal deformation due to shear and tensile faults in a half-space. *Bull. Seism. Soc. of America*, 82:1018–1040.

Olson, E. L. and Cooke, M. L. (2005). Application of three fault growth criteria to the puente hills thrust system, los angeles, california, usa. *Journal of Structural Geology*, 27:1765–1777.

Olson, J. and Pollard, D. (1989). Inferring paleostresses from natural fracture patterns: A new method. *Geology*, 17:345–348.

Olson, J. and Pollard, D. (1991). The initiation and growth of en echelon veins. *Journal of Structural Geology*, 13(5):595–608.

Press, F. (1965). Displacements, strains and tilts at tele-seismic distances. *J. Geoph. Res.*, 70:2395–2412.

Price, E. and Bürgmann, R. (2002). Interactions between the landers and hector mine, california, earthquakes from space geodesy, boundary element modeling, and time-dependent friction. *Bull. Seism. Soc. Am.*, 92:1450–1469.

Reinen, L. A. (2008). Numerical models for exploration and visualization of complex geological phenomena in an undergraduate structural geology course. volume 89 (53), pages ED53A–0582. American Geophysical Union, Fall Meeting.

Resor, P. G. (2003). *Deformation associated with continental normal faults*. PhD thesis, Stanford University, CA, USA.

Resor, P. G., Pollard, D. D., Wright, T. J., and Beroza, G. C. (2005). Integrating high-precision aftershock locations and geodetic observations to model coseismic deformation associated with the 1995 kozani-grevena earthquake, greece. *Journal of Geophysical Research*, 110:B09402.

Rigo, A., De Chabalier, J.-B., Meyer, B., and Armijo, R. (2004). The 1995 kozani-grevena (northern greece) earthquake revisited: an improved faulting model from synthetic aperture radar interferometry. *Geophysical Journal International*, 157:727–736.

Savage, H. M. and Cooke, M. L. (2003). Can flat-ramp-flat geometry be inferred from fold shape? *Journal of Structural Geology*, 25:2023–2034.

Savage, J. and Hastie, L. (1966). Surface deformation associated with dip-slip faulting. *J. Geoph. Res.*, 71:4897–4904.

Savage, J. and Hastie, L. (1969). A dislocation model for the fairview peak, nevada, earthquake. *Bull. Seism. Soc. of America*, 59:1936–1948.

Schmidt, D. A., Burgmann, R., Nadeau, R. M., and D'Alessio, M. (2005). Distribution of aseismic slip rate on the hayward fault inferred from seismic and geodetic data. *Journal of Geophysical Research*, 110:1–15.

Sempere, J. and Mac Donald, K. (1986). Overlapping spreading centers : Implications from crack growth simulation by the displacement discontinuity method. *Tectonics*, 5:151–163.

Shackleton, R. and Cooke, M. L. (2007). Is plane-strain a valid assumption in non-cylindrical fault-cored folds? *Journal of Structural Geology*, 29:1229–1240.

Soliva, R., Benedicto, A., and Maerten, L. (2006). Spacing and linkage of confined faults: the importance of mechanical thickness. *Journal of Geophysical Research*, 111.

Soliva, R., Benedicto, A., Schultz, R. A., Maerten, L., and Micarelli, L. (2008). Displacement and interaction of normal fault segments branched at depth: Implications for fault growth and potential earthquake rupture size. *Journal of Structural Geology*, 30:1288–1299.

Soliva, R., Maerten, F., J.P., P., and Auzias, V. (2010). Fault static friction and fracture orientation in extensional relays; insight from field data, photoelasticity and 3d numerical modeling. *In press in Special Edt. of J. Struct. Geol.*

Steketee, J. (1958a). On volterra's dislocations in a semi-infinite elastic medium. *Can. J. Physics*, 36:192–205.

Steketee, J. (1958b). Some geophysical applications of the elasticity theory of dislocations. *Can. J. Physics*, 36:1168–1198.

Tamagawa, T. and Pollard, D. D. (2008). Fracture permeability created by perturbed stress fields around active faults in a fractured basement reservoir. *American Association of Petroleum Geologists*, 92:743–764.

Thomas, A. L. (1993). Poly3d: a three-dimensional, polygonal element, displacement discontinuity boundary element computer program with applications to fractures, faults, and cavities in the earth's crust. Master's thesis, Stanford University.

Tselentis, G.-A. and Gkika, F. (2005). Boundary element slope instability modeling of corinth canal, greece, due to nearby faults activation. *Coastal Engineering*, 78:313–322.

Walter, T. R. (2007). How a tectonic earthquake may wake up volcanoes: Stress transfer during the 1996 earthquake-eruption sequence at the karymsky volcanic group, kamchatka. *Earth and Planetary Science Letters*, 264:347–359.

Walter, T. R. and Amelung, F. (2006). Volcano-earthquake interaction at mauna loa volcano, hawaii. *Journal of Geophysical Research*, 111:B05204.

Walter, T. R. and Amelung, F. (2007). Volcanic eruptions following m 9 megathrust earthquakes: Implications for the sumatra-andaman volcanoes. *Geology*, 35:539–542.

Weertman, J. and Weertman, J. (1964). *Elementary Dislocation Theory*. Macmillan Co.

White, I. R. and Crider, J. G. (2006). Extensional fault-propagation folds: mechanical models and observations from the modoc plateau, northeastern california. *Journal of Structural Geology*, 28:1352–1370.

Willemse, E. J. M. and Pollard, D. D. (2000). Normal fault growth: evolution of tipline shapes and slip distribution. *Aspects of Tectonic Faulting, Springer -Verlag, Berlin*, Lehner, F.K. and Urai, J.L. (eds.):193–226.

Willemse, E. J. M., Pollard, D. D., and Aydin, A. (1996). Three-dimensional analyses of slip distributions on normal fault arrays with consequences for fault scaling. *J. Struct. Geol.*, 18:295–309.

Willemse, J. M. (1997). Segmented normal faults: Correspondence between three-dimensional mechanical models and field data. *Journal of Geophysical Research*, 102:675–692.

Wong, G. and Barnett, D. (1984). A dislocation method for solvinf 3d crack and inclusion problems in linear elastic solids. In B. A. Bilby, K. J. M. and Willis, J. R., editors, *Fundamentals of Deformation and Fracture*, pages 417–438. Eshelby Memorial Symposium Sheffield, Cambridge University Press.

Wriggers, P. (2002). *Computational Contact Mechanics*. J. Wiley and sons, New York.

Wu, H. and Pollard, D. (1995). An experimental study of the relationships between joint spacing and layer thickness. *Journal of Structural Geology*, 16(6):887–905.

Yoffe, E. (1960). The angular dislocation. *Phil. Mag.*, 5:161–175.

Yun, S. H., Segall, P., and Zebker, H. (2006). Constraints on magma chamber geometry at sierra negra volcano, galapagos islands, based on insar observations. *Journal of Volcanology and Geothermal Research*, 150:232–243.

Zhang, L., Wu, J. C., Ge, L. L., Ding, X. L., and Chen, Y. L. (2008). Determining fault slip distribution of the chi-chi taiwan earthquake with gps and insar data using triangular dislocation elements. *Journal of Geodynamics*, 45.

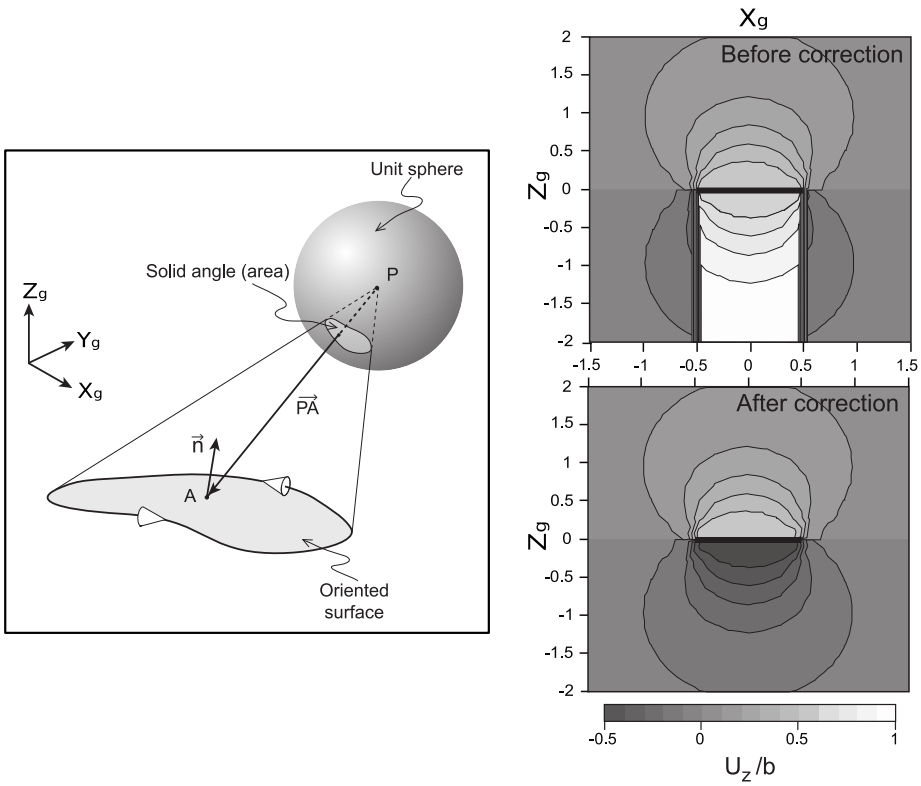


FIGURE 1.13: Shadow's effect correction. Left: representation of the solid angle at point $P$ due to a triangular dislocation loop at point $A$. Right: Displacement field computed under an horizontal dislocation before the correction (top) and after the correction (bottom)

## 1.9 Appendix: *Shadow effect correction*

### 1.9.1 Description of the problem

The dislocation surface is represented mathematically by the multivalued terms found in the displacement field expressions derived from Burgers' function $\phi$. At any point $M(x_1, y_1, z_1)$ the function $\phi$ has a value proportional to the solid angle $\Omega$ subtended at $M$ by the dislocation surface. In Fig. 1.13, left, a representation of the solid angle, $\Omega$, at point P due to a triangular dislocation loop at point $A$ is illustrated. The solid angle is the projected area of this triangle onto a unit sphere centered at $P$. Depending on which side of the surface of the triangular loop (planar case) the point $P$ is located, the solid angle will be either negative or positive. The sign depends on the orientation of the triangular surface as determined by the normal vector $\mathbf{n}$ associated with it. With the orientation convention given in Fig. 1.13, left, the sign of the solid angle $\Omega$ can be expressed by $-sign(P.A.n)$. Consider a particular component of the Burgers' vector, $\mathbf{b_i}$ , acting in the i-direction. Then, the displacement component $\mathbf{u_i}$ in the i-direction at a point $M$ is written as $\mathbf{u_i} = \mathbf{b_i}\phi + \mathbf{f(M)}$, where $f(M)$ is a function of the position of $M$

and is independent of $\phi$ (Burgers, 1939). Thus, a value $\mathbf{b_i}$ is added to the displacement component at $x = 0$ for any path that passes into the paper between the positive $z_1$ and $z_2$ axes.

For the case where the point $P$ is inside the triangular prism, the solid angle $\Omega_1$ is positive and it does not represent the solid angle associated with the triangular dislocation surface. In this region, the construction of the solid angle is not correct. Indeed, it is the solid angle, $\Omega_2$ , complementary of the solid angle $\Omega_1$, that is associated with the triangular dislocation surface. In terms of Burgers' function, for positions under the element we have

$$\phi_{calculated} = \Omega_1/4\pi \tag{1.20}$$

However, to model the triangular surface of dislocation correctly, we should have taken $\phi_{calculated} = \Omega_2/4\pi$. Furthermore, as $\Omega_2$ is negative, because of the orientation of the triangular surface of dislocation and because $\Omega_2$ is the complement of $\Omega_1$, we have $\Omega_1 - \Omega_2 = 4\pi$. Consequently

$$\phi_{calculated} = \frac{\Omega_2 + 4\pi}{4\pi} = \phi_{correct} + 1 \tag{1.21}$$

Thus, the calculated Burgers function will increase by unity for all points inside the prismatic volume and a constant value $\mathbf{b_i}$ will be added to the displacement component in the i-direction

$$\mathbf{u_i} = \mathbf{b_i}(\phi + \mathbf{1}) + \mathbf{f(M)} \tag{1.22}$$

### 1.9.2 Solution of the problem

It has been found that a constant value $b_i$ must be subtracted from the $u_i$ component of displacement for all points inside the prismatic semi-infinite volume defined by the downward projection of a triangular surface with a tipline made of the non-vertical edges of biangular dislocations. This correction must be implemented in order to create a triangular surface of displacement discontinuity and can be interpreted as the removal of rigid body translation.

#### 1.9.2.1 Corrective displacement for observation points

The displacement computed at any observation point p in the elastic field is given by:

$$\mathbf{u_p} = \sum_{\mathbf{e}} \mathbf{U_e b_e} \tag{1.23}$$

where $\mathbf{U_e}$ is the displacement influence coefficients due to the element $e$ at point $p$, and $\mathbf{b_e}$ the Burgers vector of element $e$. The shadow effect at $p$ due to a given element $e$ is corrected by adding to the computed displacement, the Burgers vector $\mathbf{b_e}$ of the element $e$ expressed into the global coordinate system. Computed displacement at $p$ receives such correction from an element $e$ if $p$ lies directly under the rigid body of $e$. The sign of the correction is related to the orientation of the normal of $e$ relative to the global coordinate system. If the normal has a positive side-up, the correction has to be subtracted to the displacement vector, otherwise it has to be added. The Burgers vector $\mathbf{b_e}$ is originally expressed in element local coordinate system, and equation $\tilde{\mathbf{b}}_\mathbf{e} = \mathbf{R_e b_e}$ allows its transformation to the global coordinate system. $\mathbf{R_e}$ represents the element matrix rotation from local to global coordinate system. Therefore, $\mathbf{u_p}$ must be corrected by the following equation:

$$\mathbf{u_p} \equiv \mathbf{u_p} - \sum_{\mathbf{e}} \delta_{\mathbf{pe}} \mathbf{R_e b_e} = \mathbf{u_p} - \sum_{\mathbf{e}} \delta_{\mathbf{pe}} \tilde{\mathbf{b}}_\mathbf{e} \tag{1.24}$$

where $\delta_{pe}$ is an extended Kronecker delta which takes the values:

$$\delta_{pe} = \begin{cases} 0 & \text{if p is outside the prismatic semi-infinite volume of e} \\ -1 & \text{if p is inside the prismatic semi-infinite volume of e } \textit{and} \text{ e has a normal side up} \\ +1 & \text{if p is inside the prismatic semi-infinite volume of e } \textit{and} \text{ e has a normal side down} \end{cases} \tag{1.25}$$

Incorporating equations (1.24) in (1.23) to take into account data points that received the "Shadow Effect" correction, gives:

$$\mathbf{u_p} = \sum_{e} (\mathbf{U_{pe}} - \delta_{\mathbf{pe}} \mathbf{R_e}) \mathbf{b_e} = \sum_{\mathbf{e}} \tilde{\mathbf{U}}_{\mathbf{pe}} \mathbf{b_e} \tag{1.26}$$

where $\tilde{\mathbf{U}}_{\mathbf{pe}} = (\mathbf{U_{pe}} - \delta_{\mathbf{pe}} \mathbf{R_e})$ is the corrected displacement influence matrix at field point $p$ due to source element $e$. Consequently, when computing the displacement vector $\mathbf{u_p}$ at any observation point $p$, one must use the corrected displacement influence matrix $\tilde{\mathbf{U}}_{\mathbf{pe}}$ instead of $\mathbf{U_{pe}}$.

Applying this correction, we calculate the displacement field as illustrated in Fig.1.13 (right). This simple correction may be applied for any boundary condition.

#### 1.9.2.2 Corrective displacement for triangular elements

For a triangular element $e$, the computed displacement $\mathbf{u_e}$ is discontinuous while going from one side to the other. In order to compute $\mathbf{u_e^+}$, the displacement on the positive side of the element, an infinitesimal shift $\xi$ of the element's center $c_e$ along its normal $\mathbf{n_e}$ is applied (equation (1.27)).

$$c_e^+ = c_e + \xi \mathbf{n_e}, \qquad \text{with} \quad 0 < \xi \ll 1. \tag{1.27}$$

This ensure that the displacement will be effectively computed onto the positive side of the element. Then, the same corrective procedure used for the observation points is applied.

# CHAPTER 2

# Solving 3D boundary element problems using constrained iterative approach

F. Maerten[1,2], L. Maerten[1], M. Cooke[3]

(1) Igeoss, Montpellier, FRANCE
(2) University of Montpellier II, Geosciences, FRANCE
(3) University of Massashussetts, Amherst, USA

Computational Geosciences (in press), 2009,
DOI: 10.1007/s10596-009-9170-x



**Preamble**

In this chapter, we use an iterative approach that leads to three major enhancements. First, the model complexity decreases from $O(n^3)$ to $O(n^2)$. Second, the resolution of the system of equations and the post-processing at observation grids can easily be parallelized on multi-core architectures. And third, adding inequality constraints on traction

(e.g. static Coulomb friction) and displacement (e.g. non-interpenetration of the elements) can be implemented in a simple way using this formulation.

## About...

Laurent Maerten participated in the testing of the new functionalities, and Michele Cooke did a comparison with her 2D code **Fric2D**. She also reviewed the manuscript before submission.

## Article Outline

## 2.1 Résumé

Certains des défis majeurs pour les géophysiciens et géologues structuralistes qui utilisent ou développent des codes d'éléments frontières en trois dimensions (3D-BEM) sont: (i) réduire la quantité de mémoire nécessaire pour résoudre de grands systèmes d'équations à matrices denses, et (ii) d'incorporer des contraintes inégalitaires sur les forces (TIC) et sur les déplacements (DIC). Ce dernier a deux buts: en premier lieu, par exemple, les contraintes inégalitaires peuvent être utilisées pour simuler des glissements par frottement (en utilisant des TICs). Deuxièmement, ces contraintes peuvent empêcher l'interpénétration des éléments tout en permettant le mode d'ouverture (en utilisant des DICs). Nous avons développé une méthode qui intègre simultanément les deux types de fonctionnalité. Nous montrons que l'utilisation d'un solveur itératif approprié évite non seulement l'allocation de mémoire importante pour résoudre le système d'équations (ce qui permet de construire de très grands modèles ainsi que de simplifier la parallélisation sur des processeurs multi-cœurs), mais admet également des fonctionnalités intéressantes telles que l'ajout simple des TICs et DICs. Comparativement aux autres techniques de gestion des contacts (par exemple, les multiplicateurs de Lagrange, la méthode de pénalisation ou de complémentarité), cette nouvelle technique, qui n'utilise pas de procédure d'erreurs et d'essais, apporte plus de souplesse, tout en rendant le système plus stable, moins sujet aux arrondis et sans calcul supplémentaire exessif.

Nous comparons et validons l'utilisation des contraintes inégalitaires avec des solutions analytiques et numériques en 2D.

## 2.2 Abstract

Some major challenges for geophysicists and structural geologists using three-dimensional Boundary Element Method codes (3D-BEM) are: (i) reducing the amount of memory required to solve large and dense systems; and (ii) incorporation of inequality constraints such as traction inequality constraints (TIC) and displacement inequality constraints (DIC). The latter serves two purposes. First, for example, inequality constraints can be used to simulate frictional slip (using TIC). Second, these constraints can prevent element interpenetration while allowing opening mode (using DIC). We have developed a method that simultaneously incorporates both types of functionality of the inequality constraints. We show that the use of an appropriate iterative solver not only avoids the allocation of significant memory for solving the system (allowing very large models computation and simplifying parallelization on multi-core processors), but also admits interesting features such as natural incorporation of TICs and DICs. Compared to other techniques of contact management (e.g. Lagrange Multipliers, Penalty Method or Complementarity Problem), this new simple methodology, which does not use any incremental trial and error procedures, brings more flexibility, while making the system more stable and less subject to round-off errors without any computational overhead.
We provide validations and comparisons of the inequality constraints implementation using 2D analytical and numerical solutions. **Keyword**: 3D-BEM, Iterative solver, Inequality constraints, Friction

## 2.3 Introduction

For geophysicists and structural geologists, easy construction and rapid computation of three-dimensional (3D) models composed of multiple frictional faults with complex geometries is fundamental to the study of earthquake triggering (e.g. (Muller et al., 2003)) and fault interactions (e.g. (Maerten, 2000; Dair and Cooke, 2009)), or to determine the deformation associated with displacement discontinuities, such as faults and fractures, in Earth's crust. For example, frictional slip along faults controls fracture orientation at extensional relay zones (e.g. (Auzias, 1995; Ohlmacher and Aydin, 1997; Soliva et al., 2010)), the seismic cycle (e.g. (Tse and Rice, 1986; Zoback et al., 1987)), the distribution and amount of slip along faults (e.g. (Burgmann and Pollard, 1994; Cowie and Scholz, 2003)), development of adjacent damage zone (e.g. (Martel, 1997; Cooke, 1997); Savage and Cooke, in press) and frictional slip along bedding contacts influences layer flexure and fracture/fault propagation (e.g. (Roering et al., 1997; Cooke and Pollard, 1997; Cooke

and Underwood, 2001)). However, these studies that demonstrate the role of fault friction are all two-dimensional investigations of relatively simple fracture networks. Most three-dimensional models of fracture systems are limited to frictionless faults because of the difficulty of implementing frictional sliding along contacts.

Among the existing 3D numerical methods, the Finite and Boundary Element Methods (FEM and BEM, respectively) are the most frequently used for investigation of crustal deformation. Boundary element methods (Crouch and Starfield, 1983) have a great advantage over finite element methods (Hughes et al., 1976) because only the boundaries of objects, and not the entire field, have to be discretized. This makes BEM model more simple to construct than FEM and requires solution of fewer unknowns. The main advantage of FEM over BEM is that the constructed global stiffness matrix, which reflects the node connectivity and boundary conditions, is sparse so that efficient techniques of storage and inversion permit fast determination of the solution. In contrast, in BEM, an element is influenced by all other elements within the model, which results in a dense stiffness matrix. Even though only object boundaries are used in BEM, the stiffness matrix may become very large and plagued with the associated problem of storage, time needed to invert the system of equations, and errors accumulated during the inversion ($n^3$ operations for a matrix of size $n \times n$).

To incorporate inequality constraints, different formulations can be used in both FEM and BEM. Major ones are Penalty Methods (e.g. (Crouch and Starfield, 1983; Wriggers, 2002)), Lagrange Multipliers (e.g. (Hughes et al., 1976)), and Complementarity Methods (e.g. (Kwak and Lee, 1988)). Although the differences between the methods may be negligible for small models, the memory requirements and time needed to find the solution increase considerably with model complexity. Consequently, the results of complex models depends on the robustness of the algorithm used to treat the inequality constraints. In order to understand the benefits and limits of each method, we give a brief review of each.

For BEM, one of the simplest and the most frequently used algorithm for inequality constraints is the penalty method (e.g. (Cooke, 1997)). In this method, an artificial stiffness is defined for each element so that penetration between two contacting boundaries is related to the normal contacting force by an arbitrary penalty factor. This method can suffer from both high structural stiffness that can significantly affect the results and ill-conditioning that worsens as penalty parameters are increased. Sometimes, solutions may fail to converge or may converge to a wrong solution (Mijar and Arora, 2000).

The Lagrange multipliers method is more stable than the penalty method (e.g. (Bathe and Chaudary, 1985)) and is primarily used in FEM. In order to enforce the normal

and tangential displacement inequality constraints, extra variables are introduced in the equations. Additional degrees of freedom make the system of equations much larger, and it is difficult to implement into existing BEM code (Mijar and Arora, 2000; Man, 1994). Furthermore, Lagrange multipliers method requires a continuous change of the number of equations during the system resolution when a non-linear contact problem is simulated (Eterovic and Bathe, 1991; Zhong, 1993).

Complementarity methods have the advantage that all boundary conditions along the contact surface are incorporated into a single variational inequality and any available minimization method can be used to solve the problem. Unlike the other methods, there is no convergence problem, no artificial stiffness parameter, a single formulation can define the boundary conditions and both small and large displacement problems can be solved (De Bremaecker and Ferris, 2000). The method can easily be applied to 3D contact problems with friction (Klarbring, 1986; Klarbring and Bjorkman, 1988). However, the dense matrix defining the system of equations needs to be explicitly constructed, which is something that we want to avoid in order to be able to run large models.

In this paper, we adopt the boundary element method because of the simplicity offered by this method to construct complex models made of multiple faults and fractures. We present a new and simple way to incorporate inequality constraints, such as contact management, within BEM using a block-iterative solver. Compared to other techniques of contact management, this method avoids the addition of new unknowns into the system of equations or the use of additional algorithms. With the new method, there is no overhead for the system to converge toward the solution, no artificial parameters and no incremental loading or trial and error procedures. Furthermore, the proposed iterative solver allows for fast computation and parallelization onto multi-core architectures.

The paper is organized as follows. Section 2.4 briefly presents the Boundary Element Method used as well as the block-iterative solver. Performance and convergence are discussed in sections 2.5 and 2.6, respectively. Finally, section 2.7 is devoted to the contact management (frictionless and static Coulomb friction) along with verifications, comparisons and discussion on the effect of an incremental loading.

## 2.4 System definition

For the boundary element method used here, we adopt the analytical solution of angular dislocation in an elastic whole- or half-space described by Comninou (Comninou and

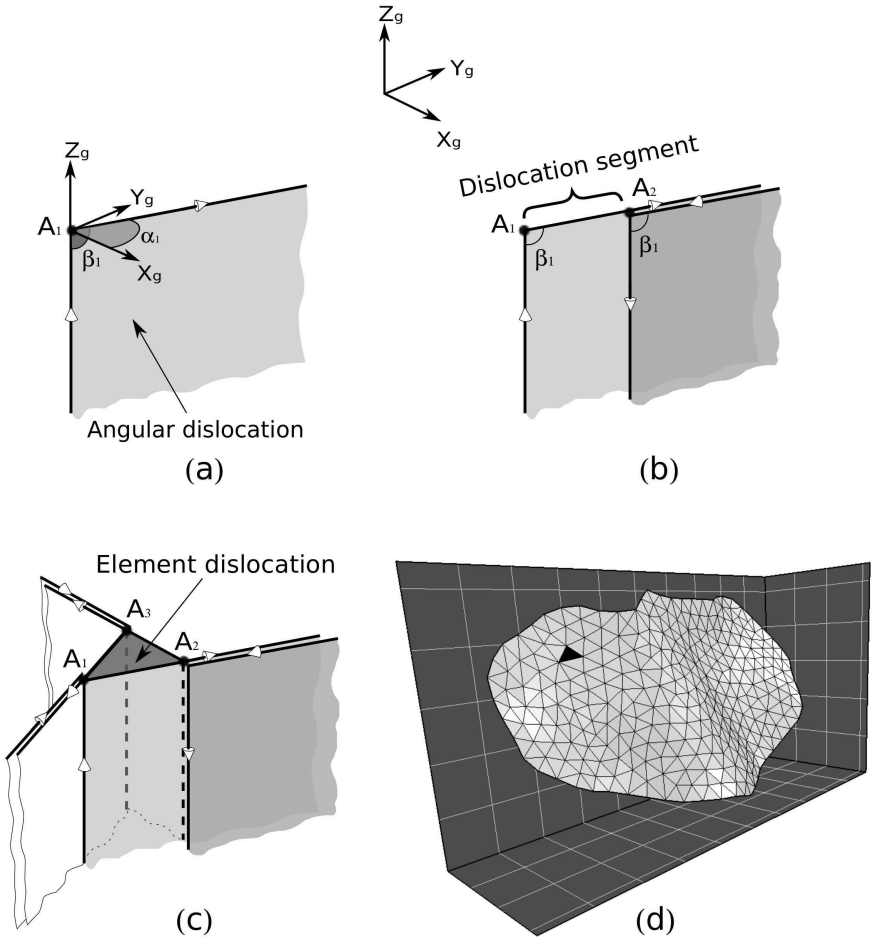


FIGURE 2.1: Construction of a polygonal element. (a) Angular dislocation. (b) Two angular dislocations are used to construct a dislocation segment. (c) Three dislocation segments are superimposed to create a triangular element. (d) Complex surface made of triangular elements

Dundurs, 1975) and implemented in the code Poly3D ((Thomas, 1993), Maerten et al., in preparation). A dislocation segment is defined as the superposition of two angular dislocations, and a polygonal element is then constructed as a sum of dislocations segments (Fig. 2.1). Mixed traction-displacement boundary conditions can be used for each constitutive element of the model. When traction boundary conditions are specified, we solve for the corresponding unknown displacement discontinuity. As soon as all displacement discontinuities are known, stress, strain and displacement can be computed at any observation point within the elastic field as a post-process.

The following conventions are adopted throughout this paper: compression is negative and a positive normal displacement means opening mode. Bold variables are for vectors or matrices, and for any variable $\mathbf{V}$ written $\mathbf{V}_{a,b}$, $a$ and $b$ are for element and vector/matrix index respectively.

### 2.4.1 Boundary Element formulation

Given a point $M$ in the elastic body, the displacement $\mathring{\mathbf{d}}$ due to an angular dislocation $(A_1, \alpha_1, \beta_1)$ at point $A_1$ is given by (see Fig. 2.1a)

$$\mathring{\mathbf{d}}(M) = \mathring{\mathbf{U}}(M, A_1, \alpha_1, \beta_1)\mathbf{u} \tag{2.1}$$

and is a linear function of the Burgers vector, $\mathbf{u}$, or displacement discontinuity vector. Angles $\alpha_1$ and $\beta_1$ are the trend and plunge of the angular dislocation at point $A_1$, respectively. Coefficients of the matrix $\mathring{\mathbf{U}}$ are directly given by Comninou and Dundurs (Comninou and Dundurs, 1975). A bi-angular dislocation, having two vertical legs, perpendicular to the free surface, is then constructed from two angular dislocations $(A_1, \alpha_1, \beta_1)$ and $(A_2, \alpha_1, \beta_1)$ (Fig. 2.1b). The total displacement at point $M$ is simply the superposition of the two angular dislocation contributions

$$\begin{aligned} \bar{\mathbf{d}}(M) &= [\mathring{\mathbf{U}}(M, A_1, \alpha_1, \beta_1) - \mathring{\mathbf{U}}(M, A_2, \alpha_1, \beta_1)]\mathbf{u} \\ &= \bar{\mathbf{U}}\mathbf{u} \end{aligned} \tag{2.2}$$

Using the same process of superposition, a triangular element $\{A_1, A_2, A_3\}$ (or a polygonal element in the general case) is built with three bi-angular dislocations (Fig. 2.1c), where the legs under each vertex have been canceled, leaving a displacement discontinuity only in the triangle. The total displacement at point $M$ resulting from a triangular dislocation made of three dislocation segments, is therefore given by

$$\begin{aligned} \mathbf{d}(\mathbf{M}) &= \sum_{i=1}^{3} \bar{\mathbf{U}}(M, A_i, A_{i+1}, \alpha_i, \beta_i)\mathbf{u} \\ &= \mathbf{U}\mathbf{u} \end{aligned} \tag{2.3}$$

Once the displacement of a triangular element is known, the total solution at a point $M$ is recovered by considering the influence of all triangular elements comprising the model.

Similarly, the strain field at point $M$, due to triangular element, can be computed by partial differentiation of (2.3) by using the linearized *Green-St Venant* strain tensor

$$\epsilon = \frac{\mathbf{1}}{\mathbf{2}}(\nabla\mathbf{d} + \nabla\mathbf{d}^{\mathbf{T}}) \tag{2.4}$$

where $\nabla \mathbf{d}$ is the deformation gradient tensor. Equation (2.4) leads to the *strain influence matrix* due to an angular dislocation

$$E_{ijk} = \frac{1}{2}\left(\frac{\partial U_{ik}}{\partial x_j} + \frac{\partial U_{jk}}{\partial x_i}\right) \tag{2.5}$$

which relates the strain at $M$ and the element Burgers vector $\mathbf{u}$ by

$$\epsilon(\mathbf{M}) = \mathbf{Eu} \tag{2.6}$$

The stress tensor is given by Hooke's law for infinitesimal deformation as

$$\sigma_{ij} = 2G\epsilon_{ij} + \lambda\epsilon_{kk}\delta_{ij} \tag{2.7}$$

where $G$ is the shear modulus, $\lambda$ is the Lamé's constant, $\delta_{ij}$ is the Kronecker delta, and $\epsilon$ is given by (2.4). Substituting (2.4) into (2.7) and using (2.6) yields the stress $\sigma$ at any point M induced by one triangular dislocation

$$\sigma(\mathbf{M}) = \mathbf{Su} \tag{2.8}$$

$\mathbf{S}$ is called the *stress influence matrix* at a point $M$ due to a triangular dislocation. The element traction can now be defined using Cauchy's formula by resolving the stress tensor $\sigma$ onto the triangular element plane using its centroid as the collocation point

$$\mathbf{t} = \sigma\mathbf{n} \tag{2.9}$$

where $n$ represents the element's normal. Combining (2.9) and (2.8), leads to

$$\mathbf{t} = \mathbf{Tu} \tag{2.10}$$

where $\mathbf{T} = \mathbf{Sn}$ is the *traction influence matrix*. Using the traction formulation for a triangular dislocation, the total traction at the center of a triangular element is simply the superposition of all tractions induced by the triangular elements within the elastic body. A system of linear equations can then be constructed to solve for the unknowns Burgers vector components

$$\{\mathbf{t}\} = [\mathbf{T}]\{\mathbf{u}\} \tag{2.11}$$

In equation (2.11), $\{\mathbf{t}\}$ represents the column of the initially prescribed traction vector components of the triangular dislocations, $[\mathbf{T}]$ is a *dense matrix* of traction influence coefficients, and $\{\mathbf{u}\}$ the column of the unknowns Burgers vector components.

### 2.4.2 Block relaxation scheme

To solve the system of equations, we use an iterative method that consists of calculating successive corrections and can be put in the framework of the successive subspace correction method (Xu, 1992). This can be done using a simple relaxation method (such as a Gauss-Seidel or Jacobi) where equations from the system $a_{ij}x_j = b_i$ are traversed one by one, and for the $i^{th}$ equation, the unknown value $x_i$ is obtained by pretending that all other variables $x_j$ for $j \neq i$ are known. This approach produces the following update scheme for the variable $x_i$

$$x_i = \frac{1}{a_{ii}}(b_i - \sum_{j \neq i} a_{ij}x_j) \tag{2.12}$$

or

$$x_i = x_i + \frac{1}{a_{ii}}(b_i - \sum_{j} a_{ij}x_j) \tag{2.13}$$

where $a_{ii}$ are scalars different from zero (the formulation (2.12) will be used in the remaining of the paper). It has been proved (Golub and Van Loan, 1996) that this scheme converges if and only if the system is strictly diagonal dominant, i.e $\forall i, |a_{ii}| > \sum_{j \neq i} |a_{ij}|$. Note that it is also possible to speed up the convergence by using a SOR (Successive Over Relaxation) version (Golub and Van Loan, 1996).

In the method developed here, the central strategy of the modified iterative solver consists of traversing the system by groups of equations instead of one by one; each group corresponds to the equations of a given triangular element. This scheme is usually called a "block relaxation scheme" (Saad, 1996), where the update reflects a sub-vector of the solution vector, instead of only one component (called "point relaxation scheme"). Consequently, coefficients $a_{ij}$ are no longer scalars but squared matrices of size the number of unknowns attached to the considered element.

Let $\mathbf{Tu} + \mathbf{t}^0 = 0$ be the system of equations to solve (e.g. equilibrium equations), where $\mathbf{T}$ is a stencil operator representing the Green's function coefficients on unstructured meshes, $\mathbf{u}$ the numerical solution and $\mathbf{t}^0$ the discretized forcing function. For a discrete model $S$ made of $N$ (triangular) elements, the system of equations can be rewritten for a given triangular element $e$ as

$$\sum_{f \in S} \mathbf{T}_{ef}\mathbf{u}_f + \mathbf{t}^0_e = 0 \tag{2.14}$$

with $\mathbf{T}_{ef}$ being the matrix of Green's functions at element centroid $e$ (*"field"*) due to element $f$ (*"source"*) in $e$ local coordinate system.

Equations for an element $e$ represent one to three lines of the global system $\mathbf{Tu} + \mathbf{t}^0 = 0$ (determined by the number of unknown displacement components). Equation (2.14) can

now be expanded as follows to give the solution for the element $e$

$$\mathbf{u}_e = -\mathbf{T}_{ee}^{-1}\{\mathbf{t}_e^0 + \sum_{f \in S-\{e\}} \mathbf{T}_{ef}\mathbf{u}_f\} \tag{2.15}$$

if we suppose that the self-effect Green's function $\mathbf{T}_{ee}$ is non-singular. Recall that solving equation (2.15) for an element $e$ depends on the previously computed values $\mathbf{u}_f$ for elements $f \in S - \{e\}$, and the initially prescribed boundary value $\mathbf{t}_e^0$. In other words, solving equation (2.15) for an element $e$ at a given iteration, means that all other constitutive elements $f$ are considered with prescribed displacement boundary conditions, i.e. by pretending that $\mathbf{u}_f$ are known.

Solving the entire system is trivial since we have to loop over all the elements, and for a current element $e$, we apply equation (2.15) to compute the unknown displacement discontinuity components. Because the solution for an element $e$ depends on the previously computed values on the other elements, the initial guess of the solution for the whole system will condition the speed of the convergence toward the final solution.

For the purpose of this work, the $\mathbf{T}$ Green's functions used here are traction influence functions (as described in section 2.4.1, equation (2.10)) and $\mathbf{t}^0$ is the initially prescribed traction vector onto the elements, while $\mathbf{u}$ is the resulting displacement discontinuity vector or Burgers vector. Note that alternative Green's functions, such as the displacement-discontinuity/strain/stress, can also be used for the methodology described above.
Equation (2.15) can be rewritten in a more compact form

$$\mathbf{u}_e = -\mathbf{T}_{ee}^{-1}\{\mathbf{t}_e^0 + \mathbf{t}_{ef}\} = -\mathbf{T}_{ee}^{-1}\mathbf{t}_e \tag{2.16}$$

in which $\mathbf{t}_{ef} = \sum_{f \in S-\{e\}} \mathbf{T}_{ef}\mathbf{u}_f$ is the superposition of the traction vectors induced by all the other triangular elements within the elastic field (induced traction), and $\mathbf{T}_{ee}^{-1}$ is called the inverse self-effect traction influence matrix for element $e$. The initial boundary value, $\mathbf{t}_e^0$, is the resolved far field stress onto the element $e$ in its local coordinate system. The vector $\mathbf{t_e} = \mathbf{t_e^0} + \mathbf{t_{ef}}$ is called the *total traction* and is defined as the sum of the initial and induced traction for a given element $e$ (Crouch and Starfield, 1983).
The Gauss-Seidel iterative solver is presented in algorithm (2.1). $\mathbf{u}_{prev}$ represents the computed displacement discontinuity for the current element $e$ at the previous iteration, and *tol* is the tolerance of the iterative solver

**forall** $e \in S$ **do**
  compute $\mathbf{T}_{ee}^{-1}$
**end**
**while** $\epsilon > tol$ **do**
  $\epsilon = 0$
  **forall** $e \in S$ **do**
    **Requires**: Traction boundary condition for at least one axis of e
    $\mathbf{u}_{prev}$ = current displacement on e
    $\mathbf{t}_e$ = initial traction on e
    **forall** $e \in S - \{e\}$ **do**
      $\mathbf{t}_e = \mathbf{t}_e + \mathbf{T}_{ef}\mathbf{u}_f$
    **end**
    $\mathbf{u}_e = -\mathbf{T}_{ee}^{-1}\mathbf{t}_e$
    $\epsilon = \epsilon + |(||\mathbf{u}_e||^2 - ||\mathbf{u}_{prev}||^2)/||\mathbf{u}_e||^2|$
    set displacement on e
  **end**
**end**

**Algorithm 2.1**: Solving iteratively the system of equations

## 2.5 Performance

Using this brute iterative solver requires calculating the traction influence matrices at each iteration and for each element, which results in a slow computation similar to a direct solver, even if its complexity is one order less. One way to speed up the computation is to estimate a first guess for the solution by using a coarser model and extrapolate the solution onto the original model. Also, we choose to allocate the influence coefficient matrices of a given element $e$ (the $\mathbf{T}_{ef}$ matrices in equation (2.16)), according to the available Random Access Memory (RAM) of the computer. At the initialization of the solver, each element $e$ will pre-compute and store all $\mathbf{T}_{ef}$. If the RAM is fully used, the remaining matrices, if any, are computed "on the fly". Furthermore, because no matrix inversion is required while the solver is running, single-precision floating-point numbers can be used (4 bytes) to store the $\mathbf{T}_{ef}$ matrices instead of double-precision (8 bytes), saving half of the memory without any lost of precision. If $n$ represents the size of the system to solve (degree of freedom), the complexity of the algorithm (number of operations needed to solve the system) goes from $O(n^3)$, for the classical LU decomposition or Gaussian elimination, to $O(mn^2)$ for the iterative solver, where $m$ is the number of iterations.

This iterative solver also allows us to take advantage of new multi-core processor architectures, by parallelizing the computation onto different threads (where the number of threads k is defined by the number of processors on the mother board times the number of cores for each processor). At the beginning, the system is split into k sub-systems of

| Solver configuration | Solver time (s) | Speedup |
|---|---|---|
| a: Direct (LU) | 1h 25mn | 1 |
| b: Iterative | 1h 13mn | 1 |
| c: (b) + Alloc | 12mn | 7 |
| d: (c) + Guess | 1mn 15s | 68 |
| e: (d) + Thread8 | 14s | 364 |

TABLE 2.1: Time needed to solve a system of 8900 unknowns using different optimizations and a tolerance of $10^{-5}$: (a) direct solver, (b) iterative solver, (c) iterative solver using memory allocation, (d) iterative solver with a guess from a coarser mesh, (e) iterative solver parallelization on 8 threads

close to equal sizes, one for each thread. Consequently, k iterative solvers are run in parallel. There is no need to update the communication between each sub-process during one iteration because they share the same model memory. The only requirement is to update the new displacement onto the elements at the end of each iteration (Jacobi method), in order to avoid read/write conflicts.

It is worth to mention that the complexity of the system can be significantly decreased by using techniques such as the Multipole-Expansion (Rokhlin, 1985; Greengard and Rokhlin, 1987), where fundamental equations are expanded into Taylor series, or $\mathcal{H}$-Matrix (Hackbusch, 1999) where algebraic manipulations of the dense system matrix combined with hierarchical partition tend to make the system sparser for long distance effects. In (Maerten, 2010), we exploit the $\mathcal{H}$-Matrix along with Adaptive Cross Approximation (Bebendorf and Rjasanow, 2003) both to solve a system of equations as well as for the post-processing at observation grids. In our opinion, this method is preferable to the Multipole-Expansion because it is simpler and faster to implement, while giving the same performance. The combination of H-Matrix along with Adaptive Cross Approximation does not rely on the kernel functions before assembling the system matrix, as do multipole methods where changing the kernel requires recoding of the approximant. The approximation is applied to the matrix entries of the system during the construction (algebraic approximation).

Table 2.1 gives an overview of the computation time using different combination of optimizations for a simple model composed of two intersecting normal faults. Models are run on a Intel Bi-Xeon 5345 64 bits quadri-core at 2.33 GHz running Linux Ubuntu 7.10. From this table, it is clear that the first guess combined with the elemental matrices allocation and parallelization play an essential role in the time required to solution.

## 2.6 Convergence

The strict diagonal dominance (SDD) of $\mathbf{T}^{-1}$ (or strict precedence rules) required for convergence by Gauss-Seidel or Jacobi type of iterative solver can be understood by considering that the influence traction matrices, $\mathbf{T}_{ef}$, are functions of both the size of $f$ and the distance from the element source $f$ to the element field $e$; $\mathbf{T}_{ef}$ decreases as this distance increases. Because the self-effect relates the influence of an element on itself, the self-effect has the minimum distance possible and therefore has the maximum coefficients. However, this does not confirm the SDD. For example, when two adjacent elements $e$ and $f$, have a small angle between them, the distance between the two centers can be small enough that SDD is not honored. In order to overcome this problem, the two systems, related to $e$ and $f$, have to be solved simultaneously.

It is interesting to mention that as long as the system is SDD, any arbitrary initial guess will make the solver to converge toward the unique solution (Golub and Van Loan, 1996).

## 2.7 Inequality constraints

At a given iteration and for a given element $e$, equation (2.16) can be worked in two ways. First, the total traction vector $\mathbf{t}_e$ can be modified by inequality constraints if necessary before multiplication by $\mathbf{T}_{ee}^{-1}$ to give $\mathbf{u}_e$. Second, the solution $\mathbf{u}_e$, which is related to displacement, can be modify to respond to user prescribed inequality constraints. We call these options respectively Traction Inequality Constraints or TICs (since they are related to traction), and Displacement Inequality Constraints or DICs. TICs are applied to the elemental induced tractions, functions of the initially prescribed boundary condition for element $e$ and the influence from the other elements, whereas DICs are applied to the elemental displacement discontinuity solution itself. Since we are working with one element at a time during an iteration, it is straight-forward to constrain the traction vector and the displacement solution with inequalities.
The assignment of the TIC and DIC is summarized in algorithm (2.2). Lines 12 and 14 show respectively the assignment of the TICs and DICs. The implementation of inequality constraints is very straightforward, in the sense that simple conditional tests can be inserted for the induced traction vector and/or the displacement discontinuity vector, which is described next.

```
1  forall e ∈ S do
2  |  compute T_ee^-1
3  end
4  while ε > tol do
5  |  ε = 0
6  |  forall e ∈ S do
7  |  |  u_prev = current displacement on e
8  |  |  t_e = initial traction on e
9  |  |  forall e ∈ S − {e} do
10 |  |  |  t_e = t_e + T_ef u_f
11 |  |  end
12 |  |  Apply TICs on t_e
13 |  |  u_e = −T_ee^-1 t_e
14 |  |  Apply DICs on u_e
15 |  |  ε = ε + |(||u_e||^2 − ||u_prev||^2)/||u_e||^2|
16 |  |  set displacement on e
17 |  end
18 end
```

**Algorithm 2.2**: Modified iterative solver algorithm in order to take into account TICs and DICs (lines 12 and 14)

### 2.7.1 Frictionless contact

In the following, $t_{e,n}$ and $u_{e,n}$ denotes the normal component of the total traction and displacement discontinuity vectors respectively for an element $e$. According to the model geometry configuration and the applied stress/strain, some elements will open whereas some others will close. Interpenetration of the side of the discontinuity is not realistic and must be avoided while allowing opening of the discontinuity. This problem of contact detection on boundaries was first formulated by Signorini (Signorini, 1959), and can be expressed in terms of complementarity relations, for an element $e$, on normal traction $t_{e,n}$ and normal displacement $u_{e,n}$ by

$$\begin{cases} u_{e,n} \geq 0 \\ t_{e,n} \geq 0 \\ u_{e,n}.t_{e,n} = 0 \end{cases} \tag{2.17}$$

or in a simple form $u_{e,n} \geq 0 \perp t_{e,n} \geq 0$, where the symbol $\perp$ means that, in addition of the inequalities in $u_{e,n}$ and $t_{e,n}$, one of the them must be null. These three conditions state that if a contact occurs, no interpenetration should take place. Either $u_{e,n} \geq 0$ and consequently $t_{e,n} = 0$, or $t_{e,n} \geq 0$ and in that case we should have $u_{e,n} = 0$. The non-interpenetration inequality constraint can be formulated in a simple way and used on a crack while prescribing normal traction boundary condition. Either a DIC or a TIC

can be employed to model frictionless contact problems as demonstrated in the appendix. These two inequality constraints are described respectively in algorithms (2.3) and (2.4).

**Requires**: Traction boundary condition for the normal axis
**if** $t_{e,n} < 0$ **then**
| $t_{e,n} = 0$
**end**

**Algorithm 2.3**: Non interpenetration using traction formulation

**Requires**: Traction boundary condition for the normal axis
**if** $u_{e,n} < 0$ **then**
| $u_{e,n} = 0$
**end**

**Algorithm 2.4**: Non interpenetration using displacement formulation

By forcing the normal displacement of the element to be zero if stresses are compressive, we imply that the induced traction will be such to prevent overlap. Thus, the total normal traction for an element $e$, after the problem is solved, will be negative according to our sign convention.

To demonstrate this we can take a simple example of one element $e$ with traction boundary conditions for the three axis. This element is subjected to a compressive far field stress ($\sigma^{\mathbf{R}}$) judiciously oriented to encourage interpenetration, and in this configuration $t^0_{e,n} < 0$. In order to avoid interpenetration, the system to solve is defined as

$$\begin{cases} \mathbf{T}_{ee}\mathbf{u}_e + \mathbf{t}^0_e = 0 \\ \text{subject to } u_{e,n} \geq 0 \end{cases} \tag{2.18}$$

with

$$\mathbf{t}^0_e = \mathbf{R}_e \sigma^{\mathbf{R}} \mathbf{n_e} \tag{2.19}$$

and $\mathbf{R}_e$ being the rotation matrix from global coordinate system to element $e$ local coordinate system, and $\mathbf{n}_e$ is its normal. Because the normal displacement is negative (interpenetration occurs), it is set to zero according to the inequality constraint, and we

determine negative total traction in the normal direction, as shown in equation (2.20):

$$\left\{ \begin{array}{l} \mathbf{t}_{e,s} \\ t_{e,n} \end{array} \right\} = \\ \left\{ \begin{array}{l} \mathbf{t}^0_{e,s} \\ t^0_{e,n} \end{array} \right\} + \left[ \begin{array}{ll} \mathbf{T}^{-1}_{ee,s} & 0 \\ 0 & T^{-1}_{ee,n} \end{array} \right] \left\{ \begin{array}{l} \mathbf{u}_{e,s} \\ u_{e,n} = 0 \end{array} \right\} = \\ \left\{ \begin{array}{l} \mathbf{t}^0_{e,s} + \mathbf{T}^{-1}_{ee,s} \mathbf{u}_{e,s} \\ t^0_{e,n} < 0 \end{array} \right\} \tag{2.20}$$

(see equation (2.27) in appendix for the special form of $\mathbf{T}^{-1}_{ee}$)

#### 2.7.1.1 Verification

In order to check the validity of the displacement inequality constraints, we create a model with connected echelon faults subjected to a compressive far field stress oriented along the oblique segments (Fig. 2.2.a). We allow both interpenetration and opening of the segments comprising the fault. To visualize the deformation field around the model, a planar rectangular observation grid cross-cuts the segments (Fig 2.2.a). Displacement is computed at each point of the observation grid, and the grid is deformed according to the computed displacement field.

In this model, horizontal and oblique segments are subjected to interpenetration and opening respectively, as shown in case (1) of Figure 2.2.b, where boundary conditions on triangular elements are set to zero traction for the dip, strike and normal directions.
To prevent interpenetration, a first solution imposes displacement boundary condition for the normal direction on all the segments, which leads to the case (2) of figure 2.2.b, where we effectively avoid interpenetration, but also opening along the oblique segments. A second approach imposes traction boundary conditions along the X- and Y- axis of all the segments, displacement boundary conditions for the Z-axis (normal to the elements) for the horizontal segments (avoiding interpenetration), and normal traction boundary conditions for the oblique segments, allowing opening (Fig 2.2.b, case (3)). This last model is then compared with the use of the DIC $u_z \geq 0$, where all elements have traction boundary conditions for the three axis (Fig. 2.2.b, case (4)). Results of case (3) and (4) are perfectly similar in magnitude and distribution of aperture along the oblique segments (left side of Fig 2.2.b) and no interpenetration occurs along the horizontal segments.

The advantage of using the DIC approach in case (4) compared to case (3), is that no assumption is made on whether segments should be locked or not in the normal direction, allowing us to build complex 3D models.

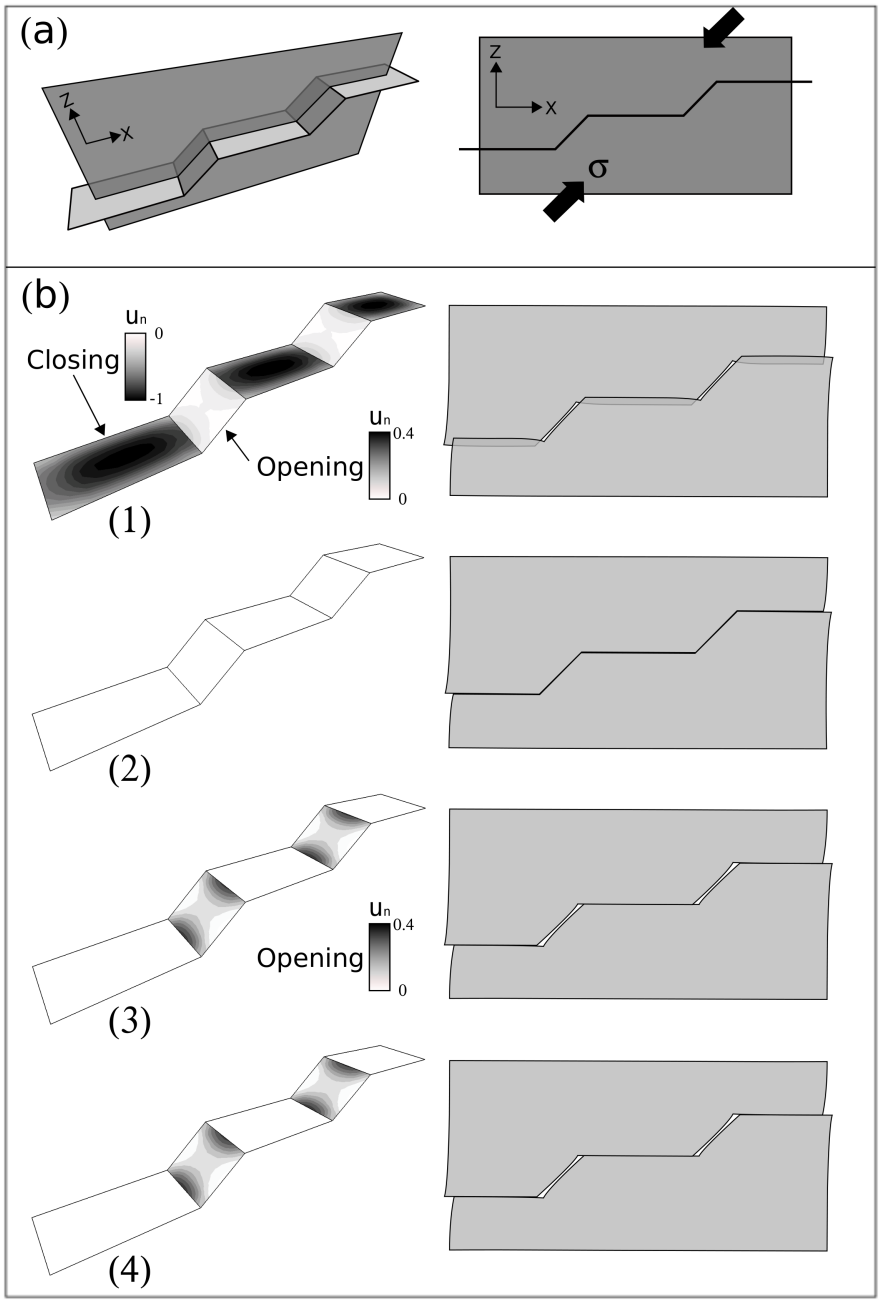


FIGURE 2.2: Verification of the non-interpenetration inequality constraint for a fault with connected echelon segments. (a) Model configuration. (b) Model results for different configurations: (1) all segments are free to slip and to open or close; (2) all segments are free to slip only; (3) horizontal segments are free to slip only, oblique ones are free to slip and to open or close; (4) same as (1) but with the DIC $u_n \geq 0$; Left: normal displacement are plotted. Right: resulting deformed observation grid

### 2.7.2 Static Coulomb friction

In this section, the quasi-static problem of contact with local Coulomb friction is formulated in term of a traction inequality constraint (note that in this paper the Coulomb friction is employed, but any other friction law can be employed). *Static friction* occurs when the tangential velocity at a contact point relative to a point on the opposite side of the discontinuity is zero; otherwise, the friction is called *dynamic friction*.
Static Coulomb friction can be formulated as follows:
Let $\mu$ and $C_o$ being the coefficient of friction and cohesion respectively, for a given polygonal element. Coulomb friction law states that the norm of the shear traction cannot exceed the criterion

$$c(t_{e,n}) = -\mu t_{e,n} + C_o \tag{2.21}$$

where $t_{e,n}$ is the normal traction at element $e$, that is $||\mathbf{t}_{e,s}|| \leq c(t_{e,n})$, where $||.||$ is the $L_2$-norm. If the shear traction is less than the Coulomb friction criteria, no slip occurs ("stick" mode). Otherwise, we have to reduce the shear traction to the value of the criteria ("slip" mode).

Conditions of friction contact can be summarized as

$$\begin{cases} u_{e,n} \geq 0 \perp t_{e,n} \geq 0 & (a) \\ ||\mathbf{t}_{e,s}|| \leq c(t_{e,n}) & (b) \end{cases} \tag{2.22}$$

Condition (2.22.a) maintains a non-interpenetrating contact while condition (2.22.b) adds frictional slip to the contact. Since both conditions can be related to tractions only, a TIC is employed for the description.
Suppose that, for a given iteration and a given element $e$, the total traction $\mathbf{t}_e = \{\mathbf{t}_e^0 + \mathbf{t}_{ef}\}$ is computed prior to multiplication by $\mathbf{T}_{ee}^{-1}$ (see eq. 3). If the normal traction is positive, the element is opening, and the constraint does not apply. On the other hand, if the normal traction is negative (interpenetration occurs), condition (2.22.a) is honored by forcing the normal traction to be zero (see the frictionless case above), and then we check the Coulomb friction criteria. If the norm of the shear traction is less than the criteria, $\mathbf{t}_{e,s}$ is forced to be zero (stick mode). Otherwise, we reduce its norm to be equal to $c(t_{e,n})$. More specifically, the norm of the shear traction can be decomposed into

$$||\mathbf{t}_{e,s}|| = c(t_{e,n}) + \delta t_{e,s} \tag{2.23}$$

where $\delta t_{e,s}$ is the excess shear traction. To remove $\delta t_{e,s}$ from $\mathbf{t}_{e,s}$, we allow a corresponding amount of displacement along the slip vector, defined by

$$\mathbf{u}_e = \mathbf{T}_{ee}^{-1} \left\{ \delta t_{e,s} \frac{\mathbf{t}_{e,s}}{||\mathbf{t}_{e,s}||} \right\} \tag{2.24}$$

This implementation is outlined in algorithm (2.5). Note that no DIC is employed in algorithm (2.5) to prevent interpenetration since this is automatically honored, as seen in the frictionless case (see also appendix). Only one TIC is used.

**Requires**: prescribed traction boundary conditions for the normal axis and at least for the dip or strike axis
**if** $t_{e,n} < 0$ **then**
  $c = -\mu t_{e,n} + C_o$
  **if** $||\mathbf{t}_{e,s}|| > c$ **then**
    $\mathbf{t}_{e,s} = \frac{(||\mathbf{t}_{e,s}|| - c)}{||\mathbf{t}_{e,s}||} \mathbf{t}_{e,s}$
  **else**
    $\mathbf{t}_{e,s} = 0$
  **end**
  $t_{e,n} = 0$
**end**

**Algorithm 2.5**: Static Coulomb friction traction inequality constraint. Note that this algorithm already incorporates the non-interpenetration constraint, as shown in appendix

#### 2.7.2.1 Verification with a 2D analytical solution

The 2D model used by Phan (Phan et al., 2003) is composed of a planar crack of length $2a$, inclined at an angle $\alpha$ from horizontal, with a constant coefficient of friction $\phi$, and subject to an horizontal compressive remote stress $\sigma$ (Figure 2.3.a). Analytical solutions of the normal traction $t_n$, shear traction $\tau_t^c$ and slip magnitude $\Delta u_t$ are given by

$$\begin{cases} t_n = -\sigma \sin^2 \alpha \\ \tau_t^c = \sigma \sin \alpha (\cos \alpha - \sin \alpha \tan \phi) \\ \Delta u_t(\eta) = \frac{4(1-\nu^2)\tau_t^c}{E} \sqrt{a^2 - (\eta - a)^2} \end{cases} \tag{2.25}$$

where $\nu$ is the Poisson's ratio and $E$ the Young's modulus.

In order to remove the boundary effect due to the comparison from 2D to 3D, the 3D model was extended far from the zone of interest (Fig. 2.3.b), where the mesh is denser. Young's modulus and Poisson's ratio are chosen to be 1 and 0.25, respectively. Two different mesh densities are used (Fig. 2.3.c and d) in order to explore the effect of

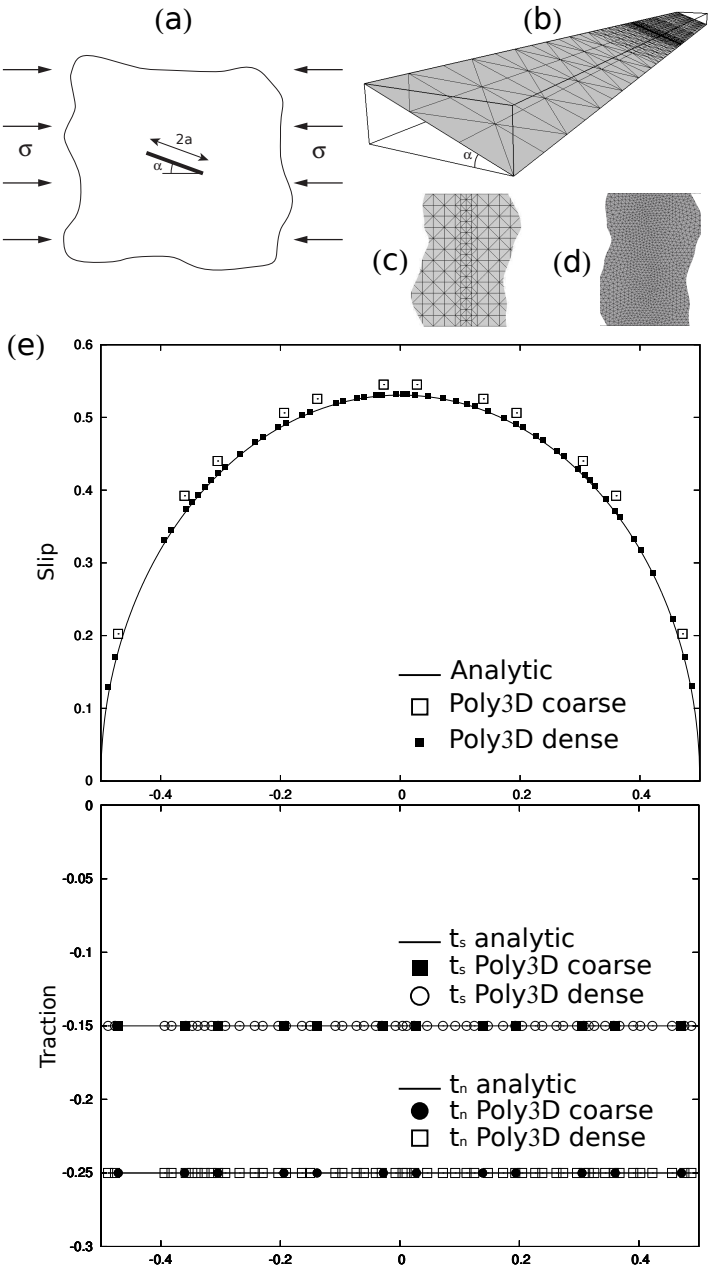


FIGURE 2.3: Comparison of the static Coulomb friction using a TIC and analytical solution of Phan (Phan et al., 2003). (a) 2D model configuration. (b) Corresponding 3D model that has been extended far from the zone of interest. (c) Close view to the coarse mesh around the zone of interest, and (d) dense mesh. (e) Comparison of slip and residual normal and shear traction

discretization. Comparison of the slip and the residual traction components is shown in Fig. 2.3.e. As we increase the mesh density, the slip results approach the analytical solution, whereas the residual traction results remain equal to the solution for both coarse and dense meshes.

#### 2.7.2.2 Comparison with the penalty method

The numerical method, Fric2D, developed by Cooke (Cooke and Pollard, 1997) is a 2D boundary element code derived from Crouch and Starfield (Crouch and Starfield, 1983), where the penalty method is employed to simulate frictional slip. Linear elements of constant displacement discontinuity comprise the fractures, faults and the boundaries to the model. The code utilized two types of elements. Along one set of elements, either the tractions or the displacement discontinuity (i.e. opening or slip) is prescribed. These elements are used for the boundaries and for conditions such as pressure filled cracks and faults with applied stress drop. Along the second type of element the user prescribes constitutive properties rather than tractions or displacement discontinuities. The four constitutive parameters along these elements are cohesion, static friction, normal stiffness and shear stiffness.

The penalty method utilizes these normal and shear stiffnesses to prevent interpenetration of the elements. Very soft values for stiffness will allow some elastic interpenetration of the elements while infinite values of stiffness forbids interpenetration. In practicality, stiffnesses several orders of magnitude greater than the host rock stiffness should be used to minimize interpenetration. One approach for determining appropriate stiffness, is to treat the prescribed stiffness as an effective stiffness equal to the host rock stiffness divided by the thickness of the fault zone (Crouch and Starfield, 1983). In this way, very thin fault zones will have less elastic interpenetration than thick fault zones. Subsequently, this interpenetration simulates the finite contraction across the thickness of the fault zone, which in the model is treated as infinitely thin.

To solve for the deformation in non-linear systems incorporating frictional slip, Fric2D iterates the solution until the percentage of shear traction change along all frictional elements between one iteration and the next is less than a prescribed tolerance (Cooke and Pollard, 1997). Additionally, the loading is applied in multiple monotonic steps to minimize the path dependency of frictional slip. The frictional elements of Fric2D have been used to solve problems of fault growth (Roering et al., 1997; Cooke and Kameda, 2002; Buczkowski and Cooke, 2004; Cooke and Murphy, 2004; Del Castello and Cooke, 2007), deformation along bedding planes (Cooke and Pollard, 1997; Cooke and

Underwood, 2001), and the development of off-fault damage ((Cooke, 1997); Savage and Cooke, in press).

In the models presented in this paper, the normal and shear stiffness were chosen to be 10 orders of magnitude greater than the host rock stiffness to prevent elastic interpenetration. The tolerance is $10^{-4}$, which required fewer than 20 iterations to reach convergence for the models presented here. The first set of models apply the load within one step. The sensitivity of loading step is explored in the next section of the paper.

#### 2.7.2.3 Model 1

The first model reproduces the fault geometry of the analytical case presented in section 2.7.2.1, but with two different friction profiles along the crack, a constant profile with $\mu = 0.6$ (Fig. 2.4), and a linear variation of $\mu$ from zero to one (Fig. 2.5). For the first case, the 2D BEM, 3D BEM and the analytical solution for the displacement and residual traction are plotted. For the second case, only the 2D and 3D BEM are compared. As with the 3D BEM (see Fig. 2.3), mesh density impacts the 2D BEM solution; as we increase the number of elements, we approach the analytical solution more closely. The major difference between the 2D and the 3D BEM solution is that the former needs more elements to approach the analytical solution than the latter (Fig. 2.4 top). For the residual tractions, the coarse and dense meshes give the same result (Fig. 2.4 bottom, where only result from the coarse model is plotted).

#### 2.7.2.4 Model 2

The second model (Fig. 2.6) is composed of two interconnected fault segments making an angle $\beta$. The larger fault, of length $4a$, makes an angle $\alpha$ with respect to the horizontal axis, and the smaller one, of length $2a$, is connected at the middle of the former. A horizontal compressive remote stress is applied to the model with magnitude $\sigma_{xx} = -1$, and a constant friction coefficient $\mu = 0.6$ is used (no cohesion).
Fig. 2.7 and 2.8 compare the results for the main and secondary fault, respectively. Again, no difference between the 2D and 3D BEM is observed for both the displacements and the residual tractions if we use a dense mesh for the 2D BEM.

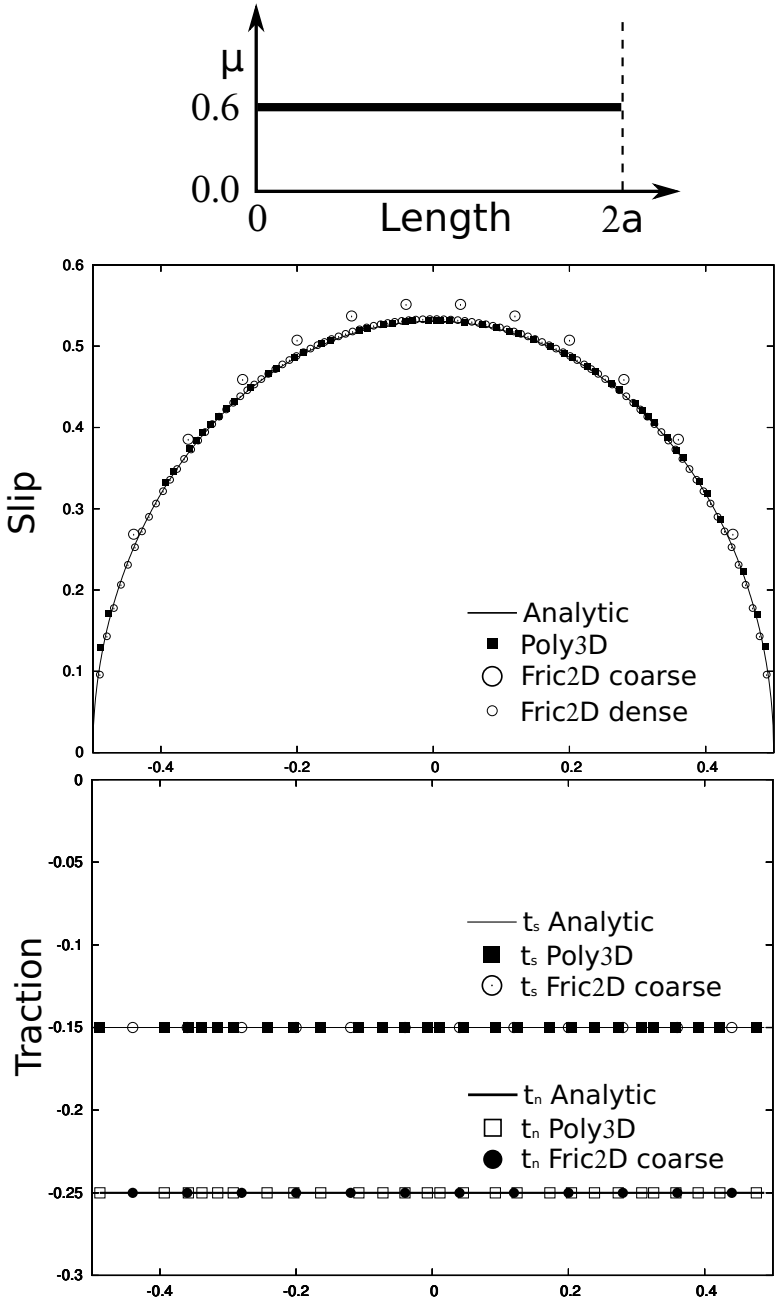


FIGURE 2.4: Constant friction coefficient profile. Comparison of the static Coulomb friction for the 2D BEM code using the penalty method and the method described in this paper (same model as in Fig. 2.3).The 2D BEM slip distribution is plotted for a coarse and dense models, showing the discretization effect

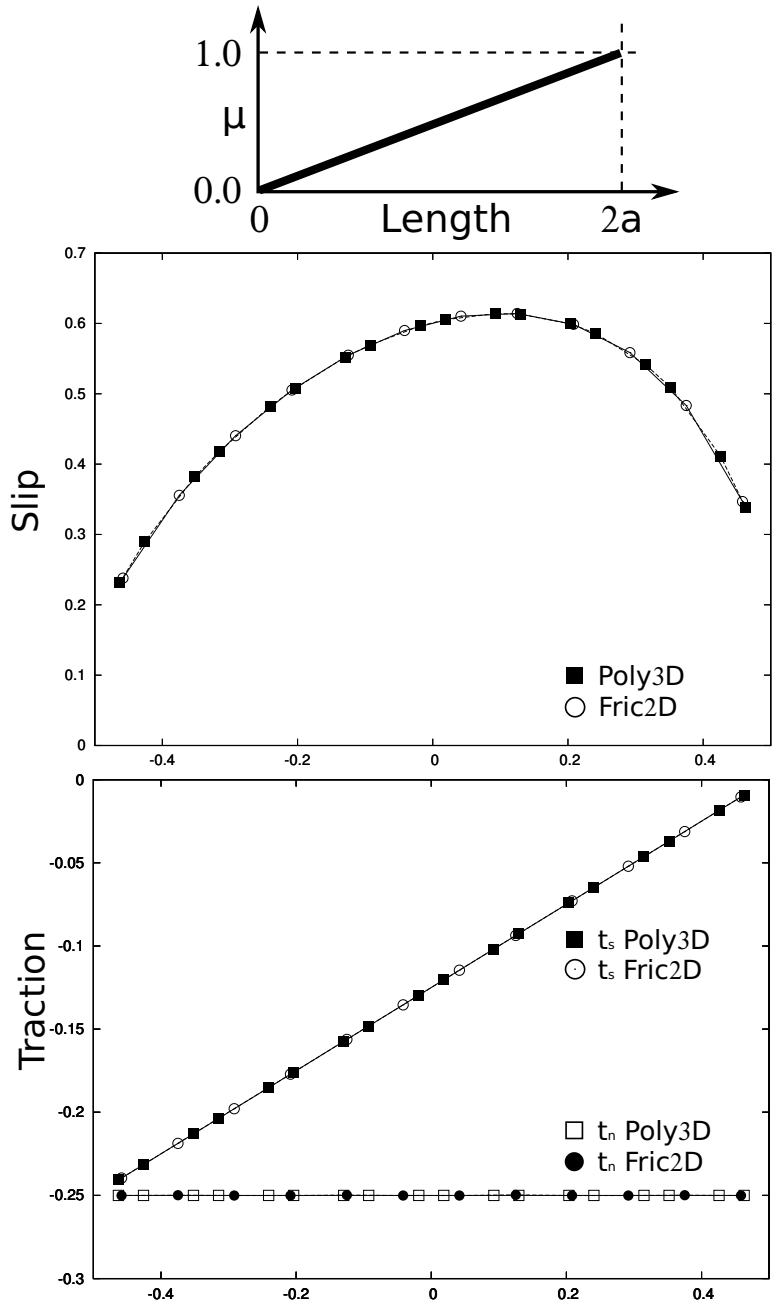


FIGURE 2.5: Linear friction profile. Comparison of the static Coulomb friction for the 2D BEM code using the penalty method and the method described in this paper with a linear variation of the friction coefficient from zero to one

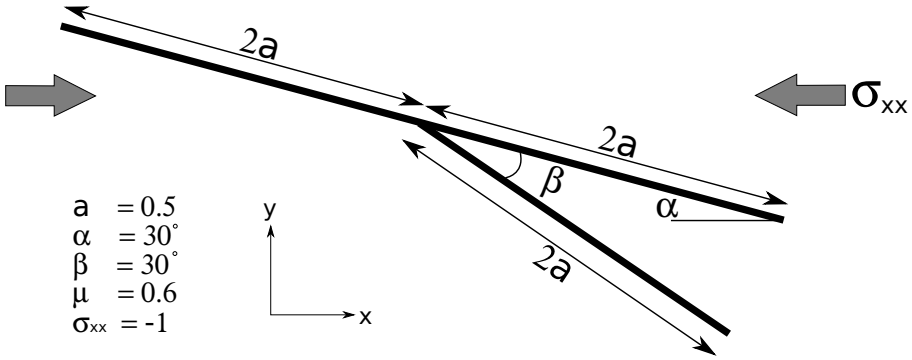


FIGURE 2.6: Branching faults model configuration

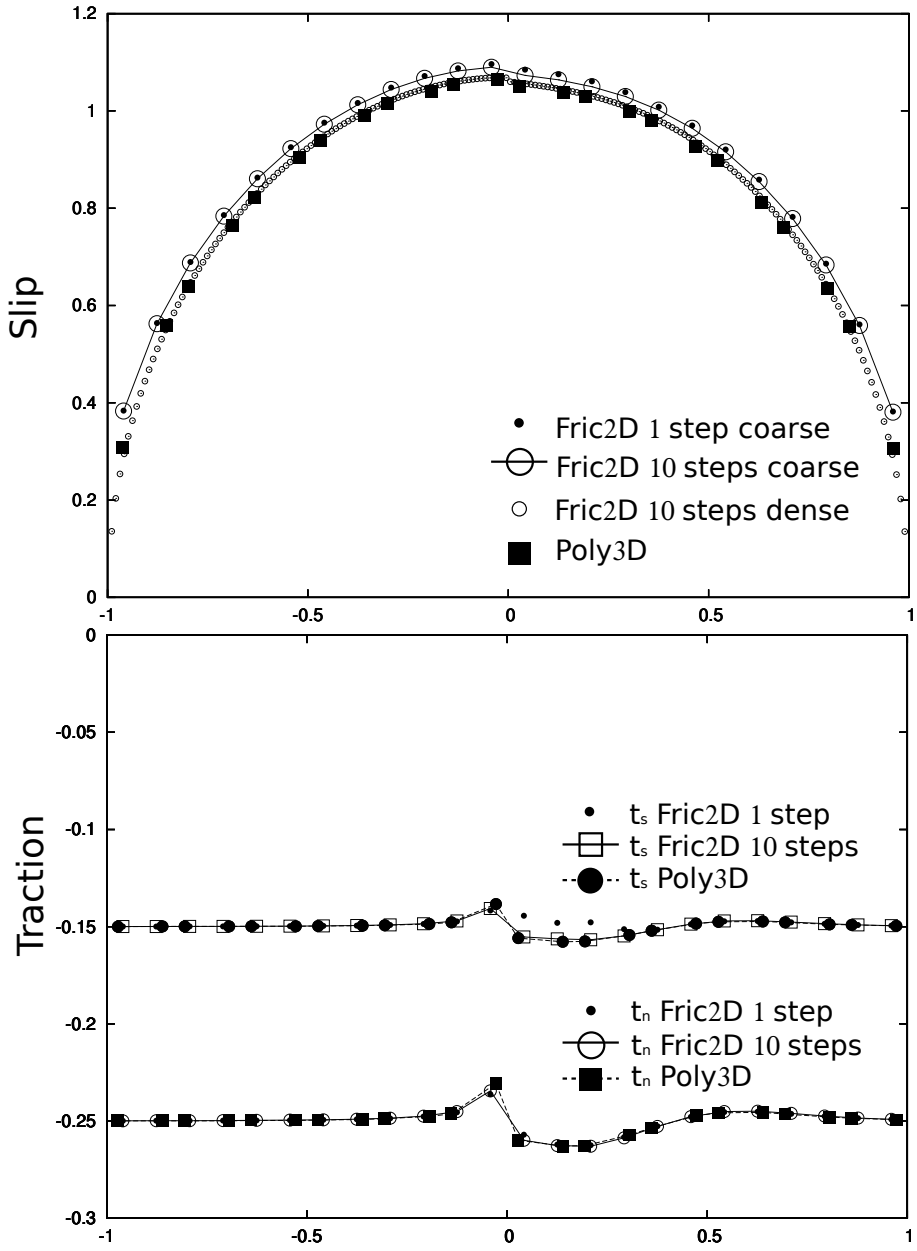


FIGURE 2.7: Main fault of the branching faults model. Comparison of the 2D and 3D BEM code. The 2D BEM slip distribution is plotted for a coarse model with 1 and 10 loading steps and for a dense model with 10 loading steps

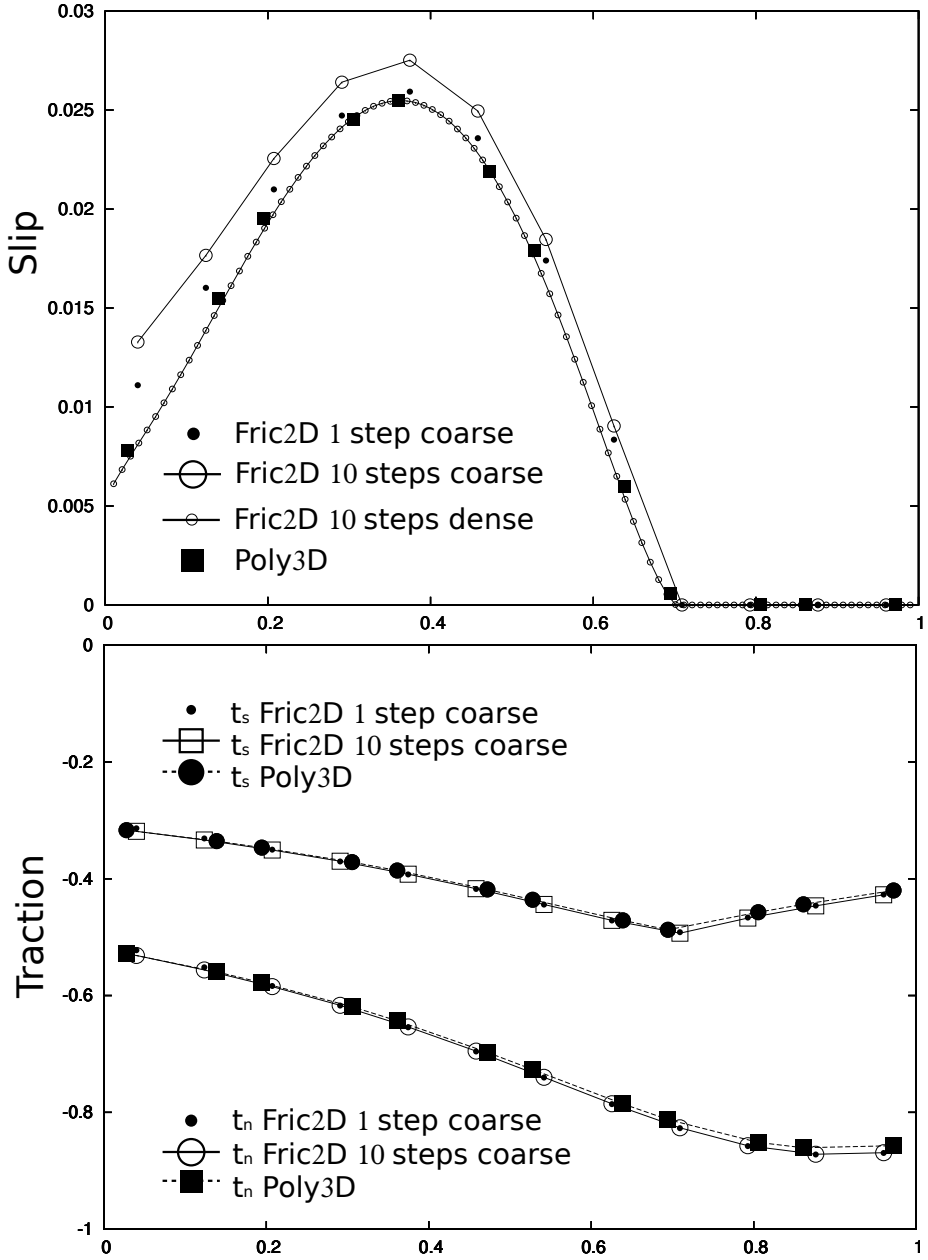


FIGURE 2.8: Secondary fault of the branching faults model. Comparison of the 2D and 3D BEM code. The 2D BEM slip distribution is plotted for a coarse model with 1 and 10 loading steps and for a dense model with 10 loading steps

### 2.7.3 Effect of an incremental remote loading

For previously presented numerical models, the remote loading was applied in one step. In order to investigate the effect of an incremental loading on the result, we ran the same models using multiple loading steps. For the new 3D BEM code, the results for any geometrical configuration are identical to applying the remote loading in one go. This suggests that the successive subspace correction method already incorporates the effect of incremental loading, and therefore, this method does not require this computationally time consuming process.

However, multiple loading increments are needed for the penalty method within the 2D BEM code as shown in the model results from section 2.7.2.4 (Fig. 2.7 and 2.8), where a one and ten step loading increments are compared for coarse mesh models. Specifically, the differences are mostly visible for the residual shear traction on the main fault (Fig. 2.7), where an incremental remote loading approaches the 3D BEM solution more closely (see the residual shear traction $t_s$ onto the main fault in Fig. 2.7).

## 2.8 Conclusion

Using an iterative method to solve a dense system, not only avoids the memory allocation for the dense matrix, but also allows the incorporation of inequality constraints in a simple, efficient and stable way. Implementing this technique avoids the use of additional algorithms to deal with inequality constraints. No new equations are incorporated into the system and no overhead is introduced for the convergence. The definition remains natural and very straight-forward to implement, and does not introduced artificial parameters as with the penalty method. No incremental loading and trial and error procedures are used, and the method provides for constraints that can evolve with time or according to another parameters (such as the cumulative slip for example) if necessary. Furthermore, such a method permits dynamic addition or removal of equations to the system (i.e. adding/removing polygonal elements), without reconstructing the entire system. This can occur, for example, with crack propagation in 3D.

The incorporation of inequality constraints on tractions and displacement now extends the existing wide range of applications of Poly3D. Three-dimensional modeling tools that incorporate frictional sliding along complex networks of fractures faults will enable investigations leading to more accurate estimation of seismic hazard in regions of active faults, better recovery of petroleum reserves from fractured reservoirs, improved access to geothermal energy and reduced costs for remediation of contaminants on fractured aquifers. Furthermore, static friction can be used to model fault cohesive end zone (CEZ) (Martel, 1997; Davatzes and Aydin, 2003; Cooke, 1997), where variation of the friction angle along a fault is used. This new feature can also be used to study frictional fault behaviors while they approach interfaces separating regions of different material properties (Maerten and Maerten, 2008). Finally, displacement inequality constraints can be employed to better constrain linear slip inversion (Maerten et al., 2005), which is part of our current research.

## 2.9 Acknowledgements

We would like to thank the anonymous reviewers for their comments. Special thanks to the Igeoss's consortium members for their support on the development of Poly3D.

## 2.10 Appendix

According to equation (2.16), the traction and displacement discontinuity for a given element $e$ are closely related through the inverse self-effect traction influence matrix $\mathbf{T}_{ee}^{-1}$, and we see that even if it is a complementary problem on traction and displacement, the special form of $\mathbf{T}_{ee}^{-1}$ allows us to formulate the problem using only one TIC by constraining $t_{e,n} \geq 0$, or one DIC by forcing $u_{e,n} \geq 0$. Both approaches are not needed.
Since the DIC formulation is trivial for non-interpenetration, we will consider only the TIC case, and show that forcing $t_{e,n} = 0$ if $t_{e,n} < 0$ is equivalent to imposing $u_{e,n} = 0$. Let $\mathbf{t}_e = \{\mathbf{t}_{e,s}, t_{e,n}\}$ be the components of the total traction vector $\{\mathbf{t}_e^0 + \mathbf{t}_{ef}\}$ from equation (2.16). For the self-effect traction influence matrix $\mathbf{T}_{ee}$ (traction influence matrix from a polygonal element on itself), the coefficients are computed at the element's centroid, which means that all dislocation segments (edges) comprising the element lie in the same plane as the centroid (Fig. 2.1.c), and, in the element local coordinate system (Fig. 2.1.c) , results in zero shearing components for the normal direction (z components of $\mathbf{T}_{ee}$). Therefore, $\mathbf{T}_{ee}$ has the following form

$$\mathbf{T}_{ee} = \begin{bmatrix} t_{ee,11} & t_{ee,12} & 0 \\ t_{ee,21} & t_{ee,22} & 0 \\ 0 & 0 & t_{ee,33} \end{bmatrix} = \begin{bmatrix} \mathbf{T}_{e,s} & 0 \\ 0 & T_{e,n} \end{bmatrix} \tag{2.26}$$

and its inverse being

$$\mathbf{T}_{ee}^{-1} = \begin{bmatrix} \mathbf{T}_{e,s}^{-1} & 0 \\ 0 & T_{e,n}^{-1} \end{bmatrix} \tag{2.27}$$

Equation (2.16) now writes

$$\mathbf{u}_e = \begin{bmatrix} \mathbf{T}_{e,s}^{-1} & 0 \\ 0 & T_{e,n}^{-1} \end{bmatrix} \begin{Bmatrix} \mathbf{t}_{e,s} \\ t_{e,n} \end{Bmatrix} \tag{2.28}$$

By constraining $t_{e,n} = 0$ if $t_{e,n} < 0$, equation (2.28) reduces to

$$\left\{ \begin{array}{c} \mathbf{u}_{e,s} \\ u_{e,n} \end{array} \right\} = \left[ \begin{array}{cc} \mathbf{T}_{e,s}^{-1} & 0 \\ 0 & T_{e,n}^{-1} \end{array} \right] \left\{ \begin{array}{c} \mathbf{t}_{e,s} \\ 0 \end{array} \right\} \tag{2.29}$$

which effectively gives $u_{e,n} = 0$.

# References


Auzias, V. (1995). *Photoelastic modeling of stress perturbations near faults and of the associated fracturing: petroleum industry application, II: Mechanism of 3D joint development in a natural reservoir analogue: the flat-lying Devonian Old Red Sandstone of Caithness (Scotland).* PhD thesis, Université de Montpellier II, France.

Bathe, K. and Chaudary, A. (1985). A solution method for planar and axisymmetric contact problems. *Numer. Meth. Engng.*, 21:65–88.

Bebendorf, M. and Rjasanow, S. (2003). Adaptive low-rank approximation of collocation matrices. *Computing*, 86(4):1–24.

Buczkowski, D. and Cooke, M. (2004). Compaction and shrinkage over buried impact craters: Implications for thickness and nature of cover material in utopia planitia, mars. *J. Geophys. Res.*, 109.

Burgmann, R. and Pollard, D. D. (1994). Slip distribution on faults: effects of stress gradients, inelastic deformation, heterogeneous host-rock stiffness, and fault interaction. *Journal of Structural Geology*, 16(12):1675–1690.

Comninou, M. and Dundurs, J. (1975). The angular dislocation in a half space. *Journal of Elasticity*, 5(3):203–216.

Cooke, M. (1997). Fracture localization along faults with spatially varying friction. *J. Geophys. Res.*, 22:425–434.

Cooke, M. and Kameda, A. (2002). Mechanical fault interaction within the los angeles basin: A two-dimensional analysis using mechanical efficiency. *J. Geophys. Res.*, 107.

Cooke, M. and Murphy, S. (2004). Assessing the work budget and efficiency of fault systems using mechanical models. *J. Geophys. Res.*, 109.

Cooke, M. and Pollard, D. (1997). Bedding-plane slip in initial stages of fault-related folding. *J. Structural Geology*, 19:567–581.

Cooke, M. and Underwood, C. (2001). Fracture termination and step-over at bedding interfaces due to frctional slip and interface opening. *J. Structural Geology*, 23:223–238.

Cowie, P., A. and Scholz, C., H. (2003). Displacement-length scaling relationship for faults: data synthesis and discussion. *J. Struct. Geol.*, 14:1149–1156.

Crouch, S. L. and Starfield, A. M., editors (1983). *Boundary element methods in solid mechanics.* George Allen and Unwin, London.

Dair, L. and Cooke, M. L. (2009). San andreas fault topology through the san gorgonio pass, california. *Geology*, 37:119–122.

Davatzes, N. C. and Aydin, A. (2003). The formation of conjugate normal fault systems in folded sandstone by sequential jointing and shearing. *J. of Geophysical Research*, 108.

De Bremaecker, J. and Ferris, M. (2000). A comparison of two algorithms for solving closed crack problems. *Engineering Fracture Mechanics*, 66:601–605.

Del Castello, M. and Cooke, M. (2007). The underthrusting-accretion cycle: Work budget as revealed by the boundary element method. *J. Geophys. Res.*, 112.

Eterovic, A. and Bathe, K. (1991). On the treatment of inequality constraints arising from contact conditions in finite element analysis. *Computer and Structures*, 40(2):203–S209.

Golub, G. H. and Van Loan, C. F. (1996). *Matrix computation*. Johns Hopkins University Press, Baltimore, MD.

Greengard, L. and Rokhlin, V. (1987). A fast algorithm for particle simulations. *J. Comput. Phys.*, 73:325–348.

Hackbusch, W. (1999). A sparse matrix arithmetic based on h-matrices: Part 1: Introduction to h-matrices. *Computing*, 62:89–108.

Hughes, T., Taylor, R., Sackman, A., and Curnier, W. (1976). A finite element method for a class of contact-impact problems. *Comput. Meth. Appl. Mech. Engng.*, 8:249–276.

Klarbring, A. (1986). A mathematical programming approach to contact problems with friction. *Computer and Structures*, 58:175–200.

Klarbring, A. and Bjorkman, G. (1988). A mathematical programming approach to contact problems with friction and varying contact surface. *Computer and Structures*, 30:1185–1198.

Kwak, B. and Lee, S. (1988). A complementarity problem formulation for two-dimensional frictional contact problems. *Computer and Structures*, 28:469–480.

Maerten, F. (2010). Adaptive cross approximation applied to the solution of system of equations and post-processing for 3d elastostatic problems using the boundary element method. *Engineering Analysis with Boundary Elements*, 34:483–491.

Maerten, F. and Maerten, L. (2008). Iterative 3d bem solver on complex faults geometry using angular dislocation approach in heterogeneous, isotropic elastic whole or half-space. In Brebbia, editor, *Boundary Elements and other Mesh Reduction Methods XXX*, pages 201–208, Southampton. BEM 30, WITpress.

Maerten, F., Resor, P. G., Pollard, D. D., and Maerten, L. (2005). Inverting for slip on three-dimensional fault surfaces using angular dislocations. *Bulletin of the Seismological Society of America*, 95:1654–1665.

Maerten, L. (2000). Variation in slip on intersectiong normal faults: Implications for paleostress inversion. *Journal of Geophysical Research*, 105(25):553–565.

Man, K. (1994). *Contact Mechanics Using Boundary Elements*. Computational Mechanics Publications, Southampton, UK.

Martel, S. (1997). Effects of cohesive zones on small faults and implications for secondary fracturing and fault trace geometry. *Journal of Structural Geology*, 19:835–847.

Mijar, A. and Arora, J. (2000). Review of formulations for elastostatic frictional contact problems. *Structural and Multidisciplinary Optimization*, 20:167–189.

Muller, J. R., Aydin, A., and Maerten, F. (2003). Investigating the transition between the 1967 mudurnu valley and 1999 izmit earthquakes along the north anatolian fault with static stress changes. *Geophysics Journal International*, 154:471–482.

Ohlmacher, G., C. and Aydin, A. (1997). Mechanics of veins, fault and solution surface formation in the appalachian valley, u.s.a.: implications for fault friction, state of stress and fluid pressure. *Journal of Structural Geology*, 19:927–944.

Phan, A.-V., Napier, J. A. L., Gray, L. J., and Kaplan, T. (2003). Symmetric-galerkin simulation of fracture with frictional contact. *Internal Journal for Numerical Methods in Engineering*, 57:835–851.

Roering, J., Cooke, M., and D., P. (1997). Why blind thrust faults don't propagate to the earth's surface: Numerical modeling of coseismic deformation associated with thrust-related anticlines. *J. Geophys. Res.*, 102:901–912.

Rokhlin, V. (1985). Rapid solution of integral equations of classical potential theory. *J Comput Phys*, 60:187–207.

Saad, Y. (1996). *Iterative Methods for Sparse Linear Systems*. PWS Publishing, New York.

Signorini, A. (1959). *Questioni de elasticita non linearizzata e semi-linearizzata*. Rend de Matematica, Rome.

Soliva, R., Maerten, F., J.P., P., and Auzias, V. (2010). Fault static friction and fracture orientation in extensional relays; insight from field data, photoelasticity and 3d numerical modeling. *In press in Special Edt. of J. Struct. Geol.*

Thomas, A. L. (1993). Poly3d: a three-dimensional, polygonal element, displacement discontinuity boundary element computer program with applications to fractures, faults, and cavities in the earth's crust. Master's thesis, Stanford University.

Tse, S., T. and Rice, J., R. (1986). Crustal earthquake instability in relation to the depth variation of frictional slip properties. *J. Geophys. Res.*, 91:9452–9472.

Wriggers, P. (2002). *Computational Contact Mechanics*. J. Wiley and sons, New York.

Xu, J. (1992). Iterative methods by space decomposition and subspace correction. *SIAM Rev.*, 34(4):581–613.

Zhong, Z. (1993). *Finite Element Procedures for Contact-Impact Problems*. Oxford University Press, Oxford.

Zoback, M., Zoback, M., Mount, V., Eaton, J., Healy, J., Oppenheimer, D., Reasonberg, P., Jones, L., Raleigh, B., Wong, I., Scotti, O., , and Wentworth, C. (1987). New evidence on the state of stress of the san andreas fault system. *Science*, 238:1105–1111.

# CHAPTER 3

# Field evidences for the role of static friction on fracture orientation in extensional relays along strike-slip faults; comparison with photoelasticity and 3D numerical modeling

R. Soliva[(2)], F. Maerten[(1,2)], J-P. Petit[(2)], V. Auzias[(3)]

(1) Igeoss, Montpellier, FRANCE
(2) University of Montpellier II, Geosciences, FRANCE
(3) Anadarko

In press in "Special Edition of Journal of Structural Geology", 2010

Reprinted from Publication , doi:10.1016/j.jsg.2010.01.008, R. Soliva, F. Maerten, J-P. Petit, V. Auzias, Field evidences for the role of static friction on fracture orientation in extensional relays along strike-slip faults; comparison with photoelasticity and 3D numerical modeling, Copyright (2010), with permission from Elsevier.
Reprinted from The Lancet, doi:10.1016/j.jsg.2010.01.008, R. Soliva, F. Maerten, J-P. Petit, V. Auzias, Field evidences for the role of static friction on fracture orientation in

**Preamble**

In this chapter, we apply the static Coulomb friction algorithm to a field example at "Les Matelles", southern France. The goal was to find natural features where the effect of the friction is clearly observable. After some discussions, we choose the outcrop at "Les Matelles" where reactivated joints and stylolites in extensional relays show different branching angles for the initiation of the jogs. This angle is intrinsically dependent on the friction coefficient. This effect was first described by Vincent Auzias in 1995 during is PhD at Montpellier.

## About...

Writing this paper gave us an opportunity to dedicate it to Maurice Mattauer, who left us in April 2009 accidentally.

# Article Outline

## 3.1 Résumé

La friction des failles est un paramètre qu'il est difficile d'évaluer le long de la zone de faille car sa détermination dépend de la connaissance de tout facteur contrôlant l'état de contrainte autour des défauts. Dans les roches homogènes cassantes, un nombre limité de ces facteurs, tels que la forme de la surface de faille, la proximité d'autres failles ou le rapport de contrainte à l'infini, sont cruciaux pour lever cette indétermination. Dans cet article, nous proposons d'analyser un exemple de terrain dans lequel toutes ces conditions sont remplies et où la nature de la structure de glissement suggère des différences de frottement statique. Nous comparons les orientations de la ramification des fractures dans les zones de relais décrochantes en échelon pour des stylolites et joints réactivés en cisaillement. Les données sont comparées à la photoélasticimétrie et des modèles numériques 3D qui tiennent compte des conditions de contrainte à l'infini ainsi que du rôle de la géométrie des segments décrochants. Sur la base des observations de terrain, ces analyses mettent quantitativement en évidence le rôle important de la friction des failles sur l'orientation des contraintes locales et sur la génération de la fracturation. Ce travail souligne que les estimations de la friction, basées sur des analyses des modes de rupture ou de contraintes in situ, doivent être accompagnées d'une étude approfondie de la forme des failles en 3D, leurs segmentations ainsi que l'état de contrainte à l'infini.

## 3.2 Abstract

Fault friction is a parameter that is difficult to asses along fault zones since its determination depends on the knowledge of any factor controlling the state of stress around faults. In brittle homogeneous rocks, a limited number of these factors, such as the shape of the fault surface, the vicinity of fault tips or the remote stress ratio, are crucial to constrain for this determination. In this paper, we propose to analyse a field example in which all these properties are met and where the nature of the slipped structure suggest differences in static friction. We compare the orientations of branching fractures at strike slip relay zones between en echelon stylolites and en echelon joints both reactivated in shear. The field data are compared with both photoelastic and 3-D numerical models that consider the remote stress conditions and the role of the geometry of the strike slip segments. Based on field observations, these analyses quantitatively demonstrate the significant role of fault friction on the local stress field orientation and subsequent fracture formation. This work points out that estimations of fault friction based on analyses of fracture patterns or in situ stresses must be accompanied with a thorough investigation of the 3-D fault shape, its segmentation and the remote stress state.

**Keyword**: Fault, friction, relay, wing cracks, damage zone

## 3.3 Introduction

Static friction along faults is an extremely important parameter for the understanding of the seismic cycle, the distribution of stresses, fracture patterns and damage zones around faults. In the past decades many efforts have been made to estimate fault friction along natural faults (e.g. (Hanks, 1977; Zoback, 1980; Brace and Kohlstedt, 1980; Lachenbruch and Sass, 1980; Zoback and Healy, 1984; Mount and Suppe, 1987; Brudy et al., 1997; Zoback et al., 1987; Scholz, 2000)). The measure of static friction estimated using laboratory tests on fault gouges is scale-limited, i.e. on gouge samples from a bore hole cutting crossing the fault, and therefore may not represent the frictional state of the whole surface. Other approaches, based on the analyses of the heat flow (Brune et al., 1969; Lachenbruch and Sass, 1980; d'Alessio M. A. et al., 2003) or numerical modeling (e.g. (T., 1985; Lovely et al., 2009)), allow discussion on the state of friction along the fault but are quite indirect. The analysis of in situ stresses from bore hole measurements or fracture patterns are considered as the best indicator of the frictional state along a fault (Zoback and Healy, 1984; Zoback et al., 1987; Scholz, 2000).

Assuming that fault cohesion can be close to zero on an active fault (Byerlee, 1978), the static friction has been approximated by Amontons first law, in which the frictional coefficient ($\mu$) is expressed as a function of the shear ($F$) and normal ($N$) components of the forces applied to a frictional surface.

$$F = \mu N \tag{3.1}$$

This law states that the friction coefficient of an infinitely long fault surface is directly related to the orientation and the magnitude of the stresses close to this surface (Figure 3.1 a). This reveals that the analysis of the stress field around a fault can be used to determine the static friction along a fault, in cases where the remote ratio of stresses applied to the sliding surface is known. Therefore, any indicators of the stress field around faults (e.g. bore hole analysis, faults or fracture patterns) provide the opportunity to quantify the static friction. However, this analytical approach, based on Amonton's first law, assumes that the fault plane is rectilinear and that the fault tips are infinitely far from the study area. Such a first order approximation is quite unrealistic for natural faults having tips, being irregular, segmented or more complex in shape (Figure 3.1 b, c, and d). The local orientation and magnitude of the stress field around a fault does not rely only on fault friction, which makes its determination non-unique unless we have knowledge of the other factors perturbing the local stress field.

In homogeneous rocks, the first parameter that has been considered as acting on the local stress field, and more precisely on the crack angle to a fault, is the static friction coefficient (e.g. (Petit and Barquins, 1988; Barquins et al., 1997; Martel, 1997; Ohlmacher and Aydin, 1997a; Willemse and Pollard, 1998; Zhou, 2006; Mutlu and Pollard, 2008)). However, the remote stress angle has been considered as very important (Barquins and Petit, 1992; Ohlmacher and Aydin, 1997a) as well as the remote stress ratio (Auzias et al., 1997; Kattenhorn et al., 2000; Zhou, 2006). Others factors more related to the geometry and behaviour of the fault surface also seem to be very influential, as the 3-D geometry of the faults (e.g. (Segall and Pollard, 1980; G.C.P. et al., 1994; Willemse, 1997; Maerten et al., 2002; Bourne and Willemse, 2001), its spatial/temporal evolution ((Willson et al., 2007; Lunn et al., 2008), Moir et al, this volume), and fault opening (Kattenhorn. S. and Marshall, 2006). Therefore, any analysis of fault zones that aims to estimate the role of fault friction on the stress field, or in contrast to determine the state of friction from stresses analysis, must know any of these factors that can perturb the local stress field.

In this paper, we analyse a field example in which these factors can be estimated. Drastic differences in fracture orientation between reactivated frictional stylolites (i.e. structures of high friction coefficient) and frictionless joints (i.e. structures of low friction coefficient)

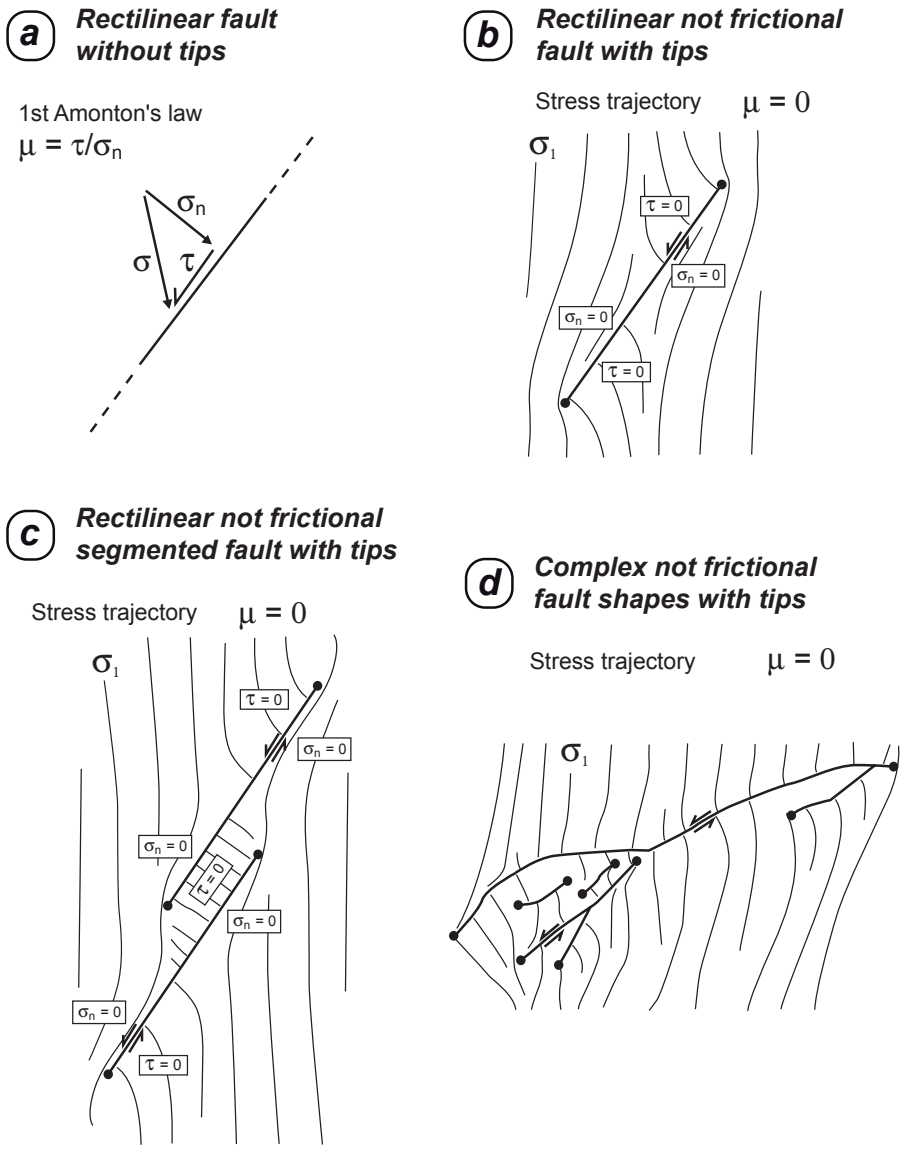


FIGURE 3.1: Comparison between the stress perturbation due to fault friction (a) and the stress perturbation due to different examples of fault geometry (b, c and d). (b), (c) and (d) are $\sigma_1$ stress patterns inferred from photoelastic modeling (Joussineau et al., 2003). The remote stress applied is uniaxial. Dots represent fault tips. This figure shows that even for $\mu = 0$, the orientation of $\sigma_1$ can be oblique and even parallel to the fault surface, rather than perpendicular as suggested by Amontons first Law.

suggest that friction is a prominent property influencing the stress perturbation at the close vicinity of a fault. We chose to study fracture orientation at extensional relay zones because the stress orientation has been described as quite stable in space along a relay zone (compared to outside) due to the juxtaposition of the two extensive fault quadrants (see Figure 3.1 c) (e.g. (Auzias et al., 1997; Ohlmacher and Aydin, 1997a)). We compare the field data to photoelastic and 3-D numerical models to demonstrate and quantify the significant role of static friction on the stress and fracture orientation at extensional relay zones.

## 3.4 Field data

### 3.4.1 Geological setting

The studied exposure, located close to Les Matelles (15 km North of Montpellier, France, Figure 3.2), is a suitable site for the study of brittle tectonics in limestones and stress perturbations around meso-scale faults (Rispoli, 1981; Fletcher and Pollard, 1981; Petit et al., 1999). The brittle tectonic structures observed (Figure 3.3 a) were formed during multiphase compressive tectonics allowing the formation of joints and stylolites. These structures of similar dimension and orientation have been reactivated as slip surfaces during a late tectonic event (Petit and Mattauer, 1995). Because of their different roughness, joints and stylolites are expected to be of different frictional properties during slip. Most of them show secondary fracturing and linkage at relay zones (Figure 3.3 b), that can be used as indicators of the palaeostress orientation (e.g. (Rispoli, 1981; Petit and Mattauer, 1995)). It is therefore worthwhile to address with particular care on the geological setting and history of the brittle structures that will be used to constrain the role of fault friction on fracture orientation.

The studied exposure has been fully described in a number of previous studies (e.g. (Rispoli, 1981; Taha, 1986; Petit and Mattauer, 1995; Petit et al., 1999)). This area is located in the vicinity of a fault branch called the Lirou fault (Figure 3.2 b). The Matelles fault zone, like many faults in the area, had both left-lateral strike slip related to the Pyrenean shortening and normal slip related to the Oligocene rift extension in the Languedoc. Middle cretaceous normal slip along the Matelles-Corconne fault zone is also expected during the Durancian tectonic events.

The brittle deformation sequence described by Petit and Mattauer (Petit and Mattauer, 1995) begins by a vertical jointing stage of the limestone layers with two principal trends, $N020$ and $N140$. The second stage is a first generation of stylolite formation oriented $N040$. The third stage, the most important for our study, is the reactivation of the previous structures as sinistral and dextral strike slips due to a last shortening creating wing cracks, en echelon veins and a second generation of stylolites around the reactivated defects. As shown by this last generation of joints and stylolites formed, the last shortening stage occurs with the maximum principal stress $\sigma_1$ oriented NorthSouth. As suggested by rock experiments, photoelastic models, numerical and analytical solutions (see (Wawersik and Brace, 1971; Petit and Barquins, 1988; Barquins and Petit, 1992; Chaker and Barquins, 1996; Lunn et al., 2008)) the presence of wing cracking around reactivated defects (see Figure 3.3 b) implies remote stress conditions close to uniaxial loading ($\sigma_1/\sigma_3 \geq 10$).

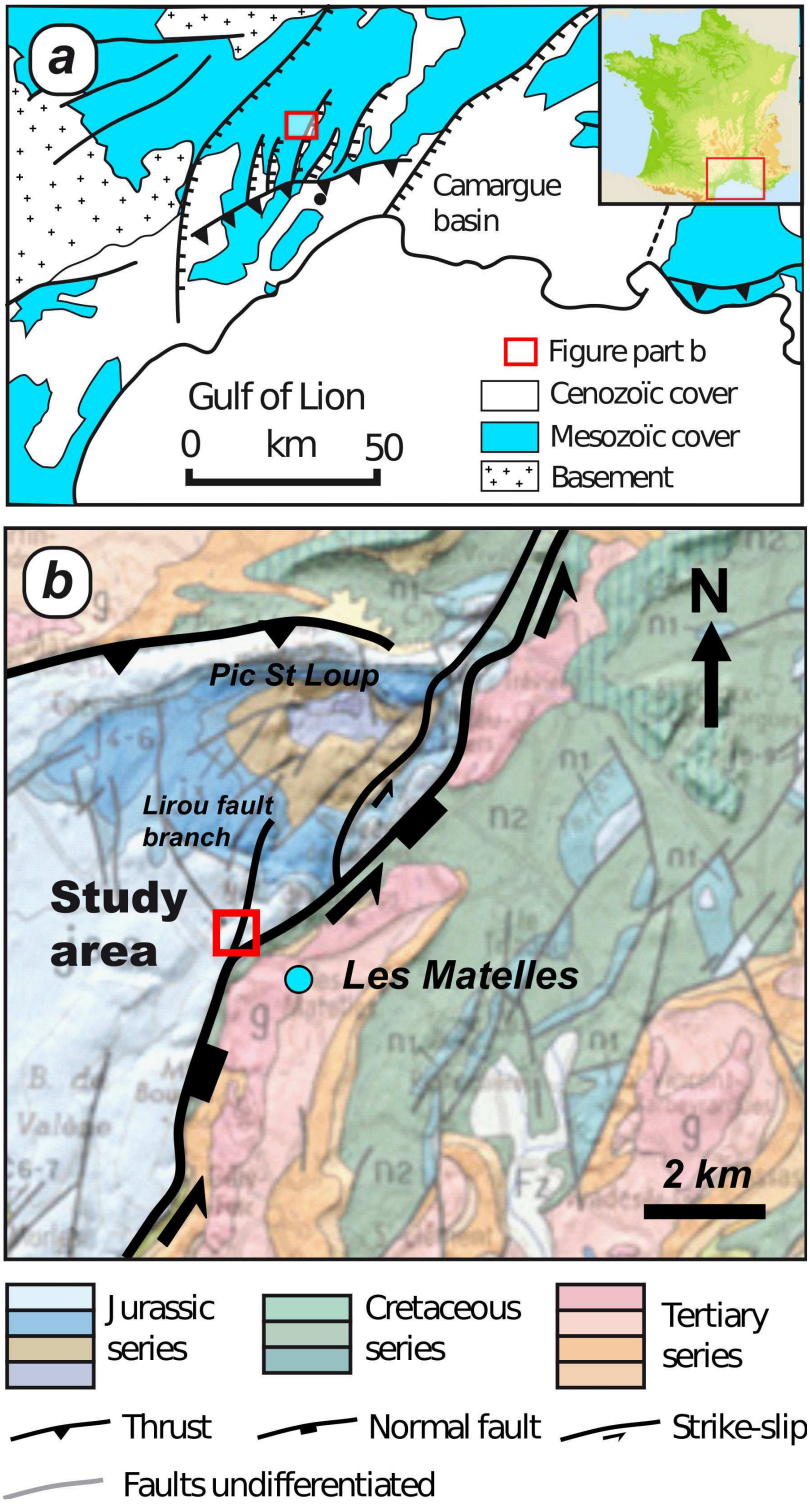


FIGURE 3.2: Location and geological context of the study area. (a) Structural scheme of the study area. (b) Geological map of the study area showing the Matelles fault and the Lirou fault branch, modified from the geological map of St Martin de Londres, 1/50 000.

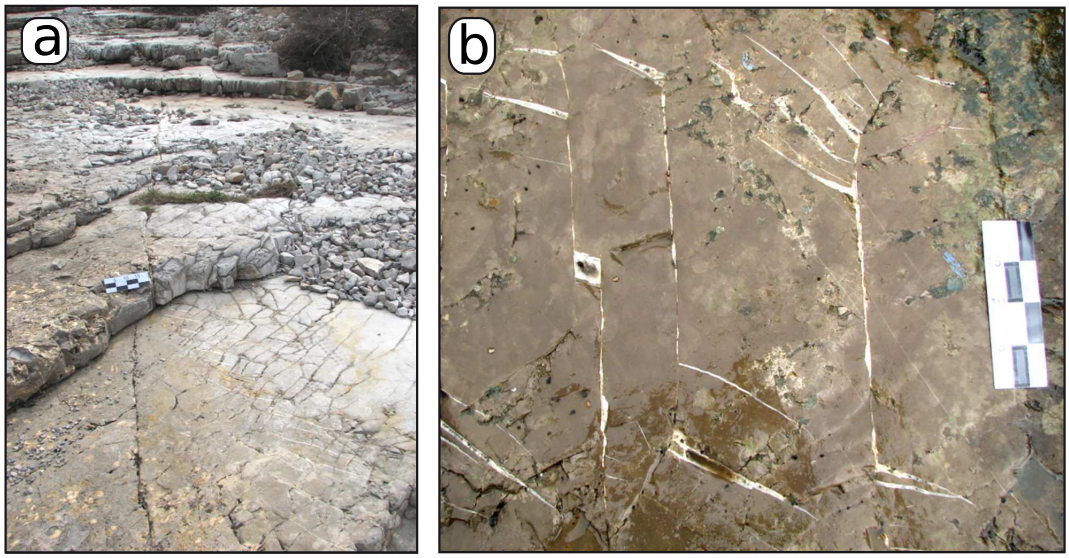


FIGURE 3.3: Field photographs of the study area. (a) Outcrop overview showing the layered upper Jurassic mudstones damaged by a dense pattern of calcite sealed fractures and stylolites. (b) First generation stylolites reactivated as sinistral strike slips showing wing cracks and branched stylolites (see (Rispoli, 1981)). The length of the scale bar is 20 cm.

Conditions close to horizontal uniaxial stresses are possible at shallow depths, i.e. for little confining pressure. The expected depth of faulting in the upper Jurassic limestone was probably less than the thickness of the lower cretaceous series ( 200 m), which was potentially yet well eroded during the Pyrenean shortening. This local stress state condition (high ratio of maximum to minimum principal stresses, $\sigma_H/\sigma_h$) and reorientation of $\sigma_1$ axis has been related to a restraining bend along the Les Matelles fault during Pyrenean strike-slip movements (Rawnsley et al., 1992; Petit et al., 1999).

### 3.4.2 Extensional relay geometries

The last stage event provides the opportunity to analyse the geometry of branching at relay zones between slipped overlapping stylolites vs. slipped overlapping joints(Figure 3.4 and 3.5a). The angle $\beta$ defined as the angle between the orientation of remote $\sigma_1$ relative to the joints or stylolites reactivated in shear (Figure 3.5 c), is quite variable (variation of 40°). A wide overlap of $\beta$ angles are therefore found for reactivated joints and stylolites containing relay zones. For similar $\beta$ angles, the branching angle $\alpha$ (defined as the angle between the slipped structure and the branching jog) is quite different with respect to the nature of the reactivated structure. More precisely, for similar $\beta$ angles, $\alpha$ is larger for joints than stylolites (Figure 3.5 a and b). These observations are verified on a $\alpha$ vs $\beta$ graph, in which additional measures from the literature were reported for comparison. Field data from stylolites and joints are consistent with the general scatter of

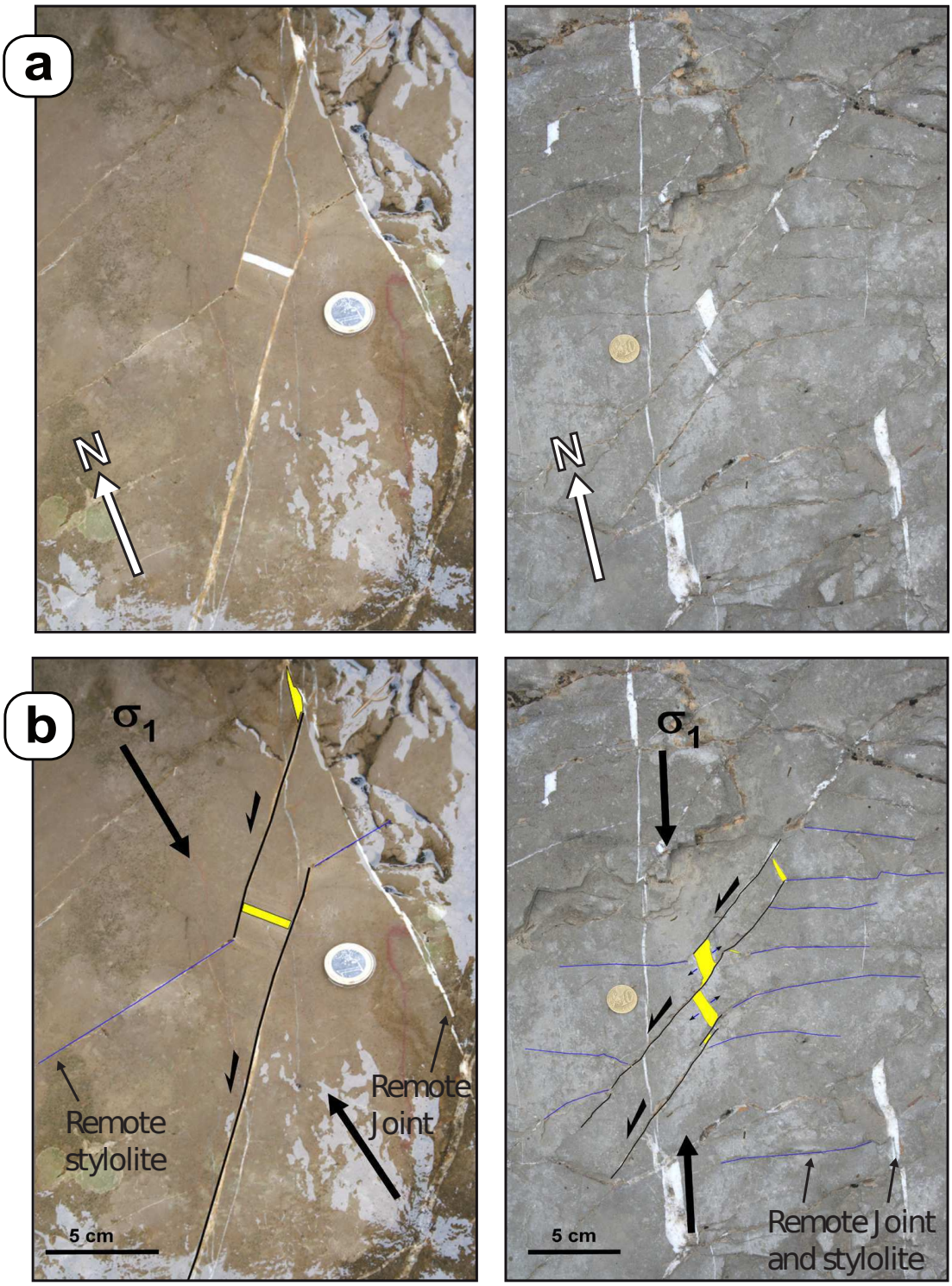


FIGURE 3.4: (a) Examples of joints (left side) and stylolites (right side) reactivated as left lateral strike slips. (b) Interpretation in terms of stress orientation using the remote orientation of syn-kinematic joints and stylolites. The "remote stress" orientation is slightly different in the two cases because they were not measured at the same location and that the larger Lirou fault probably modify the stress field orientation at this North-South last compressive stage.

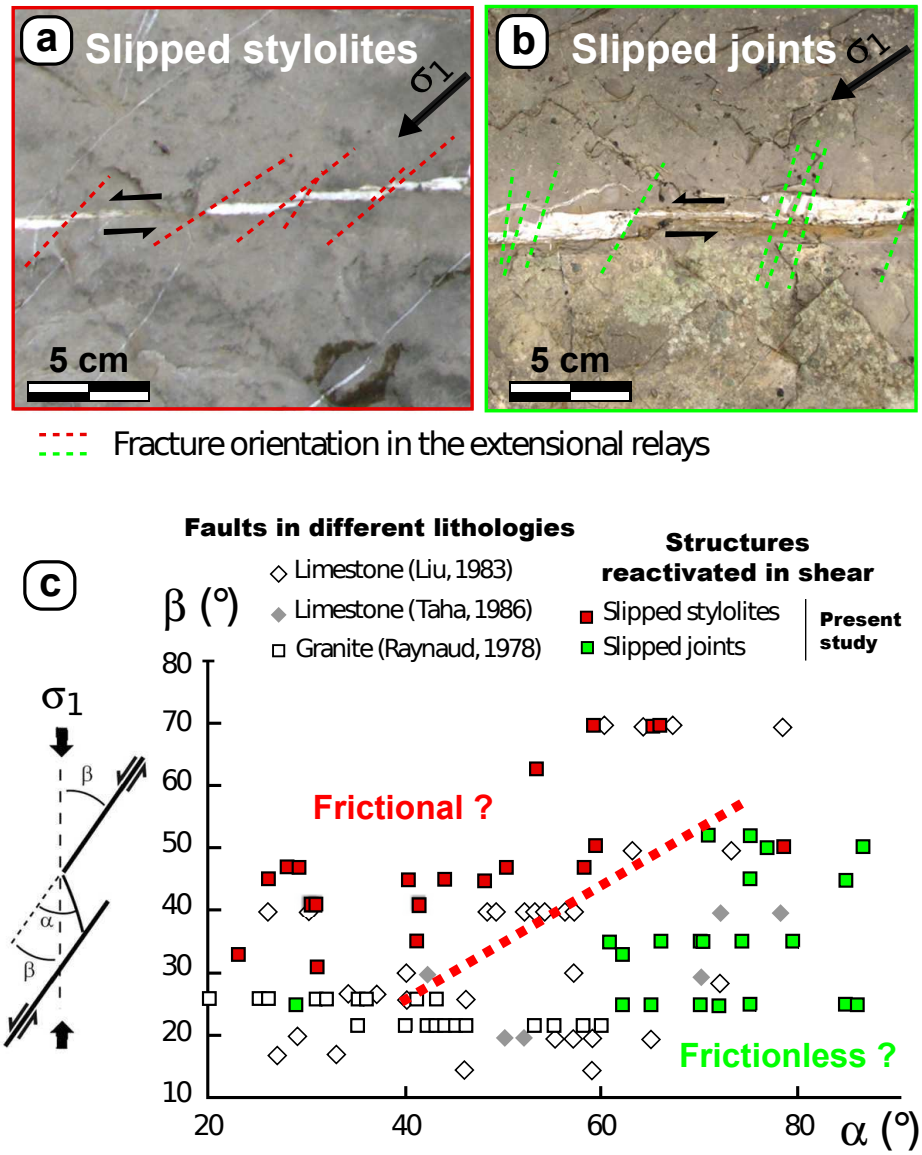


FIGURE 3.5: Variation in the geometry of extensional jogs between stylolites and joints reactivated in shear. (a) and (b) are field examples of reactivated stylolites and joints, respectively. Coloured dashed lines represent the orientation of fractures in the relay zones. (c) Graph of $\alpha$ and $\beta$ angles for all the reactivated stylolites and joints measured in the field. $\alpha$ and $\beta$ angles are represented in a small scheme at the left. Field observations show higher $\beta$ angles for reactivated stylolites

all the data, and fit in two specific fields of branching configurations as described above. Because of their different roughness (see (Delair and Leroux, 1978; Raynaud and Carrio-Schaffhauser, 1992), for the analysis of non reactivated stylolites), joints and stylolites are expected to be of different frictional properties during slip. Therefore, the question arising from these observations and treated in the next sections is the following: Is this difference of branching geometry really due to the frictional properties of the slipped structures? The local orientation of relay branching fractures ($\alpha$) gives a good approximation of the local orientation of $\sigma_1$ during fault slip of all the faults measured and at the same tectonic event (e.g. (Auzias, 1995; Ohlmacher and Aydin, 1997b; Kattenhorn et al., 2000)). The

wide range of  angle observed in the field therefore reveals wide variation in the ratio of shear stress / normal stress, probably due to variations in static friction of the slipped structures. This hypothesis will be tested below using analogue and numerical modeling.

## 3.5 Photoelastic modeling

### 3.5.1 Photoelastic method

A way to test the effect of friction is to analyze the stress field orientation using photoelastic experiments around opened (not frictional, i.e. $\mu = 0$) and closed defects (frictional). Photoelasticity is an optical method of stress analysis within elastic translucent materials like polymethylmethacrylate (PMMA), which present accidental birefringence when loaded. These materials have the property of resolving the light which falls on them at normal incidence into two components, each one coinciding with a principal plane of stress. This property, due to a higher density of the material in these stress orientations, implies a light transmitted at right angles (Hetényi, 1966). If a photoelastic sample is placed between crossed polarizers, black fringes named isoclinics (light extincted, see Figure 3.6 b for an example) are observed on the second polarizer, i.e. the analyzer. Isoclinics

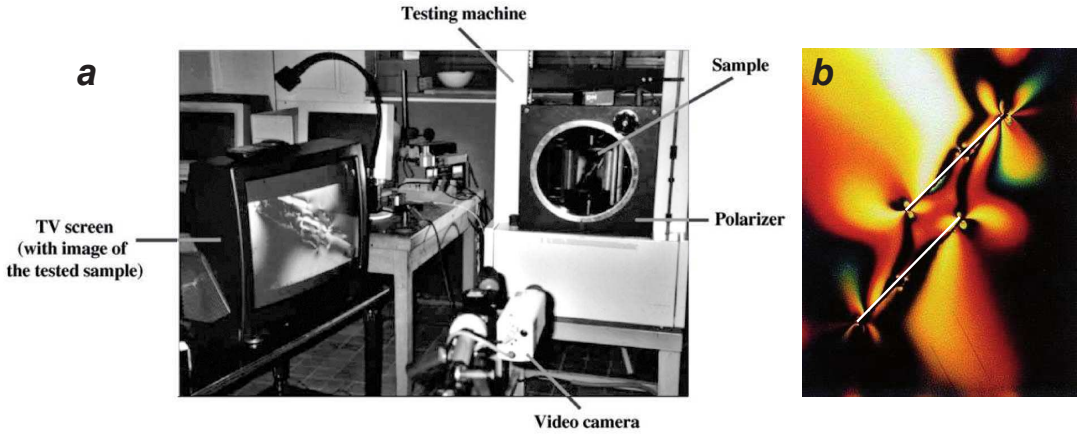


FIGURE 3.6: (a) Experimental device of the photoelastic modeling. (b) Example of isoclinic and isochromic fringes obtained in a vertical uniaxial loading experiment of slipping overlapping open defects.

correspond to locations where the plane of the incident polarized light coincides with one direction of principal stress within the sample. These isoclinics move when the polarizers rotate together. By rotating the polarizers from 0° to 90°, and drawing the corresponding isoclinics, it is possible to map the orientation of the two principal stresses. A thourough description of the same experimental device (Figure 3.6 a) and additional details about the photoelasticity method can be found in De Joussineau et al. (Joussineau et al., 2003).

To simulate the effect of fault friction on the stress field of extensional relay zone, two types of PMMA models were compared: a first one composed of closed defects and assumed to have friction, and the other one with opened defects and assumed to have negligible friction. To produce open defects, the thin plates of PMMA (0.5 $cm$ thick, 6.5 $cm$ width and 10 $cm$ high) were sawn-off with a 300 $\mu m$ thick micro-saw from central drill holes on each interacting segments of 500 $\mu m$ diameter. Closed defects were produced as planar fractures propagated along linear traces drawn with a cutter on the PMMA surface. These two types of models are subjected to loading with different $\beta$ angle such as 20°, 45° and 70°. Here $\beta$ is the angle between the axial loading and the planar defects forming the relay zone.

The models are subjected to uniaxial conditions in order to be consistent with the field conditions expected (see section 3.4). The axial compressive load is imposed by an electromechanic testing machine (Davenport 30 kN) and no lateral pressure is added. To prevent bending of the PMMA plate under vertical loading, the samples are maintained between vertical tighteners.

### 3.5.2 Experimental results of extensional relay stress pattern

The two types of models (frictional versus not frictional) show significant differences in their local stress field distribution. Figure 3.7 presents stream lines of $\sigma_1$ for not frictional (a) and frictional configuration (b) subjected to a vertical loading with $\beta = 20°$. The stress field is less perturbed in orientation for the frictional case. Without friction, the orientation of $\sigma_1$ is normal to the faults (deviation of 70° from the remote $\sigma_1$) and quite stable along the relay zone. Also note that the stress field is perturbed outside of the relay zone. In the frictional case, the stress field changes from the tip, where it is close to vertical, to the center of the relay zone, where it reaches its maximum deviation of 45°. Additional tests, not presented here and done for variable overlap and constant spacing between the defects, show the same maximum values of $\sigma_1$ deviation and a better stability of $\sigma_1$ orientation in the relay zone as the overlap increases.

All the studied tests show results generally consistent with field observations. Figure 3.8 exhibits the compilation of the $\alpha$ and $\beta$ angles data for all the tests done with constant relay geometry. Note that $\alpha$ here corresponds to the angle between the slipped defect and $\sigma_1$ at the center of the relay zone. Tests with no friction lie in the graph area of high $\alpha$ and relatively low $\beta$ angles, which corresponds to the zone of slipped joints (of low friction compared to slipped stylolites). In contrast, frictional tests data lie in the area of lower

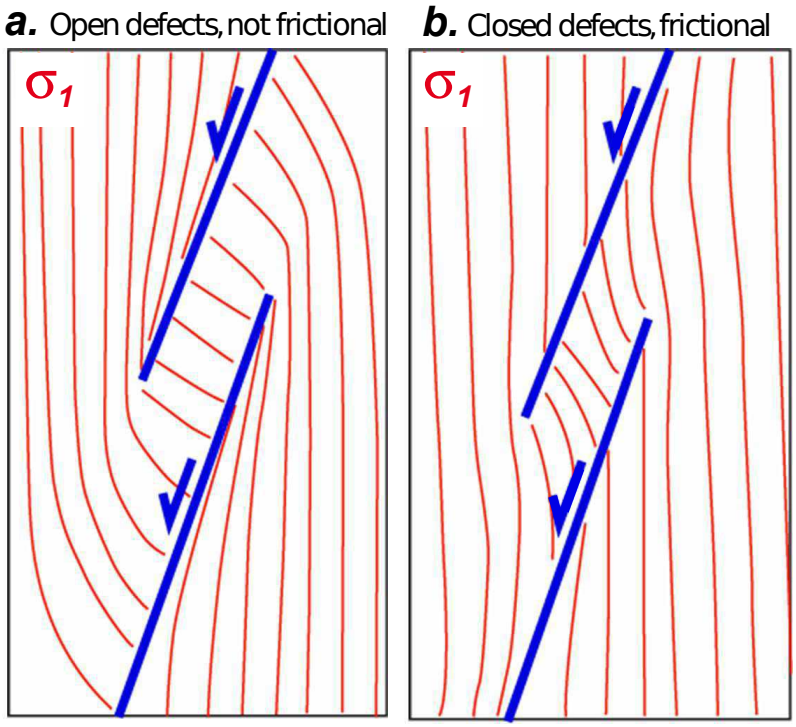


FIGURE 3.7: Drawing of $\sigma_1$ obtained from the analysis of isoclinic fringes for (a) uniaxial vertical loading of open defects, i.e. non frictional and (b) closed defects, i.e. frictional.

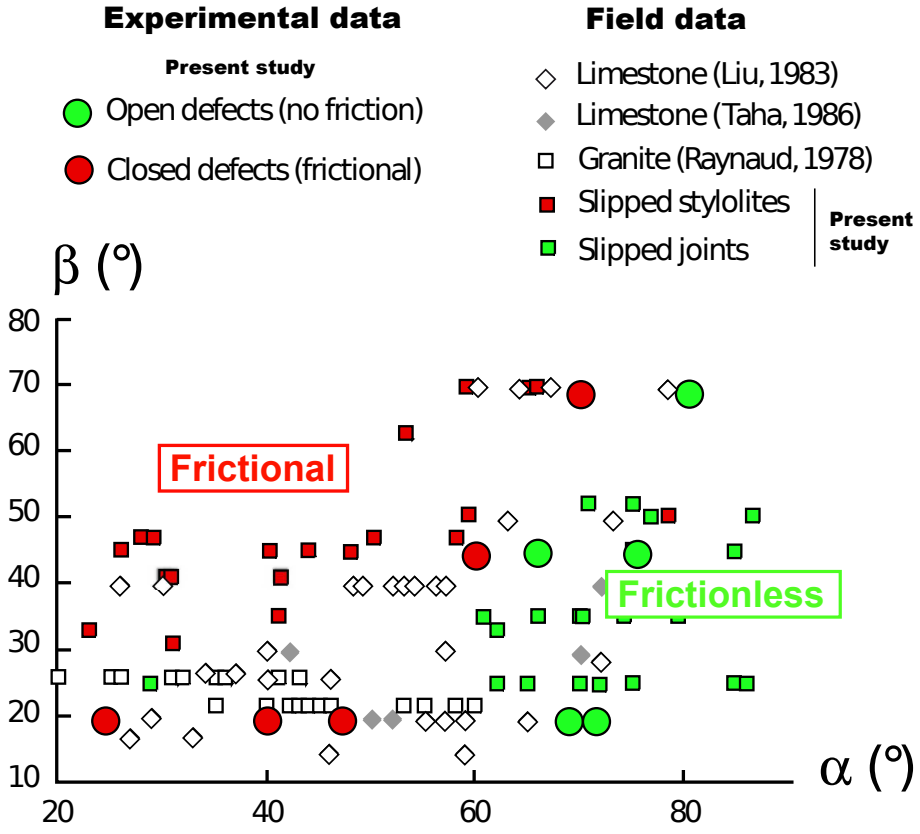


FIGURE 3.8: Comparison between $\alpha$ and $\beta$ angles obtained by photoelastic modeling with the dataset measured in the field.

$\alpha$ and relatively high $\beta$ angles, which corresponds to the zones of slipped stylolites (high friction).

## 3.6 Numerical modeling

The numerical code used to investigate fault friction is a 3-D Boundary Element Method (BEM) called Poly3D (Thomas, 1993). It relies on the analytical solution of an angular dislocation in a homogeneous elastic whole- or half-space (Comninou and Dundurs, 1975). As opposed to the Okada's code (Okada, 1985), which uses rectangular elements, Poly3D discretizes faults and fractures using triangular elements, and therefore avoids the creation of overlaps and gaps between adjacent elements which perturb the solution (Maerten et al., 2005). Mixed traction-displacement boundary conditions can be used for each constitutive element of the model (tractions are shear and normal stresses resolved on the fault surface). When traction boundary conditions are specified, we have to solve for the corresponding unknown displacement discontinuity according to the initially prescribed traction values. As soon as all displacement discontinuities are known (i.e. the slip patches), strain, stress and displacement can be computed at any observation point within the elastic field. Note that transient variations in friction coefficient or the dynamic stress field is not considered (e.g., (Poliakov et al., 2002)).

In order to have a frictional behavior, the code has been extended to support inequality constraints on traction and displacement. Specifically, the static Coulomb friction has been implemented as a traction inequality constraint and validated by comparison with analytical and numerical solutions (Maerten et al., 2009). For a given fault surface, the coefficient of friction and cohesion can be prescribed globally onto a fault surface or locally, each constitutive element having their own coefficients. Traction boundary conditions are imposed along the three axis of each triangular element local coordinate system (dip, strike and normal directions).

For a model subjected to a compressive far field stress, interpenetration of the elements has to be avoided. This is achieved by using the displacement inequality constraint $u_z \geq 0$, where $u_z$ represents the computed normal displacement of a triangular element. Again, traction boundary conditions are imposed along the three axes of each triangular element local coordinate system (Maerten et al., 2009).

### 3.6.1 Model set up

Figure 3.9a and 3.9b depict the model configurations used for the BEM modeling for joints and stylolites, respectively, and are built upon field observations (Figure 3.4). All

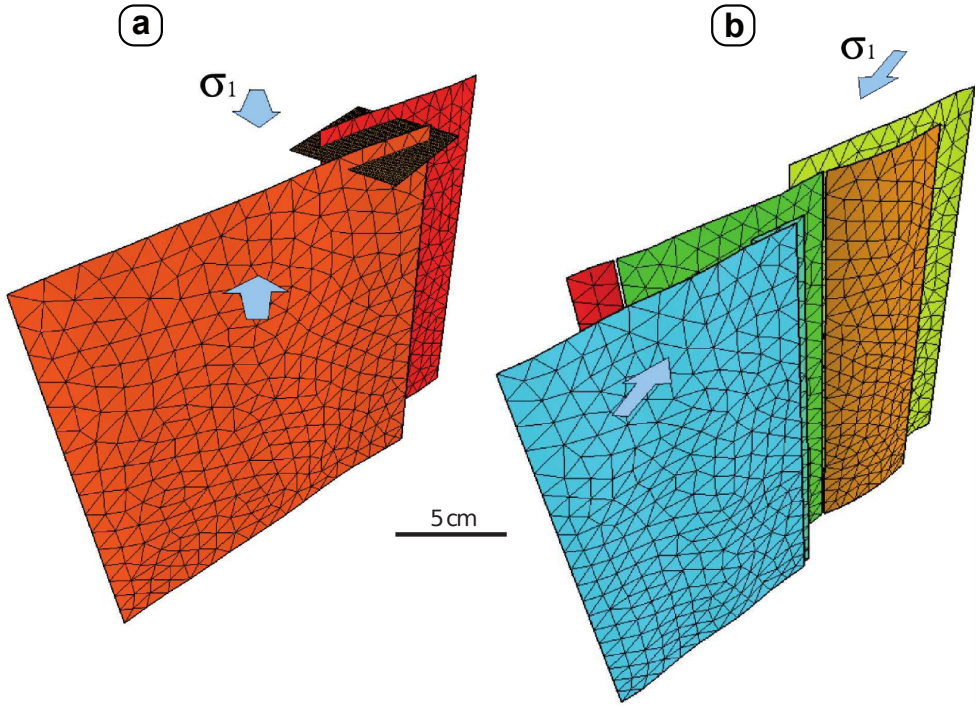


FIGURE 3.9: 3-D view of the geometry of the defects reactivated in shear used in Poly3D for the numerical simulation. (a) 3-D geometry of the reactivated joints shown in Figure 3.4 with the observation grid (dark square) on which the stresses are represented in Figure 3.10. The position of the observation grid corresponds to the position of the top of the limestone layer observed in the field. (b) 3-D geometry of the reactivated stylolites shown in Figure 3.4. The observation grids (not shown here), on which the stress field is presented in Figure 3.11, are placed at the same level than in (a).

the veins and stylolites traces in the vicinity of the zone of interest have been carefully mapped and then vertically extruded in depth all along the limestone layer thickness, giving rise to the 3D triangulated surfaces. As the Coulomb friction relates the shear to the normal components of the forces applied to a frictional surface, traction boundary condition for the three local axes (dip, strike and normal) of each constitutive triangular element is used.

### 3.6.2 Modeling of joints reactivated in shear

The joints model, depicted in Figure 3.9a, is based on the field observations shown in Figure 3.4, left side. These first generation joints are subjected to a far field remote stress with uniaxial compressive condition and $\sigma_1$ (in this area) oriented $N170$ as suggested

by the presence of surrounding joints and stylolites (third brittle deformation stage, see section 3.4). In order to display the stress orientation within the extensional relay resulting from the computed displacement discontinuities, an observation grid is placed close to the top of the model (Figure 3.9). Then, two simulations are performed: a first one, with a constant coefficient of friction $\mu = 0.6$ for all discontinuities and no cohesion, and a second without any friction but with "non-interpenetration" as a unique constraint. The elastic material properties used for the surrounding limestone are $\nu = 0.25$ and $E = 1$ GPa (see (Hatheway and Kiersch, 1989)).

Figure 3.10a and b display the frictional and not frictional models, respectively. The orientation of $\sigma_1$ axis fit better with the strike of the branching fracture in the case where the frictional coefficient equals zero. Since $\sigma_1$ should be parallel to the strike of the branching fracture, these models suggest that, at the initiation of the linkage, the slipping joints were preferably not frictional. This is consistent with the absence of macroscopic irregularities along these rectilinear structures.

### 3.6.3 Modeling of stylolite reactivated in shear

For the stylolites model depicted in Figure 3.9b, the uniaxial compressive far field stress is oriented $N015$, as proved by the presence of surrounding joints and stylolites (see Figure 3.4, right hand side, and Figure 3.9b in Petit and Mattauer (Petit and Mattauer, 1995)). Since this model is composed of two relays, two observation grids are placed in the vicinity of them close to the top of the model. A first simulation is done using only the non-interpenetration constraint (i.e. with $\mu = 0$), whereas a second one employs a constant coefficient of friction $\mu = 0.6$ without cohesion.

Figure 3.11a and b displays the results on the two observation grids for the not frictional and frictional models, respectively. As opposed to the previous joint modelling, the linking structures are more consistent with high friction stress orientations.

### 3.6.4 Parametric analysis

A series of models have been done for variable friction and constant fault geometry consistent with the overlapping segments of the experimental PMMA model. The 3-D shape of the model is shown in Figure 3.12a. The results are analyzed on the observation grid which allows to compare a configuration close to the field and the photoelastic modeling (Figure 3.12b). The models were performed with variation of static friction coefficient and

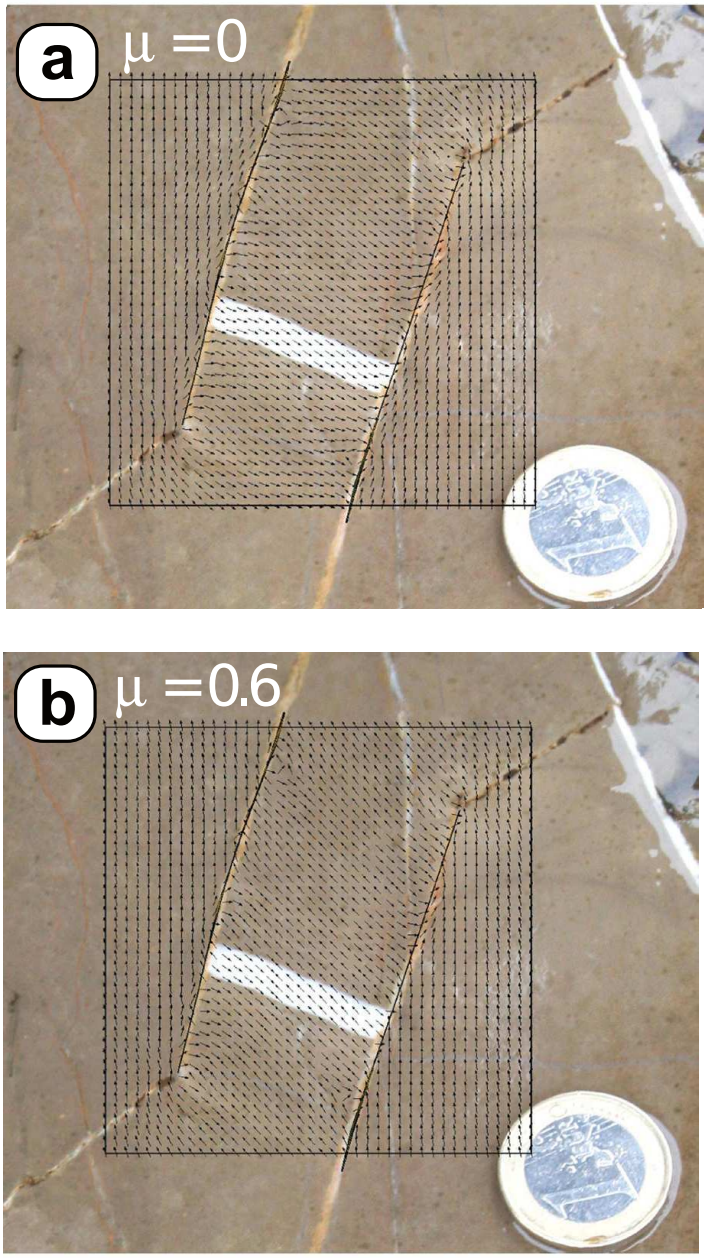


FIGURE 3.10: Model results for the joints reactivated in shear shown in Figure 3.9. (a) Modeling result for $\mu = 0$. (b) Modeling result for $\mu = 0.6$. The small arrows on the observation grid show the local orientation of $\sigma_1$.

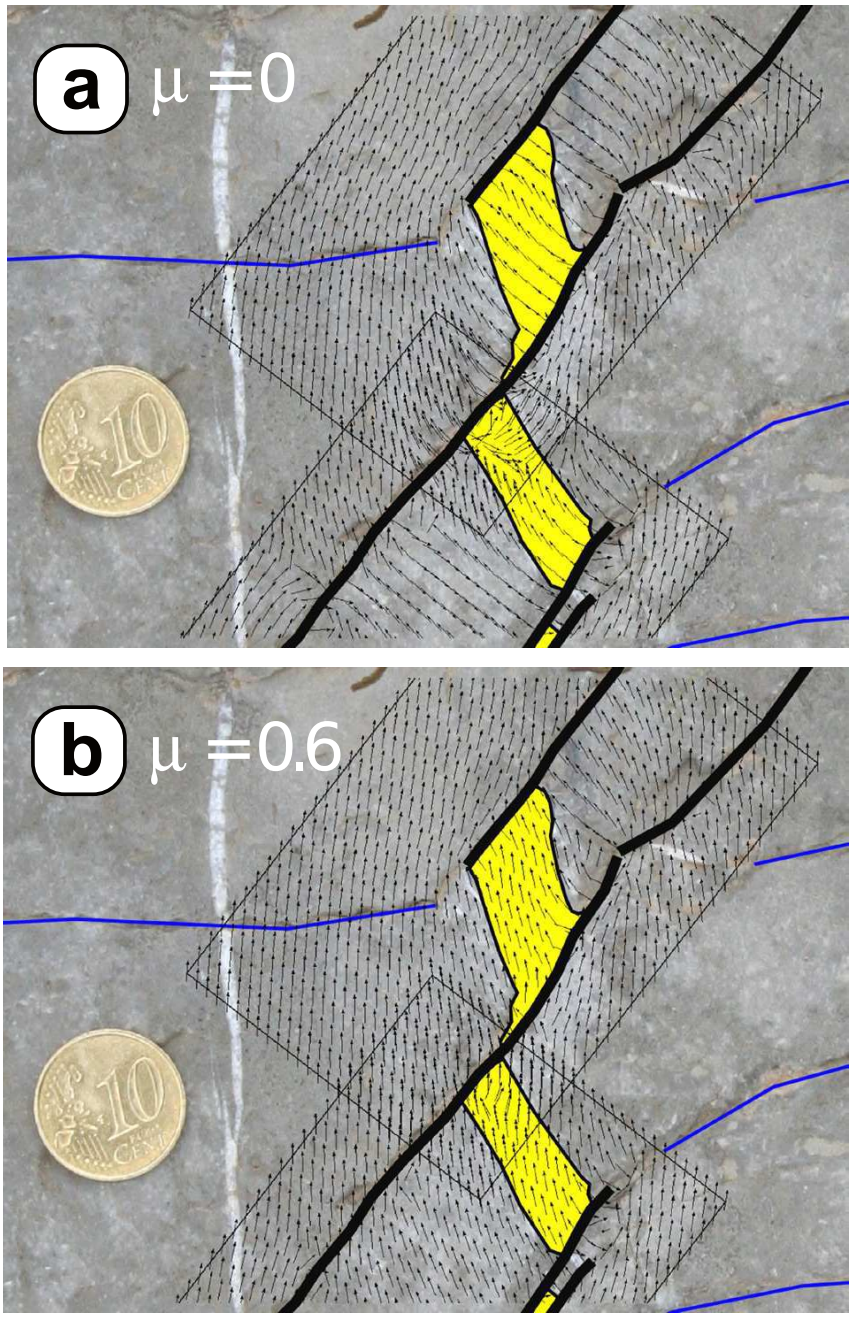


FIGURE 3.11: Model results for the stylolites reactivated in shear shown in Figure 3.9. (a) Model result for a $\mu = 0$. (b) Model result for a $\mu = 0.6$. The small arrows on the observation grid show the local orientation of $\sigma_1$.

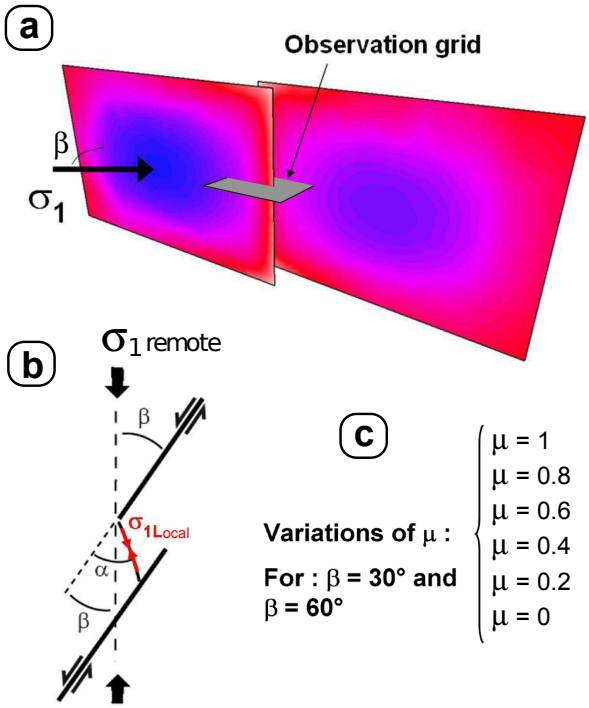


FIGURE 3.12: Input conditions for the parametric modeling. (a) Configuration of the 3-D model geometry with an example of computed displacement contours in color. (b) Horizontal view of the model configuration showing the angles $\alpha$ and $\beta$. (c) Variables used in the parametric study.

$\beta$ angles as shown in Figure 3.12c. The elastic material properties used are the same than above since a large part of the field data used for comparison were measured in limestone (Figure 3.5).

The results are in good agreement both with field and experimental data. Figure 3.13 exhibits the compilation of the $\alpha$ and $\beta$ angles data for all the tests done. As for the experimental analysis, $\alpha$ corresponds to the angle between the slipped surface and $\sigma_1$ at the center of the relay zone. The numerical models with no or little friction lay in the graph area of high $\alpha$ and relatively low $\beta$ angles, which corresponds to the zone of slipped joints (frictionless structures). In contrast, frictional models fit in the area of low $\alpha$ and relatively high $\beta$ angles, which corresponds to the zone of slipped stylolites (frictional structures).

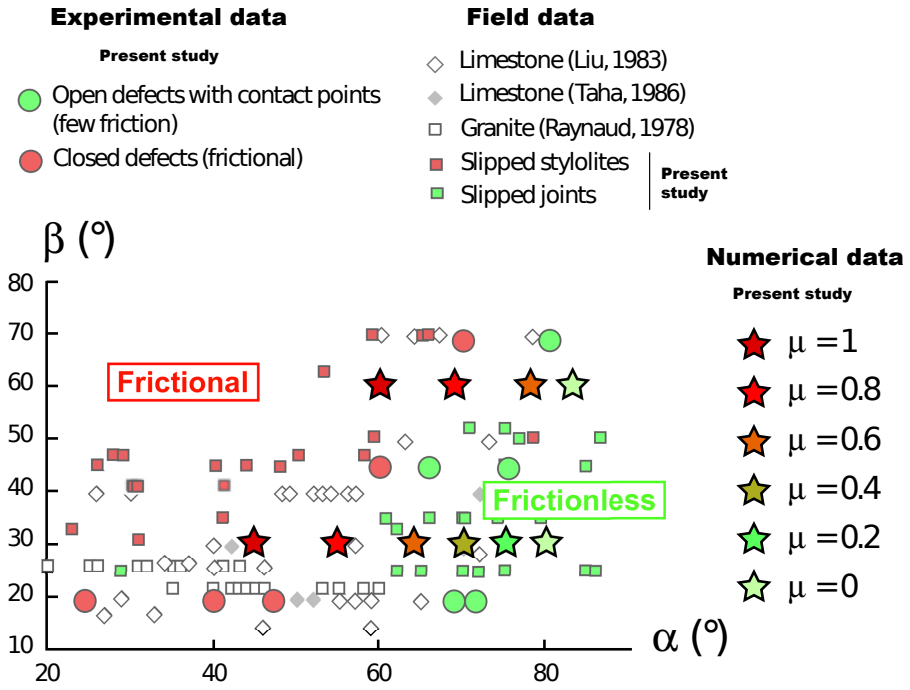


FIGURE 3.13: Comparison of $\alpha$ and $\beta$ angles between the data obtained by numerical modeling, photoelastic modeling and the dataset measured in the field. A wide part of $\alpha$ and $\beta$ spreading can be explained by variations in frictional coefficient of the slipped defects.

## 3.7 Discussion

### 3.7.1 Stress perturbation and friction of the slipping defects

The models are in good agreement with the field observations, however they do not cover the entire range of data, especially for the low $\alpha$ angles (Figure 3.13). This point can be discussed with respect to a limited number of unconstrained factors that may influence the stress field around the slipping defects.

Inelastic deformations can modify the magnitude of residual stresses in the host rock around faults, but this is probably not the explanation of the scatter observed in Figure 3.13 for two reasons. First, with respect to the brittle subsurface conditions of deformation, the studied limestone probably has negligible inelastic behaviour preceding its shear yielding strength (Rispoli, 1981; Petit and Mattauer, 1995). Second, inelastic deformation around fault, if any, has probably a larger influence on the stress magnitude than on the orientation (Burgmann and Pollard, 1994), which one close to the fault must be directly related to fault friction. This suggests that elastic models are relevant to simulate residual stresses related to fault slip in this geological context, and that the spreading of field data compared to the model is mainly due to others factors.

The effect of 3-D fault geometry, especially the fault aspect ratio, on the stress distribution around fault has probably little influence. Soliva et al. (Soliva et al., 2006) shows that the dimension of the area of stress perturbation around a fault scales linearly with the fault length since the fault growth is radial, and tends to be limited to a certain distance when the fault height reaches a constant value. This means that for vertically restricted fault by strata bounds, the 3-D shape can influence the orientation of the stress field at about a distance around the fault equivalent to the layer thickness. In the present study, for all the measures of angles made in the field (in the relay zones), the distance of the fractures around the faults is always lower than the layer thickness potentially restricting the faults (tens of cm). We therefore work in a window around the faults where the stress perturbation should not be influenced by the fault aspect ratio (3D shape), and that all the field measurements could be compared to 2-D photoelastic models or 3-D full space models proposed.

The reason of the difference of scatter between the field data and the models is potentially purely geometric. For all the model results presented in Figure 3.13 (both parametric and photoelastic), the fault configurations are idealized as two planar surfaces with constant overlap and spacing, whereas the field data are from faults more complex in shapes, with variable overlap and spacing, curved, with multiple segments and potentially more complex in 3-D.

We have shown that friction is the main factor controlling the stress perturbation and the orientation of linking fractures. However the physical cause for this variation in friction needs to be discussed. Obviously, this cause can be reasonably ascribed to the difference of surface roughness between the stylolites and the joints. However, the analysis of the roughness of the slipped defects is not very relevant on faulted stylolites since after faulting they show a smoothed irregularity that is certainly different than the initial one. The measure of roughness has been done on non reactivated stylolites (see (Delair and Leroux, 1978; Raynaud and Carrio-Schaffhauser, 1992), for the quantitative analysis of stylolites roughness in the same study area). However, these stylolites were not reactivated potentially because of a threshold friction, then different than the initial state on the faulted stylolites. On the other hand, efforts in measuring the surface roughness of the slipped defects can not be very conclusive since it represents the finite strain.

### 3.7.2 Estimation of fault friction and upscaling

From three different approaches: (1) field study, (2) experimental modeling and (3) numerical modeling, we have shown that the angle of fracture branching in strike slip relay

zones is highly dependent on the frictional state of the overlapping faults.

It is worthwhile to note that the "static" friction estimated at the relay zone corresponds to the friction of the faults in the vicinity of the relay zone and at the time of the fault interaction through the relay zone. This frictional property may therefore have evolved through time and space with the progression of fault coalescence. The "quasi-static" friction estimated must be therefore considered as the time integrated friction of the period of fault interaction through their stress field. We also must keep in mind that this approach is only suitable along faults if the remote stress conditions are well known, since the ratio of $\sigma_H/\sigma_h$ is very important for the stress orientation in the relay zone (Auzias, 1995). Any indicator of the remote and relay zone stress field are worth considering.

With regard to estimation of fault friction on large scale active faults, particular care must be taken with the stress field determined from data close to the Earths surface. For depth shallower than 300 m, the orientation of the principal stress may be different than the tectonic stresses predominant at depth (e.g. (Engelder, 1993)). On large faults (kilometric scale length), it seems therefore more appropriate to provide an estimation of fault friction based on the tectonic stress orientation or the fracture patterns measured in deep bore holes, which are more representative of the brittle crust stress state.

This approach, based on field observation and numerical modeling at the relay zone, seems therefore relevant for the estimation of fault friction along active fault segments interacting through their stress field. Its main advantage compared to rock test measures, is the in-situ estimation of the friction in its own geological context. We integrate a large part of the fault surface around the relay zone (and it can be done outside as well), as opposed to tests done on fault rocks, which correspond to a specific location of the fault surface crossed by the bore hole. Moreover, this approach provides an overall value of friction of the entire active fault zone, which may be composed of compartment with various fault rocks, as for example coarse cataclasites or gouges which can be difficult to analyze in laboratory tests. On the other hand, a limitation of this method is that permanent deformation (e.g. measured by GPS) can not be used to estimate friction with a quasi-static elastic model. Visco-elastic simulation of the lithosphere could be more appropriated if it allows to simulate the precise geometry of the fault segments.

## 3.8 Conclusion

In situ static friction can be estimated along a fault plane if its shape, the far field stress conditions and the stresses at its vicinity are well known. Joints and stylolites reactivated

in shear show roughly different angles of linking fractures at their extensional relay zones. The irregular shape of the stylolites and the rectilinear trace of the joints suggest that different frictional behaviour may explain these differences in branching angles. Photoelastic and numerical modeling confirm this phenomenon. For the same remote stress conditions, variation of the static friction along simulated faults explains a wide part of the range of branching angle measured at relay zones. In particular, our paper reveals four main points:

- A simple Amontons first law can not be used systematically to infer the static friction along natural faults,
- To discuss the amount of friction along a fault, the analysis of the local stress field must be compared to elasto-static approaches that integrate the effect of mechanical interactions along ended faults, irregular in shape, segmented or more complex,
- Both field data, photoelasticity and numerical modeling show that wide variations of friction can explain a large part of the variation in the angle of secondary fracturing in the relay zones,
- Shear-reactivated joints have lower estimated static friction than shear-reactivated stylolites.

## 3.9 Acknowledgments

We which to particularly thank and dedicate this paper to Maurice Mattauer who left us in April 2009. He discovered the studied outcrop and recently participated to discussions about this work at the laboratory and also in the field. The field work from Roger Soliva was supported by an “Action Structurante 2006” grant from the laboratory Geosciences Montpellier UMR5243. Thanks to the Igeoss’s consortium members for their support in the development of Poly3D (now renamed iBem3D). W. Ashley Griffith and Roy Schlische are thanked for their helpful comments.

# References


Auzias, V. (1995). *Photoelastic modeling of stress perturbations near faults and of the associated fracturing: petroleum industry application, II: Mechanism of 3D joint development in a natural reservoir analogue: the flat-lying Devonian Old Red Sandstone of Caithness (Scotland).* PhD thesis, Université de Montpellier II, France.

Auzias, V., Rives, T., Rawnsley, K. D., and Petit, J. . (1997). Fracture orientation modeling in the vicinity of a horizontal well. *Bulletin Elf aquitaine Production*, F64018:381–397.

Barquins, M., Chaker, C., and Petit, J.-P. (1997). Influence du frottement sur le branchement de fissures  partir de dfauts obliques soumis  une compression uniaxiale. *Compte Rendu de L'Academie des Sciences*, T324:29–36.

Barquins, M. and Petit, J.-P. (1992). Kinetic instabilities during the propagation of a branch crack: e.ects of loading conditions and internal pressure. *Journal of Structural Geology*, 14:893–903.

Bourne, S. J. and Willemse, E. J. M. (2001). Elastic stress control on the pattern of tensile fracturing around a small fault network at nash point, uk. *Journal of Structural Geology*, 23:1753–1770.

Brace, W. and Kohlstedt, D. (1980). Limits on lithospheric stress imposed by laboratory experiments. *Journal of Geophysical Research*, 85:62486252.

Brudy, M., Zoback, M. D., Fuchs, K., Rummel, F., and Baumgartner, J. (1997). Estimate of the complete stress tensor to 8 km depth in the ktb scientific drill holes: Implications for crustal strength. *J. Geophys. Res.*, 102:18453–18475.

Brune, J., Henyey, T., , and Roy, R. (1969). Heat flow, stress, and rate of slip along the san andreas fault, california. *Journal of Geophysical Research*, 74:38213827.

Burgmann, R. and Pollard, D. D. (1994). Slip distribution on faults: effects of stress gradients, inelastic deformation, heterogeneous host-rock stiffness, and fault interaction. *Journal of Structural Geology*, 16(12):1675–1690.

Byerlee, J. D. (1978). Friction of rocks. *Pure and Applied Geophysics*, 116:615626.

Chaker, C. and Barquins, M. (1996). Sliding effect on branch crack. *Physics and Chemistry of the Earth*, 21:319–323.

Comninou, M. and Dundurs, J. (1975). The angular dislocation in a half space. *Journal of Elasticity*, 5(3):203–216.

d'Alessio M. A., E., B. A., and R., B. (2003). No frictional heat along the san gabriel fault, california: Evidence from fission-track thermochronology. *Geology*, 31:541–544.

Delair, J. and Leroux, C. (1978). Méthodes de quantification de la disparition de matiére au niveau de stylolites tectoniques et mécanismes de la deformation cassante des calcaires. *Bulletin de la Sociéé Géologique de France*, 7:137–144.

Engelder, T. (1993). *Stress Regimes in the Lithosphere*. Princeton University Press.

Fletcher, R. and Pollard, D. (1981). Anticrack model for pressure solution surfaces. *Geology*, 9:419–424.

G.C.P., K., Stein, R., S., and Lin, J. (1994). Static stress changes and the triggering of earthquakes. *Bulletin of the Seismological Society of America*, 84:935953.

Hanks, T. (1977). Earthquake stress drops, ambient tectonic stress, and the stresses that drive plate motion. *Pure and Applied Geophysics*, 115:441458.

Hatheway, A. and Kiersch, G. (1989). Engineering properties of rock. in:. pages 672–715.

Hetényi, M., editor (1966). *Handbook of experimental stress analysis*. Wiley, New York.

Joussineau, G., Petit, J.-P., and Gauthier, B. (2003). Photoelastic and numerical investigation of stress distributions around fault models under biaxial compressive loading conditions. *Tectonophysics*, 363:1943.

Kattenhorn, S., Aydin, A., and Pollard, D. (2000). Joints at high angles to normal fault strike: an explanation using 3d numerical model of fault perturbated stress field. *Journal of Structural Geology*, 22:1–23.

Kattenhorn. S., A. and Marshall, S., T. (2006). Fault-induced perturbed stress fields and associated tensile and compressive deformation at fault tips in the ice shell of europa: implications for fault mechanics. *Journal of Structural Geology*, 28:22042221.

Lachenbruch, A. and Sass, J. (1980). Heat flow and energetics of the san andreas fault zone. *Journal of Geophysical Research*, 85:61856222.

Lovely, P. J., Pollard, D. D., and Mutlu, O. (2009). Regions of reduced static stress drop near fault tips for large strike-slip earthquakes. *Bulletin of the Seismological Society of America*, 99:1691–1704.

Lunn, R. J., Willson, J. P., Shipton, Z. K., and Moir, H. (2008). Simulating brittle fault growth from linkage of preexisting structures. *J. Geophys. Res.*, 113,B07403.

Maerten, F., Maerten, L., and Cooke, M. (2009). Solving 3d boundary element problems using constrained iterative approach. *Computational Geosciences*.

Maerten, F., Resor, P. G., Pollard, D. D., and Maerten, L. (2005). Inverting for slip on three-dimensional fault surfaces using angular dislocations. *Bulletin of the Seismological Society of America*, 95:1654–1665.

Maerten, L., Gillepsie, P., and Pollard, D. (2002). Effect of local stress perturbation on secondary fault development. *Journal of Structural Geology*, 24:145153.

Martel, S. (1997). Effects of cohesive zones on small faults and implications for secondary fracturing and fault trace geometry. *Journal of Structural Geology*, 19:835–847.

Mount, V. and Suppe, J. (1987). State of stress near the san andreas fault: Implications for wrench tectonics. *Geology*, 115:11431146.

Mutlu, O. and Pollard, D. (2008). On the patterns of wing cracks along an outcrop scale flaw: a numerical modeling approach using complementarity. *Journal of Geophysical Research*, 113.

Ohlmacher, G., C. and Aydin, A. (1997a). Mechanics of veins, fault and solution surface formation in the appalachian valley, u.s.a.: implications for fault friction, state of stress and fluid pressure. *Journal of Structural Geology*, 19:927–944.

Ohlmacher, G. and Aydin, A. (1997b). Mechanics of veins, fault and solution surface formation in the appalachian valley, u.s.a.: implications for fault friction, state of stress and fluid pressure. *Journal of Structural Geology*, 19:927–944.

Okada, Y. (1985). Surface deformation due to shear and tensile faults in a half-space. *Bulletin of the Seismological Society of America*, 75:1135–1154.

Petit, J., Wibberley, C., and Ruiz, G. (1999). 'crack-seal, slip': a new fault valve mechanism? *Journal of Structural Geology*, 21:1199–1207.

Petit, J.-P. and Barquins, M. (1988). Can natural faults propagate under mode ii conditions? *Tectonics*, 7:1243–1256.

Petit, J.-P. and Mattauer, M. (1995). Palaeostress superimposition deduced from mesoscale structures in limestone: the matelles exposure, languedoc, france. *Journal of Structural Geology*, 17:245256.

Poliakov, A., Dmowska, R., and Rice, J. (2002). Dynamic shear rupture interactions with fault bends and off-axis secondary faulting. *Journal of Geophysical Research*, 107.

Rawnsley, K., Rives, T., Petit, J., Hencher, S., and Lumsden, A. (1992). Joint development in perturbed stress fields near faults. *Journal of Structural Geology*, 14:939–951.

Raynaud, S. and Carrio-Schaffhauser, E. (1992). Rock matrix structures in a zone influenced by a stylolite. *Journal of Structural Geology*, 14:973–980.

Rispoli, R. (1981). Stress fields about strike-slip faults inferred from stylolites and tension gashes. *Tectonophysics*, 75:T29–T36.

Scholz (2000). Evidence for a strong san andreas fault.

Segall, P. and Pollard, D. (1980). Mechanics of discontinuous faulting. *Journal of Geophysical Research*, 85:4337–4350.

Soliva, R., Benedicto, A., and Maerten, L. (2006). Spacing and linkage of confined faults: the importance of mechanical thickness. *Journal of Geophysical Research*, 111.

T., P. (1985). Nearly frictionless faulting from unclamping in long-term interaction models. *Geology*, 30:10631066.

Taha, M. (1986). *Apport de la microtectonique cassante au problme des trajectoires de contraintes et de leurs perturbations. Exemples du Nord de Montpellier.* PhD thesis, Université de Montpellier II.

Thomas, A. L. (1993). Poly3d: a three-dimensional, polygonal element, displacement discontinuity boundary element computer program with applications to fractures, faults, and cavities in the earth's crust. Master's thesis, Stanford University.

Wawersik, W. and Brace, W. (1971). Post-failure behavior of a granite and diabase. *Rock Mechanics*, 3:61–85.

Willemse, E. and Pollard, D. (1998). On the orientation and patterns of wing cracks and solution surfaces at the tips of a sliding flaw or fault. *Journal of Geophysical Research*, 103:2427–2438.

Willemse, J. M. (1997). Segmented normal faults: Correspondence between three-dimensional mechanical models and field data. *Journal of Geophysical Research*, 102:675–692.

Willson, J., Lunn, R., and Shipton, Z. (2007). Simulating spatial and temporal evolution of multiple wing cracks around faults in crystalline basement rocks. *J. Geophys. Res.*, 113,B07403.

Zhou, X. (2006). Triaxial compressive behavior of rock with mesoscopic heterogenous behavior: Strain energy density factor approach. *Theoretical and Applied Fracture Mechanics*, 45:46–63.

Zoback, M. (1980). State of stress in the conterminous united states. *J. of Geophys. Research*, 86:6113–6156.

Zoback, M., Zoback, M., Mount, V., Eaton, J., Healy, J., Oppenheimer, D., Reasonberg, P., Jones, L., Raleigh, B., Wong, I., Scotti, O., , and Wentworth, C. (1987). New evidence on the state of stress of the san andreas fault system. *Science*, 238:1105–1111.

Zoback, M. D. and Healy, J. (1984). Friction, faulting, and in situ stress. *Annales Geophysicae*, 2:689698.

# CHAPTER 4

# Iterative 3D BEM solver on complex faults geometry using angular dislocation approach in heterogeneous, isotropic elastic whole or half-space

F. Maerten[(1,2)], L. Maerten[(1)]

(1) Igeoss, Montpellier, FRANCE
(2) University of Montpellier II, Geosciences, FRANCE

Published in Boundary Elements and other Mesh Reduction Methods 30, 2008

**Preamble**

Many simplifications are used in the formulation of the elastostatic BEM code. The major ones are linear elasticity (i.e. linear relations between the stress and infinitesimal strain components), iso-thermal conditions, isotropic and homogeneous material with respect to elastic moduli. Concerning the later, it is possible to extend the existing code to heterogeneous isotropic materials using the definition of complex 3D triangulated interfaces separating two regions of different material properties. Special boundary conditions have to be used at the interfaces in order to propagate the influence from one region to another

(i.e. continuity conditions in displacements and equilibrium conditions in traction). The following paper describes how to incorporate material heterogeneity within the boundary element code presented in chapter 1 and 2 using an iterative approach, and compares the method to a 2D analytical and numerical solution. Furthermore, it shows how to parallelize the computation on multicore architectures.

## About...

While reading Crouch and Starfield (Crouch and Starfield, 1983), I realized that implementing material heterogeneity was not so hard. What a mistake when using an iterative solver! It took me a long time to realize that, first, the self-effect was incorrectly computed in Poly3D, and, second, that the special continuity conditions at interfaces have to be solved simultaneously for a dual-element in order to have a strict precedence rule.

Laurent Maerten helped me building models for validation.

## Article Outline

## 4.1 Résumé

Basées sur la solution analytique du déplacement du à une dislocation angulaire 3D, il est possible de construire des boucles polygonales fermées avec un vecteur de Burgers constant, et où le champ de contraintes est dérivé en utilisant l'élasticité linéaire dans un milieu homogène, isotrope infini ou semi-infini. Dans ce code d'éléments frontières, chaque faille est discrétisée par un maillage triangulaire où des conditions aux limites mixtes sont prescrites.

Incorporer l'hétérogénéité des matériaux se fait en utilisant des doubles interfaces triangulées avec des conditions de continuité et d'équilibre particulières. Les interfaces et les failles peuvent donc avoir une géométrie complexe 3D sans trou ni chevauchement entre éléments.

Nous utilisons un solveur itératif où le système d'équations est décomposé au niveau de l'élément, permettant une formulation simple des conditions aux limites sur les failles et sur les interfaces. Il est démontré que la stricte dominance diagonale ne peut être atteinte que si les conditions de continuité et d'équilibre, pour un double élément donné, sont résolues simultanément. En utilisant une méthode de Gauss-Seidel, nous avons donc réduit la complexité tout en tenant compte automatiquement du caractère creux du système à résoudre. De plus, en utilisant un solveur de type Jacobi, nous montrons que la résolution du système d'équations peut simplement être parallélisée sur des procésseurs multi-cœurs. Quelques comparaisons sont faites avec des solutions analytiques et numériques en 2D.

## 4.2 Abstract

Based on the analytical solution of the induced displacement caused by a 3D angular dislocation, it is possible to construct closed polygonal loops with constant Burgers's vector, from which the stress is derived using linear elasticity in homogeneous, isotropic whole- or half-space. In this BEM code, each fault is discretized as a triangulated mesh, where mixed boundary conditions are prescribed.
Incorporate material heterogeneity is done by using triangulated interfaces made of dual-elements with prescribed continuity and equilibrium conditions. Each interface and fault can therefore have a complex 3D geometry with no gaps or overlaps between elements.
We use an interative solver where the system of equations is decomposed at the element level, allowing a simple formulation of the boundary conditions for elements making a fault, and continuity/equilibrium conditions at dual-elements making an interface. It is shown that strict diagonal dominance can be achieved only if continuity and equilibrium conditions, for a given dual-element, are solved simultaneously. Using a Gauss-Seidel-like method, we consequently reduce the complexity while automatically taking care of the sparsity of the system. Morevever, using a Jacobi-like solver, we show that the resolution of the system can simply be parallelized on multi-core processors. Some comparisons with a 2D analytical solution and a 2D BEM code are presented.

## 4.3 Introduction

In structural geology and geophysics, fault slip distributions play an important role for the induced stress perturbation. This slip distribution depends mainly on the geometrical configuration and boundary conditions along the faults, the remote boundary conditions as well as the constitutive behavior of the host rock. In particular, it was shown that the change in Young's modulus of the rock can affect the slip distribution in a non negligible way (Burgmann and Pollard, 1994). Therefore, it appears that heterogeneity cannot be ignored.
In 2D, Crouch and Starfield (Crouch and Starfield, 1983) proposed a method to add material heterogeneity into the Displacement Discontinuity Method (DDM). In 3D, it is possible to apply this method using the Okada's code (Okada, 1985) where fault surfaces are discretized into planar rectangular elements. However, this formulation necessarily introduces non-physical gaps and overlaps between adjacent elements which can perturb the solution (Maerten et al., 2005).

In this paper, we use the analytical solution of an angular-dislocation in elastic, homogeneous, isotropic whole- or half-space, where the stress is derived using linear elasticity in homogeneous, isotropic whole- or half-space (Comninou and Dundurs, 1975). A boundary element method is then formulated by discretization of all complex 3D faults into triangular elements. This BEM code (called Poly3D (Thomas, 1993)) is very similar to DDM ((Crouch and Starfield, 1983)), in which triangular elements of constant displacement discontinuity are employed. The advantage compare to Okada's code is that three-dimensional fault surfaces more closely approximate curviplanar surfaces and curved tiplines without introducing overlaps or gaps. Such formulation is very well suited to study faults interaction in 3D, since only faults surfaces have to be discretized (see for example (Maerten et al., 1999), (Maerten, 2000), (Muller et al., 2003) among others).
The addition of heterogeneous and isotropic materials is presented in this paper, and particularly an iterative method for solving the system is investigated.

## 4.4 BEM formulation

The BEM formulation employed here is derived from the analytical solution of an angular dislocation in 3D elastic whole- or half-space (Comninou and Dundurs, 1975). A triangular dislocation (or more generally a polygonal dislocation) with constant displacement discontinuity, or Burgers's vector $b$, can be constructed ((Thomas, 1993), (Jeyakumaran et al., 1992)) simply by superposition of six angular-dislocations (see Fig. 4.1).

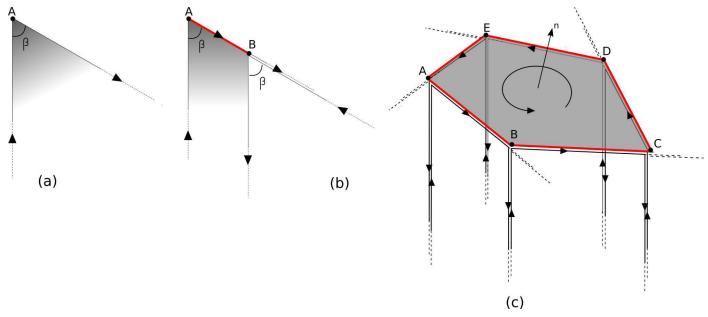


FIGURE 4.1: Construction of a polygonal element. (a) angular-dislocation ,(b) a dislocation-segment made of two angular dislocations, and (c) a polygonal-element made of five dislocation segments of 10 angular-dislocations.

Mixed boundary conditions (BC) are prescribed, and when Neumann BC are specified, we have to solve for the unknown Burgers's components. After the system is solved, it is possible to compute anywhere, within the whole- or half-space, displacement, strain or

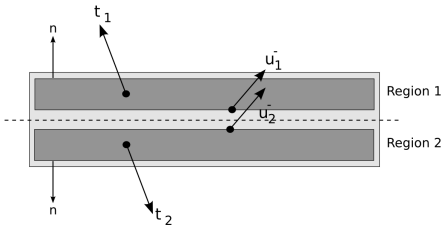


FIGURE 4.2: A dual-element part of an interface with equilibrium condition for tractions ($t_1 = -t_2$) and continuity conditions for displacement ($u_1^- = u_2^-$) on the negative side (in global coordinate system)

stress at observation points as a postprocess.

Incorporate material heterogeneity (or general piecewise inhomogeneous bodies) requires discretizing an interface between two regions of different material properties into two triangulated meshes, one for each region. These two surfaces have the particularity to be perfectly coalescent, but with opposite normals (see Fig. 4.2).

According to (Crouch and Starfield, 1983), continuity conditions on one side and equilibrium conditions on the other in element local coordinate system are applied (Crouch and Starfield, 1983) at interfaces (Fig 4.2). Doing so requires particular attention for two main reasons. First, since we are in 3D, it is impossible to have two opposite local coordinate systems. Indeed, if $x_i$ denotes the vectors of the first coordinate system ($i \in [0..2]$) and $X_i$ the second, we have $X_0 = -x_0$, $X_1 = -x_1$ and $X_2 = X_0 \times X_1 = (-x_0) \times (-x_1) = x_0 \times x_1 = x_2 \neq -X_2$ (where $\times$ denotes the vector product). Consequently, we have to express continuity conditions in global coordinate system. The second reason is that since the displacement is discontinuous when going from one side of an element to the other, we have to make sure that $U_{ee}^-$, the self displacement influence matrix at the element center on the negative side, is correctly computed. Due to the machine precision, it is not always guaranteed, and consequently, we force the element center to be on the negative side by applying an infinitesimal translation of the center along the reversed normal.

Therefore, equilibrium and continuity conditions can be written in global coordinate system as:

$$\begin{cases} \overset{1}{\tau}_e = -\overset{2}{\tau}_e \\ \overset{1}{u}_e^- = \overset{2}{u}_e^- \end{cases} \tag{4.1}$$

where polygonal elements $e$ in region 1 and 2 are perfectly coincident (they are called dual

elements in the remaining of the paper).
A global system of equations is then built, which incorporates both equlibrium, continuity and boundary conditions:

$$\begin{bmatrix} \overset{1}{T_I} & \overset{1}{T_F} & \overset{2}{T_I} & \overset{2}{T_F} \\ -\overset{1}{D_I^-} & -\overset{1}{D_F^-} & \overset{2}{D_I^-} & \overset{1}{D_F^-} \\ \overset{1}{T_I} & \overset{1}{T_F} & 0 & 0 \\ 0 & 0 & \overset{2}{T_I} & \overset{2}{T_F} \end{bmatrix} \begin{Bmatrix} \overset{1}{b_I} \\ \overset{1}{b_F} \\ \overset{2}{b_I} \\ \overset{2}{b_F} \end{Bmatrix} = \begin{Bmatrix} 0 \\ 0 \\ \overset{1}{t_F^0} \\ \overset{2}{t_F^0} \end{Bmatrix} \tag{4.2}$$

where $I$ and $F$ stands for elements at interfaces and faults respectively. $D^-$ and $T$ represent the displacement influence matrix on the negative side and the traction influence matrix respectively, both of them in global coordinate system. The two first rows define the equilibrium and continuity conditions at interfaces, while the last two represent the classical boundary conditions applied to fault surfaces, and $t_F^0$ represents the initially prescribed traction boundary values for Neumann BC.

## 4.5 Iterative solver

In order to reduce the model complexity from $O(n^3)$ to $O(n^2)$ and to take advantage of the sparsity of the system (Eq. 4.2), an iterative solver is used.
The Burgers's vector solution at a regular boundary element $e$ making a fault surface is given by:

$$b_e = T_{ee}^{-1} \left\{ t_e^0 - \sum_{f \neq e} T_{ef} b_f \right\} \tag{4.3}$$

where $T_{ef}$ denotes the traction influence matrix at the centroid of element $e$ due to element $f$.
Computing the solution for a dual-element part of an interface is tricky since we are dealing with an iterative solver for which the convergence is guaranteed if and only if the system is strict diagonal dominant (Golub and Van Loan, 1996), i.e. $\forall i, \forall j \neq i, |a_{ii}| > |a_{ij}|$. As an element $e_1$ and its dual part $e_2$ have the same geometry (only the orientation changes), $T_{e_1e_1}$ and $T_{e_2e_2}$ have the same diagonal values, and strict diagonal dominance is not honored (the same apply for $D^-$ matrices). Therefore, equilibrium condition in region $R_1$ and continuity condition in region $R_2$ have to be solved simultaneously for a given

dual-element. This leads to the following coupled elemental system:

$$\begin{Bmatrix} \overset{1}{b}_e \\ \overset{2}{b}_e \end{Bmatrix} = \begin{bmatrix} \overset{1}{T}_{ee} & \overset{2}{T}_{ee} \\ -\overset{1}{D}^{-}_{ee} & \overset{2}{D}^{-}_{ee} \end{bmatrix}^{-1} \begin{Bmatrix} -\sum_{f \neq e} \overset{1}{T}_{ef}\, b_f - \sum_{g \neq e} \overset{2}{T}_{eg}\, b_g \\ \sum_{f \neq e} \overset{1}{D}^{-}_{ef}\, b_f - \sum_{g \neq e} \overset{2}{D}^{-}_{eg}\, b_g \end{Bmatrix} \tag{4.4}$$

Eqs. (4.3) and (4.4) are then solved using a Gauss-Seidel procedure as shown in algorithm 4.1.

```
forall e ∈ S do
  | compute T_ee^{-1}
end
while ε > tolerance do
  | forall element e ∈ region R_1 do
  |   | if e ∉ interface then
  |   |   | let t = initial traction vector of e
  |   |   | forall element f ≠ e ∈ region R_1 do
  |   |   |   | t = t − T_ef b_f
  |   |   | end
  |   |   | use Eq. (4.3)
  |   |   | update ε
  |   |   | set b to e
  |   | end
  |   | else
  |   |   | let t = 0 and u^- = 0
  |   |   | forall element f ≠ e ∈ region R_1 do
  |   |   |   | t = t − T_ef b_f
  |   |   |   | u^- = u^- + D^-_ef b_f
  |   |   | end
  |   |   | forall element g ≠ e ∈ region R_2 do
  |   |   |   | t = t − T_eg b_g
  |   |   |   | u^- = u^- − D^-_eg b_g
  |   |   | end
  |   |   | use Eq. (4.4)
  |   |   | update ε
  |   |   | set 1b to e
  |   |   | set 2b to dual(e)
  |   | end
  | end
end
```

**Algorithm 4.1**: Solving iteratively the system of equations

This algorithm automatically takes care of the sparcity of the system, while allowing large model computation since practically no memory allocation is required.

## 4.6 Results

In order to check the validity of the formulation, we first compare the 2D analytical solution (Crouch and Starfield, 1983) of an annulus (with $\nu_1 = 0.25, G_1 = 1$) inside a circular hole in a large plate ($\nu_2 = 0.25, G_2 = 0.5$) (Fig. 4.3.b), with a corresponding 3D model (Fig. 4.3.a). The hole is subjected to an internal pressure of 0.001 Pa, and the computed

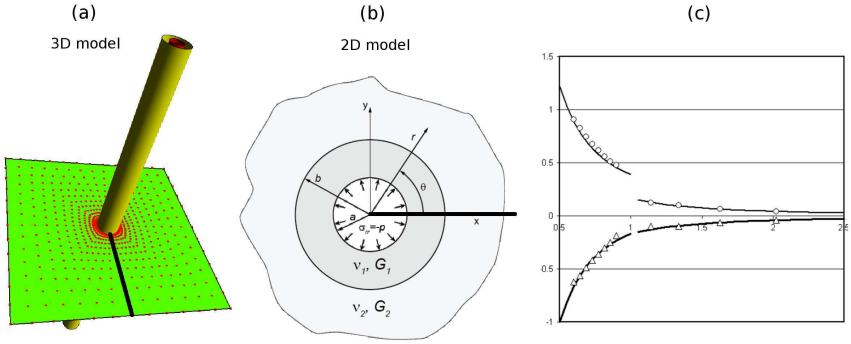


FIGURE 4.3: Comparison with a 2D analytical solution. (a) 3D model configuration, (b) 2D model, (c) comparison of normalized $\sigma_3$ (triangles) and $\sigma_1$ (circles), where solid lines are for the numerical solutions.

normalized $\sigma_3$ and $\sigma_1$ along the bold lines are compared. In order to avoid boundary effects, the tubes, defining the annulus and the hole in 2D, are extended far from the zone of interest, materialized by the squared observation plane (Fig. 4.3.a). It can be seen that the computed values along the bold line in Fig. 4.3.a match the analytical solution.
Comparison with an existing 2D BEM code (Fig. 4.4) is described in (Burgmann and Pollard, 1994). The model is composed of a penetrating fault inside an inclusion, and various configurations are computed where the ratio of the Young's modulus in the inclusion to that of the host material, was set to 1, 0.1 and 10. It is subjected to a uniform remote unit shear stress $\sigma_{yx}$ of 1 MPa. The corresponding 3D model is composed of two orthogonal vertical planar surfaces, one for the interface defining the inclusion and the other for the penetrating fault. The other five sides of the box inclusion are not taken into account. The bold lines in Fig. 4.4.a and 4.4.b represents the x-axis of Fig. 4.4.c. Computed dip-slip component are reported onto the Y-axis. Again, the results match the 2D BEM solutions.

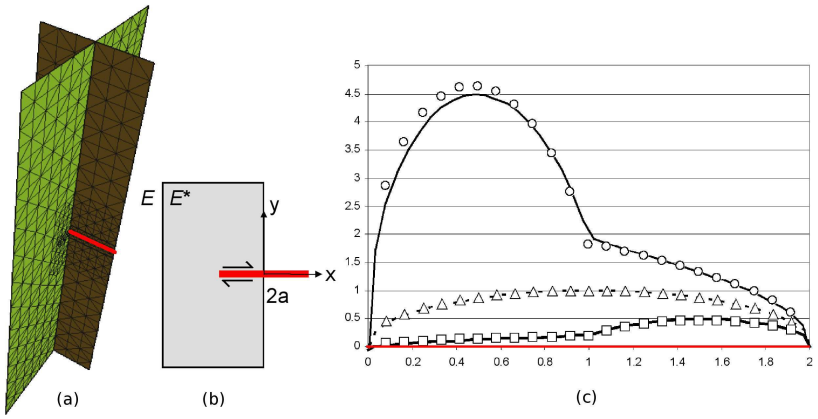


FIGURE 4.4: Comparison with a 2D BEM code. (a) 3D model configuration, (b) 2D model, (c) comparison of the computed dip-slip component onto the fault (along the bold line in (a) and (b)). Triangles is for $E^*/E = 1$, circle for $E^*/E = 0.1$, and squares for $E^*/E = 10$

.

## 4.7 Optimizations

Even if this iterative algorithm is in $O(n^2)$, it is slower than the direct solver, since at each iteration and for each element, the influence matrices (traction and displacement) due to all other elements have to be re-calculated.

### 4.7.1 Bufferized elemental matrices

We can highly increase the speed if we store elemental matrices $T_{ef}$, $D^-_{ef}$, $T_{eg}$ and $D^-_{eg}$ from Eqs. (4.3) and (4.4) for each element $e$. Of course, if we reach the maximum available RAM (Random Access Memory), the remaining matrices have to be computed "on the fly" in order to avoid memory "swapping".
Furthermore, since the global system is never constructed nor inverted, there is no cumulative roundoff error when using elemental matrices with floating precision (4 bytes) instead double (8 bytes), allowing larger models to be computed.
Table 4.1 gives some examples of the gain of speed using a direct LU solver and the iterative solver with and whitout allocation.

### 4.7.2 Parallelization on multi-core processors

The iterative solver allows taking advantage of the new multi-core processors architecture, by parallelizing the computation onto different threads using the cross-platform package

TABLE 4.1: Speed comparison (in seconds) for different model sizes, performed on Intel Xeon 2Ghz with 8 cores running Linux Ubuntu. "LU" is the classical direct solver of the whole system, "Iter" is the iterative solver with no memory allocation, "Alloc" is the iterative solver with memory allocation, and "Thread" is the parallelized version on 2 or 8 threads. Models marked "x" where stopped before the end.

| Model size | LU | Iter | Alloc | Thread 2 | Thread 8 |
|---|---|---|---|---|---|
| 2200 | 49 | 380 | 9 | 8 | 6 |
| 4200 | 466 | 1018 | 46 | 26 | 8 |
| 9000 | 1145 | 5600 | 205 | 116 | 32 |
| 16000 | x | x | 1200 | 690 | 205 |

(Trolltech, 2010) (where the number of threads $k$ is defined by number of processors on the mother board times the number of cores for each processor). At the beginning, the system is split into $k$ sub-systems (the decomposition technique is irrelevant), one for each thread. Consequently, $k$ iterative solvers are run in parallel. There is no need to update the communication between each sub-process at the end of each iteration since they share the same model memory. The only constraint is to update the new displacement onto the elements at the end of each iteration by waiting for each thread to finish its job in order to avoid read/write conflicts. This is simply achieved by using a Jacobi procedure instead of the Gauss-Seidel one. Table 4.1 gives an overview of the computation time for $k = 2$ and $k = 8$.

## 4.8 Conclusions

Indirect BEM techniques appear to be an advantageous way of modeling stress perturbation around faulted area in whole- or half-space since only the fault surfaces have to be discretized as boundary elements. Implementing material heterogeneity requires little effort and the use of an iterative solver have a great impact in terms of speed for the system resolution and memory consumption. The Jacobi version of the iterative solver also permits parallelization on multi-core processors in a simple and efficient way.
Since each dual element generates six unknowns into the system, it is necessary to reduce the complexity, which is part of our current research.

# References


Burgmann, R. and Pollard, D. D. (1994). Slip distribution on faults: effects of stress gradients, inelastic deformation, heterogeneous host-rock stiffness, and fault interaction. *Journal of Structural Geology*, 16(12):1675–1690.

Comninou, M. and Dundurs, J. (1975). The angular dislocation in a half space. *Journal of Elasticity*, 5(3):203–216.

Crouch, S. L. and Starfield, A. M., editors (1983). *Boundary element methods in solid mechanics*. George Allen and Unwin, London.

Golub, G. H. and Van Loan, C. F. (1996). *Matrix computation*. Johns Hopkins University Press, Baltimore, MD.

Jeyakumaran, M., Rudnicki, J. W., and Keer, L. M. (1992). Modeling slip zones with triangular dislocation elements. *Bulletin of the Seismological Society of America*, 82:2153–2169.

Maerten, F., Resor, P. G., Pollard, D. D., and Maerten, L. (2005). Inverting for slip on three-dimensional fault surfaces using angular dislocations. *Bulletin of the Seismological Society of America*, 95:1654–1665.

Maerten, L. (2000). Variation in slip on intersectiong normal faults: Implications for paleostress inversion. *Journal of Geophysical Research*, 105(25):553–565.

Maerten, L., Willemse, E. J. M., Pollard, D. D., and Rawnsley, K. (1999). Slip distributions on intersecting normal faults. *Journal of Structural Geology*, 21:259–271.

Muller, J. R., Aydin, A., and Maerten, F. (2003). Investigating the transition between the 1967 mudurnu valley and 1999 izmit earthquakes along the north anatolian fault with static stress changes. *Geophysics Journal International*, 154:471–482.

Okada, Y. (1985). Surface deformation due to shear and tensile faults in a half-space. *Bulletin of the Seismological Society of America*, 75:1135–1154.

Thomas, A. L. (1993). Poly3d: a three-dimensional, polygonal element, displacement discontinuity boundary element computer program with applications to fractures, faults, and cavities in the earth's crust. Master's thesis, Stanford University.

Trolltech (2010). Qtconcurrent, http://www.trolltech.com.

# CHAPTER 5

# Adaptive cross approximation applied to system resolution and post-processing for a 3D elastostatic problem using the Boundary Element Method

F. Maerten[(1,2)]

(1) Igeoss, Montpellier, FRANCE
(2)University of Montpellier II, Geosciences, FRANCE

In press in Engineering Analysis with Boundary Element, 2010,
DOI: 10.1016/j.enganabound.2009.10.016



**Preamble**

Enhancing a model using the techniques described in the previous chapters, leads to more complex systems to solve. This is especially true when using heterogeneous materials.

Since we are using boundary element techniques, the resulting system matrix is full populated (dense). This implies three drawbacks. First, the memory needed to store the system matrix grows as $O(n^2)$, where n is the number of unknowns. Second, the time needed to solve the system is $O(n^2)$. Third, the time needed to compute the displacement, strain and stress at observation grids as post-processing is $O(pn)$, where p is the number of observation points.

In this chapter, we try to reduce the complexity of such a formulation by approximation, allowing large model computations. The post-processing is also optimized using the same technique, and we show that the speed gained is a function of the position of the observation points according to the discontinuities making the model. As an example, computing the displacement and stress field at one million observation points can be done in less than 3 minutes using 9000 discontinuous elements, whereas it takes more than 17 hours using the standard method.

## About...

After giving a talk at the $30^{th}$ conference on Boundary Elements and other Mesh Reduction Methods, I discovered the $\mathcal{H}$-Matrix technique, and hense this paper where we use this thechnique for optimization of the iterative solver and post-processing...

# Article Outline

## 5.1 Résumé

Nous présentons la technique d'optimisation basée sur les matrices hiérarchiques (H-Matrix) combinée avec la méthode d'approximation adaptative croisée (ACA) appliquée à des problèmes élastostatiques en trois dimensions (3D) et utilisant la méthode des éléments frontières (BEM). Ce code est utilisé en géologie structurale et géomécanique pour évaluer la déformation et le champ de contrainte perturbé associés à des surfaces de discontinuités en déplacement. Une telle optimisation réduit significativement (i) le temps de calcul et la mémoire nécessaire pour la résolution du système d'équations, mais plus important encore (ii) le temps nécessaire pour effectuer le post-traitement aux points d'observation où la déformation et le champ de contrainte perturbé sont à évaluer. Plus précisément, il est montré que la structure H-matrix utilisée avec l'ACA, capte précisement la régularité du noyau au cours de la phase de post-traitement en fonction de la position des points d'observation, et optimise le calcul en conséquence. Combinée avec la parallélisation sur architectures multi-cœurs, cette technique permet des calculs intensifs sur ordinateurs de bureau ou portables. Des simulations numériques sont présentées, montrant les avantages d'une telle optimisation par rapport à une approche classique.

## 5.2 Abstract

We present the Hierarchical Matrix ($\mathcal{H}$-Matrix) technique combined with the Adaptive Cross Approximation (ACA) applied to a three-dimensional (3D) elastostatic problem using the Boundary Element Method (BEM). This is used in structural geology and geomechanics for the evaluation of the deformation and perturbed stress field associated with surfaces of displacement discontinuity. Such optimization significantly reduces (i) the time and memory needed for the resolution of the system of equations , but more importantly (ii) the time needed for the post-processing at observation points where the deformation and the perturbed stress field are evaluated. Specifically, it is shown that the $\mathcal{H}$-Matrix structure used with the ACA, clearly captures the kernel smoothness during the post-processing stage according to the field point positions, and optimizes the computation accordingly. Combined with the parallelization on multi-core processors, this technique allows intensive computations to be done on personal desktop and laptop computers. Numerical simulations are presented, showing the advantages of such optimizations compared to the standard method.

**Keyword**: 3D boundary element method, Geomechanics, Hierarchical matrix, Adaptive cross approximation, Multi-core parallelization

## 5.3 Introduction

For geophysicists and structural geologists, easy construction and rapid computation of three-dimensional (3D) models composed of faults and fractures with complex geometries is fundamental to the study of earthquake triggering and fault interactions, or to determining the perturbed stress field and deformation associated with displacement discontinuities in Earth's crust. Using a Boundary Element Method (BEM) greatly simplifies the model definition since only the discontinuities have to be discretized, and the surrounding rock does not need to be meshed using either triangles (2D) or tetrahedra (3D). In 2D, Crouch and Starfield (Crouch and Starfield, 1983) proposed a method called the Displacement Discontinuity Method (DDM). In 3D, a pioneering method is Okada's code (Okada, 1985) where fault surfaces are discretized into planar rectangular elements. However, this formulation necessarily introduces non-physical gaps and overlaps between adjacent elements which perturb the solution (Jeyakumaran et al., 1992; Maerten et al., 2005). Another method in 3D is the use of the analytical solution of an angular-dislocation in an elastic, homogeneous, isotropic whole- or half-space (Comninou and Dundurs, 1975).

An indirect Boundary Element Method is then formulated by discretizing all complex 3D faults into triangular elements. This BEM code, called Poly3D (Jeyakumaran et al., 1992; Thomas, 1993; Maerten et al., 2005), employs triangular elements of constant displacement discontinuity, and has been extended to incorporate heterogeneous materials (Maerten and Maerten, 2008). The advantage compared to Okada's formulation is that three-dimensional fault surfaces more closely approximate curviplanar surfaces and curved tip-lines without introducing overlaps or gaps between elements. Such a formulation is very well suited to the study of fault interactions in 3D (see for example (Maerten et al., 1999; Maerten, 2000; Muller et al., 2003) among others).

However, even if the problem dimension is one order less than the Finite Element Method (FEM), it suffers from a fully populated system matrix because each triangular element will be influenced by all the others, leading to a huge memory requirement, and long execution times to solve the system of equations ($O(kn^2)$ complexity when using an iterative solver, where $n$ is the number of triangular elements and $k$ the number of iterations).

Moreover, doing post-processing at $p$ observation points requires $O(pn)$ operations for each dependent variable, which can be considered as a penalty for users when $p$ is large. This is usually the case when studying the deformation and perturbed stress field for a model using dense 3D grids as observation points.

We apply of the Adaptive Cross Approximation method (ACA) to the resolution of the system of equations and more importantly to post-processing using multi-core architectures, leading to a drastic reduction of the computational time as well as a memory reduction, which allow large models to be computed on desktop or laptop computers.

The paper is organized as follows. Section 5.4 presents the formulation of the BEM code used for the optimization. Section 5.5 reviews the Hierarchical Matrix ($\mathcal{H}$-Matrix) technique as well as the ACA method. Section 5.6 briefly describes the ACA applied to resolution of the system of equations and section 5.7 is devoted to optimization in the post-processing stage. Finally, section 5.8 discuss the parallelization of the post-process on multi-core architectures.

## 5.4 Boundary Element formulation

For the boundary element method used here, we adopt the analytical solution of an angular dislocation in an elastic whole-space (Yoffe, 1960) or half-space as described by Comninou and Dundurs (Comninou and Dundurs, 1975), through the code Poly3D (Thomas, 1993). This formulation is derived from the elastic theory of dislocations (Steketee, 1958b,a) where a dislocation is represented by a cut in a infinite or finite elastic body. The two

faces of the cut are deformed in different ways by applying some force distribution to them, maintaining the original equilibrium state. The dislocation is then determined by the shape of the cut and by the discontinuity of the components of the displacement vector across the cut (called Burgers vector). It is obvious that the edge of the cut is a singularity in general, but does not significantly perturb the results (Jeyakumaran et al., 1992). Comninou and Dundurs (Comninou and Dundurs, 1975) give the analytical expressions for the displacement components due to an angular dislocation in a elastic whole- or half-space, which is used in our formulation to construct triangular elements made of six angular dislocations and with constant displacement discontinuity. Then, any complex discontinuous surface is discretized using such triangular discontinuous elements.

Given a point $M$ in the elastic body, the displacement $\mathring{\mathbf{u}}$ due to an angular dislocation $(A_1, \alpha_1, \beta_1)$ at point $A_1$ is given by (see Fig. 5.1a)

$$\mathring{\mathbf{u}}(M) = \mathring{\mathbf{U}}(M, A_1, \alpha_1, \beta_1)\mathbf{b} \tag{5.1}$$

and is a linear function of the Burgers vector $\mathbf{b}$ or displacement discontinuity vector. $\alpha_1$ and $\beta_1$ are the trending and plunging angles of the angular dislocation at point $A_1$, respectively. Coefficients of the matrix $\mathring{\mathbf{U}}$ are directly given by Comninou and Dundurs (Comninou and Dundurs, 1975) and are not reproduced here. A bi-angular dislocation, having two vertical legs, perpendicular to the free surface, is then constructed and is made up of two angular dislocations $(A_1, \alpha_1, \beta_1)$ and $(A_2, \alpha_1, \beta_1)$ (Fig. 5.1b). The total displacement at point M is simply the superposition of the two angular dislocation contributions

$$\begin{aligned} \bar{\mathbf{u}}(M) &= [\mathring{\mathbf{U}}(M, A_1, \alpha_1, \beta_1) - \mathring{\mathbf{U}}(M, A_2, \alpha_1, \beta_1)]\mathbf{b} \\ &= \bar{\mathbf{U}}\mathbf{b} \end{aligned} \tag{5.2}$$

Using the same process of superposition, a triangular element $\{A_1, A_2, A_3\}$ (or a polygonal element in the general case) is build with three bi-angular dislocations (Fig. 5.1c), where the legs under each vertex cancel, leaving a displacement discontinuity only in the triangle. The superposition of these dislocations are vertical surfaces defining a volume. This volume is semi-infinite and vertically trending compared to the global coordinate system (Fig. 5.1.d). The total displacement at point M induced by a triangular dislocation made

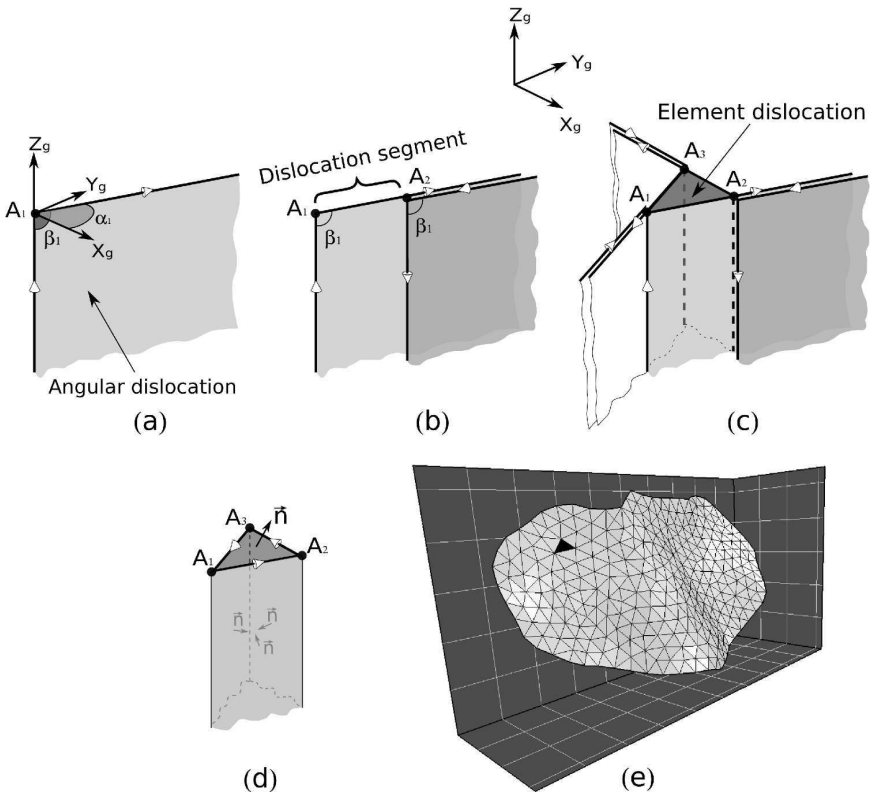


FIGURE 5.1: Construction of a polygonal element made of three dislocation segments. (a) An angular dislocation construction in global coordinate system ($x_g$,$y_g$,$z_g$) with its trending ($\alpha_1$) and plunging ($\beta_1$) angles. (b) Two angular dislocations are used to construct a dislocation segment ($A_1, A_2$). (c) Three dislocation segments are superimposed to create a triangular element ($A_1, A_2, A_3$). (d) Triangular configuration where the legs under each vertex cancel, leaving a displacement discontinuity only in the triangle. The superposition of these dislocations are vertical surfaces defining a volume. This volume is semi-infinite and vertically trending compared to the global coordinate system. (e) The discretization of a three-dimensional fault into discontinuous triangular boundary elements allows the construction of a surface with any desired tip-line and shape. The dark triangle corresponds to the element in (c) and (d)

of three dislocation segments, is therefore given by

$$\begin{aligned} \mathbf{u}(\mathbf{M}) &= \sum_{i=1}^{3} \bar{\mathbf{U}}(M, A_i, A_{i+1}, \alpha_i, \beta_i)\mathbf{b} \\ &= \mathbf{U}\mathbf{b} \end{aligned} \tag{5.3}$$

Here, $\mathbf{U}$ is called the *displacement influence matrix*. Once the displacement due to a triangular element is known, the total solution at a point $M$ is recovered by considering the influence of all triangular elements making the model.

The Burgers vector $\mathbf{b}$, for a given triangular element, can be divided into two displacement vectors, $\mathbf{u}^+$ on the positive side of the element and $\mathbf{u}^-$ on the negative side, and are related

by

$$\mathbf{b} = \mathbf{u}^{+} - \mathbf{u}^{-} \tag{5.4}$$

which shows that the use of this double-layer kernel experiences a jump in the displacement as a point $M$ passes through the boundary of the domain. The Burgers vector is expressed in the element local coordinate system constructed with $\mathbf{x}$ in the direction of greatest inclination of the element, $\mathbf{z}$ in the direction of the element's normal, and $\mathbf{y}$ is the cross-product of $\mathbf{z}$ and $\mathbf{x}$.

Similarly, the strain field at point M, due to triangular element, can be computed by partial differentiation of (5.3) using the linearized *Green-St Venant* strain tensor

$$\epsilon = \frac{\mathbf{1}}{\mathbf{2}}(\nabla\mathbf{u} + \nabla\mathbf{u}^{\mathbf{T}}) \tag{5.5}$$

where $\nabla\mathbf{u}$ is the deformation gradient tensor. Equation (5.5) leads to the *strain influence matrix* due to an angular dislocation

$$E_{ijk} = \frac{1}{2}\left(\frac{\partial U_{ik}}{\partial x_j} + \frac{\partial U_{jk}}{\partial x_i}\right) \tag{5.6}$$

which relates the strain at M and the element Burgers vector $\mathbf{b}$ by

$$\epsilon(\mathbf{M}) = \mathbf{E}\mathbf{b} \tag{5.7}$$

The stress tensor is given by Hooke's law for infinitesimal deformation as

$$\sigma_{ij} = 2G\epsilon_{ij} + \lambda\epsilon_{kk}\delta_{ij} \tag{5.8}$$

where $G$ is the shear modulus, $\lambda$ is the Lamé's constant, $\delta_{ij}$ is the Kronecker delta, and $\epsilon$ is given by (5.5). Substituting (5.5) into (5.8) and using (5.7) yields the stress $\sigma$ at any point M induced by one triangular dislocation

$$\sigma(\mathbf{M}) = \mathbf{S}\mathbf{b} \tag{5.9}$$

$\mathbf{S}$ is called the *stress influence matrix* at a point $M$ due to a triangular dislocation.

The element traction can now be defined using Cauchy's formula by resolving the stress tensor $\sigma$ onto the triangular element plane using its centroid as the collocation point

$$\mathbf{t} = \sigma\mathbf{n} \tag{5.10}$$

where $n$ represents the element's normal. Combining (5.10) and (5.9), leads to

$$\mathbf{t} = \mathbf{T}\mathbf{b} \tag{5.11}$$

where $\mathbf{T} = \mathbf{S}\mathbf{n}$ is the *traction influence matrix*.

Using the traction formulation for a triangular dislocation, the total traction at the center of a triangular element is simply the superposition of all tractions induced by the triangular elements within the elastic body plus those due to a uniform (remote) stress state. A system of linear equations can then be constructed to solve for the unknown Burgers vector components

$$\{\mathbf{t}\} = [\mathbf{T}]\{\mathbf{b}\} \tag{5.12}$$

In equation (5.12), $\{\mathbf{t}\}$ represents the column of the initially prescribed traction vector components of the triangular dislocations, $[\mathbf{T}]$ is a *dense matrix* of traction influence coefficients, and $\{\mathbf{b}\}$ is the column of unknown Burgers vector components.
The fully populated system (5.12) can be solved using an iterative solver for which the complexity is of $O(kn^2)$ where $k$ is the number of iterations and $n$ the number of unknowns.

When all displacement discontinuities are known, stress, strain and displacement can be computed within the elastic body at $p$ observation points in $O(pn)$.

## 5.5 Blockwise low-rank approximant

Among various methods of optimization (Rokhlin, 1985; Hackbusch and Nowak, 1989), the $\mathcal{H}$-Matrix technique (Hackbusch, 1999) combined with ACA (Bebendorf and Rjasanow, 2003) seems to be the most appropriate and the fastest to implement since approximation is applied to the matrix entries of the system after assembling (algebraic approximation), and does not rely on the kernel functions before assembling, as done by the multipole methods (Rokhlin, 1985; Greengard and Rokhlin, 1987).
We describe the $\mathcal{H}$-Matrix technique adopted in this paper as well as the ACA method, before concentrating on the optimization of the resolution of the system and post-processing.

### 5.5.1 $\mathcal{H}$-Matrices

$\mathcal{H}$-Matrix is a method of clustering a matrix into several blocks such that near-field block influences are evaluated in the usual way, whereas far-field blocks can be approximated by interpolation or rank reduction.
In order to construct the block decomposition, a geometrical rule has to be chosen for the clustering of the model. We adopt recursive bisection as it is fast and gives good results. Using a *kd-tree* containing all sources and fields, a subdivision by bisection is operated recursively, leading to a binary tree of *blocks*, where the root corresponds to the entire model. The recursive subdivision stops when the number of items in a block reaches a prescribed minimum. We end-up with a binary partition of the model made of blocks. Then, what remains is to determine the near- and far-field block-pairs using this decomposition. Given two blocks $C_1$ and $C_2$, the admissible condition

$$\min(diam(C_1), diam(C_2)) \leqslant dist(C_1, C_2) \tag{5.13}$$

is used to check whether $C_1$ and $C_2$ can be used for approximation. The diameter of a set of points $C$, $diam(C)$, is the maximal distance between any pair of points in $C$, and is defined as

$$diam(C) = \max_{p,q \in C} \parallel p - q \parallel \tag{5.14}$$

The distance between two sets of points, $dist(C, D)$, is defined as

$$dist(C, D) = \min_{p \in C, q \in D} \parallel p - q \parallel \tag{5.15}$$

In (5.13), $C_1$ represents a block containing source elements, and $C_2$ a block containing field points. If the condition (5.13) failed, the subdivision of these blocks continues recursively. Otherwise, $\{C_1, C_2\}$ is considered as a candidate for far-field approximation. If the blocks cannot be bisected anymore and the admissible condition is not met, near-field will be used instead (full computation). This process starts at the root of the cluster tree, and we end-up with a unique structure, called the $\mathcal{H}$-Matrix. This hierarchical structure contains:

$$\begin{cases} F_{C_1,C_2} & \text{block-pairs for near-field} \\ S_{C_1,C_2} & \text{block-pairs for far-field} \\ P_C & \text{block parents of } F_{C_1,C_2} \text{and } S_{C_1,C_2} \end{cases} \tag{5.16}$$

### 5.5.2 ACA

Once the matrix is partitioned into an $\mathcal{H}$-Matrix structure, the far field block-pair $S_{C_1,C_2}$ are approximated using the Adaptive Cross Approximation (Bebendorf and Rjasanow, 2003). According to the admissibility condition (5.13), blocks $C_1$ and $C_2$ are assumed to be far apart so the underlying functions of the kernel are asymptotically smooth. This simplification is not generated by approximating the kernel functions of the integral operator (see (Rokhlin, 1985; Hackbusch and Nowak, 1989; Greengard and Rokhlin, 1987)), but rather by finding a low-rank approximant from few of the original matrix entries. Therefore, it is not necessary to construct the whole matrix. One of the biggest advantages of this method, compared to the kernel approximant, is that only the original matrix entries are needed, and changing the kernel does not required recoding of the approximant.
Our goal is not to discuss the ACA algorithm in detail: for more informations see (Bebendorf, 2000, 2008; Bebendorf and Rjasanow, 2003).

## 5.6 $\mathcal{H}$-Matrices applied to the resolution of the system of equations

Using the $\mathcal{H}$-Matrix structure defined previously, items within each terminal block consist exclusively of triangular elements which are simultaneously sources and fields. While building the structure recursively, the matrix $\mathbf{A^F}$ related to a full block-pair $F_{C_1,C_2}$ is generated and stored without approximation. On the other hand, the matrix $\mathbf{A_k^S}$, of size $m_k \times n_k$ and related to a sparse block-pair $S_{C_1,C_2}$, is generated using the ACA technique and stored as two vector sets, $\mathbf{u} \in \mathbf{R^{n_k}}$ and $\mathbf{v} \in \mathbf{R^{m_k}}$, satisfying $\mathbf{A_k^S} = \sum_{\mathbf{l=1}}^{\mathbf{k}} \mathbf{u_l v_l^T}$, where $k$ is the rank-reduction approximation (Bebendorf and Rjasanow, 2003). $\mathbf{A_k^S}$ is determined for a prescribed accuracy $\delta$ and is related to $\mathbf{A}$ by

$$\| \mathbf{A} - \mathbf{A_k^S} \|_{\mathbf{F}} \leqslant \delta \| \mathbf{A} \|_{\mathbf{F}} \tag{5.17}$$

where $\| . \|_F$ is the Frobenius norm.

The system of equations (5.12) is then solved iteratively using a block-Gauss-Seidel solver (Saad, 1996). For geophysicists and structural geologists, this solver is preferable to the GMRES because it incorporates inequality constraints on displacement, avoiding interpenetration of the elements, and traction, allowing frictional behavior without any incremental loading, artificial parameters or new equations introduced within the system (Maerten et al., 2009). The complexity of the algorithm is close to $O(n)$, as shown in

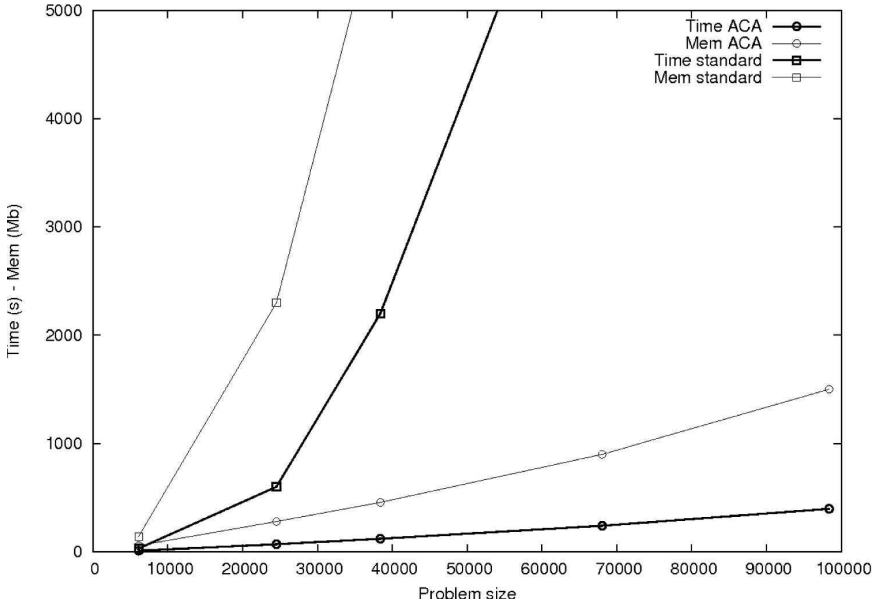


FIGURE 5.2: Time and memory versus size of the system to solve using ACA and standard methods. Bold lines represent the time in seconds, thin lines are the allocated memory in Mb. This graph suggests a complexity close to $O(n)$ for both memory and time

Fig. 5.2, for both time and memory. The ACA precision was set to $\delta = 10^{-1}$. Table 5.1 displays some results of the ACA, and these are compared to the standard iterative method for various model sizes. Elapsed time, memory allocation and the number of iterations are displayed. All models are run on a Intel bi-Xeon 2GHz with 8Gb of RAM, and

TABLE 5.1: Resolution of the system of equations : time, memory and number of iterations comparison for different model configurations.

| Dof | Standard | ACA | Ratio |
|---|---|---|---|
| 6,108 | $30s$ | $10s$ | 3 |
| | $142Mb$ | $57Mb$ | 2.49 |
| | 22 *iter* | 85 *iter* | 0.26 |
| 24,513 | $600s$ | $70s$ | 10 |
| | $2.3Gb$ | $280Mb$ | 8.2 |
| | 28 *iter* | 93 *iter* | 0.3 |
| 38,397 | $2700s$ | $120s$ | 23 |
| | $6Gb$ | $456Mb$ | 13 |
| | 41 *iter* | 116 *iter* | 0.35 |
| 68043 | – | $240s$ | – |
| | $\sim 19Gb$ | $560Mb$ | $\sim 34$ |
| | – | 151 *iter* | – |
| 98364 | – | $397s$ | – |
| | $\sim 39Gb$ | $1.5Gb$ | $\sim 26$ |
| | – | 172 *iter* | – |

running Linux Ubuntu 8.10 64 bits. When the model size is greater than 38,397 degrees of freedom (dof), we cannot launch the standard computation due to the limited size of the RAM.

## 5.7 $\mathcal{H}$-Matrices applied to post-processing at observation points

When all the unknown Burgers vectors are recovered as described in section 5.6, it is possible to compute displacement, strain and stress at observation points anywhere within the 3D elastic solid, and without any topological information attached to them.
For a model made of $n$ triangular dislocation elements, the displacement at any point $M$ is determined by superposition, i.e. by contribution of all the elements within the elastic body

$$\mathbf{u(M)} = \sum_{\mathbf{i=1}}^{\mathbf{n}} \mathbf{U_i b_i} \tag{5.18}$$

where $\mathbf{U_i}$ is the displacement influence matrix at point $M$ due to the $i^{th}$ element with $\mathbf{b_i}$ as Burgers vector.
Similarly, the strain and stress are given by

$$\epsilon(\mathbf{M}) = \epsilon^{\mathbf{R}} + \sum_{\mathbf{i=1}}^{\mathbf{n}} \mathbf{E_i b_i} \tag{5.19}$$

$$\sigma(\mathbf{M}) = \sigma^{\mathbf{R}} + \sum_{\mathbf{i=1}}^{\mathbf{n}} \mathbf{S_i b_i} \tag{5.20}$$

where $\mathbf{E_i}$ and $\mathbf{S_i}$ represent the strain and stress influence matrices at point $M$ due to an element $i$, and $\epsilon^{\mathbf{R}}$ and $\sigma^{\mathbf{R}}$ the far field strain and stress, respectively. In equations (5.19) and (5.20), the perturbed strain/stress field due to slipping triangular elements is simply superimposed on the regional strain/stress field. Since the number of observation points can be greater than the number of elements, it is desirable to reduce the computation time to be as fast as the resolution of the system of equations.

We describe here the principal contribution of this paper, that is, the use of the $\mathcal{H}$-Matrix formulation combined with the ACA technique to optimize the post-process, which is of $O(pn)$ for the standard method. Our goal is not to estimate the complexity of the optimization since it depends on too many parameters related to the distribution of the source and field points relative to each other. For the resolution of the system of equations,

the problem was straightforward because the position of the field points was exactly the same as the sources. However, we will give some benchmarks to show the potential of this approach.

### 5.7.1 Matrix representation

As in section 5.5.1, a block decomposition is done first, then the near and far field block-pairs are constructed. Compared to the method used for the resolution of the system of equations, where items are simultaneously source and field, now field points are totally different from source points, but these are added in the structure along with the sources. Another major difference is that, terminal blocks do not store full or sparse matrices. Instead, they are constructed and used "on the fly" when needed, avoiding intensive memory allocation.

When the recursive decomposition has finished and the block-pair structure has been built (see definition 5.16), the post-process computation takes place. All near field block-pairs, $F_{C_1,C_2}$, compute the displacement, strain and stress in the classical way by summing the influence of the source elements to the field points, whereas all far field block-pairs, $S_{C_1,C_2}$, use the ACA technique. To do so, we need to have a matrix representation of what has to be computed. For a given source block $C_1$ containing $n_1$ triangular elements and field block $C_2$ containing $n_2$ observation points, a way to represent the induced displacement, strain or stress in matrix form is

$$\mathbf{A} = \begin{bmatrix} \mathbf{a_{00}} & \cdots & \mathbf{a_{0n_1}} \\ \vdots & \ddots & \vdots \\ \mathbf{a_{n_20}} & \cdots & \mathbf{a_{n_2n_1}} \end{bmatrix} \tag{5.21}$$

where $\mathbf{a_{ij}}$ represents the vectorized form of the displacement, strain or stress at point $i$ due to element $j$, and are given by (5.22), (5.23) and (5.24), respectively.

$$\mathbf{a_{ij}} = \{\mathbf{u_x}\ \mathbf{u_y}\ \mathbf{u_z}\}^{\mathbf{T}}_{\mathbf{ij}} \tag{5.22}$$

$$\mathbf{a_{ij}} = \{\epsilon_{\mathbf{xx}}\ \epsilon_{\mathbf{xy}}\ \epsilon_{\mathbf{xz}}\ \epsilon_{\mathbf{yy}}\ \epsilon_{\mathbf{yz}}\ \epsilon_{\mathbf{zz}}\}^{\mathbf{T}}_{\mathbf{ij}} \tag{5.23}$$

$$\mathbf{a_{ij}} = \{\sigma_{\mathbf{xx}}\ \sigma_{\mathbf{xy}}\ \sigma_{\mathbf{xz}}\ \sigma_{\mathbf{yy}}\ \sigma_{\mathbf{yz}}\ \sigma_{\mathbf{zz}}\}^{\mathbf{T}}_{\mathbf{ij}} \tag{5.24}$$

Let $s$ be the size of $\mathbf{a_{ij}}$, i.e. $s = 3$ for displacement and $s = 6$ for strain and stress. In (5.21), each column represents a source element from $C_1$, and a block-row of size $s$ represents a field point. The total displacement, strain or stress at an observation point $i$

is computed by summing its corresponding rows from $\mathbf{A}$. For instance, the contribution at a field point $i \in C_2$ due to all elements in $C_1$, would be

$$\mathbf{w_i} = \sum_{\mathbf{j \in C_1}} \mathbf{a_{ij}} \tag{5.25}$$

Using ACA leads to a sparse representation of $\mathbf{A}$, denoted $\mathbf{A_k^S}$, and equation (5.25) is optimally computed using

$$\mathbf{A} \approx \mathbf{A_k^S} = \sum_{\mathbf{l=1}}^{\mathbf{k}} \mathbf{u_l v_l^T} \tag{5.26}$$

where $\mathbf{u_l} \in \mathbf{R^{N_2}}$ and $\mathbf{v_l} \in \mathbf{R^{n_1}}$ $\forall l \in [1, k]$, $N_2 = sn_2$, and $k$ is the rank of the low-rank approximant. The complexity of this algorithm, for a given $\mathbf{A_k^S}$, is $O(k(n_1 + N_2))$.

Algorithm 5.1 presents the optimized computation of $\mathbf{w_i}$ for all $i \in C_2$ using the Adaptive Cross Approximation.

```
set N_2 = s.n_2
Input  : set of vectors u and v from eq. (5.26)
Output: vector w = {0}_{N_2}
set r = {0}_k   // Temporary vector of dim k
for i=1 to k do
    for j=1 to n_1 do
        r_i += v_{i,j}
    end
end
for i=1 to N_2 do
    for j=1 to k do
        w_i+ = u_{j,i}.r_j
    end
end
```

**Algorithm 5.1**: Summing displacement, strain or stress from $n_1$ source points at $n_2$ field points using ACA. Notation: for a set of vectors $\mathbf{v}$, $v_{i,j}$ represents the $j^{th}$ component of the $i^{th}$ vector. The complexity is $O(k(n_1 + N_2))$, where $s = 3$ for displacement and $s = 6$ for strain or stress.

### 5.7.2 Example

The test model is composed of a single complex-shaped surface discontinuity made of 8,171 triangular elements with prescribed displacement discontinuity (computed from section 5.6), and an observation grid composed of 40,000 points for which we aim to compute the displacement vector and stress tensor at each point. This grid, named "Top", is above and close to the discontinuity. The model is embedded in a homogeneous elastic whole-space,

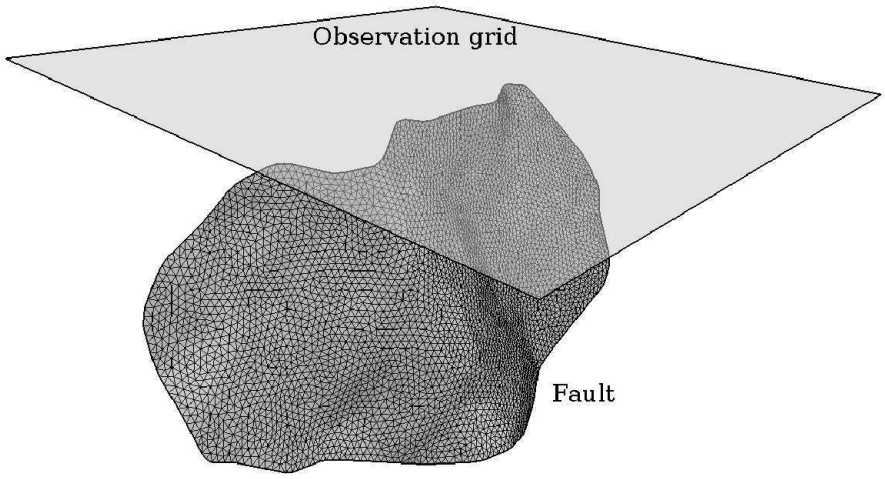


FIGURE 5.3: Post-process model configuration. The observation grid is made of 40,000 points and the fault of 8,171 triangular elements, leading to 42 billion calls to the fundamental solutions and their derivatives

and the simulation is done on the same computer as in section 5.6. This configuration leads to **42 billion** calls to the fundamental solutions and their derivatives in the whole-space, and **84 billion** calls in the half-space, and takes 40 and 80 minutes of computation using the standard method, respectively.

Fig. 5.3 shows the model configuration used for the post-processing and Fig. 5.4 compares the computed $\sigma_{xy}$ to the standard method (bottom-right) for different tolerance $\delta$ of the ACA (see equation (5.17) for the definition of $\delta$). The minimum number of sources and fields within a block is set to 16. We use a 10-band color table in order to show the small variations compared to the standard method using different precisions for the ACA. The elapsed time is $t$ and $r$ is the gained speed ratio compare to the standard method. Even for a tolerance of $\delta = 10^{-1}$ (cf. Fig. 5.4, top-left), the displayed result is comparable to the standard method (bottom-right) where the elapsed times are $t = 68s$ and $t = 2400s$, respectively, giving a speed ratio of 35. $\delta = 10^{-2}$ (bottom-left) gives a better approximation for a speed ratio of 27. Table 5.2 summarizes the speed gained as well as the error compared to the standard method. The computed overall error is given by

$$error = \frac{1}{p}.\frac{\sum_{i=1}^{p} {\Delta\sigma_i}^2}{\max({\Delta\sigma_i}^2)} \tag{5.27}$$

where

$$\Delta\sigma_i = \sigma_{i,xy}^{Standard} - \sigma_{i,xy}^{ACA} \tag{5.28}$$

for a given observation point $i$.

Even if the precision $\delta = 10^{-1}$ can be considered a good approximation, we provide the

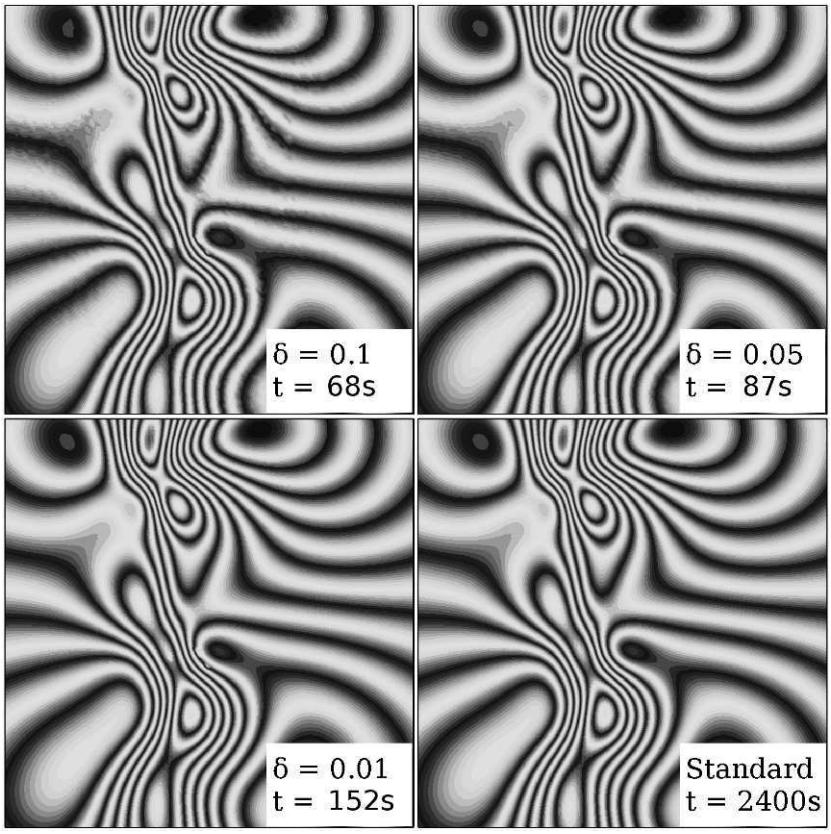


FIGURE 5.4: Comparison of $\sigma_{xy}$ computed on 40,000 observation points for a model composed of 8,171 triangular elements. Elapsed time comprises the computation of the displacement and stress at all observation points. A 10-band color table is used in order to better show the irregularities due to the approximation. Top left and right: $\delta = 10^{-1},\ t = 68s,\ r = 35$ and $\delta = 5.10^{-2},\ t = 87s,\ r = 27$, respectively. Bottom left: $\delta = 10^{-2},\ t = 152s,\ r = 16$ (see text for explanations). Bottom-right: standard method, $t = 2400s,\ r = 1$

TABLE 5.2: Post-processing: time comparison for different tolerances of the ACA. The model is composed of 8,171 elements and 40,000 observation points.

| Configuration | Time | Speedup | Error(%) |
|---|---|---|---|
| Standard | 2400s | 1 | - |
| ACA & $\delta = 10^{-1}$ | 68s | 35 | 0.27 |
| ACA & $\delta = 5.10^{-2}$ | 87s | 27 | 0.1 |
| ACA & $\delta = 10^{-2}$ | 152s | 16 | 0.04 |
| ACA & $\delta = 10^{-3}$ | 305s | 8 | 0.0052 |

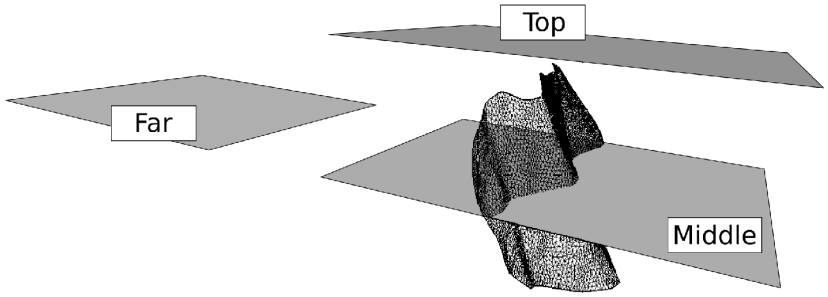


FIGURE 5.5: Perspective view for different position of the grids ("Middle", "Top" and "Far") relative to the discontinuity

elapsed time for $\delta = 10^{-3}$, showing a non-negligible increase of the computational time since a better precision leads to larger values of $k$.

### 5.7.3 Effect of field points distribution

Of course, the relative distance of the observation points to the sources controls the structure of the $\mathcal{H}$-Matrix, and therefore the speed of the post-processing. As an illustrative example, if we consider an observation grid of a given size far from the sources, the $\mathcal{H}$-Matrix structure will be such that only a few sparse block-pairs will be created. In contrast, an observation grid cross-cutting the sources, will lead to many more full and sparse block-pair, increasing the computational time. Consequently, the complexity of the post-processing is clearly dependent on the distribution of the $p$ observation points relative to the $n$ sources. This is shown in Fig. 5.5, where three identical observation grids, in terms of dimensions and number of observation points (40,000), have been placed around the same discontinuity as in section 5.7.2, but in different locations. The first grid is the same as in the previous example ("Top"), the second one cross-cuts the sources ("Middle"), and the last one ("Far") is at a distance two times the dimension of the discontinuity. Table 5.3 summarizes the computational times for each grid using an ACA precision $\delta = 10^{-1}$. For the standard method, whatever the position of the grid, the time needed for the post-process is always $2400s$. However, the $\mathcal{H}$-Matrix clearly captures the kernel smoothness: for the "Middle" grid, the elapsed time is $136s$, whereas for the "Far" grid it is only $19s$.

This can be understood by looking at the number of generated full and sparse blocks. To do so, we ran several simulations for the "Middle", "Top" and "Far" grids, varying the number of observation points from 40,000 to 160,000. We look at the number of generated full and sparse blocks (table 5.4), as well as the mean sparse matrix size, rank and sparsity (table 5.5).

TABLE 5.3: Effect of the grid position made of 40,000 points. This table shows the advantage of the $\mathcal{H}$-Matrix structure which captures the "smoothness" of the kernel for post-processing. For each grid, the standard method leads to 2400s. Using $\mathcal{H}$-Matrices, the elapsed time differs considerably according to the position of the grid.

| Grid | Time (s) | Speedup |
|---|---|---|
| Standard | 2400s | 1 |
| Middle | 136s | 18 |
| Top | 68s | 35 |
| Far | 19s | 126 |

TABLE 5.4: Number of full (F) and sparse (S) blocks generated by the $\mathcal{H}$-Matrices for different sampling and position of the grids ("Middle", "Top" and "Far"). $p$ represents the number of observation points.

| $p$ | Middle | Top | Far |
|---|---|---|---|
| 10k | $F$ 5301<br>$S$ 14828 | $F$ 2<br>$S$ 1456 | $F$ 0<br>$S$ 4 |
| 40k | $F$ 6771<br>$S$ 17762 | $F$ 0<br>$S$ 994 | $F$ 0<br>$S$ 6 |
| 90k | $F$ 8575<br>$S$ 21517 | $F$ 0<br>$S$ 957 | $F$ 0<br>$S$ 6 |
| 160k | $F$ 7740<br>$S$ 23147 | $F$ 0<br>$S$ 656 | $F$ 0<br>$S$ 10 |

For a given sparse matrix $\mathbf{A_k^s} \in \mathbb{R}^{\mathbf{n_1} \times \mathbf{n_2}}$ of rank $k$, the sparsity $S_p$ is given by

$$S_p = 100 \frac{k(n_1 + n_2)}{n_1 n_2} \tag{5.29}$$

From these two tables, it is clear that the distance of a grid relative to the sources controls the number of generated full and sparse blocks as well as the sparsity of the block-pairs. For the "Middle" grid, the number of generated sparse blocks ranges from 14,000 to 23,000, whereas for the "Far" grid it is only between 4 and 10. Furthermore, even if the sparse matrix size for the "Far" grid is large (see table 5.5), its sparsity is relatively low, ranging from 0.24% to 0.68%, enabling fast computations.

Note that for the cases of the "Top" and "Far" grids, there is no full matrix generated, avoiding $O(np)$ calculation. For the "Middle" grid, the generated full matrix size ranges from $(7 \times 9)$ for 10,000 points to $(27 \times 10)$ for 160,000 points, which is relatively small compared to the sparse matrices size. This is obviously preferable since the complexity of a full matrix is the highest.

TABLE 5.5: Sparse matrix information. Averaged matrix size ($r = s.n_2$ and $c = n_1$ stand for row and column, respectively), rank ($k$) and sparsity ($S_p$ expressed in %) for different model configurations.

| $p$ | Middle | Top | Far |
|---|---|---|---|
| 10k | $r = 116$<br>$c = 42$<br>$k = 11$<br>$S_p = 36$ | $r = 531$<br>$c = 177$<br>$k = 15$<br>$S_p = 11$ | $r = 15000$<br>$c = 4085$<br>$k = 22$<br>$S_p = 0.6$ |
| 40k | $r = 333$<br>$c = 41$<br>$k = 11$<br>$S_p = 30$ | $r = 2128$<br>$c = 267$<br>$k = 17$<br>$S_p = 7$ | $r = 25300$<br>$c = 5447$<br>$k = 19$<br>$S_p = 0.4$ |
| 90k | $r = 613$<br>$c = 35$<br>$k = 10$<br>$S_p = 30$ | $r = 4763$<br>$c = 278$<br>$k = 18$<br>$S_p = 7$ | $r = 62250$<br>$c = 5447$<br>$k = 19$<br>$S_p = 0.4$ |
| 160k | $r = 1026$<br>$c = 32$<br>$k = 9$<br>$S_p = 29$ | $r = 12946$<br>$c = 332$<br>$k = 19$<br>$S_p = 6$ | $r = 52800$<br>$c = 6537$<br>$k = 14$<br>$S_p = 0.2$ |

Finally, table 5.6 provides the elapsed time spent for the post-processing onto the different grids, and shows the speed gained compared to the standard method. Fig. 5.6 plots the corresponding times function for the number of observation points along a log-scale axis. The elapsed time for the standard method is also displayed, showing its computational inefficiency compared to the ACA method.

## 5.8 Parallelization on multi-core CPU

Today, processors are based on multi-core architectures, and the number of cores within the CPU is growing from year to year. 8-core processors are currently available, and in the near future, 16- or 32-cores will be introduced onto the market of personal desktop and laptop computers. It is obviously natural to use such architectures for parallelization when possible for any algorithms. We present the parallelization of the ACA for post-processing, the principle being the same for solving the system of equations.

TABLE 5.6: Post-process time (in seconds) for various sampling and position of a grid, and comparison with the standard method. The ACA precision is $\delta = 10^{-1}$. The second row for each value of $p$ represents the speedup ratio relative to the standard method. All grids have the same geometrical dimensions, and only the position and the sampling (number of points) change.

| $p$ | Middle | Top | Far | Standard |
|---|---|---|---|---|
| 10k | 75<br>8 | 40<br>15 | 7<br>86 | 600 |
| 40k | 136<br>18 | 65<br>37 | 10<br>240 | 2400 |
| 90k | 210<br>26 | 106<br>51 | 14<br>386 | 5400 |
| 160k | 510<br>19 | 216<br>44 | 23<br>417 | 9600 |

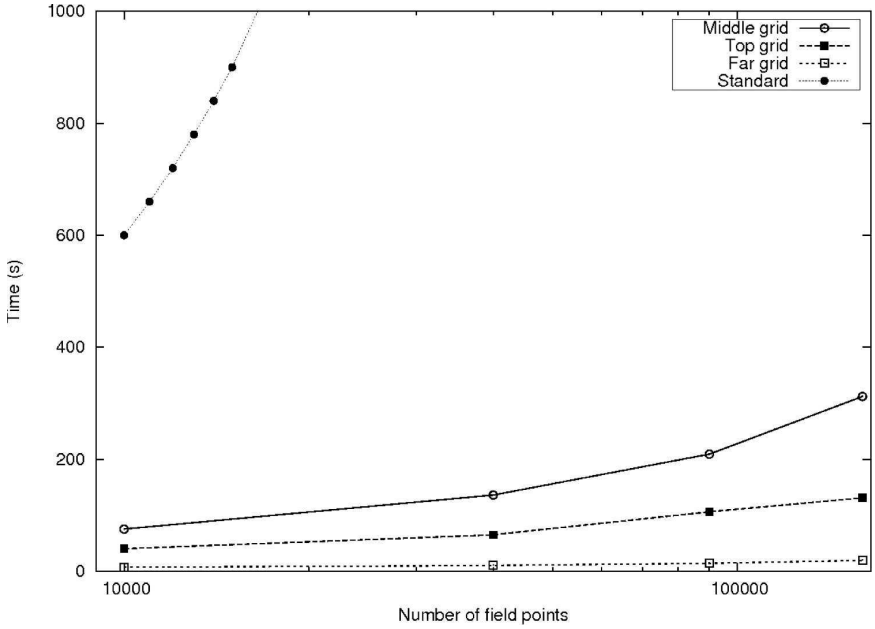


FIGURE 5.6: Post-processing optimization. Number of observation points versus time for different position of the grids ("Middle", "Top" and "Far"), and comparison with the standard method. Note the log scale for the x-axis

The basic idea is to split the set of observation points into $N_c$ groups corresponding to the number of available cores onto the CPU, and leading to $N_c$ threads that have to be run in parallel. For each thread, we use the same technique as described in section 5.7, and all threads are put into a thread-pool. The package used for the thread management is the QtConcurrent package (Trolltech, 2010), which greatly simplifies the programming and can be employed without any X-server.

Since a global update has to be done after all threads have finished their job (generally, an observation point is part of a more complex structure, where memory allocation is done for a set of observation points, requiring barrier conditions to avoid read/write conflicts), the total elapsed time will be equal to the slowest thread. Therefore, the major difficulty is to judiciously split the set of observation points in the sense of the $\mathcal{H}$-Matrix, so that all threads will have the same amount of work to do. Since the approximation at field points is based on the distance to the sources, we classify the observation points using the distance to the sources barycenter, and a priority queue based on this distance is used. While traversing the queue entirely, observation points are placed into the $N_c$ threads alternatively, leading to a more balanced representation than a naive subdivision.

Then, each thread constructs in parallel the $\mathcal{H}$-Matrix representation, where all triangular elements are introduced as sources, and runs the post-processing onto their associated field points. The thread-pool, put in *wait-condition*, waits until all threads have finished their job before effectively setting the computed values at observation points.

### 5.8.1 Example

We use the same model as described in section 5.6 and the same computer configuration. Each processor on the mother board has 4 cores, leading to 8 available cores.

Results are given in table 5.7. It can be seen that the ratio of the time needed by the ACA using 1 core and 8 cores is closed to 4 and not 7.5 as with the standard method. This is mainly due to the partition of the problem into $N_c$ sub-problems. Since the decomposition in $\mathcal{H}$-Matrix is done for each thread, the total number of block-pairs increases, and the rank-reduction for a given $S_{C_1,C_2}$ block-pair within a thread cannot be as optimal as in the non-parallelized version. Also, it can be shown that this ratio is not due to the unbalanced partition of the thread work. Table 5.8 presents the elapsed time spent for the slowest and fastest threads during the post-processing using different sampling of the observation grid, and shows that work done by the threads are almost identical. In this table, $\Delta$ represents the difference in time normalized to the time of the fastest thread.

TABLE 5.7: Parallelized post-processing on multi-core architecture: time comparison for a model composed of 8,171 elements and the "Top" grid made of 40,000 observation points. The tolerance used for the ACA is $\delta = 10^{-1}$. Columns Speedup (1) and (2) refer to the sequential standard and ACA versions, respectively.

| Config. | Cores | Time (s) | Speedup$^{(1)}$ | Speedup$^{(2)}$ |
|---|---|---|---|---|
| Standard | 1 | 2400 | 1 | – |
| Standard | 4 | 632 | 3.8 | – |
| Standard | 8 | 324 | 7.5 | – |
| ACA | 1 | 68 | 35 | 1 |
| ACA | 4 | 36 | 67 | 1.89 |
| ACA | 8 | 18 | 133 | 3.78 |

TABLE 5.8: Post-processing time needed by the threads for various number of the observation points. The number of threads is 4, and ACA precision is $\delta = 10^{-1}$. $p$ represents the number of observation points and $\Delta$ the difference in time normalized to the time of the fastest thread.

| $p$ | Min time (s) | Max time (s) | $\Delta$ (%) |
|---|---|---|---|
| 10k | 19.5 | 22.1 | 13 |
| 40k | 34.3 | 35.6 | 3.8 |
| 90k | 55.7 | 57.5 | 3.23 |
| 160k | 68.6 | 71.1 | 3.6 |

## 5.9 Conclusions and perspectives

The $\mathcal{H}$-Matrix technique combined with Adaptive Cross Approximation and parallelization on multi-core architectures, for the 3D elastostatic boundary element code, allows one to quickly solve systems that would usually require a prohibitive amount of RAM and time. This method was successfully applied to post-processing at observation grids, showing the advantage of such an approach in terms of speed and the automatic capture of kernel smoothness.

This technique has many consequences in term of future developments of the Poly3D extensions, and we just mention a few of them.

1. First, modeling of material heterogeneity (Maerten and Maerten, 2008), which requires the discretization of an interface separating two regions of different material properties as a doubly triangulated discontinuity with traction boundary conditions for the three axes (six unknowns for each doubly triangulated element), will be possible for complex models involving many regions. This kind of modelization generates

many degrees of freedom and requires a prohibitive amount of RAM when using the classical method of resolution.

2. Second, doing slip inversion (Maerten et al., 2005) using an iterative solver with inequality constraints on displacement (Maerten et al., 2009) will greatly benefit by the post-process optimization, as each triangular element is function of all observation points where a measure is used for the inversion. If we consider dense interferograms generated by satellites, the number of observation points can be considerable, and using a classical weighted damped least-squares approach without optimization is unrealistic.

Finally, it is our intention to extend the parallelization technique on GPU (Graphic Processor Unit) using CUDA (Keane, 2006) or OpenCL (Khronos-Group, 2009) language.

## 5.10 Acknowledgments

Special thanks to the Igeoss's consortium members for their support on the development of Poly3D. The author would like to thank David D. Pollard who greatly improved the text of this paper.

# References


Bebendorf, M. (2000). Approximation of boundary element matrices. *Numeri Math*, 86(4):565–589.

Bebendorf, M., editor (2008). *Hierarchical Matrices, a means to efficiently solve elliptic boundary value problems*. Springer, Berlin Heidelberg.

Bebendorf, M. and Rjasanow, S. (2003). Adaptive low-rank approximation of collocation matrices. *Computing*, 86(4):1–24.

Comninou, M. and Dundurs, J. (1975). The angular dislocation in a half space. *Journal of Elasticity*, 5(3):203–216.

Crouch, S. L. and Starfield, A. M., editors (1983). *Boundary element methods in solid mechanics*. George Allen and Unwin, London.

Greengard, L. and Rokhlin, V. (1987). A fast algorithm for particle simulations. *J. Comput. Phys.*, 73:325–348.

Hackbusch, W. (1999). A sparse matrix arithmetic based on h-matrices: Part 1: Introduction to h-matrices. *Computing*, 62:89–108.

Hackbusch, W. and Nowak, Z. (1989). On the fast matrix multiplication in the boundary element method by panel clustering. *Numeri Math*, 54(4):463–491.

Jeyakumaran, M., Rudnicki, J. W., and Keer, L. M. (1992). Modeling slip zones with triangular dislocation elements. *Bulletin of the Seismological Society of America*, 82:2153–2169.

Keane, A. (2006). Cuda (compute unified device architecture), http://developer.nvidia.com/object/cuda.html.

Khronos-Group (2009). Opencl (open computing language), http://www.khronos.org/opencl.

Maerten, F. and Maerten, L. (2008). Iterative 3d bem solver on complex faults geometry using angular dislocation approach in heterogeneous, isotropic elastic whole or half-space. In Brebbia, editor, *Boundary Elements and other Mesh Reduction Methods XXX*, pages 201–208, Southampton. BEM 30, WITpress.

Maerten, F., Maerten, L., and Cooke, M. (2009). Solving 3d boundary element problems using constrained iterative approach. *Computational Geosciences*.

Maerten, F., Resor, P. G., Pollard, D. D., and Maerten, L. (2005). Inverting for slip on three-dimensional fault surfaces using angular dislocations. *Bulletin of the Seismological Society of America*, 95:1654–1665.

Maerten, L. (2000). Variation in slip on intersectiong normal faults: Implications for paleostress inversion. *Journal of Geophysical Research*, 105(25):553–565.

Maerten, L., Willemse, E. J. M., Pollard, D. D., and Rawnsley, K. (1999). Slip distributions on intersecting normal faults. *Journal of Structural Geology*, 21:259–271.

Muller, J. R., Aydin, A., and Maerten, F. (2003). Investigating the transition between the 1967 mudurnu valley and 1999 izmit earthquakes along the north anatolian fault with static stress changes. *Geophysics Journal International*, 154:471–482.

Okada, Y. (1985). Surface deformation due to shear and tensile faults in a half-space. *Bulletin of the Seismological Society of America*, 75:1135–1154.

Rokhlin, V. (1985). Rapid solution of integral equations of classical potential theory. *J Comput Phys*, 60:187–207.

Saad, Y. (1996). *Iterative Methods for Sparse Linear Systems*. PWS Publishing, New York.

Steketee, J. (1958a). On volterra's dislocations in a semi-infinite elastic medium. *Can. J. Physics*, 36:192–205.

Steketee, J. (1958b). Some geophysical applications of the elasticity theory of dislocations. *Can. J. Physics*, 36:1168–1198.

Thomas, A. L. (1993). Poly3d: a three-dimensional, polygonal element, displacement discontinuity boundary element computer program with applications to fractures, faults, and cavities in the earth's crust. Master's thesis, Stanford University.

Trolltech (2010). Qtconcurrent, http://www.trolltech.com.

Yoffe, E. (1960). The angular dislocation. *Phil. Mag.*, 5:161–175.

# Part II

## Inverse modeling using Boundary Element Method

# Aperçu

Comme indiqué dans la partie I, la géométrie des objets actifs (discontinuités) joue un rôle important dans le comportement mécanique d'une roche. Toutefois, en plus de cette géométrie des objets (failles et fractures) qui peut être déduite de l'imagerie sismique et des études de terrain, d'autres types de mesures peuvent être utilisées pour mieux contraindre un modèle ou pour retrouver des paramètres manquants. A titre d'exemple, rien n'a été dit sur l'orientation et les magnitudes du champ de contraintes à l'infini qui est imposé à un modèle pour calculer de combien les discontinuités doivent glisser afin d'accomoder un tel chargement. L'observation des déformations en surface (données GPS, inclinomètres, images satellites, ...) peut être utilisée pour retrouver les distributions de glissement sur les failles qui ont généré ces déformations (chapitre 6). Une telle inversion, cependant, donne une estimation de la distribution des déplacements sur les failles, mais ne fournit aucune information sur la ou les paleo-contraintes (orientation et magnitudes) ayant généré de tels déplacements. Néanmoins, cette inversion linéaire en déplacement donne de très bons résultats pour les évènements co-sismiques comme démontré dans le chapitre 6, ainsi que dans le chapitre 7, où le séisme de Nias (Indonésie), qui a eu lieu en 2005, est étudié. L'annexe A présente une méthode itérative rapide pour faire de l'inversion de déplacements, et est basée sur la méthode décrite dans le chapitre 5.

Le chapitre 8 présente une technique basée sur la géomécanique pour retrouver une paléo-contrainte qui a induit les déplacements observés sur les failles. Cette technique est limitée à un évènement tectonique, mais peut donner une bonne estimation de ce qu'aurait pu être l'orientation et les magnitudes de la charge tectonique, ceci tout en utilisant les interactions mécaniques entre discontinuités.

Finalement, le chapitre 9 décrit une nouvelle technique pour faire de l'inversion de paléo-contraintes en utilisant plusieurs ensembles de données mesurées, tels les plans de fracturation, l'orientation de plans de failles secondaires (qui se sont formés dans le voisinage des failles actives majeures), les mesures GPS, InSAR et les déplacements mesurés sur les failles.

# Overview

As shown in part I, the geometry of the active objects (fault discontinuities) plays an important role in the mechanical behavior of a faulted rock mass. However, in addition to the geometry of the objects (faults and fractures) that can be deduced from seismic images and field studies, other kinds of measurements can be used to better constrain a model or to retrieve missing parameters. As an example, nothing was said about the orientation and magnitude of the far field stress or strain that has to be imposed on a model in order to calculate how the discontinuities accommodate such a tectonic loading.

Observations of deformations at the ground surface (e.g. GPS, tiltmeters, satellite images, ...) can be used to invert for slip distributions on the faults that generated such measured deformations (chapter 6). Such inversion, however, gives an estimate of the slip distribution on the faults, but does not provide any information on the tectonic loading (orientation and magnitudes) as it might be a consequence of multiple tectonic events. Nonetheless, this linear slip inversion gives very good results for co-seismic events as demonstrated in chapter 6 as well as in chapter 7, where the Nias earthquake (Indonesia), which occurred in 2005, is studied. Appendix A presents a fast iterative method for doing slip inversion, and is based on the method described in chapter 5.

Furthermore, chapter 8 presents a geomechanically-based technique to retrieve the paleostress that induced observed displacements on the faults. This technique is limited to one tectonic event, but can give a good estimate of what could have been the orientation and magnitude of the tectonic loading using mechanical interactions. Chapter 9 describes a new technique for doing paleo stress inversion using multiple data sets, such as fracture and secondary fault plane orientations (that formed in the vicinity of active larger faults), GPS, InSAR and fault slip measurements.

# CHAPTER 6

# Inverting for Slip on Three-Dimensional Fault Surfaces using Angular Dislocations

F. Maerten[(1)], P. Resor[(2)], D. D. Pollard[(3)], L. Maerten[(1)]

(1) Igeoss, Montpellier, FRANCE
(2) Department of Earth and Environmental Sciences, Wesleyan University, Middletown, Connecticut, USA
(3) Stanford University, CA, USA

Published in BSSA, 2005, v. 95(5), pp 1654-1665

With kind permission from Dr. Andrew J. Michael, BSSA Editor in Chief.

**Preamble**

Given observations of deformation at the ground surface due to an earthquake, as well the 3D geometry of the faults, is it possible to retrieve the displacement on the faults that generated such observed displacements? The following paper provides an elegant solution using complex triangulated fault surfaces, avoiding artifacts due to gaps and overlaps of elements while using rectangular element formulations. It is shown for the Hector Mine earthquake that such a formulation gives better results than a formulation using classical rectangular dislocations.

# About...

After Dave Pollard and Phil Resor asked me to study the possibility of doing slip inversion using Poly3D, I wrote down the formulation using a Least Squares approach combined with a Tikhonov regularization with Laplacian smoothing for triangulated surfaces. The conceptual model and the programming was done in few weeks, and Laurent Maerten helped me to validate the model on synthetic examples as well as on the Chichi earthquake, Taiwan (see the Stanford Structural Geology and Geomechanics web page for a poster presentation).

# Article Outline

## 6.1 Résumé

La qualité croissante des données géodésiques (InSAR, tableaux denses de mesures GPS) maintenant disponibles aux géophysiciens et géologues n'est pas pleinement exploitée lors de la procédure d'inversion du glissement sur les failles. La plupart des méthodes courantes d'inversion ustilisent des éléments de dislocation rectangulaires pour modéliser les surfaces de ruptures d'un modèle, et donc simplifient exagérément la géométrie des failles. Ces simplifications géométriques peuvent conduire à des incohérences lors de l'inversion du glissement sur les failles pour un tremblement de terre donné, et ils s'opposent à une compréhension plus complète du rôle de la géométrie des failles dans le processus d'étude des tremblements de terre. Nous avons développé une nouvelle méthode d'inversion de glissement en trois dimensions basée sur la solution analytique d'une dislocation angulaire dans un milieu semi-infini, linéaire, élastique, homogène et isotrope. Cette approche utilise le code Poly3D qui emploie un ensemble d'éléments triangulaires à déplacements constants et discontinus pour modéliser des surfaces de failles. L'utilisation de tels éléments permet de construire des modèles de failles qui approximent de façon plus précise les surfaces courbes tridimensionnelles délimitées par des bords complexes: formes qui sont couramment imagées par la réflexion sismique en trois dimensions et déduits des données de réplique de tremblements de terre. Nous démontrons le potentiel d'une telle méthode pour modéliser des géométries de ruptures en trois dimensions en inversant le glissement associé au séisme d'Hector Mine (1999). Il en résulte que le modèle évite les anomalies de déplacement liées à la superposition de dislocations rectangulaires utilisées dans les modèles précédents, améliorant l'ajustement aux données géodésiques de 32%, et honorant les surfaces de ruptures observées, ce qui permet des comparaisons plus directes entre les données géologiques et géodésiques sur les distributions de glissement.

## 6.2 Abstract

The increasing quality of geodetic data (InSAR, dense GPS arrays) now available to geophysicists and geologists are not fully exploited in slip inversion procedures. Most common methods of inversion use rectangular dislocation segments to model fault ruptures, and therefore over-simplify fault geometries. These geometric simplifications can lead to inconsistencies when inverting for slip on earthquake faults, and they preclude a more complete understanding of the role of fault geometry in the earthquake process.
We have developed a new three-dimensional slip-inversion method based on the analytical solution for an angular dislocation in a linear-elastic, homogeneous, isotropic, half-space. The approach uses the boundary element code Poly3D that employs a set of planar triangular elements of constant displacement discontinuity to model fault surfaces. The use of triangulated surfaces as discontinuities permits one to construct fault models that better approximate curved three-dimensional surfaces bounded by curved tiplines: shapes that commonly are imaged by three-dimensional reflection seismic data and inferred from relocated aftershock data.
We demonstrate the method's ability to model three-dimensional rupture geometries by inverting for slip associated with the 1999 Hector Mine earthquake. The resulting model avoids displacement anomalies associated with the overlapping rectangular dislocations used in previous models, improving the fit to the geodetic data by 32%, and honors the observed surface ruptures, thereby allowing more direct comparisons between geologic and geodetic data on slip distributions.

## 6.3 Introduction

Geodetic inversions are a useful tool for estimating kinematic source parameters of earthquakes (e.g., (Stein and Barrientos, 1985; Lin and Stein, 1989; Freymueller et al., 1994; Feigl et al., 1995; Yu and Segall, 1996; Wright et al., 1999; Reilinger et al., 2000)). Using static surface displacements associated with a given earthquake researchers seek to better understand earthquake rupture processes by inverting for fault geometry and/or slip distributions. The challenge is to find the most accurate geometry and slip distribution supported by the data. The increasing availability of spatially rich geodetic data, specifically dense GPS networks and synthetic aperture radar interferometry (InSAR), offers researchers opportunities to construct increasingly complex geometric and kinematic models of earthquake ruptures (e.g., (Johnson et al., 2001; Bürgmann et al., 2002; Jónsson

et al., 2002; Sandwell et al., 2002; Simons et al., 2002)). Inverting for both fault geometry and slip is a challenging non-linear problem. Here we prescribe a realistic geometry and carry out the linear inversion for slip. We show, in particular, how spatially dense data in the near-field admit models that incorporate realistic geometry when estimating coseismic slip.

Geological and geophysical observations reveal that faults typically are not single planar surfaces bounded by rectangular tiplines, but are composed of individual curved surfaces with curved tiplines organized as multiple echelon, conjugate, and intersecting segments. This conceptual model of fault geometry is based on observations from a variety of sources including studies of earthquake surface ruptures (e.g., (Zhang et al., 1999; Lin et al., 2001; Aydin and Kalafat, 2002; Treiman et al., 2002)), exhumed faults (e.g., (Martel, 1990; Cartwright et al., 1995; Willemse et al., 1997; Peacock, 2002)), reflection seismology (e.g., (Willemse et al., 1996; Walsh et al., 1999; Maerten et al., 2000; Kattenhorn and Pollard, 2001)), and aftershock patterns (e.g., (Waldhauser and Ellsworth, 2000; Carena and Suppe, 2002; Kilb and Rubin, 2002; Chiaraluce et al., 2003)). To more precisely estimate coseismic slip and thus to advance the understanding of earthquake source parameters we advocate the incorporation of curved fault surfaces and tiplines in geodetic inversions of coseismic deformation. Previous workers have attempted to incorporate non-planar geometry by constructing faults from multiple rectangular dislocations after the solution of Okada (e.g., (Johnson et al., 2001; Jónsson et al., 2002; Simons et al., 2002)). Although these models have proved effective in certain applications, the curved surfaces and tiplines of faults cannot be modeled with a set of rectangular dislocation segments without introducing non-physical gaps and overlaps.

In this paper we present a new method for slip inversion based on the solution for an angular dislocation in an elastic half-space, employing triangular elements of constant displacement discontinuity to model fault surfaces. Discretization of surfaces into triangular elements allows for the construction of three dimensional fault surfaces that more closely approximate curviplanar surfaces and curved tiplines without introducing overlaps or gaps, consistent with the full extent of available data. We demonstrate the strengths of this new method through a brief analysis of the fault rupture due to the 1999 Hector Mine earthquake (Mw 7.1). We start with a planar segmented fault model based on the work of Jónsson et al. (Jónsson et al., 2002) and compare these results to models that more closely honor the observed surface rupture pattern along multiple curved and intersecting fault segments. The resulting inversions show that models that more closely honor the geometry of the surface ruptures also yield significant improvements in the fit to the geodetic data.

## 6.4 Method

Displacements $d^p$ at points (p) on the Earth's surface due to slip $m^e$ on elements (e) of a buried fault can be described by a set of linear equations

$$d_p = G^{e,p} m_e + E \tag{6.1}$$

where $E$ are the observational errors and $G^{e,p}$ are the influence coefficients, or Green's functions, that describe how slip on a fault element produces displacement at the Earth's surface. This set of equations can be used to forward model surface displacements from a known fault geometry and slip distribution, or as an inverse problem to model subsurface fault geometry and slip from an observed set of surface displacements. Inversion for fault geometry is highly non-linear and thus computationally intensive even for very simple geometries (Cervelli et al., 2001), while inversion for slip is a linear inverse problem and thus relatively straight-forward. In this paper we present a new approach to solving the linear inverse problem, inverting for slip on faults with geometry that is determined a priori. Ideally the geometry is constrained through integration of multiple data sets such as mapped surface ruptures, high-precision aftershock locations, reflection seismology, and/or the results of non-linear inversion for a simplified fault geometry (e.g., for the Hector Mine earthquake, see (Hurst et al., 2000; Jónsson et al., 2002; Simons et al., 2002)).

To implement the inverse problem, we seek a solution that simultaneously minimizes the $L_2$ norm (hereafter annotated with $\|\|_2$) of the data misfit and of the model roughness. This approach allows fitting of the data to a desired threshold while introducing the geologic concept that slip distributions are relatively smooth rather than oscillatory (Harris and Segall, 1987). Minimizing the model roughness acts to prevent over-fitting of noisy data and compensates for underdetermined model parameters and geometric inaccuracies. The slip inversion problem can thus be written as

$$min\|Gm - d\|_2 + \epsilon^2 \|Dm\|_2 \tag{6.2}$$

where the first term $\|Gm - d\|_2$ is the $L_2$ norm of the data misfit and the second term $\epsilon^2\|Dm\|_2$ is a measure of the model roughness. The data misfit is calculated by subtracting the observed displacements $d$ from the predicted displacements, which are themselves calculated by multiplying the Green's functions $G$ by the modeled slip $m$. In the case of InSAR data, the model also includes apparent surface displacements that appear as

a uniform tilting associated with errors in modeling orbital parameters during data processing (Hanssen, 2001). The model roughness term $\epsilon^2\|Dm\|_2$ is composed of a scalar smoothing parameter $\epsilon$ multiplied by the $L_2$ norm of a discrete second-order difference operator $D$. Inclusion of this term acts to minimize the second derivative, or Laplacian of the modeled slip $\nabla^2 m$, and thus minimizes the non-dimensional model roughness, defined as the change in fault slip per length of fault squared and typically reported in units of $cm/km^2$ (Harris and Segall, 1987). The value of $\epsilon$ controls the amount of smoothing and may be determined either from a trade-off curve, seeking to balance smoothing with data fitting or by cross-validation (Harris and Segall, 1987; Du et al., 1992).

The approach we take to solve the slip inversion problem differs from previous work in the form of the Green's functions and the smoothing operator $D$. The Green's functions we use are based on the analytical solution for the elastic boundary value problem of an angular dislocation (Fig. 6.1a) in an infinite "whole" or semi-infinite "half" space composed of a homogeneous and isotropic linear-elastic material (Comninou and Dundurs, 1975).

Comninou and Dundurs extended the solution for an angular dislocation in a whole space (Yoffe, 1960) to an elastic half space. In the half-space solution an angular dislocation lies in a vertical plane with one leg parallel to the $z$ axis and a second leg inclined at angle $\xi$ from the first. A dislocation segment can be constructed by superimposing two coplanar angular dislocations with opposite Burger's (slip) vectors and equal angles $\beta$, at two different vertex locations, $\xi_1$ and $\xi_2$ (Fig. 6.1b). The two dislocations cancel each other except for the area of underlap, the dislocation segment. The solution for a triangular dislocation patch (Fig. 6.1c) is generated by superposition of three angular dislocation segments that share a common set of vertices, $\xi_1$ through $\xi_2$ (Jeyakumaran et al., 1992). The vertical legs of the dislocations cancel leaving only the triangular dislocation patch. Fault surfaces can be constructed by joining multiple triangular patches or elements. This solution was implemented in a C-language computer program, Poly3D (Thomas, 1993), that calculates the three dimensional components of displacement, strain, and stress anywhere in the elastic body. The first author has subsequently rewritten the code in C++ to: (i) make the code modular, thereby facilitating the development of new applications such as the inverse formulation; (ii) correct the displacement field for points located underneath dislocation elements; (iii) optimize the computation time; and (iv) develop a 3D graphical user interface (GUI) for the creation of Poly3D models and visualization of model results . For more information and to download an academic version of the code see http://pangea.stanford.edu/research/geomech/Software/Software.htm[1]. The Poly3D code provides a direct kinematic solution with prescribed displacement discontinuities on the elements making up the model faults, and a mechanical solution which prescribes

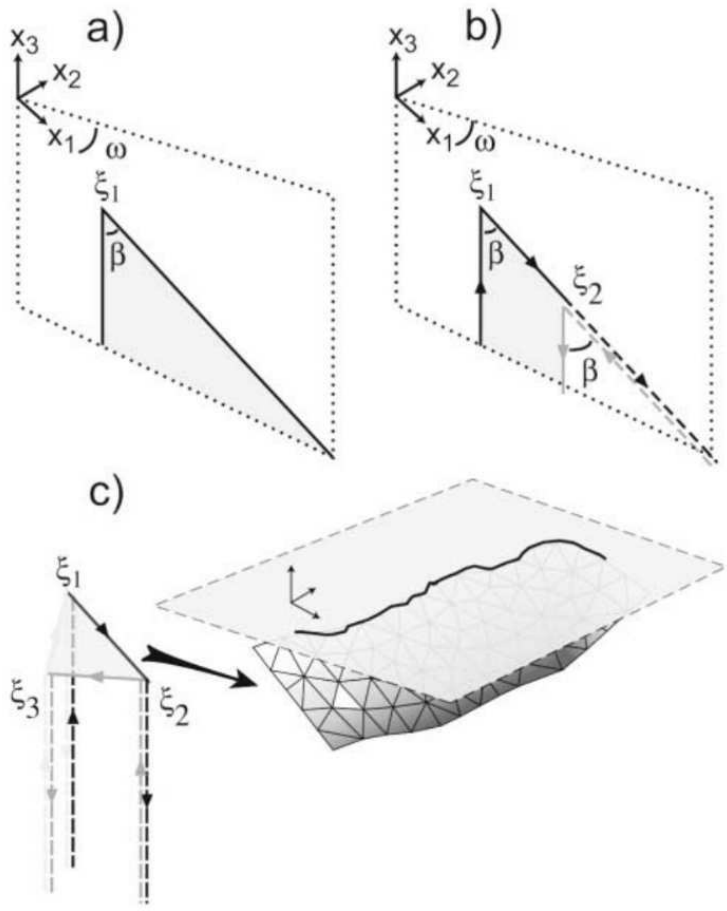


FIGURE 6.1: Construction of a triangular dislocation patch from a set of six angular dislocations. (a) A single vertical angular dislocation located at point $\xi_1$ in a homogeneous elastic half-space where Cartesian coordinate x3 is vertical, positive upward and the x1-x2 plane is the traction-free surface. $\beta_1$ is the angle between the vertical and sloping legs of the dislocation and $\omega$ is the smaller angle between the x1 axis and the strike line of the dislocation plane. (b) Two-coplanar angular dislocations of equal angles *beta* may be superimposed to create a dislocation segment with vertical legs. (c) A triangular dislocation patch can be generated by superimposing three dislocation segments that share three common locations $(\xi_1, \xi_2, \xi_3)$. The vertical dislocation lines cancel leaving a tilted triangular dislocation element (after (Thomas, 1993)).

a uniform remote stress or strain state and tractions at the midpoint of each element, or mixed boundary conditions. For slip inversion we use the kinematic solution for the Green's functions implemented in the code Poly3Dinv available with documentation at http://pangea.stanford.edu/research/geomech/Software/Software.htm.

Due to the use of triangular elements, our calculation of the discrete Laplacian operator $\nabla^2$, also differs from previous slip inversions. Instead of a finite-difference formulation we use the scale-dependent umbrella operator (Desbrun et al., 1999),

[1]Now available at https://support.igeoss.com

$$\nabla^2 m_i = \frac{2}{L_i} \sum_{j=1}^{3} \frac{m_j - m_i}{h_{ij}} \tag{6.3}$$

to approximate the discrete Laplacian for a triangulated 2-manifold. For a triangular element $i$ (Fig. 6.2), with adjacent elements $j$ on its three sides ($j = 1:3$), $h_{ij}$ represents the distance from the center of element $i$ to the center of element $j$, $m_j$ is the slip vector of element $j$, and $L_i$ is the sum of the element center distances, $L_i = \sum_{j=1}^{n} h_{ij}$.

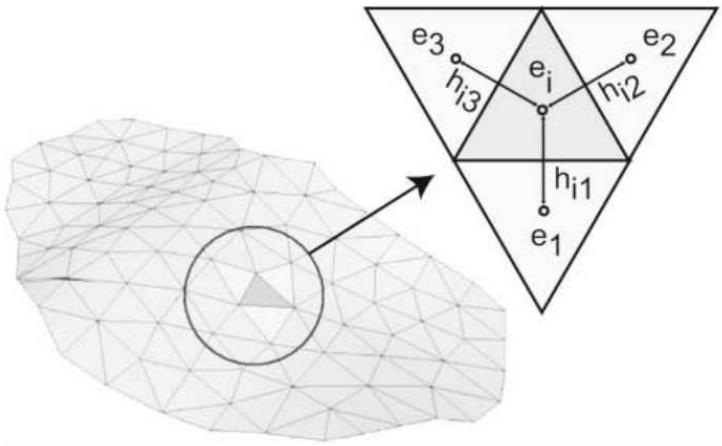


FIGURE 6.2: Discrete Laplacian operator used in Poly3Dinv to smooth the slip distribution. Each displacement discontinuity component of an element ($e_i$, dark gray) is smoothed relative to its adjoining neighbors ($e_j$, light gray). Distances between $e_i$ and $e_j$ centers are $h_{ij}$.

Rearranging to isolate diagonal ($m_i$) and off-diagonal terms ($m_j$) yields a smoothing operator of the form

$$m_j(\frac{2}{Lh_{ij}}) + m_i(\sum \frac{1}{h_{ij}}) \tag{6.4}$$

Superimposing this relation for all elements of the model yields a smoothing operator (sparse matrix) that is used within the least squares formulation to minimize the roughness of the solution. This operator is dependent on the length scale of the model, an effect that can be removed by normalizing by the average value of $h_{ij}$.

In order to solve the linear minimization problem (eq. 2), we use a weighted damped least squares approach:

$$m = (G^T W_e G + \epsilon^2 D^T D)^{-1} G^T W_e d \tag{6.5}$$

where $W_e$ is a weighting matrix that defines the relative contribution of each data point to the total prediction error (Menke, 1984). $W_e$ is typically a diagonal matrix calculated from the normalized inverse of the data measurement errors. In multiple inversions entire data sets may also be weighted relative to one another based on the relative measurement precision of each data set (e.g. InSAR vs GPS, (Jónsson et al., 2002)). Equation (6.4) is solved given the fault geometry and the input data (GPS or InSAR).
Additional constraints can be applied to reach a solution that is consistent with geological concepts of faults. For example, a zero slip constraint may be applied at known fault tips. These may include the base of the seimogenic crust and lateral fault tiplines extending downward from mapped rupture terminations at the earth's surface. In addition, individual slip components can be constrained to be unidirectional, e.g. right lateral, left lateral, reverse or normal only, or any combination of dip slip and strike slip. These constraints are imposed by using an iterative solution algorithm derived from the FNNLS solver (Bro and de Jong, 1997) to solve equation (6.4) with any combination of non-negative, non-positive, or unconstrained slip components.

## 6.5 Application to the 1999 Hector Mine Earthquake

We have chosen to evaluate the new approach to slip inversion using the October 16, 1999 Hector mine earthquake (Mw 7.1) because of the complexity of the observed surface rupture geometry (Fig. 6.3) and the availability of high-quality data (Fig. 6.4) (e.g., (Jónsson et al., 2002; Sandwell et al., 2002; Simons et al., 2002; Treiman et al., 2002)). The Harvard CMT fault plane solution for the event (Dziewonski et al., 2000) has a moment of $5.98 \times 10^{19} Nm$, a strike of 336° and dip of 80° for the inferred primary nodal plane, and a rake of 174° for slip on this plane (Table 1).

The Hector Mine Earthquake ruptured a set of fault segments with a trace length of 48 km in the Mojave Desert of California (Treiman et al., 2002). Surface ruptures occurred on portions of the Lavic Lake fault, an unnamed northeast branch fault, and two strands of the Bullion fault (Fig. 6.3). These included intersecting, echelon, and curving fault segments as well as several parallel segments at the southern terminus of the surface rupture. Observed offsets of surface features had a consistent right-lateral sense with a maximum value of $5.25 \pm 0.85$ m. The sense of vertical offsets was more variable, except in the Bullion Mountains area where there was consistent east-up offset (Treiman et al., 2002).

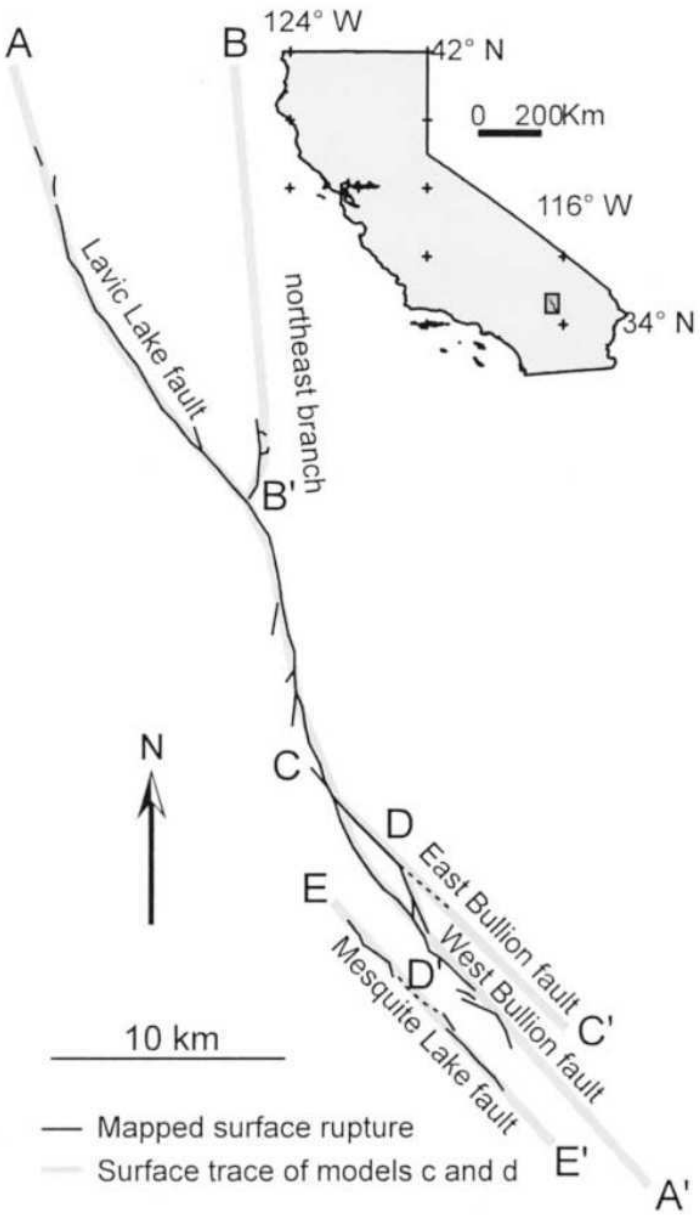


FIGURE 6.3: Map of the Hector Mine earthquake surface rupture (Treiman et al., 2002). Gray lines are surface trace of 6-segment model (Fig 6.6 C and D). Lettered sections refer to graphed segments in figure 6.6. Upper right inset shows location of Hector mine earthquake (dark gray rectangle) in southeastern California.

Moment tensor solutions (e.g, (Centroid Moment Tensor , CMT; Dziewonski et al., 2000)), geodetic inversions (Hurst et al., 2000; Jónsson et al., 2002; Simons et al., 2002), and aftershock distributions (Hauksson et al., 2002) all suggest that the faults dip steeply ( $72-84°$) to the northeast. Multiple geophysical data sets are available for modeling the coseismic rupture associated with the Hector Mine earthquake including broadband seismology, continuous and campaign GPS (Hurst et al., 2000; Agnew et al., 2002), and ascending and descending radar interferograms (InSAR) (Jónsson et al., 2002; Sandwell et al., 2002;

Simons et al., 2002). In particular, the availability of highly coherent ascending and descending interferograms permits detailed modeling of near-field deformation (Fialko et al., 2001; Sandwell et al., 2002). Our goal is primarily to evaluate slip inversions using the new method and to demonstrate how using a model that admits more realistic fault geometry may improve fault slip estimates.

A number of previous studies of the Hector Mine earthquake have inverted for coseismic source parameters incorporating geodetic data. The results of these studies are summarized in Table 1. Hurst and coworkers (Hurst et al., 2000) inverted for a single dislocation source within two weeks of the event using data from the continuously recording Southern California Integrated GPS Network (SCIGN). They solved a non-linear inversion problem for 8 source parameters (x-position, y-position, length, width, strike, dip, strike-slip, dip-slip) using a simulated annealing approach. Ji et al (Ji et al., 2002) and Kaverina et al. (Kaverina et al., 2002) performed joint inversions of geodetic and seismological data for variable fault slip on simplified dipping three-fault models made up of multiple point sources. Sandwell et al. (Sandwell et al., 2002) and Price and Bürgmann (Bürgmann et al., 2002) created models that more closely honored the geometry of the observed surface trace but with vertical faults. This approach allowed for construction of faults comprised of multiple rectangular segments including along strike heterogeneities without generating gaps or overlaps, but these models are inconsistent with the previously cited evidence for eastward dipping fault planes. Simons et al. (Simons et al., 2002) and Jónsson et al. (Jónsson et al., 2002) performed inversions using GPS and InSAR data that allowed for more realistic dipping multi-segment models. These groups both performed non-linear inversions for geometry and linear inversion for variable slip on their fault segments. The resulting fault models included dipping segments with heterogeneities, but also generated gaps and overlaps in the fault surface.

### 6.5.1 Modeling

We have created a series of fault models to compare the results of our method to published results using rectangular dislocations and to illustrate the ability of this method to incorporate more realistic three-dimensional fault geometries that more closely honor observations of surface rupture geometry and fault dip. The faults in all of the models dip 83° to the east based on the results of non-linear geodetic inversions of geodetic data by Jónsson et al. (Jónsson et al., 2002). The faults in each of the models have been discretized into meshes of triangular elements of approximately constant size and equilateral geometry. The total number of elements ( 700) was kept nearly constant between models to maintain roughly the same number of degrees of freedom and thus permit direct

statistical comparison.

We take as our starting point the geometric model of Jónsson et al. (Jónsson et al., 2002) that is comprised of 9 planar segments approximating the trace of the Lavic Lake, unnamed northeast segment and Bullion faults (Fig. 6.5a). The panels have been discretized into 783 triangular elements. The large planar panels model the fault geometry at approximately a 6-km scale and have gaps or overlaps at segment boundaries where the strike of the fault changes. The second model incorporates a curviplanar fault surface that approximates the mapped surface ruptures for the Lavic Lake and West Bullion faults and the distribution of aftershocks for the unnamed northeast fault (Fig. 6.5b). The curviplanar fault surfaces have been discretized into 683 triangular elements. The mapped fault traces have along-strike undulations that are matched by the model fault to the extent possible given the 2.3-km average element size. The minimum radius of curvature that can be modeled by a continuous mesh of equilateral elements of this size isapproximately 1.6 km. This figure is based on the radius of curvature of an open tetrahedron formed by 3 adjoining elements. A third model was constructed to illustrate the strength of this new method in modeling three-dimensional fault surfaces. This model honors the details of the observed surface ruptures at a 2-km-scale (Fig 6.5c) including all six fault segments with observed surface displacements and extends these segments to the northwest and southeast beyond the observed rupture to allow for the possibility of unobserved slip at the surface and/or subsurface slip that extended beyond the mapped surface rupture (see (Simons et al., 2002) for further discussion). The model is discretized into 612 triangular elements. The average element side is 2.6 km resulting in a maximum radius of curvature of 1.8 km.

For each geometric model we performed a joint inversion for slip using the decimated ascending and descending InSAR data sets of Jónsson et al. (Jónsson et al., 2002) and Campaign GPS data ((Agnew et al., 2002), Fig. 6.4). The SAR interferograms are treated as having a constant angle of incidence across the entire image with look vectors of [-0.38 0.07 -0.92] and [0.38 0.08 -0.92] for the descending and ascending phase data, respectively. Slip is constrained to be a combination of right lateral strike slip and east-up dip slip based on the results of previous geodetic (Hurst et al., 2000; Agnew et al., 2002; Jónsson et al., 2002; Sandwell et al., 2002), geologic (Treiman et al., 2002), and seismological investigations (Harvard CMT), (Dziewonski et al., 2000; Ji et al., 2002). Individual data sets (GPS and InSAR) are weighted relative to data uncertainty as outlined by Jónsson (Jónsson et al., 2002). We select the smoothing parameter using a trade-off curve where we seek the smoothing value that minimizes slip roughness without significantly increasing data misfit. The value $\epsilon = 0.07$ yields an average roughness of $1.7 \times 10^{-8}$ $1/km^2$ for model 1 (Fig. 6.5a) vs $5.7 \times 10^{-7}$ $1/km^2$ for the unsmoothed solution while only reducing

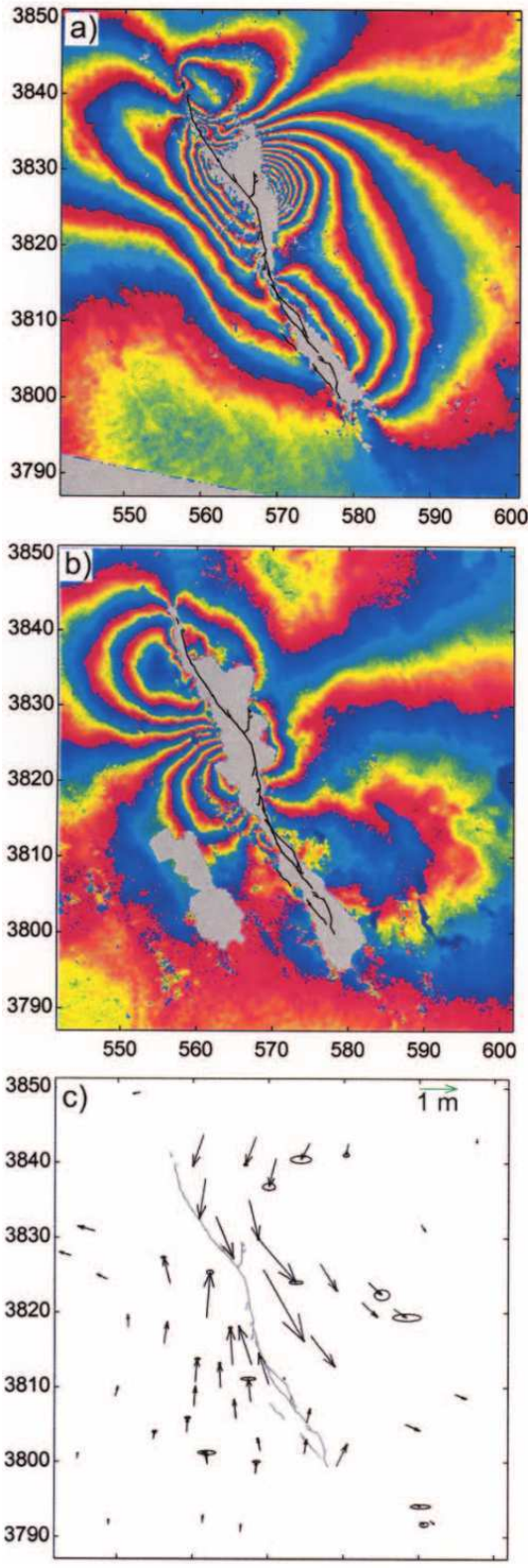


FIGURE 6.4: Geodetic data used for slip inversions. Coordinates are northing and easting for UTM zone 11. a) Descending interferogram of Hector Mine earthquake coseismic deformation (Jónsson et al., 2002) calculated from ERS-2 satellite descending passes on September 15, 1999 and October 20, 1999. b) Ascending interferogram calculated from ERS-2 satellite descending passes on November 12, 1995 and November 21, 1999. For parts a and b each color cycle represents 10 cm of displacement in the satellite line-of-site. The color gradient from blue to red to yellow is in the positive direction, toward the satellite. c) GPS displacement vectors from . Ellipses represent 2-sigma uncertainty.

the model misfit (weighted residual sum of squares, WRSS) by 22%. (All of the fault models as well as the data and parameters used for the slip inversions are available in the electronic edition of BSSA.)

### 6.5.2 Results

The resolved slip patterns in each of our models (Fig 6.5) are grossly similar to the results of Jónsson et al. (Jónsson et al., 2002) (their Fig 8a), although we have chosen a slightly rougher solution as our optimal model. For all three fault models the maximum strike-slip is located on the Lavic Lake fault just northwest of the intersection with the northeast branch at approximately 7 km depth. The magnitude of slip is 6.5 m, 6.6 m, and 7.0 m for models a, b, and c, respectively. The dip-slip maximum is also located along the Lavic Lake fault for all three models at approximately 5.5 km depth, but moves from north of the intersection with the northeast branch fault in the planar fault model to south of the intersection for the curviplanar fault models. The magnitude of the maximum dip-slip is 2.6 m for models a and b and 3.4 m for model c.

The introduction of parallel segments in the multi-segment model leads to slip partitioning between the multiple faults segments in a manner similar to geological observations. Slip on the lavic lake fault decreases to the southeast toward its intersection with the West and East Bullion faults where slip is then partitioned on to each of these parallel segments. The East Bullion fault has a maximum of 1.4 m of slip at its intersection with the Lavic Lake fault and this tapers off to zero slip over about 10 km. The majority of slip, 2.5 m, occurs on the West Bullion Fault and continues about 20 km to the south. The Mesquite Lake fault has 3.5m of slip at 18 km depth. Slip at this depth is relatively poorly resolved (Bos and Spakman, 2003) and these results are therfore not well constrained.

The seismic moment, moment magnitude, and best fit double couple (Jost and Herrman, 1989) for each of the models are presented in Table 1. All three models yield a moment magnitude of 7.1 with decreasing total seismic moments. These results are similar, but slightly lower than previous estimates of the moment using geodetic and seismic methods. The best double couple for the three models is also similar to previous estimates with primary nodal planes striking $332 - 333°$, dipping $82 - 83°$, and rakes of $175 - 176°$.

The series of models we have constructed fits the observed surface ruptures progressively better; however, we also wish to know if it yields an improved fit to the geodetic data. Goodness of fit is commonly estimated using chi squared tests that normalize the model residual (weighted residual sum of squares, WRSS) by the model degree of freedom. This second parameter, however, is difficult to estimate due to correlations between model parameters introduced by smoothing (Cervelli et al., 2001; Jónsson et al., 2002). We

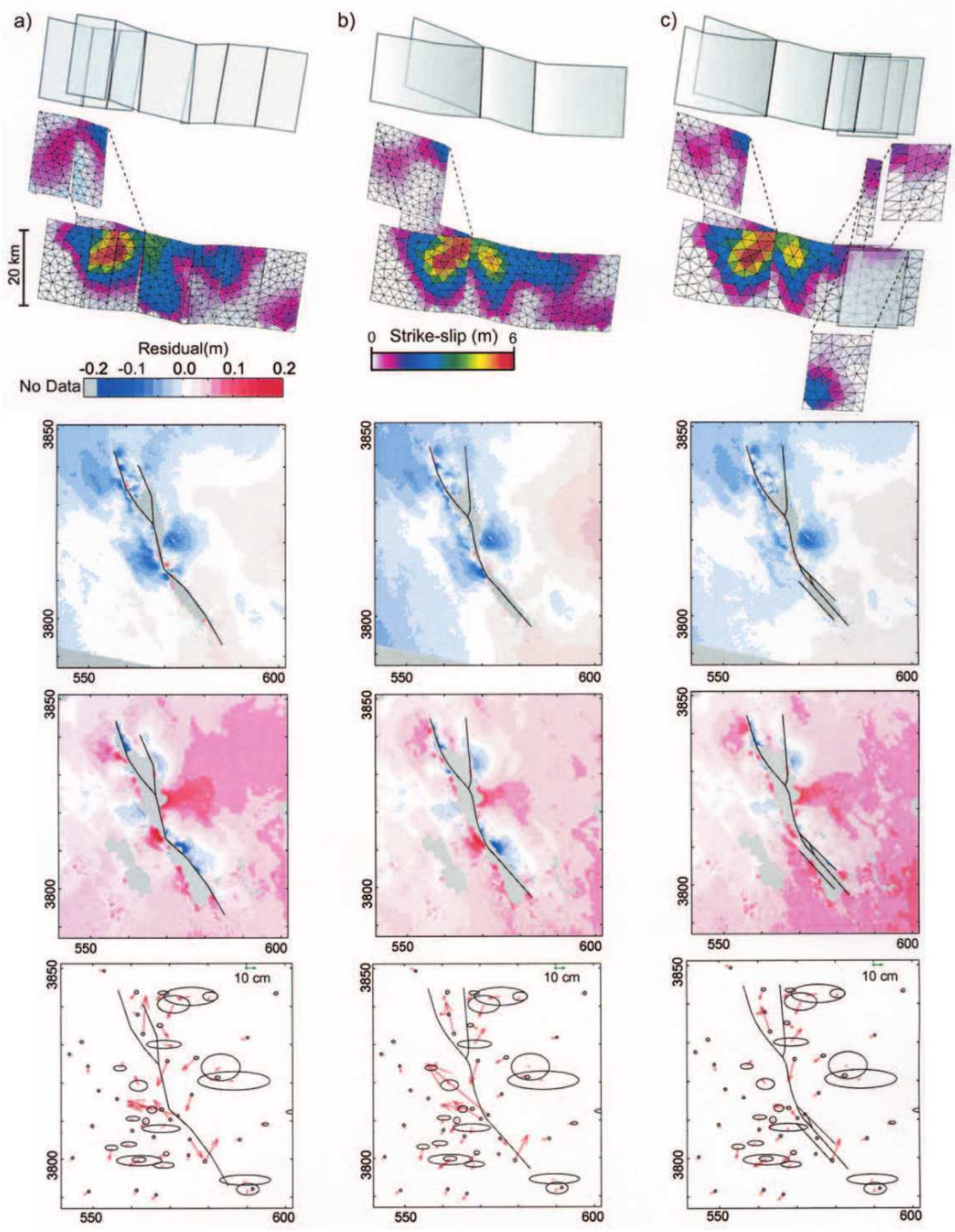


FIGURE 6.5: Comparison of fault models, modeled slip distributions, and residuals for descending and ascending phase InSAR and GPS data (from top to bottom). (a) Planar segment model after Jónsson et al. (Jónsson et al., 2002). (b) Curviplanar model approximating trace of major faults. (c) Six segment model that more closely honors the geometry of the mapped surface ruptures (Fig 6.3). Note scale change for GPS residuals in comparison to figure 6.4. Coordinates are northing and easting for UTM zone 11.

argue that by maintaining approximately the same number of elements and the same smoothing parameter that the number of model parameters remains roughly constant and therefore comparison of the WRSS between models is a reasonable estimate of the relative quality of their fit. We therefore compare our models by presenting the change in the WRSS for the combined and individual data sets as well as presenting a graphical representation of model residuals for the three geodetic data sets (Fig. 6.5).

By incorporating a single curviplanar surface (Fig. 6.5b) we obtained a 8% improvement in WRSS for the combined data sets. This model reduces the WRSS for the descending phase InSAR by 14% and the ascending phase InSAR by 22%, however it leads to a 34% increase in WRSS for the GPS data. The image of the descending phase residuals shows a clear reduction in the near-field residuals that is most obvious near the kink between the Lavic Lake and Bullion faults in the original model (Fig. 6.5a). This kink creates an area of overlapping fault segments that generates a model residual greater than 10 cm, also observable in the model of Jónsson et al. (Jónsson et al., 2002) (their Fig. 9b). In the curviplanar model the residuals in this area are less than 10 cm. Simply smoothing the initial planar-segment model, removing the overlaps and gaps removes this effect and leads to a 2% reduction in the WRSS (results not presented). The increase in the WRSS for the GPS data is largely due to a poorer fit at stations near the northeast branch fault and along the Bullion faults near their intersection with the Lavic Lake fault.

By incorporating all of the segments where surface rupture was observed (Fig. 6.5c) we obtain a 32% reduction in the total WRSS with a 23% reduction for the descending phase InSAR data, a 45% reduction for the ascending phase InSAR data, and a 57% reduction for the GPS data. This model is our preferred model as it significantly improves the fit to the observed surface ruptures and the geodetic data. The reduction in misfit for the descending phase InSAR data is most noticeable to the northwest of the intersection of the Bullion and Lavic lake faults where the previous models had residuals greater than 10 cm which are reduced to less than 5 cm. The high residuals in the ascending InSAR and GPS data near the intersection of these faults are also reduced.

The results of the multi-segment model (Fig. 6.5c) can be directly compared to geologic observations of surface slip (Fig. 6.6). The geologic slip measurements (Treiman et al., 2002) are point estimates and show significant variability over short distances while the model estimates are averages over 2.6 $km^2$ areas and are therefore smoother. The model estimates generally agree with the range of the geologic estimates with a few exceptions. The model predicts significantly more surface slip (2.4-m maximum) on the northeast branch (Fig. 6.3, B-B') than was observed (0.1-m maximum). This result suggests that there may have been significant slip in the subsurface that did not reach the surface and is consistent with previous geodetic inversions. There is a lack of geodetic data near

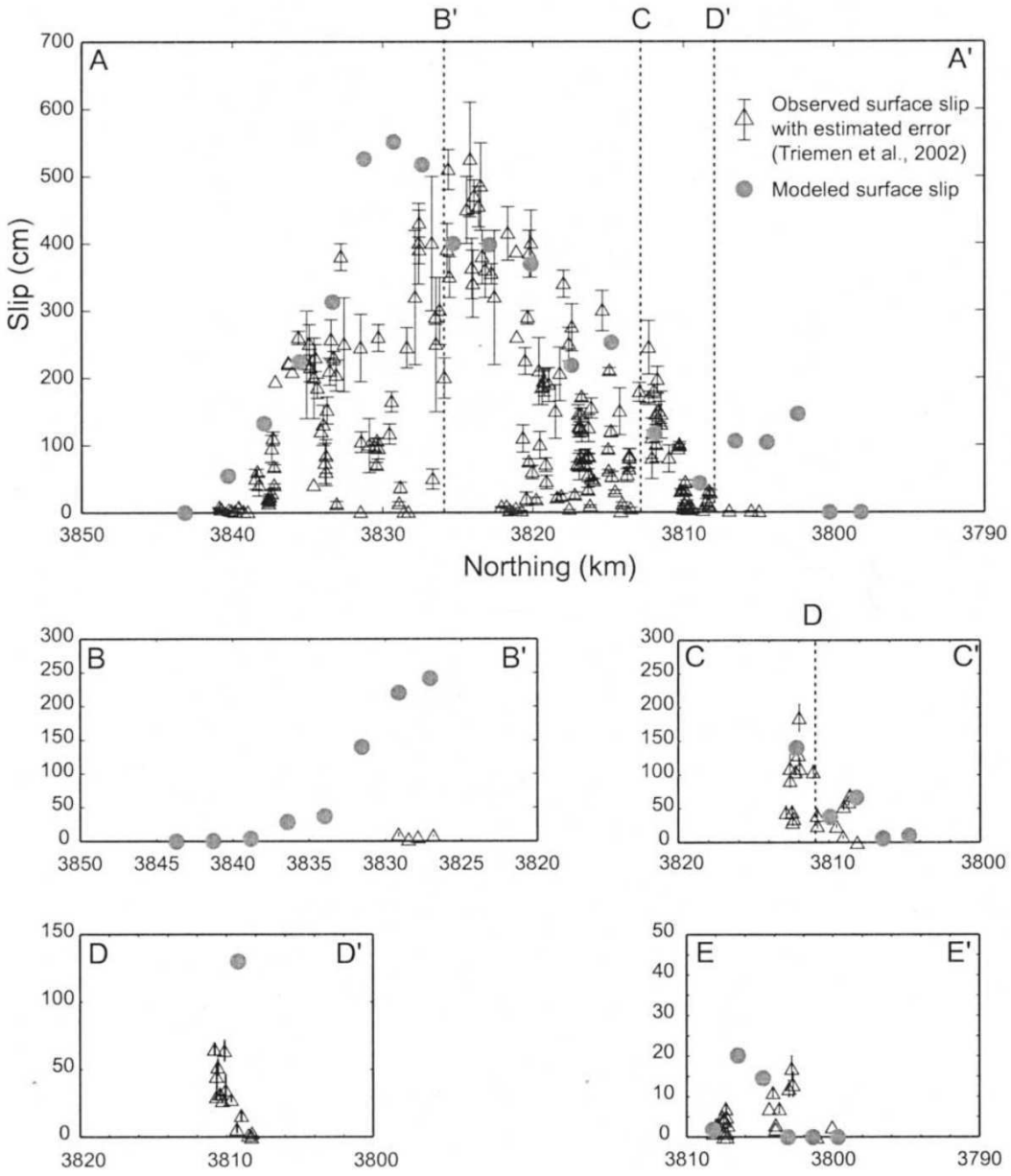


FIGURE 6.6: Comparison between the slip of elements at the surface for multi-segment fault model (Fig 6.5c) and the measured surface slip distribution from Treiman et al (Treiman et al., 2002). Fault segments are illustrated in figure 3. A-A' Lavic Lake-West Bullion faults.. B-B' northeast branch of the Lavic Lake fault. C-C' East Bullion fault. D-D' linking structure between East and West Bullion faults. E-E' Mesquite Lake fault. Note different ordinate scales for D-D' and E-E'. Fault intersections are marked with dashed lines

the surface trace of the northeast branch (Fig. 6.4) and near-surface slip in the model is therefore poorly constrained. The model also predicts more slip on the Lavic Lake fault (Fig. 6.3, northern end of A-A') just north of its intersection with the northeast branch than was observed geologically. This area is in the transition from the Bullion Mountains to younger alluvial fan deposits and may therefore have been an area where surface rupture was distributed or otherwise difficult to fully quantify. The slip on the small linking structure (D-D') is also overestimated, but is poorly constrained by near-field geodetic data. The last area of significant difference is at the southern end of the West Bullion fault (Fig. 6.3, southern end of A-A') where the geodetic model again predicts more slip than was observed at the surface. Previous researchers (e.g., see (Simons et al., 2002)) also noted this discrepancy and although additional surface rupture was identified (Treiman et al., 2002), there is still a notable deficit compared to the geodetic model results. The observed surface rupture in this region was comprised of echelon cracks in alluvial fan surfaces that may have been indicative of greater right-lateral slip at depth. The comparison between the geodetic model results and geologic slip estimates suggest that the geologic estimates are generally representative of near surface fault slip, but may have a tendency to underestimate total slip due to near surface effects such as distributed deformation in materials that may be softer and able to accommodate deformation without macroscopic fracturing.

## 6.6 Discussion and Conclusions

Inversion for coseismic slip using angular elastic dislocations allows for incorporation of more realistic geometries, and thus more realistic models of the seismic source. This approach takes advantage of the increasing quantity and quality of geodetic data, in particular the spatially dense near-field data acquired through interferometric radar techniques (InSAR). The flexibility of the method permits the construction of fault models with curved three-dimensional surfaces and tiplines. Fault surface traces can be taken into account as well as subsurface constraints such as high-precision hypocentral locations of aftershocks.

The method presented here may be modified to account for the reduced resolving power with depth of geodetic data (Bos and Spakman, 2003) by adopting an adaptive meshing algorithm (e.g., (Price and Bürgmann, 2002)). The method may also be extended to incorporate inversion for fault geometry as well as slip. This problem is highly non-linear and will require damping of the fault geometric roughness as well as slip roughness to

obtain physically reasonable solutions.

In the case of the Hector Mine earthquake we have demonstrated that the method not only provides grossly similar results to previous approaches using rectangular dislocations, but also improves upon these results by removing artifacts associated with overlaps between rectangular fault segments. By constructing a model that honors the geometry of observed surface ruptures we have demonstrated that the fault geometry suggested by these data can be incorporated into the model and also leads to an improvement in the quality of the solution.

## 6.7 Acknowledgements

We are particularly grateful to S. Jónsson, P. Segall, and H. Zebker for sharing InSAR data from the Hector Mine earthquake and modeling experience both of which were invaluable in our development and evaluation of P3Dinv. Thanks to D. Agnew for providing campaign GPS data and K. Kendrick for providing surface slip data for the Hector Mine earthquake and K. Johnson for providing data and models for the Chi-Chi earthquake. J. Muller helped with the modification of the FNNLS solver to allow for variable constraints. Funding for this research was provided in part by the USGS National Earthquake Hazard Reduction Program external grant 02HQGR0050, the ARCO Stanford Graduate Fellowship to P. Resor, and the Stanford Rock Fracture Project.

# References


Agnew, D., Owen, S., Shen, Z., Anderson, G., Svarc, J., Johnson, H., Austin, K., and Reilinger, R. (2002). Coseismic displacements from the hector mine, california, earthquake: results from survey-mode global positioning system measurements. *Bull. Seism. Soc. Am.*, 92:1355–1364.

Aydin, A. and Kalafat, D. (2002). Surface ruptures of the 17 august and 12 november 1999 izmit and duzce earthquakes in northwestern anatolia, turkey: their tectonic and kinematic significance and the associated damage. *Bull. Seism. Soc. Am.*, 92:95–106.

Bos, A. G. and Spakman, W. (2003). The resolving power of coseismic surface displacement data for fault slip distribution at depth. *Geophys. Res. Lett.*, 30,2110.

Bro, R. and de Jong, S. (1997). A fast non-negativity-constrained least squares algorithm. *J. Chemom.*, 11:393–401.

Bürgmann, R., Ergintav, S., Segall, P., Hearn, E., McClusky, S., Reilinger, R., Woith, H., and Zschau, J. (2002). Time-dependent distributed afterslip on and deep below the izmit earthquake rupture. *Bull. Seismol. Soc. Am.*, 92:126–137.

Carena, S. and Suppe, J. (2002). Three-dimensional imaging of active structures using earthquake aftershocks: the northridge thrust, california. *J. Struct. Geol.*, 24:887–904.

Cartwright, J. A., Trudgill, B. D., and Mansfield, C. S. (1995). Fault growth by segment linkage: an explanation for scatter in maximum displacement and trace length data from the canyonlands grabens of se utah. *J. Struct. Geol.*, 17:1319–1326.

Centroid Moment Tensor (CMT) Catalog (2003). last accessed August 2003, www.seismology.harvard.edu/CMTsearch.html.

Cervelli, P., Murray, M., Segall, P., Aoki, Y., and Kato, T. (2001). Estimating source parameters from deformation data, with an application to the march 1997 earthquake swarm off the izu peninsula, japan. *J. Geophys. Res.*, 11:217–237.

Chiaraluce, L., Ellsworth, W., Chiarabba, C., and Cocco, M. (2003). Imaging the complexity of an active normal fault system: the 1997 colfiorito (central italy) case study. *J. Geophys. Res.*, 108:2294.

Comninou, M. and Dundurs, J. (1975). The angular dislocation in a half space. *Journal of Elasticity*, 5(3):203–216.

Desbrun, M., Meyer, M., Schroder, P., and Barr, A. H. (1999). Implicit fairing of irregular meshes using diffusion and curvature flow. *SIGGRAPH*, 99:317–324.

Du, Y., Aydin, A., and Segall, P. (1992). Comparison of various inversion techniques as applied to the determination of a geophysical deformation model for the 1983 borah peak earthquake. *Bull. Seism. Soc. Am.*, 82:1840–1866.

Dziewonski, A., Ekstrom, G., and Maternovskaya, N. (2000). Centroid moment tensor solutions for october-december, 1999. *Phys. Earth Planet. Inter.*, 121:205–221.

Feigl, K., Sergent, A., and Jacq, D. (1995). Estimation of an earthquake focal mechanism from a satellite radar interferogram: application to the december 4, 1992 landers aftershock. *Geophys. Res. Lett.*, 22:1037–1040.

Fialko, Y., Simons, M., and Agnew, D. (2001). The complete (3-d) surface displacement field in the epicentral area of the 1999 m(w) 7.1 hector mine earthquake, california, from space geodetic observations. *Geophys. Res. Lett.*, 28:3063–3066.

Freymueller, J., King, N., and Segall, P. (1994). The coseismic slip distribution of the landers earthquake. *Bull. Seism. Soc. Am.*, 84:646–659.

Hanssen, R. F. (2001). *Radar interferometry: data interpretation and error analysis, in Remote Sensing and Digital Image Processing*. Kluwer Academic Publishers, Dordrecht, The Netherlands.

Harris, R. A. and Segall, P. (1987). Detection of a locked zone at depth on the parkfield, california, segment of the san andreas fault. *J. Geophys. Res.*, 92:7945–7962.

Hauksson, E., Jones, L., and Hutton, K. (2002). The 1999 mw 7.1 hector mine, california, earthquake sequence: complex conjugate strike-slip faulting. *Bull. Seism. Soc. Am.*, 92:1154–1170.

Hurst, K., Argus, D., Donnellan, A., Heflin, M., Jefferson, D., et al. (2000). The coseismic geodetic signature of the 1999 hector mine earthquake. *Geophys. Res. Lett.*, 27:2733–2736.

Jeyakumaran, M., Rudnicki, J. W., and Keer, L. M. (1992). Modeling slip zones with triangular dislocation elements. *Bulletin of the Seismological Society of America*, 82:2153–2169.

Ji, C., Wald, D., and Helmberger, D. (2002). Source description of the 1999 hector mine, california, earthquake, part ii: complexity of slip history. *Bull. Seism. Soc. Am.*, 92:1208–1226.

Johnson, K., Hsu, Y., Segall, P., , and Yu, S. (2001). Fault geometry and slip distribution of the 1999 chi-chi, taiwan, earthquake imaged from inversion of gps data. *Geophys. Res. Lett.*, 28:2285–2288.

Jónsson, S., Zebker, H., Segall, P., and Amelung, F. (2002). Fault slip distribution of the 1999 mw 7.1 hector mine, california, earthquake, estimated from satellite radar and gps measurements. *Bull. Seism. Soc. Am.*, 92:1377–1389.

Jost, M. L. and Herrman, R. B. (1989). A student's guide to and review of moment tensors. *Seism. Res. Lett.*, 60:37–57.

Kattenhorn, S. A. and Pollard, D. D. (2001). Integrating 3-d seismic data, field analogs, and mechanical models in the analysis of segmented normal faults in the wytch farm oil field, southern england, united kingdom. *AAPG Bull.*, 85:1183–1210.

Kaverina, A., Dreger, D., and Price, E. (2002). The combined inversion of seismic and geodetic data for the source process of the 16 october 1999 mw 7.1 hector mine, california, earthquake. *Bull. Seism. Soc. Am.*, 92:1266–1280.

Kilb, D. and Rubin, A. (2002). Implications of diverse fault orientations imaged in relocated aftershocks of the mount lewis, ml 5.7, california, earthquake. *J. Geophys. Res.*, 107:2294.

Lin, A., Ouchi, T., Chen, A., and Maruyama, T. (2001). Co-seismic displacements, folding and shortening structures along the chelungpu surface rupture zone occurred during the 1999 chi-chi (taiwan) earthquake. *Tectonophysics*, 330:225–244.

Lin, J. and Stein, R. S. (1989). Coseismic folding, earthquake recurrence, and the 1987 source mechanism at whittier narrows, los angeles basin, california. *J. Geophys. Res.*, 94:9614–9632.

Maerten, L., Pollard, D. D., and Karpuz, R. (2000). How to constrain 3d fault continuity and linkage using reflection seismic data: a geomechanical approach. *AAPG Bull.*, 84:1311–1324.

Martel, S. J. (1990). Formation of compound strike-slip fault zones, mount abbot quadrangle, california. *J. Struct. Geol.*, 12:869–882.

Menke, W. (1984). *Geophysical Data Analysis: Discrete Inverse Theory.* International Geophysics Series, Academic, San Diego.

Peacock, D. (2002). Propagation, interaction and linkage in normal fault systems. *Earth Sci. Rev.*, 58:121–142.

Price, E. and Bürgmann, R. (2002). Interactions between the landers and hector mine, california, earthquakes from space geodesy, boundary element modeling, and time-dependent friction. *Bull. Seism. Soc. Am.*, 92:1450–1469.

Reilinger, R., Ergintav, S., Bürgmann, R., McClusky, S., Lenk, O., et al. (2000). Coseismic and postseismic fault slip for the 17 august 1999,m7.5, izmit, turkey earthquake. *Science*, 289:1519–1524.

Sandwell, D., Sichoix, L., and Smith, B. (2002). The 1999 hector mine earthquake, southern california: vector near-field displacements from ers insar. *Bull. Seism. Soc. Am.*, 92:1341–1354.

Simons, M., Fialko, Y., and Rivera, L. (2002). Coseismic deformation from the 1999 mw 7.1 hector mine, california, earthquake as inferred from insar and gps observations. *Bull. Seism. Soc. Am.*, 92:1390–1402.

Stein, R. S. and Barrientos, S. E. (1985). Planar high-angle faulting in the basin and range: geodetic analysis of the 1983 borah peak, idaho, earthquake. *J. Geophys. Res.*, 90:11355–11366.

Thomas, A. L. (1993). Poly3d: a three-dimensional, polygonal element, displacement discontinuity boundary element computer program with applications to fractures, faults, and cavities in the earth's crust. Master's thesis, Stanford University.

Treiman, J., Kendrick, K., Bryant, W., Rockwell, T., and McGill, S. (2002). Primary surface rupture associated with the mw 7.1 16 october 1999 hector mine earthquake, san bernardino county, california. *Bull. Seism. Soc. Am.*, 92:1171–1191.

Waldhauser, F. and Ellsworth, W. L. (2000). A double-difference earthquake location algorithm: method and application to the northern hayward fault, california. *Bull. Seism. Soc. Am.*, 90:1353–1368.

Walsh, J. J., Watterson, J., Bailey, W. R., and Childs, C. (1999). Fault relays, bends and branch-lines. *J. Struct. Geol.*, 21:1019–1026.

Willemse, E. J. M., Peacock, D. C. P., and Aydin, A. (1997). Nucleation and growth of strike-slip faults in limestones from somerset, u.k. *J. Struct. Geol.*, 19:1461–1477.

Willemse, E. J. M., Pollard, D. D., and Aydin, A. (1996). Three-dimensional analyses of slip distributions on normal fault arrays with consequences for fault scaling. *J. Struct. Geol.*, 18:295–309.

Wright, T., Parsons, B., Jackson, J., Haynes, M., Fielding, E., England, P., and Clarke, P. (1999). Source parameters of the 1 october 1995 dinar (turkey) earthquake from sar interferometry and seismic bodywave modelling. *Earth Planet. Sci. Lett.*, 172:23–37.

Yoffe, E. (1960). The angular dislocation. *Phil. Mag.*, 5:161–175.

Yu, E. and Segall, P. (1996). Slip in the 1868 hayward earthquake from the analysis of historical triangulation data. *J. Geophys. Res.*, 101:16101–16118.

Zhang, P., Mao, F., and Slemmons, D. (1999). Rupture terminations and size of segment boundaries from historical earthquake ruptures in the basin and range province. *Tectonophysics*, 308:37–52.

# CHAPTER 7

# Co- and post-seismic deformation of the 28 March 2005 Nias Mw 8.7 earthquake from continuous GPS data

C. Kreemer[1], G. Blewitt[1], F. Maerten[2,3]

(1) Nevada Bureau of Mines and Geology and Seismological Laboratory, University of Nevada, Reno, Nevada, USA.
(2) Igeoss, Montpellier, FRANCE
(3) University of Montpellier II, Geosciences, FRANCE

Published in Geophysical Research Letters, 2006, Vol. 33, L07307, 4 PP.,
DOI:10.1029/2005GL025566



**Preamble**

This chapter presents an application of the slip inversion method described in chapter 6 for the Nias earthquake (Indonesia), which occurred in 2005. It provides an explanation

why the Nias earthquake did not produce a sizable tsunami.

## About...

Corne Kreemer contacted me few months after the publication of the paper on slip inversion. The goal was to use Poly3D-inverse and the available data to study the Nias earthquake using a complex surface rupture.

## Article Outline

## 7.1 Résumé

Les donnés GPS (Global Positioning System) ont été enregistrées avec plus de 5 m de déplacement co-sismique au cours du tremblement de terre de Nias (Mw = 8.7), le 28 mars 2005 en Indonésie. Le rejet vertical suggère de fortes contraintes sur la limite nord et sud de la zone de rupture. La distribution de glissements co-sismiques retrouvée indique des zones de glissements élevées près de l'épicentre et de la limite sud pour la rupture du 26 décembre 2004 d'Aceh-Andaman, où les répliques ont été abondantes. Six mois d'enregistrement de séries chronologiques post-sismiques sont mieux approximés avec une fonction logarithmique qu'avec une fonction exponentielle, ce qui suggère que la déformation post-sismique est probablement contrôlée par des post-glissements. Notre modèle d'inversion prédit des post-glissements concentrés au-dessus et en dessous des zones de glissements co-sismiques maximales où les répliques sont clairsemées. Le post-glissement peu profond ajoute une preuve supplémentaire que le tremblement de terre n'a sans doute pas atteint la surface (avec des conséquences pour la génération de tsunamis) mais, au contraire, à causé des déformations asismiques dans les parties peu profondes de la zone de subduction après l'évènement.

## 7.2 Abstract

Global Positioning System (GPS) measurements registered up to $> 5m$ of coseismic displacements during the 28 March 2005 $M_w = 8.7$ Nias earthquake, Indonesia. The vertical offsets put tight constraints on the northern and southern limit of the rupture. The inferred coseismic slip distribution indicates high slip patches near the epicenter and near the southern extent of the 26 December 2004 Aceh-Andaman rupture, where aftershocks have been abundant. Six months of postseismic time-series are better fit with a logarithmic instead of exponential function, suggesting that the postseismic deformation is likely controlled by afterslip. Our inversion model predicts afterslip to be concentrated both up- and down-dip from patches of maximum coseismic slip where aftershocks are sparse. The shallow afterslip adds further evidence that the earthquake probably did not break the surface (with implications for tsunami generation) and instead caused aseismic deformation in shallow parts of the subduction zone after the event.

## 7.3 Introduction

The $M_w = 8.7$ Nias earthquake of 28 March 2005 happened three months after the $M_w = 9.2$ December 26, 2004, Aceh-Andaman earthquake and may be the largest aftershock ever recorded. It was recorded by a network of nearby continuous Global Positioning System (GPS) stations, namely the Sumatra GPS Array (SuGAr), which did not record significant displacements related to the December event (Subarya et al., 2006), but was optimally located to constrain the co- and postseismic deformation associated with the March event. Here we model the co- and postseismic slip distribution for the Nias event from the analysis of the GPS time-series (mainly) from the SuGAr array. The co- and postseismic slip models are of particular interest, because of the size of this event, its relationship to the December earthquake, and the intriguing observation that this event did not create a sizable tsunami. These models provide insight into the seismic cycle (and future hazard) along the Sumatra subduction zone in particular, and on the dynamics of large subduction-type earthquakes in general.

Many studies have attributed postseismic transients in geodetic time-series to an afterslip process down-dip from the rupture (Melbourne et al., 2002), but fast-decaying shallow afterslip (Burgmann et al., 2002), as well as viscous relaxation (Pollitz et al., 2000) have also been invoked occasionally as plausible mechanisms, with the different processes acting over different time-scales (and probably concurrently) after an earthquake. Here we

fit the postseismic time-series with simple analytical functions, which are first-order representations of afterslip and relaxation processes.

## 7.4 Co- and Postseismic Displacements

Postseismic time-series for the Nias event were generated from the GPS station position estimates. These time-series were then corrected for ongoing deformation after the Aceh-Andaman event (Fig. 7.1). (The auxiliary material[1] describes the times-series analysis in

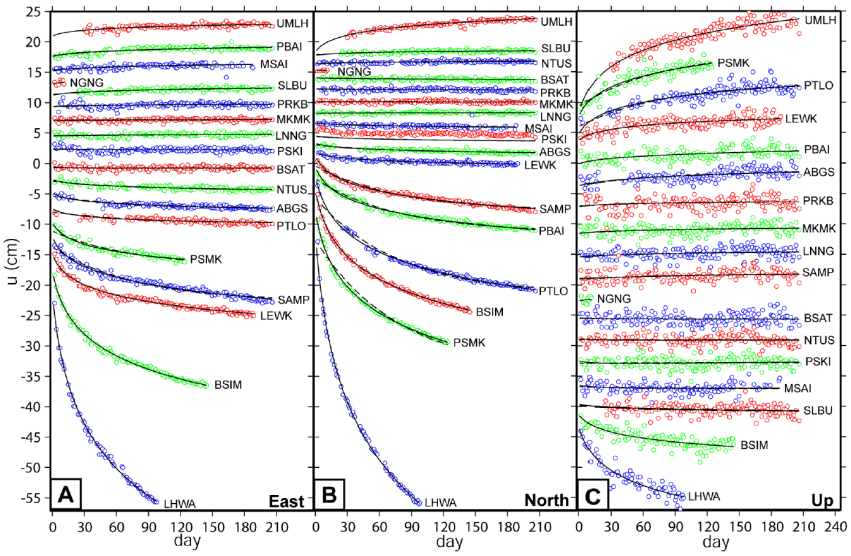


FIGURE 7.1: Postseismic time-series for the 18 analyzed stations. Note that the time-series are vertically displaced (see Table 1 for coseismic offset values). Solid and dashed lines are best-fit logarithmic and exponential functions, respectively (The relaxation predictions are not shown for newly installed stations BSIM, LEWK, LHWA, and UMLH, because the additional constant velocity that is solved for those stations differs between the two models and changes the appearance of the timeseries.): (a) east direction, (b) north direction, and (c) up direction.

detail.)

We performed a non-linear minimization scheme using the Levenburg-Marquardt method (Press, 1992) to estimate for the December and March events the coseismic offsets and postseismic deformation parameters simultaneously. The two postseismic processes we consider independently are velocity-strengthening afterslip, which follows a logarithmic decay (Marone et al., 1991),:

$$u(t) = c + a \ln(1 + t/\tau_{log}) \tag{7.1}$$

and a relaxation mechanism, which in its most simplistic form (and particularly near the rupture) follows an exponential decay (Savage and Prescott, 1978):

$$u(t) = c + a\ln(1 - e^{-t/\tau_{exp}}) \tag{7.2}$$

In (7.1) and (7.2) t is time since the earthquake, u(t) is the position (east, north, and up), c is the coseismic offset, a is the amplitude associated with the decay, and $\tau_{log}$ and $\tau_{exp}$ are the logarithmic and exponential decay time, respectively, and are assumed to be similar for all time-series. We did not assume parameters a or c to be similar between (7.1) and (7.2). For stations BSIM, LEWK, LHWA, and UMLH that were installed in the few months between the Aceh- Andaman and Nias earthquakes, we solved for an additional constant velocity term in (7.1) and (7.2) and constrained t to be that obtained from the 14 other stations. In solving for the postseismic parameters for the March event we corrected for all stations the post 28 March 2005 times-series for the ongoing postseismic deformation related to the 26 December 2004 earthquake. For this correction we assumed that the postseismic time-series after the 2004 event is controlled by a similar (logarithmic or exponential) decay mechanism as modeled for the March event.

Our estimated geodetic coseismic offsets and postseismic amplitudes for the Nias earthquake range between stations from several meters to millimeters (Fig. 7.2 and Table 7.1). (Model parameters obtained for the December event are summarized in Table S1). With

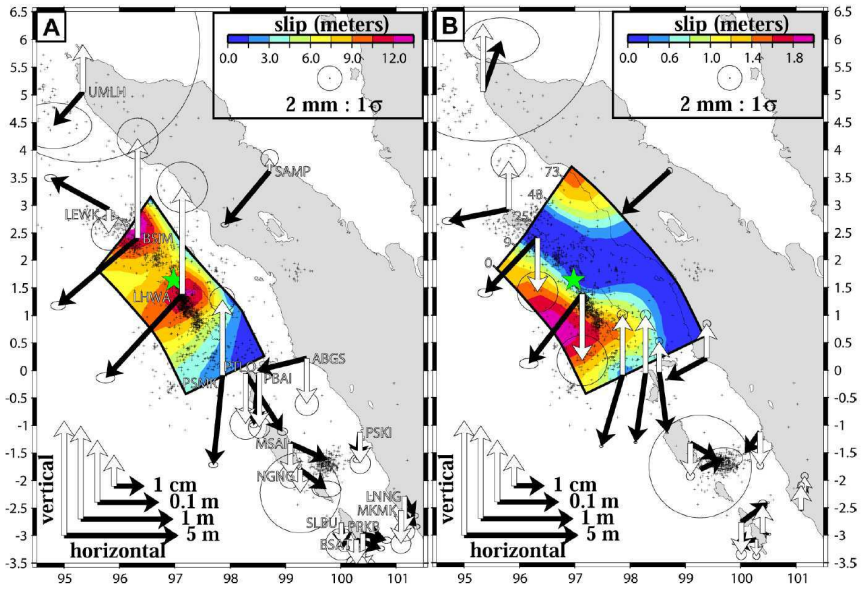


FIGURE 7.2: Horizontal (black) and vertical (white) GPS offsets, scaled with the natural log. Uncertainty ellipse is unscaled. Contours are slip magnitudes on increasingly steeper surface at depth, and crosses are aftershocks from the NEIC catalog. Green star is epicenter. (a) Coseismic, (b) postseismic from 180 days of predicted cumulative afterslip.

TABLE 7.1: Co- and Postseismic Parameters for March 28, 2005, Nias Earthquake

| Site | Lon., °E | Lat., °N | $c_{east}$,[a] mm | $c_{north}$,[a] mm | $c_{up}$,[a] mm | $a_{east}$,[b] mm | $a_{north}$,[b] mm | $a_{up}$,[b] mm | $\chi^{2c}_{\nu}$ | $\chi^{2d}_{\nu}$ |
|---|---|---|---|---|---|---|---|---|---|---|
| abgs | 99.39 | 0.22 | −44.4 ± 0.6 | −10.8 ± 0.5 | −29.5 ± 0.2 | −7.7 ± 0.2 | −4.1 ± 0.2 | 3.5 ± 0.6 | 2.1 | 2.3 |
| bsat | 100.28 | −3.08 | 6.5 ± 0.6 | −2.3 ± 0.4 | −6.4 ± 1.7 | −1.7 ± 0.2 | −0.3 ± 0.1 | −1.0 ± 0.6 | 3.2 | 3.2 |
| bsim[e] | 96.32 | 2.41 | −1809.4 ± 1.2 | −1536.5 ± 0.7 | 1600.5 ± 3.3 | −59.0 ± 0.8 | −61.9 ± 0.5 | −16.7 ± 2.2 | 3.3 | 10.9 |
| lewk[e] | 95.80 | 2.92 | −121.4 ± 1.0 | 65.8 ± 0.6 | −5.7 ± 2.8 | −28.3 ± 1.0 | −5.5 ± 0.6 | 10.4 ± 2.7 | 2.4 | 3.2 |
| lhwa[e] | 97.13 | 1.38 | −3082.7 ± 1.5 | −3356.2 ± 0.8 | 2870.0 ± 4.1 | −121.4 ± 1.2 | −157.6 ± 0.7 | −41.2 ± 3.3 | 8.5 | 44.3 |
| lnng | 101.16 | −2.29 | 2.4 ± 0.6 | −4.6 ± 0.4 | −13.7 ± 1.6 | 0.2 ± 0.2 | 0.5 ± 0.2 | 1.2 ± 0.6 | 2.7 | 2.7 |
| mkmk | 101.09 | −2.54 | 3.7 ± 0.6 | −3.8 ± 0.4 | −11.8 ± 1.6 | 0.0 ± 0.2 | 0.3 ± 0.1 | 1.8 ± 0.6 | 2.4 | 2.4 |
| msai | 99.09 | −1.33 | 18.1 ± 0.7 | −8.1 ± 0.4 | −12.0 ± 1.8 | 2.5 ± 0.2 | −1.4 ± 0.2 | −3.5 ± 0.7 | 2.3 | 2.3 |
| ngng | 99.27 | −1.80 | 9.2 ± 2.3 | −6.8 ± 1.3 | −5.6 ± 6.5 | 1.9 ± 3.0 | 0.9 ± 1.7 | 0.4 ± 8.3 | 1.8 | 1.8 |
| ntus | 103.68 | 1.35 | −8.9 ± 0.6 | −5.6 ± 0.4 | −0.1 ± 1.3 | −7.7 ± 0.2 | −4.1 ± 0.2 | 4.4 ± 0.6 | 4.0 | 4.0 |
| pbai | 98.53 | −0.03 | −5.4 ± 0.6 | −51.6 ± 0.4 | −58.9 ± 1.7 | 3.6 ± 0.2 | −28.8 ± 0.1 | 4.4 ± 0.8 | 3.3 | 3.6 |
| prkb | 100.40 | −2.97 | 6.0 ± 0.8 | −1.6 ± 0.6 | −15.5 ± 2.3 | 0.4 ± 0.3 | 0.0 ± 0.2 | 2.5 ± 0.8 | 3.0 | 3.0 |
| pski | 100.35 | −1.12 | −0.9 ± 0.7 | −7.8 ± 0.4 | −10.0 ± 1.7 | −1.2 ± 0.2 | −1.7 ± 0.1 | −3.6 ± 0.6 | 2.8 | 2.9 |
| psmk | 97.86 | −0.09 | −81.3 ± 0.8 | −796.3 ± 0.5 | 275.1 ± 2.0 | −20.6 ± 0.3 | −70.6 ± 0.2 | 26.3 ± 0.8 | 4.1 | 19.5 |
| ptlo | 98.28 | −0.05 | 90.0 ± 0.8 | −141.0 ± 0.6 | −41.4 ± 2.6 | −7.6 ± 0.3 | −52.4 ± 0.2 | 21.7 ± 0.9 | 3.6 | 5.6 |
| samp | 98.71 | 3.62 | −114.7 ± 0.7 | −136.9 ± 0.4 | 2.6 ± 1.4 | −159.6 ± 0.8 | −159.6 ± 0.8 | −159.6 ± 0.8 | 5.2 | 8.2 |
| slbu | 100.01 | −2.77 | 0.7 ± 0.9 | −6.5 ± 0.6 | −5.0 ± 2.6 | 2.7 ± 0.3 | 2.0 ± 0.2 | −3.2 ± 0.9 | 2.5 | 2.5 |
| umlh[e] | 95.34 | 5.05 | −18.2 ± 6.2 | −20.9 ± 3.7 | 32.4 ± 19.0 | 5.5 ± 7.3 | 15.4 ± 4.0 | 44.4 ± 21. | 2.5 | 2.5 |

[a]Coseismic offset from (1).
[b]Decay amplitude from (1).
[c]Reduced $\chi^2$ of fit for logarithmic decay.
[d]Reduced $\chi^2$ of fit for exponential decay.
[e]For these sites a constant secular velocity was also included in the inversion.

each model fitted separately, we find $\tau_{log} = 6.2 \pm 0.1$ days and $\tau_{exp} = 77.8 \pm 0.3$ days. The postseismic times-series are fit significantly better by (7.1) than (7.2): the data fit results in $\chi^2_\mu = 3.2$ and $\chi^2_\mu = 5.4$, respectively. The $\chi^2_\mu$ for individual stations (Table 7.1) are for all stations better (in the nearfield) or equal (in the far-field) when the logarithmic function is considered (see also Fig. 7.1). We therefore assume for the remainder of the paper that the postseismic deformation for the 6 months since the event is dominated by afterslip, although we note that both (7.1) and (7.2) are simplifications that do not fully address the intricacies of the 3-D stress and strain fields that arise for a case with a complex slip distribution on a finite fault. The data furthermore suggest that there is no temporal variation in the spatial characteristics of the afterslip process; that is, we can assume one common decay time for all timeseries combined, with single decay magnitudes for each time-series. We further note that the post 26 December 2004 time-series are fit better by (7.1) than (7.2) as well (Table S1). This result justifies our assumption to adopt a similar postseismic decay mechanism after both events when we correct the post 28 March time-series for ongoing postseismic deformation related to the December event.

## 7.5 Co- and Postseismic Slip Model

The large spatial variation in coseismic offset magnitudes (Fig. 7.2.a) places strong constraints on which to build a coseismic slip model. In particular, sites that moved up during the earthquake must be situated above the rupture plane. Consequently, the northern extension of the rupture plane must lie between stations LEWK and BSIM (which is also the exact southern limit of the Aceh-Andaman rupture (Meltzner et al., 2006; Subarya et al., 2006)), and the southern limit must lie between PSMK and PTLO, (similar to the southern extent of the 1861 M = 8.5 rupture (Natawidjaja et al., 2004)). We chose the up-dip limit of our model plane to be the trench and the down-dip width to be the 50 km

slab contour (Gudmundsson and Sambridge, 1998). We let the dip vary from $8^o$ at the surface to $23^o$ at 50 km depth.

To model the coseismic slip distribution on the fault plane described above we used our coseismic offsets as data input for the Poly3Dinv code (Maerten et al., 2005). This approach is based on a solution of an angular three dimensional dislocation in a linear, homogeneous, and isotropic elastic half-space, and during the inversion the data misfit as well as model roughness are minimized. We applied negativity constraints for left-lateral and normal slip, and set the slip to zero at the down-dip fault boundary. Our preferred coseismic slip model is shown in Fig. 7.2.a. The vertical postseismic offsets (Fig. 7.2.b) indicate that the along-trench extent of afterslip is roughly similar to that indicated by the coseismic data: the northern extent separates LEWK (which goes up) from BSIM (which goes down), and the southern extent separates LHWA (which goes down) from PSMK (which goes up). We therefore model the postseismic slip distribution on the same model surface used for the coseismic rupture, except that we extend the fault plane to larger depths to accommodate the possibility of significant deep afterslip. The decay amplitudes control the pattern of afterslip distribution and as a function of time they control the absolute magnitude of the slip distribution. We model the afterslip distribution for 180 days of accumulated postseismic deformation (Fig. 7.2.b).

## 7.6 Discussion and Conclusions

The total moment from our coseismic model is $M_w = 8.37$ for a shear modulus (m) of 30 GPa. This corresponds to a moment that is three times smaller than the Harvard CMT estimate. A reconciliation of these values is possible when it is assumed that $\mu$ increases rapidly with depth (e.g., $\mu = 100$ GPa at 50 km), which is permissible (Bilek and Lay, 1999), and has also been argued for the 2004 Aceh-Andaman event (Kreemer et al., 2006). In addition, if the slip were modeled using a layered Earth instead of half-space model, more slip would be predicted at greater depths, which would increase the moment estimate as well.

We observe maximum coseismic slip of over 10m in two distinct regions: one near the epicenter and one near the northern extent of the rupture, abutting the southern extent of the 26 December 2004 rupture. These two maxima are located underneath stations BSIM and LHWA. The slip model is largely dominated by these two data points and so our slip model may be biased. However, our solution is similar to a recent seismic model (Walker et al., 2005) in which high slip is concentrated near the same locations as in our

model, adding some confidence to our result. We observe that the areas with highest slip also saw the highest aftershock activity. To test whether our chosen maximum depth of 50 km does not influence our model result, we also perform an inversion using the same fault plane as was used in the postseismic model, and the results confirm that slip below 45-50 km is negligible. The model results are however less robust as to whether and how much slip occurred near the ocean floor. We conclude that coseismic slip is constrained to the same depths that were earlier identified as being locked for the same subduction zone further to the south (Simoes et al., 2004).

We show that at least for over 6 months after the earthquake the postseismic times-series are very well fit by a logarithmic function. They are fit significantly worse if an exponential function is used, at least for the stations closest to the rupture. Although this statistical difference may be outweighed by our use of simple first-order representations of the various physical processes at play, we conclude that the postseismic deformation thus far has likely, but not necessarily exclusively, been dominated by afterslip. Future work will need to address the interplay of the various mechanisms (Montési, 2004; Pollitz et al., 1998), which will lead to more sophisticated models of the earthquake process. Nevertheless, our postseismic inversion results show some characteristic patterns. Afterslip of $> 1m$ is constrained to depths $<\sim 9km$, with an additional zone of large afterslip below the northern part of the coseismic rupture. The deep afterslip is largely controlled by BSIM. The shallow and deep regions have experienced little aftershock activity, emphasizing the aseismic nature of the afterslip process. The total slip after 180 days adds up to a seismic moment that is 50% of the main shock, equivalent to $M_w = 8.17$. The widespread afterslip at shallow depths is profound and either reflects creep on the actual shallow fault plane and/or relates to broad postseismic adjustment in the unconsolidated sediments. If the coseismic rupture did not reach the surface, then it is expected that stresses at shallower depths have changed in such a way that they could have driven the observed shallow postseismic deformation. If true, this scenario will contribute to understanding why the Nias earthquake did not produce a sizable tsunami.

## 7.7 Acknowledgments

We thank the International GPS Service and BAKOSURTANAL for making GPS data available. We particularly wish to thank the Tectonics Observatory at Caltech and the Indonesian Institute of Sciences for establishing, maintaining and operating the SuGAr array and, with SOPAC, for archiving the data and making them available. We also thank

D. Pollard for making the Poly3D programs available, and M. Chlieh and A. Meltzner for providing preprints.

# References


Bilek, S. L. and Lay, T. (1999). Rigidity variations with depth along interplate megathrust faults in subduction zones. *Nature*, 400:443–446.

Burgmann, R., Ayhan, M., Fielding, E., Wright, T., McClusky, S., Aktug, B., Demir, C., Lenk, O., and Turkezer, A. (2002). Deformation during the 12 november 1999 duzce, turkey, earthquake, from gps and insar data. *Bull. Seism. Soc. Am.*, 92:161–171.

Gudmundsson, O. and Sambridge, M. (1998). A regionalized upper mantle (rum) seismic model. *J. Geophys. Res.*, 103:7121–7136.

Kreemer, C., Blewitt, G., Hammond, W. C., and Plag, H.-P. (2006). Global deformation from the great 2004 sumatra-andaman earthquake observed by gps: Implications for rupture process and global reference frame. *Earth Planets Space*, 58:141–148.

Maerten, F., Resor, P. G., Pollard, D. D., and Maerten, L. (2005). Inverting for slip on three-dimensional fault surfaces using angular dislocations. *Bulletin of the Seismological Society of America*, 95:1654–1665.

Marone, C. J., Scholz, C. H., and Bilham, R. (1991). On the mechanics of earthquake afterslip. *J. Geophys. Res.*, 96:8441–8452.

Melbourne, T. I., Webb, F. H., Stock, J. M., and Reigber, C. (2002). Rapid postseismic transients in subduction zones from continuous gps. *J. Geophys. Res.*, 107(B10), 2241.

Meltzner, A. J., Sieh, K., Abrams, M., Agnew, D. C., Hudnut, K. W., Avouac, J., and Natawidjaja, D. H. (2006). Uplift and subsidence associated with the great aceh-andaman earthquake of 2004. *J. Geophys. Res.*, 111(B02407).

Montési, L. G. J. (2004). Controls of shear zone rheology and tectonic loading on post-seismic creep. *J. Geophys. Res.*, 109(B10404).

Natawidjaja, D. H., Sieh, K., Ward, S. N., Cheng, H., Edwards, R. L., Galetzka, J., and Suwargadi, B. (2004). Paleogeodetic records of seismic and aseismic subduction from central sumatran microatolls, indonesia. *J. Geophys. Res.*, 109(B04306).

Pollitz, F. F., Bürgmann, R., and Segall, P. (1998). Joint estimation of afterslip rate and postseismic relaxation following the 1989 loma prieta earthquake. *J. Geophys. Res.*, 103:26975–26992.

Pollitz, F. F., Peltzer, G., and Bürgmann, R. (2000). Mobility of continental mantle: Evidence from postseismic geodetic observations following the 1992 landers earthquake. *J. Geophys. Res.*, 105:8035–8054.

Press, C. U., editor (1992). *Numerical Recipes in FORTRAN 77: The Art of Scientific Computing, 2nd ed.* Press, W. H. and Teukolsky, S. A. and Vetterling, W. T. and Flannery, B. P., New York.

Savage, J. C. and Prescott, W. H. (1978). Asthenosphere readjustment and the earthquake cycle. *J. Geophys. Res.*, 83:3369–3376.

Simoes, M., Avouac, J.-P.and Cattin, R., and Henry, P. (2004). The sumatra subduction zone: A case for a locked fault zone. *J. Geophys. Res.*, 109(B10402).

Subarya, C., Chlieh, M., Prawirodirdjo, L., Avouac, J. P., Bock, Y., Sieh, K., Meltzner, A. J., Natawidjaja, D. H., and McCaffrey, R. (2006). Plate-boundary deformation of the great aceh-andaman earthquake. *Nature*, 440:46–51.

Walker, K. T., Ishii, M., and Shearer, P. M. (2005). Rupture details of the 28 march 2005 sumatra mw 8.6 earthquake imaged with teleseismic p waves. *Geophys. Res. Lett.*, 32(L24303).

# CHAPTER 8

# Mechanical analysis of fault slip data

J. O. Kaven[(1)], F. Maerten[(2,3)], D. D. Pollard[(1)]

(1) Department of Geological and Environmental Sciences, Stanford University, Stanford, CA 94305 USA
(2) Igeoss, Montpellier, FRANCE
(3) University of Montpellier II, Geosciences, FRANCE

In preparation for Journal of Structural Geology.

**Preamble**

Having an idea of the fault geometry as well as the boundary conditions attached to them, the choice of the far field stress or strain to apply to the model is still an unknown that the user has to estimate using his intuition, existing tools, or by trial and error. In this chapter, we show that using special iteratively coupled systems, it is possible to have an estimate of the paleostress given some measures of the displacement discontinuity on the faults (e.g. throw or dip-slip measurements from seismic interpretation) using mechanical interactions. While inverting for the paleostress, we recover simultaneously the unknown displacement discontinuities on the faults. Therefore, this technique allows one to extend the fault geometry if necessary and to compute the unknown dip- and strike-slip.

# About...

My contribution was to find the idea of doing paleostress using geomechanics, to define the formulation using the iBem3D kernel functions and to do the implementation in C++. Later one, Dave Pollard told me that Ole Kaven, one of his PhD student, was working on a paleostress manuscript, mainly for doing sensitivity ananalysis and to have a nice historical background. Combining this new approach for doing paleostress inversion and what Ole already has written, was an obvious consequence.

**Note** that, in this paper in preparation, the ChiChi model will be reformulated using a more correct fault geometry. Also, as seen in Fig. 8.10 and 8.11, the model was not set correctly in half-space.

# Article Outline

## 8.1 Résumé

L'inversion de contraintes est un outil utile et populaire pour les géologues structuralistes et sismologues. Ces méthodes ont d'abord été introduites par Wallace [98] et développées par Bott [15] et des études ultérieures continuent d'être fondées sur leur première série d'hypothèses. Ces hypothèses fondamentales sont: (1) le tenseur des contraintes à l'infini est spatialement uniforme dans la roche contenant des failles et constant dans le temps au cours de l'histoire de l'évolution des failles, et (2) le glissement sur chaque surface de faille a le même sens et la même direction que la contrainte cisaillante maximum du tenseur des contraintes à l'infini résolue sur ces plans de faille. En outre, une implémentation correcte nécessite que le glissement s'accumule sur des failles d'orientations diverses. Beaucoup d'études utilisent ces méthodes pour des défauts isolés ou sur des systèmes de failles à orientations limitées, ce qui peut conduire à des résultats erronés. Nous proposons une nouvelle méthode qui intègre les effets de l'interaction mécanique de toutes les failles ou systèmes de failles, et qui résout complètement le problème mécanique plutôt que d'employer des relations empiriques entre glissement et contrainte ou déformation (ou vitesse de déformation). Nous testons la méthode sur des modèles de failles synthètiques à orientations différentes pour évaluer les effets de la non-planarité et trouvons que cette non-planarité peut introduire des erreurs importantes, même dans des cas simples idéalisés. Nous avons en outre testé l'effet de l'inversion en utilisant un jeu de failles synthétiques comportant une diversité d'orientations et trouvé que le type d'inversion de Wallace-Bott ne fonctionnait pas correctement pour ces types de modèles. Enfin, nous utilisons des données publiées sur le tremblement de terre de Chi-Chi (1999, Taiwan), et trouvons qu'en utilisant les données de surface seulement, puis les données de surface et des mécanismes au foyer, ces deux modèles donnent des résultats similaires. Les orientations de contraintes qui en résultent sont en accord avec les résultats d'inversion de Wallace-Bott. En outre, la distribution des déplacements sur la surface de faille est en accord avec les inversions cinématiques utilisant la déformation de glissements de surface co-sismiques. La méthode d'inversion de contraintes en utilisant des données de glissements de failles peut donc être améliorée de façon significative dans de nombreux cas, en utilisant une méthode de résolution mécanique qui tienne compte de la géométrie des failles ou systèmes de failles.

## 8.2 Abstract

Stress inversions are a useful and popular tool for structural geologist and seismologist alike. These methods were first introduced by Wallace (Wallace, 1951) and expanded by Bott (Bott, 1959) and subsequent studies continue to be based on their initial set of assumptions. The fundamental assumptions are: the remote stress tensor is spatially uniform for the rock mass containing the faults and temporally constant over the history of faulting in that region, and the slip on each fault surface has the same direction and sense as the maximum shear stress resolved on each surface from the remote stress tensor. Furthermore, successful implementation requires that slip accumulates on faults of diverse orientation. Many studies employ these methods on isolated faults or on fault system with limited ranges of orientations, which can lead to erroneous results. We propose a new method that incorporates the effects of mechanical interaction of the entire fault or fault system, solves the complete mechanical problem rather than employing empirical relationships between slip and stress or strain (or strain rate). We test the method on synthetic faults with various orientations to evaluate the effects of non-planarity and find that the non-planarity can introduce significant errors even for simple idealized cases. We further test the effect of diversity of fault orientations and find that Wallace-Bott type inversions do not perform as well for limited ranges of orientations when compared to the proposed method. Finally we use published data from the 1999 Chi-Chi, Taiwan, earthquake, and find that the method using surface data only and surface data and subsurface focal mechanisms produce similar results. The resulting stress orientations are in good agreement with results from Wallace-Bott inversions. Furthermore, slip distribution results are in general agreement with kinematic slip inversions using coseismic surface deformation. Stress inversion methods using fault slip data can thus be improved upon, significantly in many cases, by solving a mechanical boundary value problem that takes into account the geometry of faults or fault systems.

## 8.3 Introduction

Over the course of the 20th Century geologists sought to understand the origin and evolution of faults, and the tectonic history of faulted regions, by relating fault orientation and slip direction to the state of stress in Earths crust (e.g. (Anderson, 1942; Price, 1966; Voight, 1966; Mandl, 1988)). This relationship may be elucidated through both forward and inverse problem solving. In typical forward problems the equations of motion are solved with a prescribed remote stress state as boundary conditions, yielding the local

stress, strain, and displacement fields, and the slip distributions over the model faults (e.g. (Hafner, 1951; Sanford, 1959; Couples, 1977; Burgmann and Pollard, 1994; Willemse et al., 1996; Maerten et al., 1999)). Assumptions about the constitutive behavior, the magnitudes of the strains, and the relative magnitudes of dynamic and static forces ((Malvern, 1969), Chs. 6, 4, and 8, respectively) enable one to reduce the underlying conservation laws to the relevant equations of motion ((Pollard and Fletcher, 2005), Ch. 7). While the correspondence of such models to faulting in Earths crust depends upon the accuracy of the assumptions, each of which requires careful assessment, the efficacy of the methodology rests securely on the foundation of a complete mechanics (Fletcher and Pollard, 1990).

In typical inverse problems the directions of the remote principal stresses and a ratio of their magnitudes are constrained by analyzing field data on fault orientations and slip directions as inferred from striations such as slickenlines on exposed fault surfaces (e.g. (Carey and B., 1974; Etchecopar et al., 1981; Angelier et al., 1982; Gephart and Forsyth, 1990; Angelier, 1984; Michael, 1987; Reches, 1987; Fry, 1999; Shan et al., 2004)). The adoption of this methodology is facilitated by an instructive exposition and computer codes in the textbook by Ramsay and Lisle (Ramsay and Lisle, 2000) and by the availability of other computer codes (e.g. (Huang, 1988; Hardcastle and Hills, 1991; Orife et al., 2002)). The enthusiastic implementation of the methodology by the structural geology community is witnessed by global compilations of paleostress results from 250 sites for the World Stress Map Project (Reinecker et al., 2004) and from 2,791 independently chosen sites (Lisle et al., 2006) for a Special Issue of the Journal of Structural Geology on "New Dynamics in Palaeostress Analysis" (Blenkinsop, 2006). The equations of motion are not invoked for this inverse problem, and perturbations of the local stress field by fault slip are ignored. In other words, the mechanical role played by the faults in the tectonic deformation is not included explicitly in the analysis. Instead, two basic assumptions are made: (1) the stress field is spatially homogeneous and temporally constant; and (2) the direction of slip and the direction of the maximum shear stress resolved on each would-be fault plane are coincident. These assumptions enable the inversion, which uses Cauchys Formula ((Fung, 1977), p. 62) to relate the tangential tractions (maximum shear stresses) on planes with the measured fault orientations to the principal stresses in the corresponding homogeneous stress field.

In a remarkably prescient paper, which to our knowledge is the earliest example of paleostress inversion, Anderson (Anderson, 1905) began, without comment or justification, by simply taking one principal stress direction as vertical at any point. This assumption was addressed explicitly 37 years later by Anderson ((Anderson, 1942), p. 12 and Ch.

VII). In his 1905 paper Anderson suggested that planes carrying the maximum tangential stress "will have much to do with determining the directions of faults in the rock". He understood that there are two orientations of such planes at any point; that these planes intersect in the direction of the intermediate principal stress (Q); and that they make equal angles of 45° to the greatest principal compressive stress (P). He extended these relationships for stress at a point to rock volumes encompassing faults and conceived two conjugate sets of would-be faults corresponding to a single state of homogeneous stress. In calculating the resolved tangential stress on the conjugate planes Anderson used a variant of the Cauchy Tetrahedron ((Malvern, 1969), p. 73) with one face corresponding to a would-be fault and made an interesting analogy: "This prism we suppose to exist in the rock, somewhat as the statue exists beforehand in the block of marble..." Apparently Anderson understood that slip on an actual fault would perturb the stress away from its assumed homogeneous state. We appeal to his analogy of the would-be statue residing in the block of marble and refer to the entire class of inverse problems based on a homogeneous stress state as faultless paleostress analysis.

The next stage in the development of faultless paleostress analysis was introduced in the middle of the last century when Wallace (Wallace, 1951) analyzed the maximum shear stress (tangential traction) on planes of arbitrary orientation for a homogenous stress state using Cauchys Formula (e.g. (Jaeger et al., 2007), p. 31). He illustrated the magnitude and orientation of this shear stress on stereonets and Mohr diagrams. Appealing to laboratory results and Mohrs theory ((Nádai, 1931), p. 61), Wallace proposed that "faults will tend to concentrate at orientations tangent to a cone, with apex angle less than 90° (45° radius), which has the axis of greatest compressive stress as its axis..." and that "Orientation of net slip on faults can be correlated almost directly with orientation of maximum shearing stress...". In summary, he suggested that "If a complete picture of fault-plane orientations and net-slip orientations on several faults is available, it should be possible to determine with some degree of certainty the orientation and nature of the stress system producing the faults."

Taking a somewhat different approach conceptually, Bott (Bott, 1959) contemplates the likely presence of strength inhomogeneity in the form of older faults, joints, and cleavage. Apparently supposing that whatever perturbation in the stress field due to the formation of these structures had relaxed, he suggested "These planes would remain unnoticed until the shearing stress within them should exceed the strength...". Furthermore, Bott suggested "...fracture would occur within the preferred plane in which the strength was first exceeded, and the direction of the initial slip would be defined by the direction of the greatest shearing stress within the plane". Bott then preceded, as did Wallace (Wallace,

1951) to employ Cauchys Formula (e.g. (Jaeger et al., 2007), p. 31) to derive the equation relating the shear traction, $\tau$, to the principal stress magnitudes ($\sigma_1 \geq \sigma_2 \geq \sigma_3$):

$$\begin{aligned} \tau^2 &= \sigma_1^2 n_1^2 + \sigma_2^2 n_2^2 \sigma_3^2 n_3^2 - \left(\sigma_1^2 n_1^2 + \sigma_2^2 n_2^2 \sigma_3^2 n_3^2\right)^2 \\ & \quad (\sigma_1 - \sigma_2)^2 n_1^2 n_2^2 + (\sigma_2 - \sigma_3)^2 n_2^2 n_3^2 + (\sigma_3 - \sigma_1)^2 n_3^2 n_1^2 \end{aligned} \tag{8.1}$$

Here the principal stress directions are coincident with the coordinate axes and $(n_1, n_2, n_3)$ are the components of the unit normal to the plane bearing the shear traction. Bott concludes that oblique slip faults may occur in any orientation for a given orientation of the principal stress axes if planes of suitable weakness lie in that orientation. In some of the modern literature cited below the coincidence of the tangential traction (direction of maximum resolved shear stress) and the slip direction is referred to as the Wallace-Bott hypothesis.

A considerable effort has been made to distinguish and separate field measurements of slip directions attributable to stress states that vary in space or time, so-called heterogeneous data sets (e.g. (Armijo et al., 1982; Angelier, 1984; Huang, 1988; Hardcastle and Hills, 1991; Nemcok and Lisle, 1995; Yamaji, 2000; Shan et al., 2003; Liesa and Lisle, 2004; Shan and Fry, 2005)). At the same time methods have been devised for error estimation of the paleostress inversion (e.g. (Angelier, 1984; Choi, 1996; Orife and Lisle, 2003; Shan et al., 2006; Sato and Yamaji, 2006)), for example by comparing the misfit between the maximum shear stress directions (presumed slip directions) resolved from the preferred stress state and the measured slip directions on the respective faults. These are valuable procedures for the analysis, but they remain rooted in the two basic assumptions and therefore, while testing self-consistency and goodness of fit, they do not provide independent tests of the methodology. Shan et al. (Shan et al., 2006) have pointed out several reasons that the basic assumptions would be violated, leading "to dispersion in the parameter space of measured fault/slip data, or even possibly the presence of superficially heterogeneous fault/slip data. For the latter, we have meaningless data groups and false estimated stresses through conventional inversion methods. This is indeed the Achilles heel of stress inversion."

Two related topics must be acknowledged, because they have developed in parallel with, and sometimes intertwined with geological paleostress analysis. Seismological data are used to identify the quadrants that contain the so-called P and T axes for a given earthquake focal mechanism (e.g. (McKenzie, 1969; Whitcomb et al., 1974; Aki and Richards, 2002)). Because the fault plane generally is not available to the seismologist, they face the additional ambiguity of two orthogonal would-be fault orientations that stem from the

representation of seismic sources as double-couple force systems (Lay and Wallace, 1995; Vasseur et al., 1983; Michael, 1987; Gephart, 1990). Some researchers associate P and T with the axes of greatest shortening and greatest extension, that is principal strains or strain rates (Marrett and Allmendinger, 1990; Twiss et al., 1993; Twiss and Unruh, 1998), while others associate P and T with the axes of greatest and least compression, that is principal stresses (Angelier and Mechler, 1977; Gephart and Forsyth, 1990; Julien and Cornet, 1987; Jones, 1988; Michael, 1987; Ramsay and Lisle, 2000) for the fault in question. Whether the interpretation leads to principal strains, strain rates, or stresses, the reduction of what must be a heterogeneous field of these quantities around an active fault to a homogeneous representation (Brune, 1968; Kostrov, 1968; Molnar, 1983; Jackson and McKenzie, 1988) draws into question the first basic assumption stated above. We do not concern ourselves further with the seismological investigation of P and T, except in so far as the evaluation of this assumption might reflect upon it.

The second related topic is the interpretation of fault data by geologists in a kinematic context. That is, the orientations of faults and the slip directions inferred from striations upon them are associated with the directions of a homogeneous field of principal strains or strain rates and a ratio of their magnitudes (Reches, 1978, 1987; Aydin and Reches, 1982; Gauthier and Angelier, 1985; Wojtal, 1989; Twiss et al., 1991; Twiss and Unruh, 1998). Cladouhos and Allmendinger (Cladouhos and Allmendinger, 1993) refer to the strain due to a population of faults within a region as the fault strain and investigate this homogeneous quantity for cases where the infinitesimal strain approximation used by those mentioned above is inappropriate (see also (Gapais et al., 2000)). Again, we do not concern ourselves further with the kinematic interpretation of fault slip inversions, except in so far as the evaluation of the homogeneous assumption might reflect upon it. Because the models we employ use an isotropic and linear elastic constitutive law, the principal stress and strain directions at any point are identical and the respective components are proportional. The method of inversion proposed here, whether for remote principal stresses or strains, applies the principles of continuum mechanics to a medium with explicit surfaces of discontinuity in the displacement field, which are the model faults.

In an extensive review of fault slip inversion methodology Twiss and Unruh (Twiss and Unruh, 1998) evaluate the relative merits of stress and kinematic interpretations, emphasizing that the kinematic quantity of interest should be the rate of deformation rather than the strain or strain rate, and adding an additional unknown, the relative vorticity, to the inversion problem in order to account for local block rotations (Twiss et al., 1991). They distinguish the local scale of a single fault or earthquake rupture from the larger global scale and assert: "From a global volume we need a sufficiently large set of fault slip

data in order to find an inverse solution for the homogeneous principal deformation rates or the homogeneous principal stresses". As part of our evaluation of the second basic assumption we identify conditions under which such a global volume exists, and within which fault slip is dependent upon both the global state of stress and the mechanical interaction of the model faults. For the isotropic elastic solutions we employ, the relative vorticity is identically zero.

One purpose of this paper is to provide new evaluations of the basic assumptions of paleostress analysis. These assumptions have received some attention as the inversion method was put into practice (Carey-Gailhardis and Mercier, 1987; Dupin et al., 1993; Pollard et al., 1993; Orife and Lisle, 2003). In some studies independent data sets from seismology (earthquake focal mechanisms) or geodesy (displacements from GPS surveys) have been compared to fault slip directions (Roberts and Ganas, 2000; Kao and Angelier, 2001; Blenkinsop, 2006). A direct evaluation of the assumptions would require an independent measure of the tangential traction vector (maximum shear stress) acting on a fault surface during slip, so the direction of this vector could be compared to the slip direction. A direct evaluation also would require in-situ stress measurements at some distance from the active faults to establish the homogeneity of the remote stress field (e.g. (Zoback et al., 1987; Zoback, 1992)). Although technology exists today to infer the stress state from such measurements in active tectonic regions (Amadei and Stephansson, 1997), they are not possible for ancient faults. Instead, we evaluate the assumptions using a methodology similar to that employed in forward modeling that invokes the equations of motion and explicitly includes the faults and their associated fields of stress and deformation (Pollard et al., 1993; Maerten, 2000; Maerten et al., 2005). A second purpose of this paper is to draw attention to a new form of paleostress inversion using a complete mechanics and to encourage its use. The computer code used here is available from IGEOSS (http://www.igeoss.com/igeoss/) at a nominal cost for non-commercial research.

## 8.4 Accounting for a Complete Mechanics

The displacement discontinuity resulting from remotely applied stresses and tractions acting on fracture surfaces are governed by principles of continuum mechanics, dominantly those of linearly elastic theory that were first introduced by Inglis (Inglis, 1913), and Griffith (Griffith, 1921, 1925), and later developed by Irwin (Irwin, 1957) and Williams (Williams, 1987) and many others becoming a mature discipline (Lawn and Wilshaw, 1993; Anderson, 1995) by the end of the 20th century. The concepts of fracture mechanics have been used to explain a variety of rock fracture phenomena including aspects of faulting (see

numerous examples in Atkinson (Atkinson, 1987). From these we understand that slip on a particular segment of a fault is determined not only by the remote stress or strain tensor, but also includes the effects of material properties of the surroundings (Lamé constants), and the fault surfaces (friction) or fault zone (strength), the orientation and geometry of the fault tipline and surfaces, and the effects of all other proximal segments of the fault or fault system. Both analytical (e.g. (Rudnicki, 1980; Rice, 1980; Pollard and Segall, 1987; Burgmann and Pollard, 1994; Martel and Shacat, 2006)) and numerical (e.g. (Segall and Pollard, 1980; Willemse, 1997; Maerten et al., 2005)) models have helped to elucidate these relationships. The problem at hand (multiple three-dimensional faults that interact mechanically with one another) requires the elastic boundary value problem to be solved numerically.

Boundary element methods (Crouch and Starfield, 1983), such as the displacement discontinuity method employed in the numerical code Poly3D (Thomas, 1993; Maerten et al., 2005) permit one to solve the elastic problem as a system of algebraic equations that relate the tractions on a triangular element of the fault surface to the displacement discontinuity on that element and all other elements that make up the fault or faults (Fig. 8.1).

The system of linear equations has the following general form:

$$\begin{aligned} \tau_s^e &= \sum_{f=1}^{N} A_{ss}^{ef} D_s^f + \sum_{f=1}^{N} A_{sd}^{ef} D_d^f + \sum_{f=1}^{N} A_{sn}^{ef} D_n^f \\ \tau_d^e &= \sum_{f=1}^{N} A_{ds}^{ef} D_s^f + \sum_{f=1}^{N} A_{dd}^{ef} D_d^f + \sum_{f=1}^{N} A_{dn}^{ef} D_n^f \\ \tau_n^e &= \sum_{f=1}^{N} A_{ns}^{ef} D_s^f + \sum_{f=1}^{N} A_{nd}^{ef} D_d^f + \sum_{f=1}^{N} A_{nn}^{ef} D_n^f \end{aligned} \tag{8.2}$$

where $e, f = 1, ..., N$ and $N$ is the number of fault elements, $\tau_n$, $\tau_s$, $\tau_d$ are the normal, strike-parallel and dip-parallel traction components at the element center, respectively, and $D_n$, $D_s$, and $D_d$ are the uniform normal, strike-parallel and dip-parallel displacement discontinuity components between the two surface of the element (Fig. 8.1). The influence coefficient matrices $A_{kl}$ $(k, l = n, d, s)$ relating the corresponding displacement discontinuity to the tractions follow from the analytical solution for the angular dislocation (Yoffe, 1960) in the half-space (Comninou and Dundurs, 1975) as extended to the polygonal surface of unknown displacement discontinuities by Jeyakumaran et al. (Jeyakumaran et al., 1992). The element local quantities are expressed in terms of the local coordinate axes (Fig. 8.1) and require transformations into the global coordinate axes system, which can be done in the computation of the influence coefficients directly. In general, the problem at hand may be one with mixed boundary conditions (e.g. normal displacement discontinuity components and both strike- and dip-parallel tractions), so equation (8.2) requires restructuring to properly constrain the solution. In the remainder of this paper, $A_{ef}$ denotes the traction influence matrix at a field element $e$ due to a source element $f$ with

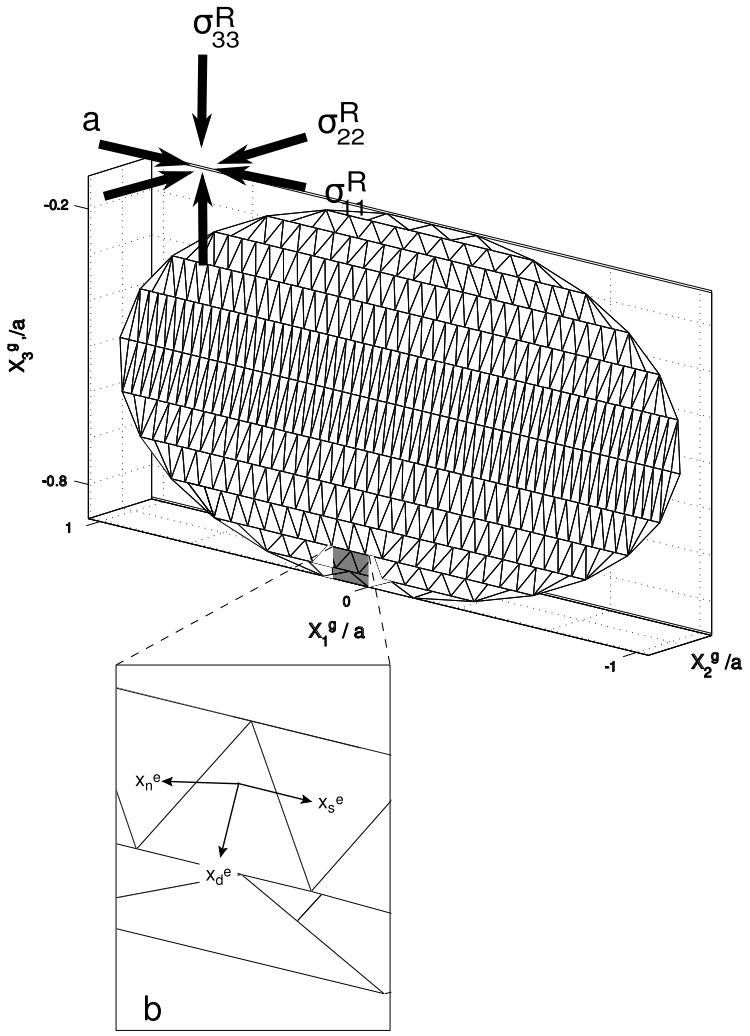


FIGURE 8.1: Displacement discontinuity discretization, global (a) and local (b) reference systems and orientations of remote stresses.

slip vector $D_f$. It is implied that these quantities account for all three vector components at a particular element.

The unknown displacement discontinuity vector at element $e$ can be computed with an iterative scheme using a block Gauss-Seidel like definition (Maerten et al., 2009):

$$\tau_e = -A_{ee} D_e - \sum_{f \neq e} A_{ef} D_f \tag{8.3}$$

which gives:

$$D_e = A_{ee}^{-1} \left\{ \tau_e^0 + \sum_{f \neq e} A_{ef} D_f \right\} \tag{8.4}$$

In general, it is assumed that some components of displacement discontinuity $D_e$ for element $e$ are unknown. In paleostress analyses, $D_e$ is known at outcrops but nowhere else along the fault. The matrix $A_{ee}^{-1}$ relates the known traction of element $e$ to the relative

displacement. $\tau_e^0$ represents the initial boundary value for an element $e$, and is determined from the resolved far field stress $\sigma^R$ onto this element in the local coordinate system using Cauchy's formula with appropriate rotation:

$$\tau_e = \omega_e \sigma^R n_e \tag{8.5}$$

where $n_e$ is the element normal unit vector. The rotation matrix $\omega_e$ relates the remote stresses to the element local along-strike, along-dip, and normal traction components and is comprised of direction cosines.

Confining pressures in the crust suppress opening of faults, so we enforce the condition that the normal relative displacement is zero. This condition is known to be violated near steps and bends in faults and near terminations of faults that are accompanied by splay cracks (Mutlu and Pollard, 2008). Using the Andersonian stress state, that is a traction-free surface and negligible topography, the vertical stress, $\sigma_{33}^R$, is a principal stress (implying $\sigma_{13}^R = 0 = \sigma_{23}^R$), so:

$$\sigma^R = \begin{bmatrix} \sigma_{11}^R & \sigma_{12}^R & 0 \\ \sigma_{21}^R & \sigma_{22}^R & 0 \\ 0 & 0 & \sigma_{33}^R \end{bmatrix} \tag{8.6}$$

By orienting the global coordinate axes so the third normal stress component is vertical we can modify the definition of the normal far field stress so the diagonal components of this tensor also depend on the magnitude of the vertical stress. Furthermore, since the addition of an isotopic stress does not change the resolved tractions on faults, (8.6) can be simplified to:

$$\sigma^R = \begin{bmatrix} \sigma_{11}^R - \sigma_{33}^R & \sigma_{12}^R & 0 \\ \sigma_{12}^R & \sigma_{22}^R - \sigma_{33}^R & 0 \\ 0 & 0 & 0 \end{bmatrix} \tag{8.7}$$

which then permits one to rewrite the sought after stress tensor components as:

$$\tilde{\sigma}^R = \begin{bmatrix} \tilde{\sigma}_{11}^R & \sigma_{12}^R \\ \sigma_{12}^R & \tilde{\sigma}_{22}^R \end{bmatrix} \tag{8.8}$$

where the tilde signifies the difference between horizontal normal stress components and the vertical normal stress. Anderson's standard state of stress thus provides the basis for the above assumptions, i.e. the horizontal perturbations to lithostatic stress with one principal stress vertical.

Now, consider a model comprised of $n$ triangular elements (Fig. 8.1) with traction boundary conditions for the strike and dip components and a displacement discontinuity condition for the normal component with magnitude zero. For a given element $e$, two equations need to be solved:

$$\begin{cases} -\tau^0_{e,1} = \left(\sum_f A_{ef} D_f\right)_1 \\ -\tau^0_{e,2} = \left(\sum_f A_{ef} D_f\right)_2 \end{cases} \tag{8.9}$$

where $\tau^0_{e,s}$, $\tau^0_{e,d}$ and some of the displacement discontinuity vectors $D$ are unknown.

Combining equations 8.5 and 8.6, and recognizing that the remote stress tensor consists of four independent components, we get:

$$-\widehat{\omega}_e \begin{Bmatrix} \sigma^R_{11} \\ \sigma^R_{12} \\ \sigma^R_{22} \\ \sigma^R_{33} \end{Bmatrix} = \begin{Bmatrix} \left(\sum_f A_{ef} D_f\right)_s \\ \left(\sum_f A_{ef} D_f\right)_d \end{Bmatrix}. \tag{8.10}$$

$$-\tilde{\omega}_e \begin{Bmatrix} \tilde{\sigma}_{11} \\ \sigma_{12} \\ \tilde{\sigma}_{22} \end{Bmatrix} = \begin{Bmatrix} \left(\sum_f A_{ef} D_f\right)_s - \omega_{e,13}\sigma_{33} \\ \left(\sum_f A_{ef} D_f\right)_d - \omega_{e,23}\sigma_{33} \end{Bmatrix} \tag{8.11}$$

where $\omega_{e,ij}$ are the direction cosines relating the element local traction components to the remote stresses. For a given known or estimated value of $\sigma^R_{33}$, in simplified form (using equation 8.9) becomes:

$$-\tilde{\omega}_e \begin{Bmatrix} \tilde{\sigma}_{11} \\ \sigma_{12} \\ \tilde{\sigma}_{22} \end{Bmatrix} = \begin{Bmatrix} \tau^o_{e,s} \\ \tau^o_{e,d} \end{Bmatrix} \tag{8.12}$$

Using a Least Squares formulation ((Aster et al., 2005), p. 16) for all elements, we find:

$$\begin{Bmatrix} \tilde{\sigma}^R_{11} \\ \sigma^R_{12} \\ \tilde{\sigma}^R_{22} \end{Bmatrix} = \left(\tilde{\omega}^\tau \tilde{\omega}\right)^{-1} \tilde{\omega}^t \begin{Bmatrix} \tau^0_{e,s} \\ \tau^o_{e,d} \end{Bmatrix} \tag{8.13}$$

We solve for the best-fitting unknown remote stress and resultant slip distribution on portions of the fault or fault system where no slip data are available.

Note that equation (8.13) solves for the unknown $\tilde{\sigma}^R$ using the computed traction vector, while equation (8.4) solves for the unknown slip vectors using the resolved traction vector $\tau^0_e$. Therefore, the solution algorithm has two steps: 1) use the initial remote stress tensor $\tilde{\sigma}^R$, resolve it onto the fault elements that have no relative displacement data, and

solve for the unknown relative displacements; 2) use the computed and known relative displacements to solve for $\tilde{\sigma}^R$. We choose an iterative solver that cycles between steps 1) and 2) until convergence. The determination of the relative displacement vectors for the elements are constrained by the resolved far field stress, which makes this method different from a linear slip inversion (Maerten et al., 2005). This process is outlined in algorithm 8.

**Data** : Known slip vectors: $D_k$
**Model**: Unknown slip vector, $D_u$, and remote stress, $\tilde{\sigma}^R$
initialization: Set starting guess for $D_u$ and $\tilde{\sigma}^R$
**while** *not converged* **do**
  → $\mathbf{S_1}$: Solve for the $D_u$ for each element $e$ using the resolved $\tilde{\sigma}^R$ and $D_k$
  → $\mathbf{S_2}$: Solve the unknown $\tilde{\sigma}^R$ using $D_u$ and $D_k$
  → **Post processing**: Resolve $\tilde{\sigma}^R$ onto each element $e$ and set as initial boundary conditions
**end**

**Algorithm 8.1**: Paleostress iterative solver

Once the algorithm has converged, the full stress tensor can be obtained by adding the isotropic normal stress to the diagonal. Then the Cartesian stress components $\sigma^R_{11}$, $\sigma^R_{12}$, $\sigma^R_{22}$ are used to retrieve the orientation of the horizontal principal axes of the stress tensor and their magnitudes.

## 8.5 Test Results for Stress Inversion

We test the proposed algorithm (Alg. 8) by comparing results of the inversion to those from a typical faultless stress inversion. We use single faults with non-planar surfaces, solve the forward problem to determine the slip on every element, randomly select varying fractions of the elements for inversion, and evaluate the errors and variances of the results. Then we use the same randomly selected slip data in a faultless inversion, and compare the results. We employ the same strategy to test a multi-fault systems with varying orientations of the individual faults. Finally, we use field data from the 1999 Chi-Chi earthquake along the Chelungpu fault in Taiwan and contrast the results from these methods.

### 8.5.1 Heuristic Example: Single Fault Inversions

To establish the validity of the results of the proposed inversion technique, we test synthetic models of isolated faults with elliptical fault tiplines, but non-planar fault surface

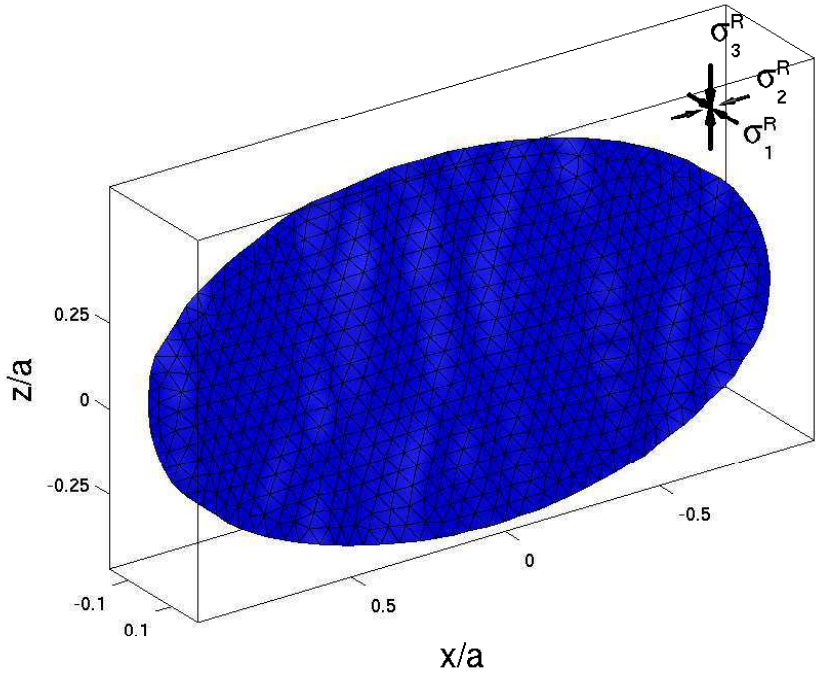


FIGURE 8.2: Anisotropically rough synthetic fault surface used in forward models to generate slip given the applied remote stresses (arrows). Lighting used to accentuate fault roughness.

topography. We evaluate the error in our inversion technique using the magnitudes and orientations of the remote stresses applied in the forward models. The fault surfaces have anisotropic, approximately fractal roughness with the slip-parallel direction being smoother than the slip-perpendicular direction (Fig. 8.2), and the roughnesses correspond to values from the faults measured by Sagy et al. (Sagy et al., 2007), which are normal faults of the Klamath Graben system with ≈100m offset. We choose a non-planar fault geometry because the available data (e.g. (Power et al., 1987; Sagy et al., 2007)) indicate faults have significant non-planarity or roughness.

We estimate error and variance bounds for the mechanics-based method for the idealized fault (Fig. 8.3) by varying the percentages of elements used. For each percentage of elements tested we first choose fractal, anisotropically rough faults and solve the problem in a forward sense for the slip magnitudes and directions on every element given a remote stress that acts to induce dip-slip on a fault. The horizontal remote stresses are $\tilde{\sigma}_1^R = \tilde{\sigma}_{11}^R = 5$MPa (recall $\tilde{\sigma}_{11}^R = \sigma_{11}^R - \sigma_{33}^R$), normal to fault strike, $\tilde{\sigma}_2^R = \tilde{\sigma}_{22}^R = 1$MPa parallel to fault strike. The elastic properties of the isotropic and homogeneous medium are Young's modulus $E = 5$GPa and Poisson's ratio $\nu = 0.25$. The boundary conditions on the fault prohibit opening or closing and result in a complete shear stress drop on all elements (1349 elements). From the resultant slip distribution we randomly select 20 constellations

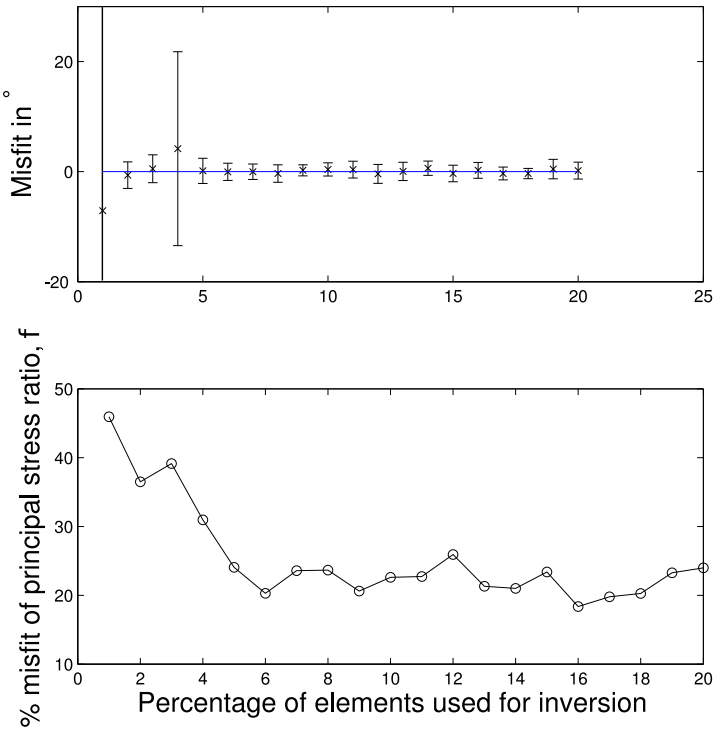


FIGURE 8.3: Validation of results for varied percentage of elements used on a rough fault. a) Misfit in degrees of orientation of horizontal principal stress from inversion. b) % error in principal stress ratio, $\phi$, from inversion results.

of elements and invert for the remote stress state using each. The we evaluate the mean stress orientation and the standard deviation.

The prescribed principal horizontal stress orientations are approximated by the proposed inversion method (Fig. 8.3a) with the greatest mean angular misfit of 7° for 1% (14) elements used and 0.5° for 20% (270) elements used. Variances (standard deviations) in the inversion results are large ($> 40°$) for few elements but steadily decrease as more elements are used to 1.5° for 20% with the exception of the 4% of elements. Here the variance is 19° due to switching of the horizontal principal stress orientations. Misfits of principal stress ratios decrease but remain greater than 20% for percentages up to 20 elements used (Fig. 8.3b). This is attributed to the modest range of orientations (spherical variance, $S_s^2 \geq 0.99$).

The mechanics-based methods permits one to solve for the slip distribution at every element on the fault (Fig. 8.4). The general distribution of the slip is elliptical as expected for an isolated planar fault with elliptical tipline (Willemse et al., 1996; Willemse, 1997).

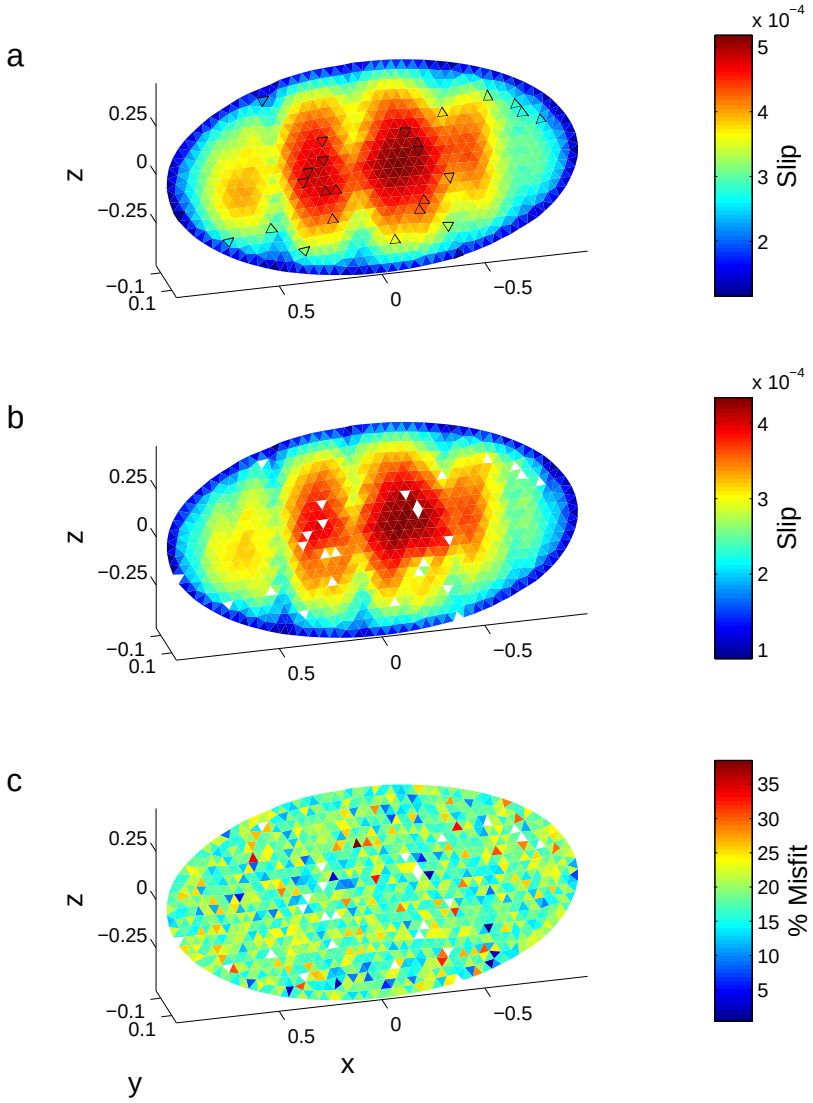


FIGURE 8.4: a) Slip magnitude on heuristic fault model from the forward model. The approximately self-affine surface roughness is larger in the direction parallel to strike. Random triangles used in inversions or outlined in black. b) Inverted slip distribution using the select elements. c) % Misfit of slip distribution between the forward model and the inversion result.

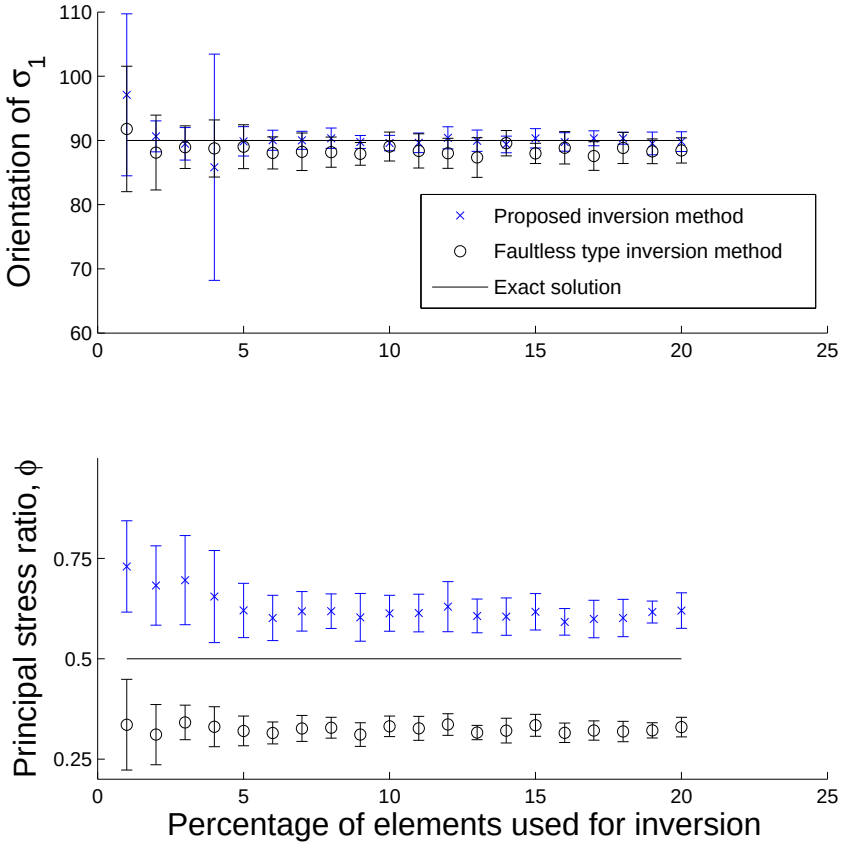


FIGURE 8.5: a) Orientation of horizontal principal stress for varied percentage of elements used in mechanics based stress inversion and faultless inversions. Error bars indicate variance within 20 model runs for each constellation of faults. Principal stress orientation imposed in forward models is 90°. b) Principal stress ratio, $\phi$ ($\phi = 0.5$ in forward models), from mechanics-based and faultless inversions for varying percentage of elements used.

Deviations can be detected which are due to the non-planar fault surface, yielding heterogeneous resolved tractions, which, in turn, induce non-elliptical slip distribution. From the known slip distribution of the forward model we randomly select elements used for an inversion, which are depicted by the triangles in Figure 8.4ab. Figure 8.4b is the slip distribution from the inversion , which exhibits small misfits (Fig. 8.4c).

We compare the remote horizontal stress magnitudes and orientations of the mechanics-based inversion technique to those from the method proposed by Michael (Michael, 1987), which solves the faultless inversion problem. We establish error and variance bounds for the idealized fault (Fig.8.2) by varying percentages of elements used for inversion (Fig. 8.5). We use the same constellations of elements, their local orientations and the slip on them to solve for the remote stress orientations (see details above).

Both methods reproduce the mean stress orientation (normal to strike, 90°) imposed in the forward models well (Fig. 8.5a). The mean orientations from faultless stress inversion methods deviate by at most 1.5° and usually as little as 0.5° for greater percentages of elements used. Meanwhile the method proposed here deviates by as much as 8° when 1% of elements are used but converges quickly on the correct orientation with more elements. The method proposed has greater variances than faultless inversion methods for models with few ($< 5\%$) elements are used but has reduced variance when more elements are used. Neither method performs well in reproducing the principal stress ratio for the given setup (Fig. 8.5b). All estimates from the proposed methods are off by 20% or more compared to greater than 30% for fault less methods. Variances in principal stress ratio decrease for both methods with increased number of elements used. The difficulty in reproducing the stress ratio in both methods underscores the importance of varied fault orientations for both methods.

### 8.5.2 Heuristic Example: Fault System with Diverse Orientations

One of the commonly unenforced requirements of the faultless inversion is the necessity to include various fault orientations within the fault system (Twiss and Unruh, 1998). Here we test the effects of diversity of fault orientations on both faultless and the proposed stress inversion results by populating the fault system with non-intersecting planar circular faults at equal centroid spacing, but varying the individual orientations of the faults (Fig. 8.6). We choose planar circular faults to minimize the effects of roughness and tipline shape and to provide insight into the effects of fault system interaction and diverse orientations. We use a ratio of spacing over fault-radius of 5% (minimum) to avoid spurious numerical results, however, the model faults are mechanically interacting (Willemse, 1997). We follow the same strategy laid out in the preceding section of running forward models to produce the reference solution and slip on every element, which is selected randomly for inversions. We acknowledge that our model setup grossly underestimates the complications and does not represent all mechanisms present in a real fault system, but contend that the multiple fault scenario is an important one to test and contrast with results of the faultless inversion.

We center 36 circular faults on an evenly spaced grid (Fig. 8.6), allow a variety of strikes and dips for each fault in each forward model, select 5% of the elements for the combined stress and slip distribution inversion using 20 randomly selected constellations, and

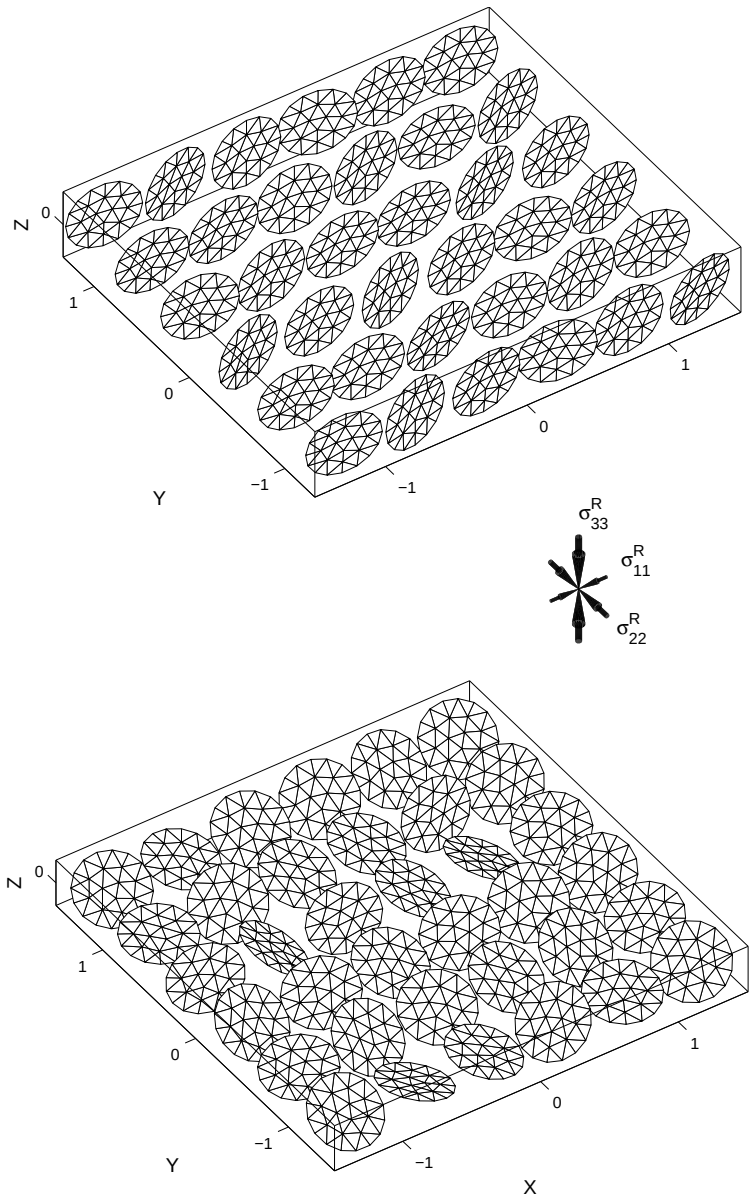


FIGURE 8.6: Setup of heuristic models using various orientations: 36 faults are centered on fixed position and allowed to randomly vary in strike and dip by (top) 20° and 5°, respectively, and (bottom) 160° and 80°, respectively. The remotely applied principal stresses are equivalent for all setups and indicated by the pairs of arrows. Boundary conditions on the faults are zero opening/closing and complete shear stress drop.

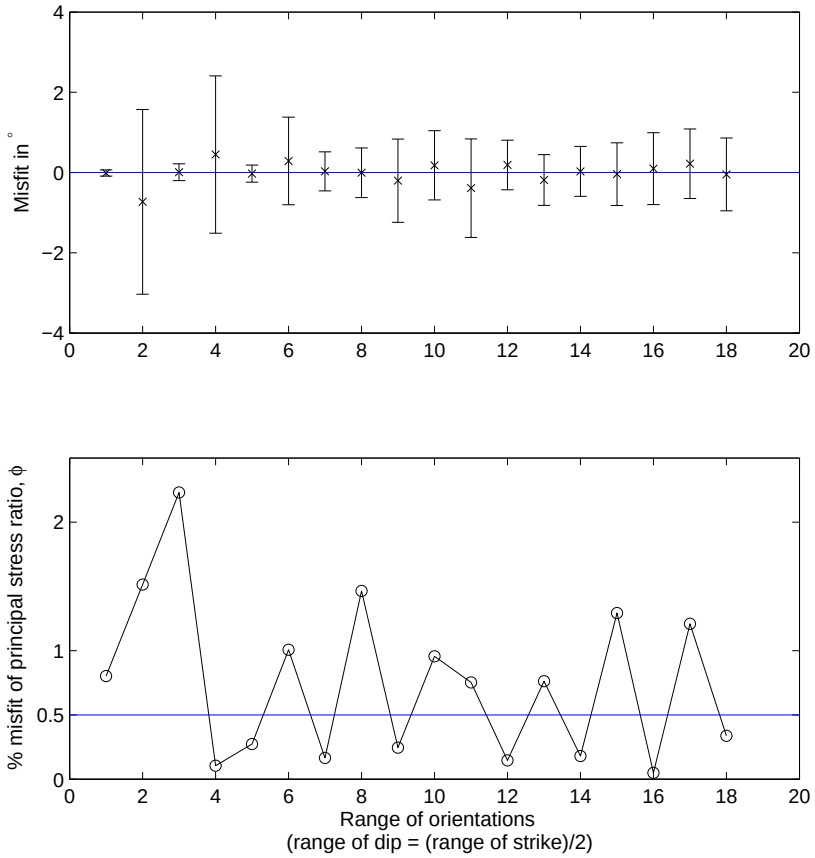


FIGURE 8.7: Validation of results for various orientations within fault system, for setup see Fig. 8.6. a) Misfit in degrees of orientation of horizontal principal stress from inversion. b) % error in principal stress ratio, $\phi$, from inversion results.

evaluate the mean errors and standard deviations for each setup. The range of strike orientations is permitted to vary 10° for each. Corresponding to the range in strike, we vary the dip of each fault in increments of 5°. The least range in orientations has strike ranging from -5° to 5° and dips ranging from 85° to 90°. The greatest range in orientations has strikes ranging from -90° to 90°, and dips ranging from 0° to 90°. This gives a total of 18 variations on range of strike and dip. The remote stresses are $\tilde{\sigma}_1^R = \sigma_{22}^R - \sigma_{33}^R = 5\text{MPa}$, $\tilde{\sigma}_2^R = \sigma_{11}^R - \sigma_{33}^R = 2.5\text{MPa}$. The boundary conditions on the fault prohibit opening or closing and result in a complete shear stress drop. The homogeneous, isotropic, and linearly elastic medium has Young's modulus $E = 5\text{GPa}$ and Poisson ratio $\nu = 0.25$.

The resulting horizontal principal stress orientations closely fit the applied stresses in the forward model (Fig. 8.7a): mean misfits are small (<0.5°) and standard deviations are all less than 2.5°. The stress ratio, $\phi = 1/2$, is reproduced well by the mechanics-based inversion, since the misfit is less than 2.5% for all fault models (Fig. 8.7b).

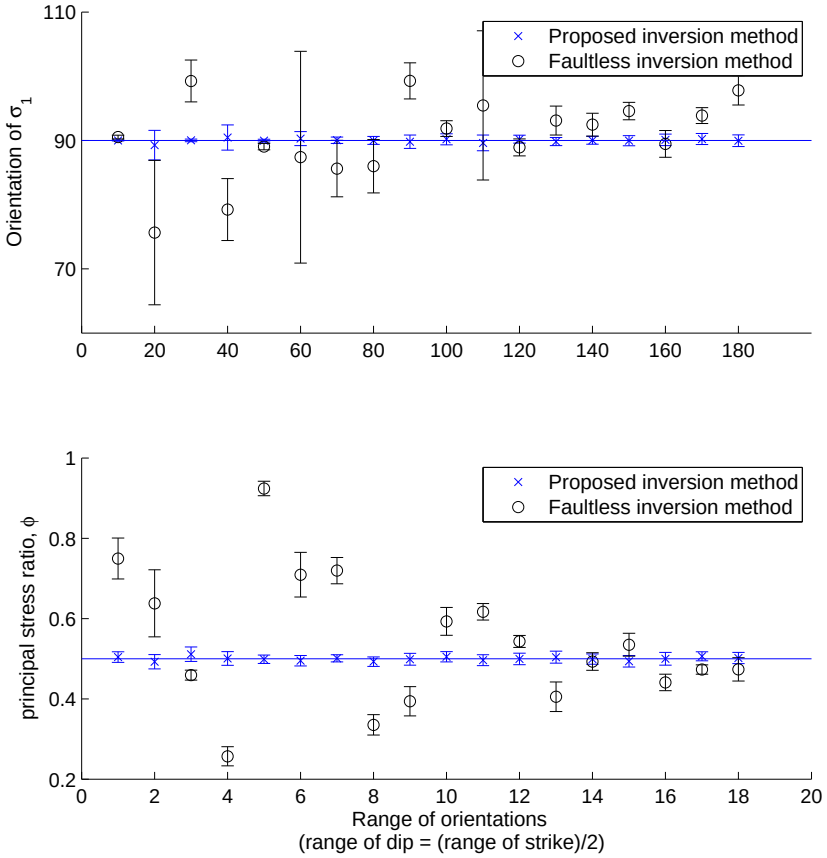


FIGURE 8.8: a) Orientation of horizontal principal stress for varied ranges of fault orientations from mechanics based stress inversion and faultless inversions. Error bars indicate variance within 20 model runs for each constellation of faults. b) Principal stress ratio, $\phi$, from mechanics-based and faultless inversions for varying orientations used.

The sensitivity of the results to the range of fault orientations is compared for both inversion methods in Figure 8.8. The mechanics-based inversion technique produces results that are both very close to the imposed principal stress orientation and exhibit a small standard variation. The greatest mean error does not exceed 1° with standard deviations less than 0.5° for all ranges of orientations plotted. The faultless inversion technique (Michael, 1987) exhibits greater mean errors and greater standard deviations (Fig. 8.8). Mean errors are as great 15° for a range of 20° in strike and 5° in dip. The principal stress ratio is in error by as much as 80%. However, both mean error and standard deviation are reduced as the diversity of orientations is increased. While we expect that our model reproduces well the forward models generated using the same methods when compared to faultless methods, these results highlight the importance of mechanical interaction in fault systems and thus address fundamental limitations to the faultless methods.

### 8.5.3 Field Example: 1999 Chi-Chi Earthquake, Taiwan

Here we highlight the capabilities of the inversion method for a fault that has been studied extensively because it hosted the 1999 ChiChi earthquake. We focus in particular, on the paleo-stress inversions (e.g. (Lee et al., 2003; Blenkinsop, 2006)). The earthquake was a consequence of the ongoing collision of the Phillipe Sea and Eurasian plates; the fault ruptured along a surface trace of about 100km and produced some of the largest surface slip ever recorded during a reverse faulting event (Lee et al., 2003). The fault trace itself is continuous except near the distal ends in the north and to a lesser degree in the south (Fig. 8.9). Along the fault trace 94 slip measurements have been reported (Lee et al., 2003) that have provided the basis for several studies of the stress orientations (e.g. (Lee et al., 2003; Blenkinsop, 2006)).

GPS surface displacements near the fault and throughout Taiwan have been used to kinematically invert for the coseismic slip on the fault (Johnson and Segall, 2004). Several studies have explored the focal mechanisms preceding, during, and after the main shock and provide a wealth of subsurface slip data, some of which occurred on the main shock rupture surface (Wu et al., 2008). Given the wealth of geologic and geophysical data available, we choose this setting to highlight the capabilities of the inversion technique to illustrate how it can incorporate surface as well as subsurface data. It is worth noting that even surface displacement away from the fault, such as GPS-derived coseismic displacements could be incorporated to find a more robust estimate of the remote stress tensor and the associated slip on the fault.

One of the limitations that is inherent to the mechanics-based method is that knowledge of the unexposed geometry of the fault is required. However, in many settings ample information exists on the increasingly accurate relocations of seismicity, providing important insight into the structure and geometry of the fault of interest (e.g. (Carena and Suppe, 2002)). In the present case, we use subsurface geometries that fit the observed surface coseismic displacements best, and combine these with the well documented geometry of the fault trace. Johnson and Segall (Johnson and Segall, 2004) fit a main fault dipping to the east at 26° to a depth of 12km, a secondary fault segment dipping south at 23 °, which joins the main fault by a third segment dipping shallowly to the southeast, and a horizontal décollement. Lee et al. (Lee et al., 2002) attempt to fit a more refined geometry at depth that smoothly joins the separate sections and invert for slip on the resultant fault. Both studies find that maximum slip occurred in the northern section, near a bend in the surface trace (Lee et al., 2002). We incorporate the detailed surface trace, and the subsurface geometry by progressively smoothing the surface trace and projecting it

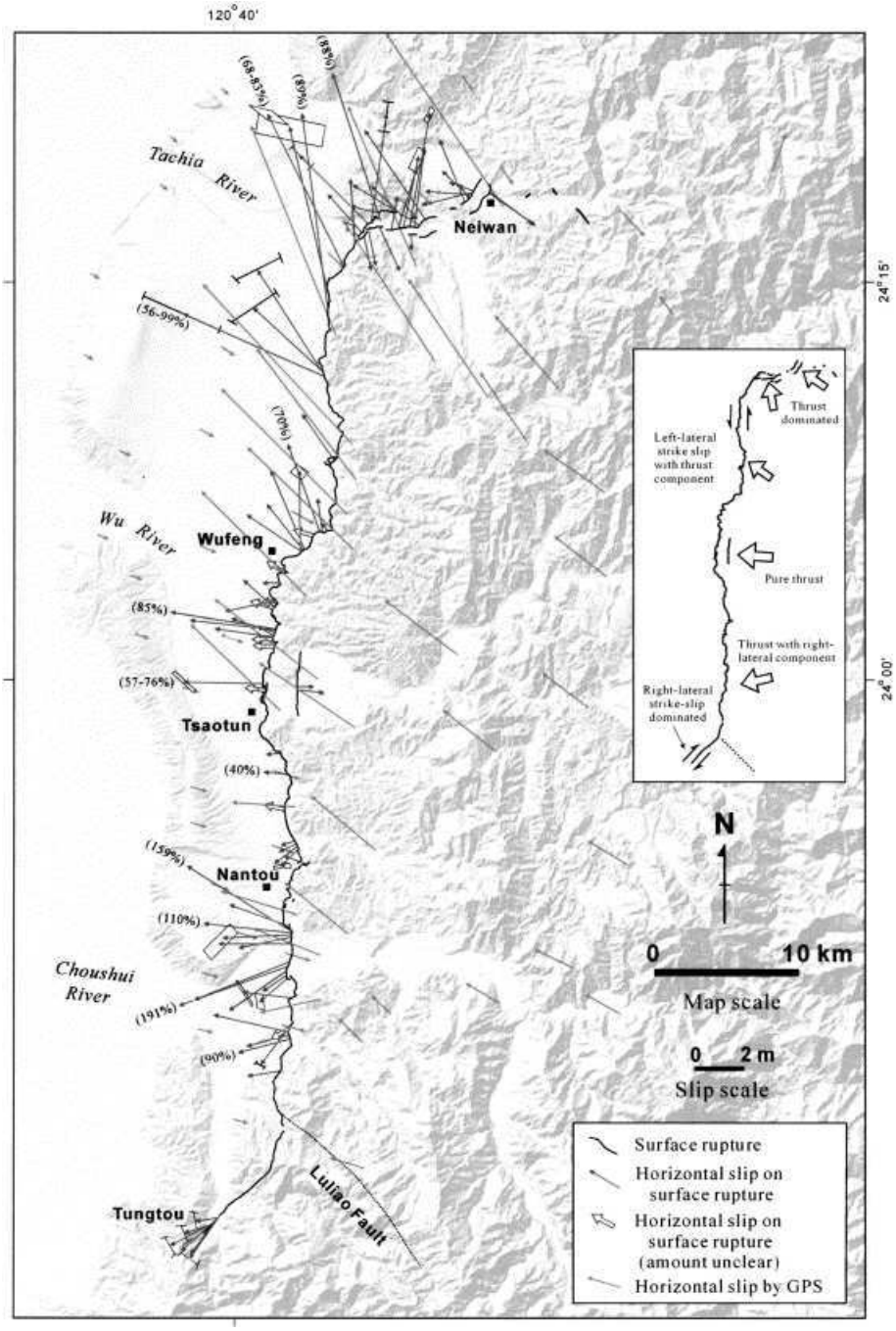


FIGURE 8.9: Example of paleostress inversion location and data from Lee et al. (Lee et al., 2003). Horizontal slip surveyed in Blenkinsop (Blenkinsop, 2006) and GPS displacement vectors. Percentage (in parenthesis) adjacent to slip vector on the rupture is the proportion of the slip to the slip recorded at the nearest GPS station on the hanging-wall side of the rupture.

at the preferred dip of 26° to a depth of 12km. We omit the horizontal décollement to simplify the analysis. We further simplify the surface trace geometry at the northern end to represent the change in strike without incorporating all the different fault strands, but rather construct the fault to be one contiguous surface.

As input we use the surface slip data published by several workers (Lee et al., 2003; Blenkinsop, 2006), resolve these on the nearest elements at the surface and enforce that the recorded local strike of the fault trace is equal to the strike of the corresponding element. We average the slip measurements at locations with more than one offset markers recorded, while at others the triangular surface elements are large enough to necessitate that local slip measurements be averaged and resolved onto the respective elements. The resolved slip measurements are then imposed as known boundary conditions in the inversion. We also include subsurface focal mechanism measurements relocated and inverted for by Wu et al. (Wu et al., 2008), use the predicted rake, and scale the slip by the magnitude of each individual event in one of the inversions to highlight the capabilities of the algorithm. The material properties of the medium surrounding the fault are homogeneous, isotropic, and linearly elastic with a Poisson's ratio of 1/4 and a Young's modulus of 5GPa. Because the lithologies across Taiwan are highly variable the values chosen should be understood as approximations to the effective material properties.

The inversion results highlight how the detailed surface slip data can produce robust remote stress orientations, while also providing an alternative method to estimating subsurface slip. The first inverse model only uses surface data and is depicted in Figure 8.10. Slip maxima occur at several locations with the largest near the bend in fault geometry at 24.2° latitude. The maximum slip is roughly 14m, which overestimates the 10m of slip in the subsurface from kinematic inversions using surface displacements records (Johnson and Segall, 2004; Lee et al., 2002). The direction of the most compressive principal stress (092.4°) indicates compression near the east-west direction and the stress ratio is $\phi = 0.169$. This result is close to that of faultless inversions (orientation of $\sigma_1 = 111°$, $\phi = 0.2$) considering the variance of stress orientation inversion results is 21°, which indicate in general that the principal stress direction, or orientation of crustal shortening, is roughly west-north-west to east-south-east (Blenkinsop, 2006). The deviation of regional principal stress orientations is likely due to averaging the slip data and simplifying the geometry near the northern end of the fault.

The second inverse model includes three focal mechanisms from the catalog of Wu et al. (Wu et al., 2008) that occurred on the day of the main shock and are resolved onto the fault (Fig. 8.11). The resultant slip on the fault is very similar to that of the inversion given above using only the surface data (Fig. 8.10). One notable difference is the slight

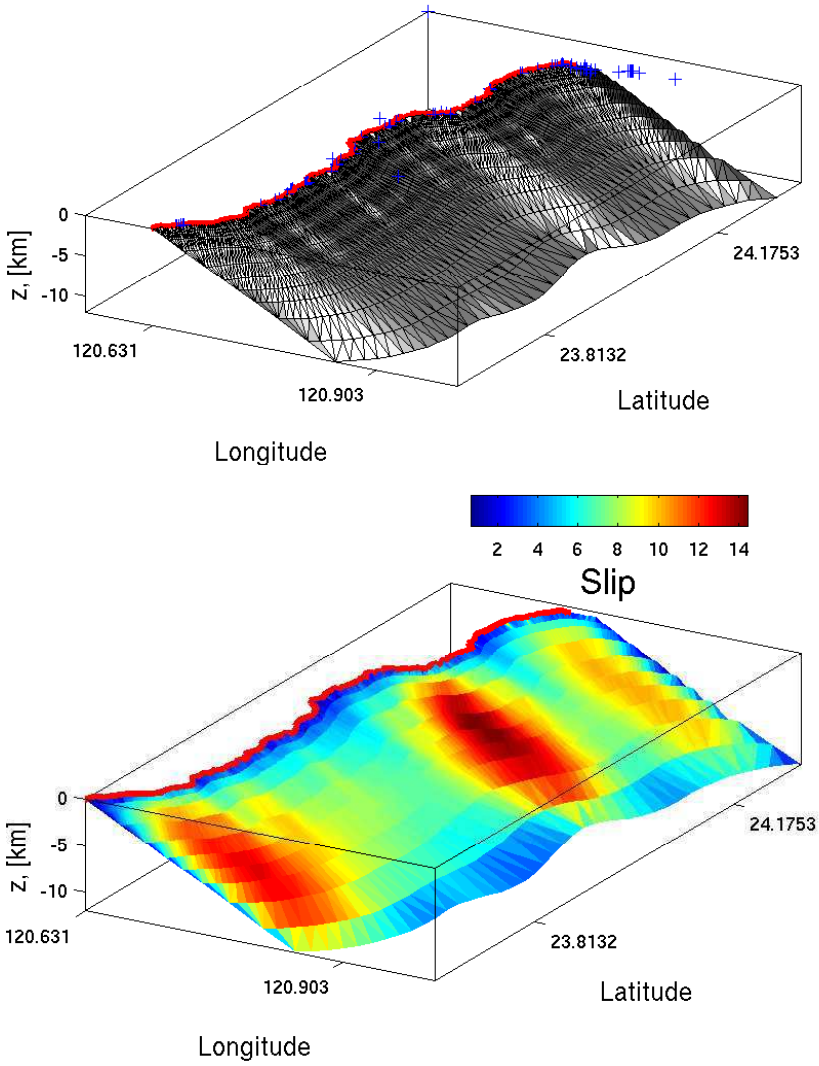


FIGURE 8.10: a) Fault trace of the Chelungpu fault and fault surface mesh used in the inversion. Blue crosses indicate locations of slip data. For slip vectors see Fig 8.9 and Blenkinsop (Blenkinsop et al., 2006). Slip distribution from the inversion using only the surface data.

deviation of slip near the resolved focal mechanisms, which are enforced exactly. The most compressive principal stress orientation is 092.4° and the stress ratio is $\phi = 0.169$, are identical to those using only the surface data (Fig. 8.11a) and the stress ratio is $\phi = 0.169$.

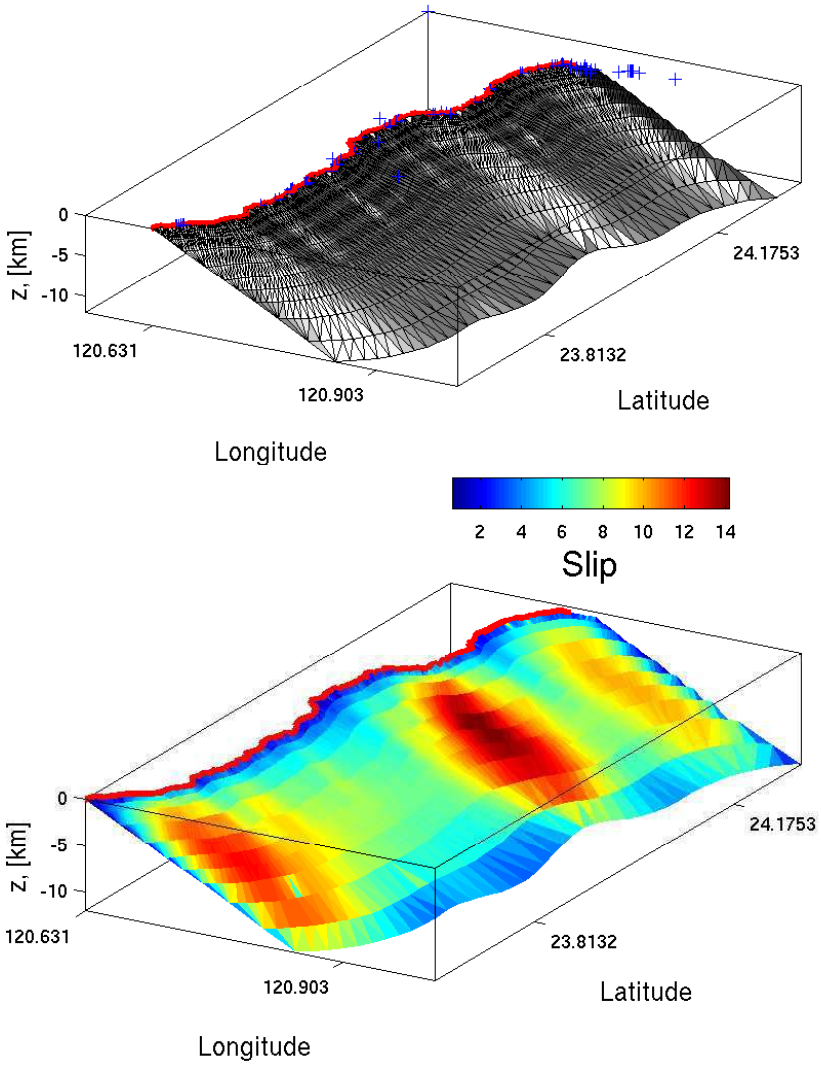


FIGURE 8.11: a) Fault trace of the Chelungpu fault and fault surface mesh used in the inversion. Blue crosses indicate locations of slip data. For slip vectors see Fig 8.9 and Blenkinsop (Blenkinsop et al., 2006). Slip distribution from the inversion using only the surface data and the subsurface focal mechanism solutions.

## 8.6 Conclusions

Faultless stress inversion methods are based on two assumptions that require careful evaluation when these methods are applied. In addition, their successful implementation requires diverse orientations of fault. The implications of ignoring this requirement have received little attention. We present a new stress inversion method that solves a complete mechanics problem explicitly including the stress perturbations of the faults.

We validate the method by solving a forward problem on two heuristic models and invert for stress and slip distributions using a subset of the elements in the forward problem. One heuristic model is that of a single fault with surface roughness similar to faults encountered in the field (Sagy et al., 2007). The second heuristic model tests an array of circular faults with varying ranges in orientations. Both models are reproduced well during the validation with principal stress orientation generally reproduced to within a few degrees, often less. Principal stress magnitude ratios are reproduced well for the heuristic model of an array of faults with varying orientation, but rather poorly for the single fault heuristic model.

When compared to commonly used faultless methods, the proposed method perform as well for the heuristic model of a single rough fault for the principal stress orientations, but better for the ratio of principal stress magnitudes. For the heuristic model of an array of faults with varying orientations, the proposed method performs better in predicting the stress orientations and principal stress magnitudes.

Inversions for stress and slip distributions simultaneously for the 1999 Chi-Chi, Taiwan, earthquake provide robust results that compare well with principal stress orientations and ratios found in previous studies. The results here also compare well with slip distributions found using independent methods. Both inversion setups, one using only surface data, the other incorporating subsurface focal mechanisms as well, yield meaningful stress orientations and slip distribution. These applications highlight the versatility and robustness of the proposed method.

# Acknowledgment

Financial support for this project was provided by the Stanford Rock Fracture Project. We thank Kaj Johnson for providing the coordinates of the Chelungpu fault trace.

# References


Aki, K. and Richards, P. (2002). *Quantitative Seismology*. University Science Books, Sausalito, CA.

Amadei, B. and Stephansson, O. (1997). *Rock stress and its measurement*. Chapman & Hall, London.

Anderson, A. (1942). *The Dynamics of Faulting and Dyke Formation with Application to Britain*. Oliver and Boyd, Edinburgh.

Anderson, E. (1905). The dynamics of faulting. *Edinburgh Geol. Soc.*, 8(3):387–402.

Anderson, T. (1995). *Fracture mechanics, Fundamentals and Applications*. CRC Press, London, U.K.

Angelier, J. (1984). Tectonic analysis of fault slip data sets. *J. Geophys. Res.*, 89:5835–5848.

Angelier, J. and Mechler, P. (1977). Sur une méthode graphique de recherche des contraintes principales également utiliable en tectonique et en séismologie: la méthode des dièdres driots. *Bulletin de la Societé Géologique de France*, 7:1309–1318.

Angelier, J., Tarantola, A., Valette, B., and Manoussis, S. (1982). Inversion of field data in fault tectonics to obtain the regional stress - i. single phase fault populations: a new method of computing the stress tensor. *J. Geophys. Res.*, 69:607–621.

Armijo, R., Carey, E., and Cisternas, A. (1982). The inverse problem in microtectonics and the separation of tectonic phases. *Tectonophysics*, 82(1-2):145–160.

Aster, R., Borchers, B., and Thurber, C. (2005). *Parameter Estimation and Inverse Problems*. Elsevier Academic Press, Burlington, MA, USA.

Atkinson, B. (1987). *Fracture mechanics of rock*. Academic Press, London, U.K.

Aydin, A. and Reches, Z. (1982). Number and orientation of fault sets in the field and in experiments. *Geology*, 10:107–112.

Blenkinsop, T. (2006). Kinematic and dynamic fault slip analyses: implications from the surface rupture of the 1999 chi-chi, taiwan, earthquake. *J. Struct. Geol.*, 28(6):1040–1050.

Blenkinsop, T., Lisle, R., and Ferrill, D. (2006). Introduction to the special issue on new dynamics in palaeostress analysis. *J. Struct. Geol.*, 28(6):941–942.

Bott, M. (1959). The mechanics of oblique slip faulting. *Geological Mag.*, 96:109–117.

Brune, J. (1968). Seismic moment, seismicity, and rate of slip along major fault zones. *J. Geophys. Res.*, 73:777–784.

Burgmann, R. and Pollard, D. D. (1994). Slip distribution on faults: effects of stress gradients, inelastic deformation, heterogeneous host-rock stiffness, and fault interaction. *Journal of Structural Geology*, 16(12):1675–1690.

Carena, S. and Suppe, J. (2002). Three-dimensional imaging of active structures using earthquake aftershocks: the northridge thrust, california. *J. Struct. Geol.*, 24:887–904.

Carey, E. and B., B. (1974). Analyse thé orique et numérique d'un modélé mecanique élémentaire appliqué à l'étude d'une population de failles. *C.r. Acad. Sci., Paris*, 279:891–894.

Carey-Gailhardis, E. and Mercier, J. (1987). A numerical method for determining the state of stress using focal mechanisms of earthquake populations: application to tibetan teleseisms and microseismicity of southern peru. *Earth Planet. Sci. Lett.*, 82:165–179.

Choi, P. (1996). *Reconstitutions des Paléocontraintes en Tectonique Cassante: Méthodes et Application aux Domaines Continentaux Déformés (Corée, Jura).* PhD thesis, Université P. & M. Curie, Paris.

Cladouhos, T. and Allmendinger, R. (1993). Finite strain and rotation from fault-slip data. *J. Struct. Geol.*, 15(6):771–784.

Comninou, M. and Dundurs, J. (1975). The angular dislocation in a half space. *Journal of Elasticity*, 5(3):203–216.

Couples, G. (1977). Stress and shear fracture (fault) patterns resulting from a suite of complicated boundary conditions with applications to the wind river mountains. *Pure and Applied Geophysics*, 115:113–133.

Crouch, S. L. and Starfield, A. M., editors (1983). *Boundary element methods in solid mechanics.* George Allen and Unwin, London.

Dupin, J.-M., Sassi, W., and Angelier, J. (1993). Homogeneous stress hypothesis and actual fault slip: a distinct element analysis. *J. Struct. Geol.*, 15(8):1033–1043.

Etchecopar, A., Vasseur, G., and Daignieres, M. (1981). An inverse problem in microtectonics for the determination of stress tensors from fault striation analysis. *J. Struct. Geol.*, 3(1):51–65.

Fletcher, R. and Pollard, D. (1990). Can we understand structural and tectonic processes and their products without appeal to a complete mechanics? *J. Struct. Geol.*, 21:1071–1088.

Fry, N. (1999). Striated faults: visual appreciation of their constraint on possible paleostress tensors. *J. Struct. Geol.*, 21(1):7–21.

Fung, Y. (1977). *A first course in Continuum Mechanics*. Prentice-Hall, Englewood Cliffs, NJ.

Gapais, D., Cobbold, P. ans Bourgeois, O., Rouby, D., and deUrreistiete, M. (2000). Tectonic significance of fault-slip data. *J. Struct. Geol.*, 22(7):881–888.

Gauthier, B. and Angelier, J. (1985). Fault tectonics and deformation: a method of quantification using field data. *Earth and Planetary Sci. Lett.*, 74(1):137–148.

Gephart, J. and Forsyth, D. (1990). An improved method for determining the regional stress tensor using earthquake focal mechanism data: Application to the san fernando earthquake sequence. *Comput. Geosci.*, 16(7):953–989.

Gephart, J. W. (1990). Fmsi: a fortran program for inverting fault/slickenside and earthquake focal mechanism data to obtain the regional stress tensor. *Computers and Geoscience*, 16(7):953–989.

Griffith, A. (1921). The phenomena of rupture and flow in solids. *Phil. Transactions of the Royal Society*, A221:163–198.

Griffith, A. (1925). Theory of rupture. In *First International Congress for Applied Mechanics*, pages 53–64. Delft. Waltham Int. Press.

Hafner, W. (1951). Stress distribution and faulting. *Geol. Soc. America Bull.*, 62:373–398.

Hardcastle, K. and Hills, L. (1991). Brute3 and select: Quickbasic 4 programs for determination of stress tensor configurations and separation of heterogeneous populations of fault-slip data. *Computers & Geosciences*, 17(1):23–43.

Huang, Q. (1988). Computer-based method to separate heterogeneous sets of fault-slip data into sub-sets. *J. Struct. Geol.*, 10(3):297–299.

Inglis, C. (1913). Stresses in a plate due to the presence of cracks and sharp corners. volume 55, pages 219–230. Inst. Naval Arch.

Irwin, G. (1957). Analysis of stresses and strain near the end of a crack traversing a plate. *J. of Appl. Mech.*, 24:361–364.

Jackson, J. and McKenzie, D. (1988). The relationship between plate motions and seismic moment tensors, and the rates of active deformation in the mediterranean and middle east. *Geophysical J.*, 88:46–73.

Jaeger, J., Cook, N., and Zimmermann, R. (2007). *Fundamentals of Rock Mechanics*. Blackwell Publ., Malden, MA.

Jeyakumaran, M., Rudnicki, J. W., and Keer, L. M. (1992). Modeling slip zones with triangular dislocation elements. *Bulletin of the Seismological Society of America*, 82:2153–2169.

Johnson, K. and Segall, P. (2004). Imaging the ramp-décollement geometry of the chelungpu fault using coseismic gps displacements from the 1999 chi-chi, taiwan earthquake. *Tectonophysics*, 378:129–139.

Jones, L. (1988). Focal mechanisms and the state of stress on the san andreas fault in southern california. *J. Geophys. Res.*, 93:8869–8891.

Julien, P. and Cornet, F. (1987). Stress determination from aftershocks of the campania-lucania earthquake of november 23, 1980. *Annales Geophysicae*, 5B(3):289–300.

Kao, H. and Angelier, J. (2001). Stress tensor inversion for the chi-chi earthquake sequence and its implications on regional collision. *Bull. of the Seism. Soc. of America*, 91(5):1028–1040.

Kostrov, V. (1968). Seismic moment and energy of earthquakes, and seismic flow of rocks. *Izvestiya Academy of Sciences of the USSR (Physics of Solid Earth)*, 1:23–40.

Lawn, B. and Wilshaw, T. (1993). *Fracture of Brittle Solids*. Cambridge University Press, New York.

Lay, T. and Wallace, T. (1995). *Modern Global Seismology*. Academic Press, London, UK.

Lee, J.-C., Chu, H.-T., Angelier, J., Chan, Y.-C., Hu, J.-C., Lu, C., and Rau, R.-J. (2002). Geometry and structure of northern surface ruptures of the 1999 mw=7.6 chi-chi taiwan earthquake: influence from inherited fold belt structures. *J. Struct. Geol.*, 24:173–192.

Lee, Y.-H., Hsieh, M.-L., Lu, S.-D., Shih, T.-S., Wu, W.-Y., Sugiyama, Y., Azuma, T., and Kariya, Y. (2003). Slip vectors of the surface rupture of the 1999 chi-chi earthquake, western taiwan. *J. Struct. Geol.*, 25(11):1917–1931.

Liesa, C. and Lisle, R. (2004). Reliability of methods to separate stress tensors from heterogeneous fault-slip data. *J. Struct. Geol.*, 26(3):559–572.

Lisle, R., Orife, T., Arlegui, L., Liesa, C., and Srivastava, D. (2006). Favoured states of palaeostress in the earth's crust: evidence from fault-slip data. *J. Struct. Geol.*, 28(6):1051–1066.

Maerten, F., Maerten, L., and Cooke, M. (2009). Solving 3d boundary element problems using constrained iterative approach. *Computational Geosciences*.

Maerten, F., Resor, P. G., Pollard, D. D., and Maerten, L. (2005). Inverting for slip on three-dimensional fault surfaces using angular dislocations. *Bulletin of the Seismological Society of America*, 95:1654–1665.

Maerten, L. (2000). Variation in slip on intersectiong normal faults: Implications for paleostress inversion. *Journal of Geophysical Research*, 105(25):553–565.

Maerten, L., Willemse, E. J. M., Pollard, D. D., and Rawnsley, K. (1999). Slip distributions on intersecting normal faults. *Journal of Structural Geology*, 21:259–271.

Malvern, I. (1969). *Introduction to the Mechanics of a Continuum Medium*. Prentice-Hall.

Mandl, G. (1988). *Mechanics of tectonic faulting. Models and basic concepts*. Elsevier, Amsterdam.

Marrett, R. and Allmendinger, R. (1990). Kinematic analysis of fault-slip data. *J. Struct. Geol.*, 12(8):973–986.

Martel, S. and Shacat, C. (2006). Mechanics and interpretations of fault slip. In Abercrombie, R., DiToro, G., Kanamori, H., and McGarr, A., editors, *Radiated Energy and the Physics of Earthquake Faulting*, pages 207–216. American Geophysical Union Monograph 170.

McKenzie, D. (1969). The relation between fault plane solutions for earthquakes and the directions of the principal stresses. *Bull. Seismol. Soc. Am.*, 59:591–601.

Michael, A. (1987). Use of focal mechanisms to determine stress: a control study. *J. Geophys. Res.*, 92(B1):357–368.

Molnar, P. (1983). Average regional strain due to slip on numerous faults of different orientations. *J. Geophys. Res.*, 88:6430–6432.

Mutlu, O. and Pollard, D. (2008). On the patterns of wing cracks along an outcrop scale flaw: a numerical modeling approach using complementarity. *Journal of Geophysical Research*, 113.

Nádai, A. (1931). *Plasticity*. McGraw-Hill, Inc., New York.

Nemcok, M. and Lisle, R. (1995). A stress inversion procedure for polyphase fault/slip data sets. *J. Struct. Geol.*, 17(10):1445–1453.

Orife, T., Arlegui, L., and Lisle, R. (2002). Dipslip: a quickbasic stress inversion program for analysing sets of faults without slip lineations. *Computers & Geosciences*, 28(6):775–781.

Orife, T. and Lisle, R. (2003). Numerical processing of palaeostress results. *J. Struct. Geol.*, 25(6):949–957.

Pollard, D. and Fletcher, R. (2005). *Fundamentals of Structural Geology*. Cambridge University Press, Cambridge, UK.

Pollard, D., Saltzer, S., and Rubin, A. (1993). Stress inversion methods: are they based on faulty assumptions? *J. Struct. Geol.*, 15:1045–1054.

Pollard, D. and Segall, P. (1987). Theoretical displacements and stresses near fractures in rock: with applications to faults, joints, veins, dikes and solution surfaces. In Academic., S. D., editor, *Fracture Mechanics of Rocks*. Atkinson, B.

Power, W., Tullis, T., Brown, S., Boitnott, G., and Scholz, C. (1987). Roughness of natural fault surfaces. *Geophy. Res. Lett.*, 14:29–32.

Price, N. J. (1966). *Fault and Joint Development in Brittle and Semi-brittle Rock*. Pergamon, London.

Ramsay, J. and Lisle, R. (2000). *The Techniques of Modern Structural Geology. Volume III. Applications of Continuum Mechanics in Structural Geology*. Academic Press, London, U.K.

Reches, Z. (1978). Number and orientation of fault sets in the field and in experiments. *Tectonophysics*, 47:109–129.

Reches, Z. (1987). Determination of the tectonic stress tensor from slip along faults that obey the coulomb yield condition. *Tectonics*, 6(4):849–861.

Reinecker, J., Heidbach, O., Müller, B., Tingay, M., and Connolly, P. (2004). The 2004 release of the world stress map, url. http://www.world-stress-map.org.

Rice, J. (1980). The mechanics of earthquake rupture. In Dziewonski, A. and Boschi, E., editors, *Physics of the Earth's Interior*, pages 555–649, North-Holland Publ. Co. International School of Physics 'Enrico Fermi', Course 78, 1979, Italian Physical Society.

Roberts, G. and Ganas, A. (2000). Fault-slip direction in central and southern greece measured from striated and corrugated fault planes: comparison with focal mechanism and geodetic data. *J. of Geophy. Res.*, 105(B10):23443–23462.

Rudnicki, J. (1980). Fracture mechanics applied to the earth's crust. *Annual Review of Earth and Planetary Sciences*, 8:489–525.

Sagy, A., Brodsky, E., and Axen, G. (2007). Evolution of fault-surface roughness with slip. *Geology*, 35(3):283–286.

Sanford, A. (1959). Analytical and experimental study of simple geologic structures. *Geol. Soc. America Bull.*, 70:19–52.

Sato, K. and Yamaji, A. (2006). Uniform distribution of points on a hypersphere for improving the resolution of stress tensor inversion. *J. Struct. Geol.*, 28(6):972–979.

Segall, P. and Pollard, D. (1980). Mechanics of discontinuous faulting. *Journal of Geophysical Research*, 85:4337–4350.

Shan, Y. and Fry, N. (2005). A hierarchical cluster approach for forward separation of heterogeneous fault/slip data into subsets. *J. Struct. Geol.*, 27(5):929–936.

Shan, Y., Li, Z., and Lin, G. (2004). A stress inversion procedure for automated recognition of polyphase fault/slip data sets. *J. Struct. Geol.*, 26(9):919–925.

Shan, Y., Lin, G., Li, Z., and Zhao, C. (2006). Influence of measurement errors on stress estimated from single-phase fault/slip data. *J. Struct. Geol.*, 28(6):943–951.

Shan, Y., Suen, H., and Lin, G. (2003). Separation of polyphase fault/slip data: an objective-function algorithm based on hard division. *J. Struct. Geol.*, 25(6):829–840.

Thomas, A. L. (1993). Poly3d: a three-dimensional, polygonal element, displacement discontinuity boundary element computer program with applications to fractures, faults, and cavities in the earth's crust. Master's thesis, Stanford University.

Twiss, R., Protzman, G., and Hurst, S. (1991). Theory of slickenline patterns based on the velocity gradient tensor and microrotation. *Tectonophysics*, 186:215–239.

Twiss, R., Souter, B., and Unruh, J. (1993). The effect of block rotations on the global seismic moment tensor and patterns of seismic p and t axes. *J. of Geophy. Res.*, 98:645–674.

Twiss, R. and Unruh, J. (1998). Analysis of fault slip inversions: Do they constrain stress or strain rate? *J. of Geophy. Res.*, 103(B6):12205–12222.

Vasseur, G., Etchecopar, A., and Philip, H. (1983). Stress state inferred from multiple focal mechanisms. *Ann. Geophys.*, 1(4-5):291–298.

Voight, B. (1966). Beziehung zwischen großen horizontalen spannungen in gebirge und der tektonik und der abtragung. In *Rock Mech., 1st Congr., Vol 2*, pages 1–56. Lisbon. Int. Soc.

Wallace, R. (1951). Geometry of shearing stress and relation to faulting. *J. of Geology*, 59:118–130.

Whitcomb, J., Garmany, J., and Anderson, D. (1974). Earthquake prediction: Variation of seismic velocities before the san fernando earthquake. *Science*, 180:632–635.

Willemse, E. J. M., Pollard, D. D., and Aydin, A. (1996). Three-dimensional analyses of slip distributions on normal fault arrays with consequences for fault scaling. *J. Struct. Geol.*, 18:295–309.

Willemse, J. M. (1997). Segmented normal faults: Correspondence between three-dimensional mechanical models and field data. *Journal of Geophysical Research*, 102:675–692.

Williams, J. (1987). On the calculation of energy release rates for cracked laminates. *Int. J. of Fracture*, 36(2):101–119.

Wojtal, S. (1989). Measuring displacement gradients and strains in faulted rocks. *J. Struct. Geol.*, 11(6):669–678.

Wu, Y.-M., Zhao, L., Chang, C.-H., and Hsu, Y.-J. (2008). Focal mechanism determination in taiwan by genetic algorithm. *Bull. of the Seism. Soc. of America*, 98(2):651–661.

Yamaji, A. (2000). The multiple inverse method: a new technique to separate stresses from heterogeneous fault-slip data. *J. Struct. Geol.*, 22(4):441–452.

Yoffe, E. (1960). The angular dislocation. *Phil. Mag.*, 5:161–175.

Zoback, M. (1992). First and second order patterns of stress in the lithosphere. the world stress map project. *J. of Geophys. Research*, 97:11703–11728.

Zoback, M., Zoback, M., Mount, V., Eaton, J., Healy, J., Oppenheimer, D., Reasonberg, P., Jones, L., Raleigh, B., Wong, I., Scotti, O., , and Wentworth, C. (1987). New evidence on the state of stress of the san andreas fault system. *Science*, 238:1105–1111.

# CHAPTER 9

# Applications of the principle of superposition for paleo-stress analysis and fault modeling

F. Maerten[1,2], L. Maerten[1], D. Pollard[3]

(1) Igeoss, Montpellier, FRANCE
(2) University of Montpellier II, Geosciences, FRANCE
(3) Standord University, Stanford, CA, USA

In preparation for Journal of Structural Geology.

Patent pending

**Preamble**

This chapter shows that using the principle of superposition, which is inherent to linear elasticity, allows one to recover paleostress using a Monte-Carlo method in a very fast way. Compared to the technique developed in chapter 8, this new method allows one to use fracture orientation from well bores, and to estimate the number of tectonic events, each measured fracture being classified into its respective event.

## About...

Few years ago, I wanted to develop an elegant application using the principle of superposition. At this time, only fast displacement and perturbed stress field computation was done using this principle (see section 9.5). After a laborious research on how to incorporate opening fractures (joints, veins, dikes) into the paleostress formulation (see chapter 8), the idea of using the principle of superposition came in my mind. As usual, Laurent Maerten helped me to validate the method, and Dave Pollard greatly enhanced the manuscript and wrote the historical part.

# Article Outline

## 9.1 Résumé

Les méthodes d'inversion de contraintes, qui utilisent des stries mesurées et/ou le rejet sur les failles, sont principalement basées sur deux hypothèses: (i) le champ de contraintes est uniforme au sein de la masse rocheuse englobant les failles (en supposant l'absence de champ de contrainte perturbé), et (ii) le déplacement sur les failles a la même direction et le même sens que le champ de contraintes à l'infini résolu sur les plans de failles. De plus, il a été montré que les directions de glissements sont affectées par: (i) l'anisotropie de la géométrie des failles; (ii) l'anisotropie du frottement sur ces failles (ondulations de surface); (iii) l'hétérogénéité de la rigidité de la roche hôte, et (iv) les perturbations du champ de contraintes local, principalement dues aux interactions mécaniques des failles entre elles. Les interactions mécaniques dues à la géométrie complexe des failles dans les milieux hétérogènes doivent donc être prises en compte lors du calcul d'inversion de contraintes. Déterminer les paramètres de ces paléo-contraintes en présence de failles interagissant entre elles nécessite de faire des milliers de simulations et requiet par conséquent un temps de calcul non négligeable afin de s'ajuster aux données observées.

Dans cet article nous approfondissons cette approche avec la méthode des éléments frontières en 3D en utilisant le principe de superposition qui s'applique à l'élasticité linéaire dans un milieu semi-infini, hétérogène et isotrope. Compte tenu du rejet sur les failles, des données de striation, des mesures de contraintes ainsi que la géométrie des failles, des données GPS, d'orientation de fractures (joints, veines, dykes, stylolites), d'orientation de plan de failles secondaires, on retrouve l'état de paleo-contrainte pour un ou plusieurs évènements tectoniques, et ceci de manière rapide.

Nous montrons qu'en utilisant le principe de superposition, chaque simulation se fait en temps constant quelle que soit la complexité du modèle sous-jacent, et que le modèle n'a pas besoin d'être recalculée à chaque simulation. Les applications de cette méthode sont multiples: interpolation de contraintes, modélisation de la fracturation, détection des évènements tectoniques, contrôle de la qualité des failles interprétées, ou calcul en temps réel du champ de contraintes perturbé lorsque l'utilisateur fait de l'estimation de paramètres.

## 9.2 Abstract

Methods for stress inversion, using measured striations and/or throw on faults, are mainly based on on the assumptions that: (i) the stress field is uniform within the rock mass embedding the faults (assuming no perturbed stress field), and that (ii) the slip on faults has the same direction and sense as the resolved far field stress on the fault plane. However, it has been shown that slip directions are affected by: (i) anisotropy in fault compliance caused by irregular tip-line geometry; (ii) anisotropy in fault friction (surface corrugations); (iii) heterogeneity in host rock stiffness; and (iv) perturbation of the local stress field mainly due to mechanical interactions of adjacent faults. Mechanical interactions due to complex faults geometry in heterogeneous media should be taken into account while doing the stress inversion. Determining the parameters of such paleostress in the presence of multiple interacting faults requires running a lot of simulations, and therefore a huge amount of computation time in order to fit the observed data. In this paper we investigate this approach with a 3D boundary element method using the principle of superposition that applies to linear elasticity for heterogeneous, isotropic whole- of half-space media. Given some measures of the fault throw, dip-slip and/or slickenline directions, stress measurements as well as fault geometry, GPS data, fractures (joints, veins, dikes, pressure solution seams with stylolites) or secondary fault plane orientations, we recover the remote stress state for multiple tectonic events in a fast way.

We show that using the principle of superposition, each simulation is done in constant time whatever the complexity of the underlying model and that the model does not need to be recomputed. Applications of this technique range from stress interpolation and fracture modeling, recovering of tectonic event(s), quality control on interpreted faults to real-time computation of perturbed stress and displacement fields when the user is doing parameters estimation.

## 9.3 Introduction

Understanding the origin and evolution of faults and the tectonic history of faulted regions can be facilitated by relating fault orientation and slip direction to the state of stress in Earths crust (Anderson, 1942; Price, 1966; Voight, 1966; Mandl, 1988). In typical inverse problems the directions of the remote principal stresses and a ratio of their magnitudes are constrained by analyzing field data on fault orientations and slip directions as inferred from striations such as slickenlines on exposed fault surfaces (e.g. Angelier, 1984; Angelier et al., 1982; Carey and B., 1974; Etchecopar et al., 1981; Fry, 1999; Reches, 1987; Shan et al., 2004; Sato and Yamaji, 2006). The equations of motion are not invoked for these

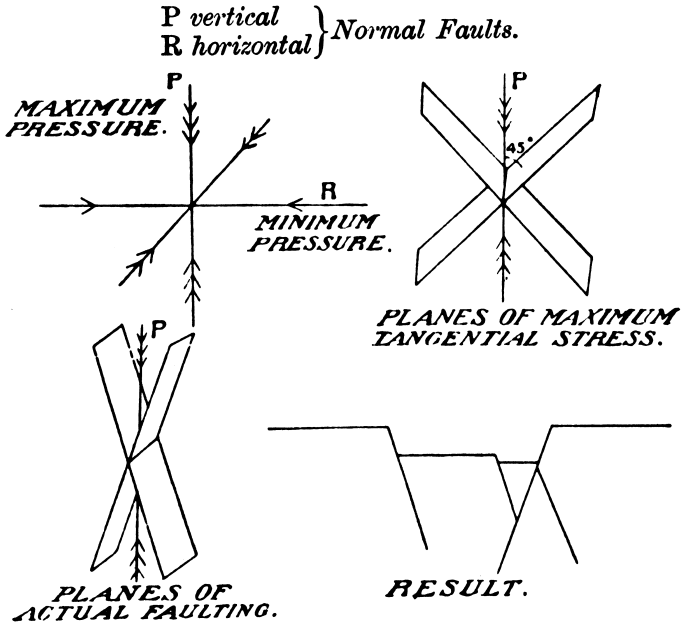


FIGURE 9.1: a) upper left - directions of principal stress axes with one vertical; b) upper right - orthogonal planes carrying the maximum shear stress at a point or in a volume with a homogeneous state of stress; c) lower left - conjugate normal fault planes; d) lower right - schematic normal fault planes. From Anderson (Anderson, 1905).

inverse problems, and perturbations of the local stress field by fault slip are ignored. The mechanical role played by the faults in the tectonic deformation is not included explicitly in the analysis.

To our knowledge paleostress analysis of this kind began with the remarkably prescient paper on the dynamics of faulting by E. M. Anderson published in 1905 (Anderson, 1905). Here we provide a brief perspective on paleostress analysis by identifying two generations in the development of this methodology, and then we distinguish a third generation, which is the focus of the paper.

### 9.3.1 Generation 1: Anderson's inversion for tectonic stress regimes

Anderson (Anderson, 1905) began, without comment or justification, by taking one principal stress direction as vertical (Fig. 9.1.a), but he addressed this assumption explicitly 37 years later in his book on the dynamics of faulting (Anderson, 1942, p. 12 and Ch. VII). In his 1905 paper Anderson suggested that planes carrying the maximum tangential stress "will have much to do with determining the directions of faults in the rock". He understood (Fig. 9.1.b) that for a triaxial stress state ($P > Q > R$) there are two orientations of such planes at a point or throughout a homogeneous stress field; that these

planes intersect in the direction of the intermediate principal stress (Q); and that they make equal angles of 45° with the direction of greatest principal compressive stress (P). These planes are geometrically orthogonal and mathematically "conjugate" (so related as to be interchangeable in the enunciation of certain properties) in the sense that the traction vectors acting upon them are equal in magnitude.

Anderson (1905) suggested that "the planes of faulting in any rock do not follow exactly the directions of maximum tangential stress, but deviate from these positions in a more or less determinate manner". Without references to the existing literature, Anderson declared: "If we suppose that the resistance which any solid (otherwise isotropic) offers to being broken by shearing along any plane consists of two parts, one part being a constant quantity and the other part proportional to the pressure across that plane, we shall arrive at results which agree very well with the observed geological facts." This resistance to breakage by shearing is equivalent to that attributed to Coulomb (Coulomb, 1773), and the so-called Coulomb failure criterion may be written (Jaeger et al., 2007, p. 90):

$$|\tau| = S_0 + \mu\sigma \tag{9.1}$$

On the left hand side is the shear stress that promotes faulting. On the right hand side are Andersons two resistance terms: $S_0$ is the constant quantity (cohesion); $\mu$ is the proportionality constant (friction); and $\sigma$ is the normal stress (pressure).

In calculating the tangential and normal stress on the conjugate planes Anderson used a variant of Cauchys tetrahedron (Malvern, 1969, p. 73), with one face corresponding to a would-be fault, and made an interesting analogy: "This prism we suppose to exist in the rock, somewhat as the statue exists beforehand in the block of marble... ." Clearly, Anderson understood that slip on a fault would perturb the stress from the assumed homogeneous state, so it is appropriate to think of his conjugate planes as would-be faults. Therefore, we appeal to Anderson's analogy and refer to his method, based on a homogeneous stress state, as 'faultless' paleostress analysis.

Anderson avoids grappling with the cohesion by "supposing a plane crack had actually formed in this direction, and that movement were just about to begin along it...", in this case resisted only by friction, so $S_0 = 0$ in Eq. 9.1. Subtracting the frictional resistance from the shear stress and introducing the principal stresses (e.g. Jaeger et al., 2007, p. 23), Anderson derived (Anderson, 1905, p. 389):

$$\frac{P-R}{2}(\sin 2\theta) - \mu\left(\frac{P+R}{2} - \frac{P-R}{2}\cos 2\theta\right) = 0 \tag{9.2}$$

Here $\theta$ is the angle from the direction of $P$ to the plane of interest. Anderson asserted that this quantity "will be a maximum in the directions in which faulting will be the most likely to occur". Using differential calculus to find the maximum of as a function of $\theta$, he derived the relationship $\tan 2\theta = 1/\mu$, which may be solved for the orientation of faulting, $\theta_c$. For example, taking $\mu = 1/\sqrt{3}$, Anderson (Anderson, 1905, p. 389) calculated $\theta_c = 30°$(Fig. 9.1.c).

While clearly recognizing that faults in nature present more complicated geometries because of sequential development and mutual cross-cutting (Fig. 9.1.d), Anderson used the relationships between the orientations of conjugate faults and those of the principal stress directions to identify three tectonic stress regimes for faulting (normal, wrench, and thrust), and he associated each with one of the principal stress axes being vertical (greatest, intermediate, and least compression, respectively). For each regime the intermediate principal stress direction was taken as coincident with the line of intersection of two conjugate fault orientations, and the greatest principal stress bisected the acute angle between these faults. Thus, this most elementary form of paleostress analysis provides the orientations of the principal stress axes (with one assumed to be vertical) and their relative magnitudes $P \geq Q \geq R$. While the necessary data for Anderson's stress inversion is the orientation of conjugate faults, the underlying theory is faultless.

### 9.3.2 Generation 2: inversion using slickenlines or focal mechanisms

The second generation of paleostress analysis was introduced in the middle of the last century when Wallace (Wallace, 1951) analyzed the maximum shear stress (tangential traction) on planes of arbitrary orientation for a homogeneous stress state using Cauchy's Formula (e.g. Jaeger et al., 2007, p.31). Appealing to laboratory results and Mohr's theory (Jaeger et al., 2007, p.94) , Wallace proposed that "faults will tend to concentrate at orientations tangent to a cone, with apex angle less than 90°, which has the axis of greatest compressive stress as its axis..." and that "Orientation of net slip on faults can be correlated almost directly with orientation of maximum shearing stress...". He suggested that "If a complete picture of fault-plane orientations and net-slip orientations on several faults is available, it should be possible to determine with some degree of certainty the orientation and nature of the stress system producing the faults."

Taking a somewhat different approach conceptually, Bott (Bott, 1959) contemplated the likely presence of strength inhomogeneity in the form of older faults, joints, and cleavage. Apparently supposing that whatever perturbation in the stress field due to the formation

of these structures had relaxed, he suggested "These planes would remain 'unnoticed' until the shearing stress within them should exceed the strength...". Furthermore, Bott suggested "...fracture would occur within the preferred plane in which the strength was first exceeded, and the direction of the initial slip would be defined by the direction of the greatest shearing stress within the plane". Bott then preceded, as Wallace (Wallace, 1951) did, to employ Cauchy's Formula (e.g. Jaeger et al., 2007, p.31) to derive the equation relating the shear stress (tangential traction), $\tau$, to the principal stress magnitudes $\sigma_1 \geq \sigma_2 \geq \sigma_3$ in a homogeneous stress field:

$$\begin{aligned} \tau^2 &= \sigma_1^2 n_1^2 + \sigma_2^2 n_2^2 + \sigma_3^2 n_3^2 - (\sigma_1^2 n_1^2 + \sigma_2^2 n_2^2 + \sigma_3^2 n_3^2)^2 \\ &= (\sigma_1 - \sigma_2)^2 n_1^2 n_2^2 + (\sigma_2 - \sigma_3)^2 n_2^2 n_3^2 + (\sigma_3 - \sigma_1)^2 n_3^2 n_1^2 \end{aligned} \tag{9.3}$$

Here the principal stress directions are coincident with the coordinate axes and $(n_1, n_2, n_3)$ are the direction cosines for the unit normal to the plane of interest. In some of the modern literature on paleostress analysis the coincidence of the tangential traction (direction of maximum resolved shear stress) and the slip direction is referred to as the 'Wallace-Bott' hypothesis.

Six quantities are necessary to define the six independent components of the stress tensor at a point or in a volume subject to a homogeneous stress state. These quantities may be taken as the three principal stresses $\sigma_1, \sigma_2, \sigma_3$ and the three Euler angles $(\psi, \theta, \phi)$ that define the principal stress axes, for example with respect to a geographic coordinate system. However, given only data on the slip direction (assumed coincident with that of the maximum resolved shear stress) on arbitrary planes, one can only constrain the Euler angles and a non-dimensional measure of the shape of the deviatoric stress tensor (Etchecopar et al., 1981; Angelier, 1984). This can be understood by noting that the direction of the maximum resolved shear stress depends on principal stress differences (Ramsay and Lisle, 2000), which can be expressed as:

$$\phi = \frac{\sigma_2 - \sigma_3}{\sigma_1 - \sigma_3} \tag{9.4}$$

In typical inverse problems following the Wallace-Bott methodology the directions of the remote principal stresses and the ratio of their magnitudes are constrained by analyzing field data on fault orientations and slip directions as inferred from striations such as slickenlines on exposed fault surfaces (e.g. Carey and B., 1974; Etchecopar et al., 1981; Angelier et al., 1982; Angelier, 1984; Gephart, 1990; Michael, 1987; Reches, 1987; Fry, 1999; Shan et al., 2006). The adoption of this methodology is facilitated by an instructive exposition and computer codes in the textbook by Ramsay & Lisle (Ramsay and Lisle,

2000) and by the availability of other computer codes (e.g. Huang, 1988; Hardcastle and Hills, 1991; Orife et al., 2002). The enthusiastic implementation of the methodology by the structural geology community is witnessed by global compilations of paleostress results from 250 sites for the World Stress Map Project (Reinecker et al., 2004) and from 2,791 independently chosen sites (Lisle et al., 2006) for a Special Issue of the Journal of Structural Geology on "New Dynamics in Palaeostress Analysis" (Blenkinsop, 2006). Readers are referred to this special issue for a more extensive coverage of this methodology and references to the literature.

A closely related methodology has developed in parallel with, and sometimes intertwined with geological paleostress analysis in which seismological data are used to identify the quadrants that contain the so-called $P$ and $T$ axes for a given earthquake focal mechanism (e.g. McKenzie, 1969; Aki and Richards, 2002). Because the fault plane generally is not available to the seismologist, they face the additional ambiguity of two orthogonal would-be fault orientations that stem from the representation of seismic sources as double-couple force systems (Vasseur et al., 1983; Michael, 1987; Gephart, 1990; Lay and Wallace, 1995). Some researchers associate $P$ and $T$ with the axes of greatest shortening and greatest extension, that is principal strains or strain rates (Marrett and Allmendinger, 1990; Twiss et al., 1993; Twiss and Unruh, 1998), while others associate $P$ and $T$ with the axes of greatest and least compression, that is principal stresses (Gephart, 1990; Julien and Cornet, 1987; Michael, 1987; Jones, 1988; Ramsay and Lisle, 2000) for the fault in question.

While this second generation of paleostress analysis employs data on the orientation of faults and slickenlines, or earthquake focal mechanisms, the underlying theory is faultless. In other words the mechanical role played by faults in the tectonic deformation is not included explicitly in the analysis.

### 9.3.3 Generation 3: inversion using heterogeneous stress fields

At the same time that faultless paleostress analysis (generations 1 and 2) was being developed and refined, geologists and geophysicists sought to understand the origin and evolution of faults, and the tectonic history of faulted regions, by relating fault orientation and slip direction to the state of stress in Earths crust using forward models. For example, Anderson (Anderson, 1942, Ch. 7) calculated and interpreted the stress perturbations near a model fault using the solution of Inglis (Inglis, 1913) for a highly eccentric elliptical hole in an elastic plate. In typical forward problems the equations of motion are solved with a prescribed remote stress state as boundary conditions, yielding the local stress, strain, and

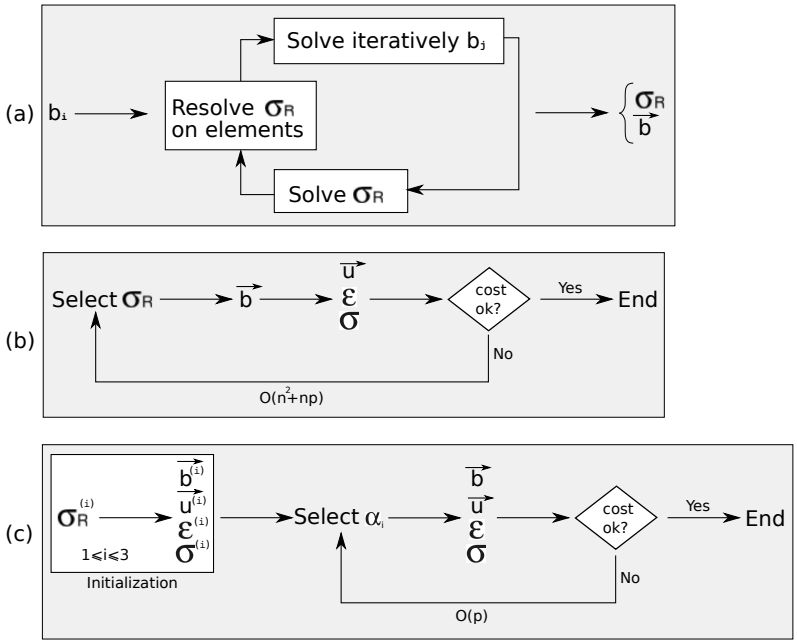


FIGURE 9.2: Various methods for recovering paleostress. (a) Technique as described by Kaven et al. (Kaven, 2009). (b) Monte-Carlo method without optimization. (c) The method described in this paper using the principle of superposition, which drastically reduces the complexity of the model.

displacement fields, and the slip distributions over the model faults (e.g. Chinnery, 1961, 1963; Pollard et al., 1993; Burgmann and Pollard, 1994; Willemse et al., 1996; Maerten et al., 1999). In these forward models the faults are explicitly defined in terms of their geometry and boundary conditions are prescribed in terms of tractions or displacement discontinuities. In this paper we take the same approach, but consider the inverse problem: given the fault geometry and data on slip, or stress perturbations as interpreted, for example, from secondary fractures, what was the tectonic (remote) stress state?

The idea of using a full mechanical scenario is not new for doing paleostress inversion (e.g., see Kaven, 2009). However, using multiple types of data to better constrain the inversion is new and is presented in this paper. Data sets are of two types. Those which provide only orientation information (such as fractures and secondary fault's planes with internal friction angle, as well as fault striations), and those which provide magnitude information (e.g., fault slip, GPS, InSAR data set).

In (Kaven, 2009), the paleostress inversion was essentially computed using slip measurements on fault's planes ($b_i$ in figure 9.2 a). The method relies on an algorithm that has two steps: (i) use the initial remote stress tensor $\sigma_R$, resolve it onto the fault elements that have no relative displacement data, and solve for the unknown relative displacements ($b_j$ in figure 9.2 a); (ii) use the computed and known relative displacements to solve for $\sigma_R$

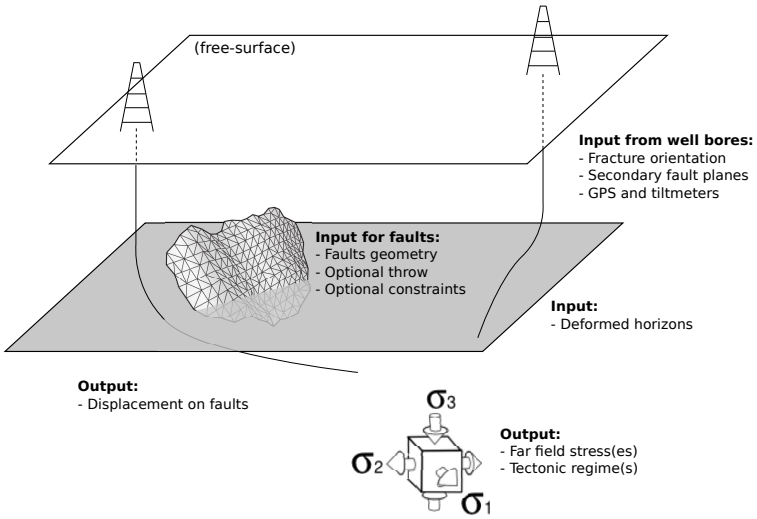


FIGURE 9.3: Sketch of a common geomechanical problem. The faults geometry is known (and optionally, measured fault throw and imposed inequality constraints such as normal, thrust, ...). The user has access to data from well bores (fracture orientation, in-situ stress measurement, secondary fault planes) geodetic data (InSAR, GPS and tilt-meter) as well as interpreted horizons. The goal of the presented technique is to recover the remote stress state and tectonic regime for the tectonic event(s) as well as the displacement discontinuity on faults, and then to have an estimate of the displacement and perturbed strain and stress fields anywhere within the model.

(Fig. 9.2.a). An iterative solver, that cycles between steps (i) and (ii) until convergence, is used.

Another method can be imagined based on a Monte-Carlo algorithm. It is outline in figure (9.2 b). However, this technique proves to be unfeasible since it requires a long computation time, and for which the complexity is of $O(n^2 + p)$, where $n$ and $p$ are the number of triangular elements making the faults and the number of data points, respectively. For a given simulation, a random far field stress $\sigma_R$ is chosen, and the corresponding displacement discontinuity $\mathbf{b}$ on faults are computed. Then, as a post-process at data points and depending on the type measurements, the cost functions are computed using either the displacement, strain or stress field. For hundreds of thousands of simulations, the best cost (close to zero) is retained as a solution.

In this paper, we extend the inversion for any kind of data that can be combined and weighted together. We show that it provides a fast and reliable way of doing stress inversion. Fig 9.3 depicts a typical problem of paleostress. The fault geometries are known as well as data from well bores (fracture orientation, secondary fault planes, GPS and tilt-meter data set). The goal of the technique detailed here is to recover the tectonic event(s) as well as the displacement discontinuity on faults using such data set, and then to have an estimate of the displacement and perturbed strain and stress field anywhere

within the medium, using only data available from seismic interpretation, well bores and field observations.

We show in the following that the use of the principle of superposition allows one to do parameter estimations in a very fast way, each simulation being done in constant time (section 9.4). Applications of such method are developed in sections 9.5, 9.6, 9.7 and 9.8.

## 9.4 Theory

In this section, we give an overview of the technique by briefly describing the numerical method (section 9.4.1), the reduced remote tensor used for the simulation (section 9.4.2) and the principle of superposition (section 9.4.3). Finally, we provide an estimate of the complexity in section 9.4.4.

### 9.4.1 Modeling using iBem3D

The formulation is done using iBem3D, the successor of Poly3D (Thomas, 1993; Maerten et al., 2005) and which is a boundary element code based on the analytical solution of an angular dislocation in a homogeneous or inhomogeneous (Maerten and Maerten, 2008) elastic whole- or half-space (Comninou and Dundurs, 1975). We choose to use an iterative solver (Maerten et al., 2009) for speed considerations (Maerten, 2010) and parallelization on multicore architectures. However, inequality constraints cannot be used as they are non linear and the principle of superposition does not apply. In this code, faults are represented by triangulated surfaces with discontinuous displacement. The advantage compared to Okada's code (Okada, 1985) is that three-dimensional fault surfaces more closely approximate curviplanar surfaces and curved tip-lines without introducing overlaps or gaps. Mixed boundary conditions are prescribed, and when traction boundary conditions are specified, we have to solve for the unknown Burgers's components. After the system is solved, it is possible to compute anywhere, within the whole- or half-space, displacement, strain or stress at observation points as a post-process. Specifically, the stress field at any observation point is given by the perturbed stress field due to slipping faults plus the contribution of the remote stress. Consequently, knowing only the perturbed stress field due to the slip on faults is not enough. Moreover, the estimation of the fault slip from seismic interpretation is only given along the dip-direction. Nothing is known along the strike-direction, and a full mechanical scenario is necessary to recover the unknown components of the slip vector as it will impact the perturbed stress field.

Changing the imposed far field stress (orientation and or relative magnitudes) will modify the slip distribution and consequently the perturbed stress field. In general, a code such as iBem3D is well suited for computing the full displacement vectors on faults (see for example Maerten et al., 1999; Maerten, 2000; Muller et al., 2003, among others), and was intensively optimized using the $\mathcal{H}$-Matrix technique (Maerten, 2010). The main unknown for the modeling remains the estimation of the far field stress that has to be imposed as boundary conditions.

### 9.4.2 Reduced far field stress tensor

A model composed of multiple fault surfaces is subjected to a constant far field stress tensor $\sigma_R$ defined in the global coordinate system by:

$$\sigma_R = \begin{bmatrix} a_{11} & a_{12} & a_{13} \\ & a_{22} & a_{23} \\ & & a_{33} \end{bmatrix} \tag{9.5}$$

If we suppose a sub-horizontal far field stress (Anderson, 1905) (the present methodology is not restricted to that case), Eq. 9.5 simplify into:

$$\sigma_R = \begin{bmatrix} a_{11} & a_{12} & 0 \\ & a_{22} & 0 \\ & & a_{33} \end{bmatrix} \tag{9.6}$$

Since the addition of an hydrostatic stress does not change $\sigma_R$, it is written:

$$\sigma_R = \begin{bmatrix} a_{11} - a_{33} & a_{12} & 0 \\ & a_{22} - a_{33} & 0 \\ & & 0 \end{bmatrix} = \begin{bmatrix} \bar{a}_{11} & a_{12} \\ & \bar{a}_{22} \end{bmatrix} \tag{9.7}$$

Consequently, we end up with the definition of a far field stress with three unknowns, namely $\{\bar{a}_{11}, \bar{a}_{22}, a_{12}\}$.

The far field stress tensor, as defined in Eq. 9.7, can be computed using only two parameters instead of the three $\{\bar{a}_{11}, \bar{a}_{22}, a_{12}\}$. Using the spectral decomposition of the reduced $\sigma_R$, we have:

$$\sigma_R = R_\theta^T \sigma R_\theta \tag{9.8}$$

where

$$\sigma = \begin{bmatrix} \sigma_1 & 0 \\ 0 & \sigma_2 \end{bmatrix} \tag{9.9}$$

is the matrix of principal values, and

$$R_\theta = \begin{bmatrix} \cos\theta & -\sin\theta \\ \sin\theta & \cos\theta \end{bmatrix} \tag{9.10}$$

is the rotation matrix around the global z-axis (since we assume a sub-horizontal stress tensor). By writing:

$$\sigma_2 = k\sigma_1 \tag{9.11}$$

eq. 9.8 transforms into:

$$\sigma_R(\theta, k) = \sigma_1 R_\theta^T \begin{bmatrix} 1 & 0 \\ 0 & k \end{bmatrix} R_\theta \tag{9.12}$$

Omitting the scaling factor $\sigma_1$ due to Property 1 (see section 9.6.2.2), $\sigma_R$ can be expressed as a functional of two parameters $\theta$ and $k$:

$$\sigma_R(\theta, k) = R_\theta^T \begin{bmatrix} 1 & 0 \\ 0 & k \end{bmatrix} R_\theta \tag{9.13}$$

These two parameters are naturally bounded by:

$$\begin{cases} -\pi/2 & \leq \theta \leq \pi/2 \\ -10 & \leq k \leq 10 \end{cases} \tag{9.14}$$

if we suppose that uniaxial remote stress starts to occur when $k \geq 10$. Note that for $k = 1$, we find an hydrostatic stress tensor, which has no effect on a model. Note also that using a lithostatic far field stress tensor (therefore a function of depth $z$), does not invalidate the presented technique, and Eq. 9.13 transforms into:

$$\sigma_R(\theta, k, z) = z R_\theta^T \begin{bmatrix} 1 & 0 \\ 0 & k \end{bmatrix} R_\theta \tag{9.15}$$

and is linearly dependent on $z$.

We will use the simplified tensor definition given by Eq. 9.13 in the coming sections to determine $(\theta, k)$, or equivalently $(\alpha_1, \alpha_2, \alpha_3)$, according to measurements.

### 9.4.3 Principle of superposition

The basic idea of the method proposed in this paper is to use the principle of superposition, a well known principle in linear elasticity, to recover the displacement, strain and stress at any observation point $P$ using the pre-computed specific values from linearly independent simulations. This principle stipulates that a given value $f$ can be determined by a linear combination of specific solutions. In the present method, recovering a far field stress implies to recover the three parameters $\{\bar{a}_{11}, \bar{a}_{22}, a_{12}\}$. Therefore, the number of linearly independent solutions must be three. In other words:

$$\begin{aligned} f = F(\sigma) &= F\left(\alpha_1\sigma^{(1)} + \alpha_2\sigma^{(2)} + \alpha_3\sigma^{(3)}\right) \\ &= \alpha_1 F\left(\sigma^{(1)}\right) + \alpha_2 F\left(\sigma^{(2)}\right) + \alpha_3 F\left(\sigma^{(3)}\right) \\ &= \alpha_1 f_1 + \alpha_2 f_2 + \alpha_3 f_3 \end{aligned} \tag{9.16}$$

where $(\alpha_1, \alpha_2, \alpha_3)$ are real numbers, and $\sigma^{(i)}$ (for $i = 1$ to 3) are three linearly independent remote stress tensors. If we choose $F$ to be the strain, stress or displacement Green's functions, then the resulting values $\epsilon$, $\sigma$ and $u$ at $P$ can be expressed as a combination of three specific solutions:

$$\left\{ \begin{array}{lcll} \epsilon_P &=& \alpha_1\epsilon_P^{(1)} + \alpha_2\epsilon_P^{(2)} + \alpha_3\epsilon_P^{(3)} & (a) \\ \sigma_P &=& \alpha_1\sigma_P^{(1)} + \alpha_2\sigma_P^{(2)} + \alpha_3\sigma_P^{(3)} & (b) \\ u_P &=& \alpha_1 u_P^{(1)} + \alpha_2 u_P^{(2)} + \alpha_3 u_P^{(3)} & (c) \end{array} \right. \tag{9.17}$$

Similarly, using $(\alpha_1, \alpha_2, \alpha_3)$ allows one to recover the displacement discontinuities on the faults:

$$b_e = \alpha_1 b_e^{(1)} + \alpha_2 b_e^{(2)} + \alpha_3 b_e^{(3)} \tag{9.18}$$

and any far field stress is also given by as a combination of the three parameters:

$$\sigma_R = \alpha_1\sigma_R^{(1)} + \alpha_2\sigma_R^{(2)} + \alpha_3\sigma_R^{(3)} \tag{9.19}$$

### 9.4.4 Complexity estimate

Changing $\sigma_R$ usually requires recomputing the entire model in order to determine the corresponding unknown displacement discontinuities. Then, at any observation point $P$, the stress is determined as a super imposition of the far field stress $\sigma_R$ and the perturbed stress field due to slipping elements. For a model made of $n$ triangular discontinuous elements, computing the stress state at point $P$ requires first to solve for the unknown displacement

discontinuities on triangular elements (for which the complexity is of $O(n^2)$), and then approximately $350n$ multiplications using the standard method. Using the principle of superposition does not required recomputing the unknown displacement discontinuities on triangular elements, and only 18 multiplications are needed. Note that the complexity is independent of the number of triangular elements within the model, and is constant in time.

We now give some direct applications of the method for real time evaluation of the deformation and perturbed stress field while the user changes the far field stress (section 9.5). Paleostress estimation using different data sets is presented in section 9.6. A method to recover multiple tectonic phases is explained in section 9.7, and we show how this method can be used for quality control on fault interpretation in section 9.8.

## 9.5 Real time computation

Before developing the paleostress inversion, we briefly give a method to compute in real time the displacement discontinuity on faults as well as the displacement, strain and stress fields at observation points while varying the orientation and/or magnitude of the far field stress.

If the tectonic stress $\sigma_R$ is given and three independent solutions are known, there exist a unique triple $(\alpha_1, \alpha_2, \alpha_3)$ for which Eq. 9.19 is honored, and Eq. 9.17 and 9.18 can be applied. In matrix form, Eq. 9.19 writes:

$$\begin{bmatrix} \sigma_{00}^{(1)} & \sigma_{00}^{(2)} & \sigma_{00}^{(3)} \\ \sigma_{01}^{(1)} & \sigma_{01}^{(2)} & \sigma_{01}^{(3)} \\ \sigma_{11}^{(1)} & \sigma_{11}^{(2)} & \sigma_{11}^{(3)} \end{bmatrix} \begin{Bmatrix} \alpha_1 \\ \alpha_2 \\ \alpha_3 \end{Bmatrix} = \begin{Bmatrix} \sigma_{00}^{R} \\ \sigma_{01}^{R} \\ \sigma_{11}^{R} \end{Bmatrix} \tag{9.20}$$

or in compact form:

$$A_\sigma \alpha = \sigma_R \tag{9.21}$$

Since the three particular solutions $\sigma^{(i)}$ are linearly independent, the system can be inverted, which gives:

$$\alpha = A_\sigma^{-1} \sigma_R \tag{9.22}$$

In Eq. 9.22, $A_\sigma^{-1}$ is pre-computed at initialization. Given a user remote stress $\sigma_R$, we recover the three parameters $(\alpha_1, \alpha_2, \alpha_3)$, then the fault slip as well as the displacement,

strain and stress field are computed in real time using Eq. 9.18 and 9.17, respectively. To do so, it is necessary to store, at initialization, the three particular solutions of the displacement, strain and stress at each observation point, as well as the displacement discontinuity on the faults. This technique allows the user to vary the orientation and magnitude of $\sigma_R$, and to display interactively the associated deformation and perturbed stress field.

## 9.6 Paleostress inversion using field measurements

As seen in section 9.4.1, the main unknown while doing forward modeling for the estimation of the slip distribution on faults, and consequently the associated perturbed stress field, are the orientation and relative magnitudes of the far field stress $\sigma_R$.

If field measurements are known at some given observation points (e.g. displacement, strain and/or stress, fractures orientation, secondary fault planes that formed in the vicinity of major faults), then it is possible to recover the triple $(\alpha_1, \alpha_2, \alpha_3)$ and therefore for the tectonic stress $\sigma_R$ (section 9.6.2) and the corresponding tectonic regime (see appendix). This section describes the method of resolution as well as the cost functions to minimize different types of data.

### 9.6.1 Method of resolution

Using a Monte Carlo method (Hammersley and Handscomb, 1975; Rubinstein, 1981) allows one to find the parameters $(\alpha_1, \alpha_2\, \alpha_3)$ which minimize the cost functions given three independent far field stresses (see Eq. 9.19). However, even if $(\alpha_1, \alpha_2\, \alpha_3)$ is a 3-dimensional parameters-space, we saw in section 9.4.2 that it can be reduced to two dimensions (namely, the parameters $\theta$ and $k$), the conversion being given by Eq. 9.22 (see also figure (9.2.c) and algorithm 9.1 for a detailed description). Consequently, we drastically speedup the searching method by reducing the parameters-space by one dimension.

A simple sampling method can be done by considering a two-dimensional rectangular domain for which the axes correspond to $\theta$, and $k$. The 2D-domain is sampled randomly with $n_p$ points, and the associated cost function (defined in the coming sections) is used to determine the point where we obtain the minimum cost. A refinement is then created around the selected point and the procedure is repeated with a smaller domain. Algorithm 9.1 depicts a simplified version of the procedure, for which there is no refinement.

Of course, the sampling method presented here can be greatly optimized by various techniques (McKay et al., 1979).

**Algorithm 9.1**: Paleostress estimation

**Input:** Faults geometry
**Input:** Data set
**Output:** $\sigma_R$ // *the estimated paleostress*
**Initialization:** Compute 3 simulations using 3 linearly independent $\sigma_R^{(i)}$ $(1 \leq i \leq 3)$ and the faults. Store the resulting displacement and stress fields at data points, and displacement discontinuity at faults if necessary.
**Initialization:** Pre-compute $A_\sigma^{-1}$ (see Eq. 9.22)
**Let** c= 1 // *initial cost*
**Let** $\bar{\alpha} = (0, 0, 0)$ // *initial* $(\alpha)$ *solution*
**for** $i = 1$ *to* $n_p$ **do**
    Randomly generate $\theta \in [-\pi/2, \pi/2]$
    Randomly generate $k \in [-10, 10]$
    // *Convert* $(\theta, k) \in \Re^2$ *to* $(\alpha) \in \Re^3$:
    Compute $R_\theta$ using Eq. 9.10
    Compute $\sigma_R(\theta, k)$ using Eq. 9.13
    Compute $\alpha$ using Eq. 9.22
    // *Compute the corresponding cost*:
    $d =$ *cost*($\alpha$, data set)
    **if** $d \leq c$ **then**
        $\bar{\alpha} = \alpha$
        $c = d$
    **end**
**end**
$\sigma_R = \sum_{i=1}^{3} \bar{\alpha}_i \sigma_R^{(i)}$

To see the benefit of the principle of superposition combined with a Monte Carlo method (Fig. 9.2.c) compared to a naive method (Fig. 9.2.b), we can imagine a model composed of $3,000$ triangular elements. To compute the displacement discontinuity on faults, the model takes approximately $30s$, and $5s$ to compute the stress at 200 data points. Using the principle of superposition, recovering the paleostress using $10,000$ random simulations takes $1mn40s$. Using the naive method (i.e. recomputing the displacement discontinuity on faults for each simulation), would required 4 days.

### 9.6.2 Geologic, geophysical, and geodetic data sets

The particularity of this method lies in a fact that many different kinds of data sets can be used to constrain the inversion. We present in the following sections two groups of

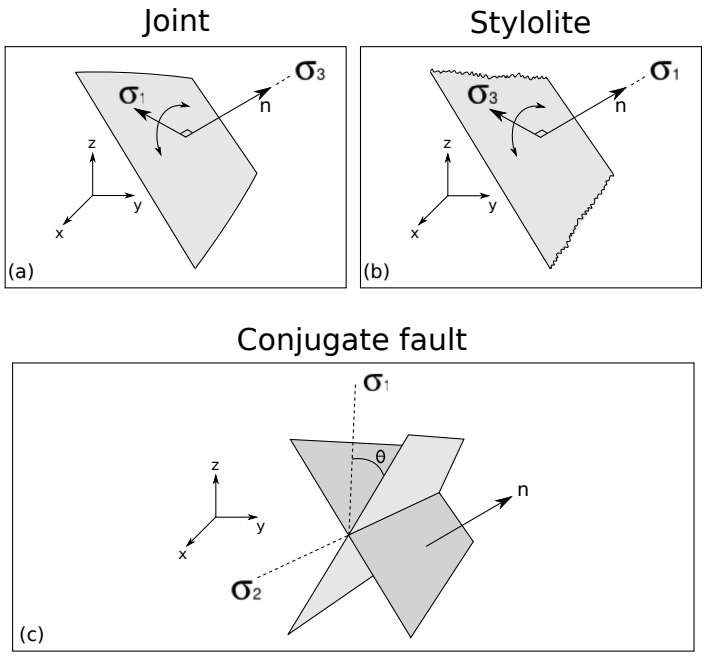


FIGURE 9.4: Fracture and conjugate fault-planes. (a) Orientation of $\sigma_3$ relatives to an opening fracture (joints, veins, dikes) given by its normal $\mathbf{n}$ in 3D. (b) same as (a) but for a pressure solution seam with stylolites. (c) Orientation of $\sigma_1$ and $\sigma_2$ relative to a conjugate fault-planes given by one of the normal $\mathbf{n}$ in 3D and the internal friction angle $\theta$.

data: the first one includes only orientation information and the second includes with displacement and/or stress magnitude information.

#### 9.6.2.1 Data sets containing only orientation information

**Using fractures and stylolites orientations** For opening fractures (joints, veins, dikes) the orientation of the normal to the fracture plane indicates the direction of the least compressive stress direction ($\sigma_3$). Similarly, the normals to pressure solution seams and stylolites indicate in the direction of the most compressive stress ($\sigma_1$). We show that using measurements of the orientations of fractures, pressure solution seams and stylolites allows one to recover the tectonic regime which generated such features.

At any observation point $P$, the local perturbed stress field can be determined easily from a numerical point of view by using three linearly independent simulations. The goal is to determine the best fit of the far field stress $\sigma_R$, therefore parameters $\alpha_1$, $\alpha_2$ and $\alpha_3$, given some orientations of opening fracture planes for which the normals coincide with the directions of the least compressive stress $\sigma_1^P$ at $P$, or equivalently for which the plane of the fracture contains the most compressive stress $\sigma_3$ (see Fig. 9.4.a and b). By varying $(\alpha_1, \alpha_2, \alpha_3)$, the state of stress at any observation point $P$ can be computed quickly using

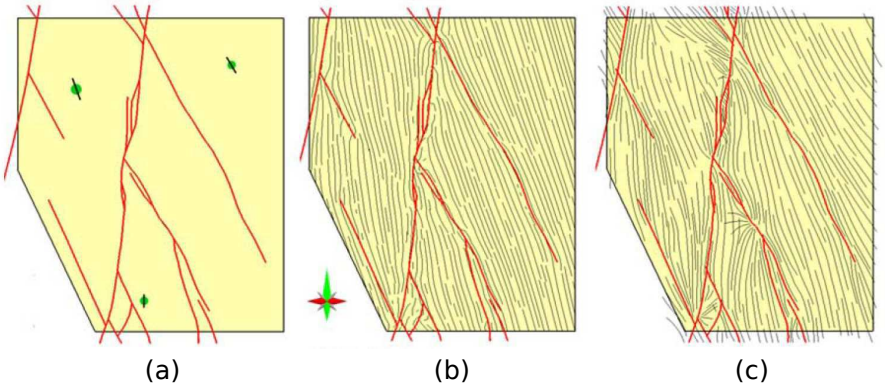


FIGURE 9.5: Example of a geomechanically-based fracture modeling from outcrop fault data and observed three fracture data points using the method describe in this paper. (a) model configuration showing the three fracture orientations used for the inversion (green dots) as well as the interpreted faults (red lines). (b) computed fracture network. (c) observed fracture network in the entire field.

the three pre-computed models. The cost function to minimize is:

$$f_{frac}(\alpha_1, \alpha_2, \alpha_3) = \frac{1}{m} \sum_P \left[1 - \left(\sigma_{\mathbf{3}}^{\mathbf{P}} . \mathbf{n}^{\mathbf{P}}\right)^2\right] \tag{9.23}$$

where . is the dot-product, $\mathbf{n}$ is the normal to a fracture plane, and $m$ is the number of observation points. We end up with the minimization of a function of three parameters:

$$F_{frac} = \min_{\alpha_1,\alpha_2,\alpha_3} \{f_{frac}(\alpha_1, \alpha_2, \alpha_3)\} \tag{9.24}$$

Similarly, for pressure solution seams and stylolites, the cost function is defined as in equation 9.23 using the most compressive stress $\sigma_1$ (see Fig. 9.4.c and d):

$$f_{styl}(\alpha_1, \alpha_2, \alpha_3) = \frac{1}{m} \sum_P \left[1 - \left(\sigma_{\mathbf{1}}^{\mathbf{P}} . \mathbf{n}^{\mathbf{P}}\right)^2\right] \tag{9.25}$$

**Example: Nash Point (UK)** Figure 9.5 displays an example using fracture orientations to determine the far field stress and consequently the perturbed stress field around a complexly faulted outcrop. The right figure presents the observed fracture pattern at NashPoint (Rawnsley et al., 1992) which apparently formed in the presence of the perturbed stress field due to active faults (red lines). In this example, we use only three measurements of fracture orientation (left, green dots) to recover the paleostress and the fault slip distributions. The recovered paleo stress is oriented $N161$ with a ratio of $-1.5$ (strike-slip faulting regime). After the paleostress has been resolved, the predicted fracture pattern (lines perpendicular to the local least compressive stress) is computed on

a dense observation grid (middle figure) and this is compared to the observed fracture pattern.

**Using secondary fault planes** The orientation of secondary fault planes that develop in the vicinity of larger active faults may be estimated using the Coulomb failure criteria (Jaeger et al., 2007; Maerten et al., 2002) defined by:

$$\tan(2\theta) = \frac{1}{\mu} \tag{9.26}$$

where $\theta$ is the angle of the failure planes to the maximum principal compressive stress ($\sigma_1$) and $\mu$ is the coefficient of internal friction. Two conjugate failure planes intersect along $\sigma_2$ and the fault orientation is influenced only by the orientation of the principal stresses and the value of the friction.

The cost function is therefore defined by:

$$f_{fault}(\alpha_1, \alpha_2, \alpha_3) = \frac{1}{2m} \sum_P \left[ \left(\sigma_{\mathbf{2}}^{\mathbf{P}} . \mathbf{n}^{\mathbf{P}}\right)^2 + \left( \frac{|\sin^{-1}\left(\sigma_{\mathbf{1}}^{\mathbf{P}} . \mathbf{n}^{\mathbf{P}}\right)| - \theta}{\pi} \right)^2 \right] \tag{9.27}$$

where $\sigma_1$ is the direction of the most compressive stress and $\sigma_2$ is the direction of the intermediate principal stress. The first term of the right hand side in Eq. 9.27 maintains an orthogonality between the computed $\sigma_2$ and the normal of the fault plane, whereas the second term ensures that the angle between the computed $\sigma_1$ and the fault plane is close to $\theta$ (see Fig. 9.4.e).

**Example 1: Normal and thrust fault** Figure 9.6 shows two synthetic examples of the same model using an inclined planar fault. Initially, the model is constrained by a far field stress and at 200 observation points, where the two conjugate planes are computed using an internal friction angle of 30°. Then, for each observation point, one of the conjugate fault planes is chosen randomly and used as input data for the stress inversion. Figure 9.6 presents the inclination of the two conjugate fault planes for a normal (Fig. 9.6.a) and a thrust (Fig. 9.6.b) fault regime, respectively. For each of them, the plot of the cost function at each observation point is displayed in Fig. 9.7. The recovered tectonic regime, stress ratio and orientation match for both cases.

**Example 2: Oseberg-Syd (Norway)** Figure 9.8 presents an application to faulting in the Oseberg-Syd field off-shore Norway (Maerten et al., 2002). Here the secondary

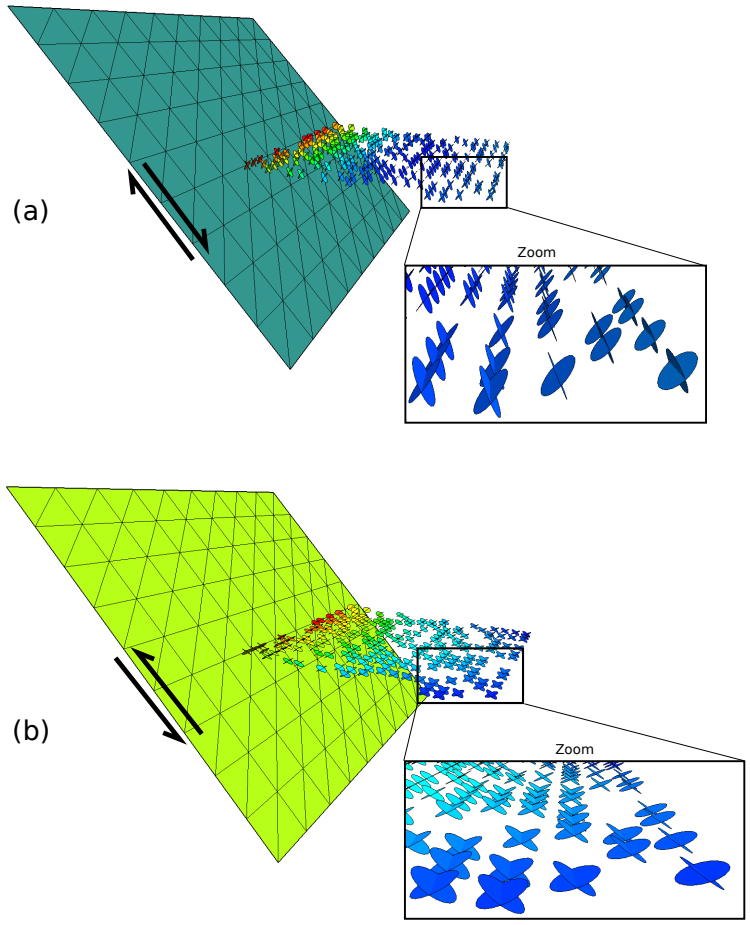


FIGURE 9.6: Method applied to a synthetic example using two conjugate fault planes selected randomly. Dip-azimuth and dip-angle of each conjugate fault planes are used to do the inversion and the internal friction angle is $\theta = 30$. The main active fault is represented by the inclined rectangular plane. (a) Normal fault configuration and (b) thrust configuration.

faults imaged on a seismic survey are used to recover the paleostress state. Figure 9.9 shows the cost distribution for each of the 2063 triangular elements making up the secondary fault surfaces. The plot on top of the figure shows that some fault planes are not well oriented according the recovered far field stress (reddish cost between 0.8 and 1). The recovered paleostress is oriented $N350$ and has a stress ratio of 2.85 (corresponding to a normal faulting regime).

The plot on bottom shows the distribution after removing those anomalous fault planes from the simulation. The new recovered remote stress is now oriented $N346.5$ and has a ratio of 2.7 (normal faulting regime). Estimated paleostress by Maerten et al. (Maerten et al., 2002) using palinspastic restoration for the same region was estimated $N350$ with a ratio of 1.4 (normal faulting regime).

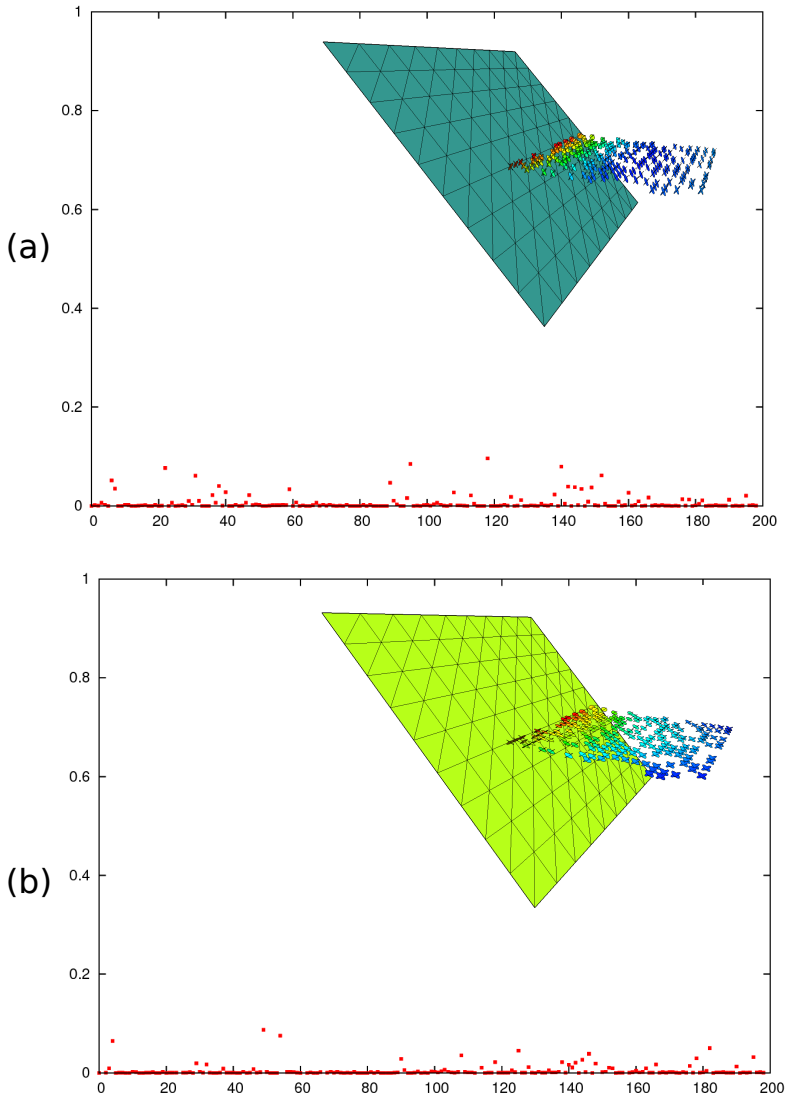


FIGURE 9.7: Cost function for the synthetic example from Fig. 9.6. (a) Normal fault and (b) thrust fault. In both cases, the recovered regional stress tensor, displacement on fault and predicted conjugate fault planes perfectly match the initial synthetic model.

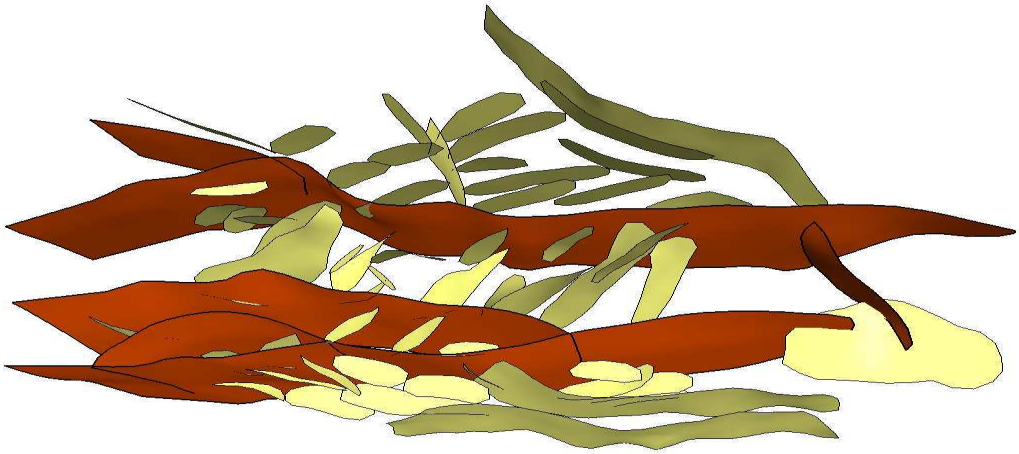

FIGURE 9.8: Method applied to the Oseberg-Syb field, Norway. Major and secondary faults are represented in red and yellow, respectively.

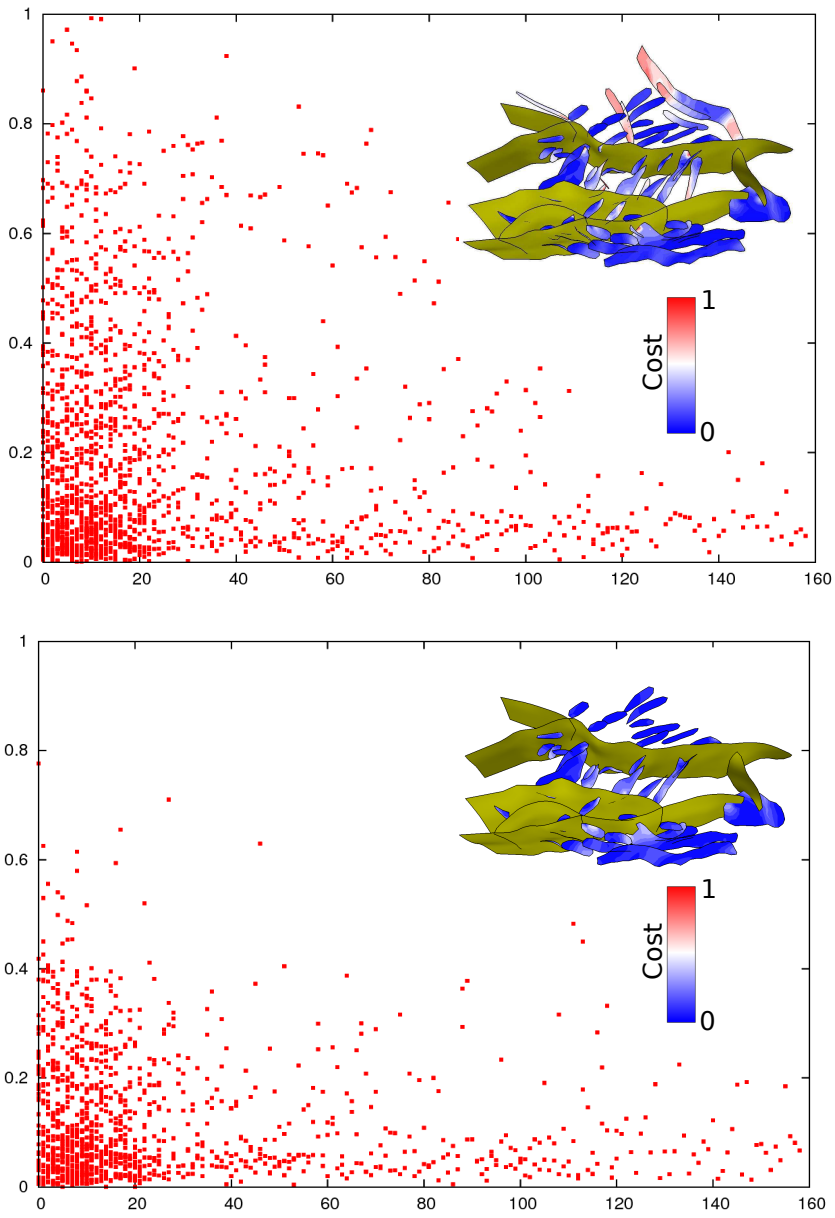


FIGURE 9.9: Plot of the cost for each triangular element making the secondary fault planes for the Oseberg-Syb field. Top: all fault planes are used for the simulation. Bottom: only secondary faults below a given user cost threshold are used.

**Using fault striations** In this case, the cost function is defined as:

$$f_{stri}(\alpha_1, \alpha_2, \alpha_3) = \frac{1}{m} \sum_e (1 - \mathbf{d_e^c}.\mathbf{d_e^m})^2 \tag{9.28}$$

where $\mathbf{d_e^c}$ and $\mathbf{d_e^m}$ represent the normalized slip vector from a simulation and the measured one, respectively.

#### 9.6.2.2 Data sets containing magnitude information

The magnitude of displacements may be used to determine not only the stress orientation, but also the magnitude of the remote stress tensor, instead of just the principal stress ratio. To do so, the procedure is similar to that described previously. However, given Eq. 9.17.c and 9.18, it can be seen that there exists a parameter $\delta$ for which the computed displacement discontinuity on faults and the displacement, strain and stress fields at observation points scale linearly with the imposed far field stress. In other words:

$$\begin{cases} \delta.\sigma_R \Rightarrow \delta.\mathbf{b_e} \\ \delta.\sigma_R \Rightarrow \delta.\mathbf{u_P} \\ \delta.\sigma_R \Rightarrow \delta.\epsilon_P \\ \delta.\sigma_R \Rightarrow \delta.\sigma_P \end{cases} \tag{9.29}$$

This leads to the following property:

**Property 1**:

> Scaling the far field stress by $\delta \in \Re$ scales the displacement discontinuity on faults as well as the displacement, strain and stress fields at observation points by $\delta$.

Using this property, all measurements at data points are globally normalized before any computation and the scaling parameter is noted $\delta_m$ (the simulations are also normalized, but the scaling factor is irrelevant). After the system is solved, the recovered far field stress, displacement and stress fields are scaled back by a factor of $\delta_m^{-1}$.

**Using GPS data** In this case, the cost function is defined as:

$$f_{gps}(\alpha_1, \alpha_2, \alpha_3) = \frac{1}{2m} \sum_P \left[ \left( 1 - \frac{\mathbf{u_P^c}.\mathbf{u_P^m}}{||\mathbf{u_P^c}||.||\mathbf{u_P^m}||} \right)^2 + \left( 1 - \frac{||\mathbf{u_P^m}||}{||\mathbf{u_P^c}||} \right)^2 \right] \tag{9.30}$$

where $u_P^m$ is the measured elevation changed at point $P$ from the horizon and $u_P^c$ is the computed elevation change for a given set of parameters $(\alpha_1, \alpha_2, \alpha_3)$. The first term on the right hand side in Eq. 9.30 represents a minimization of the angle between the two displacement vectors, whereas the second term represents a minimization of the difference of the norm.

**Using InSAR data** In this case we are faced with two possibilities. Either the *global* displacement vectors of the measures are computed using the displacement $u$ along the direction of the satellite line of sight $\mathbf{s}$, which gives:

$$\mathbf{u_P^m} = \mathbf{u_{insar}} = \mathbf{u.s} \tag{9.31}$$

Then the same procedure used for the GPS case is employed with the computed $\mathbf{u_P^c}$.
Or, the computed displacement vectors are computed *along* the satellite line of sight giving:

$$u_P^c = \mathbf{u.s} \tag{9.32}$$

where . is the dot product. The cost function is consequently given by:

$$f_{insar}(\alpha_1, \alpha_2, \alpha_3) = \frac{1}{m} \sum_P \left(1 - \frac{u_P^c}{u_P^m}\right)^2 \tag{9.33}$$

**Example** Figure 9.10 presents a synthetic example using an InSAR data set. First a forward model is run using one fault plane (Fig. 9.10.a) and one observation grid at the surface of the half-space (red dots in Fig. 9.10.a). A satellite direction is chosen, and for each observation points, the displacement along the satellite line of sight is computed. Then, the procedure described in this paper is applied using the second form of the InSAR cost function (Eq. 9.33). Figure (9.10.b) compares the original interferograms (left) to the recovered one (right). Figure (9.10.c) shows how complex the cost surface can be, even for a simple synthetic model. The surface is a function of $\theta$ and $k$, and the solution is marked by a small black circle. The cost surface was sampled with $500,000$ points (number of simulations), and took 18s on a laptop 2GHz processor with 2GB of RAM running on Linux Ubuntu 8.10 32 bits.

**Using flattened horizon** Using the mean plane of a given horizon (flattened horizon), we compute the change in elevation for each points making the horizon, and use it as in a similar way to the GPS data for which only the $u_z$ component is provided.

**Example** Figure 9.11 shows the result when using such data. Initially, a complex shaped fault is constrained by a far field stress, and will consequently slip to accommodate the remote stress. At each point of an observation plane cross-cutting the fault, we compute the resulting displacement vector and deform the grid accordingly. Then, the inversion takes place using the fault geometry. After flattening the deformed grid, the change in elevation for each point is used to constrain the inversion and to recover the

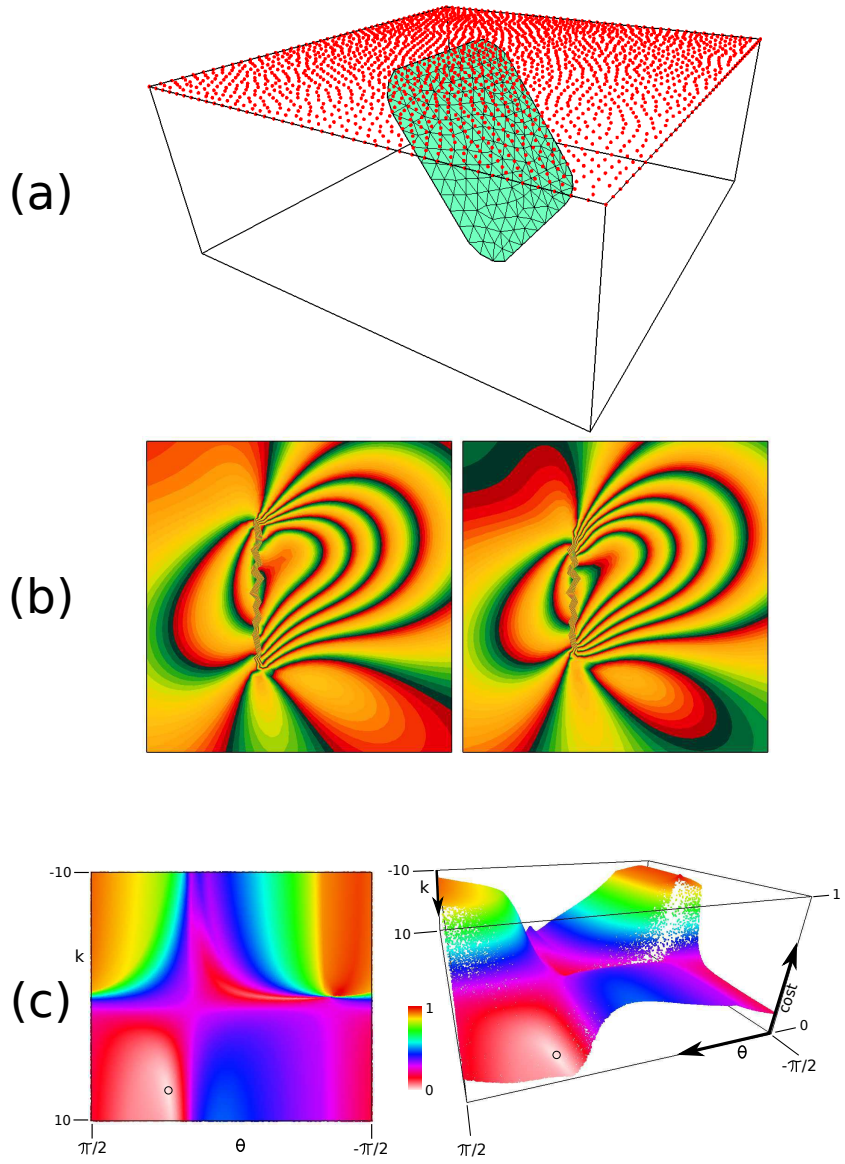


FIGURE 9.10: Method applied to a synthetic example using an InSAR data set. (a) model configuration showing the InSAR data points (red dots) as well as the fault surface. (b) comparison of the fringes from original (left) and recovered (right) InSAR grid. (c) Plot of the cost surface, function of $\theta$ (x-axis) and $k$ (y-axis). Left: top view. Right: perspective. The solution is marked by a small black circle.

previously imposed far field stress as well as the fault slip and the displacement field. The comparison of the original and inverted dip-slip (Fig. 9.11.b) and strike-slip (Fig. 9.11.c) match well (same scale). A good match is also observed for the displacement field at the observation grid (Fig. 9.11.d).

**Using dip-slip information** In this case, the cost function is defined as:

$$f_{ds}(\alpha_1, \alpha_2, \alpha_3) = \frac{1}{m} \sum_e \left(1 - \frac{b_e^c}{b_e^m}\right)^2 \tag{9.34}$$

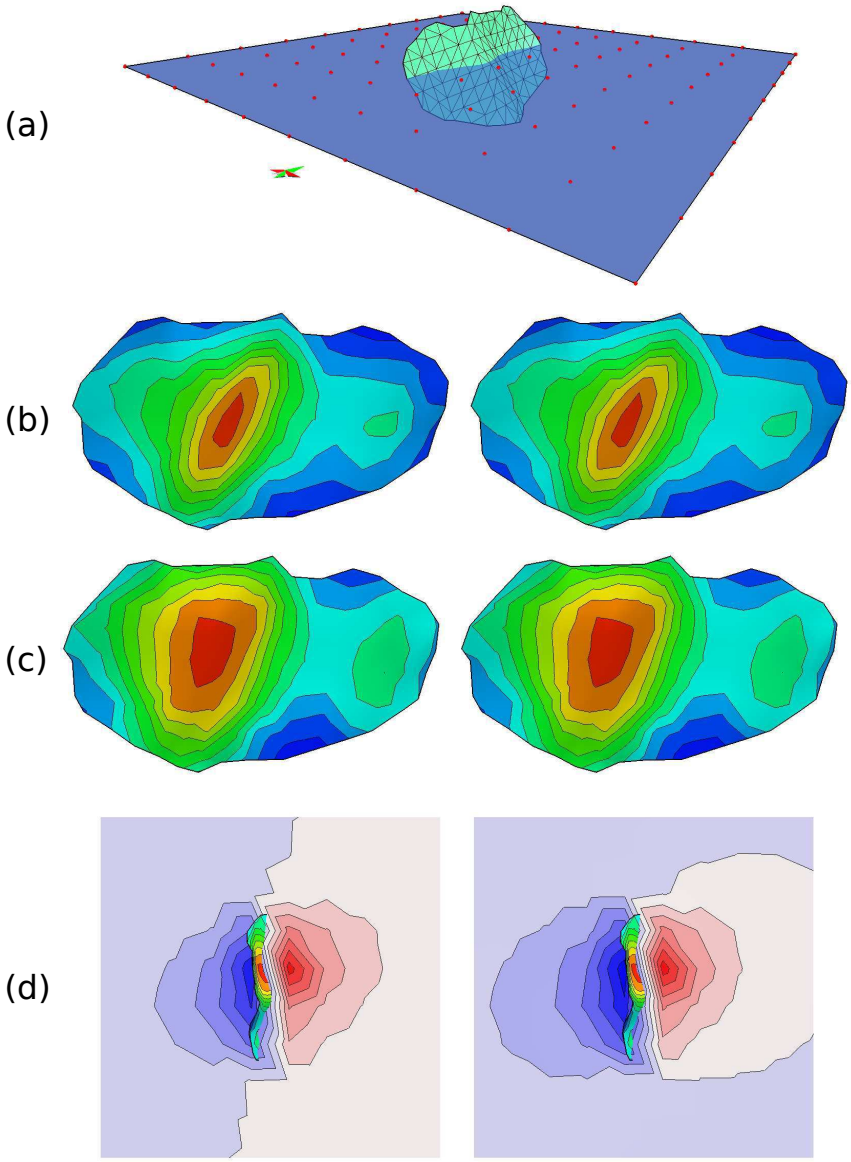


FIGURE 9.11: Method applied to a synthetic example using a flattened horizon. (a) model configuration showing the horizon (red dots) as well as the fault surface. (b) comparison of the original (left) and recovered (right) dip-slip. (c) comparison of the original (left) and recovered (right) strike-slip. (d) original vertical displacement from flattened horizon (left) and recovered (right).

where $b_e^m$ is the measured dip-slip magnitude for a triangular element e, and $b_e^c$ is the computed.

#### 9.6.2.3 Using all available information

Previously described cost functions can be combined to better constrained stress inversion by available data (fault and fracture plane orientation, GPS, InSAR, flattened horizons,

dip-slip measurements from seismic reflection and fault striations). Furthermore, data can be weighted differently, and each datum can also support a weight for each coordinate.

## 9.7 Multiple tectonic events

For multiple tectonic events, it is possible to recover the major ones, e.g. those for which the tectonic regime and/or the orientation and/or magnitude are noticeably different. The algorithm 9.2 presents a way to determine different events from fractures orientation (joints, stylolites, conjugate fault planes) measure along well bores. After doing a first simulation, a cost is attached at each observation point which shows the confidence of the recovered tectonic stress relative to the data attached to that observation point. A cost of zero and one means a good and a bad confidence, respectively (see Fig. 9.7 for an example plot of the cost). By selecting only data points that are under a given threshold value and running another simulation with these points, it is possible to extract a more precise paleostress. Then, the remaining data points above the threshold value are used to run another simulation and the paleostress state to recover another tectonic event. If the graph of the new cost shows disparities, the above procedure is repeated until satisfactory results are achieved. It is worth mentioning that during the determination of the tectonic phases, the observation points are classified in there respective tectonic event. However, the chronology of the tectonic phases remains undetermined.

### 9.7.1 Example

Two overlapping dipping faults are subjected to two tectonic regimes (see Fig. 9.12.a and b). The first one, a normal fault regime, is oriented $N115$ with $S_H/S_h = 0.2$ (Fig. 9.12.c, top). The corresponding fracture orientations (see Fig. 9.12.d) are computed on a grid above the model (red dots in Fig. 9.12.a). The second tectonic regime is oriented $N150$ with $S_H/S_h = -1.5$ (see Fig. 9.12.c, bottom) and corresponds to a strike-slip fault regime. The fractures orientation (Fig. 9.12.d) are computed on a second grid (green dots in Fig. 9.12.a). After a first paleostress estimation is done using the two fracture sets, the corresponding cost is displayed in Figure 9.12.e. It clearly shows two distinct clusters of points (top and bottom of the graph). At this stage the resulting paleo-orientation and stress ratio is irrelevant. Points that have a cost$\leq 0.1$ are selected for a new paleostress estimation (gray box in Fig. 9.12.e). The paleostress is now oriented $N115.1$ with a ratio $S_H/S_h = 0.198$. This effectively corresponds to the first normal fault regime imposed to the synthetic forward model. Using the estimated parameters $\alpha_i$ from this

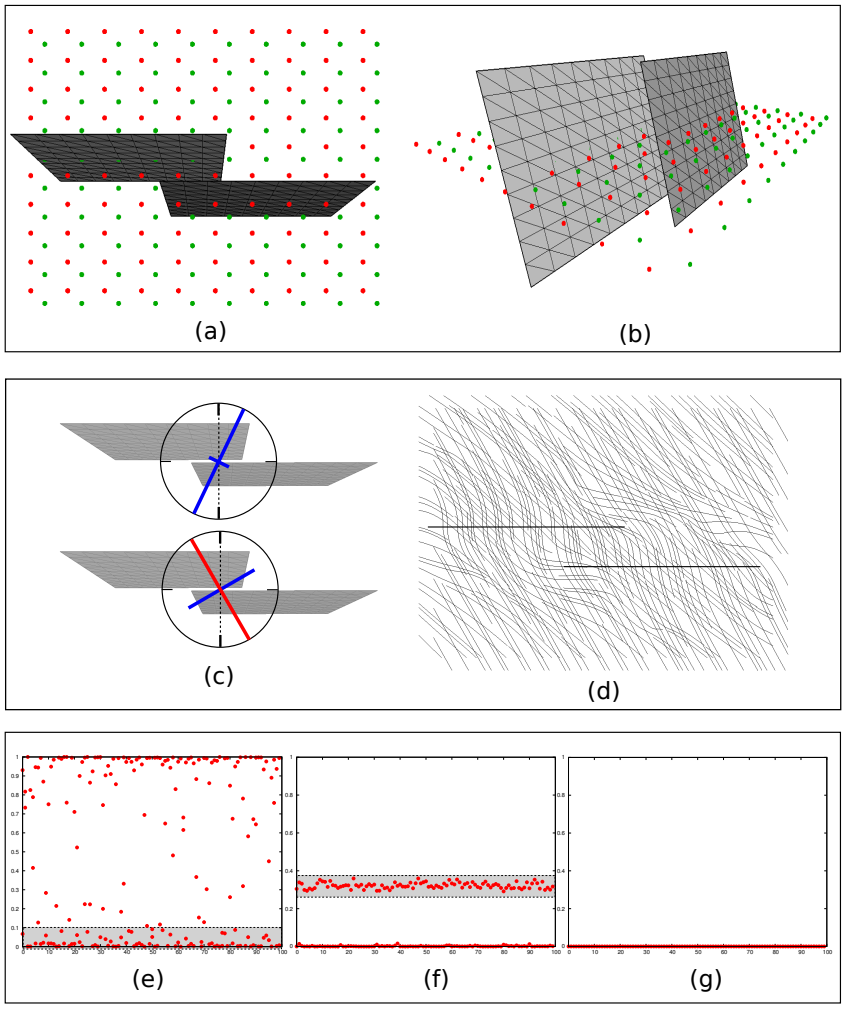


FIGURE 9.12: Different tectonic events. (a) Model configuration showing the two overlapping normal faults (meshes) as well as the two observation grids(red and green dots). On each grid, joint orientations are computed using a given tectonic event (see text). (b) Perspective view of the model. (c) Orientation of the first (top) and second (bottom) far field stresses with relative magnitudes. Blue is for tension and red for compression. (d) Resulting joint sets used for paleostress estimation. (e) Cost function (y-axis) after recovery of a paleostress using joints orientation from the two grids. The x-axis corresponds to the id of the grid points. (f) Resulting cost function after selection of the best points in gray box from (e). (g) Resulting cost function after selection of the remaining points in gray box from (f).

last simulation, a new cost is computed for the two grids (Fig. 9.12.f) which allows to further discriminate the two clusters. Finally, the remaining points (gray box in Fig. 9.12.f) are used to determine the second tectonic event. The recovered paleo-stress is now oriented $N149.98$ with a ratio $S_H/S_h = -1.501$, which corresponds to the second far field stress applied to the synthetic model, and for which the cost is close to zero for all data points (see Fig. 9.12.g).

**Algorithm 9.2**: Detecting multiple tectonic events

**Input:** $\epsilon$ a user threshold in $]0, 1[$
**Input:** $S$ = all fractures from all wells
**Let:** $T = \varnothing$
**while** $S \neq \varnothing$ **do**
    *Simulation:* Compute the cost for each fracture in $S$
    **if** $\max(cost) < \epsilon$ **then**
        **if** $T = \varnothing$ **then**
            Terminate
        **else**
            **Let:** $V = S \cup T$
            **Let:** $S = T = \varnothing$
            **foreach** *point* $p$ *in* $V$ **do**
                **if** $cost(p) \leq \epsilon$ **then** $S$+=$p$
                **else** $T$+=$p$
            **end**
            $\Rightarrow$ Found a tectonic event $\sigma_R$ for fractures in $S$
            $S = T$
            $T = \varnothing$
            **continue**
        **end**
    **end**
    $S$ = fractures below $\epsilon$
    $T$ += fractures above $\epsilon$
**end**

## 9.8 Seismic interpretation quality control

It is useful to have a method for quality control (QC) on interpreted faults geometries from seismic interpretation. The basic idea is to use the fracture orientations from well bores to recover the far field stress and the displacement discontinuities on active faults. Then, the computed displacement field is used to deform the initially flattened horizons. We then compare the geometry of the resulting deformed horizons to the interpreted ones. If some mismatches are clearly identified (e.g., interpreted uplift and computed subsidence), the fault interpretation is possibly false. For example, an interpreted fault might dip in the wrong direction. Note that an unfolded horizon can be approximated by its mean plane, as done in section 9.6.2.2.

## 9.9 Conclusion and perspectives

We have shown using the simple property of superposition inherent to linear elasticity, it is possible to do real-time computation of the perturbed stress and displacement field around a complexly faulted area, as well as the displacement discontinuity on faults. Furthermore, the formulation enables one to do rapid paleostress inversion using multiple types of data such as fracture orientation, secondary fault planes, GPS, InSAR, fault throw and fault slickenlines. Specifically, it was shown that using only fracture orientation and/or secondary fault planes from well bores allows one to recover one or more tectonic events, the recovered stress tensor being given by the orientation and ratio of the principal magnitudes. Applications of these methods ranges from stress interpolation in a complexly faulted reservoir, fractures prediction, quality control on interpreted faults as well as real-time computation of perturbed stress and displacement fields while doing interactive parameter estimation.

## 9.10 Acknowledgments

The authors would like to thank Paul Gillespie from StatoilHydro who providing us data for the Oseberg Syd field and Nash Point.

# References

Aki, K. and Richards, P. (2002). *Quantitative Seismology.* University Science Books, Sausalito, CA.

Anderson, A. (1942). *The Dynamics of Faulting and Dyke Formation with Application to Britain.* Oliver and Boyd, Edinburgh.

Anderson, E. (1905). The dynamics of faulting. *Edinburgh Geol. Soc.*, 8(3):387–402.

Angelier, J. (1984). Tectonic analysis of fault slip data sets. *J. Geophys. Res.*, 89:5835–5848.

Angelier, J., Tarantola, A., Valette, B., and Manoussis, S. (1982). Inversion of field data in fault tectonics to obtain the regional stress - i. single phase fault populations: a new method of computing the stress tensor. *J. Geophys. Res.*, 69:607–621.

Blenkinsop, T. (2006). Kinematic and dynamic fault slip analyses: implications from the surface rupture of the 1999 chi-chi, taiwan, earthquake. *J. Struct. Geol.*, 28(6):1040–1050.

Bott, M. (1959). The mechanics of oblique slip faulting. *Geological Mag.*, 96:109–117.

Burgmann, R. and Pollard, D. D. (1994). Slip distribution on faults: effects of stress gradients, inelastic deformation, heterogeneous host-rock stiffness, and fault interaction. *Journal of Structural Geology*, 16(12):1675–1690.

Carey, E. and B., B. (1974). Analyse thé orique et numérique d'un modélé mecanique élémentaire appliqué à l'étude d'une population de failles. *C.r. Acad. Sci., Paris*, 279:891–894.

Chinnery, M. (1961). The deformation of the ground around surface faults. *Bull. of Seism. Soc. of America*, 51:355–372.

Chinnery, M. (1963). The stress changes that accompany strike-slip faulting. *Bull. of Seism. Soc. of America*, 53:921–932.

Comninou, M. and Dundurs, J. (1975). The angular dislocation in a half space. *Journal of Elasticity*, 5(3):203–216.

Coulomb, C. A. (1773). Sur une application des régles de maximis et minimis à quelques problèmes de statique relatifs à l'architecture. *Acad. Roy. des Sciences Memoires de math. et de physique par divers savans*, 7(343-382).

Etchecopar, A., Vasseur, G., and Daignieres, M. (1981). An inverse problem in microtectonics for the determination of stress tensors from fault striation analysis. *J. Struct. Geol.*, 3(1):51–65.

Fry, N. (1999). Striated faults: visual appreciation of their constraint on possible paleostress tensors. *J. Struct. Geol.*, 21(1):7–21.

Gephart, J. W. (1990). Fmsi: a fortran program for inverting fault/slickenside and earthquake focal mechanism data to obtain the regional stress tensor. *Computers and Geoscience*, 16(7):953–989.

Hammersley, J. M. and Handscomb, D. C. (1975). *Monte Carlo Methods*. Fletcher, Norwich, England.

Hardcastle, K. and Hills, L. (1991). Brute3 and select: Quickbasic 4 programs for determination of stress tensor configurations and separation of heterogeneous populations of fault-slip data. *Computers & Geosciences*, 17(1):23–43.

Huang, Q. (1988). Computer-based method to separate heterogeneous sets of fault-slip data into sub-sets. *J. Struct. Geol.*, 10(3):297–299.

Inglis, C. (1913). Stresses in a plate due to the presence of cracks and sharp corners. volume 55, pages 219–230. Inst. Naval Arch.

Jaeger, J., Cook, N., and Zimmermann, R. (2007). *Fundamentals of Rock Mechanics*. Blackwell Publ., Malden, MA.

Jones, L. (1988). Focal mechanisms and the state of stress on the san andreas fault in southern california. *J. Geophys. Res.*, 93:8869–8891.

Julien, P. and Cornet, F. (1987). Stress determination from aftershocks of the campania-lucania earthquake of november 23, 1980. *Annales Geophysicae*, 5B(3):289–300.

Kaven, O. (2009). *Geometry and mechanics of three-dimensional faults: implications for slip, aftershocks, and paleostress*. PhD thesis, Stanford University, CA, USA.

Lay, T. and Wallace, T. (1995). *Modern Global Seismology*. Academic Press, London, UK.

Lisle, R., Orife, T., Arlegui, L., Liesa, C., and Srivastava, D. (2006). Favoured states of palaeostress in the earth's crust: evidence from fault-slip data. *J. Struct. Geol.*, 28(6):1051–1066.

Maerten, F. (2010). Adaptive cross approximation applied to the solution of system of equations and post-processing for 3d elastostatic problems using the boundary element method. *Engineering Analysis with Boundary Elements*, 34:483–491.

Maerten, F. and Maerten, L. (2008). Iterative 3d bem solver on complex faults geometry using angular dislocation approach in heterogeneous, isotropic elastic whole or half-space. In Brebbia, editor, *Boundary Elements and other Mesh Reduction Methods XXX*, pages 201–208, Southampton. BEM 30, WITpress.

Maerten, F., Maerten, L., and Cooke, M. (2009). Solving 3d boundary element problems using constrained iterative approach. *Computational Geosciences*.

Maerten, F., Resor, P. G., Pollard, D. D., and Maerten, L. (2005). Inverting for slip on three-dimensional fault surfaces using angular dislocations. *Bulletin of the Seismological Society of America*, 95:1654–1665.

Maerten, L. (2000). Variation in slip on intersectiong normal faults: Implications for paleostress inversion. *Journal of Geophysical Research*, 105(25):553–565.

Maerten, L., Gillepsie, P., and Pollard, D. (2002). Effect of local stress perturbation on secondary fault development. *Journal of Structural Geology*, 24:145153.

Maerten, L., Willemse, E. J. M., Pollard, D. D., and Rawnsley, K. (1999). Slip distributions on intersecting normal faults. *Journal of Structural Geology*, 21:259–271.

Malvern, I. (1969). *Introduction to the Mechanics of a Continuum Medium*. Prentice-Hall.

Mandl, G. (1988). *Mechanics of tectonic faulting. Models and basic concepts*. Elsevier, Amsterdam.

Marrett, R. and Allmendinger, R. (1990). Kinematic analysis of fault-slip data. *J. Struct. Geol.*, 12(8):973–986.

McKay, M. D., Beckman, R. J., and Conover, W. J. (1979). A comparison of three methods for selecting values of input variables in analysis of output from a computer code. *Technometrics*, 21:239–245.

McKenzie, D. (1969). The relation between fault plane solutions for earthquakes and the directions of the principal stresses. *Bull. Seismol. Soc. Am.*, 59:591–601.

Michael, A. (1987). Use of focal mechanisms to determine stress: a control study. *J. Geophys. Res.*, 92(B1):357–368.

Muller, J. R., Aydin, A., and Maerten, F. (2003). Investigating the transition between the 1967 mudurnu valley and 1999 izmit earthquakes along the north anatolian fault with static stress changes. *Geophysics Journal International*, 154:471–482.

Okada, Y. (1985). Surface deformation due to shear and tensile faults in a half-space. *Bulletin of the Seismological Society of America*, 75:1135–1154.

Orife, T., Arlegui, L., and Lisle, R. (2002). Dipslip: a quickbasic stress inversion program for analysing sets of faults without slip lineations. *Computers & Geosciences*, 28(6):775–781.

Pollard, D., Saltzer, S., and Rubin, A. (1993). Stress inversion methods: are they based on faulty assumptions? *J. Struct. Geol.*, 15:1045–1054.

Price, N. J. (1966). *Fault and Joint Development in Brittle and Semi-brittle Rock*. Pergamon, London.

Ramsay, J. and Lisle, R. (2000). *The Techniques of Modern Structural Geology. Volume III. Applications of Continuum Mechanics in Structural Geology*. Academic Press, London, U.K.

Rawnsley, K., Rives, T., Petit, J., Hencher, S., and Lumsden, A. (1992). Joint development in perturbed stress fields near faults. *Journal of Structural Geology*, 14:939–951.

Reches, Z. (1987). Determination of the tectonic stress tensor from slip along faults that obey the coulomb yield condition. *Tectonics*, 6(4):849–861.

Reinecker, J., Heidbach, O., Müller, B., Tingay, M., and Connolly, P. (2004). The 2004 release of the world stress map, url. http://www.world-stress-map.org.

Rubinstein, R. Y. (1981). *Simulation and the Monte Carlo Method*. John Wiley and Sons, Inc.

Sato, K. and Yamaji, A. (2006). Uniform distribution of points on a hypersphere for improving the resolution of stress tensor inversion. *J. Struct. Geol.*, 28(6):972–979.

Shan, Y., Li, Z., and Lin, G. (2004). A stress inversion procedure for automated recognition of polyphase fault/slip data sets. *J. Struct. Geol.*, 26(9):919–925.

Shan, Y., Lin, G., Li, Z., and Zhao, C. (2006). Influence of measurement errors on stress estimated from single-phase fault/slip data. *J. Struct. Geol.*, 28(6):943–951.

Thomas, A. L. (1993). Poly3d: a three-dimensional, polygonal element, displacement discontinuity boundary element computer program with applications to fractures, faults, and cavities in the earth's crust. Master's thesis, Stanford University.

Twiss, R., Souter, B., and Unruh, J. (1993). The effect of block rotations on the global seismic moment tensor and patterns of seismic p and t axes. *J. of Geophy. Res.*, 98:645–674.

Twiss, R. and Unruh, J. (1998). Analysis of fault slip inversions: Do they constrain stress or strain rate? *J. of Geophy. Res.*, 103(B6):12205–12222.

Vasseur, G., Etchecopar, A., and Philip, H. (1983). Stress state inferred from multiple focal mechanisms. *Ann. Geophys.*, 1(4-5):291–298.

Voight, B. (1966). Beziehung zwischen großen horizontalen spannungen in gebirge und der tektonik und der abtragung. In *Rock Mech., 1st Congr., Vol 2*, pages 1–56. Lisbon. Int. Soc.

Wallace, R. (1951). Geometry of shearing stress and relation to faulting. *J. of Geology*, 59:118–130.

Willemse, E. J. M., Pollard, D. D., and Aydin, A. (1996). Three-dimensional analyses of slip distributions on normal fault arrays with consequences for fault scaling. *J. Struct. Geol.*, 18:295–309.

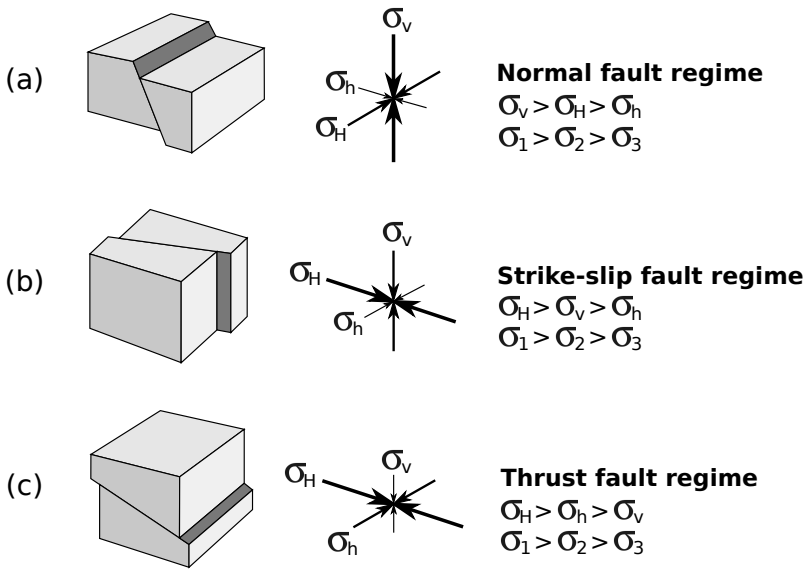


FIGURE 9.13: Tectonic regimes by considering one axis vertical. (a) Normal fault regime: $\sigma_1$ is vertical. (b) Strike-slip fault regime: $\sigma_2$ is vertical. (c) Thrust fault regime: $\sigma_3$ is vertical.

# Appendix

For a given far field stress tensor, the *tectonic regime* can be determined easily using the principal values $\sigma_i$ and vectors $\boldsymbol{\sigma}_i$ (ordered in decreasing order). Since one axis is vertical, we have (see Fig. 9.13 a, b and c):

$$Tectonic\ regime = \begin{cases} \text{Normal} & : \text{ if } \boldsymbol{\sigma_1} \text{ is vertical} \\ \text{Strike-slip} & : \text{ if } \boldsymbol{\sigma_2} \text{ is vertical} \\ \text{Thrust} & : \text{ if } \boldsymbol{\sigma_3} \text{ is vertical} \end{cases} \tag{9.35}$$

# Part III

## Structural restoration using Finite Element Method

# Aperçu

Faire de la modélisation directe et inverse, comme vu dans les parties I et II, montre l'importance de la géométrie des failles sur les déplacements discontinus calculés, et par conséquent sur les champs de déplacement et de contraintes perturbés associés. Pour la majorité des simulations numériques, il est donc recommandé de valider la géométrie d'un modèle **avant** toute simulation numérique. Le chapitre 10 présente un moyen de valider une interprétation à l'aide d'une technique de restauration géomécanique. Ce code est différent de la méthode des éléments frontières vue précédemment, en ce sens que les plis sont considérés comme les principaux générateurs de fractures. Il est également démontré que cette méthode permet d'estimer la chronologie des failles entre elles.

Lorsque les surfaces utilisées viennent de l'interprétation sismique, les horizons extraits peuvent être aussi très bruités, et peuvent présenter des bosses et effets d'escaliers, avec des traces de failles et gradients de déplacement irréguliers. Le chapitre 11 présente un filtrage basé sur un lissage géomécanique pour corriger les irrégularités sur les horizons 3D faillés et plissés, et par conséquent sur la reconstruction des surfaces de failles qui en découlent.

# Overview

Doing forward and inverse modeling, as seen in part I and II, shows the importance of the faults geometry to the resulting computed displacement discontinuity, and consequently to the associated displacement and perturbed stress field. For the majority of the numerical simulations, it is mandatory to validate such geometry **before** analyzing the results of any numerical simulation. Chapter 10 presents a way of validating an interpretation using a geomechanically-based restoration technique. This code is different from the Boundary Element method described previously, in the sense that folds are considered as the main driver for the generation of fractures. It is also shown that such a method allows one to estimate fault chronology.

When using surfaces from seismic interpretation, the extracted horizons can be very noisy, and can present bumps and steps with irregular fault cut-offs and displacement gradient at fault tips. Chapter 11 presents a geomechanically-based smoothing filter to correct such irregularities on 3D faulted horizons, and consequently on the reconstructed of fault surfaces.

# CHAPTER 10

# Chronologic modeling of faulted and fractured reservoirs using geomechanically-based restoration: Technique and industry applications

L. Maerten[(1)], F. Maerten[(1,2)]

(1) Igeoss, Montpellier, FRANCE
(2) University of Montpellier II, Geosciences, FRANCE

Published in American Association of Petroleum Geologist Bulletin, 2006, v. 90, p. 1201-1226.

**Preamble**

Structural verification of geometry can be done in 2D using balanced cross sections, which is the goal of the restoration algorithm describes in this chapter, where a Finite Element Method is employed.

Specifically, the advantage of using geomechanically-based restoration is studied on the MacClay experiment for a sandbox model, where initial and final configurations are known, as well as the complete kinematic, sediment deposition, boundary conditions and material

properties. It is shown that this technique can help to elucidate fault development and chronology, and help the user to check the validity of the interpretation of seismic images. The extension to 3D is straightforward, but will not be discussed here.

## About...

In this paper, my contribution was to define the conceptual model using an innovative iterative solver which allows the incorporation of contact management using a master/slave procedure. The initial implementation was done using the Java language, and later in C++, allowing fast computation. Laurent Maerten used the software to study a MacClay experiment as well as the Coulasou fold (near Montpellier, France).

# Article Outline

## 10.1 Résumé

Nous avons développé une méthode de restauration basée sur la géomécanique pour modéliser la déformation des réservoirs. L'approche, fondée sur la méthode des éléments finis (FEM), simule le comportement physique des masses rocheuses et prend en considération l'hétérogènéité des propriétés des matériaux, le glissement banc sur banc ainsi que l'interaction mécanique des failles entre elles. Pour démontrer le potentiel d'une telle méthode, nous analysons la déformation et la croissance des failles dans le compartiment supérieur (*hanging wall*) d'une faille normale listrique syn-sédimentaire d'un modèle de bac à sable, qui fournit un analogue pour l'étude des réservoirs complexes. Les résultats du modèle numérique sont ensuite analysés pour investiguer sur la chronologie des failles. Le modèle numérique correspond bien au modèle physique et fournit des informations supplémentaires quant à l'évolution du réservoir et sa déformation associée. L'approche est aussi testée sur un exemple naturel de plissement en utilisant les données d'affleurement pour l'étude de la déformation dans un régime compressif.

Ces exemples illustrent comment les failles et fractures indétectables, le cloisonnement des réservoirs, les chemins de migration et pièges des hydrocarbures peuvent être compris dans le contexte des processus tectoniques et comment cette compréhension peut être exploitée dans la prise de décisions et la réduction des risques. Nous concluons que la restauration géomécanique des réservoirs faillés et fracturés a un potentiel important pour les applications industrielles par rapport aux techniques de restauration géométriques conventionelles, qui n'ont pas de base mécanique.

## 10.2 Abstract

We have developed a geomechanically-based restoration method to model reservoir deformation. The approach, founded on the finite element method (FEM), simulates the physical behavior of the rock mass and takes into consideration heterogeneous material properties, bedding slip and the mechanical interaction of faults. To demonstrate the method's potential, we analyze deformation and fault growth in the hanging wall of a syn-sedimentary listric normal fault from a sandbox model, which provides an analog for evaluating complex faulted reservoirs. The numerical model results are then analyzed to investigate the chronology of faulting. The numerical model corresponds well to the physical model and provides additional insights about reservoir evolution and deformation. The approach also is tested on a natural example of folding using outcrop data to study contractional deformation.

These examples illustrate how undetected faults and fractures, reservoir compartmentalization, hydrocarbon migration pathways, and hydrocarbon traps can be understood in the context of tectonic processes and how this understanding can be exploited in decision making and reducing risk. We conclude that the geomechanically-based restoration of faulted and fractured reservoirs has significant potential for industry applications compared to common geometric restoration techniques, which lack a mechanical basis.

## 10.3 Introduction

Whether faults and fractures act as seals or conduits, and whether they are resolvable or not on seismic reflection surveys, they can significantly affect hydrocarbon migration and trap location as well as flow of hydrocarbons to wells during production. Therefore, understanding the evolution of faults and fractures and physical properties through time should improve reservoir simulation models and, in turn, significantly improve decision making and reduce production risks.

Structural heterogeneities such as faults and fractures are known to be capable of significantly altering the flow of hydrocarbons, either during the migration from the source to the reservoir rock or during production of the reservoir. Therefore, understanding and quantifying the spatial and temporal development of these features as well as their properties (e.g. geometry, throw, aperture, permeability, etc.) can have great economical impact on the recovery of natural reserves. However, despite the tremendous detail now available from 3D seismic reflection techniques (Dorn, 1998), many of these features cannot be detected at the current resolution of the seismic reflection data, typically about 20 to 30

m of throw for faults in North Sea reservoirs. Furthermore, while these geophysical techniques adequately image the major geological structures, this only provides the present day structural geometry of the subsurface, which often has resulted from multiple tectonic events, thereby increasing the complexity of the analysis. In order to more realistically model the spatial and temporal development of structural heterogeneities and to address these economical issues, a variety of numerical techniques have been developed. They fall into three main categories: 1) the geometric and kinematic approaches; 2) the stochastic approaches, and; 3) the physical and geomechanic approaches.

The first category includes most of the restoration techniques used by structural geologists to check the consistency of the subsurface structural interpretations. Measures of gaps and overlaps between the restored parts of a model give qualitative values to check the strength of the geological interpretation. The geometrical methods proposed to restore geological structures are based on a variety of algorithms, which aim at reproducing natural deformation. For instance, the methods include balancing cross sections by flexural slip (Dahlstrom, 1969; Hossack, 1979; Davison, 1986) to model deformation accommodated by slip along infinite number of bedding interfaces. Vertical (Gibbs, 1983; Williams and Vann, 1987) or inclined shear (White et al., 1986; Dula, 1991) techniques have been developed to simulate deformation accommodated by slip along infinite number of vertical or inclined parallel faults respectively. Geometrical (Gratier et al., 1991; Samson, 1996; Williams et al., 1997) unfolding methods for 3D surfaces have been proposed, based on flexural slip and homogeneous inclined shear (Kerr et al., 1993). More simply, map view restoration has been done using rigid translation and rotation of fault blocks (Dokka and Travis, 1990; Rouby et al., 1993) to model larger scale deformation. An analytical approach for 3D surface unfolding has been proposed, based on surface parameterization and global deformation minimization (Lévy, 2000). These methods are based on geometrical assumptions (Rouby et al., 2000) such as preservation of area, minimization of deformation, of changes in segment length or minimization of shearing, constant fault slip, fixed faults in space, or discontinuous rigid blocks.

Lately, the use of these techniques has been extended to predict areas that have undergone large strains at subseismic reservoir scales and to relate the strains to structural heterogeneities such as faults and fractures (Hennings et al., 2000; Sanders et al., 2002, 2004). Although they have the attractiveness of modeling the kinematic evolution of deformed sedimentary basins back in time, these methods are not appropriate to compute fault block deformation and fault slip distributions, which are necessary to model both the fault development and the subseismic fractures. Natural deformation is a physical phenomenon that involves parameters such as the initial geometry, the distribution of mass, rock mechanical properties, and the forces that cause the deformation. Therefore, it is uncertain

which geometric restoration algorithm should be used to model rock deformation (Hauge and Gray, 1996; Bulnes and McClay, 1999). Furthermore, these techniques are not based on the fundamental principles of conservation of mass and momentum, which govern rock deformation. Consequently, no rock mechanical properties can be incorporated in the model, no stress boundary condition can be applied to simulate tectonic loading, and no mechanical interaction among the faults is taken into account. In addition, only strain, which is strongly dependent on the geometric restoration algorithm used, is calculated (Erickson et al., 2000; Hennings et al., 2000; Rouby et al., 2000; Sanders et al., 2004) while fracture mechanics tells us that the state of stress is required to explain how fractures develop and interact.

Stochastic techniques often are based on the fracture power-law size distribution, calibrated using field or seismic data (Childs et al., 1990; Walsh and Watterson, 1991; Schlische et al., 1996). For instance, the fractal model for faulting is used to predict the number of subseismic faults by extrapolation of the power-laws (Sassi et al., 1992; Yielding et al., 1992; Gauthier and Lake, 1993; Gillespie et al., 1993). Although the size distributions are predictable, these techniques pay little or no consideration to physical concepts that govern fault development. Consequently, they can not take advantage of the constraints imposed by physical laws to predict the orientations and the location of these geological features.

Recent studies ((Maerten et al., 1999; Bourne et al., 2000), Maerten et al., in press) have shown that adding a geomechanical rationale to stochastical techniques improves their predictive capability and leads to more realistic faulted and fractured reservoir models. A finite element approach for 3D surface unfolding has been proposed, based on strain minimization (Dunbar and Cook, 2003). These techniques fall into the third category. As opposed to the geometric approach, the geomechanical approach takes into account mechanical concepts and the fundamental physical laws that govern fracture and fault development. The basic methodology consists of calculating the stress distribution at the time of fracturing using the available reservoir structure data such as faults, fractures and folds, and rock properties and the tectonic setting that can be characterized by stress or strain magnitude and orientation. Then, the calculated stress fields, perturbed by the main structures, combined with rock failure criteria are used to model fracture networks (i.e. orientation, location, and spatial density). Applications to both outcrops (Kattenhorn et al., 2000; Bourne and Willemse, 2001; Bai et al., 2002; Guiton et al., 2003b; Healy et al., 2004; Davatzes et al., 2005) and reservoirs ((Maerten et al., 1999; Bourne et al., 2000; Guiton, 2001; Maerten et al., 2002), Maerten et al., in press) demonstrate how geomechanics can provide a high degree of predictability of natural fracture and fault networks. The 3D boundary element method (FEM) has been successfully applied to model

subseismic faults ((Maerten et al., 1999), Maerten et al., in press) in Northern North Sea highly faulted reservoirs as well as undetected fractures in naturally fractured carbonate reservoirs (Bourne et al., 2000). 3D FEM has been recently developed to forward model diffuse fracture networks in folded sedimentary layers (Guiton et al., 2003a) and applied to a Middle East folded hydrocarbon reservoir (Guiton, 2001). However, while numerical models of rock deformation based on continuum mechanics provide an important tool for characterizing geologic structures in the context of hydrocarbon exploration and production, they do not effectively model past fracture development because of their geometric dependence on the available present-day sub-surface structural model of the reservoir to infer stress distribution.

In this contribution, we propose a new numerical method developed by L. Maerten and F. Maerten (2001, personal communication) that combines the restoration of geological structures with geomechanics. This technique allows computing geologic deformation and perturbed stresses through time for key geologic settings and tectonic episodes. The method, based on the FEM, simulates the geomechanical behavior of complex geological structures such as folded and faulted rock. It honors the full complement of physical laws that govern geological deformation, including conservation of momentum, mass and energy. Therefore, physical laws and linear elastic theory replace kinematic and geometric constraints used by the existing methods for the restoration of geological structures.

We apply the 2D FEM to analyze deformation and fault growth in the hanging wall of a syn-sedimentary listric normal fault from a sandbox experiment (McClay, 1990). The physical model constitutes a good quality analog for evaluating complex faulted and fractured reservoirs. It provides good controls on both the interpretation of the observed structures and the analysis of their development through time. The restoration methodology is described and we explain how fault chronology can be inferred and undetected faults can be modeled. We also show how this technique applies to a natural example of contractional structures and how it can help petroleum engineers to define reservoir compartmentalization, hydrocarbon migration pathways, and trap geometries with the goals of reducing production risks and improving the decision-making process.

## 10.4 Principles and Method

The geomechanically-based restorations described in this paper were performed with Dynel, a 2D and 3D geomechanical computer program, which has been developed to model complex geological structures with a variety of boundary conditions or constraints. In this paper, we only consider the 2D formulation to restore geological cross sections.

### 10.4.1 Principles

Dynel is a continuum code based on FEM (Hughes, 1987) for modeling the behavior of complex geological structures such as folded, fractured and faulted rock. Its formulation can accommodate large displacements and strains for a heterogeneous, anisotropic and discontinuous medium. Stresses that would exceed the elastic limit, and thereby subject the model to non-recoverable deformation, are not taken into account (Novozhilov, 1953). Models are discretized with linear triangular elements in 2D, which form a mesh that is adjusted by the user to fit the shape of the structures under consideration. Each element has assigned material properties that may differ from element to element, and each behaves according to a prescribed linear elastic law in response to constraints such as applied and/or internal forces, displacements, and interface contact reactions. As opposed to the standard implicit FEM (Hughes, 1987), where a global stiffness matrix is built for solving for the unknown displacements, we use an iterative solver based on the Gauss-Seidel method (Golub and Van Loan, 1996). This solver allows forces to be transmitted from node to node through the entire system until equilibrium is obtained. Nodal forces are computed using the stress state of each connected element, and take into account other forces such as external and contact forces.
This explicit formulation of the FEM used here makes it ideally suited for modeling complex geological and geomechanical problems that consist of several stages, such as restoration, sedimentation and erosion. Furthermore, this formulation results in much less memory allocation and computation can easily be distributed among computers in a cluster. The explicit solution scheme, also gives a stable solution to unstable numerical processes. It permits one to develop new complex constraints such as unfolding on non planar surfaces, contact interaction and mixing of different boundary conditions (i.e. displacement and stress (traction) boundary conditions).

### 10.4.2 Method

#### Determination of the element and nodal deformation

Initially, the system is at rest in equilibrium ($\sum f = 0$). Applying local forces, displacements and/or stresses will make the system evolve. At iteration i, and according to the prescribed boundary conditions, the nodes subjected to forces are displaced, causing deformation of the connected elements. Next, the homogeneous displacement field associated with the deformation of the elements is calculated. Then, the strain is derived from the

linear displacement field using the kinematic equations for finite or infinitesimal strain. Using Hooke's law (Jaeger et al., 2007), the stress tensor is calculated for each triangular element. Nodal forces are then derived as a function of the element stress tensor. For infinitesimal deformation, tensors and forces are computed in the global coordinate system. For finite deformation, the displacement field, strain and stress tensors are computed in the local coordinate system of each element in order to take into account rigid body rotation. Finally, the forces are rotated back to the global coordinate system and contact forces are added for each node.

### Contacts at interfaces

Contacts are modeled using the concept of slave nodes and master segments (or master surfaces in 3D), which is used in almost all FEM contact algorithms (Wriggers, 2002). Consider two fault blocks in contact. If a node of the interface mesh of one block penetrates a segment from the interface mesh of the second block, the node is considered a slave node whereas the segment is considered a master segment. A contact force is then applied to push the node back toward the outside of the element containing the master segment. Thus, the contact force is directed toward the master segment along the normal to that segment. The master-slave concept implemented here allows nodes to be both slave nodes for an iteration and part of a master segment for other iterations. Therefore, to solve fault-block contact problems, it is not necessary to assign the master and slave roles to boundary surfaces.

### Solving the system

The explicit solver is based on the Gauss-Seidel method, which allows nodal forces to be transmitted from node to node, until equilibrium is reached. Each node is treated independently from the others, and the order in which they are checked is irrelevant. Gauss-Seidel is an iterative method for solving partial differential equations on a triangulated surface (2D) or tetrahedrized volume (3D). When a node is checked, its new position depends on the current positions of the connected neighboring nodes (Fig. 10.1). The key feature of this algorithm is that it uses new information, for instance updated mesh node positions, as soon as they become available, as opposed to the Jacobi's method (Golub and Van Loan, 1996) in which the update of each node depends only on the values at neighboring nodes from the previous iteration.

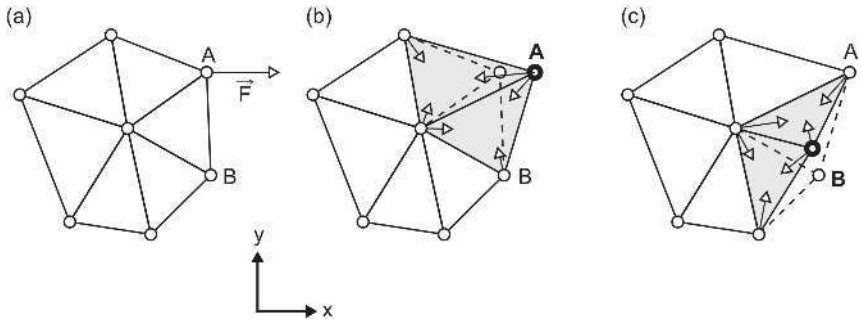


FIGURE 10.1: Iterative solver principle. (a) Initial mesh configuration with applied force at node A. (b) At first iteration, node A is displaced according to force and the two connected triangular elements are deformed accordingly. (c) At second iteration, node B is displaced according to the sum of forces and the two connected triangular elements are deformed accordingly.

For a given node, we calculate the force resulting from the deformation of each connected element. The contact forces are then added. This force is then transformed back to a displacement vector using the nodal stiffness matrix. This matrix is defined as the sum of the stiffness matrices of the connected elements, for which the other nodes are considered fixed. Then, the displacement constraints or displacement boundary conditions, such as fixity, unfolding and unfaulting, are applied to the computed displacement vector. Finally, the node is moved according to the new displacement vector and the iteration jumps to the next node. The algorithm stops when the sum of the squared norm of the nodal displacement vector is below a given threshold value.

### Advantages and pitfalls

Linear elasticity is used as a tool for restoration because its fundamental properties are well suited for such modeling. It is the most intuitive mechanical behavior that provides a unique solution. Therefore, model results can easily be comprehended. Linear elasticity honors the full complement of physical laws that govern geological deformation, including conservation of momentum, mass and energy. As a result, physical laws replace kinematic or geometric assumptions commonly used for restoring geological structures, such as preservation of segment length, surface area or volume. Linear elasticity is reversible, which allows one to go back and forth from the restored to the initial state. Furthermore, since one usually does not know the path of deformation that should be used for restoration, linear elasticity provides the simplest guess. Heterogeneous elastic properties are taken into account to honor vertical and lateral variations in rock rheology, which could have a significant effect on the restoration results (see below). In addition, mechanical boundary conditions can be prescribed using linear elasticity. For instance, there is no need to prescribe ad hoc conditions such as a pin plane, a fixed transport direction,

discontinuous rigid blocks, or fixed faults. Moreover, stress boundary conditions can be added to the model in order to take into account the far field tectonic stresses necessary for modeling structural heterogeneities (Maerten et al., 2002).
The main limitation of using linear elasticity is that we know from laboratory experiments (Jaeger et al., 2007) that rock does not behave as a perfectly elastic solid for all loading conditions. Indeed, non-linear and non-recoverable stress-strain relations are observed beyond the elastic limit. To some extent these inelastic behaviors can be approximated by suitable reductions of the elastic stiffness, and by introducing explicit displacement discontinuities into models that account, for example, for slip on faults.

## 10.5 Application to restoration and example tests

We applied the FEM to restore a simple 2D geological structure. The following examples illustrate the effectiveness of the method to treat contact interfaces and to model heterogeneous material properties. They highlight that different solutions are obtained although the model initial geometry is otherwise identical.

### 10.5.1 Model configurations

Three model configurations, which consist of symmetric folds with constant thickness, have been investigated. The first is a three-layer model with bedding slip (Fig. 10.2.a).

The modeled bedding interfaces can slip with no friction but are constrained to stay in mechanical contact to prevent any opening (i.e. gaps) and interpenetration (i.e. overlaps). In this configuration the layers can mechanically interact, translate, rotate and deform during the restoration. The mechanical properties of the model are homogeneous with a Poisson's ratio of 0.25 and a Young's modulus of 10 GPa. The second configuration (Fig. 10.3.a) is a one-layer model with homogeneous material properties identical to the first configuration. The third configuration (Fig. 10.3.a) is a one-layer model in which a stiffer inclusion has been added. The mechanical properties of the inclusion are defined by a Poisson's ratio of 0.35 and a Young's modulus of 100 GPa, while the rest of the model is identical to the previous configurations. The base and the sides of the three models are free surfaces and we use a finite plane strain deformation.

The basic 2D cross-section restoration procedure consists in constraining each node of a stratigraphic horizon bounding a sedimentary layer (here the top one), to displace to a target curve (here horizontal) representing the depositional topography. Each of the

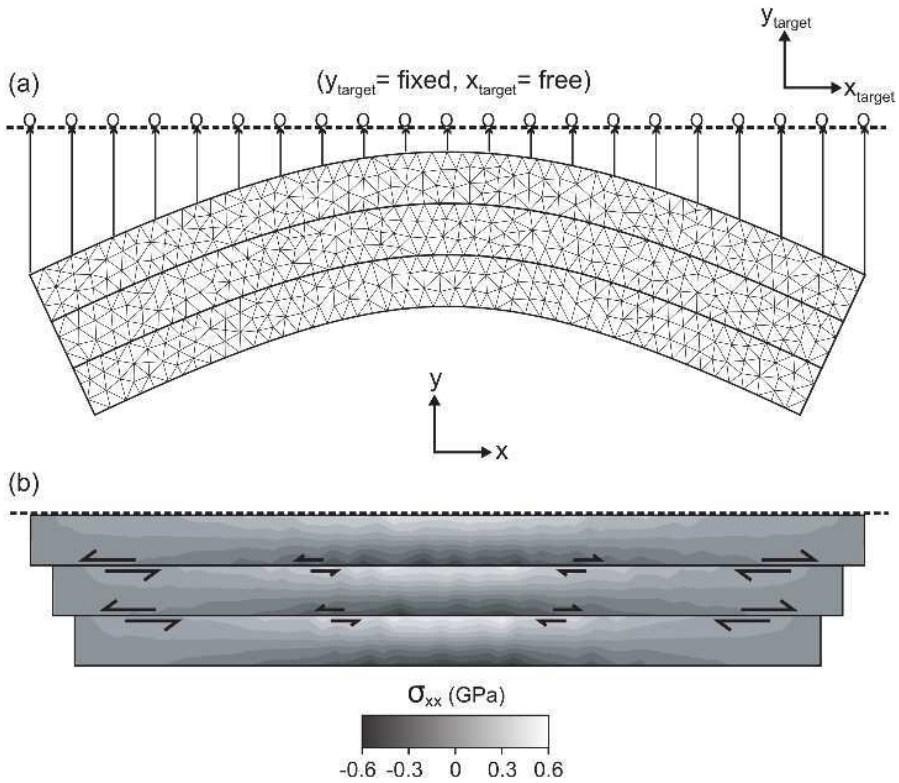


FIGURE 10.2: Restoration of a three layer folded beam with bedding slip interfaces. (a) Mesh of the folded layers with homogeneous properties (E = 10 GPa, $\nu$ = 0.25). Slip is allowed between layer interfaces. (b) Iso-contours of the computed $\sigma_{xx}$. Black is tension and white is compression.

displaced nodes is constrained to stay on the target curve but is free to move parallel to that curve. All the other nodes of the model, unless otherwise constrained, are free to move until the system converges and equilibrium is reached.

### 10.5.2 Results

The result of the first model (see Fig. 10.2.b) shows flat restored layers with bedding slip that increases to the right and to the left side of the model and in opposite sense. The deformation is distributed among the three layers and produces bed-parallel compression and tension at the layer top and bottom respectively. The unfolded lower layer is shorter than the unfolded upper layer giving an overall inverted pyramid shape.
The single layer model however, gives notably different results (see Fig. 10.3.b). One still observes bed-parallel compression and tension at the layer top and bottom respectively. However, the magnitude of the stress is about 5 times greater than that for the slipping layers, because those layers are thinner: layer parallel strain is proportional to the distance from the middle (neutral) surface of a bending layer, and the stress in proportional to the strain. Furthermore, the top boundary length is 2.3% shorter than this of the previous

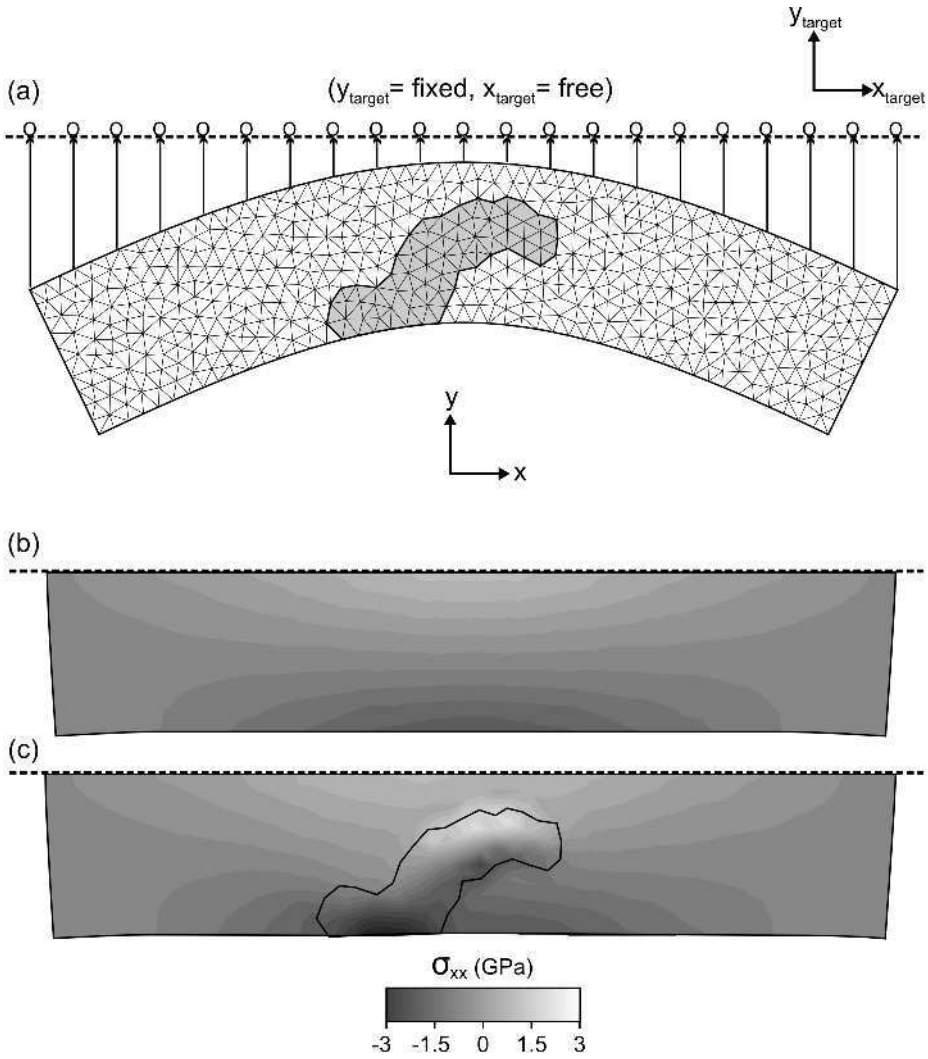


FIGURE 10.3: Restoration of a one layer folded beam. (a) Mesh of the folded beam with location of an inclusion. (b) Iso-contours of the computed $\sigma_{xx}$ for a model with homogeneous properties (E = 10 GPa, $\nu = 0.25$). (c) Iso-contours of the computed $\sigma_{xx}$ for a model with heterogeneous properties (E = 100 GPa, $\nu = 0.35$ for the inclusion). Black is tension and white is compression.

model whereas the bottom boundary is 7.2% longer. Therefore, although the initial geometry is the same, the two first models give different restored geometries and different perturbed stress field distributions. The purpose of the third model was to test the effect of heterogeneous material properties. The result (Fig. 10.3.c) shows that a stiffer inclusion perturbs the stress when the layer is unfolded. Near the top boundary of the inclusion there is a large compression while near the lower boundary there is a large tension. The geometry of the restored fold is similar to the previous model. However, the bottom boundary of the fold is undulating rather than being straight as in the first and second models. For the following set of experiments we use homogeneous material properties. Changing the homogeneous mechanical properties of a model will not significantly change the results, except for the computed stress magnitude since stress is linearly dependent of

the Young modulus. As seen in Figure Fig. 10.3, only contrast in mechanical properties would affect the results.

## 10.6 Experiment 1

We have evaluated the potential industry applications of this new technique by restoring a section across a laboratory experiment. This has many advantages over a natural example because: (i) the initial and final configurations are known; (ii) the complete kinematic and sediment deposition path are recorded; (iii) the boundary conditions are well controlled; and, (iv) the mechanical properties are known. The analogue modeling experiment analyzed in this section consists of a syn-sedimentary listric normal fault with rigid footwall. Because of its quality and applicability, this model has already been used as a restoration case study (Bulnes and McClay, 1999; Erickson et al., 2000; Yamada and McClay, 2003). The laboratory experiment is described in (McClay, 1990), we nonetheless summarize it in the following section for the sake of clarity.

Simple listric fault detachment surfaces were simulated by using a molded footwall block above which a plastic sheet, attached to the moving wall, translates the hanging wall at a constant rate of 4.16 $10^{-3} cm.s^{-1}$ (see Fig. 10.4.a). The plastic sheet models a constant-displacement condition on the base of the model, which implies a zero elongation parallel to the fault surface and a strong décollement surface (see (Medwedeff and Krantz, 2002)). The rigid nature of the footwall block means that the detachment surface has a constant geometry throughout the experiment, thus limiting the deformation to the hanging wall block. Homogeneous dry quartz sand has been used to simulate the brittle behavior of the upper crust. Dry quartz sand ($300\mu m$) has essentially linear Coulomb rheology with a friction angle of 31° (Ellis and McClay, 1988). During the 50% extension of the model, 28 sand layers with alternating colors were added incrementally in order to maintain a constant, horizontal upper free surface and to simulate syn-rift sedimentation that would infill an extensional basin. The serial section of the completed and impregnated model (Figure 10.4.b) shows the well established geometry of a roll-over anticline. In this experiment, where the displacement is uniform over the entire fault surface, a crestal graben system is developed. The fault sequence diagram of Figure 10.4.c shows nucleation of new faults into this crestal graben.

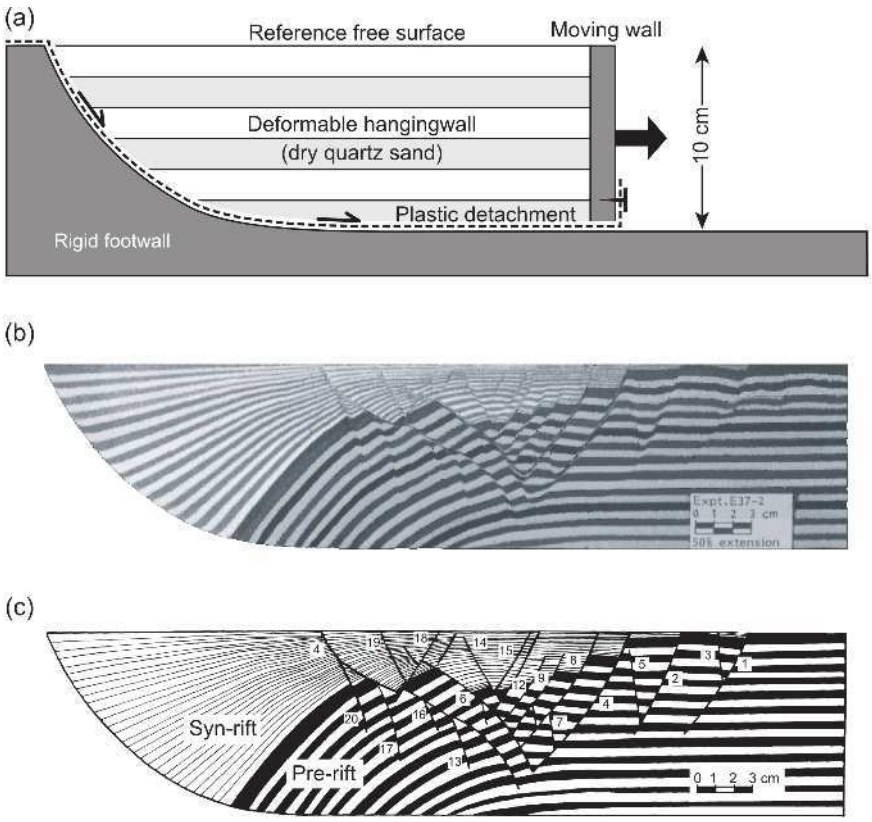


FIGURE 10.4: Physical experiment after McClay, 1990 (McClay, 1990). (a) Details of the model apparatus with a simple listric detachment formed by pulling the plastic sheet (attached to the moving wall) down and along the detachment surface. (b) Serial section of the impregnated sand model after 50% of extension. (c) Line drawing showing the deformed hanging wall and fault sequence inferred from sediment thickness variation (McClay, 1990).

### 10.6.1 Numerical model configuration

The geometry of the completed analogue model was carefully interpreted and a finite element mesh model was built (Fig. 10.5.a) honoring the geometry of both the faults and the boundaries of the sediment layers. The syn-rift sequence has been divided into 6 packages, each with 5 increments of sedimentation, except for the youngest which is comprised of 3 increments. These packages are used for the 6 stage restoration models described below.

The mechanical properties throughout the model are homogeneous and are those of dry quartz sand, with a Poisson's ratio of 0.3, a Young's modulus of $2MPa$ (Clark, 1966), and a friction angle of 31°. The base of the model is constrained to follow the shape of the fixed listric basal fault (see Fig. 10.5.b) with no constant slip imposed. Nodes of the base of the model can slide with no friction along the curved basal boundary in order to accommodate the displacement during the restoration and to mimic the sandbox model configuration. The modeled faults of the hanging wall block can slip with no friction but

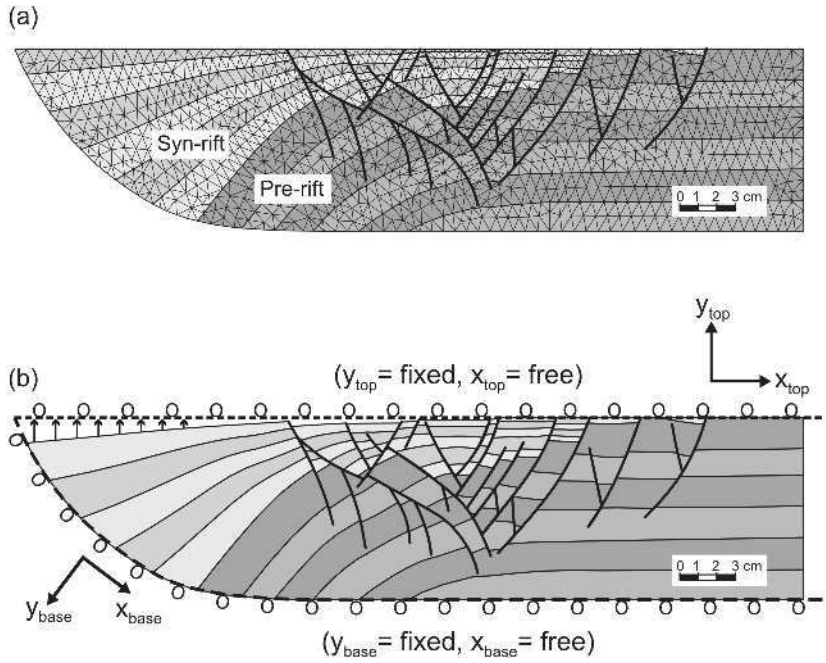


FIGURE 10.5: Configuration of the geomechanically-based restoration. (a) Finite element mesh (triangular elements) of the physical experiment with homogeneous properties (E = 2 MPa, $\nu = 0.3$). (b) Boundary conditions constraining the base of the model to follow the shape of the fixed listric basal fault, the faults of the hanging wall block to slip with no friction but to stay in mechanical contact, and the top of the model to flatten along a horizontal target line.

are constrained to stay in mechanical contact, thus preventing any opening (i.e. gaps) and interpenetration (i.e. overlap) of the fault walls. This configuration allows a degree of freedom where the faults can mechanically interact, translate, rotate and deform during the restoration. The right side of the model is a free surface.

The restoration consists on sequentially removing the upper syn-rift sedimentary layer packages one by one, and to constrain the top of the next package to flatten along a horizontal target line. This target line (see Fig. 10.5.b) corresponds to the constant horizontal upper free surface of the analogue model. The nodes can slide with no friction along the target line in order to accommodate the displacement during the restoration. For each stage of the restoration, all the nodes of the model are free to displace with respect to the constraints stated above and the faults are free to accommodate any slip until the model equilibrates ($\sum f = 0$) and the energy is globally minimized. We assume a plane strain model with no material motion in and out of the cross section. In order to simulate the flow behavior of the dry quartz sand approximately during the deformation, we set the accumulated stress to zero with no associated strain after each restoration stage, and the deformed geometry is used as input for the next restoration increment.

### 10.6.2 Restoration results

We mapped the picture of the completed sandbox experiment onto the finite element mesh using a texture mapping tool. This allows one to follow the deformation of the layers at each stage of the restoration. The results of the restoration are shown in Figure 10.6. The faults located in the roll-over anticline translate, rotate and deform as the restoration

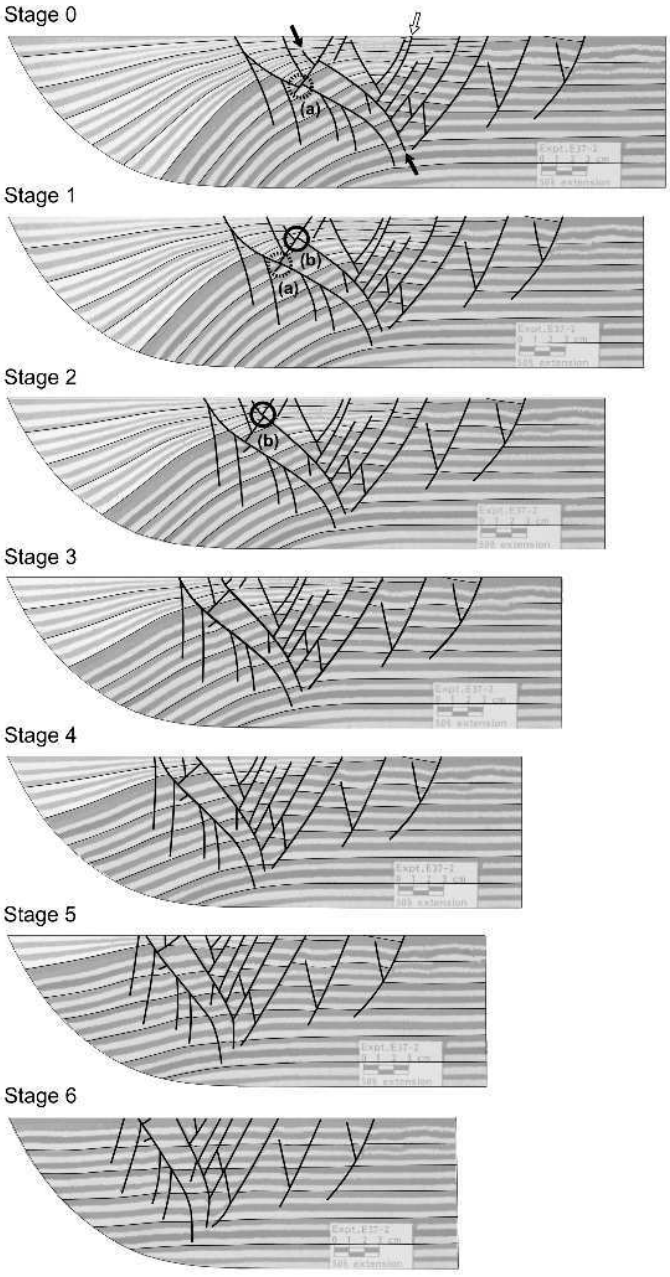


FIGURE 10.6: Results of the geomechanically-based restoration from stage 0 to stage 6. The picture of the physical experiment section has been mapped onto the finite element mesh. White arrow indicates the antithetic normal fault interacting with studied fault (see Fig. 10.8) marked with a black arrow. (a) and (b) indicates the locations of studied cross-cutting relationships between intersecting faults.

sequence progresses, whereas faults located to the right in the model, only exhibit a

translation. The changes in fault cross-cutting relationships through time, as observed in Figure 10.6 (a) and (b), demonstrate how geomechanically-based restoration can deal with complex fault geometry and interaction. For instance, the right-dipping fault of intersection (b) in Figure 10.6, cross-cuts a left-dipping fault at stage 1, whereas it is the left-dipping fault that cross-cuts the right-dipping fault at the next stage 2. These cross-cutting relationships between faults help us understand the chronological development of faults that is described below.

When analyzing the evolution of the sand layers, one observes that they roll back along the basal listric fault to their original horizontal position, while the free right border of the model translates without any rotation. In the final restored state (stage 6 of Figure 10.6), the pre-rift beds are sub-horizontal, which is consistent with the initial configuration of the physical sandbox experiment. However, close to the main bounding listric normal fault, some beds dip slightly to the left ($\sim 1.5°$). Some mismatches also are seen in the continuity of the bedding interfaces across some of the faults. The origin of these discrepancies can cautiously be attributed to different sources. First, the mechanical behavior of the dry quartz sand might not be effectively modeled using elastic behavior. Second, remobilized sand close to the faults may be involved in normal or reverse drag attributed to inelastic deformation, which is not modeled. Third, we have not imposed a constant slip on the décollement as in the physical model. And finally, the plane strain constraint used in the numerical model may not necessarily be appropriate. Indeed, some motion of the dry quartz sand parallel to the strike of the basal listric fault probably occurred during the physical experiment.
Each of the 28 syn-rift sand layer increments of the physical experiment corresponds to 0.5 cm of displacement at a constant rate of 4.16 $10^{-3} cm.s^{-1}$. Therefore, one time-increment is about 120 seconds. This time-increment has been combined with the measure of shortening after each restoration stage to produce Figure 10.7. This graph compares the displacement rate imposed in the sandbox experiment with the displacement rate inferred from the restoration, and it provides a quantitative means for evaluating the restoration. The inferred displacement rate is constant and closely matches the one imposed in the sandbox experiment. The best linear fit is given by

$$y = 4.11\ 10^{-3}x + 0.0.248 \tag{10.1}$$

with $R = 0.99915$ and where 4.11 $10^{-3}$ is the computed displacement rate in $cm.s^{-1}$.

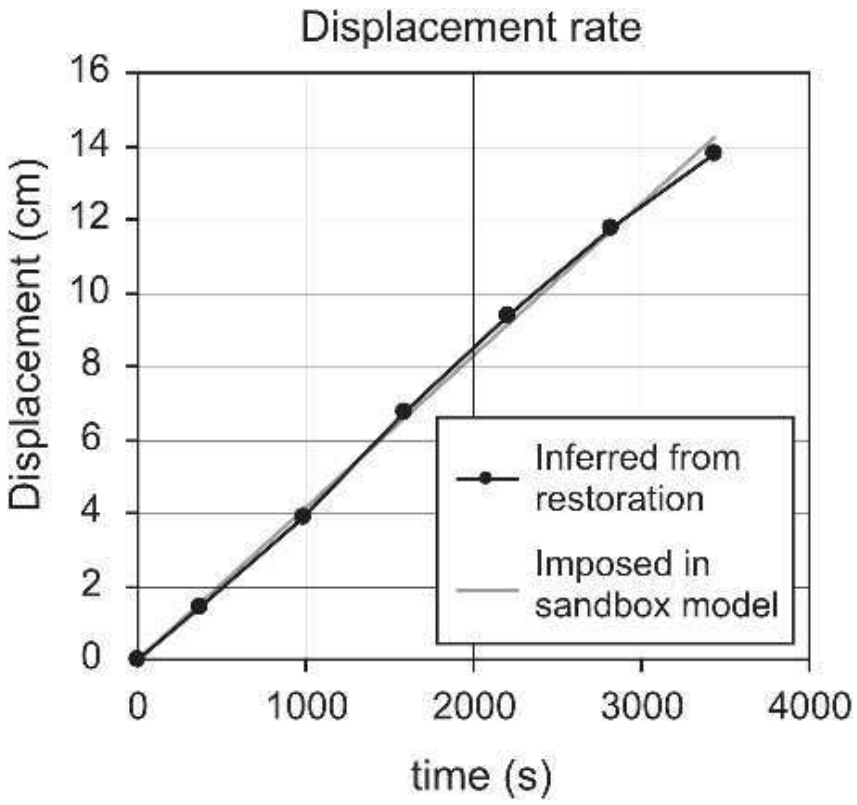


FIGURE 10.7: Graph comparing the displacement rate imposed in the sandbox experiment with the displacement rate inferred from the restoration. The inferred displacement rate is constant and closely matches the one imposed in the sandbox experiment.

### 10.6.3 Fault development analysis

For each restoration stage we computed the slip distribution along the faults in order to estimate the amount of fault activity through time. Since there is no mesh regeneration between each restoration stage, we used the relative (x, y) coordinates of the nodes on both sides of the faults to compute the slip distribution along the faults. Cumulative slip distributions illustrate how the faults initiate, propagate, mechanically interact and lock through time. As an example, Figure 10.8 shows for each stage, the cumulative slip distribution along fault (c), which is also marked by a black arrow in Figure 10.6 (stage 0). For the sake of simplicity, the modeled fault is analyzed in a forward sense.

Initially there is no slip along the fault (c). Between stages 6 and 5, slip accumulates along the upper 6.5 cm of the fault. There is little or no slip computed along the lower 2 cm of the fault, therefore the fault has not yet reached its final length. The fault propagates within the syn-rift sequence and offsets the top free surface as illustrated by the open slip distribution curve. Between stages 5 and 4, slip quickly accumulates along the fault, except in the lower centimeter. This highlights the highest intensity of fault activity, which clearly shows an asymmetric slip distribution with maximum slip near the top free surface

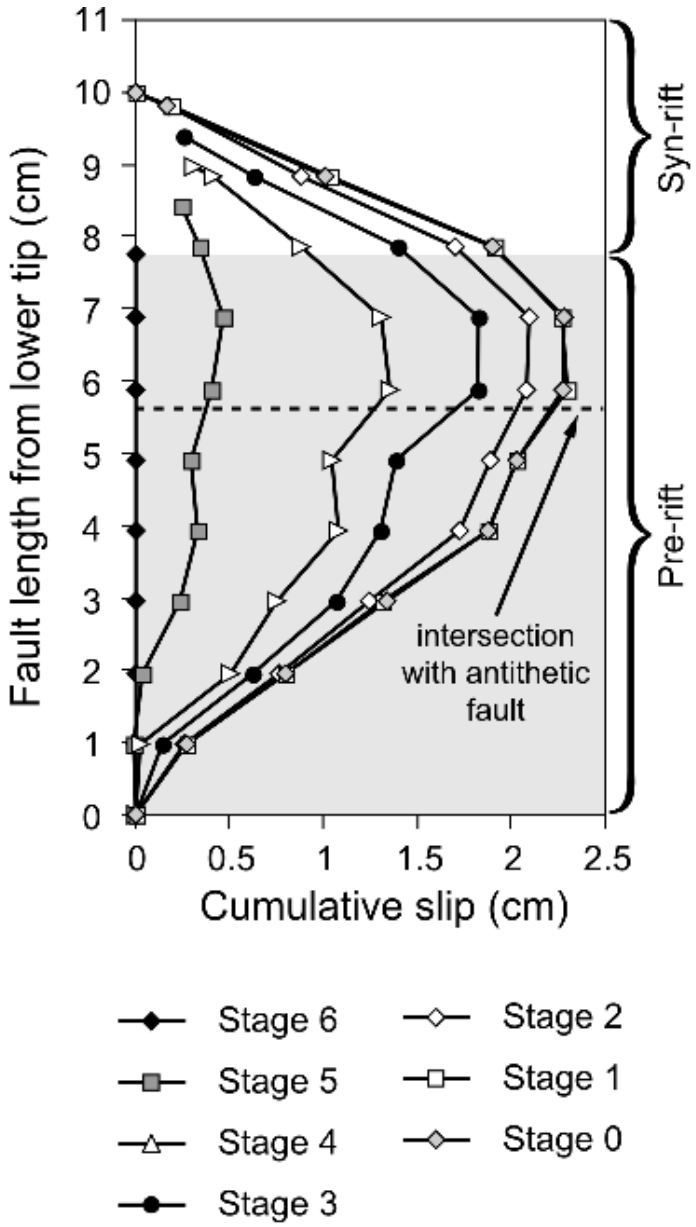


FIGURE 10.8: Cumulative slip distribution, for each stage of the restoration, computed along the fault marked as a black arrow in Fig. 10.6. Dashed line locates the intersection with the mechanically interacting antithetic normal fault marked as a white arrow in Fig. 10.6.

as described in other studies (Childs et al., 1993; Maerten et al., 1999). Between stages 4 and 2, slip keeps accumulating and the fault reaches its final length in both the post-rift and the syn-rift sequence. At stage 2, the fault does not offset the top free surface as illustrated by the slip distribution that goes to zero in the syn-rift sequence. Between stages 2 and 1, slip accumulates everywhere except along the lower 2 cm of the fault, where the fault starts to lock. Between stages 1 and 0, the fault has entirely locked since no slip has accumulated. This corresponds to the change in fault cross-cutting relationship observed in Figure 10.6 (b) and described earlier.

The dashed line of Figure 10.8 shows the location of the intersection with a major antithetic fault marked by a white arrow in Figure 10.6 (stage 0). This fault mechanically interacts with the studied fault and perturbs its slip distribution as illustrated by a higher slip gradient. The fault interaction is the strongest between stages 5 and 3, where the slip gradient is the highest. This also corresponds to the highest activity of the antithetic intersecting fault. The perturbed slip distribution is consistent with previous independent observations (Nicol et al., 1995; Maerten, 2000) and mechanical analyses (Maerten et al., 1999). The mechanical interaction responsible for the perturbed slip distribution is attributed, at least in part, to elastic deformation that modifies the local shear stress acting on one fault as induced by slip on the other fault (Willemse, 1997; Maerten, 2000). The entire model was analyzed in a forward sense in order to sequentially investigate the development of the faults in the hanging wall of the basal listric fault. Slip distribution along each fault was computed for each stage. It was then possible to infer the evolution of deformation, the propagation and locking history of the faults, and the fault chronology (see Fig. 10.9).

### 10.6.4 Active deformation area

The analysis of fault development, which has been inferred from the computed fault slip distributions, shows that through time, the deformation or fault activity is always localized close to the top free surface and just to the right of the base of the ramp (see Fig. 10.9). This has been observed in many natural examples (Shelton, 1984; Williams and Vann, 1987), in sandbox experiments (Ellis and McClay, 1988; McClay, 1990; Withjack et al., 1995) and has been explained using elastic and elasto-plastic geomechanical simulations (Erickson et al., 2001). The location and magnitude of the deformation is directly related to the shape of the basal listric normal fault that controls the rollover anticline geometry, and therefore the distribution of the perturbed stress fields.

### 10.6.5 Fault propagation

The analysis shows that faults initiate close to the top free surface and propagate downwards in the pre-rift sequence and upwards in the syn-rift sequence, as observed for faults (a) and (c) of Figure 10.9. The full length of the faults is attained at an early stage of the deformation. The analysis also shows that new active segments of the faults always form with a dip angle close to 60°. This is consistent with the Coulomb failure criterion

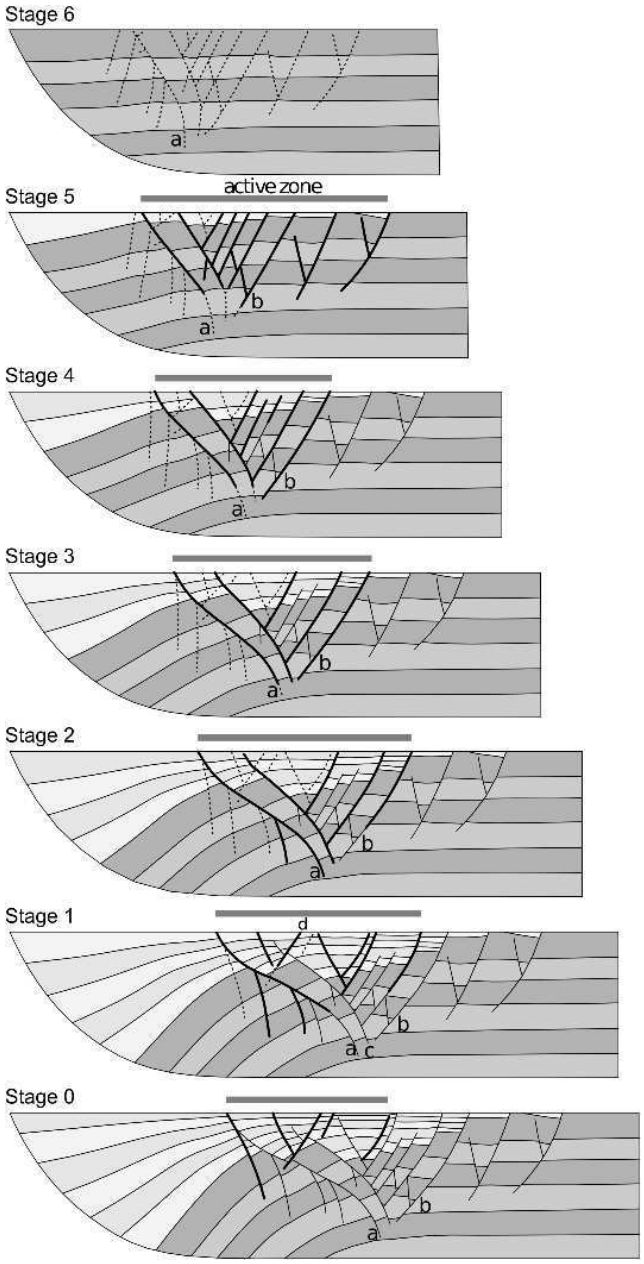


FIGURE 10.9: Sequential fault development analysis inferred from computed fault slip distributions. Dashed faults are incipient faults, thick black faults are active faults, and thin black faults are locked. Faults marked as a, b, c and d are referred in the text.

(modified from (Jaeger et al., 2007), p. 95) defined by:

$$tan(\pi - 2\delta) = \pm \frac{1}{tan\phi} \tag{10.2}$$

where $\delta$ is the dip angle of the fault plane, $\phi$ is the friction angle, and with the maximum compressive stress ($\sigma_{max}$) vertical. This criterion predicts that for dry quartz sand ($\phi = 31°$) that $\delta = 60°$. The final observed S-shaped geometry of faults, (a) and (c), can therefore be explained in part by the propagation of the faults upwards and downwards at 60 degrees to the vertical as the model rotates over the listric normal fault (i.e. rollover

anticline).

### 10.6.6 Locking faults

Results from the fault slip analysis illustrate how the faults start to lock. When a fault is fully developed, after initiating close to the top free surface and propagating downwards in the pre-rift sequence, it starts to lock close to the base. Then, the locked segment of the fault spreads upwards as seen for faults (a) and (b) (Figure 10.9). Another locking mechanism observed in the restoration occurs when a fault is cross-cut by a propagating fault. This is clearly observed for faults (a) and (c), locked by the propagating fault (d) (Figure 10.9).

### 10.6.7 Fault chronology

The above observations based on the analysis of the computed fault slip distributions permit one to infer the deformation and the fault development chronology of the entire model. This chronology is in good agreement with the chronology inferred from the sedimentation thickness variation analysis of the physical model (see Fig. 10.4.c). However, the geomechanical model adds more than a fault chronology based on sediment thickness analysis, since it tells us when and where faults propagate and lock in space and through time.

### 10.6.8 Conclusions and applications to reservoir exploration and production

The numerical model corresponds well to the physical model and provides additional insights about the physics of the process and quantitative values of physical parameters. The geomechanically-based restoration provides a way to quickly and efficiently assess the development of the geological structures (i.e. faults) through time. This tool has significant potential for understanding complex geological structures and for evaluating hydrocarbon migration through time. Indeed, if one expects hydrocarbons to migrate along the active segments of faults, one could infer hydrocarbon migration pathways directly and locate areas of potential structural traps that could be economically interesting.

## 10.7 Experiment 2

The objective of the following experiment is to predict fault location and geometry as observed in the physical model. Therefore, a model without the faults is restored and attributes of the computed perturbed stress field are compared with the location and geometry of the faults, observable in the physical experiment.

### 10.7.1 Numerical model configuration

The geometry of the model corresponds to stage 0 of the previous experiment, where the first package of the syn-rift sequence has been removed (see Fig. 10.10.a and 10.10.b). All the faults of the deformed hanging wall have been omitted and the top boundary has been interpreted as a smooth surface without any offsets caused by the observed faults. This experiment could be viewed as a demonstration of how to interpret poor quality seismic data, where faults cannot be detected from sedimentary interface offsets.

The mechanical properties throughout the model are homogeneous and similar to the previous experiment with a Poisson's ratio of 0.3, a Young's modulus of 2 MPa, and a friction angle of 31°. The nodes at the base of the model are constrained to slide with no friction and to follow the shape of the fixed listric basal fault (see Fig. 10.10.b). The left side of the model is a free surface. The restoration consists on constraining the top of the model to flatten along the horizontal target line that corresponds to the constant horizontal upper free surface of the analogue model. The nodes can slide with no friction along the target line in order to accommodate the displacement during the restoration. All the other nodes of the model are free to displace until the energy is globally minimized. We assume a plane strain model with no material motion in and out of the cross section. A second model (see Fig. 10.11.a), similar to the previous one, has been setup in which the base has not been constrained to follow the listric fault. This experiment could be viewed as a demonstration of how to interpret poor quality seismic data, where faults as well as the basal décollement cannot be detected.

### 10.7.2 Restoration results

Based on the restoration boundary conditions and mechanical parameters, one computes the perturbed elastic stress field at the finite elements. Note that computed stresses are the stresses produced by restoring the model. The inverse of these stresses corresponds to the stresses that are computed if we deform the initial model geometry to the observed

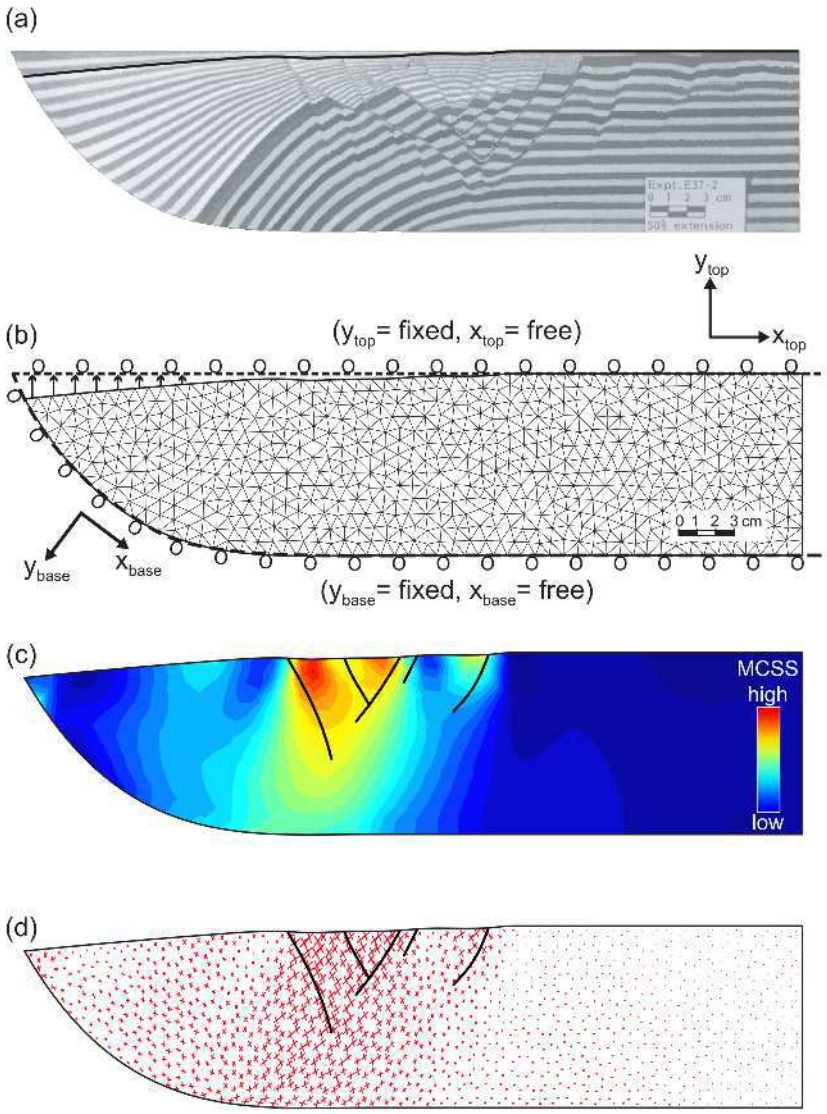


FIGURE 10.10: Model configuration and results of the second geomechanically-based restoration. (a) Serial section of the impregnated physical experiment. The black line corresponds to the smoothed interpreted sedimentary layer without fault offsets. (b) Finite element mesh with homogeneous properties (E=2 GPa, $\nu$=0.3) and boundary conditions. The faults have been omitted in the model. (c) Iso-contours of the computed maximum Coulomb shear stress (MCSS) resulting from the restoration and plotted over the initial unrestored geometry. (d) Orientation of the predicted shear planes scale to the MCSS. The size of the shear planes is proportional to the MCSS. Thick black lines are the superimposed active faults predicted from stage 0 of figure 10.9. They closely matched the highest values of MCSS and the orientation of the computed shear planes.

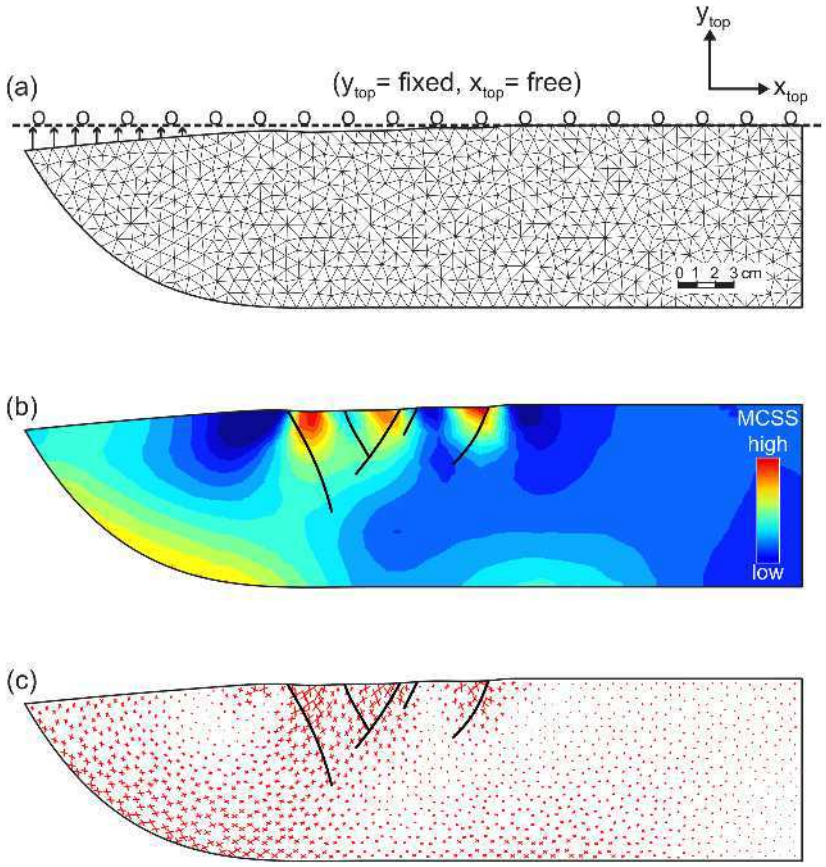


FIGURE 10.11: Model configuration and results of experiment 2 without constraining the base of the model. (a) Finite element mesh with homogeneous properties (E=2 GPa, $\nu$=0.3) and boundary conditions. The faults have been omitted in the model and the base is free. (b) Iso-contours of the computed maximum Coulomb shear stress (MCSS) resulting from the restoration and plotted over the initial unrestored geometry. (c) Orientation of the predicted shear planes scale to the MCSS. The size of the shear planes is proportional to the MCSS. Thick black lines are the superimposed active faults predicted from stage 0 of figure 10.9.

deformed geometry. Linear elasticity allows such back and forth analysis of the stresses from the deformed to the undeformed states. The principal stresses (i.e. inverse) are then combined with a failure criterion to create maps of both the predicted fault geometry and the predicted fault location.

The modeled fault geometry can be estimated using the Coulomb failure criterion defined in equation (10.2). Two conjugate failure planes intersect and the fault dip-angles are influenced only by the angle of friction $\phi$ and the orientation of the local maximum and minimum principal stresses, $\sigma_{max}$ and $\sigma_{min}$, respectively. We chose the maximum Coulomb shear stress (MCSS) as an index for fault location because it has been effectively used by (Maerten et al., 2001) and Maerten et al. (in press) to model secondary normal faulting in a North Sea reservoir. The MCSS is the maximum shear stress that would occur on optimally oriented conjugate shear fractures as defined above. The value of the MCSS is

determined by (Jaeger et al., 2007), p. 95:

$$MCSS = (\frac{\sigma_{max} - \sigma_{min}}{2}\sqrt{1 + tan^2\phi}) - tan\phi(\frac{\sigma_{max} + \sigma_{min}}{2}) \tag{10.3}$$

where $\phi$ is the friction angle.

Figure 10.10.c shows the contours of the MCSS over the entire model. The highest stress concentration is localized close to the top free surface and just to the right of the base of the ramp. This corresponds to the area of highest fault activity inferred from the previous restorations and is similar to the elastic and elasto-plastic geomechanical simulations carried out by (Erickson et al., 2001). The right side of the model displays the lowest MCSS stress values and corresponds to the region that has only been translated during the extension. When the active fault segments, predicted from stage 0 of the previous restoration experiment, are superimposed onto the map, they match with the highest computed MCSS values.

Figure 10.10.d shows the orientation of the two shear failure planes derived from the computed stresses over the entire model. The sizes of the displayed shear planes are proportional to the computed MCSS. When the active faults, predicted from stage 0 of the previous restoration experiment, are superimposed onto the map, their geometry closely follows the curved path of the computed shear plane orientations.

Figure 10.11.b also shows that without constraining the base of the model, highest stress concentration still localizes close to the top free surface, which corresponds to the area of highest fault activity inferred from the previous restorations. Orientation of the two shear failure planes remains identical to the previous model close to the top free surface. However, the orientation of the conjugate shear planes tends to deviate from the previous model towards the traction free base of the model.

### 10.7.3 Conclusions and applications to reservoir exploration and production

The geomechanically-based restoration not only provides a complete and robust set of tools for inferring fault development chronology but also a tool to compute deformation between the restored and the deformed states. The analysis of deformation (i.e. perturbed stress field) can be used effectively in the oil industry to model undetected or sub-seismic faults ((Maerten et al., 2002), Maerten et al., in press). These predictions may serve to infer reservoir compartmentalization and to locate and exploit faulted regions of reservoirs.

## 10.8 Experiment 3

As an application of the geomechanically-based restoration technique to model contractional structures, we restore a decameter-scale fold, which crops out in the Coulazou gully located near the Montpellier thrust fault, Southern France (see Fig. 10.12).

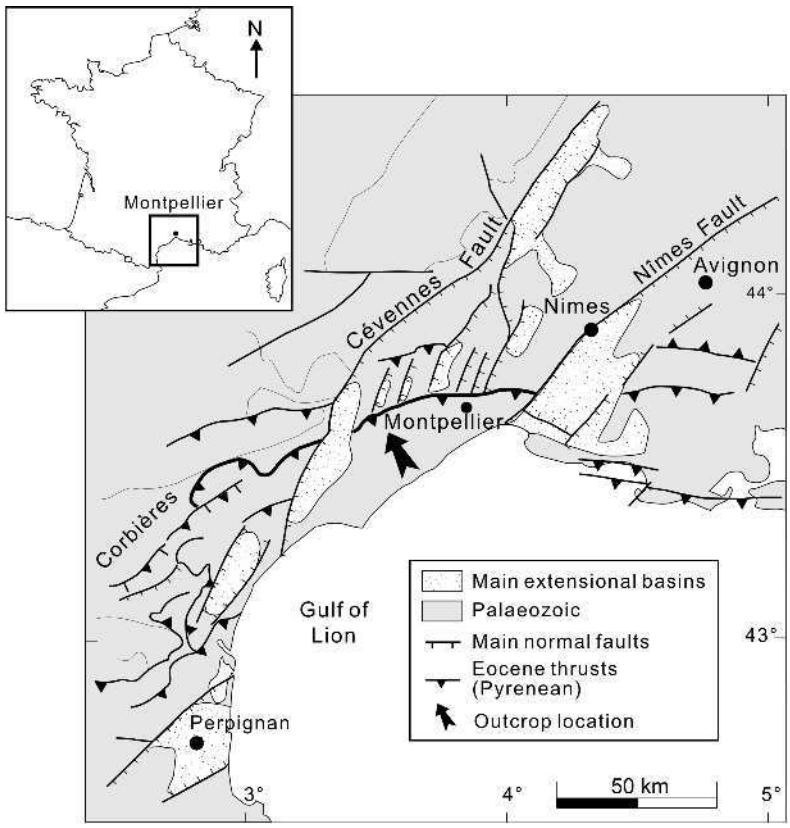


FIGURE 10.12: Simplified structural map of the central part of Gulf of Lion margin, showing the contractional and extensional structures as well as the outcrop location. Paleozoic basement is marked with crosses.

The Montpellier thrust fault is part of the thrusts and folds of the Pyrenean foreland (Arthaud and Séguret, 1981) formed during Eocene. The thrusts have later been truncated by NS-striking extensional structures developed throughout the late Oligocene-Early Miocene rifting of the Gulf of Lion continental passive margin. The Mesozoic limestone cover, which was involved in thin-skinned compressional tectonics during the Pyrenean orogeny, outcrops in the Coulazou gully. The structural style of the area is characterized by a succession of EW trending, decameter-scale folds affecting mechanical units of limestone layers that are several meters thick (Bazalgette, 2004). Figure 10.13 shows a fold cropping out along the cliff bounding the Coulazou gully, and its interpretation in a vertical cross section. The fold has a gentle concave downward shape affecting a 7 to 9 m thick competent limestone unit vertically bounded by softer marly units. The lower marly calcareous unit, visible in the cross section, corresponds to a décollement level above

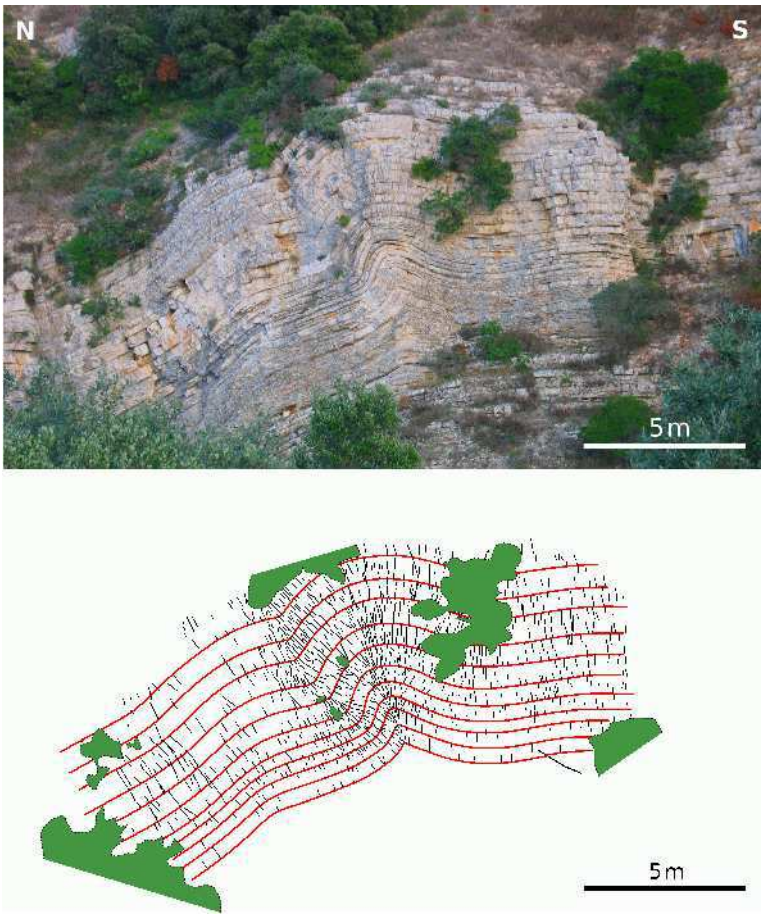


FIGURE 10.13: Contractional fold of the Coulazou gully, southern France. (a) Outcrop photograph. (b) Structure interpretation showing the main bedding interfaces and the observed fractures.

which the fold has initiated. Layer-bounded mode I fractures cluster near the fold hinge. Field observations (Bazalgette, 2004) suggest that some of the fractures are reactivated pressure solution surfaces, probably developed during the Pyrenean compression prior to folding.

### 10.8.1 Numerical model configuration

A finite element mesh (Fig. 10.14.a) was developed from the interpretation of the fold that fits the geometry of the sedimentary layers. A finer mesh has been used near the hinge in order to honor the highest fold curvature geometry. The mechanical properties throughout the model are homogeneous and are those of limestone, with a Poisson's ratio of 0.25, a Young's modulus of 30 GPa (Clark, 1966).

The modeled bedding interfaces can slip with no friction but are constrained to stay in mechanical contact, thus preventing any opening and interpenetration of the layers. This configuration allows a degree of freedom where the layers can slip, translate, rotate and

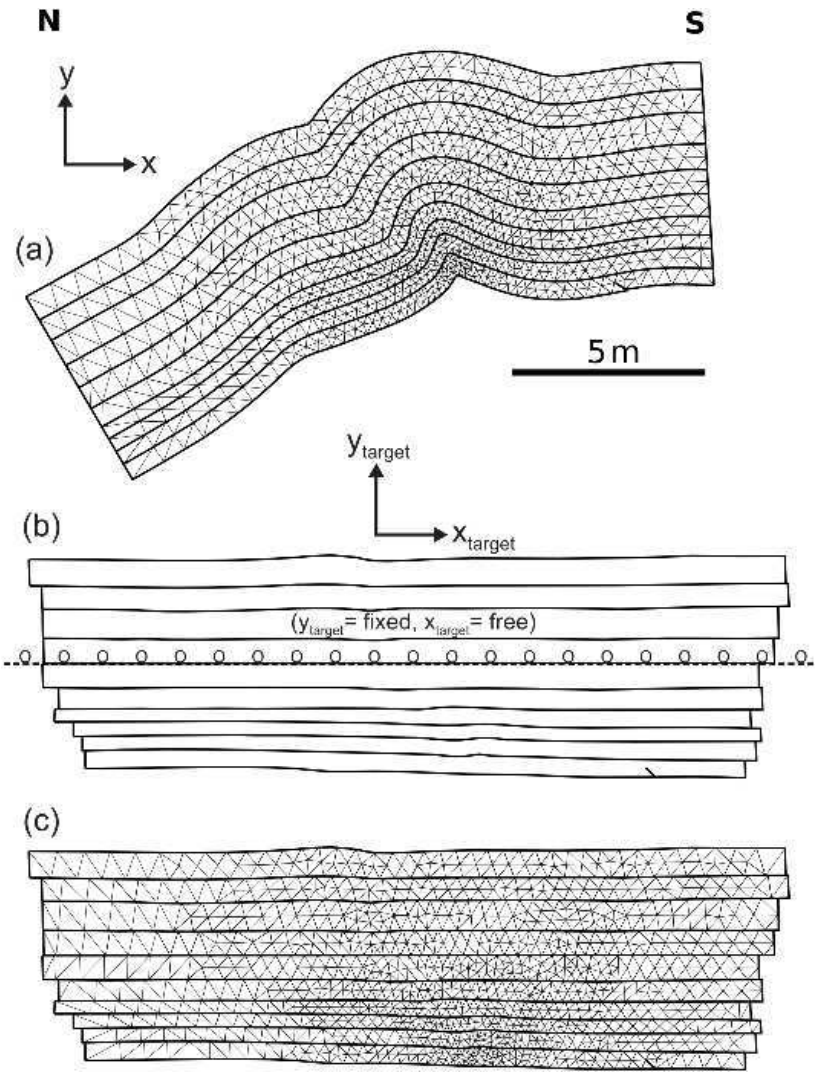


FIGURE 10.14: Model configuration of the contractional fold restoration. (a) Finite element mesh (triangular elements) with homogeneous properties (E=30 GPa, $\nu$=0.25). (b) Boundary conditions constraining the middle bedding interface of the model to flatten along a horizontal target line. The boundary conditions sketched on the unfolded model for clarity. (c) Unfolded finite element mesh.

deform during the restoration while they mechanically interact. The outside boundaries of the model are free surfaces. We justify the free lower and upper boundaries by the fact that the mechanical competent limestone unit is bounded by softer marly layers, where décollement has probably occurred. In this example, the restoration consists of constraining all the nodes of the middle bedding interface to displace to a target horizontal line representing the hypothetic pre-deformed geometry (Fig. 10.14.b). Each of the displaced nodes can slide with no friction along the target line in order to accommodate the displacement during the restoration. All the other nodes of the model are free to move until equilibrium is reached. We assume a plane strain model with no material motion in and out of the cross section.

### 10.8.2 Restoration results

The result of the restoration (Fig. 10.14.c) shows sub-horizontal layers with a constant thickness throughout the model. There is a small thickness variation with an increased thickness from north to south, which is also observed in the structural interpretation. This could be natural lateral thickness variation or artificial variation caused by the imperfect perpendicularity between the camera direction and the cliff face (i.e. perspective distortion). Slip occurred in all bedding interfaces giving an overall inverted pyramid shape as observed in the synthetic example of Figure 10.2, where the unfolded lower layers are shorter than the unfolded upper layers.

We mapped both the outcrop image of the fold and the fracture interpretation (Fig. 10.15 and Fig. 10.16.d) onto the finite element mesh in order to display the observed fractures and bedding interfaces of the structure in what could have been its pre-deformed geometry. They show rotated fractures that appear perpendicular to bedding.

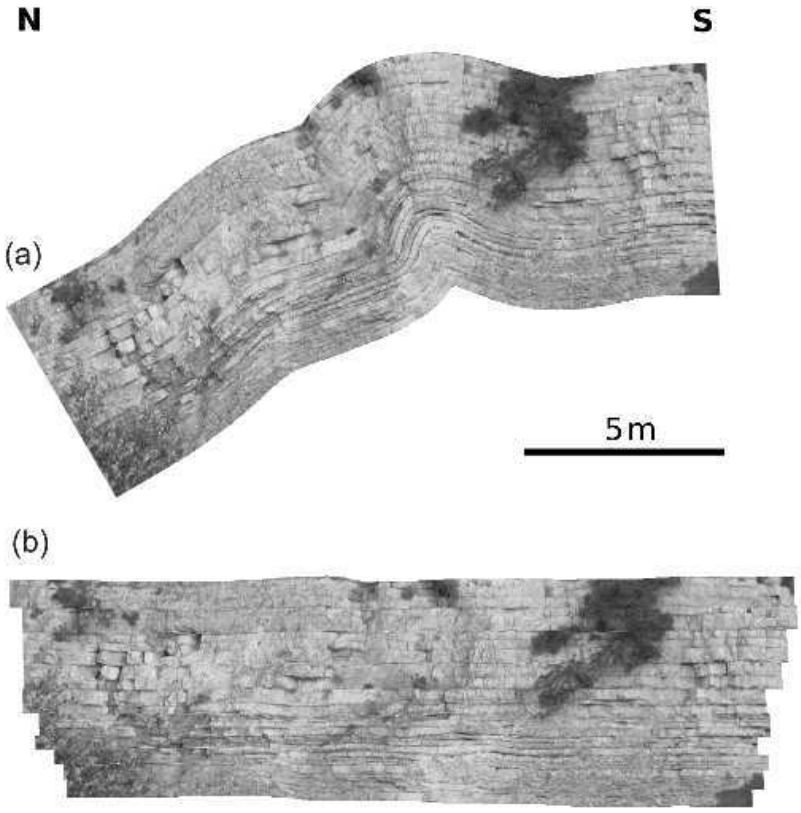


FIGURE 10.15: Results of the geomechanically-based restoration. (a) The outcrop photograph has been mapped onto the finite element mesh. (b) Unfolded photograph showing sub-horizontal beds.

For sake of clarity, the stress displayed on Figure 10.16 (i.e. least principal stress $\sigma_3$) is the stress produced by folding the beds. The inverse of that stress corresponds to

the maximum compressive stress ($\sigma_1$) that is computed by unfolding the beds to sub-horizontal beds. The deformation caused by the folding is distributed among the ten layers and produces bed-parallel tension and compression at the layer top and bottom respectively. Results show stress concentrations (tension) localized along the fold hinge and articulations and in the extrados of the folds, which reasonably correlate with the location of the observed fracture clusters. The restoration produces bed-parallel tension that could ultimately reactivate preexisting bed-perpendicular stylolites or develop joints (opening mode fractures) normal to bedding, as observed in Figure 10.16.a and b. The high stress concentration magnitude computed from the unfolding can be explained by the fact that stresses that exceed the elastic limit, and would be subject to non-linear elastic deformation, are not taken into account. We would expect fractures developing in such areas in response to the stress concentration. It is important to note that no far field tectonic stresses have been added to the model. Therefore, the computed stresses only reflect the deformation caused by unfolding.

Figure 10.17 shows the quantitative comparison between fracture frequency (i.e. fracture/m) measured along 3 beds and computed stress $\sigma_3$ along the same beds. The maximum fracture frequency matches the location of the highest value of $\sigma_3$ for the 3 layers. The asymmetric nature of fracture frequency with higher frequency to the left of the maximum is reproduced for layers A and B. Layer C displays a symmetric fracture frequency graph that is also reproduced by the restoration.

### 10.8.3 Conclusions and applications to reservoir exploration and production

We have shown that the geomechanically-based restoration technique can be applied to restore both extensional and contractional structures. The technique provides a robust tool for efficiently modeling diffuse deformation (i.e. undetected joints) from computed stress field. These modeling efforts may serve to locate and exploit fractured regions of reservoirs.

## 10.9 Conclusions

The restoration method presented here combines fundamental physical laws that govern rock deformation, including conservation of momentum and mass, with the kinematic constraints necessary for restoring geological structures. The physical laws and linear elastic

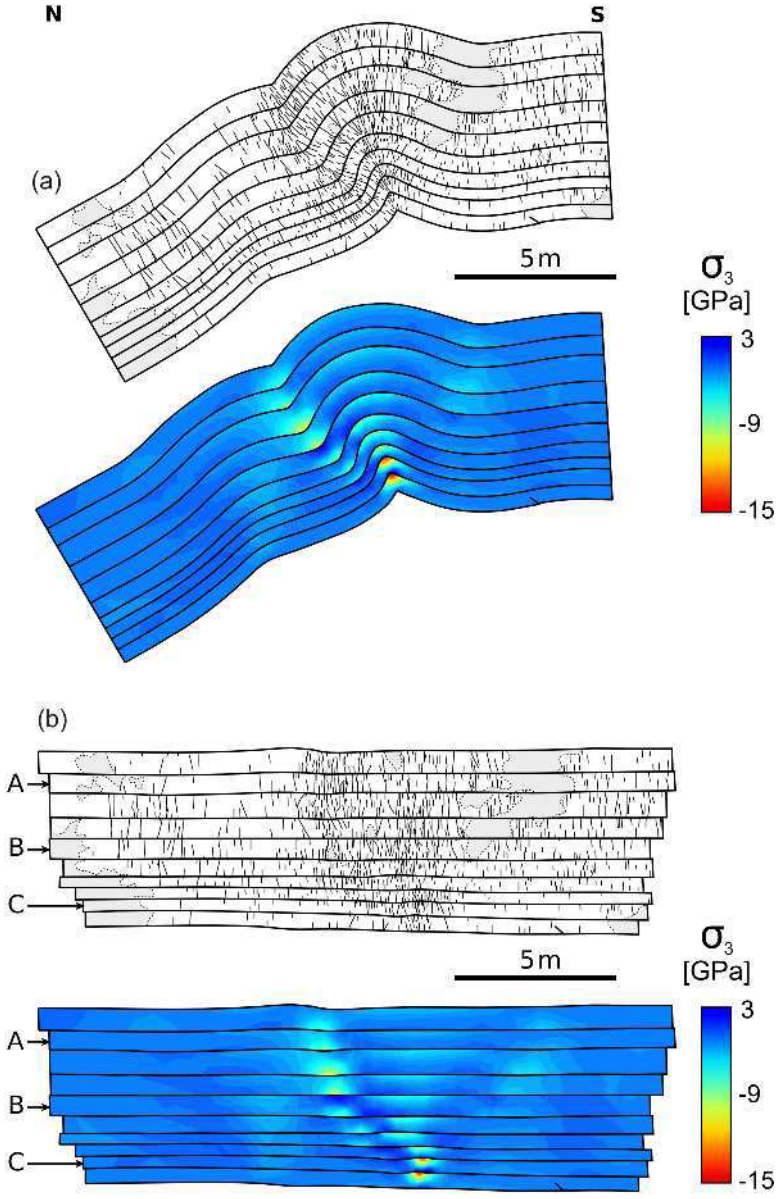


FIGURE 10.16: Comparison between observed fractures and computed stress. (a) Observed fractures and iso-contours of the computed least principal stress ($\sigma_3$) resulting from the restoration and plotted over the initial unrestored geometry. (b) Observed fractures and iso-contours of computed $\sigma_3$ on the actual fold geometry. Note that $\sigma_3$ is the stress produced by folding the beds. The inverse of that stress corresponds to the maximum principal stress ($\sigma_1$) that is computed when we restore the folded beds to the sub-horizontal beds. Fracture closely matched the highest values of $\sigma_3$. A, B, and C represents the graphs of figure 10.17.

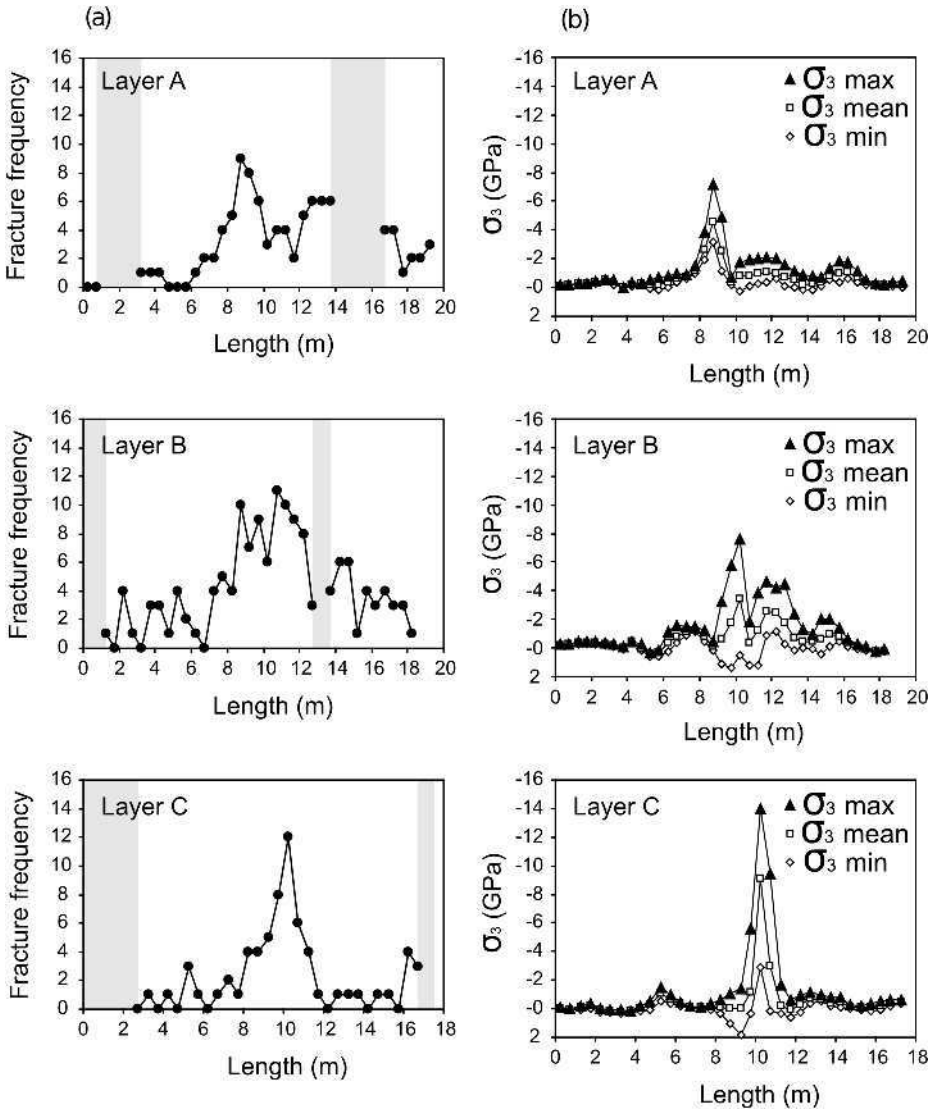


FIGURE 10.17: Comparison between observed fractures and computed stress. (a) Observed fracture frequency (i.e. fracture per meter) for 3 different layers A, B and C. Gray bands are area of no data because of vegetation. (b) Computed $\sigma_3$ along the 3 layers A, B, and C. Fracture frequency closely matched the values of the least principal stress $\sigma_3$.

theory replace ad hoc kinematic and geometric assumptions commonly used by other methods, including preservation of segment length, area, or volume. The main benefits of such an approach are: (i) rock mechanical properties and their variation throughout the geological model are taken into account; (ii) the mechanical interaction of faults and slipping bedding surfaces are modeled; and (iii) the method applies the same principles to restore geological structures from any tectonic setting. In contrast, kinematic and geometric models typically adopt different mechanisms and constraints to mimic the deformation in different tectonic settings. In addition this method computes stresses from the restoration and these can be related to small-scale structural heterogeneities (i.e. sub-seismic faults, joints).

The results of this study have shown that the geomechanically-based restoration approach, despite its limitations in terms of inelastic deformation, allows one to successfully model fault chronology as well as small-scale joints during restoration. We have demonstrated, through the restoration of sand layers in a laboratory experiment, that the approach provides an efficient way to assess fault development through time. We suggest that the approach could have significant potential for evaluating hydrocarbon migration pathways through time and for locating structural traps. Using the same example, we have demonstrated that such an approach could be used in the oil industry to model sub-seismic faults. These predictions may serve to infer reservoir compartmentalization and to locate and exploit faulted regions of reservoirs.
Finally, we have shown that this restoration technique can be applied to restore contractional structures and that it provides a robust tool for efficiently modeling diffuse deformation (i.e. jointing) necessary to exploit fractured reservoirs. Geological restoration based on geomechanics appears a promising route towards improved reservoir characterization.

## 10.10 Acknowledgments

We are grateful to David Pollard for his encouragement and review, Ken McClay for his agreement to use one of his figures, and Loïc Bazalgette for providing the data of the Coulazou's fold. We thank the Structural Geology and Geomechanics Team of Stanford University as well as the IGEOSS's development team for their hard work. We also thank ChevronTexaco, Conoco-Phillips, ExxonMobile, Repsol, Shell, and Total for supporting and funding the project through a research and development consortium.

# References


Arthaud, F. and Séguret, M. (1981). Les structures pyrénéennes du languedoc et du golfe du lion (sud de la france). *Bulletin de la Société Géologique de France*, 23:51–63.

Bai, T., Maerten, L., Gross, M. R., and Aydin, A. (2002). Orthogonal cross joints: Do they imply a regional stress rotation? *Journal of Structural Geology*, 24:77–88.

Bazalgette, L. (2004). *Relations plissement/fracturation multi échelle dans les multi-couches sédimentaires du domaine élastique/fragile: Accommodation discontinue de la courbure par la fracturation de petite échelle et par les articulations. Possibles implications dynamiques dans les écoulements des réservoirs.* PhD thesis, Université de Montpellier II, France.

Bourne, S. J., , Rijkels, A., Stephenson, B. J., and Willemse, E. J. M. (2000). Predictive modeling of naturally fractured reservoirs using geomechanics and flow simulation. *GeoArabia*, 6(1):87–102.

Bourne, S. J. and Willemse, E. J. M. (2001). Elastic stress control on the pattern of tensile fracturing around a small fault network at nash point, uk. *Journal of Structural Geology*, 23:1753–1770.

Bulnes, M. and McClay, K. (1999). Benefits and limitations of different 2d algorithms used in cross-section restoration of inverted extensional faults: application to physical experiments. *Tectonophysics*, 312:175–189.

Childs, C., Easton, S. J., Vendeville, B. C., Jackson, M. P. A., Lin, S. T., Walsh, J. J., and Watterson, J. (1993). Kinematic analysis of faults in a physical model of growth faulting above a viscous salt analogue. *Tectonophysics*, 228:313–329.

Childs, C., Walsh, J. J., and Watterson, J. (1990). A method for estimation of the density of fault displacements below the limits of seismic resolution in reservoir formations. *North Sea oil and gas reservoirs: Liverpool, The Norwegian Institute of Technology*, 2:193–203.

Clark, S. P. (1966). *Handbook of physical constants (revised edition)*, volume 97. Geological Society of America Memoir.

Dahlstrom, C. D. A. (1969). Balanced cross section. *Canadian Journal of Earth Sciences*, 6:743–757.

Davatzes, N. C., Eichhubl, P., and Aydin, A. (2005). Structural evolution of fault zones in sandstone by multiple deformation mechanisms: Moab fault, southeast utah. *Geological Society of America Bulletin*, 117:135–148.

Davison, I. (1986). Listric normal fault profiles: Calculation using bed-length balance and fault displacement. *Journal of Structural Geology*, 8:209–210.

Dokka, R. K. and Travis, C. J. (1990). Late cenozoic strike-slip faulting in the mojave desert, california. *Tectonics*, 9:311–340.

Dorn, G. A. (1998). Modern 3d seismic interpretation. *The Leading Edge*, 17:1262–1272.

Dula, W. F. (1991). Geometric models of listric normal faults and rollover folds. *AAPG Bulletin*, 75:1609–1625.

Dunbar, J. A. and Cook, R. W. (2003). Palinspastic reconstruction of structure maps: An automated finite element approach with heterogeneous strain. *Journal of Structural Geology*, 26:1021–1036.

Ellis, P. G. and McClay, K. (1988). Listric extensional fault system - results of analogue model experiments. *Basin Research*, 1:55–70.

Erickson, G. S., Strayer, L. M., and Suppe, J. (2001). Mechanics of extension and inversion in the hanging walls of listric normal faults. *Journal of Geophysical Research*, 106:26,655–26,670.

Erickson, S. G., Hardy, S., and Suppe, J. (2000). Sequential restoration and unstraining of structural cross sections: Application to extensional terranes. *AAPG Bulletin*, 84:234–249.

Gauthier, B. D. M. and Lake, S. D. (1993). Probabilistic modeling of faults below the limit of seismic resolution in pelican field, north sea, offshore united kingdom. *AAPG Bulletin*, 77:761–776.

Gibbs, A. D. (1983). Balanced cross-section construction from seismic sections in areas of extensional tectonics. *Journal of Structural Geology*, 5:153–160.

Gillespie, P. A., Howard, C., Walsh, J. J., and Watterson, J. (1993). Measurement and characterisation of spatial distributions of fractures. *Tectonophysics*, 226:113–141.

Golub, G. H. and Van Loan, C. F. (1996). *Matrix computation*. Johns Hopkins University Press, Baltimore, MD.

Gratier, J.-P., Guillier, B., Delorme, A., and Odonne, F. (1991). Restoration and balance of a folded and faulted surface by bestfitting of finite elements: Principle and applications. *Journal of Structural Geology*, 13:111–115.

Guiton, M. L. E. (2001). *Contribution of pervasive fractures to the deformation during folding of sedimentary rocks: Thése de Doctorat.* PhD thesis, École Polytechnique, Paris, France.

Guiton, M. L. E., Leroy, Y. M., and Sassi, W. (2003a). Activation of diffuse discontinuities and folding of sedimentary layers. *Journal of Geophysical Research*, 108.

Guiton, M. L. E., Sassi, W., Leroy, Y. M., and Gauthier, B. D. M. (2003b). Mechanical constraints on the chronology of fracture activation in folded devonian sandstone of the western moroccan anti-atlas. *Journal of Structural Geology*, 25:1317–1330.

Hauge, T. A. and Gray, G. G. (1996). A critique of techniques for modelling normal-fault and rollover geometries. *Modern developments in structural interpretation, validation and modelling: Geological Society (London) Special Publication*, 99:89–97.

Healy, D., Yielding, G., and Kusznir, N. (2004). Fracture prediction for the 1980 el asnam, algeria earthquake via elastic dislocation modeling. *Tectonics*, 23:1–21.

Hennings, P. H., Olson, J. E., and Thompson, L. B. (2000). Combining outcrop data and three-dimensional structural models to characterize fractured reservoirs: An example from wyoming. *AAPG Bulletin*, 84:830–849.

Hossack, J. R. (1979). The use of balanced cross section in the calculation of orogenic contraction: A review. *Journal of the Geological Society (London)*, 136:705–711.

Hughes, T. J. R. (1987). *The finite element method: linear static and dynamic finite element analysis.* Prentice-Hall, New Jersey.

Jaeger, J., Cook, N., and Zimmermann, R. (2007). *Fundamentals of Rock Mechanics.* Blackwell Publ., Malden, MA.

Kattenhorn, S., Aydin, A., and Pollard, D. (2000). Joints at high angles to normal fault strike: an explanation using 3d numerical model of fault perturbated stress field. *Journal of Structural Geology*, 22:1–23.

Kerr, H., White, N., and Brun, J.-P. (1993). An automatic method for determining 3-d normal fault geometry. *Journal of geophysical Research*, 98:17,837–17,857.

Lévy, B. (2000). *Topologie algorithmique combinatoire et plongement.* PhD thesis, University of Nancy, Nancy, France.

Maerten, L. (2000). Variation in slip on intersectiong normal faults: Implications for paleostress inversion. *Journal of Geophysical Research*, 105(25):553–565.

Maerten, L., Gillepsie, P., and Pollard, D. (2002). Effect of local stress perturbation on secondary fault development. *Journal of Structural Geology*, 24:145153.

Maerten, L., Pollard, D. D., and Maerten, F. (2001). Digital mapping of three-dimensional structures of the chimney rock fault system, central utah. *Journal of Structural Geology*, 23:585–592.

Maerten, L., Willemse, E. J. M., Pollard, D. D., and Rawnsley, K. (1999). Slip distributions on intersecting normal faults. *Journal of Structural Geology*, 21:259–271.

McClay, K. R. (1990). Extensional fault systems in sedimentary basins: A review of analogue model studies. *Marine and Petroleum Geology*, 7:206–233.

Medwedeff, D. A. and Krantz, R. W. (2002). Kinematic and analog modeling of 3-d extensional ramps: Observations and a new 3-d deformation model. *Journal of Structural Geology*, 24:763–772.

Nicol, A., Walsh, J. J., Watterson, J., and Bretan, P. G. (1995). Three dimensional geometry and growth of conjugate normal faults. *Journal of Structural Geology*, 17:847–862.

Novozhilov, V. V. (1953). *Foundations of the nonlinear theory of elasticity*. Graylock Press.

Rouby, D., Cobbold, P. R., Szatmari, P., Demerican, S., Coelho, D., and Rici, J. A. (1993). Least-squares palinspastic restoration of region of normal faulting - application to the campos basin (brasil). *Tectonophysics*, 221:439–452.

Rouby, D., Xiao, H., and Suppe, J. (2000). 3-d restoration of complexly folded and faulted surfaces using multiple unfolding mechanisms. *AAPG Bulletin*, 84:805–829.

Samson, P. (1996). Equilibrage de structures géologiques 3d dans le cadre du projet gocad. Master's thesis, Institut National Polytechnique de Lorraine, Lorraine, France.

Sanders, C., Bonora, M., Kozlowski, E., and Sylwan, C. (2002). From 2d to 4d fracture network model, structural modeling of a complex thrust trap: A case study from the tarija basin, argentina. *Society of Petroleum Engineers*, ISRM78184:1–8.

Sanders, C., Bonora, M., Richards, D., Kozlowski, E., Sylwan, C., and Cohen, M. (2004). Kinematic structural restorations and discrete fracture modeling of a thrust trap: A case study from the tarija basin, argentina. *Marine and Petroleum Geology*, 21:845–855.

Sassi, W., Livera, S. E., and Caline, B. P. R. (1992). Quantification of the impact of subseismic scale faults on cormorant block iv. *R. M. Larsen, H. Brekke, B. T. Larsen, and E. Talleraas, eds., Structural and tectonic modeling and its application to petroleumgeology: Norwegian PetroleumSociety (NPS), Special Publication, Elsevier, Amsterdam*, 1:355–364.

Schlische, R. W., Young, S. S., Ackermann, R. V., and Gupta, A. (1996). Geometry and scaling relations of a population of very small rift-related normal faults. *Geology*, 24:683–686.

Shelton, J. W. (1984). Listric normal faults: An illustrated summary. *AAPG Bulletin*, 68:801–815.

Walsh, J. J. and Watterson, J. (1991). Geometric and kinematic coherence and scale effects in normal fault systems. *A. M. Roberts, G. Yielding, and B. Freeman, eds., The geometry of normal faults: Geological Society (London) Special Publication*, 56:193–203.

White, N. J., Jackson, J. A., and McKensie, D. P. (1986). The relationship between the geometry of normal faults and that of sedimentary layers in their hanging walls. *Journal of Structural Geology*, 8:897–909.

Willemse, J. M. (1997). Segmented normal faults: Correspondence between three-dimensional mechanical models and field data. *Journal of Geophysical Research*, 102:675–692.

Williams, G. D., Kane, S. J., Buddin, T. S., and Richards, A. J. (1997). Restoration and balance of complex folded and faulted rock volumes: Flexural flattening, jigsaw fitting and decompaction in three dimensions. *Tectonophysics*, 273:203–218.

Williams, G. D. and Vann, I. (1987). The geometry of listric normal faults and deformation in their hanging walls. *Journal of Structural Geology*, 9:789–795.

Withjack, M. O., Islam, Q. T., and La Pointe, P. R. (1995). Normal faults and their hanging-wall deformation: An experimental study. *AAPG Bulletin*, 79:1–18.

Wriggers, P. (2002). *Computational Contact Mechanics*. J. Wiley and sons, New York.

Yamada, Y. and McClay, K. (2003). Application of geometric models to invert listric fault systems in sandbox experiments: Paper 1 - 2d hanging wall deformation and section restoration. *Journal of Structural Geology*, 25:1551–1560.

Yielding, G., Walsh, J. J., and Watterson, J. (1992). The prediction of small-scale faulting in reservoirs. *First Break*, 10:449–460.

# CHAPTER 11

# Geomechanically smoothing noisy horizons

F. Maerten[1,2], L. Maerten[1]

(1) Igeoss, Montpellier, FRANCE
(2) University of Montpellier II, Geosciences, FRANCE

In preparation for AAPG Bulletin

**Preamble**

This chapter presents a geomechanically-based smoothing filter for noisy 3D horizons. It is shown that the filter removes geometrical artifacts where, for example, high stress concentration occurs after unfolding and unfaulting, while smoothing fault cut-offs and transforming high displacement gradients at crack-tips to more realistic values.

## About...

Laurent Maerten, as usual, did most of the modeling. Paul Griffith, from BG-Group, participated to fruitful discussions.

# Article Outline

## 11.1 Résumé

Nous présentons un filtre de lissage d'horizons 3D faillés et plissés basé sur la géomécanique. Ce filtre corrige de façon adaptative la géométrie en fonction d'un critère prescrit par l'utilisateur et basé sur le changement d'aire, de déformation ou de contrainte. Un code de restauration, s'appuyant sur une méthode itérative d'éléments finis (FEM) et basé sur la géomécanique avec gestion des contacts, est utilisé comme outil pour détecter les anomalies géométriques sur les surfaces 3D. Il est montré que ce type de filtrage supprime les irrégularités géométriques où, par exemple, une concentration de contraintes élevées est décelée après dépliage et défaillage, tout en lissant la trace des failles et les forts gradients de déplacement en bout de faille en une géométrie plus plausible. Les surfaces de faille 3D ainsi reconstruites depuis ces horizons filtrés sont par conséquent moins buitées.

## 11.2 abstract

We present a mechanically-based smoothing filter for complex three-dimensional (3D) folded and faulted horizons which adaptively corrects the geometry according to a user prescribed criteria based on area change, strain or stress. A restoration code, built upon an iterative Finite Element Method (FEM) in *geostructural* mechanics with contact management, is used as a tool to detect anomalous geometrical configurations on 3D surfaces. It is shown that the filter removes geometrical artifacts where, for example, high stress concentration occurs after unfolding and unfaulting, while smoothing fault cut-off and transforming high displacement gradient at crack-tip into a more plausible geometry. Reconstructed fault surfaces from such filtered horizons are consequently less corrugated.
**Keyword**: Finite Element Method, Iterative solver, Geomechanics, Filtering

## 11.3 Introduction

When using numerical codes in geomechanics for the determination of the perturbed stress field or for the validation of interpretations, the geometry of the underlying model is critical. As an example, using the Boundary Element Method (BEM) code iBem3D (Maerten and Maerten, 2008; Maerten et al., 2005, 2009a,b; Maerten, 2010) requires a non-noisy geometry of faults as they will mainly control the characteristic of the perturbed stress field due to slipping surfaces. Noisy input geometries, such as corrugated or bumped surfaces, will inevitably introduced artifacts within the result. Another example is given by Dynel (Maerten and Maerten, 2006), a Finite Element Method (FEM) restoration tool in 2D and 3D that allows validating seismic interpretations using geomechanics. If input horizons are noisy in geometry, the resulting restored cross section or volume will inevitably show high strain or stress concentration at bumps, or artifacts where steps are present.

Therefore, it is necessary to filter input surfaces from eventual distorted geometries, while keeping the natural features unchanged (e.g. opened crack-tips). Fig. 11.1 shows some commonly observed distortions on a 3D interpreted seismic horizon, and are sevenfold. First, some **steps** are observable (rectangles Fig. 11.1, and are mainly due to the bad quality of the seismic images as well as the manually or semi-automatic detection of horizons from the 3D seismic image. Second, **fault cut-off** (ellipsis in Fig. 11.1) are generally wavy with kink angle due to the discretization of the surface. Third, **fault tips** (squares in Fig. 11.1) can have exaggerated displacement gradient. Fourth, **bumps** (circles in Fig. 11.1) can be observed at some places which can be natural or resulting from the missed

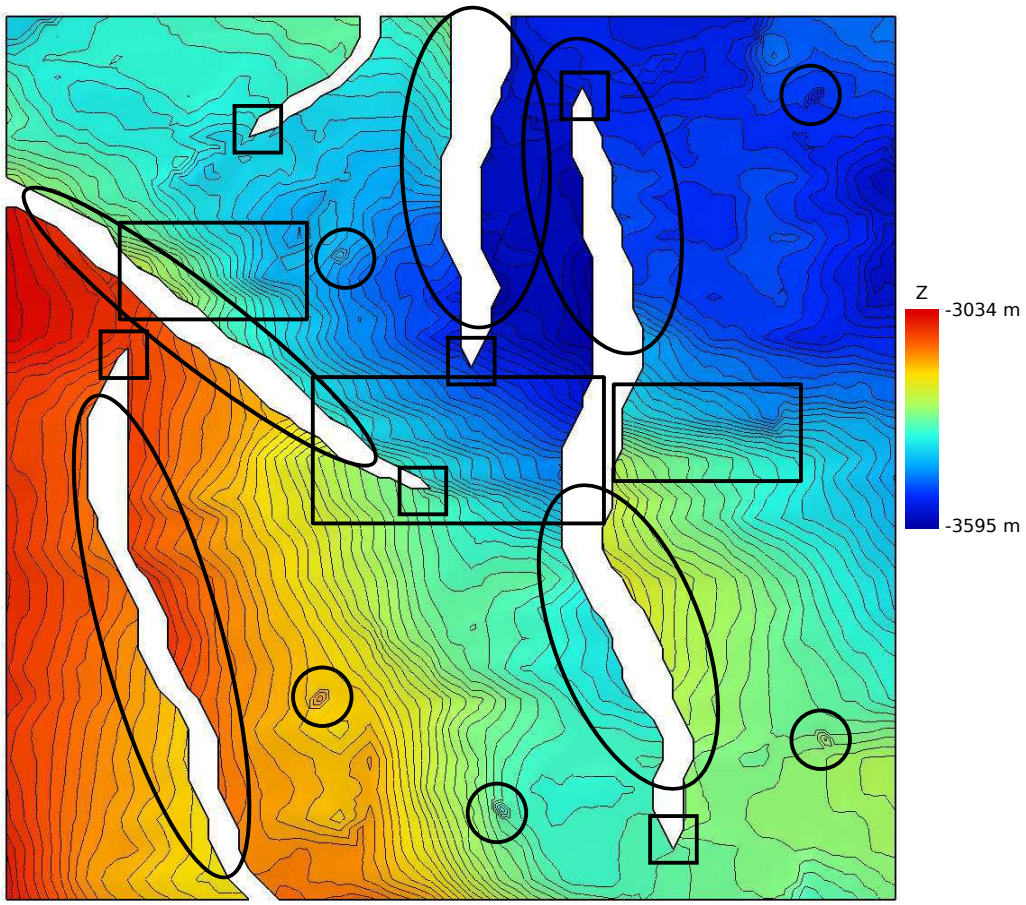


FIGURE 11.1: Example of a 3D horizon with geometrical irregularities. Top view of the 3D horizon with displayed iso-contours of elevation. Four potential problems can be observed: (1) *steps* on the surfaces (rectangles), (2) wavy fault *cut-off* with sharp angles (ellipses), (3) *bumps* (circles), and (4) unrealistic fault *tips* geometries (squares).

interpretation. Fifth, the **mesh discretization** (density and topology) can leads to some artifacts. Sixth, even if it is not used in present study, **material heterogeneity** can have an impact, especially for high contrast of the Young's modulus. Finally, **material anisotropy** (e.g. material orthotropy), can also generate perturbations.

Different type of algorithms exist for noise removal. Some of them deal directly from acquired data before the conversion into a mesh or meshes: mean and Gaussian linear filters, conservative-smoothing, trimmed-mean, mode, median and symmetric-nearest-neighbor non-linear filters (Hall, 2007).

Other methods work directly on triangulated meshes. When a mesh is constructed from acquired data, measurement error can result in a rough mesh, and smoothing can attenuate this noise. But in general, mesh post-processing algorithms may introduce undesirable artifacts. The most common method for smoothing meshes is the Laplacian (Taubin, 1995;

Desbrun et al., 1999), also known as *diffusion*. This filter has a couple of desirable properties. First, it does not modify the connectivity of a mesh, but only the position of the vertices. The triangulation remains unchanged. Second, the discrete Laplacian can be formulated so that smoothing a given vertex only requires direct connectivity information. As the size of the mesh increases, the number of neighbors of a vertex remains constant. Consequently, the Laplacian smoothing can be linear in space and time. The Laplacian smoothing also suffers from undesirable properties. Shape distortion and shrinkage of the mesh are the common ones.

We present a new method that can answers the previous pitfalls by using the rock mechanics on triangulated 3D folded and faulted surfaces (2-manifold of genus 0 with external and internal borders). This algorithm is based on the Finite Element Method for 3D surfaces that are unfolded and unfaulted at the same time on a target surface (e.g., a plane), and which provides relevant information about anomalous geometries. The method does geometrical corrections of the surface geometry in the initial space by minimizing a user selected criteria (e.g. area variation or high strain/stress concentration) in the restored space.

## 11.4 Features classification

In order to develop the mechanically-based smoothing filter, some remarkable features have to be described first. For the moment, we are not interested in the magnitude of a given criteria, but rather on the detection of the potential geometrical irregularities of an horizon.

1. *Perfectly developable surface*
   For a developable surface without any corrugation and fault traces, the result of the unfolding process leads to no area-changed as shown in Fig. 11.2. In this example, a crumpled squared thin sheet of paper, that has been digitalized using the Stanford digital scanner, is unfolded on an horizontal and planar target plane. As expected, unfolding this mesh produces a non-distorted planar surface, where the final area is identical to the original one within an error of 0.0005%.

2. *Bumps*
   However, for a artificially distorted surface, stress concentration are well localized at the asperities. This is shown in Fig. 11.3, which uses the same triangulated surface as in Fig. 11.2 and where we artificially created an asperity.

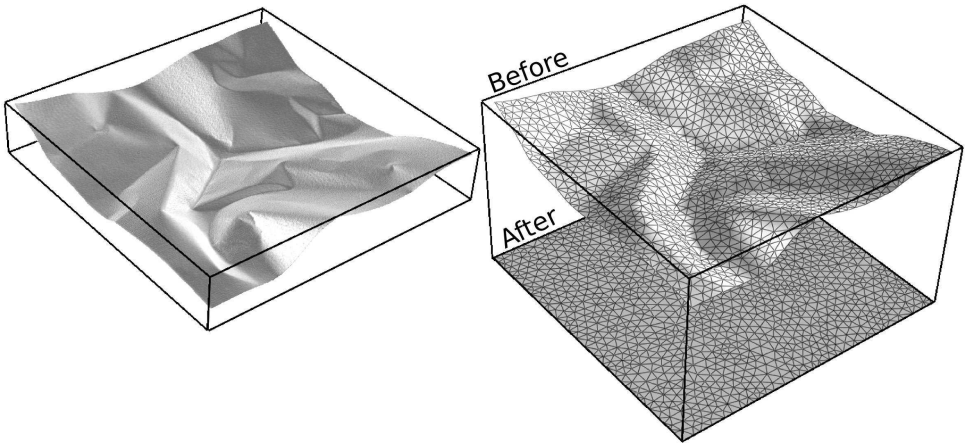


FIGURE 11.2: A developable surface. Left: crumpled squared thin sheet of paper that has been digitalized using the Stanford digital scanner. Right-top: mesh used for the unfolding. Right-bottom: Unfolded surface on a planar horizontal target. The change in area is 0.0005

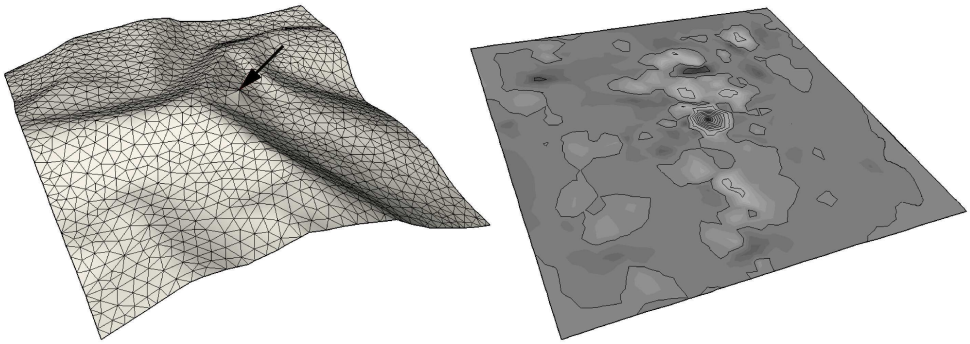

FIGURE 11.3: A developable surface with an artificial asperity. Left: marked asperity. Right: after unfolding, high stress concentration is visible

3. *Steps*

   From Fig. 11.1 (rectangles), "steps" can be observable and are mainly due to the interpretation discretization. These features are obviously not natural and are a side effect of the segmentation process.

4. *Fault tips*

   Fault tips usually present low displacement gradient since they represent the termination of a fault. Therefore, unrealistic high angle should be reduced to a lower value (squares in Fig. 11.1).

5. *Fault cut-off*

   The shape of the fault cut-off should be altered if necessary as shown in modified "Big Smile" model (ellipses in Fig. 11.1 and Fig. 11.4, left), where the fault trace was made irregular intentionally.

6. *Discretization effect*

   Of course, the mesh density will control the overall aspect of the surface. For a coarse

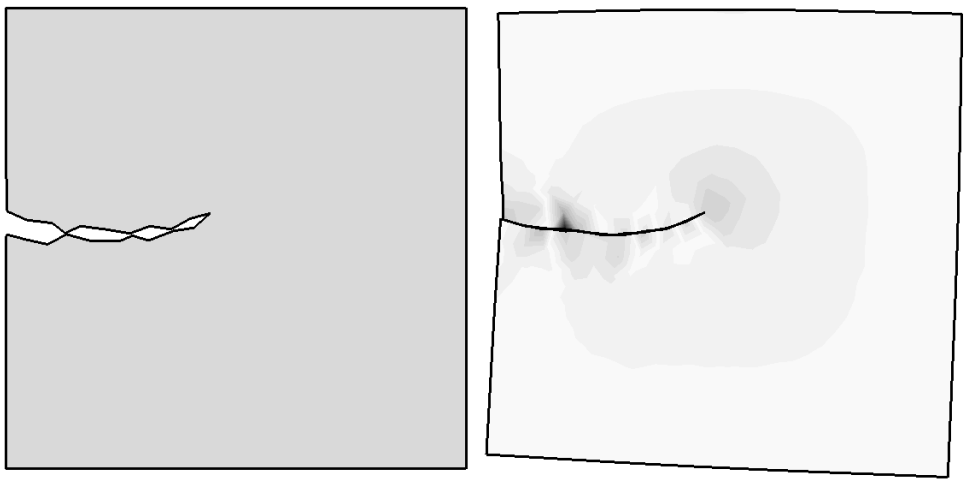

FIGURE 11.4: Irregular fault cut-off for the "Big Smile" surface. Left: initial planar surface before unfaulting. Right: unfaulted cut-off showing the presence of a high stress concentrations

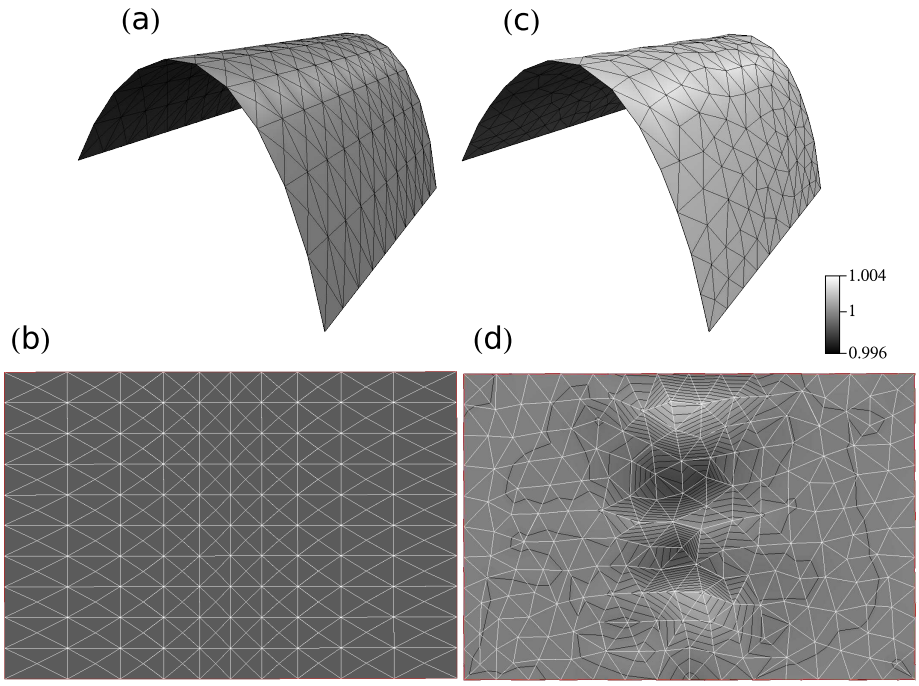


FIGURE 11.5: Mesh effect. Effect of the topological configuration and mesh density after unfolding the surface. (a) Initial regular mesh of a developable surface and (b) after unfolding, no concentration is observable. The surface is perfectly developable. (c) Initial irregular mesh of a developable surface and (d) corresponding concentration due to a bad topological configuration and coarse mesh discretization. Note that the area change is relatively small (4%)

mesh, the topology as well as the fault cut-off cannot be represented precisely. For features such as valley and ridges, triangular edges have to pass through them, in order to minimize the distortions (Fig. 11.5).

7. *Material heterogeneity*

   Even if we can generally consider seismic horizons as an interface between two

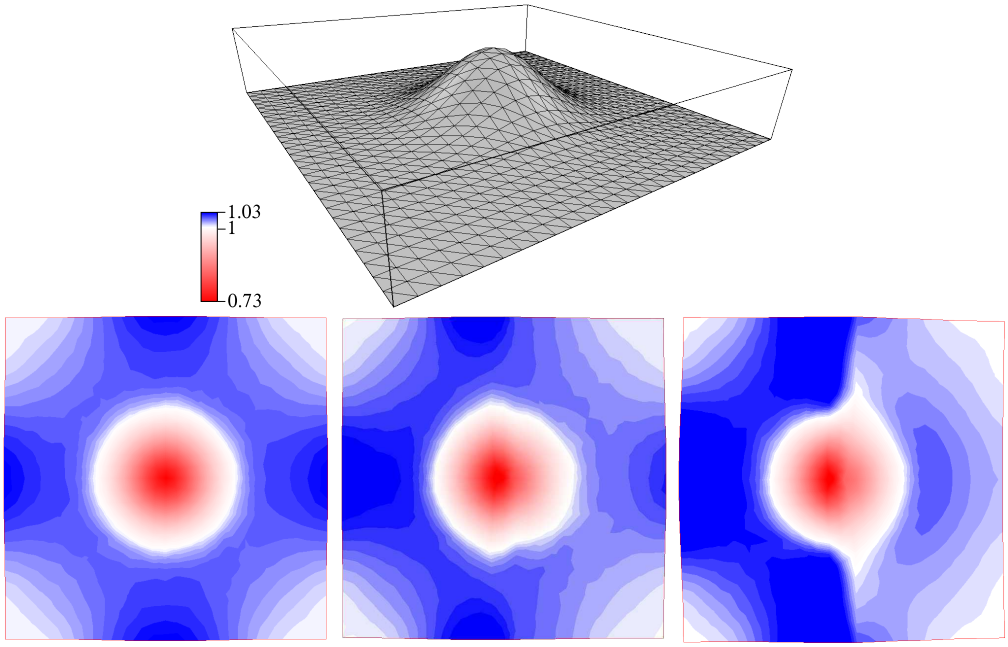


FIGURE 11.6: Effect of mechanical properties. Unfolding of a non-developable (Gaussian) surface with homogeneous (left), heterogeneous Poisson's ratio (middle) and Young's modulus (right).

different materials, it is worth to mention the effect of the contrast in material properties, as shown in Fig. 11.6. A 3D Gaussian is constrained to be unfolded on a target plane, and three different scenarios are studied. The first one (left of Fig. 11.6) supposes an homogeneous material ($E = 1$ and $\mu = 0.25$), and the unfolding leads to symmetric iso-values of change in area. The second and third one, play with the variation of the Poisson's ratio and Young's modulus (Fig. 11.6, middle and right, respectively). For half of the Gaussian, the Poisson's ratio is set to $\mu = 0.49$ and the other part to $\mu = 0.01$, the Young's modulus being the same for the two parts. After unfolding, stress concentration is observable when the Poisson's ratio changes. Similarly (right of Fig. 11.6), the change in Young's modulus ($E = 1$ for the right part, and $E = 3$ for the other) creates perturbed stress, while the Poisson's ratio remains the same for the whole Gaussian. Note that in both heterogeneous cases, the resulting unfolded surfaces contour are different from the homogeneous case.

8. *Material anisotropy*

   Anisotropic materials can also generate perturbed stress field. Consider an orthotropic material with a given angle of orthotropy and different value of the Young's modulus and Poisson's ratio for the two local axis. This material will preferably will stiffer in one direction than the other, leading to a stretched unfolded surface in the direction of softer Young's modulus.

## 11.5 Iterative FEM method

The method described in this paper follows the same principles as the one presented in (Maerten and Maerten, 2006). Rather that working in 2D, we extended the method to 3D surfaces (denoted 2.5D in the remaining of this paper) and volumes, but are only interested in the former. In order to detect geometrical irregularities, we employs Dynel, a restoration technique on a planar target surface for folded and faulted surfaces while unfaulting the fault traces at the same time without friction.

Dynel is a continuum code based on FEM (Hughes, 1987) for modeling the behavior of complex geological structures such as folded, fractured and faulted rock. Its formulation can accommodate large displacements and strains for a linear, heterogeneous, anisotropic and discontinuous medium.
Models are discretized with linear triangular elements in 2.5D, which form a 3D mesh. Each element has assigned material properties, if necessary, that may differ from element to element, and each behaves according to a prescribed linear elastic law in response to constraints such as applied and/or internal forces, displacements, and interface contact reactions. As opposed to the standard implicit FEM (Hughes, 1987), where a global stiffness matrix is built for solving for the unknown displacements, we use an iterative solver based on the block Gauss-Seidel method (Golub and Van Loan, 1996). This solver allows forces to be transmitted from node to node through the entire system until equilibrium is obtained. Nodal forces are computed using the stress state of each connected element, and take into account other forces such as external and contact reaction forces. We will see in section 11.6 that this formulation allows fast update of the local stiffness matrices, without the need to reconstruct the entire global matrix, leading in fast computations.

### 11.5.1 Determination of the element and nodal deformation

Even if the processes of unfolding and unfaulting is done in 2D, we have to take into account the 3D nature of the triangles. To do so, the stiffness matrix associated to each element is computed using the initial nodes position in the element's local coordinate system. For a given node the nodal stiffness is determined using the stiffness matrices of the incident elements after a rotation into the global coordinate system, and by pretending that, for a given node, all the other neighboring nodes are fixed. Elemental and nodal stiffness matrices are computed at initialization, which greatly improves the speed of the solver.

Initially, the system is at rest in equilibrium. Unfolding and unfaulting will make the system evolve by deforming the elements and consequently by generating internal strain at elements. The strain is then transformed to a stress by using the Hooke's law (Jaeger et al., 2007). Nodal forces are then derived as a function of the element stress tensor. Using the element local coordinate system is twofold. First, it takes into account rigid body rotation. Second, it allows fast computations by avoiding the use of the rotation matrix from global to local and local to global coordinate system.

At iteration i, and according to the prescribed boundary conditions, the nodes subjected to internal and external forces are displaced, causing deformation of the incident elements. The stress state associated to an incident element is computed at the considered node. This process is done for every connected elements, and the corresponding forces at the node are summed-up in the global coordinate system. The total nodal force is then transform back to a displacement vector using the nodal compliance matrix being the inverse of the nodal stiffness matrix and pre-computed at initialization. Then, and according to the node boundary conditions, the node is virtually displaced in order to detect eventual contacts using the master/slave technique. Finally, the contact forces are added at the involved nodes.

### 11.5.2 Contacts at interfaces

Contacts are modeled using the concept of slave nodes and master segments, which is the same technique used in (Maerten and Maerten, 2006). Consider two fault blocks in contact. If a node of the interface mesh of one block penetrates a segment from the interface mesh of the second block, the node is considered a slave node whereas the segment is considered a master segment. A contact force is then applied to push the node back toward the outside of the element containing the master segment. Thus, the contact force is directed toward the master segment along the normal to that segment. The master-slave concept implemented here allows nodes to be both slave nodes for an iteration and part of a master segment for other iterations. Therefore, to solve fault-block contact problems, it is not necessary to assign the master and slave roles to boundary surfaces. During the restoration process nothing is imposed about the movement of the fault traces. Only the closing of traces is imposed, while they are allowed to slip with no friction as the mesh deform.

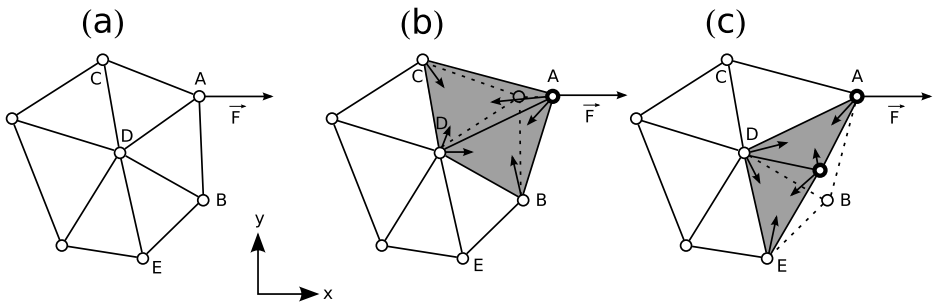


FIGURE 11.7: Force propagation in Dynel. (a) Initial geometry and external force applied to node A. (b) After the node has moved, internal forces, due to the deformation of the incident triangular elements, appear at nodes A, B, C and D. (d) At next iteration, the node B is moved according to its force, generating new internal forces at nodes A, B, D and E. This process continue for all nodes until all the system is at equilibrium

### 11.5.3 Solving the system

The explicit solver is based on the block Gauss-Seidel method, which allows nodal forces to be transmitted from node to node, until equilibrium is reached. Each node is treated independently from the others in order to allow fast nodal stiffness update, and the order in which they are checked is irrelevant. Gauss-Seidel is an iterative method for solving partial differential equations on a triangulated surface (2D) or tetrahedrized volume (3D). When a node is checked, its new position depends on the current positions of the connected neighboring nodes (Fig. 11.7). The key feature of this algorithm is that it uses new information, for instance updated mesh node positions, as soon as they become available, as opposed to the Jacobi's method (Golub and Van Loan, 1996) in which the update of each node depends only on the values at neighboring nodes from the previous iteration. For a given node, we calculate the force resulting from the deformation of each connected element. The contact forces are then added. This force is then transformed back to a displacement vector using the nodal stiffness matrix. This matrix is defined as the sum of the stiffness matrices of the connected elements, for which the other nodes are considered fixed. Then, the displacement constraints or displacement boundary conditions, such as fixity, unfolding and unfaulting, are applied to the computed displacement vector. Finally, the node is moved according to the new displacement vector and the iteration jumps to the next node. The algorithm stops when the sum of the squared norm of the nodal displacement vector is below a given threshold value.

## 11.6 Geomechanical smoothing filter

In this section, we describe the main algorithm to correct the geometry of a noisy surface using the processes of unfolding and unfaulting.

After the unfolding and unfaulting processes have finished to converge, i.e. the nodal mean squared displacement is less than a user prescribed threshold, the geometrical correction algorithm takes place while the previous two others processes continue to be activated.

The goal of this algorithm is to modify the nodes geometry in initial space, and therefore the associated stiffnesses (nodal and at the incident elements), in order to minimize a user selected criteria (area change, stress, strain) within a given range in the restored space. Since the direction of the minimization is unknown, some preliminary tests have to be launched for the six possible directions ($-\mathbf{x}$, $\mathbf{x}$, $-\mathbf{y}$, $\mathbf{y}$, $-\mathbf{z}$, $\mathbf{z}$). To do so, and for a given direction vector $\mathbf{d}$, a candidate node is virtually moved in the initial space of $\delta\mathbf{d}$, where $\delta$ is a small value compare to the incident edges length to the node. Then, the criteria is computed at this node and compared to the reference value at the same node to see if it has been reduced. The direction which minimize the best the criteria is retained as the candidate and the node is effectively moved of $\delta\mathbf{d}$, changing its geometry in the initial space. Incident element stiffnesses are then updated, as well as the nodal stiffness. The unfolding and unfaulting processes are run until the new forces, resulting of the change in geometry of the considered node, are in equilibrium. Then, the algorithm goes to another anomalous node.

It is worth to mention that this algorithm converge for any geometrical configuration (given a range of correction), since the initial geometry modifications can accommodate the criteria. The overall process is presented in algorithm (11.8), whereas the nodal minimization is outlined in algorithm (11.9).

As it is hard to evaluate the complexity of such method, we give timing for some models. Table 11.1 resumes the timing of some models presented in this paper using the corrective algorithm or not. Timing on horizon from Fig. 11.15 shows that user interaction remains possible.

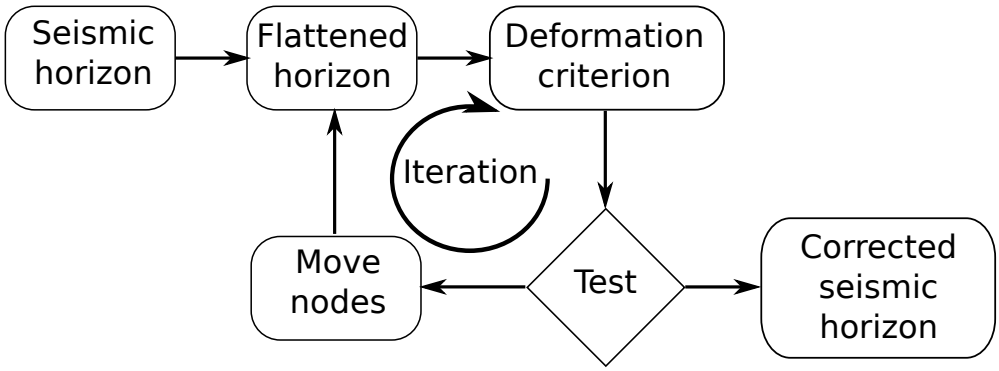


FIGURE 11.8: Overall mechanically-based filter Algorithm combined by the unfolding and unfaulting processes

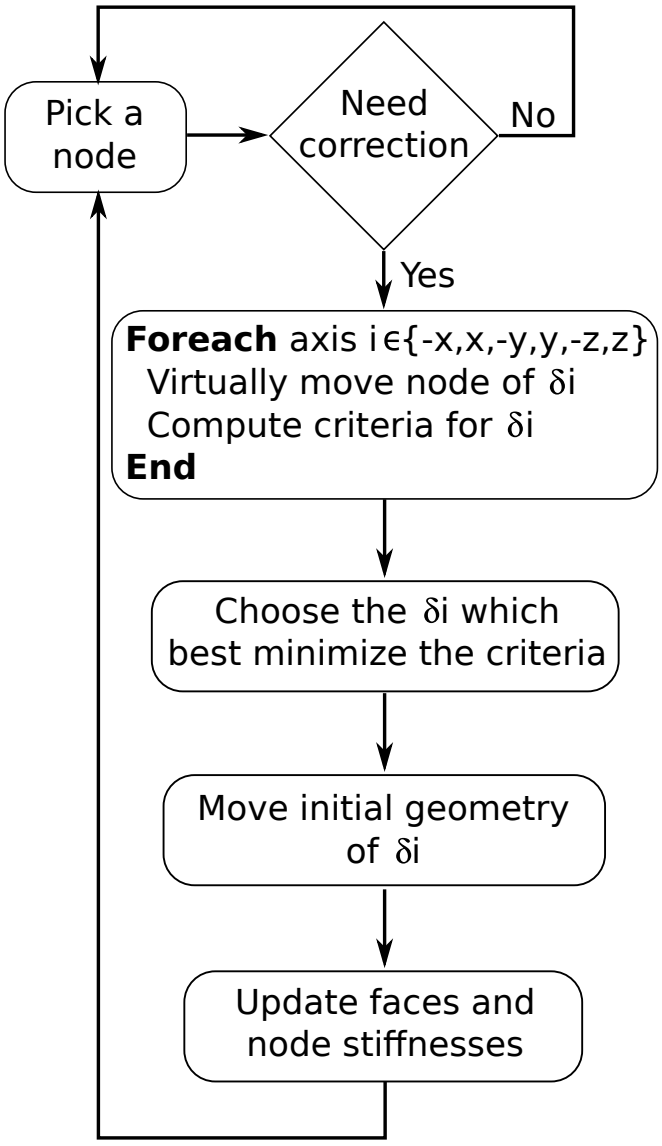


FIGURE 11.9: Mechanically-based filter Algorithm for a given node candidate. The six possible directions of correction are tested before choosing the right one. Then, the initial node position is modified accordingly

TABLE 11.1: Elapsed time (in seconds) for some models presented in this paper. Algorithms "Fold", "Fault" and "Corr" correspond to unfold, unfault and the geometrical correction, respectively. Models "Sheet of paper", "Sheet of paper+bump", "Gauss", "Big smile" and "Horizon" refers to models in figures 11.1, 11.2, 11.3, 11.6, 11.11 and 11.15, respectively.

| Model | Nb nodes | Algo | Time (s) |
|---|---|---|---|
| Sheet of paper | 2000 | Fold | 2 |
| Sheet pf paper+bump | 2000 | Fold+Corr | 2 |
| Gauss | 1000 | Fold | 0.5 |
| Big smile | 800 | Fold+Fault+Corr | 0.2 |
| Horizon | 14000 | Fold+Fault+Corr | 5 |

## 11.7 Verifications

In order to check the validity of the proposed algorithm, we tested it for some of the features described in section 11.4 on synthetic examples.

### 11.7.1 Bumps

Fig. (11.10) shows the geometrical correction applied to the artificially created bump on a 3D surface. Before correction (Fig. 11.10 top right), a high change in area is observable, whereas after correction (Fig. 11.10 bottom left), the bump is removed and the remaining nodes are not altered by the algorithm, significantly reducing the user selected criteria concentration (Fig. 11.10, bottom right).

### 11.7.2 Fault's tip

Fig. 11.11 show the effect on the "Big Smile" model. After unfaulting, area-change concentration occurs at the tip of the fault after unfaulting. This concentration cannot be removed by the algorithm, since a small change along $x$ or $y$ (in-plane) increases the area-change (Fig. 11.11 bottom right).

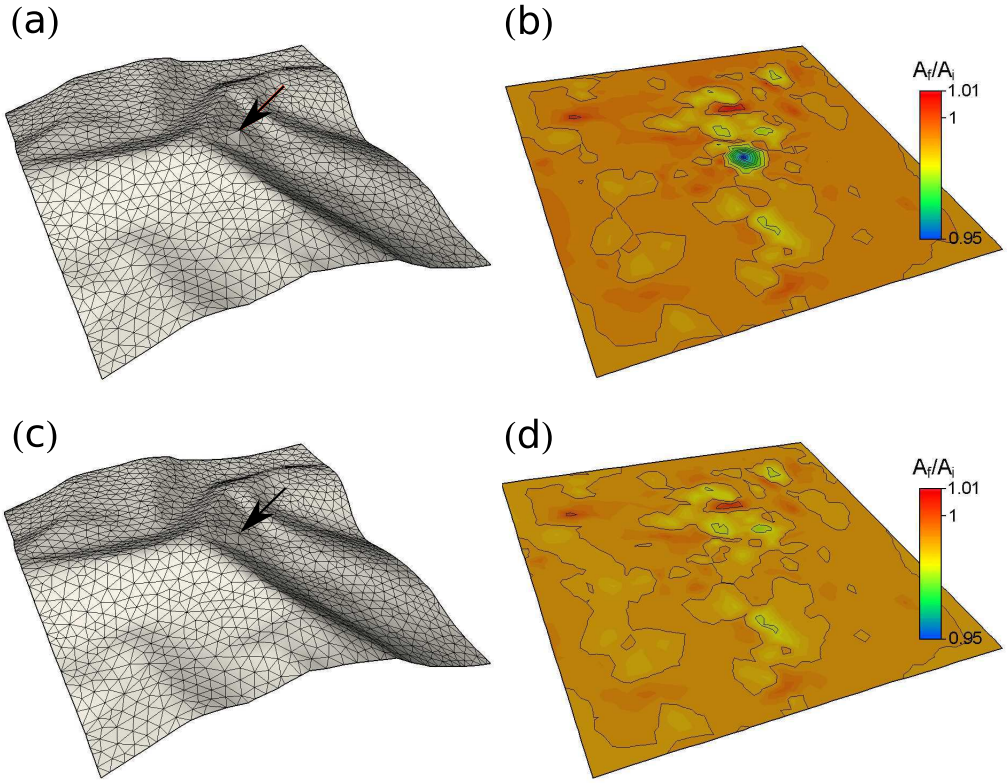


FIGURE 11.10: Bump correction. (a) initial modified geometry pointed by the black arrow; (b) resulting area change after unfolding where a high concentration is observable at the bump location; (c) after geometrical correction of the mesh (the removed bump is pointed by the black arrow); (d) corresponding area change iso-contours, where the high concentration has disappeared

### 11.7.3 Wavy fault cut-off

Using the same modified "Big Smile" model from Figure 11.11, the algorithm smooths the fault cut-off, reducing the high area-change concentration at kink angles, leading to smooth lines (Fig. 11.11 bottom left).

## 11.8 Application

The following model describes a complete example applied to a noisy interpreted 3D seismic horizons. It is shown that bumps, steps, fault cut-off and tips are altered by the algorithm.

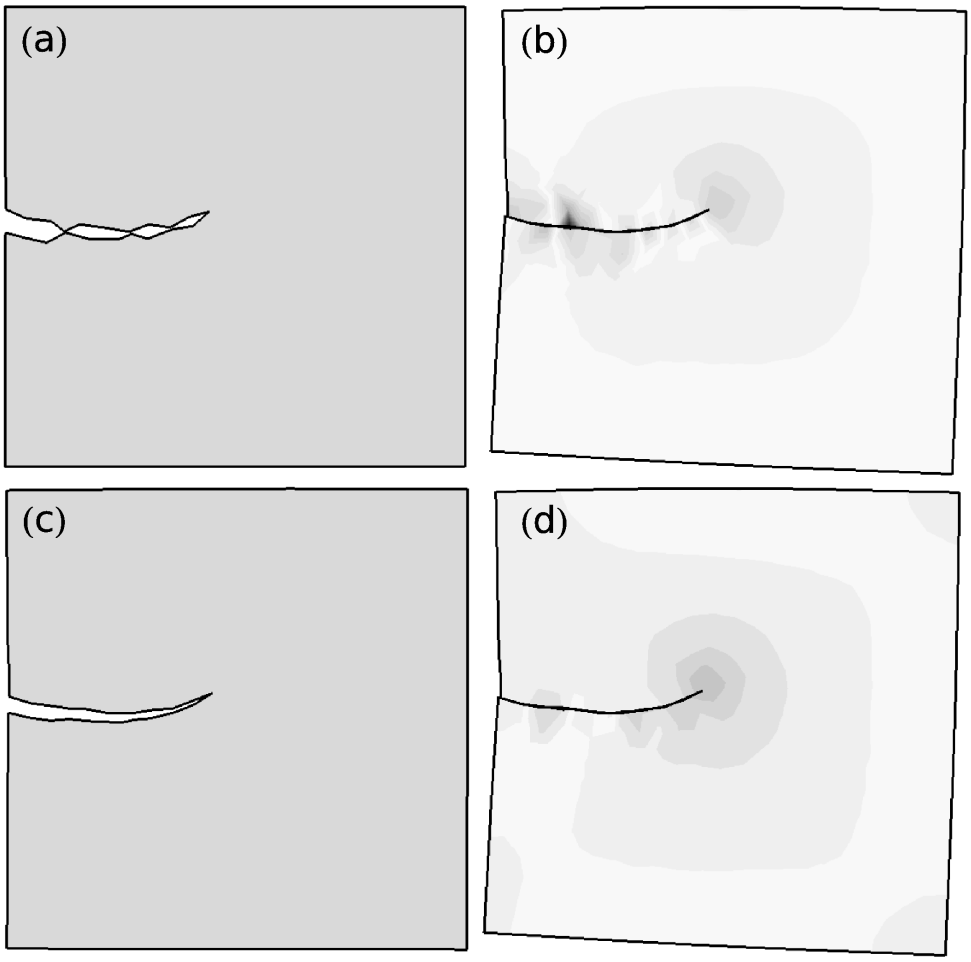


FIGURE 11.11: Fault cut-off correction. (a) initial geometry of the noisy fault cut-off; (b) corresponding area-change concentration close to the sharp angles of the fault trace; (c) after geometrical correction, the fault trace is smoothed, and (d) corresponding area change where the high concentration has disappeared leaving only the concentration at the crack tip.

### 11.8.1 Local surface correction

The input surface is the one used in the introduction to present some of the commonly observed anomalous features, and is shown in Fig. 11.1 (see also Fig. 11.12 for a 3D exaggerated (x2) perspective view). The goal is to remove in one go the observed anomalous geometries such as bumps, steps, fault cut-off and tips. Unfolding and unfaulting the horizon shows many perturbations, especially at fault cut-off (Fig. 11.13). Applying the geometrical correction algorithm reduces significantly the perturbation (Fig. 11.14), where only concentrations at fault tips remain visible. Figure 11.15 compares the horizon with iso-contours of elevation before (top) and after (bottom) correction. Bumps and steps have been removed, fault cut-off are now smoothed, and displacement gradient at fault tip are reduced. Figure 11.16 presents iso-contours of the displacement in $x$ (top), $y$ (middle) and $z$ (bottom) of the nodes using the initial geometry. Specifically, the z-

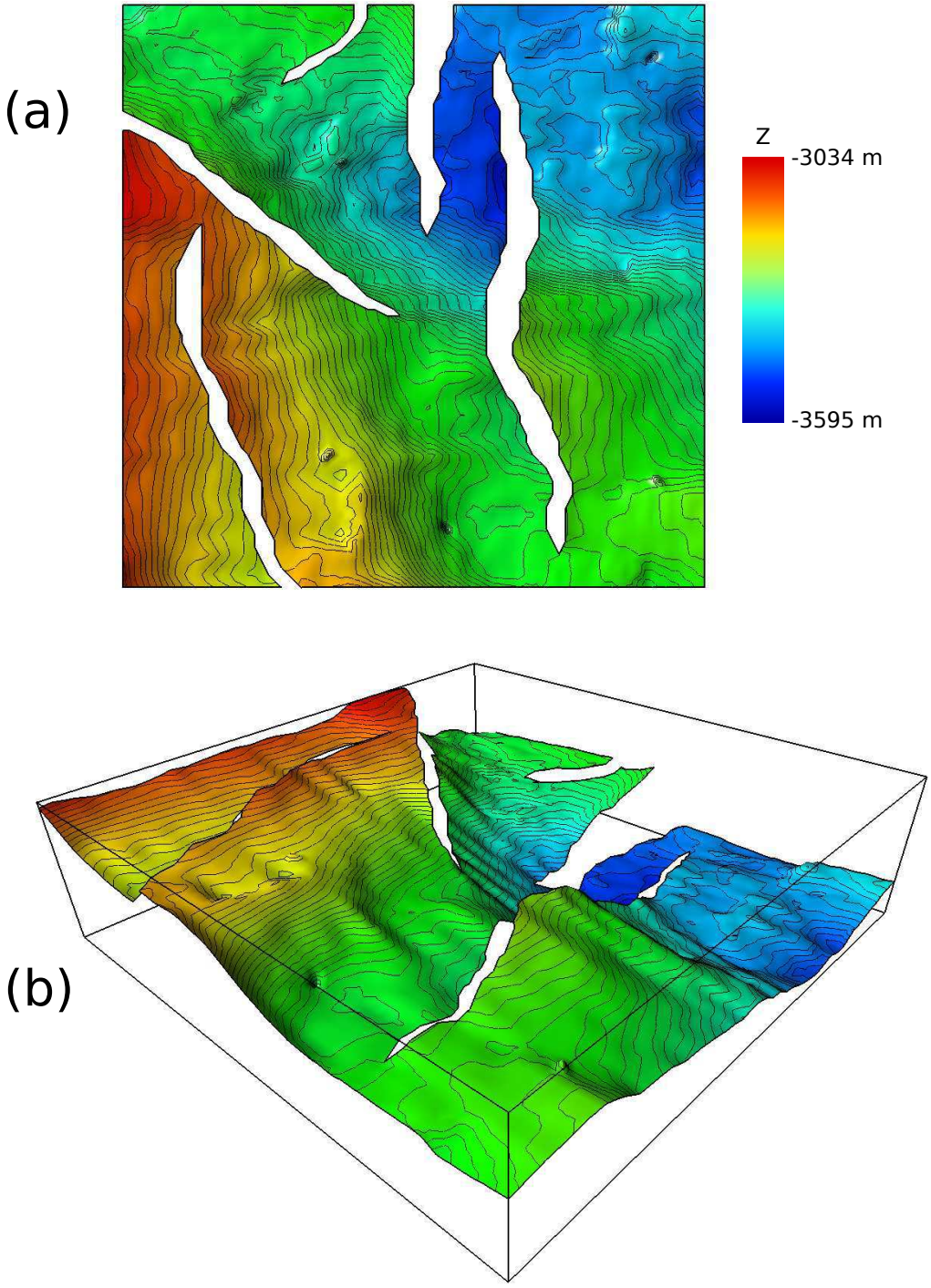


FIGURE 11.12: Folded and faulted horizon. (a) Top view (orthographic) with iso-contours of elevation; (b) Perspective 3D view (2x exaggeration).

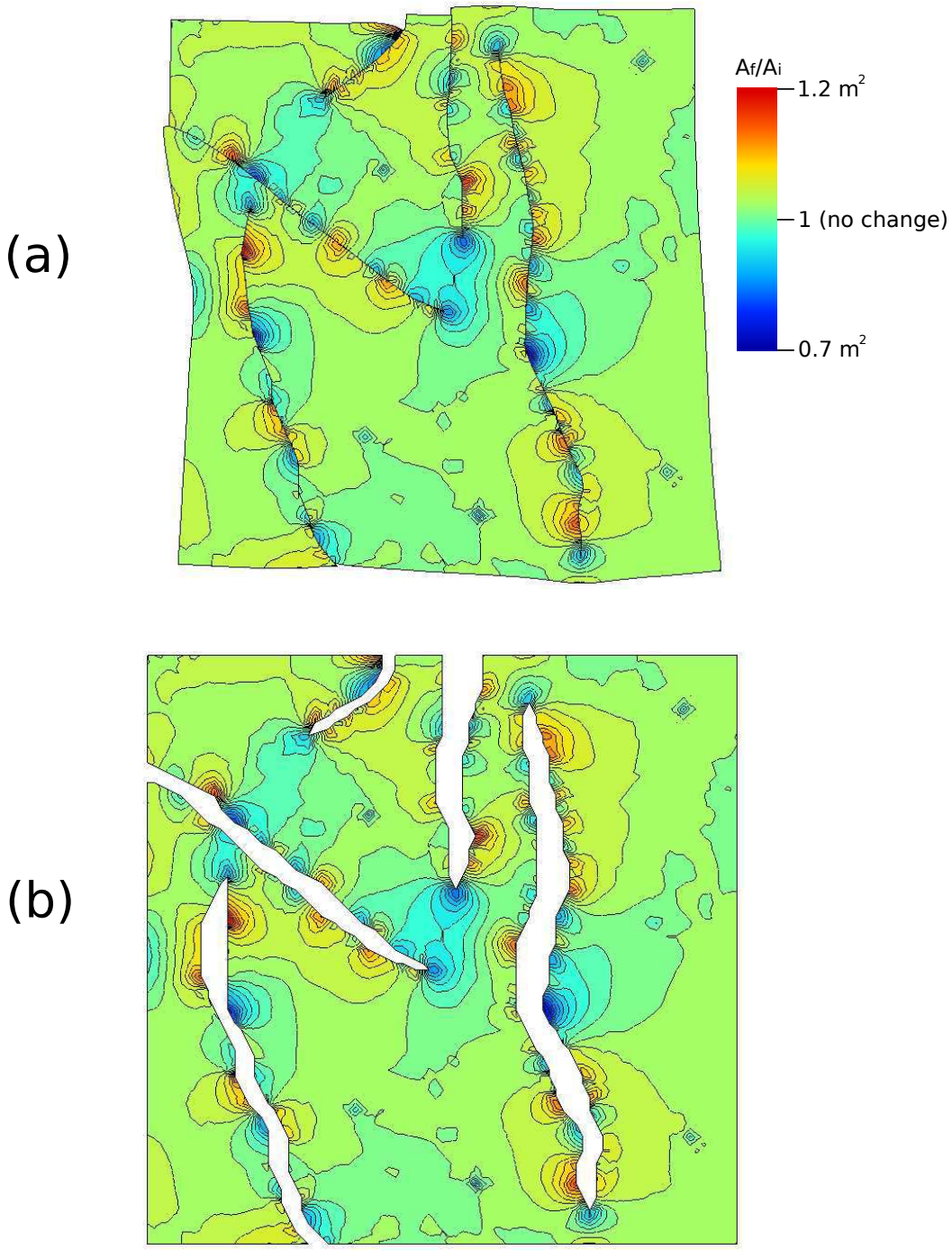


FIGURE 11.13: Area-change perturbation before correction. After unfolding and unfaulting, high area-change perturbation are localized at bumps, steps, kink-angle of fault cut-off and fault tips. (a) restored space and (b) initial space.

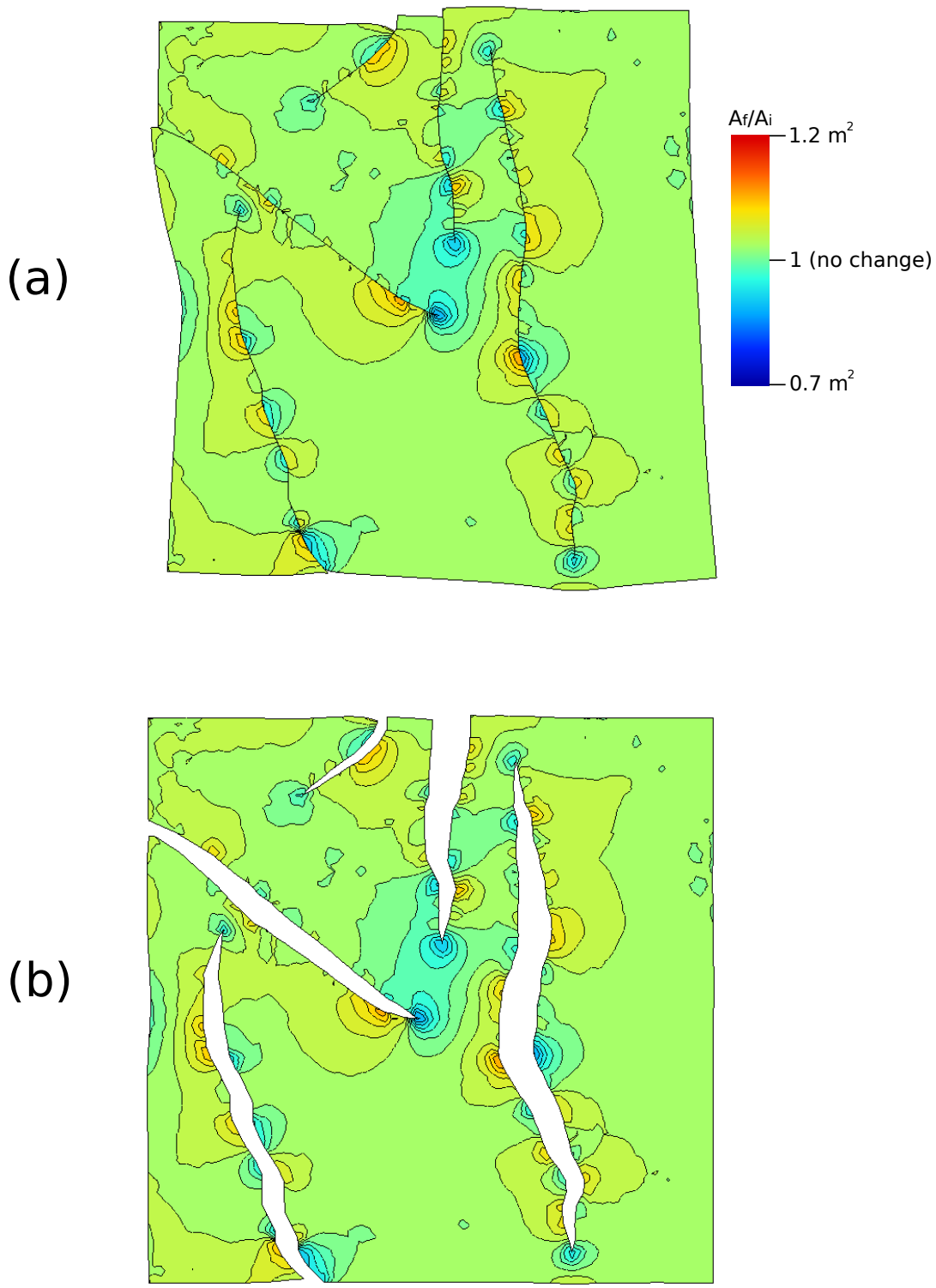


FIGURE 11.14: Area-change perturbation after correction. (a) iso-contours of perturbations in restored space (same scale as in Fig. 11.13) and (b) in initial space.

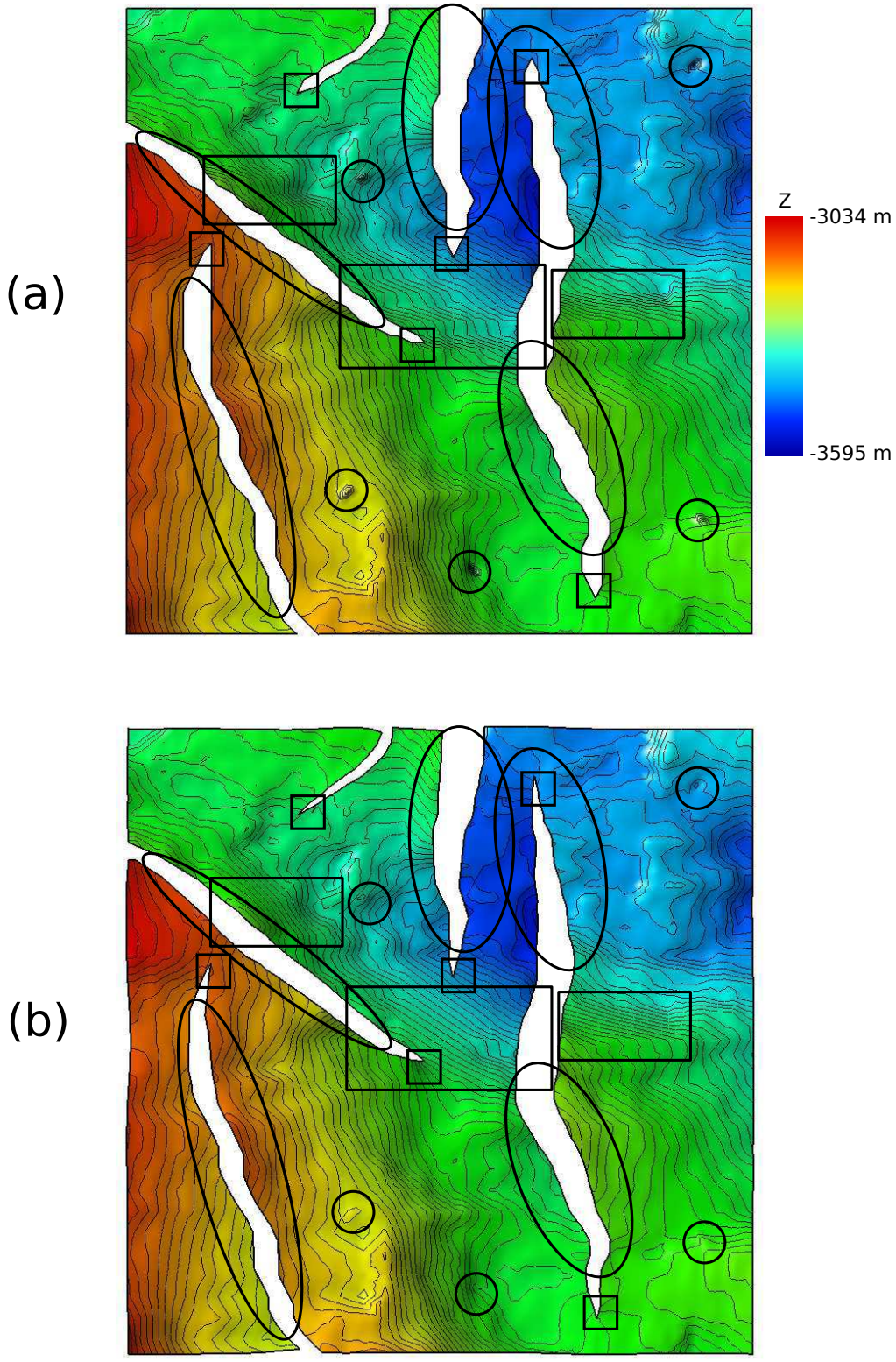


FIGURE 11.15: Comparison of the elevation iso-contours for the (a) initial geometry and (b) corrected geometry.

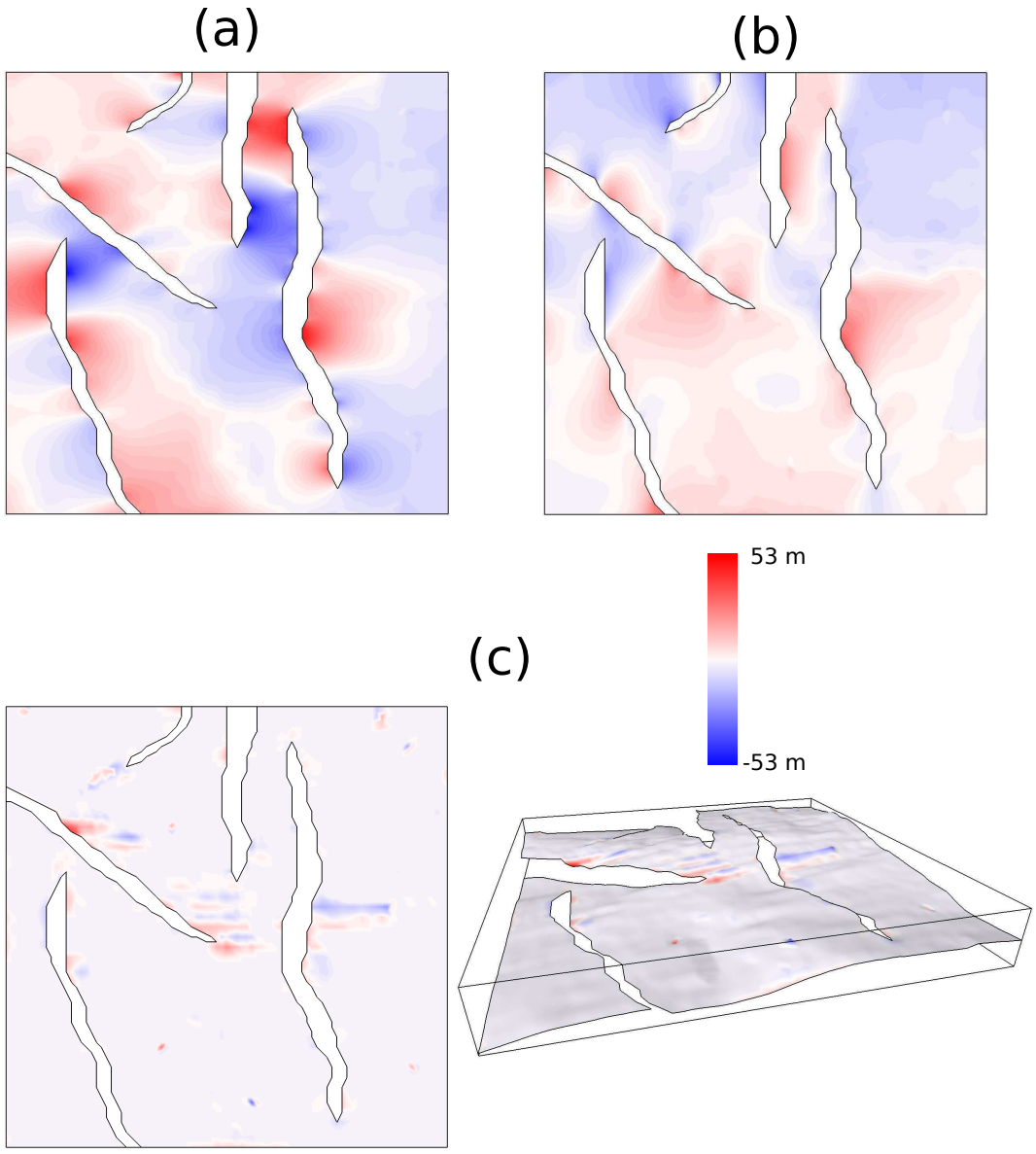


FIGURE 11.16: Iso-contours of the corrective displacement components: (a) along the x-axis; (b) along the y-axis and (c) along the z-axis with a perspective view.

correction clearly shows that the correction was preferentially applied to bumps and steps. Figure 11.17 shows displacement field for the whole surface (top), and at specific locations close to fault cut-off (bottom left) and fault tip (bottom right). Consequently, smoothing the fault cut-off implies that the 3D fault traces will be smoothed as well. Fig. 11.18 (top) presents the initial geometry of the reconstructed part of a fault, showing a corrugated surface. After correction, the reconstructed fault surface is smoothed (Fig. 11.18 middle). A close view to both surfaces (Fig. 11.18 bottom) shows that the presence of steps in the original geometry of the horizon generate a wavy fault surface, whereas after correction, this side effect is removed, leading to a more plausible fault surface.

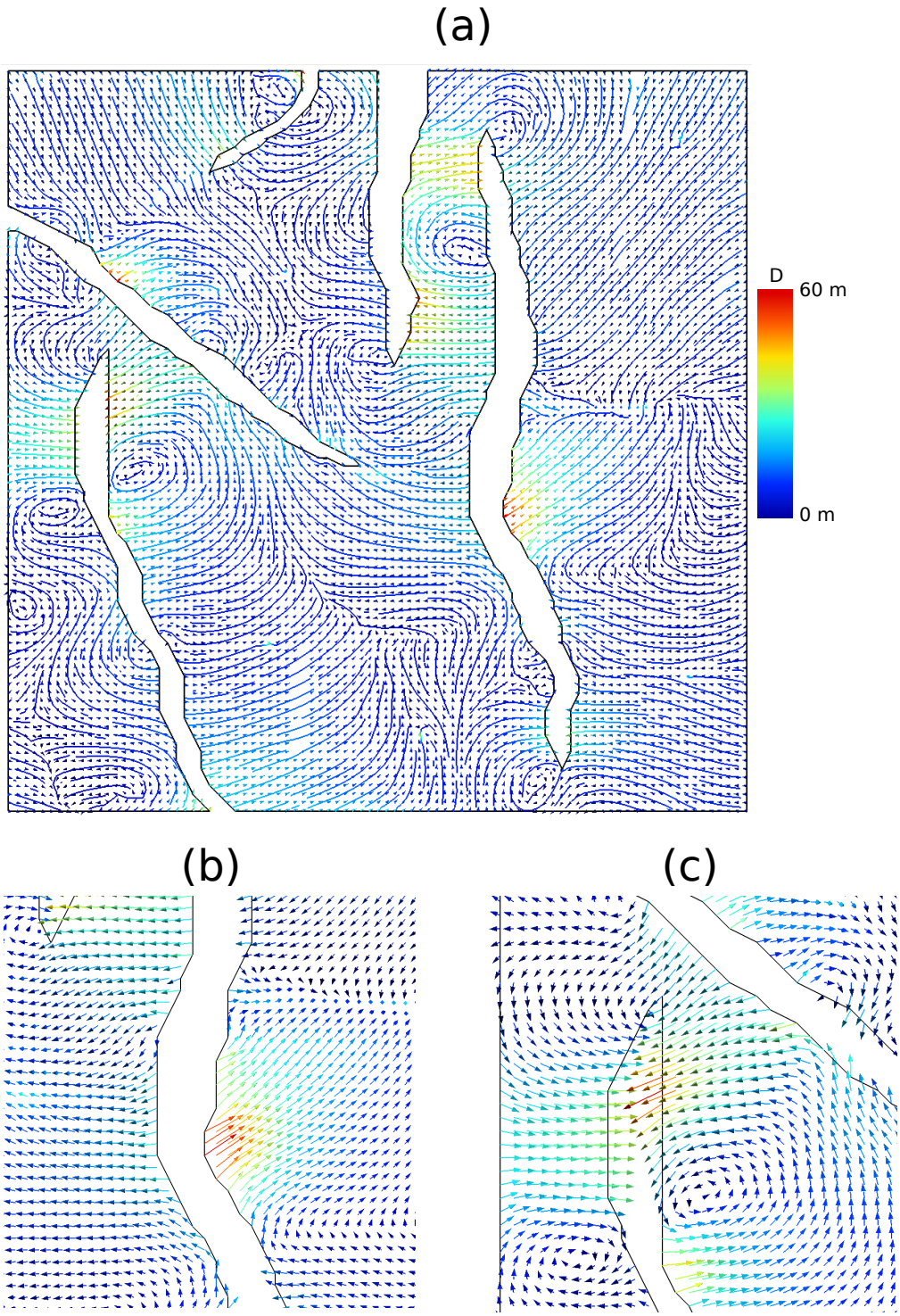


FIGURE 11.17: Displacement field showing the in-plane correction. (a) stream-lines for the whole horizon; (b) close view of the vector field at a kink angle along a fault cut-off, and (c) vector field at a fault's tip.

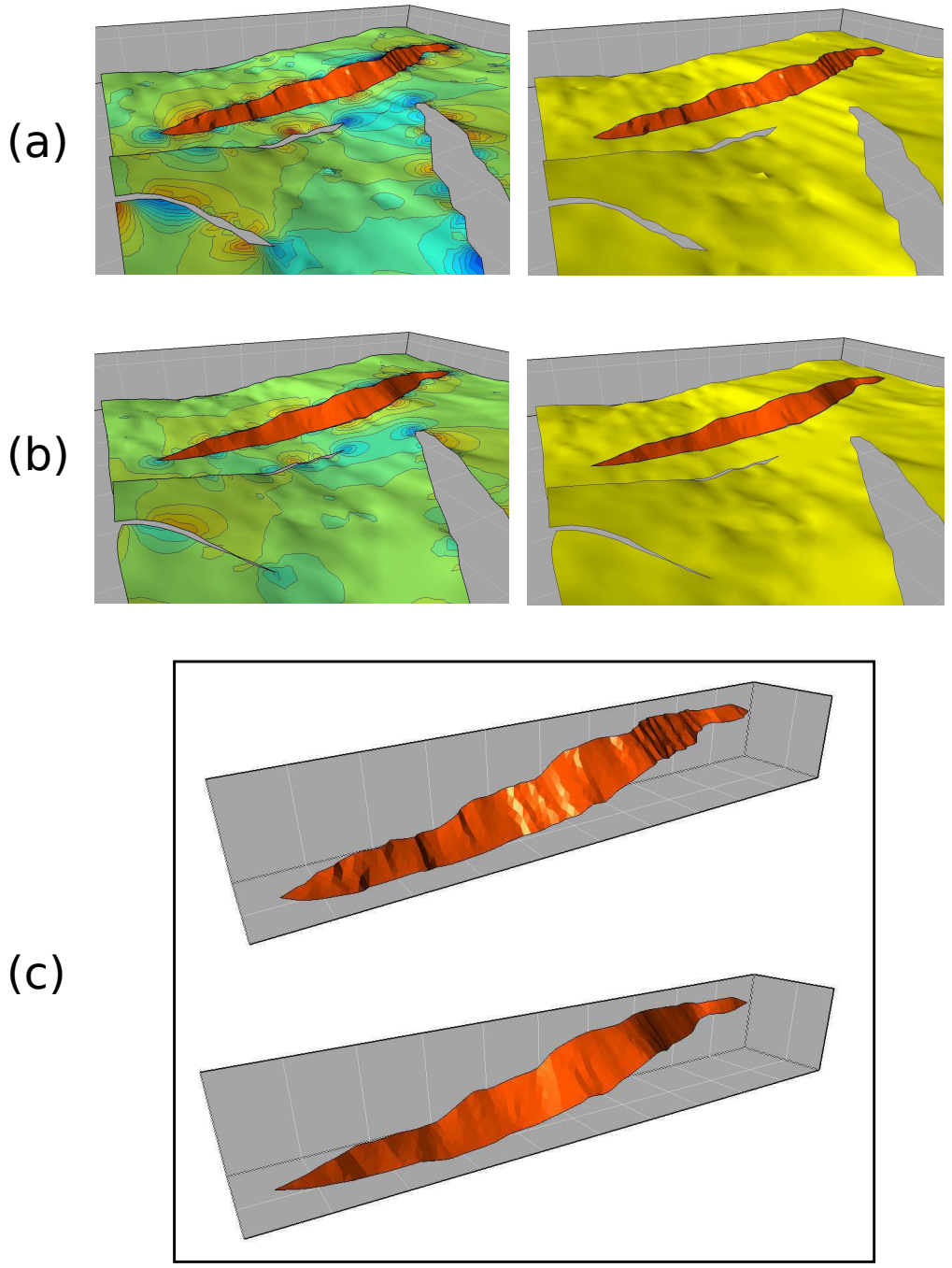


FIGURE 11.18: Smoothing a fault surface. Effect of the geometry correction (steps, fault cut-off and fault's tip) on the reconstruction of a fault surface: (a) initial geometry with iso-contours of area-change perturbation (left); (b) final geometry where the fault-cut-off has been smoothed and steps have been removed; (c) close view of the reconstructed part of the fault surface using the initial (top) and final geometry (bottom).

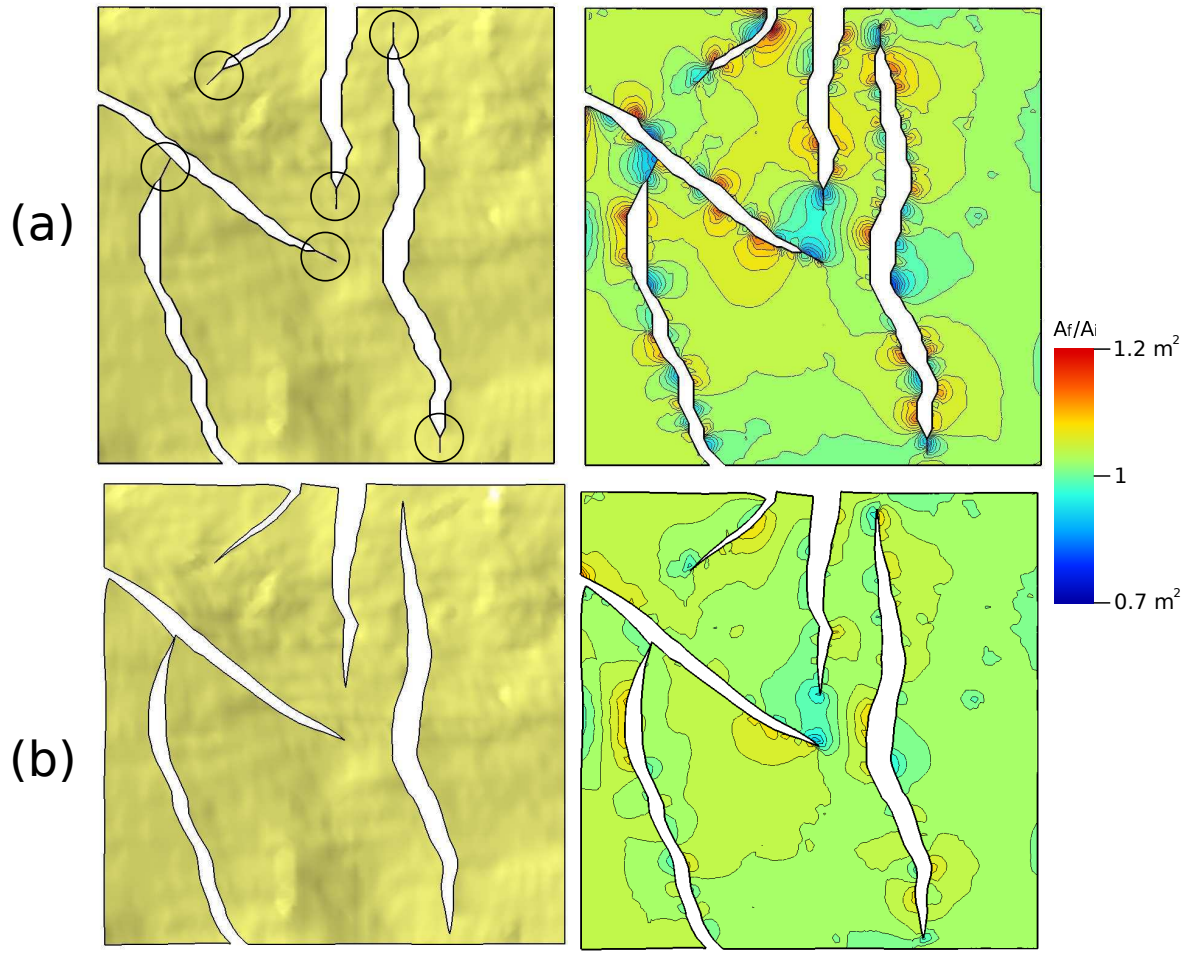


FIGURE 11.19: Extended fault's tips. (a) Before correction. The extended fault's tips are circled. (b) After correction, displacement gradients at fault's tips have been increased.

### 11.8.2 Extending fault tips

In order to see the strength of such method to correct fault cut-off and displacement gradient at tips, we extended some fault traces by cutting the triangulated surface at the fault tips, resulting in an implausible geometry (Fig. 11.19, top left) while maintaining a high area-changed concentration. After running the algorithm, fault traces are smoothed as expected, and the extended parts recover a more natural displacement gradient, (see Fig. 11.19 bottom left). Figure 11.19 top right and bottom right shows iso-contours of the criteria used to detect anomalous regions (i.e. area-changed). It is shown that high concentration have been reduced and globally smoothed.

## 11.9 Conclusions

We have shown that using a geomechanical smoothing filter to correct for anomalous geometry has positive effects. The filter automatically remove steps that can occur from the picking resolution of the interpretation. Anomalous bumps are also erased and kink angle at fault cut-off as well as fault displacement gradient at tips are smoothed. Reconstructed fault surfaces are globally less corrugated. Instead of doing a global correction, the user have the possibility to locate and select zones of anomalous geometry and apply the presented algorithm to the selection only. As it is fast enough, user interaction allows to pick a threshold value for the correction, and see the corresponding result in real time.

## Acknowledgments

We would like to thanks Marc Levoy from the Stanford Computer Graphics Laboratory, for helping us to scan the crumpled squared thin sheet of paper, as well as Paul Griffith from BG-Group for contributing to the discussions.

# References


Desbrun, M., Meyer, M., Schroder, P., and Barr, A. H. (1999). Implicit fairing of irregular meshes using diffusion and curvature flow. *SIGGRAPH*, 99:317–324.

Golub, G. H. and Van Loan, C. F. (1996). *Matrix computation*. Johns Hopkins University Press, Baltimore, MD.

Hall, M. (2007). Smooth operator: Smoothing seismic interpretations and attributes. *The Leading Edge*, January:16–20.

Hughes, T. J. R. (1987). *The finite element method: linear static and dynamic finite element analysis*. Prentice-Hall, New Jersey.

Jaeger, J., Cook, N., and Zimmermann, R. (2007). *Fundamentals of Rock Mechanics*. Blackwell Publ., Malden, MA.

Maerten, F. (2010). Adaptive cross approximation applied to the solution of system of equations and post-processing for 3d elastostatic problems using the boundary element method. *Engineering Analysis with Boundary Elements*, 34:483–491.

Maerten, F. and Maerten, L. (2008). Iterative 3d bem solver on complex faults geometry using angular dislocation approach in heterogeneous, isotropic elastic whole or half-space. In Brebbia, editor, *Boundary Elements and other Mesh Reduction Methods XXX*, pages 201–208, Southampton. BEM 30, WITpress.

Maerten, F., Maerten, L., and Cooke, M. (2009a). Solving 3d boundary element problems using constrained iterative approach. *Computational Geosciences*.

Maerten, F., Maerten, L., Pollard, D., and Lagalaye, Y. (2009b). ibem3d, a three-dimentional boundary element method using angular dislocations for sub-surface structures modeling. *In preparation for Journal of Geophysical Research*.

Maerten, F., Resor, P. G., Pollard, D. D., and Maerten, L. (2005). Inverting for slip on three-dimensional fault surfaces using angular dislocations. *Bulletin of the Seismological Society of America*, 95:1654–1665.

Maerten, L. and Maerten, F. (2006). Chronologic modeling of faulted and fractured reservoirs using geomechanically-based restoration: Technique and industry applications. *AAPG Bulletin*.

Taubin, G. (1995). A signal processing approach to fair surface design. SIGGRAPH.

# Part IV

Conclusions and perspectives

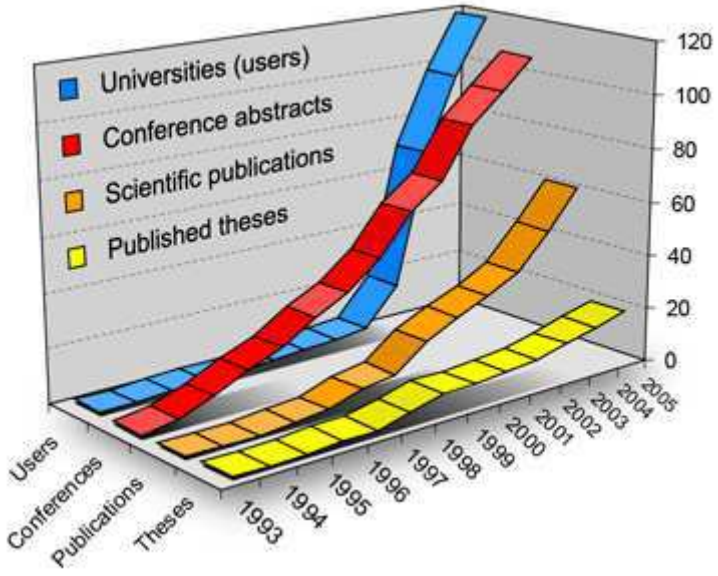


FIGURE 11.20: Evolution of the number of publications, conference abstracts, theses and users using iBem3D (Poly3D) since 1993 and until 2005

As seen in the three main parts of this thesis, linear elasticity still can be considered a *useful* tool for sub-surface modeling as it gives a first good approximation of the geological phenomena. This is demonstrated by the growing number of publications and thesis based on these tools: iBem3D (formally called Poly3D) and Dynel2D/3D. Fig. 11.20 shows the evolution of the international scientific publications, thesis and conference abstracts for iBem3D (Poly3D) in research and industry from 1993 to 2005.

Linear elasticity can be used as a forward tool (part I) and allows one to estimate the perturbed stress field in a complexly faulted area in a efficient way, given the geometry and boundary conditions on the faults making a model, as well as the far field stress. Direct applications range from the study of earthquake triggering and volcanoes modeling, fault interactions, the determination of the deformation associated with displacement discontinuities, such as faults and fractures, in Earth's crust, sub-seismic fault modeling, joint modeling, interpretation/validation, fault connectivity and reservoir compartmentalization, depleted area and fault reactivation, pressurized well bore stability, and mine and mine-shaft modeling (chapter 1). Implemented within a BEM code (e.g., iBem3D), it allows one to add frictional and non-interpenetration behaviors (chapter 2). Frictional slip along faults controls fracture orientation at extensional relay zones (chapter 3), the seismic cycle, the distribution and amount of slip along faults, development of adjacent damage zone and frictional slip along bedding contacts influences layer flexure and fracture/fault propagation. Heterogeneous materials with complex geometrical interfaces separating meddia with different material properties is investigated and implemented in chapter 4.

Finally, model complexity reduction is presented in chapter 5 for both the resolution of the system of equations and the post-processing at observation points.

Linear elasticity also allows one to do inverse modeling, i.e., to recover for the unknowns model parameters using geologic, seismologic and geodetic data (part II). Given the faults geometry as well as the rapidly increasing number of geodetic data with high precision, slip inversion offers a way to determine the slip distribution which induced the input geodetic observations to a precision that is consistent with the data (chapter 6). This technique was successfully applied to the Nias earthquake (Indonesia) which occurred in 2005 (chapter 7). The method for fast optimization presented in chapter 5 is used for linear slip inversion in appendix A in combination with displacement inequatily constraints (DICs). This new formulation permits one to use the large data sets as well as more complex faults geometry made of thousands of triangular elements. A second type of inversion is to determine the remote stress given the geometry of the faults as well as some measure of the slip distribution from seismic interpretation (chapter 8). This tool can give a good approximant of what could have been the far field stress (magnitudes and orientations) which produced such observed displacement on faults. The principle of superposition is used in chapter 9, and provides an efficent, stable and fast way of doing far field stress estimation using multiple types of data.

Finally, linear elasticity makes possible restoration modeling in a simple and efficient way (chapter 10), e.g. to determine the perturbed stress field due to folding (and eventually to faulting). This technique can help to understand fault development and chronology, and help the user to check the validity of their interpretation from seismic images. In chapter 11, we use the principle of geomechanically unfolding and unfaulting 3D surfaces to detect anomalous geometries in noisy horizons from seismic interpretation. An iterative algorithm is then applied to the horizon to correct for the 3D geometry in its initial space. It is shown that bumps, steps and fault cut-off are smoothed, while fault tips are modified such that they present a more plausible displacement gradient. Since the constraint of restoration of an horizon onto a target is not a natural boundary condition, it generates residual tractions at the free surface that perturb the stress field. Therefore, fractures prediction have to be carefully used in such a case (see for instance Lovely et al., Geomechanical analysis of the Volcanic Tableland extensional fault system, Bishop, CA and evaluation of mechanics-based restoration methods, In preparation for AAPG Bulletin).

Of course, linear elasticity has many limits, as it is based on infinitesimal deformations. Complex models with large deformations (involving plastic zones) cannot be handle by

such codes, and other formulations have to be used. Specifically, the user must be aware that linear elasticity accurately represents deformations of few percents, and for the case of iBem3D, one has to make sure that the computed displacement discontinuities on a fault do not exceed a few percents of the fault size.

## Perspectives for forward modeling

Within the field of linear elasticity, our goal is to extend the functionality of such modeling tools in order to incorporate a way to do Discrete Fracture Network (DFN) generation using the perturbed stress field due to slipping faults as well as the remote far field stress. One way of generating such fractures is to combine BEM and FEM, the former to compute the perturbed stress field and the later to create fracture patterns (see for example Iben et al., 2006, Generating Surface Crack Patterns, Proceedings of the ACM SIGGRAPH/Eurographics Symposium on Computer Animation).

Using the same perturbed stress field, we think that it is possible to determine the optimum well path in a complex faulted reservoir, avoiding collapse of the well bore. Having the perturbed stress field due to slipping faults (computed from a numerical simulation), a well bore trajectory can be computed efficiently by avoiding regions where the stress field will plausibly collapse the well bore.

Fracture propagation in mode I is another problem that should be amenable to such tools, and especially iBem3D for which the crack grow can be computed efficiently without remeshing of the entire elastic medium.

Another interesting feature is to implement the thermo-poro-elasticity in iBem3D, but this functionality is still under investigation.

## Perspectives for inverse modeling

One of our current research investigations is the use of an iterative solver for doing slip inversion, as it will use the new features developed in chapter 2 (specifically the displacement inequality constraints), chapter 4 (for the addition of heterogeneous materials) and chapter 5 (for fast optimization). We give a brief overview of this on-going project in appendix A.

## Perspectives for restoration modeling

For this type of modeling, we investigate the possibility of adding plasticity during the restoration of highly folded structures. Also, even if the Finite Element Method is relatively well suited for doing restoration, we investigate the use of a MeshLess (or MeshFree)

method, as it offers many advantages compare to FEM. This method allows one to do very large deformations, and has the ability to avoid the use of topological structures which are critical in three dimensions for the stability of the simulations.

# Part V

Appendices

In appendix A, we provide a paper in preparation, and which fit in part II ("Inverse modeling using Boundary Element Method").

Appendix B presents an application of parameter estimation for fault sealing and leakage for both nuclear waste disposal and exploitation of natural resources, using the static Coulomb friction (chapter 2).

The last appendix C provides three other publications along with a list of conferences abstacts and titles of internal publications from the Rock Fracture Project (RFP) at Stanford.

# APPENDIX A

## Fast iterative slip inversion

F. Maerten[1,2]

(1) Igeoss, Montpellier, FRANCE
(2) University of Montpellier II, Geosciences, FRANCE

*In preparation for EABE*

**Preamble:**
This appendix shows that the combination of the iterative solver (chapter 2) with the optimization presented in chapter 5 can drastically decrease the computation time when doing slip inversion and allow the use of displacement inequality constraints (chapter 2) to better constrain the inversion. The inequality on displacements allows to specify if a fault is normal or reverse, left or right lateral, and bound the norm of the displacement within a user prescribed range.

# About...

The main goal of this research is to find a way for reducing the model complexity in order to do slip inversion in inhomogeneous bodies using complexly shaped interfaces (chapter 4). Another goal is to see if the displacement inequality constraints, as defined in chapter 2, can be used in such a code.

# Article Outline

## A.1 Résumé

Retrouver la distribution de glissements sur des failles en trois dimensions étant donné certaines mesures du déplacement (donnés GPS ou InSAR) associée à des événements tectoniques tels que les tremblements de terre, est d'un grand intérêt. La méthode indirecte des éléments frontières en trois dimensions se révèle être un bon candidat pour opérer cette inversion. Habituellement, une approche des moindres carrés pondérés, combinée à une régularisation de Tikhonov, est utilisée. Puis, le système doit être résolu sous contraintes inégalitaires afin de converger le modèle vers une solution réaliste. Toutefois, en raison du vaste ensemble de données disponibles (en particulier de données InSAR) et de la complexité du système de failles utilisé, le temps nécessaire pour construire le système d'équations peut être relativement long et la mémoire nécessaire pour le stockage de la matrice se révéler insuffisant. En outre, le solveur sous contraintes peut présenter un temps de calcul non négligeable et qui est fonction de la complexité géométrique du modèle utilisé ainsi que des contraintes inégalitaires associées.

Dans cet article, nous montrons que grâce à l'utilisation d'une approche itérative combinée aux méthodes des matrices hiérarchiques et d'approximation adaptative croisée, le système d'équations peut être construit et résolu de manière très rapide, tout en permettant l'utilisation de contraintes inégalitaires en déplacement . Nous montrons un exemple avec une analyse comparative de ce nouvel algorithme à une méthode classique des moindres carrés sous contraintes.

## A.2 Abstract

Retrieving the slip distribution onto three-dimensional faults given some measures of the ground displacements (e.g. GPS or synthetic aperture radar interferometry) associated with tectonic events such as earthquakes is of great interest. Three dimensional indirect boundary element methods reveal to be a good candidate to operate the inversion. Usually, a weighted least squares approach combined with a Tikhonov regularization is used. Then, the system has to be solved with inequality constraints in order to better converge toward a realistic solution. However, due to the large set of data available (especially from InSAR) and the more complex fault system used, the time needed to construct the system of equations can be relatively long, and the memory needed for the storage grows as a squared of the number of unknowns. Furthermore, the constrained solver can exhibit a long computation time depending of the model complexity and the inequalities used.

In this paper, we show that using an iterative approach combined with the H-Matrix and Adaptive Cross Approximation methods, the system of equations can be constructed and solved in a very fast way, while allowing the incorporation of the displacement inequality constraints. We show an example along with benchmarking, and compare this new algorithm to an existing direct inverse method using a classical constrained least-squares solver.
**Keywords:** earthquake, slip inversion, iterative method, H-Matrix, Adaptive Cross Approximation

## A.3 Introduction

Modern methods of data acquisition allow denser measurement of ground surface displacements with better precision. Recovering for slip onto the faults that produced such observed displacements is of main interest for the geophysicists for the comprehension of earthquake triggering (see for example (G.C.P. et al., 1994)). To do so, numerical methods are widely used either in forward sens (e.g. (Muller et al., 2003)) or by doing slip inversion (e.g. (Johnson et al., 2001; Jónsson et al., 2002; Maerten et al., 2005)). Boundary Element Method (BEM) seems to be the most appropriate technique for modeling inverse problems (Okada, 1985; Maerten et al., 2005) since only the fault discontinuities have to be discretized and not the entire volume of interest as done by the Finite Element Method. The solution presented by Maerten et al. (Maerten et al., 2005) reveals to be better suited for that purpose than the Okada's code (Okada, 1985) since it uses triangular elements to model complex fault geometry, avoiding gaps and overlaps between adjacent elements

(Jeyakumaran et al., 1992; Maerten et al., 2005) which can perturbed the solution. This method takes advantage of GPS and InSAR data set to recover for the slip distribution, and is combined with a Fast Non-Negative Least Squares solver (FNNLS). The strenghs was demonstrated through a brief analysis of the fault rupture due to the 1999 Hector Mine earthquake (Mw 7.1).

Nowadays, due to the available dense data acquisition resulting from satellite interferometry, as well as the possibility to model more complex fault systems (therefore increasing the number of unknowns), the computation time to construct and to solve the system of equations becomes a drawback using a direct approach. Our intention, in this paper, is to show that using an iterative approach (Maerten et al., 2009a) combined with $\mathcal{H}$-Matrix (Hackbusch, 1999) and Adaptive Cross Approximation (ACA) (Bebendorf and Rjasanow, 2003), it is possible to solve inverse problems in a fast way, allowing, for example, a quick parameters estimation (e.g. fault geometry) if necessary. Furthermore, as demonstrated in (Maerten et al., 2009a), the iterative approach allows the use of displacement inequality to better constrain the model to converge toward a realistic solution.

The paper is organized as follow. After reviewing the formulation of the inverse problem using an iterative approach, we apply the $\mathcal{H}$-Matrix and ACA to the construction and resolution of the least squares problem. Finally, an example is provided along with benchmarks.

## A.4 BEM formulation

For the boundary element method, we employ the analytical solution of an angular dislocation in a homogeneous elastic whole- or half-space (Comninou and Dundurs, 1975), which has been extended to account for heterogeneous materials (Maerten and Maerten, 2008). In this code, each fault is discretized as a triangulated mesh, where mixed boundary conditions are prescribed. This BEM code (called iBem3D (Maerten et al., 2009b)) is very similar to the 2D Displacement Discontuinuity Method (DDM) (Crouch and Starfield, 1983), in which triangular elements of constant displacement discontinuity are employed. The advantage compare to Okada's code, which uses rectangular and planar elements, is that three-dimensional fault surfaces more closely approximate curviplanar surfaces and curved tiplines without introducing overlaps or gaps between adjacent elements. Such a formulation is very well suited to study faults interaction in 3D, as only faults surfaces have to be discretized (see for example (Maerten et al., 1999), (Maerten, 2000), (Muller

et al., 2003) among others).

As described by Maerten et al. (Maerten et al., 2005), a linear slip inversion can be done by using a weighted damped least squares approach. Displacements $u_p$ at points $p$ on the Earth's surface due to slip $b_e$ on elements $e$ of a buried fault can be described by a set of linear equations:

$$u_p = D_{pe} b_e + E \tag{A.1}$$

where $E$ are the observational errors and $D_{pe}$ are the influence coefficients, or Green's functions, that describe how slip on a fault element produces displacement at the Earth's surface.

To implement the inverse problem, we seek a solution that simultaneously minimizes the $L_2$ norm (hereafter annotated with $\|\|_2$) of the data misfit and of the model roughness. This approach allows fitting of the data to a desired threshold while introducing the geologic concept that slip distributions are relatively smooth rather than oscillatory. Minimizing the model roughness acts to prevent over-fitting of noisy data and compensates for underdetermined model parameters and geometric inaccuracies. The slip inversion problem can thus be written as

$$min\|Db - u\|_2 + \epsilon^2 \|S\|_2 \tag{A.2}$$

where the first term $\|Db - u\|_2$ is the $L_2$ norm of the data misfit and the second term $\epsilon^2\|S\|_2$ is a measure of the model roughness. The data misfit is calculated by subtracting the observed displacements $u$ from the predicted displacements, which are themselves calculated by multiplying the Green's functions $D$ by the modeled slip $b$.

However, this technique suffers from the limited amount of RAM of the computers necessary to store the system of equations, and the long time needed for its construction and its resolution due to the use of a Fast Non-Negative Least Squares solver (Maerten et al., 2005).

### A.4.1 Iterative formulation

The displacement at the an observation point located at the earth surface depends on the displacement discontinuity from all triangular elements making the faults, and is expressed as:

$$u_p = \sum_f D_{pf} b_f \tag{A.3}$$

Extracting a single triangular element $e$ from Eq. A.3 gives:

$$D_{pe}b_e = u_p - \sum_{f \neq e} D_{pf}b_f \tag{A.4}$$

Using a least-squares approach for all observation points $p$ and a given element e, we have:

$$\sum_p \left[D_{pe}^T W_p D_{pe}\right] b_e = \sum_p D_{pe}^T W_p \left\{ u_p - \sum_{f \neq e} D_{pf}b_f \right\} \tag{A.5}$$

where $u_p$ is the observed displacement at point $p$, $D_{pe}$ the displacement influence matrix at $p$ due to element $e$, and $b_f$ the current displacement discontinuity or Burgers's vector at elements $f$. $W_p$ represents the weight matrix that defines the relative contribution of each data point $p$ to the total prediction error (Menke, 1984).

Equation A.5 can now be written:

$$b_e = A_e^{-1} \left\{ u_e - \sum_{f \neq e} B_{ef}b_f \right\} \tag{A.6}$$

with

$$\begin{cases} A_e &= \sum_p D_{pe}^T W_p D_{pe} \\ u_e &= \sum_p D_{pe}^T W_p u_p \\ B_{ef} &= \sum_p D_{pe}^T W_p D_{pf} \end{cases} \tag{A.7}$$

The naive construction of this system of equations is given in algorithm A.1. In equation A.6, matrices $B_{ef}$, for all elements $f$, are stored in row-wise since $b_f$ are successively refined at each iteration (see algorithm A.2), and has dimensions $n_e \times n_e$, where $n_e$ is the degree of freedom of the element $e$. Therefore, for a given element $e$, it is stored in the form $[B_{ef}] = \left[B_{ef_0} ... B_{ef_{n-1}}\right]$.

### A.4.2 Tikhonov regularization

Instead of using a Tikhonov regularization into the least-squares formulation as done in (Maerten et al., 2005), we choose to separate the implementation from the normal equation. For a given iteration, we first recover for the unknown Burgers's vector for each element. Then, a post-processing regularization is applied at each element $e$ using its adjacent elements $g$. The computed displacement $b_e$ at element $e$ is smoothed according

```
forall element e do
    forall observation point p do
        compute D_pe
        A_e += D_pe^T W_p D_pe
        u_e += D_pe^T W_p u_p
        forall element f ≠ e do
            compute D_pf
            B_ef += D_pe^T W_p D_pf
        end
    end
end
```

**Algorithm A.1**: Naive algorithm to compute the elemental matrices at the intialization stage of the iterative solver

to elements $g$ using equation A.8:

$$b_e = \frac{1}{(1-\epsilon)w_e + \epsilon \sum_g w_g} \left[ (1-\epsilon) w_e b_e + \epsilon \sum_g w_g b_g \right] \tag{A.8}$$

with $w_g$ being a weighting parameter for the adjacent elements g (e.g. area), and $\epsilon$ a smoothing parameter such that $\epsilon \in [0, 1[$. This process is described in algorithm A.2.

It can be noted that the best value of $\epsilon$ can be iteratively refined using an iterative Tikhonov regularization algorithm (Henn and al., 2001). This thechnique prevents the user to search for the best smoothing parameter, since it will be found automatically by minimizing the objective (or misfit) function.

In Appendix A.6, we propose a formulation with the Tikhonov regularization in the normal equation. This formulation was not tested yet, but will be compared soon to the previous implementation in terms of stability and speed of the convergence.

### A.4.3 Solving the system with inequality constraints

After the system of equations is built, the model is solved using a block Jacobi, as described in (Maerten et al., 2009a), which allows the incorporation of displacement inequality constraints or DICs (e.g. non interpenetration of elements) and traction inequality constraints or TICs (e.g. static friction). In order to better constrained the inversion, our interrest here is to use some special forms of the DICs for a given element $e$ with Burgers's vector $b_e$, i.e:

$$A \leq b_{e,i} \leq B \tag{A.9}$$

where $b_{e,i}$ represents the $i^{th}$ component of the element's Burgers's vector $b_e$, and $A$ and $B$ are the user prescribed bounding values. The overall process for solving the system iteratively is presented in algorithm A.2.

```
call algorithm (A.1) or (A.3) // Construction of the system
while not converge do
    forall element e do
        apply equation (A.6) // Solve for b̄_e
        apply the displacement inequalities
    end
    forall element e do
        apply equation (A.8) // Tikhonov regularization on b̄_e
    end
    forall element e do
        b_e = b̄_e // Set the solution
    end
end
```

**Algorithm A.2**: Inequality constraints, Tikhonov regularization and method of resolution of the system using a Jacobi iterative solver

## A.5 Reducing the model complexity

Compare to the direct inversion, which is in $O(pn)$, where n and p are the number of elements and data points respectively, the model construction using the naive algorithm A.1 is in $O(pn^2)$, and for each element and each observation point, the displacement influence matrix has to be computed, which makes it very slow. On way to reduce the computation time (but not the complexity) is to use the fact that for a given observation point $p$, the $D_{pf}$ influence matrices, for all element $f$, have to be computed only once. Hense, the algorithm A.1 is transformed into algorithm A.3. But still, the complexity remains hight.

Among various methods of optimization (Rokhlin, 1985; Hackbusch and Nowak, 1989), the $\mathcal{H}$-Matrix technique (Hackbusch, 1999) combined with ACA (Bebendorf and Rjasanow, 2003) seems to be the most appropriate and the fastest to implement since approximation is applied to the matrix entries of the system after assembling (algebraic approximation), and does not rely on the kernel functions before assembling, as done by the multipole methods (Rokhlin, 1985; Greengard and Rokhlin, 1987).

```
forall observation point p do
    set row matrices R_n = 0
    forall element e do
        compute D_pe
        set R[e] = D_pe
    end
    forall element e do
        A_e += R[e]^T W_p R[e]
        u_e += R[e]^T W_p u_p
        forall element f ≠ e do
            // Use the pre-calculated D_pf stored in R
            B_ef += R[e]^T W_p R[f]
        end
    end
end
```

**Algorithm A.3**: System construction speedup

### A.5.1 $\mathcal{H}$-Matrices

$\mathcal{H}$-Matrix is a method of clustering a matrix into several blocks such that near-field block influences are evaluated in the usual way, whereas far-field blocks can be approximate by interpolation or rank reduction.

In order to construct the block decomposition, a geometrical rule has to be chosen for the clusterization of the model, and we adopt recursive bisection as it is fast and gives good results.

Using a *kd-tree* containing all sources and fields, a subdivision by bisection is operated recursively, leading to a binary tree of *blocks* where the root corresponds to the entire model. The recursive subdivision stops when the number of items in a block reaches a prescribed minimum. We end-up with a binary partition of the model made of blocks, and what remains to do is the determination of the near- and far-field block-pairs using this decomposition. Given two blocks $C_1$ and $C_2$, the admissible condition

$$\min(diam(C_1), diam(C_2)) \leq dist(C_1, C_2) \tag{A.10}$$

is used to check whether $C_1$ and $C_2$ can be used for approximation. $diam(C)$, the diameter of a set of points $C$, is the maximal distance between any pair of points in $C$, and is defined as $diam(C) = \max_{p,q \in C} \parallel p - q \parallel$, where $dist(C, D)$ is the distance between two sets of points, and is defined as $dist(C, D) = \min_{p \in C, q \in D} \parallel p - q \parallel$. In Eq. (A.10), $C_1$ represents a block containing source elements, and $C_2$ a block containing field points. If the condition (A.10) failed, the subdivision of these blocks continues recursively. Otherwise, $\{C_1, C_2\}$ is considered as a candidate for far-field approximation. If the blocks cannot be bisected

anymore and the admissible condition is not met, near-field will be used instead (full computation). This process is started at the root of the cluster tree, and we end-up with a unique structure, called $\mathcal{H}$-Matrix.

### A.5.2 ACA

Once the matrix is partitioned into an $\mathcal{H}$-Matrix structure, the far field block-pair $\mathcal{P}_{C_1,C_2}$ are approximated using the Adaptive Cross Approximation (Bebendorf and Rjasanow, 2003). According to the admissibility condition (A.10), blocks $C_1$ and $C_2$ are assumed to be far apart so the underlying functions of the kernel are asymptotically smooth. This low rank approximant is not generated by approximating the kernel functions of the integral operator (see (Rokhlin, 1985; Hackbusch and Nowak, 1989; Greengard and Rokhlin, 1987)), but rather by finding a low-rank from few of the original matrix entries. Therefore, it is not necessary to construct the whole matrix. One of the biggest advantages of this method, compared to the kernel approximant, is that only the original matrix entries are needed, and changing the kernel does not required recoding of the approximants. Our goal is not to discuss the ACA algorithm in detail: for more informations see (Bebendorf, 2000, 2008; Bebendorf and Rjasanow, 2003).

### A.5.3 Applying $\mathcal{H}$-Matrix and ACA to the system construction

Since a long computation time is expected during the system construction for the evaluation of the displacement influence matrices at observation points due to triangular elements (matrices $\mathbf{D_{pe}}$ and $\mathbf{D_{pf}}$ from Eq. A.6), they are approximated using the $\mathcal{H}$-Matrix and ACA techniques.

A block decomposition is done using both source elements (triangular elements) and field points (observation points from grids). While building the structure recursively, the matrix $\mathbf{A^F}$ related to a full block-pair $\mathcal{P}_{I/J}$ is generated and stored without approximation. On the other hand, the matrix $\mathbf{A_k^S}$, of size $m_k \times n_k$ and related to a sparse block-pair $\mathcal{P}_{I/J}$, is generated using the ACA technique and stored as two vector set, $\mathbf{u} \in \mathbf{R^{n_k}}$ and $\mathbf{v} \in \mathbf{R^{m_k}}$, satisfying

$$\mathbf{A_k^S} = \sum_{\mathbf{l=1}}^{\mathbf{k}} \mathbf{u_l v_l^T} \tag{A.11}$$

where $k$ is the rank-reduction approximation (Bebendorf and Rjasanow, 2003).

For a sparse block-pair $\mathcal{P}_{I/J}$, where $I$ and $J$ are a set of field points and sources respectively, we have:

$$[\mathbf{A^T W A}]\mathbf{b} = \mathbf{A^T W}(\mathbf{d} - \mathbf{c}) \tag{A.12}$$

with

$$\begin{cases} \mathbf{A} = \begin{bmatrix} \mathbf{D_{p_1 e_1}} & \cdots & \mathbf{D_{p_1 e_n}} \\ \vdots & & \vdots \\ \mathbf{D_{p_m e_1}} & \cdots & \mathbf{D_{p_m e_n}} \end{bmatrix} & (a) \\ \mathbf{c} = \left\{ \sum_{g \in J} \mathbf{D_{p_1 g}} \mathbf{b_g} \ \cdots \ \sum_{\mathbf{g \in J}} \mathbf{D_{p_m g}} \mathbf{b_g} \right\}^T & (b) \\ \mathbf{d} = \{ \mathbf{d_{p_1}} \ \cdots \ \mathbf{d_{p_m}} \}^T & (c) \\ \mathbf{b} = \{ \mathbf{b_{e_1}} \ \cdots \ \mathbf{b_{e_n}} \}^T & (d) \end{cases} \tag{A.13}$$

In the following sub-sections, we study the model partition as well as the optimization of the left and right hand side of Eq. (A.12). We use the notation $u_{i,j}$ to denote the $i^{th}$ component of the $j^{th}$ vector of the ACA decomposition given in Eq. (A.11).

#### A.5.3.1 Model partitioning

We use the same technique as the one described in (Maerten et al., 2009b) for the post-processing optimization. A block decomposition is done using both source elements (triangular elements) and field points (observation points from data set). Compared to a method used for the system resolution of a forward modeling where items are simultaneously source and field, now we clearly make the distinction while building recursively the block decomposition. For instance, when a block has to be bisected, we make sure that the newly created blocks will contain field points. When the recursive decomposition is done, the computation of the influence matrices takes place. All near field block-pairs $\mathcal{P}_{I/J}$ compute the displacement influence matrices in the classical way, whereas all far field block-pairs use the ACA technique. For a given far field block-pair $\mathcal{P}_{I/J}$ containing $n_J$ triangular elements and $n_I$ observation points, a way to represent the induced displacement in matrix form is:

$$\mathbf{A} = \begin{bmatrix} \mathbf{D_{00}} & \cdots & \mathbf{D_{0 n_J}} \\ \vdots & \ddots & \vdots \\ \mathbf{D_{n_I 0}} & \cdots & \mathbf{D_{n_I n_J}} \end{bmatrix} \tag{A.14}$$

where $\mathbf{D_{ij}}$ represents the displacement influence matrix at point $i$ due to element $j$. Using ACA leads to a sparse representation of $\mathbf{A}$, denoted $\mathbf{A^S_k}$, and matrix (A.14) is optimally

computed using

$$\mathbf{A} \approx \mathbf{A_k^S} = \sum_{\mathbf{l=1}}^{\mathbf{k}} \mathbf{u_l v_l^T} \tag{A.15}$$

Assuming that each source element in $\mathcal{P}_{I/J}$ have two degrees of freedom (unknown in-plane displacement discontinuity) and that each field point is provided with a measure of the displacement in one direction, then $\mathbf{u_l} \in \mathbf{R^{n_I}}$ and $\mathbf{v_l} \in \mathbf{R^{2n_J}}$ $\forall l \in [1..k]$, where $k$ is the low-rank approximation. The complexity of this algorithm, for a given $\mathbf{A_k^S}$, is $O(k(n_I + N_{2J}))$.

#### A.5.3.2 Fast evaluation of $\mathbf{A^T W A}$ for an element $e$

Given an admissible block-pair $\mathcal{P}_{I/J}$, the matrix $\mathbf{A^T W A}$ is fast evaluated for each element $e \in J$ having two degrees of freedom (slip vector) using the ACA decomposition with rank $k$ from Eq. (A.11):

$$[\mathbf{A^T W A}]_\mathbf{e} = \sum_{\mathbf{l=1}}^{\mathbf{k}} \tilde{\mathbf{u}}_\mathbf{l} \begin{bmatrix} v_{j,l}^2 & v_{j,l}v_{j+1,l} \\ sym & v_{j+1,l}^2 \end{bmatrix}_\mathbf{e} \tag{A.16}$$

where $e$ is a source in $\mathcal{P}_{I/J}$ with index $j$, and $\tilde{u}_l$ is given by:

$$\tilde{u}_l = \sum_{p \in I} w_p u_{p,l}^2 \tag{A.17}$$

For all block-pairs $\mathcal{P}_{I/J}$ (admissible or not), the resulting $[\mathbf{A^T W A}]_\mathbf{e}$ are summed-up for a given element $e$:

$$\mathbf{A_e} = \sum_{\mathbf{q} \in \{\mathcal{P}_{\mathbf{I/J}}\}} [\mathbf{A^T W A}]_\mathbf{e}^{(\mathbf{q})} \tag{A.18}$$

$\mathbf{A_e}$ is then inverted and stored for the element $e$ at initialization.

#### A.5.3.3 Fast evaluation of $\mathbf{A^T W(d - c)}$ for an element $e$

For the right hand side of equation (A.12), we use the classical ACA product of matrix-vector. Since unknown displacement discontinuities $\mathbf{b}$ are successively corrected at each iteration, we need to reevaluate the right hand side in a fast way. Having computed, in ACA sense, the matrix $\mathbf{A}$ for the admissible block-pair $\mathcal{P}_{I/J}$ (see equation A.13.a), the vector $\mathbf{c} = \mathbf{Ab}$ is first computed in $O(k(p+n))$ using all field points $p \in I$ and elements $f \in J$. Since sub-matrices $\mathbf{D_{pe}}$ from $\mathbf{A}$ are the same as those used in the evaluation of $\mathbf{c}$, storage can be saved. Then, for each element $e$, the product $[\mathbf{A^T W(d - c)}]_\mathbf{e}$ is evaluated

and summed-up for all block-pairs:

$$\mathbf{c_e} = \sum_{\mathbf{q}\in\{\mathcal{P}_{\mathbf{I/J}}\}} [\mathbf{A^T W(d-c)}]_{\mathbf{e}}^{(\mathbf{q})} \tag{A.19}$$

## A.6 Conclusions

We have shown that doing linear slip inversion on complex fault geometry using an iterative approach can be optimized using $\mathcal{H}$-Matrix and Adaptive Cross Approximation, and leads to fast inversions. This method does not need to use an auxiliary constrained least squares solver (such as the FNNLS) to incorporate displacement inequalities. Compare to a classical approach, the Tikhonov regularization is not incorporated into the normal equation, but as a post-processing at each iteration of the block Jacobi iterative solver. Results perform well compare to a direct inversion, and the gain in speed and memory allows modeling more complex systems using denser data set.

Future developments include (i) the iteratively refinement of the smoothing parameter $\epsilon$ using an Iterative Tikhonov Regularization algorithm (Henn and al., 2001), (ii) the use of tiltmeters and stress/strain (Flodin et al., 2005) data set, as well as (iii) the parallelization on multi-core architectures (Maerten, 2010).

# References


Bebendorf, M. (2000). Approximation of boundary element matrices. *Numeri Math*, 86(4):565–589.

Bebendorf, M., editor (2008). *Hierarchical Matrices, a means to efficiently solve elliptic boundary value problems*. Springer, Berlin Heidelberg.

Bebendorf, M. and Rjasanow, S. (2003). Adaptive low-rank approximation of collocation matrices. *Computing*, 86(4):1–24.

Comninou, M. and Dundurs, J. (1975). The angular dislocation in a half space. *Journal of Elasticity*, 5(3):203–216.

Crouch, S. L. and Starfield, A. M., editors (1983). *Boundary element methods in solid mechanics*. George Allen and Unwin, London.

Flodin, A. E., Maerten, F., and Maerten, L. (2005). A geomechanically-based inverse method for interpolating the three-dimensional stress field in a faulted reservoir. volume 37, page 51. Proceeding of Geological Society of America, Rocky Mountain.

G.C.P., K., Stein, R., S., and Lin, J. (1994). Static stress changes and the triggering of earthquakes. *Bulletin of the Seismological Society of America*, 84:935953.

Greengard, L. and Rokhlin, V. (1987). A fast algorithm for particle simulations. *J. Comput. Phys.*, 73:325–348.

Hackbusch, W. (1999). A sparse matrix arithmetic based on h-matrices: Part 1: Introduction to h-matrices. *Computing*, 62:89–108.

Hackbusch, W. and Nowak, Z. (1989). On the fast matrix multiplication in the boundary element method by panel clustering. *Numeri Math*, 54(4):463–491.

Henn, S. and al. (2001). Iterative multigrid regularization tehniques for image matching. *SIAM*, 23(4):1077–1093.

Jeyakumaran, M., Rudnicki, J. W., and Keer, L. M. (1992). Modeling slip zones with triangular dislocation elements. *Bulletin of the Seismological Society of America*, 82:2153–2169.

Johnson, K., Hsu, Y., Segall, P., , and Yu, S. (2001). Fault geometry and slip distribution of the 1999 chi-chi, taiwan, earthquake imaged from inversion of gps data. *Geophys. Res. Lett.*, 28:2285–2288.

Jónsson, S., Zebker, H., Segall, P., and Amelung, F. (2002). Fault slip distribution of the 1999 mw 7.1 hector mine, california, earthquake, estimated from satellite radar and gps measurements. *Bull. Seism. Soc. Am.*, 92:1377–1389.

Maerten, F. (2010). Adaptive cross approximation applied to the solution of system of equations and post-processing for 3d elastostatic problems using the boundary element method. *Engineering Analysis with Boundary Elements*, 34:483–491.

Maerten, F. and Maerten, L. (2008). Iterative 3d bem solver on complex faults geometry using angular dislocation approach in heterogeneous, isotropic elastic whole or half-space. In Brebbia, editor, *Boundary Elements and other Mesh Reduction Methods XXX*, pages 201–208, Southampton. BEM 30, WITpress.

Maerten, F., Maerten, L., and Cooke, M. (2009a). Solving 3d boundary element problems using constrained iterative approach. *Computational Geosciences*.

Maerten, F., Maerten, L., Pollard, D., and Lagalaye, Y. (2009b). ibem3d, a three-dimentional boundary element method using angular dislocations for sub-surface structures modeling. *In preparation for Journal of Geophysical Research*.

Maerten, F., Resor, P. G., Pollard, D. D., and Maerten, L. (2005). Inverting for slip on three-dimensional fault surfaces using angular dislocations. *Bulletin of the Seismological Society of America*, 95:1654–1665.

Maerten, L. (2000). Variation in slip on intersectiong normal faults: Implications for paleostress inversion. *Journal of Geophysical Research*, 105(25):553–565.

Maerten, L., Willemse, E. J. M., Pollard, D. D., and Rawnsley, K. (1999). Slip distributions on intersecting normal faults. *Journal of Structural Geology*, 21:259–271.

Menke, W. (1984). *Geophysical Data Analysis: Discrete Inverse Theory*. International Geophysics Series, Academic, San Diego.

Muller, J. R., Aydin, A., and Maerten, F. (2003). Investigating the transition between the 1967 mudurnu valley and 1999 izmit earthquakes along the north anatolian fault with static stress changes. *Geophysics Journal International*, 154:471–482.

Okada, Y. (1985). Surface deformation due to shear and tensile faults in a half-space. *Bulletin of the Seismological Society of America*, 75:1135–1154.

Rokhlin, V. (1985). Rapid solution of integral equations of classical potential theory. *J Comput Phys*, 60:187–207.

## A.7 Appendix: Tikhonov regularization in the normal equation

For an element $e$ having three adjacent elements $f_i,\ i \in [1..3]$, the Laplacian writes

$$\mathbf{S_{ef}} = \begin{bmatrix} s_{ee} & s_{ef_1} & s_{ef_2} & s_{ef_3} \\ s_{ef_1} & s_{f_1f_1} & 0 & 0 \\ s_{ef_2} & 0 & s_{f_2f_2} & 0 \\ s_{ef_3} & 0 & 0 & s_{f_3f_3} \end{bmatrix}_{\mathbf{e}} \tag{A.20}$$

where $s_{ij}$ is a weighting parameter relating element $i$ and $j$ and is function of the distance from center to center. Incorporating $\mathbf{S_{ef}}$ into the normal equation A.2, Eq. A.5 changes to:

$$\mathbf{A_e b_e} = \mathbf{u_e} - \mathbf{u_e^\epsilon} \tag{A.21}$$

where

$$\begin{cases} \mathbf{A_e} &= \sum_p \mathbf{D_{pe}^T W_p D_{pe}} + \left(\epsilon^\mathbf{2} \sum_{\mathbf{i=0}}^{\mathbf{3}} \mathbf{s_{ef_i}^2}\right) \mathbf{I} \\ \mathbf{u_e} &= \mathbf{D_{pe}^T W_p} \left\{ \mathbf{u_p} - \sum_{\mathbf{f \neq e}} \mathbf{D_{pf} b_f} \right\} \\ \mathbf{u_e^\epsilon} &= \sum_{i=1}^{3} [\epsilon^2 s_{ef_i}(s_{ee} + s_{f_if_i}) \mathbf{I b_{f_i}}] \end{cases} \tag{A.22}$$

and $\mathbf{I}$ is the matrix identity. Using the center to center as weighting parameters, and $s_{ef}$ writes:

$$\begin{cases} s_{ee} = -2\bar{L}/L \\ s_{ef} = 2/L/d_{ef} \end{cases} \tag{A.23}$$

with $L = \sum_i d_{ef_i}$ and $\bar{L} = \sum_i d_{ef_i}^{-1}$.

# APPENDIX B

# Fault reactivation and fault properties: 3D geomechanical modeling approach and application to nuclear waste disposal

R. Soliva[(1)], L. Maerten[(2)], F. Maerten[(1,2)], I. Aaltonen, L. Wilkström[(3)] and J. Mattila[(4)]

(1) Géosciences Montpellier, Université Montpellier 2, Place E. Bataillon, 34095 Montpellier cedex 5, France
(2) IGEOSS, Parc Euromédecine, 340 rue Louis Pasteur, 34790 Grabels, France
(3) Posiva Oy, Olkiluoto, FIN-27160 Eurajoki, Finland
(4) Geological Survey of Finland, P.O. Box 96, FIN-02151 Espoo, Finland

2nd International Conference on Fault and Top Seals - From Pore to Basin Scale, Montpellier, France, 2009.

**Preamble:**
Fault sealing and leakage are key parameters for both nuclear waste disposal and exploitation of natural resources. These parameters are related to mechanism of deformation that change in space along the fault planes and through time as the overall deformation of the subsurface area evolves. The challenging methodology described in this contribution aims at relating computed fault reactivation (i.e. fault slip and residual stresses) to potential

fault sealing and/or leakage through time.

This extended abstract is the contribution to the 2nd International Conference on Fault and Top Seals - From Pore to Basin Scale, held in Montpellier, France, 21 - 24 September 2009. It presents the application of *Scribble*, the Java-script language for iBem3D (former Poly3D), to quickly run thousands of models for sensitivity analysis. In this particular modeling, three inter-dependent parameters are analyzed: (1) ice thickness above the faults, (2) fault friction and (3) fault cohesion.

## B.1 Résumé

Les défauts d'étanchéité et de fuites sur les failles sont les deux paramètres clés pour l'étude du stockage des déchets nucléaires et l'exploitation des ressources naturelles. Ces paramètres sont liés au mécanisme de déformation qui change dans l'espace le long des plans de faille et dans le temps lorsque la déformation globale du sous-sol évolue. La méthodologie décrite dans cette contribution vise à relier la réaction des failles (c'est à dire le déplacement sur les failles et les contraintes résiduelles) au potentiel d'étanchéité et de fuites de celles-ci dans le temps.

Ce résumé étendu est notre contribution à la $2^{eme}$ Conférence internationale sur *Fault and Top Seals - From Pore to Basin Scale*, qui s'est tenue à Montpellier, France, du 21 au 24 septembre 2009. Elle présente une application de *Scribble*, le langage Javascript pour iBem3D (ex- Poly3D), afin d'exécuter rapidement des milliers de modèles dans le but de faire une analyse de sensibilité de paramètres. Dans cette modélisation particulière, trois paramètres interdépendants sont analysés: (1) l'épaisseur de la glace au-dessus d'un système de failles, (2) la friction et (3) la cohésion sur ces failles.

## B.2 Abstract

We present Poly3D, a three-dimensional elastostatic code using the Boundary Element Method in heterogeneous elastic whole- or half-space, with application in structural geology and geomechanics for the evaluation of the deformation and perturbed stress field associated with surfaces of displacement discontinuity. After the presentation of the theory behind Poly3D and its wide range of applications, we describe the recent developments such as (i) the incorporation of static friction and non-interpenetration, (ii) the incorporation of material heterogeneity using complex 3D interfaces separating regions of different material properties, (iii) a module for doing slip inversion using GPS and InSAR dataset, (iv) a module for doing paleo-stress and slip recovery, and (v) optimizations and parallelization on multi-core architectures. Each new feature will be illustrated with examples showing their importance for the comprehension of natural phenomenons.

## B.3 Introduction

Fault sealing and leakage are key parameters for both nuclear waste disposal and exploitation of natural resources. These parameters are related to mechanism of deformation that change in space along the fault planes and through time as the overall deformation of the subsurface area evolves. The challenging methodology described in this contribution aims at relating computed fault reactivation (i.e. fault slip and residual stresses) to potential fault sealing and/or leakage through time. As a test case, we use the fast 3D boundary element code Poly3D (Thomas, 1993; Maerten et al., 2005) from IGEOSS, for modeling fault reactivation in the Olkiluoto nuclear waste repository site, Finland.

## B.4 Methodology

The methodology can be resumed as follow:

1. Building of 3D fault model that must be as close as possible to the geological reality. Faults are triangulated surfaces suited for Poly3D;
2. Setting the constant parameters such as the rock type and half space options;
3. Setting the fault variable parameters that can be friction, cohesion and fluid pressure;

4. Setting the 3D far field stress as a variable. This far field stress coming tectonic forces or ice load can be heterogeneous (i.e. gradients);

5. Run of hundreds of simulations with varying parameters;

6. Global automatic analyzes of the results (i.e. 3D graph) in order to evaluate which combinations of parameters lead to fault reactivation;

7. Spatial analyzes of the results looking at individual fault that have been reactivated (i.e. slip and residual stresses);

8. Establish a relationship between fault slip or residual stresses and deformation mechanisms in order to infer fault seal and leakage capacity.

## B.5 Example case study

The Olkiluotto repository site is located in faulted and fractured gneisses, which has been deformed during several tectonic phases (Andersson et al., 2007). These tectonic deformations allowed the formation of interacting and intersecting ductile thrust faults formed at depth. These deformation zones were exhumed and reactivated during late extensional and compressional events in a more brittle context. Kilometre scale brittle deformation zones therefore formed during poly phased tectonic events and are subjected to be reactivated in the future during glacial loading and unloading cycles.

## B.6 Model configuration

The 3D model geometry has been build from surface mapping, well bore, tunnels and seismic reflection data. It includes 10 intersecting thrust faults with dip angles varying from 30 to 70 degrees (see Fig. B.1a).

Since the aim is to model the effect of a vertical ice sheet, the principal parameter to use as a variable is the applied state of stress, which is strongly dependent on the thickness of the mass above the faults (see Fig. B.1b). Extrapolating the present stresses to the future (i.e. 115 000 yr) and with the addition of a variable ice sheet thickness, a resulting stress gradients can be calculated and applied to the model. Data derived from in situ bore hole measurements and rock tests were provided and used as constant (i.e. elastic moduli) or variable (i.e. cohesion, friction) parameters in this preliminary study (Hudson and Johansson, 2006).

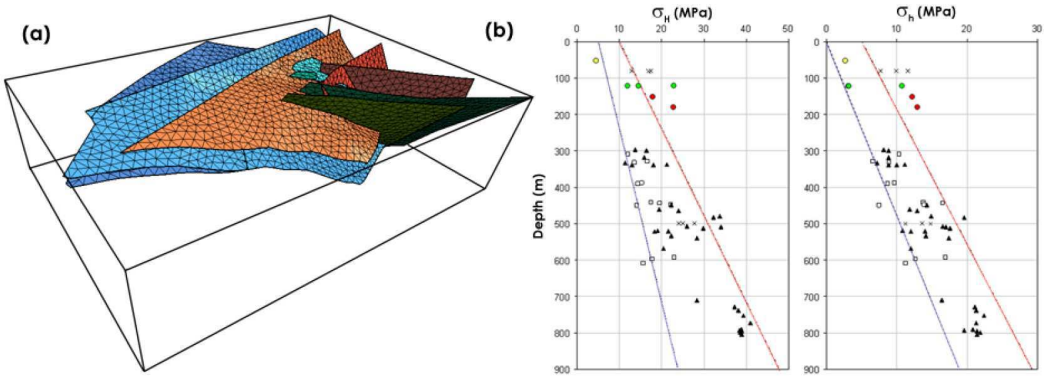


FIGURE B.1: Model configuration. (a) 3D fault model as triangulated surfaces and (b) measured in-situ stresses used as a base for the far field stress boundary conditions.

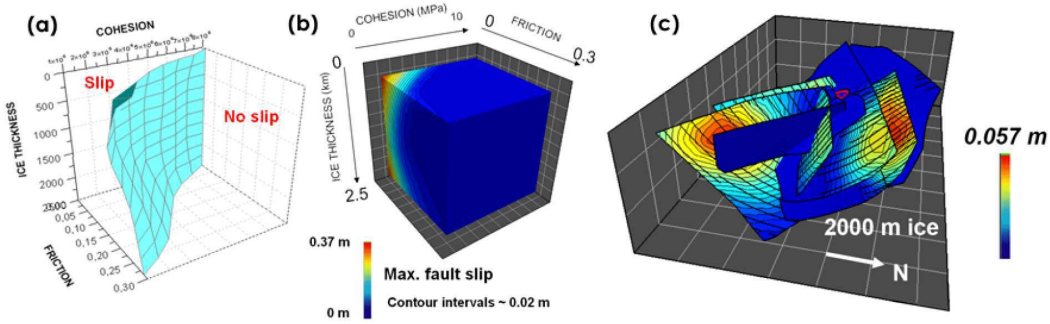


FIGURE B.2: Model results. (a) 3D rupture envelope. (b) Iso-surfaces of maximum slip for the entire model. (c) Fault slip distribution computed for 2000 m of ice, a friction of 0.085 and a cohesion of 2 MPa.

## B.7 Model results analysis

A total of 1331 Poly3D simulations have been run using the far filed stresses, the friction and the cohesion as variables. Each run in which at least one triangular element of the fault surfaces has slipped is identified as a "slipping model". The runs, in which no triangular element has slipped is identified as "non slipping models". Figure B.2a and b shows 3D graphs illustrating slipping and non slipping models as 3D fields separated by a rupture envelope, which is function of friction, cohesion and ice thickness.

Figure B.2c illustrates how individual run can be analyzed. Here fault slip distribution is displayed with slip vectors. Only some zone of the faults have slipped in response too fault mechanical interaction, friction, cohesion and far field stress.

## B.8 Conclusions

The preliminary results of the methodology presented here appear promising. The methodology aims at relating computed slip or residual stress along reactivated faults with fault sealing and leakage capacity. The methodology has been applied and tested on the Olkiluoto nuclear waste repository site, Finland but could be applied to petroleum reservoirs, where depletion can affects fault reactivation, hence fault leakage.

# References

Andersson, J., Ahokas, H., Hudson, J., Koskinen, L., Luukkonen, A., Löfman, J., Keto, V., Pitkänen, P., Mattila, J., Ikonen, A., and Ylä-Mella, M. (2007). Olkiluoto site description, part1. Technical report, Posiva report 2007-3.

Hudson, J. A. and Johansson, E. (2006). Summary of rock mechanics work completed for posiva before 2005. Technical report, Posiva report 2006-4.

Maerten, F., Resor, P. G., Pollard, D. D., and Maerten, L. (2005). Inverting for slip on three-dimensional fault surfaces using angular dislocations. *Bulletin of the Seismological Society of America*, 95:1654–1665.

Thomas, A. L. (1993). Poly3d: a three-dimensional, polygonal element, displacement discontinuity boundary element computer program with applications to fractures, faults, and cavities in the earth's crust. Master's thesis, Stanford University.

# APPENDIX C

Other publications and conferences

The reader might find it interesting to see all the other publications, proceedings and conferences that I participated since 2000, and will find other useful information related to the developed softwares and applications.

## C.1 Other international publications

### Maerten, L., Pollard, D.D., and *Maerten, F.*, 2001, Digital mapping of three-dimensional structures of the Chimney Rock fault system, central Utah: Journal of Structural Geology, v. 23, p. 585-592.

**Abstract**

*Part of the Chimney Rock fault system, located on the northern San Rafael Swell, Utah, was mapped by integrating air photograph interpretation and differential global positioning system (GPS) location data. Fault slip, slip directions, and hanging wall subsidence/footwall uplift were digitally recorded in the field along and between the normal faults using Trimble PathFinder equipment and software. GPS was used to record (with sub-meter precision) the location of each measurement as well as the UTM coordinates and elevation of stratigraphic markers at the top of the Jurassic Navajo Sandstone and near the base of the overlying Carmel Formation. The fault system, as well as the associated deformation of the sedimentary layers within the fault blocks, have been precisely characterized using this technique. The geographic coordinates and local elevation were transferred to gOcad to produce a three-dimensional surface representation of a selected resistant limestone layer, by interpolating the elevation between the collected data points using imposed constraints such as the dips of the layers and the locations of the major faults. Separations of the selected horizon from the footwall to the hanging wall were used to calculate the dip-slip distribution along the faults. The digital field data were compared with the results of numerical modeling based on continuum mechanics to study the mechanical interaction among intersecting normal faults and the effects of this interaction on slip distribution and direction. This project illustrates the complete circle from digital mapping to data analysis to numerical modeling to quantitative comparison of theoretical models and field data.*

**Muller, J.R., Aydin, A., and *Maerten, F.*, 2003, Static stress changes on the 17 August 1999 Kocaeli (Izmit) earthquake rupture segments due to the 22 July 1967 Mudurnu Valley earthquake, Turkey. International Journal of Geophysics.**

**Abstract**

*The last major rupture along the North Anatolian fault (NAF) prior to the Izmit and Dzce earthquakes in 1999 was the Ms= 7.1 1967 July 22 Mudurnu Valley Earthquake, which ruptured approximately 80 km along the surface of the west-central NAF. The geographic continuity of the Mudurnu Valley and Izmit ruptures corresponds to the historical westward progression of major earthquakes along the NAF and encourages us to test the stress-triggering effects of the 1967 earthquake on the 1999 earthquake. Although the triggered earthquake sequence from 1939 to 1999 has been investigated by earlier workers, this study addresses several outstanding problems related to this most recent earthquake interaction in light of more detailed fault configurations and a posteriori knowledge of the 1999 events. The questions we hope to answer are: (1) did the stress perturbation caused by the 1967 Mudurnu Valley earthquake promote failure at the 1999 Izmit earthquake hypocentre and along Izmit fault segments? (2) Why did the 1999 Izmit earthquake rupture along faults in the centre of the IzmitAkyazi depression rather than along the western continuation of the Mudurnu Valley fault that ruptured in 1967? (3) What is the rupture configuration at the western end of the 1967 earthquake fault that would most favour slip on the 1999 August 17 Izmit earthquake fault? Using a 3-D boundary element method, we test three possible rupture configurations for the 1967 Mudurnu Valley earthquake. Coulomb stress changes are calculated on major faults within the region due to non-uniform slip associated with the 1967 Mudurnu Valley earthquake. We find that for all three potential 1967 Mudurnu Valley rupture geometries there are positive Coulomb stress changes at the hypocentre of the 1999 Izmit earthquake. We also find, however, that only when subsurface rupture of the 1967 Mudurnu Valley earthquake deviates from the mountain-front fault and extends towards Lake Sapanca does an Izmit rupture segment (Sakarya segment) receive greater Coulomb stress changes than the mountain-front fault west of the Mudurnu rupture.*

**Lovely, P. and Flodin, E. and Guzofski, C. and *Maerten, F.* and Pollard, D.D, 2010, Geomechanical analysis of the Volcanic Tableland extensional fault system, Bishop, CA and evaluation of mechanics-based restoration methods. In preparation for AAPG Bulletin.**

**Abstract**

*Numerical models and field data are integrated to perform a geomechanical analysis of the Volcanic Tableland fault array, an outcrop analogue for subsurface normal fault systems. A geomechanical approach is used to infer 3D fault geometry from outcrop data, and a paleostress inversion technique is employed to establish appropriate physical boundary conditions for forward models. Past studies suggest that larger Tableland faults developed through linkage of smaller faults, implying that small faults may be the oldest in the study area. While this mechanism of fault growth is clear from mapped traces of some faults, other large faults are relatively linear. We provide evidence in the form of throw distributions that even long, linear fault traces likely grew by linkage of smaller faults. Other studies suggest that geomechanical models may be used to understand stress perturbations due to slip on large (seismic-scale) faults, and thus to infer density and orientation of subseismic-scale faulting. Regions of densest subseismic faulting on the Tableland correlate with tensile stress shadows, suggesting that it would be inappropriate in the case of this field site to predict subseismic faulting from stress perturbations due to slip on larger faults, and that the growth of larger faults has not led to initiation of new subseismic-scale faults, but may inhibit the growth of existing faults. Further geomechanical models corroborate previous work that suggests Tableland faulting results from flexural stresses in the rollover anticline in the hanging wall of the Basin and Range-scale White Mountain fault, several kilometers to the east. We conclude by comparing forward model kinematics with results of mechanics-based restoration models. A critical evaluation suggests that restoration models may not accurately reflect the kinematics of forward deformation.*

## C.2 Rock Fracture Project abstracts, Stanford, CA

1. **Maerten, F.** and Maerten, L., 2002, Poly3DGUI, a new graphical interface for industrial use: architecture and functionality. In D. Pollard & A. Aydin, eds., Proceedings of the Stanford Rock Fracture Project, v. 13, p. F1-F4.

2. Maerten, L. and **Maerten, F.**, 2002, Dynel: New tools for the restoration of 2D and 3D geological structures. In D. Pollard & A. Aydin, eds., Proceedings of the Stanford Rock Fracture Project, v. 13, p. G1-G5.

3. **Maerten, F.** and Maerten, L., 2001, DYNEL: a new 3-D geomechanical method for modeling geological structures. In D. Pollard & A. Aydin, eds., Proceedings of the Stanford Rock Fracture Project, v. 12, p. E1-E10.

4. **Maerten, F.** and Maerten, L., 2001, Poly3D: a 3D geomechanical program for fault related problems in petroleum reservoirs. In D. Pollard & A. Aydin, eds., Proceedings of the Stanford Rock Fracture Project, v. 12, p. F1-F4.

5. Du Bernard Rochy, X. and **Maerten, F.**, 2001, Grain-scale deformation mechanics. In D. Pollard & A. Aydin, eds., Proceedings of the Stanford Rock Fracture Project, v. 12, p. G1-G7.

6. **Maerten, F.**, 2000, Current status of Poly3D: In D. Pollard & A. Aydin, eds., Proceedings of the Stanford Rock Fracture Project, v. 11, p. M1-M8.

7. **Maerten, F.**, 2000, Improved Poly3DPro interface (Graphical Interface for Poly3D). In D. Pollard & A. Aydin, eds., Proceedings of the Stanford Rock Fracture Project, v. 11, p. R1-R7.

## C.3 Conference abstracts

1. **Maerten, F., Maerten, L., D. D. Pollard, 2010, Paleostress analysis using full mechanical scenario : Stress Controls on Faulting, Fracturing, and Igneous Intrusion in the Earth's Crust, Anderson conference, University of Glasgow**

   **Abstract**

   *Methods for stress inversion (originally initiated by Anderson in 1905) using measured striations and/or throw on faults, are mainly based on on the assumptions that: (1) the stress field is uniform within the rock mass embedding the faults (assuming no perturbed stress field), and that (2) the slip on faults has the same direction and sense as the resolved far field stress on the fault plane. However, it has been shown that slip directions are affected by: (1) anisotropy in fault compliance caused by irregular tip-line geometry; (2) anisotropy in fault friction (surface corrugations); (3) heterogeneity in host rock stiffness; and (4) perturbation of the local stress field mainly due to mechanical interactions of adjacent faults. Mechanical interactions due to complex faults geometry in heterogeneous media should be taken into account while doing stress inversion. Determining the parameters of such paleostress in the presence of multiple interacting faults requires running a lot of simulations, and therefore a huge amount of computation time in order to fit the observed data.*

*In this contribution we investigate paleostress analysis using a linear elastic 3D boundary element method for heterogeneous, isotropic whole- of half-space media. Given the complex triangulated fault geometries as well as some measures of the fault throw or dip-slip, slickenline directions, stress measurements, GPS or InSAR data, open fractures (joints, veins, dikes), pressure solution seams with stylolites, or secondary fault plane orientations, we interactively recover the remote stress state for multiple tectonic events. Synthetic and field examples are presented which validate the proposed technique.*

2. **Maerten, F., Maerten, L., P. Gillespie, 2010, Interactive determination of perturbed stress field in complex reservoirs using geomechanics and data from well-bores: AAPG Geosciences, Technology Workshop on The Role of Fracture and Geomechanical Characterization in the Hydrocarbon Industry, Rome**

   **Abstract**

   *We use a 3D elastic computer code to recover for complex perturbed stress field in reservoirs. Multiple types of data can be used to constrain the computation such as fractures orientation, secondary fault planes with internal friction angle, GPS data, measured fault throw from seismic interpretation as well as fault slickenlines. We show that this innovative technique allows to recover for orientation and magnitude (or ratio) of each recovered tectonic event, and permits fracture prediction in complex reservoirs.*

3. **Soliva, R., Maerten, L., Maerten, F., Aaltonen, I., 2009, Wilkstrm, L., Mattila, J., Fault reactivation and fault properties: 3D geomechanical modeling approach and application to nuclear waste disposal: 2nd International Conference on Fault and Top Seals From Pore to Basin Scale, Montpellier, France**

   **Abstract**

   *We present the preliminary results of a methodology that consists on modeling 3D fault reactivation and to relate both the computed fault slip and residual stresses to fault seal and leakage capacity. A series of geomechanical simulations is run on a 3D fault model, which integrates friction, cohesion, far field stress and fluid pressure as variables. The hundreds of simulations are analyzed as a whole in order to determine the likelihood of fault reactivation with respect to the variable parameters. Each reactivated fault is then analyzed independently. Fault sealing and/or leakage capacity can be estimated when the relationship between computed fault slip and/or residual stresses and fault zone deformation mechanisms is known. The methodology has been applied and tested on the Olkiluoto nuclear waste repository site, Finland.*

*The method can be applied to petroleum reservoirs, where depletion can affects fault reactivation, hence fault sealing and leakage reliability.*

4. **Maerten, F., 2009, Poly3D, a 3D elastostatic code using the boundary element method with applications in structural geology and geomechanics, USGS, Denver**

   **Abstract**

   *We present Poly3D, a three-dimensional elastostatic code using the Boundary Element Method in heterogeneous elastic whole- or half-space, with application in structural geology and geomechanics for the evaluation of the deformation and perturbed stress field associated with surfaces of displacement discontinuity. After the presentation of the theory behind Poly3D and its wide range of applications, we describe the recent developments such as (i) the incorporation of static friction and non-interpenetration, (ii) the incorporation of material heterogeneity using complex 3D interfaces separating regions of different material properties, (iii) a module for doing slip inversion using GPS and InSAR dataset, (iv) a module for doing paleo-stress and slip recovery, and (v) optimizations and parallelization on multi-core architectures. Each new feature will be illustrated with examples showing their importance for the comprehension of natural phenomenons.*

5. **Maerten, F., Maerten, L., 2009, PaleoStress and slip recovery on complex faults geometry using mechanical interactions: Application to fractures prediction: AAPG annual convention. Denver**

   **Abstract**

   *Methods for stress inversion, using measure striation and/or throw, are mainly based on the assumptions that (i) the stress field is uniform within the rock mass embedding the faults (assuming no perturbed stress field), and that (ii) the shear traction has the same direction and sens as the resolved far field stress onto the fault plane. However, it has been shown that slip direction are highly affected by (i) anisotropy in fault compliance caused by irregular tipline geometry, (ii) anisotropy in fault friction (surface corrugations), (iii) heterogeneity in host rock stiffness and (iv) perturbation of the local stress field mainly due to mechanical interactions of adjacent faults. Therefore, mechanical interactions due to complex faults geometry in heterogeneous media have to be taken into account while doing stress inversion.*

   *We investigate this approach using Poly3D, a 3D Boundary Element Method (3D-BEM) using linear elasticity in heterogeneous, isotropic whole- of half-space. Given some measures of the fault throw and/or dip-slip (plus constraints such as slikenline*

*directions if any), as well as the faults geometry, we recover for paleo-stress directions and magnitudes as well as for the unknown slip components onto the faults.*

*Having the paleo-stress as well as for the slip distribution onto the faults, it is then possible to compute anywhere within the 3D elastic field, the strain, stress and displacement. Particularly, the perturbed stress field can be used to predict fractures and subseismic faults. We show examples from different field areas, such as complex faulted reservoirs.*

6. **Lepage, F., Laverne, T., Maerten, F., Desmarest, D., Quetelard, E., Palomas, M., Maerten, L., 2007, 3-D model building and geomechanically-based volume restoration: The next generation tool: American Association of Petroleum Geologists Annual Convention**
   **Abstract**
   *For many years structural geologists have been using computer tools to construct balanced 2D and 3D structural models. The tools available to restore geological structures are based on a variety of geometric techniques, which aim at reproducing natural deformation, constrained by assumptions such as preservation of area or volume, minimization of deformation, minimization of changes in segment length. While the challenge of restoring structural models could be attributed to inadequate data, hardware, and software in the past, the challenge today is to integrate a complete mechanics into the methodology. Indeed, it is established that rock deformation is a physical process that involves parameters such as the initial geometry, the distribution of mass, rock properties, and the constitutive laws that govern the deformation.*

   *Therefore, we propose the next generation tool that allows elastically-based 3-D volume restoration. The method, when realistically well constrained, honors the fundamental physical laws that govern deformation, that are (i) conservation of mass, (ii) conservation of momentum and (iii) conservation of energy. Mechanically-based decompaction as been implemented based on both the heterogeneous rock properties assigned to the model and the compaction rule chosen. This innovation permits fault slip during decompaction and does not unrealistically deform the model. We describe the complete workflow from interpreted horizons and faults, to 3-D model building, to model setup, to volume restoration. We offer examples to illustrate the applications in the oil and gas industry for the characterization of structurally complex reservoirs.*

7. **Maerten, L., Maerten, F., Griffiths, P., Pike, N., 2007, A methodology for automated correction and validation of seismic horizon and fault interpretation using DYNEL, a geomechanically-based 3-D restoration tool:**

**American Association of Petroleum Geologists Annual Convention Abstract**

*To reduce exploration risk and optimize production in structurally complex areas, the geological interpretation must be physically and mechanically reliable. Despite the advances in 3D seismic techniques and in the availability of computationally-robust interpretation software, the challenge associated with interpreting complex structures in seismic reflection data is that highly deformed areas surrounding faults, folds and salt surfaces are often poorly imaged.*

*We present a methodology to help geophysicists quickly check the mechanical strength and weakness of their interpretation and to automatically correct the faulted horizon geometry. The workflow consists on restoring interpreted seismic horizons and relating the concentrations of computed attributes such as stress or strain to areas of interpretation uncertainty. The technique used, based on the finite element method, allows unfolding and unfaulting of 3D horizons using the physical behaviour of rock mass. A fast algorithm has been developed to automatically correct the interpreted structures in zones that exhibit anomalous stress or strain concentrations after restoration. The modified horizons are then imported back to the seismic data interpretation software for comparison with the seismic volume.*

*This approach is able to mechanically check and correct seismic data interpretation. Its application to both synthetic and reservoir data demonstrates a high degree of reliability in the characterization of structurally complex reservoirs.*

8. **Maerten, F., Maerten, L., Davatzes, N. C., 2007, Poly3D boundary element code with inequality constraints: More potential to model natural structures: European Geosciences Union, Geophysical research abstracts, v. 9, p. 06729**

**Abstract**

*Some of the major challenges using boundary element codes are: (i) limiting the amount of memory necessary to solve large and dense systems; and (ii) incorporating traction inequality constraints (TIC) and displacement inequality constraints (DIC). The latter serves two purposes: first to simulate friction using the Coulomb criteria (TIC) for instance; and second to bound the displacement discontinuity onto the modelled fractures (using DIC). Since Poly3D is now widely used around the world as a research tool for studying fracture mechanics, rock deformations, earthquakes and volcanoes, we have developed a method that addresses these two purposes at the same time. We show that the use of a discrete iterative solver not only permits to compute very large model by avoiding allocation of significant memory while solving the system, but also authorizes new unexpected features to be implemented such as*

*TIC and DIC. To illustrate these new potential, we give an example of one particular TIC, the static Coulomb friction, for the modeling of cohesive end zones (CEZ) to explain the low value of the kink angles observed in the faults in the Waterpocket monocline (Utah, USA). We also give an application of one DIC for characterizing secondary features such as stylotites around curving and overlapping fractures, in Jurassic limestone from Montpellier area, Southern France.*

9. **Maerten, F., Maerten, L., 2006, Improved understanding of observed 2D and 3D geological structures using geomechanically-based approaches: EGU, Vienna, Austria**

   **Abstract**

   *Recent advances in geologic mapping techniques, reflection seismology, aftershock location and GPS measurements allow geoscientists to image surface and subsurface structures with greater precision. We present 2 numerical approaches that help improving the understanding of these imaged structures by bringing rational physical principles to the geological interpretations.*

   *Poly3Dinv is a 3D slip-inversion method based on the analytical solution of an angular dislocation in a linear-elastic, homogeneous, isotropic, half-space. The approach uses the boundary element method (BEM) that employs planar triangular elements to model complex fault surfaces. Slip inversion techniques are used by geophysicists to invert for coseismic slip associated with earthquakes. We used this first technique to investigate the 3D geometry of normal faults by integrating high-precision aftershock locations and published geological and geodetic data sets from the 1995 Kozani-Grevena earthquake in Greece.*

   *Dynel is a new generation restoration tool based on the finite element method (FEM), which allows unfolding and unfaulting of complex 2D and 3D structures using the physical behavior of rock mass and taking into account rock heterogeneous mechanical properties as well as physical boundary conditions. The technique has been used to understand the development and the geometry of a decameter-scale fold, which crops out in the Coulazou gully located near the Montpellier thrust fault, Southern France.*

   *Through these two examples we show that the geometric flexibility of the geomechanical techniques and the ability to integrate available data sets can lead to improved understanding of observed 2D and 3D geological structures.*

10. **Delaval, C., Maerten, L., Subsol, G., Micallef, J.-P., Goudot, P., Yachouh, J., Maerten, F., Chemouny, S., 2006, A 3d computer-assisted method for the strategy and assessment of therapy of the weakened mandible: Proceedings of Computer Aided Radiology and Surgery, 12th Computed.**

**International Journal of Computer Assisted Radiology and Surgery, v. 1, p. 433-435**

**Abstract**

*Departments of Maxillofacial Surgery and Stomatology receive every year patients with mandible which are lysed, resected or edentulous because of age or a tumoral disease. The loss of substance due to cysts or tumors weakens the ramus and corpus of the mandible. This weakness leads to fracture risk during chewing, especially when the Maxillo-Facial surgeon cuts a part of the mandibular bone in an interrupting way or not. Moreover, the loss of teeth induces the resorption of the bone surrounding the roots, named alveolar bone. This bone height diminution also leads to a mandibular weakness that increases the fracture risk and makes the repair harder.*

*The goal of our research is to set-up and to assess a suite of computerized tools that will analyze the 3D CT-Scan images of the patient and assist the practitioner, in clinical routine:*

*(a) to design patient-specific geometrical and biomechanical models of the mandible;*

*(b) to apply masticatory forces and stresses which are specific to the patient to be treated (with respect to age, alimentary habits and anatomy);*

*(c) to analyze bone strains with the Finite Elements Method.*

*In order to:*

*(a) predict the threshold of the fracture risk that will allow to decide a treatment;*

*(b) plan and simulate a therapy if it is required (for example by defining the critical height of the mandible to preserve in the case of a tumoral surgery);*

*(c) assess the therapy by a retrospective evaluation of the clinical case and a correlation with the computed results.*

*Many studies have used Finite Element Models to evaluate the mechanical strains developed within the mandibular bone [Weingrtner et al., 1997; Vollmer, 2000; Erkmen, 2005] but most of them deal with the behavior of the bone material located near dental implants [Ftterling et al., 1998; Nagasao et al., 2002]. Thus, the biomechanics of the edentulous mandible remains not well known so far [Veyrune, 2000].*

11. **Maerten, L., Maerten, F., Arbeaumont, A., Mutlu, O., Pollard, D. D., 2006, What should be balanced in the construction and restoration of cross sections?: Geological Society of America Abstracts with Programs, p. 49-6**

    **Abstract**

*Advances in 3D seismic reflection surveying, in the power of desktop computers, and in the availability of computationally-robust software support the development of the next generation of cross section construction and restoration tools. While the challenge of quantifying magnitudes of deformation in diverse tectonic settings could be attributed to inadequate data, hardware, and software in the past, the challenge today is to integrate a complete mechanics into the methodology.*

*As an example we review the classic reconstruction of the Sprsel fold from the Jura Mountains of Switzerland by Laubscher based upon conservation of line length and area. This methodology is compared to a geomechanical reconstruction using the finite element method (FEM) and based upon conservation of mass in which the material time derivative of density balances the product of mass density and the divergence of the velocity field. In Laubscher's reconstruction the Mesozoic strata are kinematically constrained to form two complementary kink bands terminating downward at a mobile layer resting on a detachment at the top of a rigid basement. The FEM analysis is based upon conservation of linear and angular momentum in which the product of density and the material time derivative of velocity balances the resultant surface and body forces. The kinematics of folding and deformation of the mobile layer and basement follow from these laws of nature rather than being pre-supposed. The equations of motion, derived by combining the conservation laws with appropriate constitutive laws, can be solved to extract deformational histories from diverse tectonic environments so one can compare model rates and geologic rates of deformation.*

*We offer three examples to illustrate the power of the geomechanical methodology: 1) restoration of detached sedimentary strata over salt from the North Sea extensional province to evaluate the evolution of the salt body and associated structures through time; 2) restoration of normal faults of the Rhine graben to mechanically validate the structural interpretation and relationships between intersecting normal faults; and 3) restoration of contractional structures in the deep-water fold and thrust belts of the Niger Delta, to elucidate thrust fault propagation and quantify the magnitude of shortening.*

12. **Flodin, A. E., Maerten, F., Maerten, L., 2005, A geomechanically-based inverse method for interpolating the three-dimensional stress field in a faulted reservoir: Geological Society of America, Rocky Mountain Section, Abstracts with Programs, v. 37, p. 51**

    **Abstract**

    *Information concerning the nature of the stress field in a reservoir is necessary for many oilfield applications, such as pre-drill wellpath planning and fault seal analysis.*

*Available data usually include stress orientation and magnitude estimates of various quality along a limited number of wellbores. Current methods to map the reservoir volume stress field from these point and/or line data range from simplistic averaging to more sophisticated interpolation and geostatistical techniques. We present a new method to interpolate stress throughout a reservoir volume using a geomechanically-based numerical boundary element code, Poly3D, coupled with a weighted damped least-squares inverse solver. The primary advantage of this methodology over others is that the stress solution includes the effect of elastic interactions among faults. The code uses as input a 3D fault framework, with or without mapped displacements, and estimates of stress orientation and magnitude from wellbores, which can be weighted to data quality. Output is in the form of a best-fit' remote stress field, which is in turn used to forward model the volumetric stress field. Results illustrating the utility of our tool are presented for a number of faulted reservoir scenarios.*

13. **Resor, P. G., Maerten, F., Pollard, D. D., Maerten, L., 2005, Coseismic slip estimate for the 1999 Hector Mine earthquake using a multi-segment fault model: Penrose Conferences, Mammoth Lakes, California**
**Abstract**
*Reconciling geologic and geophysical observations of coseismic slip for modern earthquakes is critical in order to evaluate the significance of paleoseismic observations and thus understand the role that coseismic slip plays in long-term strain distribution of the Eastern California Shear Zone. In order to make a more direct comparison between estimates of coseismic slip for the 1999 Hector Mine earthquake (Mw 7.1) we have created a three-dimensional fault model using triangular dislocation patches in place of the more commonly used rectangular patches. This geometric model includes dipping fault segments that honor the observed surface rupture geometry at a kilometer-scale including fault bends, intersections, and parallel segments without introducing artificial overlaps or gaps. Coseismic slip on this model is estimated using a damped least squares linear inversion. The resulting model yields an improved fit to the geodetic data (32% reduction in weighted residuals) over more simplified fault models. The resulting slip distribution can be directly compared to geologic observations of surface slip (Figure). The geologic slip measurements (Treiman et al., 2002) are point estimates and show significant variability over short distances while the geodetic model estimates are averages over 2.6 km2 areas and are therefore smoother. Geodetic model estimates generally agree with the upper range of the geologic estimates with a few exceptions. The majority of these exceptions are regions where the geodetic model estimates exceed the geologic estimates. At least in some*

*cases these discrepancies appear to be in areas of poorly-consolidated surface materials that may lead to distributed deformation rather than localized faulting. These results suggest that geologic estimates may tend to under-estimate coseismic slip.*

14. **Maerten, F., Maerten, L., 2004, 3-D Geomechanical Techniques to Better Characterizing Complex Structural Models: (i) Slip Inversion and (ii) Restoration: American Association of Petroleum Geologists Annual Convention, v. 13, p. A90**

    **Abstract**

    *We present 2 geomechanical approaches to better characterizing 3-D structural models by bringing rational physical principles to the geological interpretation.*

    *The first one is a 3-D slip-inversion method based on the analytical solution of an angular dislocation in a linear-elastic, homogeneous, isotropic, half-space. The approach uses the boundary element method (BEM) that employs planar triangular elements to model complex fault surfaces. Slip inversion techniques, usually used by geophysicists to invert for coseismic slip associated with earthquakes, is used here to determine the characteristics of faults, where they are poorly imaged. We have tested the method on a field case study from the Bishop Tuff, California, where the unseen 3-D fault geometries and slip distributions have been predicted using the only available data; (i) the fault pattern (fault trace map) and, (ii) the measured surface deformation (structure contour map).*

    *The second technique is based on the restoration of interpreted geological structures. The method, based on the finite element method (FEM), allows unfolding and unfaulting complex 2-D and 3-D structures using the physical behavior of rock mass and taking into account rock heterogeneous mechanical properties as well as physical boundary conditions. New algorithms have been developed to automatically correct the interpreted structures in zones that exhibit anomalous stress and/or strain concentrations subsequent to restoration. The technique has been tested on several 2-D and 3-D cases and we show how such geomechanically-based restoration can lead to better characterization of structural models.*

15. **Maerten, L., Maerten, F., 2004, Chronologic modeling of faulted and fractured reservoirs using geomechanically-based restoration: American Association of Petroleum Geologists Annual Convention, v. 13, p. A90**

    **Abstract**

    *We present a new geomechanical tool that allows chronologic modeling of reservoir deformation. The method aims at restoring complex geological structures such as folded and faulted rock. It is based on the finite element method and simulates*

*the physical behavior of rock mass and takes into consideration rock heterogeneous mechanical properties, fault mechanical interaction as well as tectonic stresses.*

*To illustrate the method's potential for evaluating faulted and fractured reservoirs, we analyze deformation and fault development, though time, in the hanging wall of a syn-sedimentary listric normal fault. As a case study example, we use one of the sandbox experiments carried out by McClay in 1990. A model of the final deformed stage of the analogue experiment was created and restored chronologically by removing the sedimentary layers one after the other. At each restoration stage, fault slip distributions are computed to facilitate the understanding of fault nucleation, propagation and sealing. The model is then analyzed in a forward sense so as to chronologically investigate fault development and deformation in the hanging wall of the basal listric fault. The numerical model corresponds well to the physical model and provides additional insights about the basin (reservoir) evolution and deformation.*

*We conclude that the geomechanically-based 2-D and 3-D restoration of complex geological structures, has considerable potential for industry applications on fractured reservoir characterization and production. This method allows to characterizing, for key geologic and tectonic episodes, subseismic faults and fractures, reservoir compartmentalization, hydrocarbon migration pathways, and hydrocarbon traps.*

16. **Maerten, F., Maerten, L., Resor, P. G., Muller, J. R., Pollard, D. D., 2003, A new method for slip inversion for faults with complex geometry: European Geophysical Society, Nice, France, Geophysical Research Abstracts, v. 5, p. 07473**

    **Abstract**

    *The increasing data quality now available to the geophysicist and geologist (fault trace mapping, high quality InSAR data, GPS measurement, and aftershock relocations) are not today fully exploited in slip inversion procedures. Most commonly used methods use idealized rectangular dislocation segments to model complex fault ruptures, which requires simplified fault geometries. These geometrical simplifications can often lead to inconsistencies when inverting for slip on earthquake faults. We have developed a new three-dimensional slip-inversion method based on the analytical solution of an angular dislocation in a linear-elastic, homogeneous, isotropic, half-space. The approach uses the boundary element code Poly3D that employs planar triangular elements of constant displacement to model fault surfaces. The use of triangulated surfaces as the discontinuities, permits one to construct fault models with complex three-dimensional shapes and irregular tiplines with no overlaps or gaps, which better honor fault surface traces as well as subsurface constraints such as*

*relocated aftershocks or refletcion/refraction seismic data. We have used the method to invert for coseismic slip associated with several earthquakes, employing a variety of observational data including: (i) GPS data, (ii) InSAR measurements of coseismic displacements, and (iii) relocated aftershocks. We show that the method yields similar results to previous inversions, but improves the fit to data in areas of complex fault geometry.*

17. **Resor, P. G., Maerten, F., Pollard, D. D., 2003, Inverting for heterogeneous slip on three-dimensional fault systems: a first step toward understanding fault mechanics: Geological Society of America Abstracts with Programs, v. 35(6), p. 112**

**Abstract**

*Many studies of earthquake triggering and fault interaction have relied on highly-idealized fault geometries and slip distributions. Geological and geophysical observations, however, reveal that faults typically are not single planar surfaces with uniform slip bounded by rectangular tiplines, but are composed of multiple curved surfaces with curved tiplines and heterogeneous slip distributions. The segments typically are organized into echelon, conjugate, and intersecting patterns. The discontinuities, bends, intersections, and slip heterogeneities generate stress concentrations that may promote or inhibit slip on nearby faults and thus play an important role in the mechanics of fault systems. It is therefore important to incorporate both realistic fault geometry and slip distributions when evaluating models of fault mechanics.*

*We have developed a new three-dimensional slip-inversion method based on the analytical solution for an angular dislocation in a linear-elastic, homogeneous, isotropic, half-space. The approach uses the boundary element code Poly3D that employs a set of planar triangular elements of constant displacement discontinuity to model fault surfaces. The use of triangulated surfaces as discontinuities permits construction of fault models that better approximate curved three-dimensional surfaces with no overlaps or gaps, bounded by curved tiplines. Slip inversion on three-dimensional surfaces therefore allows investigations of fault models that incorporate more realistic geometry and heterogeneous slip.*

*We have applied the method to invert for coseismic slip associated with the 1999 Hector Mine and 1995 Kozani-Grevena earthquakes, using InSAR and GPS observations of surface displacements. Three dimensional fault models were constructed by integrating available data sets including mapped surface ruptures, relocated aftershocks, and previous inversions for subsurface geometry. The resulting models improve the fit to the near-field geodetic data and more faithfully honor observations*

*of fault rupture geometry. Models such as these form the starting point for more complete evaluations of fault mechanics and failure criteria.*

18. **Maerten, F., Maerten, L., Resor, P. G., 2002, Slip Inversion on Complex Fault Surfaces Using Angular Elastic Dislocations: American Geophysical Union Fall Meeting, Eos Transaction, v. 83(47), p. F361**
**Abstract**
*We present a new 3D slip-inversion method based on the analytical solution of an angular dislocation in a linear-elastic, homogeneous, isotropic, whole- or half-space. The approach uses a boundary element method (BEM) that employs planar triangular elements of constant displacement to model fault surfaces. Discretization of surfaces into triangular boundary elements allows the construction of complex 3D fault surfaces with irregular tipline and no overlaps or gaps. A damped least squares method is used to minimize the functional —C.b-d— + E—Z.b—, where b represents the slip distribution on the faults, C the influence coefficient matrix and d the observed deformation data. Z is a discrete Laplacian operator for triangulated 2- manifolds, which serves as the measure of the roughness of the slip distribution, and E represents the smoothing parameter. We have tested the method on synthetic forward elastic models using complex 3D fault geometry. Only one component of the computed displacement field (Ux, Uy, or Uz) was needed to constrain the inversion. Slip inversion results were used to refine initially simple models, developing more complex models that approached the fault geometry of the original forward model. We have also used the method to invert for fault slip on several natural examples employing a variety of observational data including: (i) field measurements of deformed stratigraphic layers, (ii) GPS and (iii) inSAR measurements of coseismic displacements.*

19. **Maerten, L., Maerten, F., 2002, New Numerical Tool for Inverse and Forward Modeling of Complex Geological Structures: Application to the Analysis of a Sandbox Experiment: Geological Society of America Abstracts with Programs**
**Abstract**
*We present a new geomechanical computer tool based on the finite element technique, which simulates the behavior of complex geological structures such as folded and faulted rock. The model undergoes infinitesimal or finite linear elastic deformation and is composed of a heterogeneous, anisotropic medium. Inelastic deformation is accommodated by discontinuities (faults and fractures). Applications of this new tool include the forward analysis of tectonic folding and faulting in sedimentary basins and mechanically-based 2D and 3D structural restoration.*

*To demonstrate the capability of the new tool we analyzed fault development in the hanging wall of a syn-sedimentary listric normal fault. Because the complete deformation history is known, an example was taken from one of the sandbox experiments carried out by McClay (1990). A model of the final deformed stage of this analogue model was created and restored sequentially by removing the upper sedimentary layers one by one. The top of the next upper sedimentary layer was constrained to be horizontal while the base of the model was constrained to follow the shape of the listric basal fault. The faults were constrained to stay in contact and for simplicity to have zero friction. The elastic properties were homogeneous throughout the model. For each step the faults were free to accommodate any slip until the model equilibrated (F=0) and the elastic deformations were minimized. We mapped the picture of the final stage of the sandbox experiment onto the numerical model grid in order to follow the deformation of the layers during each step of the restoration. The model also was analyzed in a forward sense in order to sequentially investigate the development of the faults in the hanging wall of the basal listric fault. The chronology of the numerical fault development is compared to the chronology inferred from the analysis of sedimentation thickness variations and both fault geometry and slip distribution are described.*

*The numerical model corresponds well to the physical model and provides additional insights about the physics of the process and quantitative values of physical parameters. We conclude that this tool has significant potential for analyzing physical models and natural examples of complex geological structures.*

20. **Muller, J. R., Aydin, A., Maerten, F., 2002, Rupture Progression Along Discontinuous Oblique Fault Sets: Implications for the Karadere Rupture Segment of the 1999 Izmit Earthquake, and a Future Rupture in the Marmara Sea: 1st International Symposium of the Faculty of Mines (ITU) on Earth Sciences and Engineering, Istanbul, Turkey**
**Abstract**
*Understanding the mechanical interaction of obliquely intersecting fault segments is imperative for assessing the seismic hazard along the North Anatolian fault and within the Marmara Sea. The 1999 Mw=7.4 Izmit, Turkey earthquake offers an opportunity to study how coseismic rupture can transfer across two fault sets with an oblique intersection angle of at least 20 to produce a surface rupture of 150 km. The so-called double-bend transition between the Arifiye-Karadere-Glyaka segments provides an interesting example of fault interaction in that the Karadere fault extends further to the southwest and northeast than the limits of coseismic surface rupture. We test the both the effects of the double-bend fault geometry as well as*

*the mechanical interaction with neighboring discontinuous fault segments on confining slip to a reduced region of the Karadere fault and allowing the double-bend rupture to occur. We use boundary element modeling to characterize the fault geometry and stress boundary conditions most favorable for rupture on oblique fault sets. Our investigation involves first analysis of the effects of regional stress direction on rupture of oblique faults as well as the effects of rupture on one fault on triggering slip on a vertical and dipping oblique segments. We then characterize the Karadere segment rupture transition in light of these results in addition to testing the effects of changing dip along the length of the Karadere fault as its northern portion forms the southwestern margin of the Dzce basin and its southern portion forms the southeastern margin of the Sakarya basin.*

*Finally, we comment on the implications of our results on a future rupture in the Marmara Sea and how fault interaction may increase or decrease the tendency of such a rupture in utilizing the intersecting oblique fault sets there.*

21. **Pollard, D. D., Maerten, F., Maerten, L., Resor, P. G., Allward-Fiore, P., 2002, Forward 3D Modeling of Complex Fault Systems Using an Elastic Boundary Element Method: Geological Society of America Abstracts with Programs**

    **Abstract**

    *Poly3D, a fast 3D boundary element numerical code and Poly3DGUI a graphical user interface, facilitate the forward modeling of multiple mechanically interacting faults with complex 3D tiplines and irregular surface geometries, limited only by data precision and computing power and memory. Poly3D is based on the analytical solution for an angular dislocation in a half space composed of a homogeneous and isotropic linear-elastic material (Comninou & Dunders, 1975). Six angular dislocations are superimposed to define triangular dislocation elements that are combined to model complex 3D fault shapes without gaps or overlaps. Boundary conditions on these elements are either a uniform displacement discontinuity or the traction vector at the element center. Tectonic deformation can be simulated using remote strain boundary conditions. The GUI runs under the Windows operating system on a PC using OpenGL and Open Inventor technologies. The power of the C++ language combined with fast PC graphics cards and gigahertz CPUs enable real-time 3D simulations of the faulting process and stunning visualizations of deformed horizons, slip distributions, and displacement vector and stress tensor fields.*

    *Forward modeling results from three recent studies use a variety of geologic and geophysical data sets to constrain fault geometries and tectonic histories. 1) GPS data*

*on faults and deformed limestone beds within the Carmel formation are used to investigate fault slip distributions and fault interaction for four sets of intersecting normal faults at Chimney Rock, Utah. 2) GPS measurements and a high resolution DEM are used to analyze the 3D geometry of deformed sandstone beds within the upper Esplanade formation in both the hanging and foot wall of a crustal-scale normal fault in the western Grand Canyon, Arizona. 3) Digital orthoquad photographs, digital topographic maps, and GPS field data on sandstone beds of the Frontier formation within the Emigrant Gap anticline, Wyoming, are used to investigate the relationship between fold shape and the underlying thrust fault geometry and slip distribution. In each study the geometric flexibility of Poly3D and the visualization capabilities of Poly3DGUI have led to new insights into the processes of faulting, fault interaction, and fault-related folding.*

22. **Pollard, D. D., Maerten, F., Resor, P. G., 2002, Using Aftershock Relocations and 3D Mechanical Models to Understand the Integrated Behavior of Normal, Antithetic, and Strike-Slip Faults During Crustal Extension: USGS presentation**
**Abstract**

23. **De Joussineau, G., Maerten, F., Maerten, L., Bouissou, S., Barquins, M., 2001, Modeling Faults as Frictional Surfaces : Effect of Fault Surface Morphology on Sliding Regime and Slip Distribution: Workshop "Fault Zone Characterization for Tectonic Numerical Modelling", Frankfurt, Germany**
**Abstract**
*Slip is often irregularly distributed along faults after seismic events even if theoretical models predict symmetric and smooth profiles. Among the various mechanical heterogeneities that can explain such irregular slip distribution, those in fault surface morphology are very likely agents. However, because it is difficult to investigate fault surface morphology at depth, the relation between surface morphology and slip distribution heterogeneities has been poorly studied.*

*In order to give some phenomenological ideas on this relationship, a new type of experiments was developed consisting in analyzing slip distribution along fault models of known morphology. Both analogue and a numerical modeling were carried out to characterize the role of sliding surface morphology in sliding regime and slip distribution along faults. The analogue experiments consisted in uniaxial compression tests at constant loading rate on PMMA (polymethylmethacrylate) plates (16x10x0.6 cm3)*

*containing finite oblique defects (4 cm-long) representing faults. Two types of fault models were used: fault models with ground surfaces (FMGS), where asperities worn by the surfaces are geometrically similar and regularly spaced, and fault models with natural fracture surfaces (FMNS), where surfaces exhibit fractographic structures and hence irregular asperities; this morphology was obtained by propagating natural mode I cracks in the plates. During the experiments, slip distribution profiles were constructed by measuring the relative displacement of markers perpendicular to the sliding surfaces for different stages of shortening in the sample.*

*Results show that fault morphology determines both the sliding regime and the types of slip distribution along these sliding surfaces. In the analogue experiments, along FMGS, stable sliding giving a symmetric smooth distribution was observed. Conversely, for FMNS, stickslip was observed, and the slip distribution exhibited significant irregularities in a globally symmetric profile (see Fig.1). These slip heterogeneities ranged from 0.01 L (for the smallest ones) to 0.1 L (for the largest ones), L being the fault model length. This can be compared with slip heterogeneities exhibited by the Superstition Hills Sequence (California) after the 1987 event, which range from 0.02 L to 0.1 L, L being the fault length. The analysis of such slip heterogeneities evidences four types of local slip behavior, which seem to be present on slip profiles along active faults. These types are interpreted in terms of interplay between local asperities of various size and spatial distribution.*

*The numerical models come in complement to the analogue experiments and are used here to understand, at a smaller scale, the effects of a known fault surface morphology on the sliding regime, the slip profile, and the stress distribution through time. The models were done with DYNEL, an 2D explicit finite element code, where the process of solving a global stiffness matrix is replaced by a multi-agent system algorithm, which allows forces to be transmitted from node to node through the entire system until equilibrium is obtained. The flexibility of the method permits to simulate the behavior of complex geometrical structures using a model that undergoes infinitesimal linear elastic deformation in a heterogeneous, anisotropic and discontinuous medium, where discontinuities and contacts are well handled. The model configuration consisted on sliding a rectangular object along a fixed one, so that one edge of each object stays in contact with one edge of the other object. Different models were realized to simulate contrasted contact surface geometries, ranging from an idealized sinusoidal surface morphology to more irregular and more realistic surfaces. For each model, we calculated the relative displacement between the two sliding surfaces for different stages. We also computed the absolute motion through time of several points along the irregular interfaces as well as the stresses in order to*

*characterize the interactions between asperities during displacement. Results clearly show that the geometry of the asperities in contact during sliding controls the small-scale slip distribution variations (see Fig.2). Mechanical contacts and interactions are associated with a stress perturbation as well as a reduction of slip compared to the slip that would occur along perfectly smoothed surface. The models also show that the contacts of the asperities control the sliding regime as observed in the analogue experiments.*

*In spite of the non scaled conditions of the experiments and the marked differences between experimental and natural faults, these experiments may help to interpret the discrepancy observed between theoretical slip distribution profiles and the displacement measured along active faults. They also evidence the role played by surface morphology in sliding regime and slip distribution along faults.*

24. **Maerten, L., Maerten, F., Muller, J. R., Pollard, D. D., 2001, Modeling three-dimensional (3D) complex fault geometries using elastic boundary element code: Workshop "Fault Zone Characterization for Tectonic Numerical Modelling", Frankfurt, Germany**

**Abstract**

*For geomechanical studies, a first order approximation is to treat a faulted rock mass as a homogeneous isotropic linear elastic material cut by discontinuities. Even though this approximation ignores sedimentological heterogeneities and the inelastic part of the rock deformation, it captures the first-order relationship among fault geometry, slip distributions, and structure contours by accurately representing the 3D geometry of the mapped faults. Recent advances in geologic mapping, aftershock location, and reflection seismology allow geoscientists to image surface and subsurface structures with greater precision. These images demonstrate that earthquake ruptures typically occur along faults or fault systems that display complex 3D geometries.*

*A good candidate for such studies is the three-dimensional boundary element method (BEM) based on the displacement discontinuity and the governing equations of linear elasticity theory. The advantage of the BEM, as opposed to the Finite Element Method (FEM) is that only the "boundary" surfaces themselves are discretized by polygonal elements, while the surrounding material need not be modeled explicitly. Poly3D, a 3D boundary element code and user interface developed at Stanford University, enables the integration of these varied data sets to constrain fault geometry and accurately models the complex geometries, limited only by data precision and*

*computing power. Poly3D is based on the analytical solution for the elastic boundary value problem of an angular dislocation in a half space composed of a homogeneous and isotropic linear-elastic material (Comninou & Dunders, 1975). One of the major advantages that such 3D BEM has over other commonly-used dislocation models (e.g. based on Okada, 1985) is the use of a triangular rather than rectangular uniform dislocation patch. The triangular shape enables one to model complex 3D surfaces without gaps or overlaps (see Fig.1). A further advantage is the possibility of using remote strain boundary conditions to simulate tectonic deformation and/or traction boundary conditions to simulate stress drop on fault segments, which allow for the effect of mechanical interaction between the faults.*

*Poly3D has been applied to numerous fault related problems over the last 5 years. We present results from three recent studies that have focused on fault interaction, fault related deformation and earthquake triggering using a variety of geologic and geophysical data sets to constrain fault geometries and deformation. 1) GPS field mapping of faults and deformed strata is used to investigate fault slip and fault interaction around a set of normal faults at Chimney Rock, Utah (see Fig.2). 2) Large-scale geologic mapping and measured slip distributions are integrated with published geophysical data to study the interaction between the 1967 Mudurnu Valley and 1999 Kocaeli earthquakes in Turkey (see Fig.3). 3) Industrial 3D seismic refection data is used for modeling the subseismic deformations in the inter-well regions of an oil reservoir (see Fig.4). In each of these studies the geometric flexibility of Poly3D and the ability to integrate available data sets has led to new insights into the processes of faulting, fault interaction, and earthquake triggering.*

25. **Maerten, F., Maerten, L., 2001, Unfolding and Restoring Complex Geological Structures Using Linear Elasticity Theory: American Geophysical Union Fall Meeting, Eos Transaction, v. 82(47), p. F1150**

**Abstract**

*We present a new method to unfold and restore geological structures in 2D and 3D using elasticity theory. A primary motivation for such restoration is to check the consistency of the geological interpretations. Also, measures of the deformation between the restored state and the deformed state give quantitative estimates of strain that can be compared with observed strain markers. Different geometrical and kinematic methods have been proposed in the past 30 years to restore geological structures. Most restorations have been performed in 2D, either in cross section or in map view, based primarily on area conservation. The methods include (1) unfolding in cross section by flexural slip or by vertical or inclined shear; and (2) unfaulting in map*

*view by rigid block translation and rotation of fault blocks. Geometrical and analytical unfolding methods for 3D surfaces have been proposed, based on flexural slip and homogeneous inclined shear.*

*In this new method, structures are unfolded onto a datum defined by the user. The datum can assume any shape. One advantage of using elasticity for the unfolding process is that the solution is unique. The second advantage is that the surface is treated as continuous and deformable, as opposed to other methods where the surface needs to be subdivided into rigid elements. The last and most important advantage is that the method does not use the commonly assumed geometrical assumptions that are (i) conservation of area, (ii) minimization of the changes in segment length (or minimization of the shearing) and (iii) minimization of the deformation energy. Instead, this method honors the fundamental physical laws that govern deformation, that are (i) conservation of mass, (ii) conservation of momentum and (iii) conservation of energy. Therefore, physical laws and linear elastic theory replace geometrical assumptions used by the existing methods for the restoration of geological structures. Examples illustrate how unfolding can be accomplished for 2D cross-sections, 3D surfaces and 3D volumes. Heterogeneous material properties as well as varying boundary conditions yield different but unique solutions even if the model is otherwise identical. One can compute stresses and strains within the deformed surface and these can be related to smaller scale fractures and faults, which might have a large economic impact.*

26. **Pollard, D. D., Maerten, F., Maerten, L., Resor, P. G., Muller, J. R., Aydin, A., 2001, Improved 3D Modeling of Complex Fault Geometries Using Poly3D, an Elastic Boundary Element Code: American Geophysical Union Fall Meeting, Eos Transaction, v. 82(47), p. F835**
**Abstract**
*Recent advances in geologic mapping, aftershock location, and reflection seismology allow geoscientists to image surface and subsurface structures with greater precision. These images demonstrate that earthquake ruptures typically occur along faults or fault systems that display complex 3D geometries. Poly3D, a 3D boundary element code and user interface, enables the integration of these varied data sets to constrain fault geometry and accurately models the complex geometries, limited only by data precision and computing power. Poly3D is based on the analytical solution for the elastic boundary value problem of an angular dislocation in a half space composed of a homogeneous and isotropic linear-elastic material (Comninou & Dunders, 1975). One of the major advantages that Poly3D has over other commonly used dislocation models (e.g. based on Okada, 1985) is the use of a triangular rather than rectangular*

*uniform dislocation patch. The triangular shape enables one to model complex 3D shapes without gaps or overlaps. A further advantage of Poly3D is the possibility of using remote strain boundary conditions to simulate tectonic deformation and traction boundary conditions to simulate stress drop on fault segments. Poly3D has been applied to numerous problems of fault interaction and earthquake deformation over the last 5 years. We present results from three recent studies that have focused on fault interaction and earthquake triggering using a variety of geologic and geophysical data sets to constrain fault geometries and deformation. 1) GPS field mapping of faults and deformed strata is used to investigate fault slip and fault interaction around a set of normal faults at Chimney Rock, Utah. 2) Large-scale geologic mapping and measured slip distributions are integrated with published geophysical data to study the interaction between the 1967 Mudurnu Valley and 1999 Kocaeli earthquakes in Turkey. 3) Aftershock triggering and the development of normal fault systems are investigated by integrating high-precision aftershock locations and published geological and geodetic data sets from the 1995 Kozani- Grevena earthquake in Greece. In each of these studies the geometric flexibility of Poly3D and the ability to integrate available data sets has led to new insights into the processes of faulting, fault interaction, and earthquake triggering.*

27. **Maerten, L., Maerten, F., Gillespie, P., 2000, Poly3D: a 3D Geomechanical Program Used to Solve Fault Related Problems in Petroleum Reservoirs: NPF Meeting, Stavanger, Norway.**

**Abstract**

*Spatial continuity and linkage of faults may substantially affect fluid flow either by compartmentalizing the reservoir, or by increasing the tortuosity of flow pathways, according to whether the faults act as seals or conduits. Therefore, understanding fault linkage geometry and predicting subseismic faults should improve reservoir flow simulation models and, in turn, significantly improve well planning.*

*Methods have been developed to infer, in three dimensions, the fault tip-line geometry below the seismic resolution and potential fault linkage as well as subseismic faults in reservoirs, using 3D seismic data and Poly3D, a boundary element elastic model.*

*The purpose of the demo is to show how Poly3D can be used to treat these problems. Two examples from the North Sea oil field, illustrate how such geomechanical analyses can predict fault connectivity, reservoir compartmentalization and subseismic fault prediction. In the first, a 3D numerical model of the faulted reservoir and its surroundings is constructed using seismic interpretation. Such a model, combined with an appropriate set of boundary conditions is used to compute the fault slip distribution as well as the vertical displacement field. By comparing the interpreted*

*fault slip distribution to the computed slip distribution adjacent to potential intersection lines, the geomechanical models can constrain the geometry of the faults as well as the location of the intersection line between faults.*

*The second example describes a method for predicting the positions and orientations of subsesimic faults in the rock volume. The large seismic faults and their associated observed slip distributions are brought into Poly3D in order to determine what the stress conditions were around the seismic faults at the time of faulting. The computed stress field is then combined with the Coulomb failure criterion in order to predict the orientations and densities of the smaller faults; this information is represented as a pair of grids (e.g. density and strike grid). The grids can then be used to condition 3D stochastic model of faulting which uses a power-law distribution to simulate the sizes of the subseismic faults.*

28. **Muller, J. R., Aydin, A., Maerten, F., 2000, Mechanical interaction between the July 1967 Mudurnu Valley and August 1999 Izmit earthquakes using detailed fault mapping and 3-D BEM modeling: American Geophysical Union Fall Meeting, Eos Transaction, v. 81(48)**
**Abstract**
*The last major rupture prior to the Izmit and Duzce earthquakes in 1999 was the Ms = 7.1 July 22 1967 Mudurnu Valley earthquake to the southeast. The mechanical interaction between the 80 km long 1967 rupture and the next potential rupture (the 130 km long 1999 Izmit rupture) was modeled by earlier workers. These models, however, didn't identify and address several interesting problems related to this interaction due primarily to the lack of detailed fault configurations and couldn't have the knowledge of recent events available today. The geometric relationship between the two rupture traces poses two interesting problems. First, why did slip not continue to extend along the western continuation of the fault that ruptured in 1967? In its easternmost portion, the 80 km Mudurnu Valley surface rupture overlapped 25 km of a fault segment that ruptured in 1957 (Ambraseys and Zatopek, 1969). To the west, the generally continuous rupture terminated near Kanlicay with additional minor slip segments located to as far north and west as Lake Sapanca. Past the western termination of the 1967 rupture, the geomorphological and structural suggests that the Mudurnu Valley fault extends further to the west along the mountain front that marks the boundary between basement and cover which reaches the Bay of Izmit near Golcuk. We suggest that the change in orientation of the Mudurnu Valley fault near Karapucek reduces the tendency for continued westward propagation of slip along that fault. Boundary element modeling shows that the tendency for right-lateral slip is instead favored along the Izmit earthquake fault segments within the broad valley*

*to the north. Second, if the 1967 earthquake enhanced the failure along the Izmit earthquake fault, why did the Izmit earthquake epicenter appear to be on the Gulcuk segment to the west instead of segments closer the termination of the 1967 rupture? We calculate changes in Coulomb stress on the five major Izmit fault segments due to interpolated slip during the Mudurnu Valley earthquake. The greatest increases in the tendency for right-lateral slip on the Izmit fault segments occurs in a region near the town of Arifiye, approximately 50 km east of Golcuk. This region of right-lateral Coulomb stress increase corresponds with a local maximum of surface slip (4.3 m). This suggests that if the Mudurnu Valley earthquake were to trigger failure on the Izmit fault, the area near Arifiye would be a likely epicentral region. These results match well with the seismic inversion analysis of Cemen, et al. (2000) which suggests two subevents of moment release during the Izmit earthquake, the first and larger of which is located near Arifiye, the second and smaller near Golcuk.*

# APPENDIX D

## Résumé étendu

Les théories physiques utilisent toujours une simplification des lois de la nature, simplement parce que modéliser des structures complexes, telle la Terre à une large échelle en utilisant un modèle atomistique à l'échelle moléculaire, est irréaliste. Les chercheurs tendent donc à capturer les propriétés importantes des objets à modéliser, et les utilisent dans un concept théorique, analytique et numérique, le but étant d'expliquer et de prédire les phénomènes naturels.

Nous pouvons distinguer deux types de modèles physiques qui sont les fondements de toutes les théories physiques pour modéliser le comportement des matériaux: (1) le modèle microscopique discret, et (2) le modèle macroscopique continu. A l'échelle microscopique, les particules bougent en fonction de l'influence des forces d'interactions mutuelles et sont régies par la mécanique quantique. A une échelle beaucoup plus grande, les objets sont régis par des théories continues (mécanique des solides, des fluides, élasticité, thermodynamique, électromagnétisme, acoustique, etc...). Ces théories tentent de décrire le comportement d'objets tels que nous les percevons dans notre monde espace-temps à quatre dimensions. Matière et énergie sont considerées comme continues et donc la représentation mathématique des quantités physiques s'opère grâce à l'utilisation de fonctions continues (ou continues par morceaux) de l'espace et du temps.

Ces problèmes peuvent êtres résolus par des manipulations mathématiques (modèles analytiques), mais ces outils se limitent souvent à des sur-simplifications des modèles. Par conséquent, diverses techniques de discrétisation ont été proposées et développées, donnant lieu à des modèles numériques et utilisant des approximations proches des solutions analytiques lorsque le nombre de variables discrètes augmente. Le but de ces méthodes est de résoudre des équations aux dérivées partielles (PDE). Les méthodes les plus connues sont les Différences Finis (FDM), les Eléments Finis (FEM) et les Eléments Frontières (BEM).
La méthode FDM est la méthode de traitement classique des PDE. Elle remplace la solution continue par une grille de points. En chaque point, tous les opérateurs différentiels sont remplacés par des opérations de différence finies, donnant lieu à un groupe d'équations qui peut être facilement résolu.
Dans la méthode FEM, le domaine de solution est discrétisé en un nombre uniforme et non-uniforme d'éléments finis qui sont connectés par l'intermédiaire de nœuds. Le changement des variables dépendantes, au regard de la position, est approximé dans chaque élément en utilisant des fonctions de forme.
La méthode BEM utilise le fait que les équations sous forme différentielle peuvent souvent être transformées sous forme intégrale. Elle transforme donc l'opérateur différentiel défini dans le domaine, en opérateur integral défini sur le bord du domaine. Donc, dans cette

méthode, seule les frontières des domaines d'intérêt ont besoin d'être discrétisées.
Les méthodes FEM et FDM peuvent être considérées comme similaires dans le sens où tout le domaine de solution doit être discrétisé, et qu'un maillage est nécessaire (structuré ou non). Pour la méthode BEM, seules les surfaces des bords (en 3D) sont utilisées.

Le but de cette thèse est l'étude de la mécanique des milieux continus appliquée à la compréhension des phénomènes géologiques, en utilisant des modélisations basées sur les équations aux dérivées partielles avec conditions aux limites. Plus précisément, nous nous intéressons aux phénomènes 'quasi-statiques' dans la croute superficielle de la terre (par exemple les évenements co-sismiques), en utilisant l'élasticité linéaire, qui a prouvée être trés fiable en première approximation pour la plupart des structures étudiées pour la compréhension des tremblements de terre et volcans, ou pour étudier l'état du champ de contrainte perturbé autour de régions complexes et faillées.

Trois types de codes numériques sont développés au travers de cette thèse sous forme de trois grandes parties: (I) les modèles directs, (II) les modèles inverses, et (III) les modèles de restauration.

La première partie est dediée à la modélisation directe en utilisant un code elasto-statique d'éléments frontières (BEM), appelé iBem3D (le successeur de Poly3D originalement développé a l'université de Stanford). Ce type de modélisation permet d'étudier la réponse faite par des failles soumises à un champ de contraintes regional, étant donné la géométrie des failles et des conditions aux limites sur celles-ci. Les résulats de telles simulations peuvent être utilisés, par exemple, pour prédire la fracturation due à la déformation associée aux glissements des failles, ou pour étudier la réactivation de failles lors d'un processus d'étude de tremblements de terre.
Le premier chapitre présente les fondements de cette thèse. Nous montrons qu'en utilisant une formulation analytique du calcul du champ de déplacement induit par une dislocation angulaire dans un milieu infini ou semi-infini, homogène, élastique et isotrope, il est possible de construire des surfaces triangulées complexes en 3D avec des déplacements discontinus. Une telle formulation permet d'avoir des surfaces de discontinuités de forme et de bord complexes, s'opposant au modèle d'Okada, actuellement considéré comme la méthode standard en géophysique, et où les éléments ont une forme rectangulaire induisant des recouvrements et trous dans le maillage. Les applications d'un tel code sont vastes dans le domaine de la géologie structurale et de la géophysique. Nous présentons quelques applications clefs qui sont publiées depuis quelques années par une large communauté scientifique de part le monde.
Le deuxième chapitre propose une méthode itérative pour la résolution du système d'équations d'iBem3D à $n$ degrés de libertés. Cette technique permet de reduire la complexité du

modèle de $O(n^3)$ à $O(k.n^2)$, où $k$ représente le nombre d'itérations nécessaires. De plus, cette méthode permet d'incorporer les contraintes inégalitaires en force (par exemple, la contrainte de friction Coulombienne) et en déplacement (par example, la non-interpénétration des éléments lorsque soumis à une contrainte compressive). Cette méthode permet aussi une paralélisation simplifiée sur des architectures multi-coeurs.
Le chapitre trois présente une application des contraintes inégalitaires pour l'étude des fractures branchées dans des zones de relais extensifs formés de stylolites ou de joints en échelon. La localisation géographique choisie est celle des "Matelles", située près de Montpellier. Il est montré que l'orientation des dominos dans ces zones de relais est fonction de la friction au niveau des fractures en échelon.
Le chapitre quatre montre que l'implémentation d'origine du code iBem3D, qui était fait pour des milieux élastiques homogènes et isotropes, peut être étendue à des milieux hétérogènes, ceci en utilisant des conditions aux limites particulières au niveau des interfaces entre deux régions à contraste rhéologique différent. Ces interfaces sont discrétisées en surfaces triangulées pouvant avoir des géométries complexes.
Le chapitre cinq est dédié à l'optimisation du code iBem3D. En effet, même si l'utilisation d'un processus itératif décroit la complexité du modèle à $O(k.n^2)$, il reste tout de même un problème majeur pour l'étude de gros modèles faits de centaines de milliers d'éléments triangulaires, la mémoire nécessaire étant du même ordre que la résolution du système, c'est-à-dire en $O(n^2)$. De plus, le post-traitement au niveau des grilles d'observation peut pénaliser l'utilisateur, plus particulièrement si le nombre de points d'observation est grand. Ce chapitre présente l'optimisation de calculs par l'utilisation d'approximations et de la parallélisation sur architecture multi-coeurs, pour la résolution du système d'équations ainsi que pour le post-traitement. Il est montré que la compléxité d'un modèle passe de $O(k.n^2)$ à $\sim O(k.n)$ pour le temps d'exécution, et de $O(n^2)$ à $\sim O(n)$ pour la mémoire. De même, le post-traitement au niveau des points d'observation est reduit considérablement et est fonction de la position de la grille par rapport aux surfaces de discontinuités (c'est à dire les failles).

La deuxième partie de la thèse étudie la modélisation inverse, encore appelée estimation de paramètres, en s'appuyant sur le même code déléments frontières. Ce type de modélisation est donc une estimation de paramètres de ce qui est générallement imposé ou calculé en modélisation directe (par exemple, le tenseur des contraintes en des points de l'espace 3D, le déplacement mesuré le long des failles, etc...). Etant donné des déformations mesurées à la surface de la terre ou en profondeur dues à des glissements de failles, le but est de retrouver les déplacements associés le long de ces failles qui ont induit de telles déformations, ou de retrouver le ou les évènements tectoniques qui ont activé les failles, qui à leur tour, ont déformé la surface de la terre.

Le chapitre six présente un modèle d'inversion de déplacement sur les failles étant donné des données GPS et/ou InSAR, et expose les avantages d'une telle formulation basée sur iBem3D et utilisant des géometries complexes. Plus précisement, il est montré qu'une telle approche, basée sur des éléments triangulaires, est beaucoup plus précise que celle se basant sur des éléments rectangulaires (Okada). Ce code est appliqué au tremblement de terre Hector Mine (1999), CA, et donne des résultats beaucoup plus précis qu'avec la formulation Okada. Parallèlement, nous montrons indirectement que même pour un tremblement de terre de grande magnitude comme celui-ci (M7.1), la plupart des déformations sont élastiques.
Le chapitre sept présente une application de ce code d'inversion des déplacements pour le tremblement de terre de Nias qui se produisit en 2005 en Indonésie. Cette étude met en évidence que ce tremblement de terre n'a certainement pas atteint la topographie de surface, ce qui a des implications pour la génération de tsunamis.
Le chapitre huit présente une méthode geomécanique pour retrouver la paleo-contrainte régionale qui a induit des déplacements observés le long des surfaces de faille (à partir d'interprétations d'images sismiques). Cette technique, bien que limitée à un seul évenement tectonique et pour un seul type de mesure, peut donner une bonne estimation de ce que furent l'orientation et les magnitudes du tenseur des contraintes, estimation qui utilise les interactions mécaniques entre failles. Lors de l'inversion du champ de contrainte, les déplacements inconnus sur les surfaces de failles sont simultanément retrouvés (par exemple, les déplacements décrochants).
Le chapitre neuf présente une autre façon de faire de l'estimation de paleo-contraintes en utilisant le principe de superposition qui s'applique à l'élasticité linéaire. Cette nouvelle méthode peut prendre en compte divers types de données telles que l'orientation de fractures, de stylolites, de failles secondaires qui se sont formées proche des failles actives, mais aussi des données GPS, InSAR ou de déplacements sur les failles avec ou sans information de striation. Il est montré que plusieurs évènements tectoniques peuvent être retrouvés et que les données sont automatiquement classées dans leur évènement respectif. De plus, une telle méthode permet de calculer de façon interactive les déplacements sur les failles ainsi que les champs de déplacement et de contrainte pertubés associés lorsque l'utilisateur change les magnitudes et l'orientation du champ de contrainte regional appliqué au modèle.

La troisième partie de cette thèse est consacrée à la restauration de structures complexes et utilise la méthode des éléments finis (FEM).
Le chapitre dix est dédié à la validation d'interprétations en utilisant la technique de restauration. Faire de la modélisation directe, comme vu précédemment, a montré l'importance

de la géometrie des failles et fractures sur les résulats des calculs des déplacements discontinus sur les failles, et par voie de conséquence, sur les champs de déplacement et de contrainte associés. Pour la majorité des simulations numériques, il est primordial de valider de telles interprétations avant toute analyse des resulats de modèlisation directe. Ce chapitre présente donc un outil de vérification 'pré-simulation' basé sur la géomécanique.
Le chapitre onze, quant à lui, propose une méthode de lissage d'horizons sismiques faillés et plissés, basée sur la restauration de surfaces triangulées 3D. Il est montré qu'un tel filtre gomme les artefacts géométriques où, par exemple, une forte concentration de conraintes apparait après dépliage et défaillage. Les traces de failles sont lissées et les trop faibles ou forts gradients de déplacement sont réajustés en conséquence, produisant des terminaisons de failles réalistes.

Finalement, en annexe est présenté un projet de recherche sur une méthode numérique permettant de faire de l'inversion linéaire du déplacement sur les failles en utilisant diverses méthodes développées dans cette thèse: (1) utilisation d'un solveur itératif pour pouvoir utiliser les contraintes inégalitaires en déplacement; (2) la méthode d'optimisation par approximation afin de résoudre des problèmes beaucoup plus conséquents et plus rapidement.

# BIBLIOGRAPHY


Agnew, D., Owen, S., Shen, Z., Anderson, G., Svarc, J., Johnson, H., Austin, K., and Reilinger, R. (2002). Coseismic displacements from the hector mine, california, earthquake: results from survey-mode global positioning system measurements. *Bull. Seism. Soc. Am.*, 92:1355–1364.

Aki, K. and Richards, P. (2002). *Quantitative Seismology.* University Science Books, Sausalito, CA.

Akoglu, A. M., Cakir, Z., Meghraoui, M., Belabbes, S., El Alami, S. O., Ergintav, S., and Akyuz, H. S. (2006). The 1994-2004 al hoceima (morocco) earthquake sequence: Conjugate fault ruptures deduced from insar. *Earth and Planetary Science Letters*, 252:467–480.

Allward-Fiore, P. (2006). *3D characterization and mechanics of brittle deformation in thrust fault related folds.* PhD thesis, Stanford University, CA, USA.

Amadei, B. and Stephansson, O. (1997). *Rock stress and its measurement.* Chapman & Hall, London.

Anderson, A. (1942). *The Dynamics of Faulting and Dyke Formation with Application to Britain.* Oliver and Boyd, Edinburgh.

Anderson, E. (1905). The dynamics of faulting. *Edinburgh Geol. Soc.*, 8(3):387–402.

Anderson, T. (1995). *Fracture mechanics, Fundamentals and Applications.* CRC Press, London, U.K.

Andersson, J., Ahokas, H., Hudson, J., Koskinen, L., Luukkonen, A., Löfman, J., Keto, V., Pitkänen, P., Mattila, J., Ikonen, A., and Ylä-Mella, M. (2007). Olkiluoto site description, part1. Technical report, Posiva report 2007-3.

Angelier, J. (1984). Tectonic analysis of fault slip data sets. *J. Geophys. Res.*, 89:5835–5848.

Angelier, J. and Mechler, P. (1977). Sur une méthode graphique de recherche des contraintes principales également utiliable en tectonique et en séismologie: la méthode des dièdres driots. *Bulletin de la Societé Géologique de France*, 7:1309–1318.

Angelier, J., Tarantola, A., Valette, B., and Manoussis, S. (1982). Inversion of field data in fault tectonics to obtain the regional stress - i. single phase fault populations: a new method of computing the stress tensor. *J. Geophys. Res.*, 69:607–621.

Armijo, R., Carey, E., and Cisternas, A. (1982). The inverse problem in microtectonics and the separation of tectonic phases. *Tectonophysics*, 82(1-2):145–160.

Arthaud, F. and Séguret, M. (1981). Les structures pyrénéennes du languedoc et du golfe du lion (sud de la france). *Bulletin de la Société Géologique de France*, 23:51–63.

Aster, R., Borchers, B., and Thurber, C. (2005). *Parameter Estimation and Inverse Problems*. Elsevier Academic Press, Burlington, MA, USA.

Atkinson, B. (1987). *Fracture mechanics of rock*. Academic Press, London, U.K.

Auzias, V. (1995). *Photoelastic modeling of stress perturbations near faults and of the associated fracturing: petroleum industry application, II: Mechanism of 3D joint development in a natural reservoir analogue: the flat-lying Devonian Old Red Sandstone of Caithness (Scotland)*. PhD thesis, Université de Montpellier II, France.

Auzias, V., Rives, T., Rawnsley, K. D., and Petit, J. . (1997). Fracture orientation modeling in the vicinity of a horizontal well. *Bulletin Elf aquitaine Production*, F64018:381–397.

Aydin, A. and Kalafat, D. (2002). Surface ruptures of the 17 august and 12 november 1999 izmit and duzce earthquakes in northwestern anatolia, turkey: their tectonic and kinematic significance and the associated damage. *Bull. Seism. Soc. Am.*, 92:95–106.

Aydin, A. and Reches, Z. (1982). Number and orientation of fault sets in the field and in experiments. *Geology*, 10:107–112.

Bai, T., Maerten, L., Gross, M. R., and Aydin, A. (2002). Orthogonal cross joints: Do they imply a regional stress rotation? *Journal of Structural Geology*, 24:77–88.

Barnett, D. (1985). The displacement of a triangular dislocation loop. *Phil. Mag. A*, 51:383–387.

Barquins, M., Chaker, C., and Petit, J.-P. (1997). Influence du frottement sur le branchement de fissures  partir de dfauts obliques soumis  une compression uniaxiale. *Compte Rendu de L'Academie des Sciences*, T324:29–36.

Barquins, M. and Petit, J.-P. (1992). Kinetic instabilities during the propagation of a branch crack: e.ects of loading conditions and internal pressure. *Journal of Structural Geology*, 14:893–903.

Bathe, K. and Chaudary, A. (1985). A solution method for planar and axisymmetric contact problems. *Numer. Meth. Engng.*, 21:65–88.

Bazalgette, L. (2004). *Relations plissement/fracturation multi échelle dans les multicouches sédimentaires du domaine élastique/fragile: Accommodation discontinue de la courbure par la fracturation de petite échelle et par les articulations. Possibles implications dynamiques dans les écoulements des réservoirs.* PhD thesis, Université de Montpellier II, France.

Bebendorf, M. (2000). Approximation of boundary element matrices. *Numeri Math*, 86(4):565–589.

Bebendorf, M., editor (2008). *Hierarchical Matrices, a means to efficiently solve elliptic boundary value problems.* Springer, Berlin Heidelberg.

Bebendorf, M. and Rjasanow, S. (2003). Adaptive low-rank approximation of collocation matrices. *Computing*, 86(4):1–24.

Bellahsen, N., Allward-Fiore, P., and Pollard, D. D. (2006). From spatial variation of fracture patterns to fold kinematics: A geomechanical approach. *Geophysical Research Letters*, 33:L02301.

Bilek, S. L. and Lay, T. (1999). Rigidity variations with depth along interplate megathrust faults in subduction zones. *Nature*, 400:443–446.

Bilham, R. and King, G. (1989). The morphology of strike slip faults: examples from the san andreas fault, california. *J. Geophys. Res.*, 94:10204–10226.

Blenkinsop, T. (2006). Kinematic and dynamic fault slip analyses: implications from the surface rupture of the 1999 chi-chi, taiwan, earthquake. *J. Struct. Geol.*, 28(6):1040–1050.

Blenkinsop, T., Lisle, R., and Ferrill, D. (2006). Introduction to the special issue on new dynamics in palaeostress analysis. *J. Struct. Geol.*, 28(6):941–942.

Bos, A. G. and Spakman, W. (2003). The resolving power of coseismic surface displacement data for fault slip distribution at depth. *Geophys. Res. Lett.*, 30,2110.

Bott, M. (1959). The mechanics of oblique slip faulting. *Geological Mag.*, 96:109–117.

Bourne, S. J., , Rijkels, A., Stephenson, B. J., and Willemse, E. J. M. (2000). Predictive modeling of naturally fractured reservoirs using geomechanics and flow simulation. *GeoArabia*, 6(1):87–102.

Bourne, S. J. and Willemse, E. J. M. (2001). Elastic stress control on the pattern of tensile fracturing around a small fault network at nash point, uk. *Journal of Structural Geology*, 23:1753–1770.

Brace, W. and Kohlstedt, D. (1980). Limits on lithospheric stress imposed by laboratory experiments. *Journal of Geophysical Research*, 85:62486252.

Brankman, C. M. and Aydin, A. (2004). Uplift and contractional deformation along a segmented strike-slip fault system: the gargano promontory, southern italy. *Journal of Structural Geology*, 26:807–824.

Bro, R. and de Jong, S. (1997). A fast non-negativity-constrained least squares algorithm. *J. Chemom.*, 11:393–401.

Brudy, M., Zoback, M. D., Fuchs, K., Rummel, F., and Baumgartner, J. (1997). Estimate of the complete stress tensor to 8 km depth in the ktb scientific drill holes: Implications for crustal strength. *J. Geophys. Res.*, 102:18453–18475.

Brune, J. (1968). Seismic moment, seismicity, and rate of slip along major fault zones. *J. Geophys. Res.*, 73:777–784.

Brune, J., Henyey, T., , and Roy, R. (1969). Heat flow, stress, and rate of slip along the san andreas fault, california. *Journal of Geophysical Research*, 74:38213827.

Buczkowski, D. and Cooke, M. (2004). Compaction and shrinkage over buried impact craters: Implications for thickness and nature of cover material in utopia planitia, mars. *J. Geophys. Res.*, 109.

Bulnes, M. and McClay, K. (1999). Benefits and limitations of different 2d algorithms used in cross-section restoration of inverted extensional faults: application to physical experiments. *Tectonophysics*, 312:175–189.

Burgers, J. (1939). Internal strains in solids. *Proc. Acad. Science*, 42:293.

Burgmann, R., Ayhan, M., Fielding, E., Wright, T., McClusky, S., Aktug, B., Demir, C., Lenk, O., and Turkezer, A. (2002). Deformation during the 12 november 1999 duzce, turkey, earthquake, from gps and insar data. *Bull. Seism. Soc. Am.*, 92:161–171.

Bürgmann, R., Ergintav, S., Segall, P., Hearn, E., McClusky, S., Reilinger, R., Woith, H., and Zschau, J. (2002). Time-dependent distributed afterslip on and deep below the izmit earthquake rupture. *Bull. Seismol. Soc. Am.*, 92:126–137.

Burgmann, R. and Pollard, D. D. (1994). Slip distribution on faults: effects of stress gradients, inelastic deformation, heterogeneous host-rock stiffness, and fault interaction. *Journal of Structural Geology*, 16(12):1675–1690.

Burgmann, R., Schmidt, D. A., Nadeau, R. M., D'Alessio, M., Fielding, E. J., Lawrence, S., Manaker, D., McEvilly, T., and Murray, M. H. (2000). Earthquake potential along the northern hayward fault. *Science*, 289:1178–1182.

Byerlee, J. D. (1978). Friction of rocks. *Pure and Applied Geophysics*, 116:615626.

Cailleau, B., La Femina, P. C., and Dixon, T. H. (2007). Stress accumulation between volcanoes: an explanation for intra-arc earthquakes in nicaragua? *Geophysical Journal International*, 169:1132–1138.

Cakir, Z., Meghraoui, M., Akoglu, A. M., Jabour, N., Belabbes, S., and Ait-Brahim, L. (2006). Surface deformation associated with the mw 6.4, february 24, 2004 al hoceima (morocco) earthquake deduced from insar: Implication for the active tectonics along north africa. *Bulletin of Seismological Society of American*, 96:59–68.

Carena, S. and Suppe, J. (2002). Three-dimensional imaging of active structures using earthquake aftershocks: the northridge thrust, california. *J. Struct. Geol.*, 24:887–904.

Carey, E. and B., B. (1974). Analyse thé orique et numérique d'un modélé mecanique élémentaire appliqué à l'étude d'une population de failles. *C.r. Acad. Sci., Paris*, 279:891–894.

Carey-Gailhardis, E. and Mercier, J. (1987). A numerical method for determining the state of stress using focal mechanisms of earthquake populations: application to tibetan teleseisms and microseismicity of southern peru. *Earth Planet. Sci. Lett.*, 82:165–179.

Cartwright, J. A., Trudgill, B. D., and Mansfield, C. S. (1995). Fault growth by segment linkage: an explanation for scatter in maximum displacement and trace length data from the canyonlands grabens of se utah. *J. Struct. Geol.*, 17:1319–1326.

Centroid Moment Tensor (CMT) Catalog (2003). last accessed August 2003, www.seismology.harvard.edu/CMTsearch.html.

Cervelli, P., Murray, M., Segall, P., Aoki, Y., and Kato, T. (2001). Estimating source parameters from deformation data, with an application to the march 1997 earthquake swarm off the izu peninsula, japan. *J. Geophys. Res.*, 11:217–237.

Chaker, C. and Barquins, M. (1996). Sliding effect on branch crack. *Physics and Chemistry of the Earth*, 21:319–323.

Cheng, L.-W., Lee, J.-C., Hu, J. C., and Chen, H.-Y. (2009). Coseismic and postseismic slip distribution of the 2003 mw = 6.5 chengkung earthquake in eastern taiwan: Elastic modeling from inversion of gps data. *Tectonophysics*, 466:335–343.

Chiaraluce, L., Ellsworth, W., Chiarabba, C., and Cocco, M. (2003). Imaging the complexity of an active normal fault system: the 1997 colfiorito (central italy) case study. *J. Geophys. Res.*, 108:2294.

Childs, C., Easton, S. J., Vendeville, B. C., Jackson, M. P. A., Lin, S. T., Walsh, J. J., and Watterson, J. (1993). Kinematic analysis of faults in a physical model of growth faulting above a viscous salt analogue. *Tectonophysics*, 228:313–329.

Childs, C., Walsh, J. J., and Watterson, J. (1990). A method for estimation of the density of fault displacements below the limits of seismic resolution in reservoir formations. *North Sea oil and gas reservoirs: Liverpool, The Norwegian Institute of Technology*, 2:193–203.

Chinnery, M. (1961). The deformation of the ground around surface faults. *Bull. of Seism. Soc. of America*, 51:355–372.

Chinnery, M. (1963). The stress changes that accompany strike-slip faulting. *Bull. of Seism. Soc. of America*, 53:921–932.

Choi, P. (1996). *Reconstitutions des Paléocontraintes en Tectonique Cassante: Méthodes et Application aux Domaines Continentaux Déformés (Corée, Jura)*. PhD thesis, Université P. & M. Curie, Paris.

Cladouhos, T. and Allmendinger, R. (1993). Finite strain and rotation from fault-slip data. *J. Struct. Geol.*, 15(6):771–784.

Clark, S. P. (1966). *Handbook of physical constants (revised edition)*, volume 97. Geological Society of America Memoir.

Comninou, M. and Dundurs, J. (1975). The angular dislocation in a half space. *Journal of Elasticity*, 5(3):203–216.

Cooke, M. (1997). Fracture localization along faults with spatially varying friction. *J. Geophys. Res.*, 22:425–434.

Cooke, M. and Kameda, A. (2002). Mechanical fault interaction within the los angeles basin: A two-dimensional analysis using mechanical efficiency. *J. Geophys. Res.*, 107.

Cooke, M. and Murphy, S. (2004). Assessing the work budget and efficiency of fault systems using mechanical models. *J. Geophys. Res.*, 109.

Cooke, M. and Pollard, D. (1997). Bedding-plane slip in initial stages of fault-related folding. *J. Structural Geology*, 19:567–581.

Cooke, M. and Underwood, C. (2001). Fracture termination and step-over at bedding interfaces due to frctional slip and interface opening. *J. Structural Geology*, 23:223–238.

Coulomb, C. A. (1773). Sur une application des régles de maximis et minimis à quelques problèmes de statique relatifs à l'architecture. *Acad. Roy. des Sciences Memoires de math. et de physique par divers savans*, 7(343-382).

Couples, G. (1977). Stress and shear fracture (fault) patterns resulting from a suite of complicated boundary conditions with applications to the wind river mountains. *Pure and Applied Geophysics*, 115:113–133.

Cowie, P., A. and Scholz, C., H. (2003). Displacement-length scaling relationship for faults: data synthesis and discussion. *J. Struct. Geol.*, 14:1149–1156.

Crider, J. G. (2001). Oblique slip and the geometry of normal fault linkage: mechanics and a case study from the basin and range in oregon. *Journal of Structural Geology*, 23:1997–2009.

Crider, J. G. and Pollard, D. D. (1998). Fault linkage: Three-dimensional mechanical interaction between echelon normal faults. *Journal of Geophysical Research*, 103:24,373–24,391.

Crouch, S. L. and Starfield, A. M., editors (1983). *Boundary element methods in solid mechanics*. George Allen and Unwin, London.

Dahlstrom, C. D. A. (1969). Balanced cross section. *Canadian Journal of Earth Sciences*, 6:743–757.

Dair, L. and Cooke, M. L. (2009). San andreas fault topology through the san gorgonio pass, california. *Geology*, 37:119–122.

d'Alessio M. A., E., B. A., and R., B. (2003). No frictional heat along the san gabriel fault, california: Evidence from fission-track thermochronology. *Geology*, 31:541–544.

Davatzes, N. C. and Aydin, A. (2003). The formation of conjugate normal fault systems in folded sandstone by sequential jointing and shearing. *J. of Geophysical Research*, 108.

Davatzes, N. C., Eichhubl, P., and Aydin, A. (2005). Structural evolution of fault zones in sandstone by multiple deformation mechanisms: Moab fault, southeast utah. *Geological Society of America Bulletin*, 117:135–148.

Davis, P. (1983). Surface deformation associated with a dipping hydrofracture. *J. Geoph. Res.*, 88:5826–5834.

Davison, I. (1986). Listric normal fault profiles: Calculation using bed-length balance and fault displacement. *Journal of Structural Geology*, 8:209–210.

De Bremaecker, J. and Ferris, M. (2000). A comparison of two algorithms for solving closed crack problems. *Engineering Fracture Mechanics*, 66:601–605.

Del Castello, M. and Cooke, M. (2007). The underthrusting-accretion cycle: Work budget as revealed by the boundary element method. *J. Geophys. Res.*, 112.

Delair, J. and Leroux, C. (1978). Méthodes de quantification de la disparition de matiére au niveau de stylolites tectoniques et mécanismes de la deformation cassante des calcaires. *Bulletin de la Sociéé Géologique de France*, 7:137–144.

Delaney, P. and Pollard, D. (1981). Deformation of host rocks and flow of magma during growth of minette dikes and breccia-bearing intrusions near ship rock, new mexico. *U.S. Geological Survey Professional Paper*, 1202:61p.

Desbrun, M., Meyer, M., Schroder, P., and Barr, A. H. (1999). Implicit fairing of irregular meshes using diffusion and curvature flow. *SIGGRAPH*, 99:317–324.

Diez, M., La Femina, P. C., Connor, C. B., Strauch, W., and Tenorio, V. (2005). Evidence for static stress changes triggering the 1999 eruption of cerro negro volcano, nicaragua and regional aftershock sequences. *Geophysical Research Letters*, 32:L04309.

Dokka, R. K. and Travis, C. J. (1990). Late cenozoic strike-slip faulting in the mojave desert, california. *Tectonics*, 9:311–340.

Dorn, G. A. (1998). Modern 3d seismic interpretation. *The Leading Edge*, 17:1262–1272.

Du, Y., Aydin, A., and Segall, P. (1992). Comparison of various inversion techniques as applied to the determination of a geophysical deformation model for the 1983 borah peak earthquake. *Bull. Seism. Soc. Am.*, 82:1840–1866.

Dula, W. F. (1991). Geometric models of listric normal faults and rollover folds. *AAPG Bulletin*, 75:1609–1625.

Dunbar, J. A. and Cook, R. W. (2003). Palinspastic reconstruction of structure maps: An automated finite element approach with heterogeneous strain. *Journal of Structural Geology*, 26:1021–1036.

Dupin, J.-M., Sassi, W., and Angelier, J. (1993). Homogeneous stress hypothesis and actual fault slip: a distinct element analysis. *J. Struct. Geol.*, 15(8):1033–1043.

Dziewonski, A., Ekstrom, G., and Maternovskaya, N. (2000). Centroid moment tensor solutions for october-december, 1999. *Phys. Earth Planet. Inter.*, 121:205–221.

Ellis, P. G. and McClay, K. (1988). Listric extensional fault system - results of analogue model experiments. *Basin Research*, 1:55–70.

Engelder, T. (1993). *Stress Regimes in the Lithosphere*. Princeton University Press.

Erickson, G. S., Strayer, L. M., and Suppe, J. (2001). Mechanics of extension and inversion in the hanging walls of listric normal faults. *Journal of Geophysical Research*, 106:26,655–26,670.

Erickson, S. G., Hardy, S., and Suppe, J. (2000). Sequential restoration and unstraining of structural cross sections: Application to extensional terranes. *AAPG Bulletin*, 84:234–249.

Etchecopar, A., Vasseur, G., and Daignieres, M. (1981). An inverse problem in microtectonics for the determination of stress tensors from fault striation analysis. *J. Struct. Geol.*, 3(1):51–65.

Eterovic, A. and Bathe, K. (1991). On the treatment of inequality constraints arising from contact conditions in finite element analysis. *Computer and Structures*, 40(2):203–S209.

Feigl, K., Sergent, A., and Jacq, D. (1995). Estimation of an earthquake focal mechanism from a satellite radar interferogram: application to the december 4, 1992 landers aftershock. *Geophys. Res. Lett.*, 22:1037–1040.

Fialko, Y., Simons, M., and Agnew, D. (2001). The complete (3-d) surface displacement field in the epicentral area of the 1999 m(w) 7.1 hector mine earthquake, california, from space geodetic observations. *Geophys. Res. Lett.*, 28:3063–3066.

Fielding, E. J., Lundgren, P., Burgmann, R., and Funning, G. J. (2009). Shallow fault-zone dilatancy recovery after the 2003 bam earthquake in iran. *Nature*, 458:64–68.

Fielding, E. J., Wright, T. J., Muller, J. R., Parsons, B. E., and Walker, R. (2004). Aseismic deformation of a fold-and-thrust belt imaged by synthetic aperture radar interferometry near shahdad, southeast iran. *Geology*, 32:577–580.

Fletcher, R. and Pollard, D. (1981). Anticrack model for pressure solution surfaces. *Geology*, 9:419–424.

Fletcher, R. and Pollard, D. (1990). Can we understand structural and tectonic processes and their products without appeal to a complete mechanics? *J. Struct. Geol.*, 21:1071–1088.

Flodin, A. E., Maerten, F., and Maerten, L. (2005). A geomechanically-based inverse method for interpolating the three-dimensional stress field in a faulted reservoir. volume 37, page 51. Proceeding of Geological Society of America, Rocky Mountain.

Freymueller, J., King, N., and Segall, P. (1994). The coseismic slip distribution of the landers earthquake. *Bull. Seism. Soc. Am.*, 84:646–659.

Fry, N. (1999). Striated faults: visual appreciation of their constraint on possible paleostress tensors. *J. Struct. Geol.*, 21(1):7–21.

Fung, Y. (1977). *A first course in Continuum Mechanics*. Prentice-Hall, Englewood Cliffs, NJ.

Gapais, D., Cobbold, P. ans Bourgeois, O., Rouby, D., and deUrreistiete, M. (2000). Tectonic significance of fault-slip data. *J. Struct. Geol.*, 22(7):881–888.

Gauthier, B. and Angelier, J. (1985). Fault tectonics and deformation: a method of quantification using field data. *Earth and Planetary Sci. Lett.*, 74(1):137–148.

Gauthier, B. D. M. and Lake, S. D. (1993). Probabilistic modeling of faults below the limit of seismic resolution in pelican field, north sea, offshore united kingdom. *AAPG Bulletin*, 77:761–776.

G.C.P., K., Stein, R., S., and Lin, J. (1994). Static stress changes and the triggering of earthquakes. *Bulletin of the Seismological Society of America*, 84:935953.

Gephart, J. and Forsyth, D. (1990). An improved method for determining the regional stress tensor using earthquake focal mechanism data: Application to the san fernando earthquake sequence. *Comput. Geosci.*, 16(7):953–989.

Gephart, J. W. (1990). Fmsi: a fortran program for inverting fault/slickenside and earthquake focal mechanism data to obtain the regional stress tensor. *Computers and Geoscience*, 16(7):953–989.

Gibbs, A. D. (1983). Balanced cross-section construction from seismic sections in areas of extensional tectonics. *Journal of Structural Geology*, 5:153–160.

Gillespie, P. A., Howard, C., Walsh, J. J., and Watterson, J. (1993). Measurement and characterisation of spatial distributions of fractures. *Tectonophysics*, 226:113–141.

Golub, G. H. and Van Loan, C. F. (1996). *Matrix computation*. Johns Hopkins University Press, Baltimore, MD.

Grant, J. V. and Kattenhorn, S. A. (2004). Evolution of vertical faults at an extensional plate boundary, southwest iceland. *Journal of Structural Geology*, 26:537–557.

Gratier, J.-P., Guillier, B., Delorme, A., and Odonne, F. (1991). Restoration and balance of a folded and faulted surface by bestfitting of finite elements: Principle and applications. *Journal of Structural Geology*, 13:111–115.

Greengard, L. and Rokhlin, V. (1987). A fast algorithm for particle simulations. *J. Comput. Phys.*, 73:325–348.

Griffith, A. (1921). The phenomena of rupture and flow in solids. *Phil. Transactions of the Royal Society*, A221:163–198.

Griffith, A. (1925). Theory of rupture. In *First International Congress for Applied Mechanics*, pages 53–64. Delft. Waltham Int. Press.

Griffith, W. A. and Cooke, M. L. (2004). Mechanical validation of the three-dimensional intersection geometry between the puente hills blind-thrust system and the whittier fault, los angeles, california. *Bulletin of the Seismological Society of America*, 94:493–505.

Gudmundsson, O. and Sambridge, M. (1998). A regionalized upper mantle (rum) seismic model. *J. Geophys. Res.*, 103:7121–7136.

Guiton, M. L. E. (2001). *Contribution of pervasive fractures to the deformation during folding of sedimentary rocks: Thése de Doctorat*. PhD thesis, École Polytechnique, Paris, France.

Guiton, M. L. E., Leroy, Y. M., and Sassi, W. (2003a). Activation of diffuse discontinuities and folding of sedimentary layers. *Journal of Geophysical Research*, 108.

Guiton, M. L. E., Sassi, W., Leroy, Y. M., and Gauthier, B. D. M. (2003b). Mechanical constraints on the chronology of fracture activation in folded devonian sandstone of the western moroccan anti-atlas. *Journal of Structural Geology*, 25:1317–1330.

Hackbusch, W. (1999). A sparse matrix arithmetic based on h-matrices: Part 1: Introduction to h-matrices. *Computing*, 62:89–108.

Hackbusch, W. and Nowak, Z. (1989). On the fast matrix multiplication in the boundary element method by panel clustering. *Numeri Math*, 54(4):463–491.

Hafner, W. (1951). Stress distribution and faulting. *Geol. Soc. America Bull.*, 62:373–398.

Hall, M. (2007). Smooth operator: Smoothing seismic interpretations and attributes. *The Leading Edge*, January:16–20.

Hammersley, J. M. and Handscomb, D. C. (1975). *Monte Carlo Methods*. Fletcher, Norwich, England.

Hanks, T. (1977). Earthquake stress drops, ambient tectonic stress, and the stresses that drive plate motion. *Pure and Applied Geophysics*, 115:441458.

Hanssen, R. F. (2001). *Radar interferometry: data interpretation and error analysis, in Remote Sensing and Digital Image Processing*. Kluwer Academic Publishers, Dordrecht, The Netherlands.

Hardcastle, K. and Hills, L. (1991). Brute3 and select: Quickbasic 4 programs for determination of stress tensor configurations and separation of heterogeneous populations of fault-slip data. *Computers & Geosciences*, 17(1):23–43.

Harris, R. A. and Segall, P. (1987). Detection of a locked zone at depth on the parkfield, california, segment of the san andreas fault. *J. Geophys. Res.*, 92:7945–7962.

Hatheway, A. and Kiersch, G. (1989). Engineering properties of rock. in:. pages 672–715.

Hauge, T. A. and Gray, G. G. (1996). A critique of techniques for modelling normal-fault and rollover geometries. *Modern developments in structural interpretation, validation and modelling: Geological Society (London) Special Publication*, 99:89–97.

Hauksson, E., Jones, L., and Hutton, K. (2002). The 1999 mw 7.1 hector mine, california, earthquake sequence: complex conjugate strike-slip faulting. *Bull. Seism. Soc. Am.*, 92:1154–1170.

Healy, D., Yielding, G., and Kusznir, N. (2004). Fracture prediction for the 1980 el asnam, algeria earthquake via elastic dislocation modeling. *Tectonics*, 23:1–21.

Henn, S. and al. (2001). Iterative multigrid regularization tehniques for image matching. *SIAM*, 23(4):1077–1093.

Hennings, P. H., Olson, J. E., and Thompson, L. B. (2000). Combining outcrop data and three-dimensional structural models to characterize fractured reservoirs: An example from wyoming. *AAPG Bulletin*, 84:830–849.

Hetényi, M., editor (1966). *Handbook of experimental stress analysis*. Wiley, New York.

Hossack, J. R. (1979). The use of balanced cross section in the calculation of orogenic contraction: A review. *Journal of the Geological Society (London)*, 136:705–711.

Huang, Q. (1988). Computer-based method to separate heterogeneous sets of fault-slip data into sub-sets. *J. Struct. Geol.*, 10(3):297–299.

Hudson, J. A. and Johansson, E. (2006). Summary of rock mechanics work completed for posiva before 2005. Technical report, Posiva report 2006-4.

Hughes, T., Taylor, R., Sackman, A., and Curnier, W. (1976). A finite element method for a class of contact-impact problems. *Comput. Meth. Appl. Mech. Engng.*, 8:249–276.

Hughes, T. J. R. (1987). *The finite element method: linear static and dynamic finite element analysis*. Prentice-Hall, New Jersey.

Hurst, K., Argus, D., Donnellan, A., Heflin, M., Jefferson, D., et al. (2000). The coseismic geodetic signature of the 1999 hector mine earthquake. *Geophys. Res. Lett.*, 27:2733–2736.

Inglis, C. (1913). Stresses in a plate due to the presence of cracks and sharp corners. volume 55, pages 219–230. Inst. Naval Arch.

Irwin, G. (1957). Analysis of stresses and strain near the end of a crack traversing a plate. *J. of Appl. Mech.*, 24:361–364.

Jackson, J. and McKenzie, D. (1988). The relationship between plate motions and seismic moment tensors, and the rates of active deformation in the mediterranean and middle east. *Geophysical J.*, 88:46–73.

Jaeger, J., Cook, N., and Zimmermann, R. (2007a). *Fundamentals of Rock Mechanics*. Blackwell Publ., Malden, MA.

Jaeger, J., Cook, N., and Zimmermann, R. (2007b). *Fundamentals of Rock Mechanics*. Blackwell Publ., Malden, MA.

Jeyakumaran, M., Rudnicki, J. W., and Keer, L. M. (1992). Modeling slip zones with triangular dislocation elements. *Bulletin of the Seismological Society of America*, 82:2153–2169.

Ji, C., Wald, D., and Helmberger, D. (2002). Source description of the 1999 hector mine, california, earthquake, part ii: complexity of slip history. *Bull. Seism. Soc. Am.*, 92:1208–1226.

Johnson, K., Hsu, Y., Segall, P., , and Yu, S. (2001). Fault geometry and slip distribution of the 1999 chi-chi, taiwan, earthquake imaged from inversion of gps data. *Geophys. Res. Lett.*, 28:2285–2288.

Johnson, K. and Segall, P. (2004). Imaging the ramp-décollement geometry of the chelungpu fault using coseismic gps displacements from the 1999 chi-chi, taiwan earthquake. *Tectonophysics*, 378:129–139.

Jones, L. (1988). Focal mechanisms and the state of stress on the san andreas fault in southern california. *J. Geophys. Res.*, 93:8869–8891.

Jónsson, S., Zebker, H., Segall, P., and Amelung, F. (2002). Fault slip distribution of the 1999 mw 7.1 hector mine, california, earthquake, estimated from satellite radar and gps measurements. *Bull. Seism. Soc. Am.*, 92:1377–1389.

Jost, M. L. and Herrman, R. B. (1989). A student's guide to and review of moment tensors. *Seism. Res. Lett.*, 60:37–57.

Joussineau, G., Petit, J.-P., and Gauthier, B. (2003). Photoelastic and numerical investigation of stress distributions around fault models under biaxial compressive loading conditions. *Tectonophysics*, 363:1943.

Julien, P. and Cornet, F. (1987). Stress determination from aftershocks of the campania-lucania earthquake of november 23, 1980. *Annales Geophysicae*, 5B(3):289–300.

Kao, H. and Angelier, J. (2001). Stress tensor inversion for the chi-chi earthquake sequence and its implications on regional collision. *Bull. of the Seism. Soc. of America*, 91(5):1028–1040.

Kattenhorn, S., Aydin, A., and Pollard, D. (2000). Joints at high angles to normal fault strike: an explanation using 3d numerical model of fault perturbated stress field. *Journal of Structural Geology*, 22:1–23.

Kattenhorn, S. A. and Pollard, D. D. (2001). Integrating 3-d seismic data, field analogs, and mechanical models in the analysis of segmented normal faults in the wytch farm oil field, southern england, united kingdom. *AAPG Bull.*, 85:1183–1210.

Kattenhorn. S., A. and Marshall, S., T. (2006). Fault-induced perturbed stress fields and associated tensile and compressive deformation at fault tips in the ice shell of europa: implications for fault mechanics. *Journal of Structural Geology*, 28:22042221.

Kaven, O. (2009). *Geometry and mechanics of three-dimensional faults: implications for slip, aftershocks, and paleostress*. PhD thesis, Stanford University, CA, USA.

Kaverina, A., Dreger, D., and Price, E. (2002). The combined inversion of seismic and geodetic data for the source process of the 16 october 1999 mw 7.1 hector mine, california, earthquake. *Bull. Seism. Soc. Am.*, 92:1266–1280.

Keane, A. (2006). Cuda (compute unified device architecture), http://developer.nvidia.com/object/cuda.html.

Kerr, H., White, N., and Brun, J.-P. (1993). An automatic method for determining 3-d normal fault geometry. *Journal of geophysical Research*, 98:17,837–17,857.

Khronos-Group (2009). Opencl (open computing language), http://www.khronos.org/opencl.

Kilb, D. and Rubin, A. (2002). Implications of diverse fault orientations imaged in relocated aftershocks of the mount lewis, ml 5.7, california, earthquake. *J. Geophys. Res.*, 107:2294.

Klarbring, A. (1986). A mathematical programming approach to contact problems with friction. *Computer and Structures*, 58:175–200.

Klarbring, A. and Bjorkman, G. (1988). A mathematical programming approach to contact problems with friction and varying contact surface. *Computer and Structures*, 30:1185–1198.

Klügel, A., Walter, T. R., Schwarz, S., and Geldmacher, J. (2005). Gravitational spreading causes en-echelon diking along a rift zone of madeira archipelago: an experimental approach and implications for magma transport. *Bulletin of Volcanology*, 68:37–46.

Kostrov, V. (1968). Seismic moment and energy of earthquakes, and seismic flow of rocks. *Izvestiya Academy of Sciences of the USSR (Physics of Solid Earth)*, 1:23–40.

Kreemer, C., Blewitt, G., Hammond, W. C., and Plag, H.-P. (2006a). Global deformation from the great 2004 sumatra-andaman earthquake observed by gps: Implications for rupture process and global reference frame. *Earth Planets Space*, 58:141–148.

Kreemer, C., Blewitt, G., and Maerten, F. (2006b). Co- and postseismic deformation of the 28 march 2005 nias mw 8.7 earthquake from continuous gps data. *Geophysical Research Letters*, 33:L07307.

Kwak, B. and Lee, S. (1988). A complementarity problem formulation for two-dimensional frictional contact problems. *Computer and Structures*, 28:469–480.

La Pointe, P., Cladouhos, T., and Follin, S. (2002). Development, application, and evaluation of a methodology to estimate distributed slip on fractures due to future earthquakes for nuclear waste repository performance assessment. *Bulletin of the Seismological Society of America*, 92:923–944.

Lachenbruch, A. and Sass, J. (1980). Heat flow and energetics of the san andreas fault zone. *Journal of Geophysical Research*, 85:61856222.

Lawn, B. and Wilshaw, T. (1993). *Fracture of Brittle Solids*. Cambridge University Press, New York.

Lay, T. and Wallace, T. (1995). *Modern Global Seismology*. Academic Press, London, UK.

Lee, J.-C., Chu, H.-T., Angelier, J., Chan, Y.-C., Hu, J.-C., Lu, C., and Rau, R.-J. (2002). Geometry and structure of northern surface ruptures of the 1999 mw=7.6 chi-chi taiwan earthquake: influence from inherited fold belt structures. *J. Struct. Geol.*, 24:173–192.

Lee, Y.-H., Hsieh, M.-L., Lu, S.-D., Shih, T.-S., Wu, W.-Y., Sugiyama, Y., Azuma, T., and Kariya, Y. (2003). Slip vectors of the surface rupture of the 1999 chi-chi earthquake, western taiwan. *J. Struct. Geol.*, 25(11):1917–1931.

Lévy, B. (2000). *Topologie algorithmique combinatoire et plongement*. PhD thesis, University of Nancy, Nancy, France.

Liesa, C. and Lisle, R. (2004). Reliability of methods to separate stress tensors from heterogeneous fault-slip data. *J. Struct. Geol.*, 26(3):559–572.

Lin, A., Ouchi, T., Chen, A., and Maruyama, T. (2001). Co-seismic displacements, folding and shortening structures along the chelungpu surface rupture zone occurred during the 1999 chi-chi (taiwan) earthquake. *Tectonophysics*, 330:225–244.

Lin, J. and Stein, R. S. (1989). Coseismic folding, earthquake recurrence, and the 1987 source mechanism at whittier narrows, los angeles basin, california. *J. Geophys. Res.*, 94:9614–9632.

Lisle, R., Orife, T., Arlegui, L., Liesa, C., and Srivastava, D. (2006). Favoured states of palaeostress in the earth's crust: evidence from fault-slip data. *J. Struct. Geol.*, 28(6):1051–1066.

Lovely, P. J., Pollard, D. D., and Mutlu, O. (2009). Regions of reduced static stress drop near fault tips for large strike-slip earthquakes. *Bulletin of the Seismological Society of America*, 99:1691–1704.

Lundgren, P. and Lu, Z. (2006). Inflation model of uzon caldera, kamchatka, constrained by satellite radar interferometry observations. *Geophysical Research Letters*, 33:L06301.

Lunn, R. J., Willson, J. P., Shipton, Z. K., and Moir, H. (2008). Simulating brittle fault growth from linkage of preexisting structures. *J. Geophys. Res.*, 113,B07403.

Ma, X. and Kusznir, N. (1993). Modeling of near-field subsurface displacements for generalized faults and fault arrays. *Journal of structural geology*, 15:1471–1484.

Maerten, F. (2010). Adaptive cross approximation applied to the solution of system of equations and post-processing for 3d elastostatic problems using the boundary element method. *Engineering Analysis with Boundary Elements*, 34:483–491.

Maerten, F. and Maerten, L. (2008a). Iterative 3d bem solver on complex faults geometry using angular dislocation approach in heterogeneous, isotropic elastic whole or half-space. In Brebbia, editor, *Boundary Elements and other Mesh Reduction Methods XXX*, pages 201–208, Southampton. BEM 30, WITpress.

Maerten, F. and Maerten, L. (2008b). Iterative 3d bem solver on complex faults geometry using angular dislocation approach in heterogeneous, isotropic elastic whole or half-space. In Brebbia, editor, *Boundary Elements and other Mesh Reduction Methods XXX*, pages 201–208, Southampton. BEM 30, WITpress.

Maerten, F., Maerten, L., and Cooke, M. (2009a). Solving 3d boundary element problems using constrained iterative approach. *Computational Geosciences*.

Maerten, F., Maerten, L., Pollard, D., and Lagalaye, Y. (2009b). ibem3d, a three-dimentional boundary element method using angular dislocations for sub-surface structures modeling. *In preparation for Journal of Geophysical Research*.

Maerten, F., Resor, P. G., Pollard, D. D., and Maerten, L. (2005). Inverting for slip on three-dimensional fault surfaces using angular dislocations. *Bulletin of the Seismological Society of America*, 95:1654–1665.

Maerten, L. (2000). Variation in slip on intersectiong normal faults: Implications for paleostress inversion. *Journal of Geophysical Research*, 105(25):553–565.

Maerten, L., Gillepsie, P., and Pollard, D. (2002). Effect of local stress perturbation on secondary fault development. *Journal of Structural Geology*, 24:145153.

Maerten, L., Gillespie, P., and Daniel, J.-M. (2006). 3-d geomechanical modeling for constraint of subseismic fault simulation. *AAPG Bulletin*, 90:1337–1358.

Maerten, L. and Maerten, F. (2006). Chronologic modeling of faulted and fractured reservoirs using geomechanically-based restoration: Technique and industry applications. *AAPG Bulletin*.

Maerten, L., Pollard, D. D., and Karpuz, R. (2000). How to constrain 3d fault continuity and linkage using reflection seismic data: a geomechanical approach. *AAPG Bull.*, 84:1311–1324.

Maerten, L., Pollard, D. D., and Maerten, F. (2001). Digital mapping of three-dimensional structures of the chimney rock fault system, central utah. *Journal of Structural Geology*, 23:585–592.

Maerten, L., Willemse, E. J. M., Pollard, D. D., and Rawnsley, K. (1999). Slip distributions on intersecting normal faults. *Journal of Structural Geology*, 21:259–271.

Malvern, I. (1969). *Introduction to the Mechanics of a Continuum Medium*. Prentice-Hall.

Man, K. (1994). *Contact Mechanics Using Boundary Elements*. Computational Mechanics Publications, Southampton, UK.

Mandl, G. (1988). *Mechanics of tectonic faulting. Models and basic concepts*. Elsevier, Amsterdam.

Mansinha, L. and Smylie, D. (1971). The displacement fields of inclined faults. *Bull. Seism. Soc. of America*, 61:4731–4743.

Marone, C. J., Scholz, C. H., and Bilham, R. (1991). On the mechanics of earthquake afterslip. *J. Geophys. Res.*, 96:8441–8452.

Marrett, R. and Allmendinger, R. (1990). Kinematic analysis of fault-slip data. *J. Struct. Geol.*, 12(8):973–986.

Marshall, S. T. and Cooke, M. L. (2008). Effects of nonplanar fault topology and mechanical interaction on fault-slip distributions in the ventura basin, california. *Bulletin of the Seismological Society of America*, 98:1113–1127.

Martel, S. (1997). Effects of cohesive zones on small faults and implications for secondary fracturing and fault trace geometry. *Journal of Structural Geology*, 19:835–847.

Martel, S. and Shacat, C. (2006). Mechanics and interpretations of fault slip. In Abercrombie, R., DiToro, G., Kanamori, H., and McGarr, A., editors, *Radiated Energy and the Physics of Earthquake Faulting*, pages 207–216. American Geophysical Union Monograph 170.

Martel, S. J. (1990). Formation of compound strike-slip fault zones, mount abbot quadrangle, california. *J. Struct. Geol.*, 12:869–882.

Martel, S. J. (2004). Mechanics of landslide initiation as a shear fracture phenomenon. *Marine Geology*, 203:319–339.

Martel, S. J. and Boger, W. A. (1998). Geometry and mechanics of secondary fracturing around small three-dimensional faults in granitic rock. *Journal of Geophysical Research*, 103:21,299–21,314.

Maruyama, T. (1964). Statical elastic dislocations in an infinite and semi-infinite medium. *Tokyo Daigaku Jishin Kankyoso Iho*, 42:289–368.

Mavko, G. (1982). Fault interaction near hoolister, california. *J. Geoph. Res.*, 87:7807–7816.

McClay, K. R. (1990). Extensional fault systems in sedimentary basins: A review of analogue model studies. *Marine and Petroleum Geology*, 7:206–233.

McKay, M. D., Beckman, R. J., and Conover, W. J. (1979). A comparison of three methods for selecting values of input variables in analysis of output from a computer code. *Technometrics*, 21:239–245.

McKenzie, D. (1969). The relation between fault plane solutions for earthquakes and the directions of the principal stresses. *Bull. Seismol. Soc. Am.*, 59:591–601.

Medwedeff, D. A. and Krantz, R. W. (2002). Kinematic and analog modeling of 3-d extensional ramps: Observations and a new 3-d deformation model. *Journal of Structural Geology*, 24:763–772.

Meigs, A. J., Cooke, M. L., and Marshall, S. T. (2008). Using vertical rock uplift patterns to constrain the three-dimensional fault configuration in the los angeles basin. *Bulletin of the Seismological Society of America*, 98:106–123.

Melbourne, T. I., Webb, F. H., Stock, J. M., and Reigber, C. (2002). Rapid postseismic transients in subduction zones from continuous gps. *J. Geophys. Res.*, 107(B10), 2241.

Meltzner, A. J., Sieh, K., Abrams, M., Agnew, D. C., Hudnut, K. W., Avouac, J., and Natawidjaja, D. H. (2006). Uplift and subsidence associated with the great aceh-andaman earthquake of 2004. *J. Geophys. Res.*, 111(B02407).

Menke, W. (1984). *Geophysical Data Analysis: Discrete Inverse Theory*. International Geophysics Series, Academic, San Diego.

Michael, A. (1987). Use of focal mechanisms to determine stress: a control study. *J. Geophys. Res.*, 92(B1):357–368.

Mijar, A. and Arora, J. (2000). Review of formulations for elastostatic frictional contact problems. *Structural and Multidisciplinary Optimization*, 20:167–189.

Molnar, P. (1983). Average regional strain due to slip on numerous faults of different orientations. *J. Geophys. Res.*, 88:6430–6432.

Montési, L. G. J. (2004). Controls of shear zone rheology and tectonic loading on post-seismic creep. *J. Geophys. Res.*, 109(B10404).

Mount, V. and Suppe, J. (1987). State of stress near the san andreas fault: Implications for wrench tectonics. *Geology*, 115:11431146.

Muller, J. R. and Aydin, A. (2004). Rupture progression along discontinuous oblique fault sets: implications for the karadere rupture segment of the 1999 izmit earthquake, and future rupture in the sea of marmara. *Tectonophysics*, 391:283–302.

Muller, J. R. and Aydin, A. (2005). Using geomechanical modeling to constrain the fault geometry within the marmara sea, turkey. *Journal of Geophysical Research*, 110:B03407.

Muller, J. R., Aydin, A., and Maerten, F. (2003). Investigating the transition between the 1967 mudurnu valley and 1999 izmit earthquakes along the north anatolian fault with static stress changes. *Geophysics Journal International*, 154:471–482.

Muller, J. R., Aydin, A., and Wright, T. J. (2006). Using an elastic dislocation model to investigate static coulomb stress change scenarios for earthquake ruptures in the eastern marmara sea region, turkey, buiter, s. j. h. & schreurs, g. (eds). *Geological*

*Society of London Special Publication - Analogue and Numerical Modelling of Crustal-Scale Processes*, 253:397–414.

Mutlu, O. and Pollard, D. (2008). On the patterns of wing cracks along an outcrop scale flaw: a numerical modeling approach using complementarity. *Journal of Geophysical Research*, 113.

Mynatt, I., Hilley, G., and Pollard, D. D. (2007). Inferring fault characteristics using fold geometry constrained by airborne laser swath mapping at raplee ridge, utah. *Geophysical Research Letters*, 34:L16315.

Nádai, A. (1931). *Plasticity*. McGraw-Hill, Inc., New York.

Natawidjaja, D. H., Sieh, K., Ward, S. N., Cheng, H., Edwards, R. L., Galetzka, J., and Suwargadi, B. (2004). Paleogeodetic records of seismic and aseismic subduction from central sumatran microatolls, indonesia. *J. Geophys. Res.*, 109(B04306).

Nemcok, M. and Lisle, R. (1995). A stress inversion procedure for polyphase fault/slip data sets. *J. Struct. Geol.*, 17(10):1445–1453.

Nicol, A., Walsh, J. J., Watterson, J., and Bretan, P. G. (1995). Three dimensional geometry and growth of conjugate normal faults. *Journal of Structural Geology*, 17:847–862.

Novozhilov, V. V. (1953). *Foundations of the nonlinear theory of elasticity*. Graylock Press.

Ohlmacher, G., C. and Aydin, A. (1997a). Mechanics of veins, fault and solution surface formation in the appalachian valley, u.s.a.: implications for fault friction, state of stress and fluid pressure. *Journal of Structural Geology*, 19:927–944.

Ohlmacher, G. and Aydin, A. (1997b). Mechanics of veins, fault and solution surface formation in the appalachian valley, u.s.a.: implications for fault friction, state of stress and fluid pressure. *Journal of Structural Geology*, 19:927–944.

Okada, Y. (1985). Surface deformation due to shear and tensile faults in a half-space. *Bulletin of the Seismological Society of America*, 75:1135–1154.

Okada, Y. (1992). Internal deformation due to shear and tensile faults in a half-space. *Bull. Seism. Soc. of America*, 82:1018–1040.

Olson, E. L. and Cooke, M. L. (2005). Application of three fault growth criteria to the puente hills thrust system, los angeles, california, usa. *Journal of Structural Geology*, 27:1765–1777.

Olson, J. and Pollard, D. (1989). Inferring paleostresses from natural fracture patterns: A new method. *Geology*, 17:345–348.

Olson, J. and Pollard, D. (1991). The initiation and growth of en echelon veins. *Journal of Structural Geology*, 13(5):595–608.

Orife, T., Arlegui, L., and Lisle, R. (2002). Dipslip: a quickbasic stress inversion program for analysing sets of faults without slip lineations. *Computers & Geosciences*, 28(6):775–781.

Orife, T. and Lisle, R. (2003). Numerical processing of palaeostress results. *J. Struct. Geol.*, 25(6):949–957.

Peacock, D. (2002). Propagation, interaction and linkage in normal fault systems. *Earth Sci. Rev.*, 58:121–142.

Petit, J., Wibberley, C., and Ruiz, G. (1999). 'crack-seal, slip': a new fault valve mechanism? *Journal of Structural Geology*, 21:1199–1207.

Petit, J.-P. and Barquins, M. (1988). Can natural faults propagate under mode ii conditions? *Tectonics*, 7:1243–1256.

Petit, J.-P. and Mattauer, M. (1995). Palaeostress superimposition deduced from mesoscale structures in limestone: the matelles exposure, languedoc, france. *Journal of Structural Geology*, 17:245256.

Phan, A.-V., Napier, J. A. L., Gray, L. J., and Kaplan, T. (2003). Symmetric-galerkin simulation of fracture with frictional contact. *Internal Journal for Numerical Methods in Engineering*, 57:835–851.

Poliakov, A., Dmowska, R., and Rice, J. (2002). Dynamic shear rupture interactions with fault bends and off-axis secondary faulting. *Journal of Geophysical Research*, 107.

Pollard, D. and Fletcher, R. (2005). *Fundamentals of Structural Geology*. Cambridge University Press, Cambridge, UK.

Pollard, D., Saltzer, S., and Rubin, A. (1993). Stress inversion methods: are they based on faulty assumptions? *J. Struct. Geol.*, 15:1045–1054.

Pollard, D. and Segall, P. (1987). Theoretical displacements and stresses near fractures in rock: with applications to faults, joints, veins, dikes and solution surfaces. In Academic., S. D., editor, *Fracture Mechanics of Rocks*. Atkinson, B.

Pollitz, F. F., Bürgmann, R., and Segall, P. (1998). Joint estimation of afterslip rate and postseismic relaxation following the 1989 loma prieta earthquake. *J. Geophys. Res.*, 103:26975–26992.

Pollitz, F. F., Peltzer, G., and Bürgmann, R. (2000). Mobility of continental mantle: Evidence from postseismic geodetic observations following the 1992 landers earthquake. *J. Geophys. Res.*, 105:8035–8054.

Power, W., Tullis, T., Brown, S., Boitnott, G., and Scholz, C. (1987). Roughness of natural fault surfaces. *Geophy. Res. Lett.*, 14:29–32.

Press, C. U., editor (1992). *Numerical Recipes in FORTRAN 77: The Art of Scientific Computing, 2nd ed.* Press, W. H. and Teukolsky, S. A. and Vetterling, W. T. and Flannery, B. P., New York.

Press, F. (1965). Displacements, strains and tilts at tele-seismic distances. *J. Geoph. Res.*, 70:2395–2412.

Price, E. and Bürgmann, R. (2002). Interactions between the landers and hector mine, california, earthquakes from space geodesy, boundary element modeling, and time-dependent friction. *Bull. Seism. Soc. Am.*, 92:1450–1469.

Price, N. J. (1966). *Fault and Joint Development in Brittle and Semi-brittle Rock*. Pergamon, London.

Ramsay, J. and Lisle, R. (2000). *The Techniques of Modern Structural Geology. Volume III. Applications of Continuum Mechanics in Structural Geology*. Academic Press, London, U.K.

Rawnsley, K., Rives, T., Petit, J., Hencher, S., and Lumsden, A. (1992). Joint development in perturbed stress fields near faults. *Journal of Structural Geology*, 14:939–951.

Raynaud, S. and Carrio-Schaffhauser, E. (1992). Rock matrix structures in a zone influenced by a stylolite. *Journal of Structural Geology*, 14:973–980.

Reches, Z. (1978). Number and orientation of fault sets in the field and in experiments. *Tectonophysics*, 47:109–129.

Reches, Z. (1987). Determination of the tectonic stress tensor from slip along faults that obey the coulomb yield condition. *Tectonics*, 6(4):849–861.

Reilinger, R., Ergintav, S., Bürgmann, R., McClusky, S., Lenk, O., et al. (2000). Coseismic and postseismic fault slip for the 17 august 1999,m7.5, izmit, turkey earthquake. *Science*, 289:1519–1524.

Reinecker, J., Heidbach, O., Müller, B., Tingay, M., and Connolly, P. (2004). The 2004 release of the world stress map, url. http://www.world-stress-map.org.

Reinen, L. A. (2008). Numerical models for exploration and visualization of complex geological phenomena in an undergraduate structural geology course. volume 89 (53), pages ED53A–0582. American Geophysical Union, Fall Meeting.

Resor, P. G. (2003). *Deformation associated with continental normal faults*. PhD thesis, Stanford University, CA, USA.

Resor, P. G., Pollard, D. D., Wright, T. J., and Beroza, G. C. (2005). Integrating high-precision aftershock locations and geodetic observations to model coseismic deformation associated with the 1995 kozani-grevena earthquake, greece. *Journal of Geophysical Research*, 110:B09402.

Rice, J. (1980). The mechanics of earthquake rupture. In Dziewonski, A. and Boschi, E., editors, *Physics of the Earth's Interior*, pages 555–649, North-Holland Publ. Co. International School of Physics 'Enrico Fermi', Course 78, 1979, Italian Physical Society.

Rigo, A., De Chabalier, J.-B., Meyer, B., and Armijo, R. (2004). The 1995 kozani-grevena (northern greece) earthquake revisited: an improved faulting model from synthetic aperture radar interferometry. *Geophysical Journal International*, 157:727–736.

Rispoli, R. (1981). Stress fields about strike-slip faults inferred from stylolites and tension gashes. *Tectonophysics*, 75:T29–T36.

Roberts, G. and Ganas, A. (2000). Fault-slip direction in central and southern greece measured from striated and corrugated fault planes: comparison with focal mechanism and geodetic data. *J. of Geophy. Res.*, 105(B10):23443–23462.

Roering, J., Cooke, M., and D., P. (1997). Why blind thrust faults don't propagate to the earth's surface: Numerical modeling of coseismic deformation associated with thrust-related anticlines. *J. Geophys. Res.*, 102:901–912.

Rokhlin, V. (1985). Rapid solution of integral equations of classical potential theory. *J Comput Phys*, 60:187–207.

Rouby, D., Cobbold, P. R., Szatmari, P., Demerican, S., Coelho, D., and Rici, J. A. (1993). Least-squares palinspastic restoration of region of normal faulting - application to the campos basin (brasil). *Tectonophysics*, 221:439–452.

Rouby, D., Xiao, H., and Suppe, J. (2000). 3-d restoration of complexly folded and faulted surfaces using multiple unfolding mechanisms. *AAPG Bulletin*, 84:805–829.

Rubinstein, R. Y. (1981). *Simulation and the Monte Carlo Method*. John Wiley and Sons, Inc.

Rudnicki, J. (1980). Fracture mechanics applied to the earth's crust. *Annual Review of Earth and Planetary Sciences*, 8:489–525.

Saad, Y. (1996). *Iterative Methods for Sparse Linear Systems*. PWS Publishing, New York.

Sagy, A., Brodsky, E., and Axen, G. (2007). Evolution of fault-surface roughness with slip. *Geology*, 35(3):283–286.

Samson, P. (1996). Equilibrage de structures géologiques 3d dans le cadre du projet gocad. Master's thesis, Institut National Polytechnique de Lorraine, Lorraine, France.

Sanders, C., Bonora, M., Kozlowski, E., and Sylwan, C. (2002). From 2d to 4d fracture network model, structural modeling of a complex thrust trap: A case study from the tarija basin, argentina. *Society of Petroleum Engineers*, ISRM78184:1–8.

Sanders, C., Bonora, M., Richards, D., Kozlowski, E., Sylwan, C., and Cohen, M. (2004). Kinematic structural restorations and discrete fracture modeling of a thrust trap: A case study from the tarija basin, argentina. *Marine and Petroleum Geology*, 21:845–855.

Sandwell, D., Sichoix, L., and Smith, B. (2002). The 1999 hector mine earthquake, southern california: vector near-field displacements from ers insar. *Bull. Seism. Soc. Am.*, 92:1341–1354.

Sanford, A. (1959). Analytical and experimental study of simple geologic structures. *Geol. Soc. America Bull.*, 70:19–52.

Sassi, W., Livera, S. E., and Caline, B. P. R. (1992). Quantification of the impact of subseismic scale faults on cormorant block iv. *R. M. Larsen, H. Brekke, B. T. Larsen, and E. Talleraas, eds., Structural and tectonic modeling and its application to petroleumgeology: Norwegian PetroleumSociety (NPS), Special Publication, Elsevier, Amsterdam*, 1:355–364.

Sato, K. and Yamaji, A. (2006). Uniform distribution of points on a hypersphere for improving the resolution of stress tensor inversion. *J. Struct. Geol.*, 28(6):972–979.

Savage, H. M. and Cooke, M. L. (2003). Can flat-ramp-flat geometry be inferred from fold shape? *Journal of Structural Geology*, 25:2023–2034.

Savage, J. and Hastie, L. (1966). Surface deformation associated with dip-slip faulting. *J. Geoph. Res.*, 71:4897–4904.

Savage, J. and Hastie, L. (1969). A dislocation model for the fairview peak, nevada, earthquake. *Bull. Seism. Soc. of America*, 59:1936–1948.

Savage, J. C. and Prescott, W. H. (1978). Asthenosphere readjustment and the earthquake cycle. *J. Geophys. Res.*, 83:3369–3376.

Schlische, R. W., Young, S. S., Ackermann, R. V., and Gupta, A. (1996). Geometry and scaling relations of a population of very small rift-related normal faults. *Geology*, 24:683–686.

Schmidt, D. A., Burgmann, R., Nadeau, R. M., and D'Alessio, M. (2005). Distribution of aseismic slip rate on the hayward fault inferred from seismic and geodetic data. *Journal of Geophysical Research*, 110:1–15.

Scholz (2000). Evidence for a strong san andreas fault.

Segall, P. and Pollard, D. (1980). Mechanics of discontinuous faulting. *Journal of Geophysical Research*, 85:4337–4350.

Sempere, J. and Mac Donald, K. (1986). Overlapping spreading centers : Implications from crack growth simulation by the displacement discontinuity method. *Tectonics*, 5:151–163.

Shackleton, R. and Cooke, M. L. (2007). Is plane-strain a valid assumption in non-cylindrical fault-cored folds? *Journal of Structural Geology*, 29:1229–1240.

Shan, Y. and Fry, N. (2005). A hierarchical cluster approach for forward separation of heterogeneous fault/slip data into subsets. *J. Struct. Geol.*, 27(5):929–936.

Shan, Y., Li, Z., and Lin, G. (2004). A stress inversion procedure for automated recognition of polyphase fault/slip data sets. *J. Struct. Geol.*, 26(9):919–925.

Shan, Y., Lin, G., Li, Z., and Zhao, C. (2006). Influence of measurement errors on stress estimated from single-phase fault/slip data. *J. Struct. Geol.*, 28(6):943–951.

Shan, Y., Suen, H., and Lin, G. (2003). Separation of polyphase fault/slip data: an objective-function algorithm based on hard division. *J. Struct. Geol.*, 25(6):829–840.

Shelton, J. W. (1984). Listric normal faults: An illustrated summary. *AAPG Bulletin*, 68:801–815.

Signorini, A. (1959). *Questioni de elasticita non linearizzata e semi-linearizzata*. Rend de Matematica, Rome.

Simoes, M., Avouac, J.-P.and Cattin, R., and Henry, P. (2004). The sumatra subduction zone: A case for a locked fault zone. *J. Geophys. Res.*, 109(B10402).

Simons, M., Fialko, Y., and Rivera, L. (2002). Coseismic deformation from the 1999 mw 7.1 hector mine, california, earthquake as inferred from insar and gps observations. *Bull. Seism. Soc. Am.*, 92:1390–1402.

Soliva, R., Benedicto, A., and Maerten, L. (2006). Spacing and linkage of confined faults: the importance of mechanical thickness. *Journal of Geophysical Research*, 111.

Soliva, R., Benedicto, A., Schultz, R. A., Maerten, L., and Micarelli, L. (2008). Displacement and interaction of normal fault segments branched at depth: Implications for fault growth and potential earthquake rupture size. *Journal of Structural Geology*, 30:1288–1299.

Soliva, R., Maerten, F., J.P., P., and Auzias, V. (2010). Fault static friction and fracture orientation in extensional relays; insight from field data, photoelasticity and 3d numerical modeling. *In press in Special Edt. of J. Struct. Geol.*

Stein, R. S. and Barrientos, S. E. (1985). Planar high-angle faulting in the basin and range: geodetic analysis of the 1983 borah peak, idaho, earthquake. *J. Geophys. Res.*, 90:11355–11366.

Steketee, J. (1958a). On volterra's dislocations in a semi-infinite elastic medium. *Can. J. Physics*, 36:192–205.

Steketee, J. (1958b). Some geophysical applications of the elasticity theory of dislocations. *Can. J. Physics*, 36:1168–1198.

Subarya, C., Chlieh, M., Prawirodirdjo, L., Avouac, J. P., Bock, Y., Sieh, K., Meltzner, A. J., Natawidjaja, D. H., and McCaffrey, R. (2006). Plate-boundary deformation of the great aceh-andaman earthquake. *Nature*, 440:46–51.

T., P. (1985). Nearly frictionless faulting from unclamping in long-term interaction models. *Geology*, 30:10631066.

Taha, M. (1986). *Apport de la microtectonique cassante au problme des trajectoires de contraintes et de leurs perturbations. Exemples du Nord de Montpellier*. PhD thesis, Université de Montpellier II.

Tamagawa, T. and Pollard, D. D. (2008). Fracture permeability created by perturbed stress fields around active faults in a fractured basement reservoir. *American Association of Petroleum Geologists*, 92:743–764.

Taubin, G. (1995). A signal processing approach to fair surface design. SIGGRAPH.

Thomas, A. L. (1993). Poly3d: a three-dimensional, polygonal element, displacement discontinuity boundary element computer program with applications to fractures, faults, and cavities in the earth's crust. Master's thesis, Stanford University.

Treiman, J., Kendrick, K., Bryant, W., Rockwell, T., and McGill, S. (2002). Primary surface rupture associated with the mw 7.1 16 october 1999 hector mine earthquake, san bernardino county, california. *Bull. Seism. Soc. Am.*, 92:1171–1191.

Trolltech (2010). Qtconcurrent, http://www.trolltech.com.

Tse, S., T. and Rice, J., R. (1986). Crustal earthquake instability in relation to the depth variation of frictional slip properties. *J. Geophys. Res.*, 91:9452–9472.

Tselentis, G.-A. and Gkika, F. (2005). Boundary element slope instability modeling of corinth canal, greece, due to nearby faults activation. *Coastal Engineering*, 78:313–322.

Twiss, R., Protzman, G., and Hurst, S. (1991). Theory of slickenline patterns based on the velocity gradient tensor and microrotation. *Tectonophysics*, 186:215–239.

Twiss, R., Souter, B., and Unruh, J. (1993). The effect of block rotations on the global seismic moment tensor and patterns of seismic p and t axes. *J. of Geophy. Res.*, 98:645–674.

Twiss, R. and Unruh, J. (1998). Analysis of fault slip inversions: Do they constrain stress or strain rate? *J. of Geophy. Res.*, 103(B6):12205–12222.

Vasseur, G., Etchecopar, A., and Philip, H. (1983). Stress state inferred from multiple focal mechanisms. *Ann. Geophys.*, 1(4-5):291–298.

Voight, B. (1966). Beziehung zwischen großen horizontalen spannungen in gebirge und der tektonik und der abtragung. In *Rock Mech., 1st Congr., Vol 2*, pages 1–56. Lisbon. Int. Soc.

Waldhauser, F. and Ellsworth, W. L. (2000). A double-difference earthquake location algorithm: method and application to the northern hayward fault, california. *Bull. Seism. Soc. Am.*, 90:1353–1368.

Walker, K. T., Ishii, M., and Shearer, P. M. (2005). Rupture details of the 28 march 2005 sumatra mw 8.6 earthquake imaged with teleseismic p waves. *Geophys. Res. Lett.*, 32(L24303).

Wallace, R. (1951). Geometry of shearing stress and relation to faulting. *J. of Geology*, 59:118–130.

Walsh, J. J. and Watterson, J. (1991). Geometric and kinematic coherence and scale effects in normal fault systems. *A. M. Roberts, G. Yielding, and B. Freeman, eds., The geometry of normal faults: Geological Society (London) Special Publication*, 56:193–203.

Walsh, J. J., Watterson, J., Bailey, W. R., and Childs, C. (1999). Fault relays, bends and branch-lines. *J. Struct. Geol.*, 21:1019–1026.

Walter, T. R. (2007). How a tectonic earthquake may wake up volcanoes: Stress transfer during the 1996 earthquake-eruption sequence at the karymsky volcanic group, kamchatka. *Earth and Planetary Science Letters*, 264:347–359.

Walter, T. R. and Amelung, F. (2006). Volcano-earthquake interaction at mauna loa volcano, hawaii. *Journal of Geophysical Research*, 111:B05204.

Walter, T. R. and Amelung, F. (2007). Volcanic eruptions following m 9 megathrust earthquakes: Implications for the sumatra-andaman volcanoes. *Geology*, 35:539–542.

Wawersik, W. and Brace, W. (1971). Post-failure behavior of a granite and diabase. *Rock Mechanics*, 3:61–85.

Weertman, J. and Weertman, J. (1964). *Elementary Dislocation Theory*. Macmillan Co.

Whitcomb, J., Garmany, J., and Anderson, D. (1974). Earthquake prediction: Variation of seismic velocities before the san fernando earthquake. *Science*, 180:632–635.

White, I. R. and Crider, J. G. (2006). Extensional fault-propagation folds: mechanical models and observations from the modoc plateau, northeastern california. *Journal of Structural Geology*, 28:1352–1370.

White, N. J., Jackson, J. A., and McKensie, D. P. (1986). The relationship between the geometry of normal faults and that of sedimentary layers in their hanging walls. *Journal of Structural Geology*, 8:897–909.

Willemse, E. and Pollard, D. (1998). On the orientation and patterns of wing cracks and solution surfaces at the tips of a sliding flaw or fault. *Journal of Geophysical Research*, 103:2427–2438.

Willemse, E. J. M., Peacock, D. C. P., and Aydin, A. (1997). Nucleation and growth of strike-slip faults in limestones from somerset, u.k. *J. Struct. Geol.*, 19:1461–1477.

Willemse, E. J. M. and Pollard, D. D. (2000). Normal fault growth: evolution of tipline shapes and slip distribution. *Aspects of Tectonic Faulting, Springer -Verlag, Berlin*, Lehner, F.K. and Urai, J.L. (eds.):193–226.

Willemse, E. J. M., Pollard, D. D., and Aydin, A. (1996). Three-dimensional analyses of slip distributions on normal fault arrays with consequences for fault scaling. *J. Struct. Geol.*, 18:295–309.

Willemse, J. M. (1997). Segmented normal faults: Correspondence between three-dimensional mechanical models and field data. *Journal of Geophysical Research*, 102:675–692.

Williams, G. D., Kane, S. J., Buddin, T. S., and Richards, A. J. (1997). Restoration and balance of complex folded and faulted rock volumes: Flexural flattening, jigsaw fitting and decompaction in three dimensions. *Tectonophysics*, 273:203–218.

Williams, G. D. and Vann, I. (1987). The geometry of listric normal faults and deformation in their hanging walls. *Journal of Structural Geology*, 9:789–795.

Williams, J. (1987). On the calculation of energy release rates for cracked laminates. *Int. J. of Fracture*, 36(2):101–119.

Willson, J., Lunn, R., and Shipton, Z. (2007). Simulating spatial and temporal evolution of multiple wing cracks around faults in crystalline basement rocks. *J. Geophys. Res.*, 113,B07403.

Withjack, M. O., Islam, Q. T., and La Pointe, P. R. (1995). Normal faults and their hanging-wall deformation: An experimental study. *AAPG Bulletin*, 79:1–18.

Wojtal, S. (1989). Measuring displacement gradients and strains in faulted rocks. *J. Struct. Geol.*, 11(6):669–678.

Wong, G. and Barnett, D. (1984). A dislocation method for solvinf 3d crack and inclusion problems in linear elastic solids. In B. A. Bilby, K. J. M. and Willis, J. R., editors, *Fundamentals of Deformation and Fracture*, pages 417–438. Eshelby Memorial Symposium Sheffield, Cambridge University Press.

Wriggers, P. (2002). *Computational Contact Mechanics*. J. Wiley and sons, New York.

Wright, T., Parsons, B., Jackson, J., Haynes, M., Fielding, E., England, P., and Clarke, P. (1999). Source parameters of the 1 october 1995 dinar (turkey) earthquake from sar interferometry and seismic bodywave modelling. *Earth Planet. Sci. Lett.*, 172:23–37.

Wu, H. and Pollard, D. (1995). An experimental study of the relationships between joint spacing and layer thickness. *Journal of Structural Geology*, 16(6):887–905.

Wu, Y.-M., Zhao, L., Chang, C.-H., and Hsu, Y.-J. (2008). Focal mechanism determination in taiwan by genetic algorithm. *Bull. of the Seism. Soc. of America*, 98(2):651–661.

Xu, J. (1992). Iterative methods by space decomposition and subspace correction. *SIAM Rev.*, 34(4):581–613.

Yamada, Y. and McClay, K. (2003). Application of geometric models to invert listric fault systems in sandbox experiments: Paper 1 - 2d hanging wall deformation and section restoration. *Journal of Structural Geology*, 25:1551–1560.

Yamaji, A. (2000). The multiple inverse method: a new technique to separate stresses from heterogeneous fault-slip data. *J. Struct. Geol.*, 22(4):441–452.

Yielding, G., Walsh, J. J., and Watterson, J. (1992). The prediction of small-scale faulting in reservoirs. *First Break*, 10:449–460.

Yoffe, E. (1960). The angular dislocation. *Phil. Mag.*, 5:161–175.

Yu, E. and Segall, P. (1996). Slip in the 1868 hayward earthquake from the analysis of historical triangulation data. *J. Geophys. Res.*, 101:16101–16118.

Yun, S. H., Segall, P., and Zebker, H. (2006). Constraints on magma chamber geometry at sierra negra volcano, galapagos islands, based on insar observations. *Journal of Volcanology and Geothermal Research*, 150:232–243.

Zhang, L., Wu, J. C., Ge, L. L., Ding, X. L., and Chen, Y. L. (2008). Determining fault slip distribution of the chi-chi taiwan earthquake with gps and insar data using triangular dislocation elements. *Journal of Geodynamics*, 45.

Zhang, P., Mao, F., and Slemmons, D. (1999). Rupture terminations and size of segment boundaries from historical earthquake ruptures in the basin and range province. *Tectonophysics*, 308:37–52.

Zhong, Z. (1993). *Finite Element Procedures for Contact-Impact Problems*. Oxford University Press, Oxford.

Zhou, X. (2006). Triaxial compressive behavior of rock with mesoscopic heterogenous behavior: Strain energy density factor approach. *Theoretical and Applied Fracture Mechanics*, 45:46–63.

Zoback, M. (1980). State of stress in the conterminous united states. *J. of Geophys. Research*, 86:6113–6156.

Zoback, M. (1992). First and second order patterns of stress in the lithosphere. the world stress map project. *J. of Geophys. Research*, 97:11703–11728.

Zoback, M., Zoback, M., Mount, V., Eaton, J., Healy, J., Oppenheimer, D., Reasonberg, P., Jones, L., Raleigh, B., Wong, I., Scotti, O., , and Wentworth, C. (1987). New evidence on the state of stress of the san andreas fault system. *Science*, 238:1105–1111.

Zoback, M. D. and Healy, J. (1984). Friction, faulting, and in situ stress. *Annales Geophysicae*, 2:689698.

**This thesis comprises a total of 393 citations.**

**TITRE: Utilisation de la géomécanique pour résoudre des problèmes liés aux structures géologiques: modélisation direct, inversion et restauration**

**RÉSUMÉ:** Différentes applications de l'élasticité linéaire en géologie structurale sont présentées dans cette thèse à travers le développement de trois types de codes numériques. Le premier utilise la modélisation directe pour étudier les déplacements et champs de contraintes autour de zones faillées complexes. On montre que l'ajout de contraintes inégalitaires, telles que la friction de Coulomb, permet d'expliquer l'angle d'initiation des dominos dans les relais extensifs. L'ajout de matériaux hétérogènes et d'optimisations, telles la parallélisation sur processeurs multi-cœurs ainsi que la réduction de complexité des modèles, permettent l'étude de modèles beaucoup plus complexes. Le second type de code numérique utilise la modélisation inverse, aussi appelée estimation de paramètres. L'inversion linéaire de déplacements sur les failles ainsi que la détermination de paléo-contraintes utilisant une approche géomécanique sont développées. Le dernier type de code numérique concerne la restauration de structures complexes plissés et faillées. Il est notamment montré qu'une telle méthode permet de vérifier l'équilibre de coupes géologiques, ainsi que de retrouver la chronologie des failles. Finalement, nous montrons que ce même code permet de lisser des horizons 3D faillés, plissés et bruités en utilisant la géomécanique.

**ABSTRACT:** Different applications of linear elasticity in structural geology are presented in this thesis through the development of three types of numerical computer codes. The first one uses forward modeling to study displacement and perturbed stress fields around complexly faulted regions. We show that incorporating inequality constraints, such as static Coulomb friction, enables one to explain the angle of initiation of jogs in extensional relays. Adding heterogeneous material properties and optimizations, such as parallelization on multicore architectures and complexity reduction, admits more complex models. The second type deals with inverse modeling, also called parameter estimation. Linear slip inversion on faults with complex geometry, as well as paleo-stress inversion using a geomechanical approach, are developed. The last type of numerical computer code is dedicated to restoration of complexly folded and faulted structures. It is shown that this technique enables one to check balanced cross-sections, and also to retrieve fault chronology. Finally, we show that this code allows one to smooth noisy 3D interpreted faulted and folded horizons using geomechanics.

**DISCIPLINE:** Science de la terre: Géophysique

**MOTS-CLÉS:** Géologie structurale, élasticité linéaire, modélisation directe, inversion, restauration

**KEYWORDS:** Structural geology, linear elasticity, forward modeling, inverse modeling, restoration modeling

**INTITULÉ ET ADRESSE DE L'U.F.R OU DU LABORATOIRE:** Laboratoire dynamique de la lithosphère, Université Montpellier II, place Eugène Bataillon, 34095 Montpellier cedex 5, France